

6-18-93
E 7551

NASA Conference Publication 3210

Proceedings of the XII Space Photovoltaic Research and Technology Conference (SPRAT XII)

*Proceedings of a conference held at
Lewis Research Center
Cleveland, Ohio
October 20-22, 1992*

The NASA logo, consisting of the word "NASA" in a bold, sans-serif font, is positioned at the bottom right of the page. A horizontal line runs across the page just above the logo.

NASA Conference Publication 3210

Proceedings of the XII Space Photovoltaic Research and Technology Conference (SPRAT XII)

*NASA Lewis Research Center
Cleveland, Ohio*

Proceedings of a conference held at
Lewis Research Center
Cleveland, Ohio
October 20-22, 1992



National Aeronautics and
Space Administration
Office of Management
Scientific and Technical
Information Program

1993

Page Intentionally Left Blank

FOREWORD

Dennis J. Flood
NASA Lewis Research Center

The Twelfth Space Photovoltaic Research and Technology Conference marks another first in the series. This meeting was the first time we had an international participation, with invited talks from representatives of the Japanese National Space Development Agency, and the United Kingdom's Defence Research Agency. There was in addition, a contributed paper from the UK on the development of high efficiency GaAs and InP cells. The input from our colleagues from outside the U.S. was informative and welcome.

Apart from the new element mentioned above, the meeting can best be summarized by noting that substantial progress was reported in a variety of areas, from GaAs/Ge cells as commercial items to flexible, thin film solar cells in the early stages of pilot production, to a variety of high efficiency, multiple bandgap cells under consideration for making the transition from the laboratory environment to a production environment. Space flight data on a variety of cells are also beginning to accrue, and for the most part satisfy earlier predictions of cell behavior. All of these topics, and many more, are covered in this volume, which still forms one of the most up-to-date compendiums of space solar cell and array literature found anywhere in the U.S. and abroad.

The conference was chaired by Dr. Sheila Bailey, who was ably assisted by David Wilt as logistics chairman and Navid Fatemi as publications chairman. Their careful attention to detail and hard work were very much in evidence, and appreciated by all.

Page Intentionally Left Blank

Contents

Foreword

Dennis J. Flood, Chief, Photovoltaic Branch, NASA Lewis Research Center	iii
---	-----

Session 1 - InP Solar Cells

A Detailed Study of the Photo-Injection Annealing of Thermally Diffused InP Solar Cells R. J. Walters, G. P. Summers, and J. Bruening	1
High Temperature Annealing of Minority Carrier Traps in irradiated MOCVD n^+p InP Solar Cell Junctions S. R. Messenger, R. J. Walters, and G. P. Summers	8
Radiation Effects in Heteroepitaxial InP Solar Cells I. Weinberg, H. B. Curtis, C. K. Swartz, D. J. Brinker, and C. Vargas-Aburto	16
Progress in p^+n InP Solar Cells Fabricated by Thermal Diffusion Mircea Faur, Maria Faur, C. Goradia, M. Goradia, D. J. Flood, D. J. Brinker, I. Weinberg, C. Vargas-Aburto, and N. S. Fatemi	23
Electrochemical Characterization of p^+n and n^+p Diffused InP Structures Maria Faur, Mircea Faur, M. Goradia, C. Vargas-Aburto, and D. M. Wilt	33
Activation Energy and Capture Cross Section for Majority Carrier Traps in Zn doped InP G. Rybicki and W. Williams	43
Effects of Solar Cell Environment on Contact Integrity N. S. Fatemi and V. G. Weizer	54
Measurement of Minority Carrier Diffusion Length and Edge Surface Recombination Velocity in InP R. Hakimzadeh and S. G. Bailey	64
Surface Passivation of InP Solar Cells with InAlAs Layers R. K. Jain, G. A. Landis, and D. J. Flood	78

Session 2 - Amorphous Silicon and Thin Film Solar Cells

Polyimide Based Amorphous Silicon Solar Modules F. R. Jeffrey, D. P. Grimmer, S. A. Martens, K. Abudagga, M. L. Thomas, and M. Noak	88
---	----

Investigation of the Radiation Resistance of Triple-Junction α -Si:H Alloy Solar Cells Irradiated with 1.00 MeV Protons	
K. R. Lord II, M. R. Walters, and J. R. Woodyard	98
Results of Some Initial Space Qualification Testing on Triple Junction α -Si and CuInSe ₂ Thin Film Solar Cells	
R. L. Mueller and B. E. Anspaugh	108
Flexible Polycrystalline Thin-Film Photovoltaics for Space Applications	
J. H. Armstrong, B. R. Lanning, M. S. Misra, V. K. Kapur, and B. M. Basol	118

Session 3 - Laser Power Converters

InGaAs Concentrator Cells for Laser Power Converters and Tandem Cells	
S. J. Wojtczuk, S. M. Vernon, and E. D. Gagnon	119
The Efficiency of Photovoltaic Cells Exposed to Pulsed Laser Light	
R. L. Lowe, G. A. Landis, and P. Jenkins	129
Response of Si Solar Cell to Pulsed Laser illumination	
D. Willowby, D. Alexander, T. Edge, and K. Herren	147
Approaches to Solar Cell Design for Pulsed Laser Beam Receivers	
G. A. Landis, and R. K. Jain	155

Session 4 - Solar Cell and Array Technology

EOL Performance comparison of GaAs/Ge and Si BSF/R Solar Arrays	
T. W. Woike	167
A High Specific Power Solar Array for Low to Mid-Power Spacecraft	
P. A. Jones, S. F. White, T. J. Harvey, and B. S. Smith	177
TAB Interconnects for Space Concentrator Solar Arrays	
J. Avery, J. S. Bauman, P. Gallagher, and J. W. Yerkes	188
Space Station Freedom Advanced Photovoltaic and Battery Technology Development Planning	
S. M. Cox, M. T. Gates, S. A. Verzwylt, and K. D. Bender	196
Recent Developments in Refractive Concentrators for Space Photovoltaic Power Systems	
M. F. Piszczor and M. J. O'Neill	206

New Experimental Techniques for Solar Cells	
R. Lenk	217

Session 5 - Heteroepitaxial Solar Cells

Radiation Effects in $\text{Ga}_{0.47}\text{In}_{0.53}\text{As}$ Solar Cells	
R. J. Walters, G. J. Shaw, G. P. Summers, and S. R. Messenger	226
Investigation of ZnSe-Coated Silicon Substrates for GaAs Solar Cells	
D. A. Huber, L. C. Olsen, G. Dunham, and F. W. Addis	235
Heteroepitaxial InP, and Ultrathin, Directly Glassed, GaAs III-V Solar Cells	
C. M. Hardingham and T. A. Cross	249

Session 6 - Non-Photovoltaic Energy Conversion

Review of Betavoltaic Energy Conversion	
L. C. Olsen	256

Session 7 - Space Environmental Effects on Solar Cells

UV Testing of Solar Cells: Effects of Anti-Reflective Coating, Prior Irradiation, and UV Source	
A. Meulenber	268
The UOSAT-5 Solar Cell Experiment - First Year in Orbit	
C. Goodbody	280
Results of Thermal Vacuum Tests for the PASP+ Flight Modules	
H. Curtis, D. Guidice, P. Severance, and M. Piszczor	289
Computation of Photovoltaic Parameters Under Lunar Temperature Variation	
N. G. Dhere and J. V. Santiago	298

Program Reviews

An Overview of the Defence Research Agency Photovoltaic Programme	
C. Goodbody and M. A. Davies	307
NASDA Activities in Space Solar Power System Research, Development and Applications	
S. Matsuda, Y. Yamamoto, M. Uesugi	318

Workshop Summaries

Summary - Workshop on Heteroepitaxial InP Solar Cells	
I. Weinberg and R. W. Walters	326
Thin Film Solar Cell development	
J. Armstrong and F. Jeffrey	329
Workshop on Solar Electric Propulsion	
D. Marvin and D. Bents	331
Workshop Summary - New Silicon Cells	
A. Meulenber and P. A. Iles	334
Multi-Band Gap and New Solar Cell Options Workshop	
J. Hutchby, M. Timmons, and J. M. Olson	337
Receivers for Laser Power Beaming	
G. A. Landis	340

A DETAILED STUDY OF THE PHOTO-INJECTION ANNEALING OF THERMALLY DIFFUSED InP SOLAR CELLS

R.J. Walters and G.P. Summers
Naval Research Laboratory
Washington, DC 20375

J. Bruening
Naval Postgraduate School
Monterey, CA 93943

ABSTRACT

A detailed analysis of the annealing of thermally diffused InP solar cells fabricated by the Nippon Mining Co. is presented. The cells were irradiated with 1 MeV electrons, and the induced degradation is measured using deep level transient spectroscopy and low temperature (86 K) IV measurements. Clear recovery of the photovoltaic parameters is observed during low temperature ($T < 300$ K) solar illuminations (1 sun, AM0) with further recovery at higher temperatures ($300 < T < 500$ K). For example, the output of a cell which was irradiated up to a fluence of $1 \times 10^{16} \text{ cm}^{-2}$ was observed to recover to within 5% of the pre-irradiation output. An apparent correlation between the recovery of I_{sc} and the annealing of the H4 defect and of the minority carrier trapping centers is observed. An apparent correlation between the recovery of V_{oc} and the annealing of the H5 defect is also observed. These apparent correlations are used to develop a possible model for the mechanism of the recovery of the solar cells.

INTRODUCTION

It is well known that single crystal InP solar cells not only display record high beginning of life efficiencies but also display a resistance to irradiation which is superior to that of Si and GaAs cells (ref.1-3). Furthermore, it has been shown by Yamaguchi et al. that InP solar cells grown by thermal diffusion rapidly recover the radiation-induced degradation under solar illumination (ref 3). However, it has also been shown that InP cells grown by MOCVD, while exhibiting a marked decrease in the radiation-induced defect concentration due to photo-illumination, display no corresponding recovery of the solar cell output (ref 1). Although much detailed information has been obtained about the behavior of MOCVD InP solar cells, the published data on diffused junction cells is not complete enough to understand the observed different behavior. This paper presents new results on the recovery of irradiated, diffused junction InP cells which enable further conclusions to be drawn.

A major difficulty is that to determine the radiation-induced solar cell degradation, one must illuminate the cell with simulated solar light which is capable of annealing the thermally diffused cells. To avoid this annealing, the samples here were held at 86 K during the IV measurements. DLTS measurements before and after an IV measurement showed that the solar illumination at 86 K does not anneal the cell. Furthermore, repeated IV measurements at 86 K showed no recovery in the solar cell output. Effectively, any photo-injection annealing of the cells has, therefore, been "frozen out" at 86 K.

A related problem exists in the measurement of the minority carrier trapping centers by the DLTS technique. For DLTS to detect minority traps, minority charge carriers must be injected into the depletion region.

This is commonly done by applying a forward bias fill pulse to the sample during the measurement. However, since this establishes a current through the junction, it causes injection annealing of the defect spectrum (ref 1). In the present experiments, this effect is avoided by creating electron-hole pairs in the depletion region by pulsed laser excitation. The junction field quickly separates the charges, leaving the minority carriers available for capture at a defect level. In this way, the minority trapping centers can be detected without annealing the sample.

The present study determines the changes in the radiation-induced defect spectrum associated with the annealing stages of the irradiated solar cell IV curves. This is accomplished by measuring the DLTS spectrum of the actual solar cells after each annealing step. The results provide insight into the response of InP solar cells to a harsh space radiation environment which was previously unavailable. It is detailed investigations like this which will allow a full exploitation of the unique qualities of InP solar cells.

EXPERIMENTAL NOTES

The samples studied in this research are InP solar cells grown by the Nippon Mining Co (ref 4). They are the NS12B type. The initial cell dimensions were 1cm x 2cm x 400 μ m. The cells have a SiO₂/ZnS antireflective coating. The shadow loss is stated by the manufacturer to be approximately 5%. The cell specifications indicated efficiencies of 16.2 % (AM0, 25° C), short circuit currents (I_{sc}) of 64.3 mA, and open circuit voltages (V_{oc}) of 0.823 V. The cells are n⁺p junctions, so a positive DLTS signal (which indicates a majority carrier trap) signifies the capture of holes. A negative signal (which indicates a minority carrier trap) signifies the capture of electrons.

In order to mount these cells into the DLTS cryostat used in the present research, it was necessary to reduce the size of the cells. This was done by sawing the cells into 0.4 x 1 cm pieces. This had little effect on the short circuit current density and the open circuit voltage. Unfortunately, the sawing introduced a series resistance into the cells which reduced the fill factor and the efficiency of the samples. This is most likely due to dislodging the metalization grid of the cells. Therefore, the present study concentrates on changes in I_{sc} and V_{oc} and avoids any discussion of the efficiency.

The IV measurements were made under 1 sun, AM0 conditions at 86 K. The simulator used was an Oriel, 1000 W Xe arc lamp, portable solar simulator. The DLTS equipment used was a Bio-rad DL4600 Deep Level Transient Spectrometer. All the DLTS measurements were made with a -2 V reverse bias. The 1 MeV electron irradiations were performed at the National Institute of Standards and Technology (NIST). A Faraday cup was used for dosimetry. The fluences were determined to an accuracy of about 15%.

EXPERIMENTAL RESULTS

Prior to irradiation, one minority carrier trapping center was detected in the InP solar cells (dashed line in figure 1), and no majority carrier trapping centers were evident. The activation energy of minority trap was found to be about 0.32 ± 0.01 eV below the conduction band. This energy is close to that of the defect labeled ED, measured in electron irradiated MOCVD InP (ref 1), so a tentative identification with that defect is made here.

The defect spectrum induced by 1 MeV electron irradiation is indicated by solid lines in figure 1. The electron fluence was 6×10^{15} cm⁻². Except for the relatively weak EE and EF signals, this spectrum is virtually identical to that measured on irradiated MOCVD InP (ref. 1), so the defects are labeled accordingly. This data shows a clear resemblance between the minority trap measured before irradiation and the ED defect. Note that the signal of H5 and of all the minority traps is multiplied by 10 to make them more visible. Also, since the negative DLTS signal is most clear after the positive signal has been removed, the minority trap spectrum shown was measured on a cell which had been annealed at 500 K for 1 hour under 1 sun, AM0 illumination. The EC, EA, and ED centers were evident directly after irradiation and before annealing of the cells. However, the EE and EF centers were not detected until the H4 and H5 centers had been substantially annealed.

Since the EE and EF signals are weak and located directly below the H4 and H5 peaks in the spectrum, their detection is difficult. A full investigation of their properties will be reported later. The H3 defect level is not discussed in detail for similar reasons. Because the H3 defect is so close to H4 in the spectrum, it is difficult to monitor.

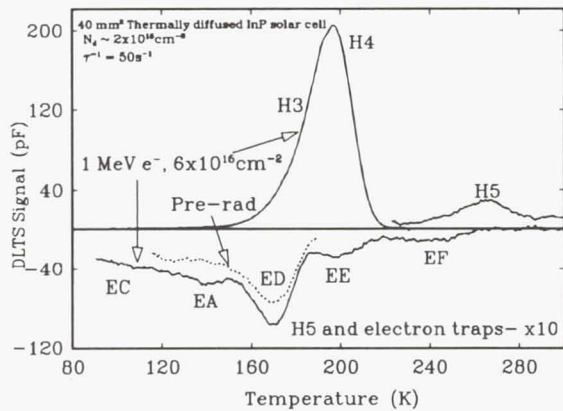


Figure 1: Radiation-induced defects in thermally diffused InP solar cells. The defects are labeled according to ref. 1. The H5 and the minority carrier trap signal is multiplied by a factor of 10.

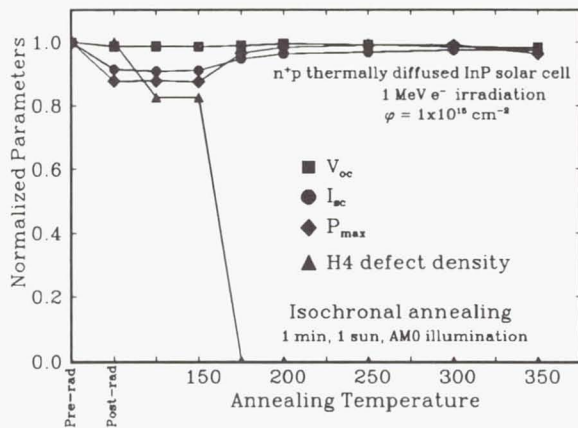


Figure 2: The annealing induced in a thermally diffused InP solar cell by solar illumination. The PV parameters are normalized to their pre-rad values and the H4 defect density to its maximum value.

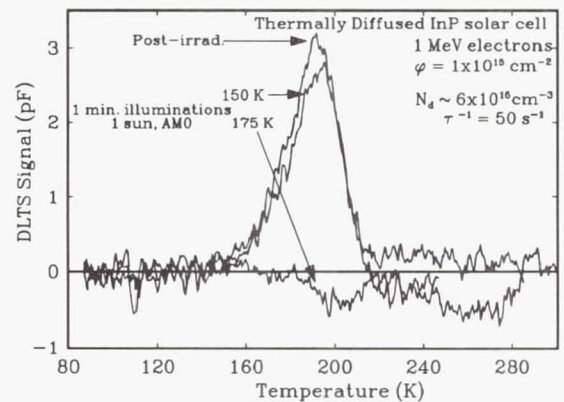


Figure 3: The photo-injection annealing of the H4 defect in the solar cell of figure 2.

Both majority and minority trap spectra were measured along with the IV curves (at 86 K). The results are shown in figures 4 and 5. The irradiation degraded V_{oc} from 1.198 V to 1.151 V. The photo-injection had no effect on V_{oc} . The irradiation degraded I_{sc} by about 8%, but an hour of illumination induced almost full recovery. An hour of illumination is seen to almost completely remove the H4 defect as well. However, the concentration of the H5 defect does not change during the experiment. The concentration of the ED defect seems to increase, but since the minority trap spectrum in figure 5 is multiplied by 5 to make it visible beneath the H4 signal, any apparent changes in the ED peak height are quite small relative to the H4 signal. H5 is not scaled in this figure.

A second isothermal annealing experiment was done on a cell which had been irradiated up to a fluence of

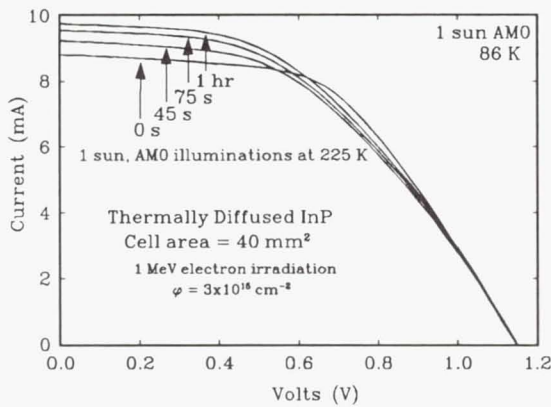


Figure 4: The isothermal, photo-injection annealing of the IV curves of an irradiated InP solar cell. The illuminations cause an increase in I_{sc} but not V_{oc} .

$1 \times 10^{16} \text{ cm}^{-2}$. The illuminations were done at 275 K for cumulative times up to 4.25 hours. The results are shown in figure 6. The open symbols on the left hand vertical axis of figure 6 are the pre-rad values for the PV parameters. The open symbols on the right hand axis are the values of the PV parameters after 4.25 hours of illumination. This is a revealing set of data because the high fluence has caused a significant degradation in all of the PV parameters, so the recovery under illumination is quite clear. Each parameter shows steady recovery for the first 25 minutes of illumination. After 25 minutes, the recovery continues but at a much slower rate. It seems that there is an asymptotic limit to the recovery.

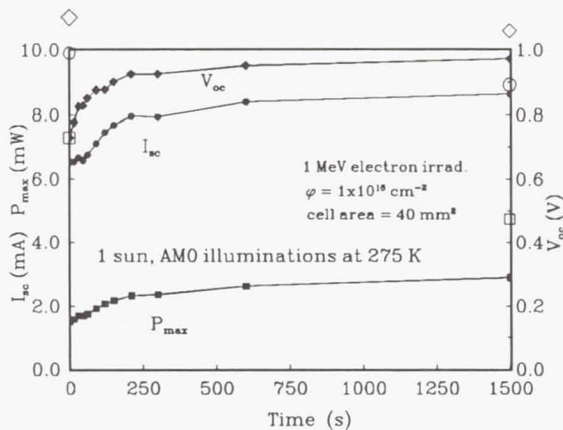


Figure 6: The annealing of a heavily irradiated InP solar cell. The open symbols on the right vertical axis are the BOL values while on the left axis are the values after 4.25 hours of annealing.

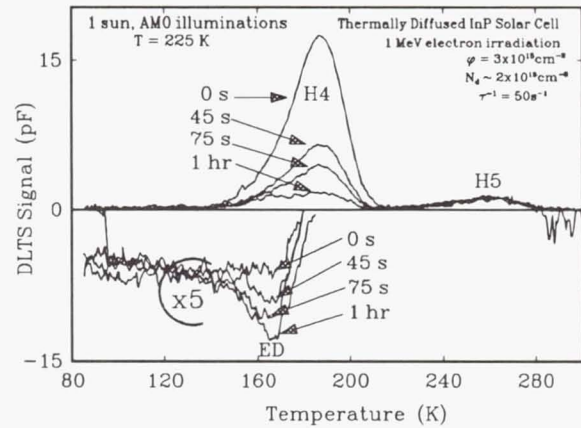


Figure 5: The photo-injection annealing of the DLTS spectra of the cell of figure 4. The electron trap signal is multiplied by 5. The H4 defect concentration decreases but H5 is unchanged.

To investigate this asymptotic limit, after the 4.25 hours of illumination at 275 K, the cell was illuminated at progressively higher temperatures. Illumination for 30 minutes at 300 K and one hour at 373 K induced further recovery in V_{oc} but none in I_{sc} . Illumination for 1 hour at 450 K caused a large increase in the entire IV curve (figure 7). This increase was accompanied by the complete removal of all the majority traps and a reduction in the concentration of the minority traps (figure 8). This is interesting because, as shown in the following paper in this conference by S.R. Messenger et al., annealing treatments in the dark on electron irradiated MOCVD InP at temperatures in excess of 600 K does not remove all of the majority carrier signal. Illumination at 500 K for one hour is seen to further reduce the minority trap concentration and to cause more recovery in I_{sc} . V_{oc} was unaffected by the 500 K illumination. During a second 500 K annealing attempt, the cell failed.

Figure 9 shows the overall history of this cell. The results are dramatic. The thick line is the IV curve measured before irradiation. The irradiation up to $1 \times 10^{16} \text{ 1 MeV electrons cm}^{-2}$ is seen to almost destroy the cell. However,

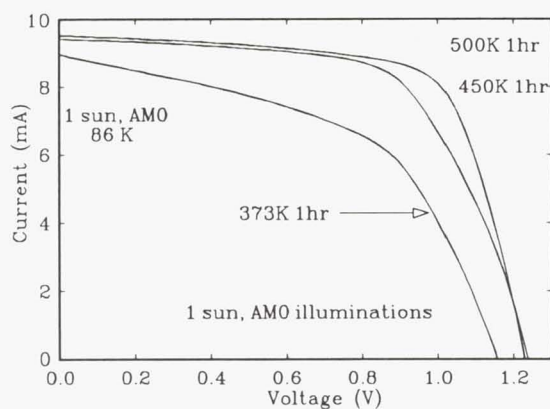


Figure 7: The high temperature photo-injection annealing of an InP cell. The illumination at 450 K caused recovery in all of the PV parameters while annealing at 500 K only increased I_{sc} .

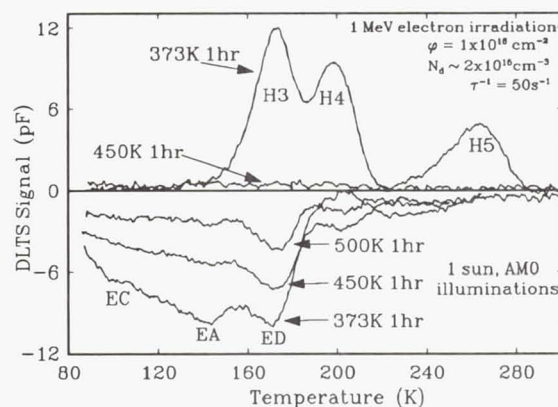


Figure 8: The annealing of the DLTS spectrum of the cell in figure 7. Illumination at 450 K removed all of the majority carrier traps. The 500 K illumination further reduced the minority carrier trap density.

the illuminations at increasingly higher temperatures cause significant recovery in the IV curves until after 1 hour at 450 K, the cell has achieved almost full recovery.

DISCUSSION

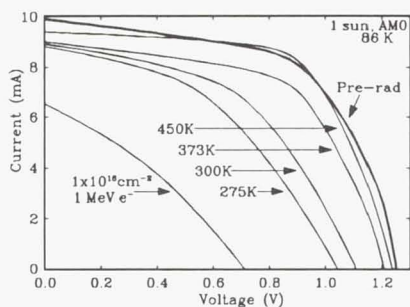


Figure 9: The full history of the annealing of the cell in figures 6-8. Even though the irradiation almost completely destroyed the cell, the illuminations caused almost full recovery.

minority carrier trapping centers, which this study has shown to affect the solar cell performance, have yet to be seriously investigated.

The results of the present annealing study clearly show that irradiated thermally diffused InP solar cells recover significantly when a current exists in the junction. The annealing occurs through a thermally activated process in which electron-hole pair recombination induces defect annealing which in turn induces recovery in the PV parameters. Furthermore, figures 1 and 2 seem to support the conclusion of Yamaguchi et al. that the H4 defect is the controlling factor (ref 3,6). However, the present study shows that this cannot be the entire story.

Considering equations 1 and 2, a recovery in I_{sc} indicates an increase in minority carrier lifetime (τ_n) (assuming the depletion layer width does not change significantly). Since I_{sc} is recovering in figure 4, the implication is that the defect annealing brought on by the solar illumination causes recovery in the τ_n . Considering equation 3, V_{oc} is controlled by the junction dark current. InP has a band-gap of 1.34 eV, so the dark current is expected to be dominated by recombination. Therefore, since V_{oc} is observed not to recover, the suggestion is that the recombination current in the junction is not significantly changing. The strong correlation between the decrease in the H4 defect concentration (fig. 5) and the recovery of I_{sc} (fig. 4) suggests that the H4 defect acts to degrade τ_n . However, since the recombination current does not seem to be changing, H4 must not be acting as an efficient recombination center. Instead, it might be concluded that it is the H5 defect which increases the dark current and thus decreases V_{oc} . It is not unreasonable for H5 to be an efficient recombination center since it has an activation energy of 0.54 eV which is not far from mid-gap. Furthermore, McKeever et al. have shown that the H5 defect has a larger capture cross-section for minority than for majority charge carriers (ref 7). This is also supported by the data of figures 7 and 8 where V_{oc} is seen to almost completely recover at the same time that the H5 defect signal is removed.

$$L_n = \sqrt{D_n \times \tau_n}$$

$$L_n \equiv \text{minority carrier diffusion length} \quad (1)$$

$$D_n \equiv \text{minority carrier diffusion coefficient}$$

$$\tau_n \equiv \text{minority carrier lifetime}$$

$$I_{sc} \sim (W + L_n)$$

$$W \equiv \text{depletion layer width} \quad (2)$$

$$V_{oc} = \frac{kT}{q} \ln\left(\frac{I_{sc}}{I_o}\right)$$

$$k \equiv \text{boltzmann's constant} \quad (3)$$

$$q \equiv \text{the electronic charge}$$

$$I_o \equiv \text{junction dark current}$$

The data of figures 7 and 8 also support the correlation between the H4 defect and I_{sc} . When the H4 defect was completely removed, I_{sc} showed a large recovery. However, as seen in figure 9, the recovery is not complete. This may be due to the effect of the remaining minority carrier defect centers. The 1 hour anneal at 500 K caused the concentration of the minority carrier defects to decrease while I_{sc} increased but V_{oc} remained the same. This suggests that the electron traps are also acting to decrease τ_n . Since H4 has such a large introduction rate, it initially controls the solar cell output, but after H4 has significantly annealed, the effect of the minority traps becomes dominant. Furthermore, since the minority traps are the residual traps seen in the spectrum, they are expected to control the asymptotic limit on the recovery of the PV parameters. It is important to note that it is not known if longer illuminations at 500 K would induce further recovery. Thus, the ultimate limit on the cell recovery is yet to be determined.

Clearly, the radiation-induced degradation of thermally diffused InP solar cells anneals under solar illumination, and there are obvious trends in the DLTS spectra which link several of the defect levels to the particular annealing stages. Also, the measured defect spectrum shown in figure 1 is basically identical to that measured in MOCVD InP. However, irradiated MOCVD InP solar cells do not show this dramatic recovery under solar illumination (ref 1). This is quite puzzling and at present, no adequate explanation has presented itself.

CONCLUSIONS

The results of this research have clearly shown the radiation-induced degradation of thermally diffused InP solar cells to anneal under solar illumination. Therefore, under normal operating conditions, the InP cells would be expected to show virtually no degradation in a typical space radiation environment. Furthermore, apparent correlations between the recovery in the PV parameters and changes in the DLTS spectra have given significant insight into the mechanism by which these cells recover. The suggestion is that the H4 defect center acts to reduce τ_n which degrades I_{sc} . The minority carrier trapping centers were seen to also affect I_{sc} , presumably by also decreasing τ_n , and since the H4 defect anneals more rapidly than the electron traps, it is the electron traps which will set an upper limit on the cell recovery. The data also suggests that H4 does not act as a recombination center, but instead it may be the H5 defect which increases the dark current. This implies that it is the H5 defect, acting as an efficient recombination center, which causes a degradation of V_{oc} . It must be noted that since no direct measurements of the junction current (i.e. the dark IV curves) have yet been made, these conclusions are tentative. Nevertheless, these cells display an annealing property which makes them virtually insensitive to irradiation while in operation. With this property, InP technology is dramatically superior to Si and GaAs in a radiation environment. By exploiting the radiation resistance of InP solar cells, it will be possible to fly missions in severe radiation orbits which were previously inaccessible.

REFERENCES

1. R.J. Walters, S.R. Messenger, G.P. Summers, E.A. Burke, and C.J. Keavney, "Proton and Electron Irradiation of MOCVD InP Solar Cells: Experimental Results and Modeling", Proc. of the 22nd IEEE Photovoltaic Spec. Conf., Las Vegas, NV, October 1991, p.1560.
2. I. Weinberg, C. K. Swartz, R. E. Hart, and R. L. Statler, "Radiation and Temperature Effects in Gallium Arsenide, Indium Phosphide, and Silicon Solar Cells," Proc. 19th IEEE Photovoltaic Spec. Conf., New Orleans, May 1986, p. 548.
3. M. Yamaguchi, K. Ando, "Mechanism for radiation resistance of InP solar cells", J. Appl. Phys. 63, 5555 (1988).
4. A. Yamamoto, M. Yamaguchi, C. Uemura, "High Efficiency Homojunction InP Solar Cells", Appl. Phys. Lett. 46, 1 Nov, 975 (1985).
5. R.J. Walters and G.P. Summers, "Deep Level Transient Spectroscopy Study of Proton Irradiated p-type InP", J. of Appl. Phys. 69 (9), 1 May 1991.
6. M. Yamaguchi, K. Ando, A. Yamamoto, and C. Uemura, "Injection-Enhanced Annealing of InP Solar Cell Radiation Damage", J. Appl. Phys. 58, 1 July, 568 (1985)
7. S.W.S McKeever, R.J Walters, S.R. Messenger, and G.P. Summers, "Deep Level Transient Spectroscopy of Irradiated p-type InP Grown by Metalorganic Chemical Vapor Deposition", J. Appl. Phys. 69 (3), 1 February 1991.

HIGH TEMPERATURE ANNEALING OF MINORITY CARRIER TRAPS IN IRRADIATED MOCVD n^+p InP SOLAR CELL JUNCTIONS

S.R. Messenger¹, R.J. Walters², and G.P. Summers^{2,3}

¹ SFA Inc., Landover, MD 20785

² Naval Research Lab, Washington, DC 20375

³ Department of Physics, University of Maryland
Baltimore County, Baltimore, MD 21228

Deep level transient spectroscopy has been used to monitor thermal annealing of trapping centers in electron irradiated n^+p InP junctions grown by metalorganic chemical vapor deposition, at temperatures ranging from 500 up to 650K. Special emphasis is given to the behavior of the minority carrier (electron) traps EA (0.24 eV), EC (0.12 eV), and ED (0.31 eV) which have received considerably less attention than the majority carrier (hole) traps H3, H4, and H5, although this work does extend the annealing behavior of the hole traps to higher temperatures than previously reported. It is found that H5 begins to anneal above 500K and is completely removed by 630K. The electron traps begin to anneal above 540K and are reduced to about half intensity by 630K. Although they each have slightly different annealing temperatures, EA, EC, and ED are all removed by 650K. A new hole trap called H3' (0.33 eV) grows as the other traps anneal and is the only trap remaining at 650K. This annealing behavior is much different than that reported for diffused junctions.

INTRODUCTION

Interest in the use of InP as a possible space photovoltaic material was stimulated in the early 1980's when Yamaguchi and co-workers discovered the superior radiation resistance of InP solar cells (refs. 1-3). These cells were made by diffusing S into Zn-doped p-type substrates and had beginning-of-life (BOL) conversion efficiencies near 16% at AM1.5. Both current-voltage (I-V) and deep level transient spectroscopy (DLTS) results were used to show that the presence and annealing of the radiation-induced defects were correlated with solar cell degradation and recovery. In particular, the behavior of the majority carrier DLTS trap H4 appeared to be the cause of both the degradation and recovery (upon annealing) of the solar cell parameters.

Recent research efforts by the present authors using Zn-doped p-InP junctions grown by Spire Corporation using metalorganic chemical vapor deposition (MOCVD) have shown results different from those of Yamaguchi et al. (refs. 4-8). Although the same basic defect structure exists after irradiation, the presence of the radiation-induced defect H4 is seen to correlate only minimally with solar cell recovery following either thermal or injection treatments. It has been suggested recently, however, that it is

the presence of another radiation-induced hole trap, H5, which contributes to solar cell recovery in MOCVD material (ref. 9). H5 can be seen following irradiation of more heavily doped cells ($\sim 10^{17}$ cm⁻³) and grows upon the annealing of H4 in lower doped cells ($\sim 10^{16}$ cm⁻³). It is possible that other related defects would also contribute to solar cell recovery. It will be shown below that several electron (minority carrier) traps called EA, EC, and ED seem to be related to H5 and therefore might also be important to solar cell behavior.

Many recently published results have considered the introduction and annealing of the majority carrier defects induced by irradiation in p-InP. The effects of minority carrier defects have been largely ignored, until now. This was the motivation for this work because, if minority carrier defects are present, they might be expected to dominate minority carrier diffusion in actual solar cell operation. In p-InP grown by MOCVD, minority carrier defects are formed both following irradiation and annealing and therefore need to be considered in any complete model for the radiation response of InP solar cells (refs. 4,5,7).

McKeever et al. (ref. 4) have shown an interesting correlation between the majority carrier trap H5 and the minority carrier trap EA. DLTS results were presented showing that, as the forward bias across the junction was gradually increased, the intensity of the H5 peak decreased with a corresponding increase in EA. At a forward bias high enough to completely turn the diode on (~ 0.7 V), H5 could not be observed and EA had reached a maximum intensity. This process was completely reversible suggesting that: 1) similar defects are involved, and 2) H5 is an efficient recombination center. It was inferred that, if minority carrier electrons were present, they became trapped at the defect site which then acted as an efficient recombination center for majority carrier holes. Hole emission could not then be observed although electron emission was still possible due to the high concentration present under the forward bias conditions. This observation was important because it suggests that electron traps were also expected to contribute to solar cell degradation and recovery, along with H5.

This paper will present high temperature isochronal thermal annealing results over the range from 500 up to 650K, which is sufficient to completely anneal H5, EA, EC, and ED, leaving behind a new residual defect called H3'.

EXPERIMENT

The devices used in this study were MOCVD n⁺p mesa diodes fabricated adjacent to solar cells of the same construction. These solar cells, which were produced by Spire Corporation, have recently yielded efficiencies of greater than 19% at AM0 (ref. 4). The reader can refer to reference 4 for a more complete description of the samples.

DLTS measurements were taken using a Bio-Rad model DL4600 instrument with both liquid nitrogen and helium cryostatic capabilities, enabling measurements to be made over the temperature

range 20-500K. Unless otherwise stated, majority carrier measurements were taken using reverse and forward biases of -2 and 0V, respectively, while those for minority carriers were taken using -2 and 1V, respectively. Pulse widths of 50mS were sufficient to ensure a complete filling of the defects.

Thermal annealing up to 500K was performed in situ in the liquid nitrogen cryostat. Above 500K a Lindberg tube furnace was used, in which the samples were annealed in air at atmospheric pressure. The samples were placed in a ceramic tube (alumina) and isochronally heated for 10 minutes while wrapped in aluminum foil. The sample reached the annealing temperature and cooled back to room temperature in times that were negligible compared with the 10 minute anneals. Temperature calibrations were determined using both thermocouple and thermometer measurements. DLTS measurements were performed immediately following each anneal. Capacitance-voltage (C-V) data were also obtained following each successive annealing step in order to monitor the carrier concentration.

1 MeV electron irradiations were performed using a van de Graaff accelerator at NASA Goddard Space Flight Center. The electron fluxes were low enough ($\sim 10^{12}$ cm⁻²s⁻¹) to ensure that no sample heating occurred during irradiations. 10 MeV proton irradiations were performed at the Brookhaven National Labs on Long Island, NY. Dosimetry was accomplished using both Faraday cups and radiachromic films.

RESULTS

Injection Behavior

Particle irradiation of p-InP produces several defects which can be detected using DLTS. Figure 1 shows the typical majority carrier trap DLTS spectrum induced following 1 MeV electron irradiation to a fluence of 10^{16} e⁻/cm², and then successive thermal annealing treatments up to 500K. Shown are the majority carrier traps H3 and H4, and H5, which have been shown to be associated with displacements in the P- and the In-sublattices, respectively (ref 10). There is little known about actual defect structures in InP. (Although DLTS is a sensitive technique for studying the behavior of deep traps in semiconductor junctions, it does not give information on the actual nature of the defects. This kind of information can only be obtained using such techniques as electron spin resonance and positron annihilation.) The sample used to obtain the data shown in Figure 1 had a pre-irradiation base carrier concentration of $\sim 10^{17}$ cm⁻³, which causes the peak of majority carrier trap H4 to occur at a temperature below that of majority carrier trap H3 due to junction electric field effects, as reported in reference 8. It can be seen in Fig. 1 that an annealing temperature of 375K substantially reduces the concentration of H4, while only slightly increasing that of H5. This is typical behavior for a junction having a base carrier concentration near 10^{17} cm⁻³. H3 appears to remain at the same intensity until the sample is heated to 500K, at which it then

starts to grow. The activation energy also increases, so the resulting defect appears to be different from H3 and is therefore labelled H3'. The evidence to date indicates that H4, H3, and H3' are closely related defects associated in some way with P vacancies. Figure 2 shows both the majority and minority carrier DLTS spectra obtained following thermal annealing at 500K for 20 minutes. The main traps remaining at this temperature are the minority carrier traps EC, EA, and ED, and majority carrier traps H5. H3, H3', and H2 are also present, although in much smaller concentrations.

Figure 3 shows more detailed information on the injection correlation of H5 with the electron traps than given by McKeever et al. Starting with the spectrum shown in Fig. 2, the forward bias was gradually increased and the DLTS spectrum was measured at several injection levels. The same general correlation is observed as reported by McKeever et al., except that the behavior of three different traps can be closely seen. The reason that McKeever et al. saw only EA is that their samples had been only injection annealed and the residual concentrations of H3 and H4 were large enough to interfere with the DLTS measurements, making EC and ED undetectable. Only when the concentrations of H3 and H4 are sufficiently reduced by thermal annealing, can all three electron traps be seen clearly.

Thermal Annealing

The correlation between H5 and EA, EC, and ED can be further investigated through thermal annealing above 500K. Figure 4 shows high temperature isochronal annealing results from 500 to 650K. The DLTS results show some correlation between the annealing of H5 and EA, EC, and ED, although a one-to-one correspondence is not observed. Not shown in Figure 4 is a DLTS spectrum taken following an annealing temperature of 540K where, although H5 is already annealed to two-thirds of its initial concentration, the electron traps have not yet started to anneal. The electron traps only start to anneal after an annealing temperature of 586K, where H5 is at half the initial intensity. Following the isochronal anneal at 627K, H5 is completely eliminated while EA, EC, and ED are reduced to half intensity. The electron traps are not completely annealed until the temperature is raised to 650K. It should also be noted that majority carrier trap H3' grows during this entire process and becomes the residual defect, not saturating until 650K, when all the other traps have been removed.

DISCUSSION AND CONCLUSIONS

The results presented here have extended the range over which annealing data have been reported for irradiated InP junctions to 650K, at which all the defects except H3' are annealed. The presence of H3' as a residual defect in solar cells made in a way similar to these diodes would probably prevent complete recovery of cell efficiency. It should be noted that an almost complete recovery is observed in diffused junction solar cells where H3' is

not formed (see previous paper). Similarly, the inability to anneal H5 in Spire samples at temperatures below 500K has led to Drevinsky's suggestion (ref. 9) that the presence of H5 prevents significant recovery of cells made in this way until the annealing is performed at the high temperatures shown in Figure 4. Drevinsky's results show that there is still substantial radiation-induced carrier removal in the cells even following annealing at 500K. As discussed previously, the defects causing the DLTS peaks H5 and EA, EC, and ED have not yet been identified, although H5 is thought to be associated with displacements in the In sublattice. The high temperature at which these centers anneal suggest, however, that they are not point defects, which are known to anneal in InP at much lower temperatures. Possible candidate defects include complexes of In vacancies or interstitials with impurities.

The different annealing temperatures observed for EA, EC, and ED, and H5, indicate that the correlation between these defects suggested by Figure 3 may be only partial. The disappearance of H5 under injection certainly indicates, however, that it is an efficient recombination center, which supports Drevinsky's conclusion that the presence of H5 reduces solar cell efficiency. It should be noted that H4 is also an efficient recombination center, but the capture of minority carriers leads to rapid injection annealing of H4 in all InP samples even at temperatures far below room temperature. The low temperature at which H4 anneals thermally and the ease with which it is removed by injection shows that H4 is a simple point defect, a conclusion supported by its high introduction rate under 1 MeV electron irradiation.

The different defect annealing behavior observed in the Spire n⁺p InP junctions fabricated by MOCVD and the NTT junctions made by diffusion is still unexplained. The different behavior leads to much more efficient recovery at much lower temperatures and injection levels in the photovoltaic parameters of solar cells made by diffusion than by MOCVD. The only obvious difference in the two structures is in the n-type dopant used in the emitter, which is Si in the Spire cells and S in the NTT cells. However, only a fraction of the photocurrent is generated in the emitter region in InP cells under AM0 solar illumination, so it is not immediately apparent why the emitter dopant should have such a profound effect on cell behavior.

It would be interesting to compare the results presented here with the recovery of irradiated Spire solar cells over the same temperature range. It is hoped that this data will be available in the near future.

REFERENCES

1. M. Yamaguchi, C. Uemura, A. Yamamoto, and A. Shibukawa, "Electron Irradiation Damage in Radiation-Resistant InP Solar Cells", Jpn. J. Appl. Phys. **23**, 30 (1984).
2. K. Ando, M. Yamaguchi, Y. Ito, and C. Uemura, "Radiation Defect Properties in Solar Cell Material InP", in Technical Digest of the 1st International Photovoltaic Science and Engineering Conference, Kobe, Japan (1984), p. 479.
3. M. Yamaguchi and K. Ando, "Mechanism for radiation resistance of InP solar cells", J. Appl. Phys. **63**, 5555 (1988).
4. S.W.S. McKeever, R.J. Walters, S.R. Messenger, and G.P. Summers, "Deep Level Transient Spectroscopy of Irradiated p-type InP Grown by Metalorganic Chemical Vapor Deposition", J. Appl. Phys. **69**, 1435 (1991).
5. R.J. Walters and G.P. Summers, "Deep Level Transient Spectroscopy Study of Proton Irradiated p-type InP", J. Appl. Phys. **69**, 6488 (1991).
6. R.J. Walters, S.R. Messenger, and G.P. Summers, "DLTS Study of Proton and Electron Irradiated n⁺p InP MOCVD Mesa Diodes", Proceedings of the 3rd International Conference on InP and Related Materials, Cardiff, Wales (1991), p. 159.
7. R.J. Walters, S.R. Messenger, G.P. Summers, E.A. Burke, and C.J. Keavney, "Proton and Electron Irradiation of MOCVD InP Solar Cells: Experimental Results and Radiation Modelling", Proceedings of the 22nd IEEE Photovoltaic Specialists Conference, Las Vegas, NE (1991), p. 1560.
8. S.R. Messenger, R.J. Walters, and G.P. Summers, "Effect of Carrier Concentration on the Properties of Irradiation-Induced Defects in p-type InP Grown by Metalorganic Chemical Vapor Deposition", J. Appl. Phys. **71**, 4201 (1992).
9. P.J. Drevinsky, C.E. Caefer, and C.J. Keavney, "Processing- and Radiation-Produced Defects in InP Solar Cells", Proceedings of the 3rd International Conference on InP and Related Materials, Cardiff, Wales (1991), p. 56.
10. B. Massarani and J.C. Bourgoin, "Threshold for Atomic Displacement In InP", Phys. Rev. **B34**, 2470 (1986).

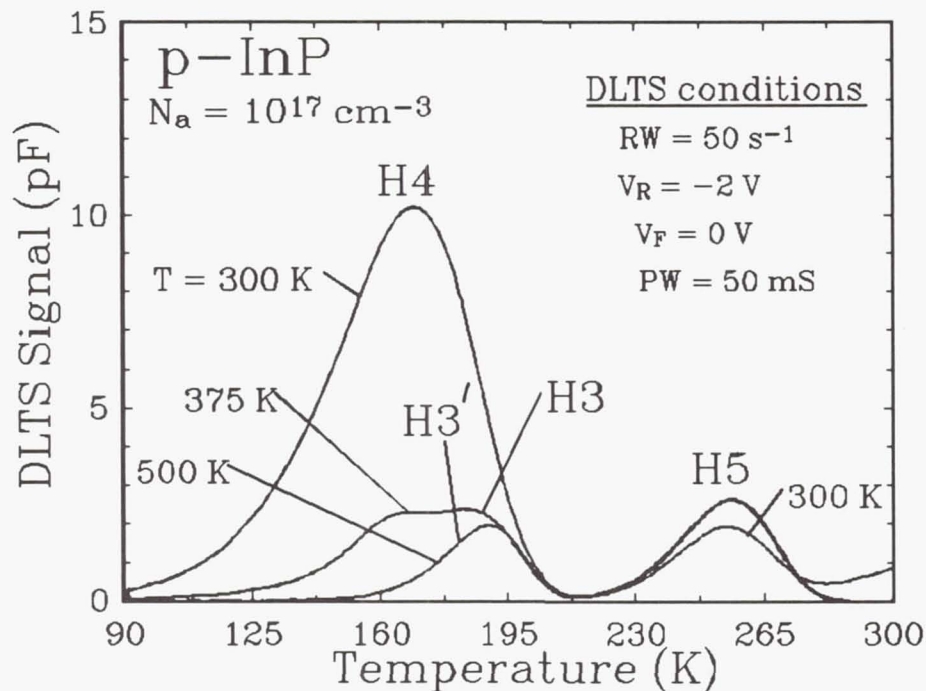


Figure 1 Typical DLTS spectrum of p-InP following 1 MeV electron irradiation and subsequent isochronal thermal annealing steps.

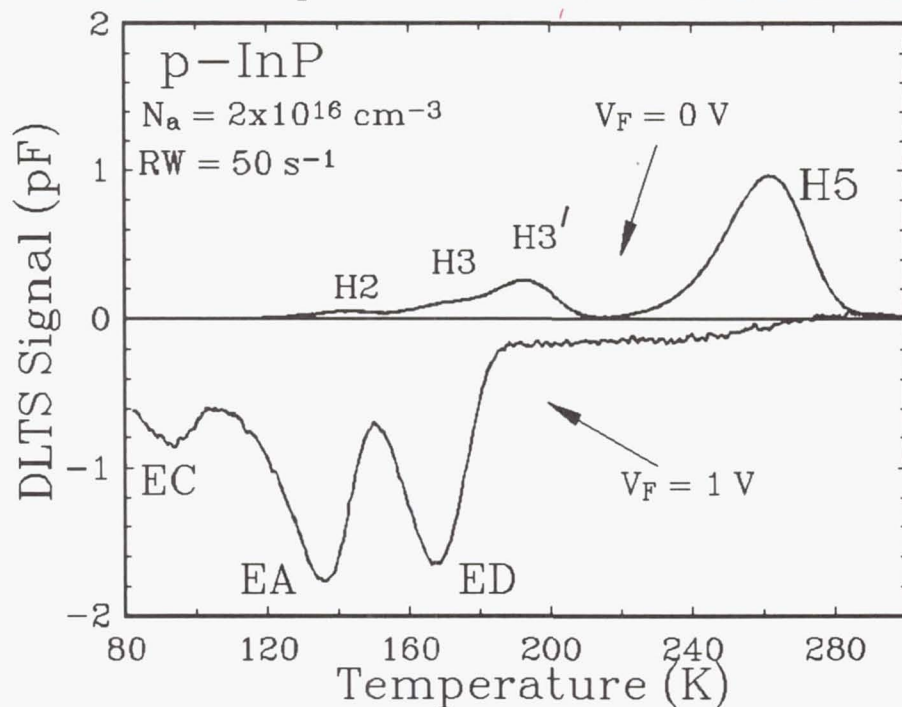


Figure 2 DLTS spectrum showing remaining traps, both majority carrier (hole) and minority carrier (electron), after a thermal anneal at 500K for 20 minutes.

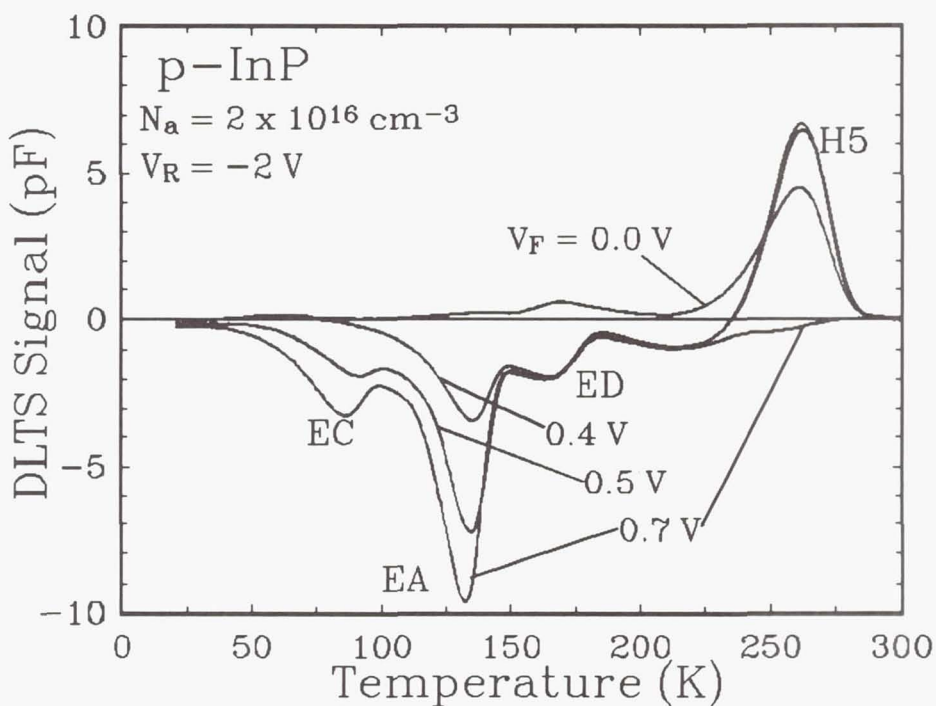


Figure 3 Effect of gradually increasing the forward bias across the junction causing the electron traps to get filled at the expense of H5.

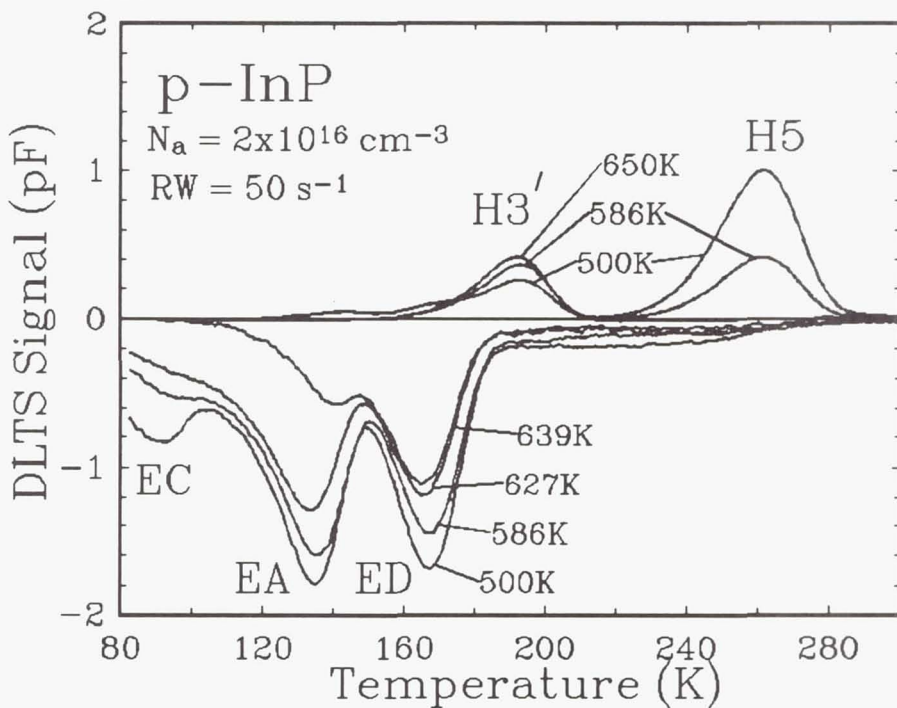


Figure 4 High temperature annealing (>500K) DLTS data showing the eventual anneal of all defects, except for H3', by 650K.

RADIATION EFFECTS IN HETEROEPITAXIAL InP SOLAR CELLS

I.Weinberg, H.B.Curtis, C.K.Swartz and D.J.Brinker

NASA Lewis Research Center
Cleveland, Ohio

And

C.Vargas-Aburto

Kent State University
Kent, Ohio

ABSTRACT

Heteroepitaxial InP solar cells, with GaAs substrates, were irradiated by 0.5 and 3 MeV protons and their performance, temperature dependency and carrier removal rates determined as a function of fluence. The radiation resistance of the present cells was significantly greater than that of non-heteroepitaxial InP cells at both proton energies. A clear difference in the temperature dependency of V_{oc} , was observed between heteroepitaxial and homoepitaxial InP cells. The analytically predicted dependence of dV_{oc}/dT on V_{oc} was confirmed by the fluence dependence of these quantities. Carrier removal was observed to increase with decreasing proton energy. The results obtained for performance and temperature dependency were attributed to the high dislocation densities present in the heteroepitaxial cells while the energy dependence of carrier removal was attributed to the energy dependence of proton range.

INTRODUCTION

Although air mass zero (AMO) efficiencies over 19% have been achieved for InP homojunction cells,¹ there still remains the problem of high wafer cost and relative cell fragility. For these reasons, several groups have been conducting research programs aimed at producing InP cells heteroepitaxially grown on cheaper, preferably stronger, substrates.^{2,3,4} To date, cells have been processed using Si and GaAs as starting substrates.^{2,3,4} However, in the current state of the art, lattice and thermal expansion mismatch tend to introduce performance limiting high dislocation densities. These have limited cell AMO, total area efficiencies, to 9.9% and 13.7% for heteroepitaxial InP cells, using Si and GaAs substrates respectively.^{2,3,4} Our previous work on these cell types included research on the effects of 1 MeV electron and 10 MeV proton irradiations.^{5,6,7} An objective of this latter work

lay in determining the role of dislocations on cell performance, temperature dependency and carrier removal. In the present case, we consider the effects of lower energy proton irradiations on the properties of InP heteroepitaxial cells processed with GaAs as the starting substrate .

EXPERIMENTAL

The cells were processed by MOCVD at the Spire corporation under contract to NASA Lewis. They consisted of a heavily doped p-type GaAs substrate followed by several layers of $\text{Ga}_x\text{In}_{1-x}\text{As}$ with lattice matching to InP occurring at $x=0.47$.^{3,4} This is followed by deposition of n^+pp^+ InP cells. Cell details are shown in figure 1. The cells were irradiated by 0.5 and 3 MeV protons to a fluence of 10^{13} cm^{-2} . Proton ranges for these energies and for 10 MeV protons are shown in the figure. Cell base carrier concentrations, at the edge of the depletion region, were determined by C-V measurements. Pre-irradiation parameters for these cells are shown in table I. The table also includes data for an n^+p InP cell whose emitter region was processed by sulfur diffusion into p-type substrates.⁸ The efficiencies of the present InP/GaAs cells are somewhat lower than the 13.7% reported for cells of a similar structure.^{2,3} It is noted that the higher efficiency cells had dislocations densities as low as $3 \times 10^7/\text{cm}^2$ while dislocations densities in the present cells were approximately an order of magnitude higher.^{3,4}

RESULTS AND DISCUSSION

Cell performance:

From figures 2 and 3 it is seen that the radiation resistance of the heteroepitaxial cell is significantly greater than that of the non-heteroepitaxial homojunction cell. An exception exists at the highest 0.5 MeV proton fluence where only a slight difference exists. Data for the remaining cell parameters, at the highest fluence are shown in table II. The improved radiation resistance of the InP/GaAs cell is due to a short BOL cell base diffusion length of approximately 0.4 micrometers. This is attributed to the high dislocation density present in this cell.

Temperature Dependency:

Temperature dependencies of V_{oc} and I_{sc} , over the measured temperature range from 25 to 75 °C, are shown in figures 4 and 5. The remaining parameters show the linear behavior exhibited by dV_{oc}/dT over this temperature range. However, because of the nonlinearity exhibited by dI_{sc}/dT at the lower temperatures, all temperature dependencies were determined at 55 °C. The results are shown in table III along with our previous results for InP/GaAs and homoepitaxial InP/InP cells.^{6,9} Comparing the temperature dependency data for the two cell types, the only clear cut difference occurs in dV_{oc}/dT . In the past, we have used Fan's

analytical model for a more detailed analysis of the V_{oc} temperature dependency.^{7,10} The analytical model predicts that the absolute magnitude of dV_{oc}/dT increases with decreasing open circuit voltage. The data shown in table IV is in agreement with this prediction. The fluence dependence of dV_{oc}/dT , shown in figure 6, indirectly confirms the prediction of the analytical model inasmuch, as seen from tables I and II, V_{oc} decreases with increasing fluence. Aside from the fluence dependence the high dislocation densities in the heteroepitaxial cells result in reduced values of V_{oc} and therefore higher values for the absolute magnitude of dV_{oc}/dT . Hence, the difference in V_{oc} temperature dependencies between the hetero- and homoepitaxial cell is attributed to the high dislocation density present in the latter cell.

Carrier Removal:

Carriers removed, in the present InP/GaAs cell, at 0.5 and 3 MeV, are shown in figure 7. Carrier removal rates R_C , where $R_C = \Delta p / \Phi$, are shown in table V for the present cells together with previously obtained 10 MeV proton data for InP/GaAs and InP/InP cells.^{6,9} The 10 MeV data shown in the table indicates that carrier removal in the heteroepitaxial cell is greater than that measured for the homoepitaxial cells at this proton energy. The excess carrier removal is attributed to the greater dislocation density, and hence increased defect density, present in the irradiated heteroepitaxial cells. The data also indicates that, under proton irradiation, carrier removal rates tend to increase with decreasing proton energy. From the proton ranges shown in figure 1, and plots of defects created as a function of distance, it is seen that the lower energy protons create more defects in the active cell region as compared to those created by the higher energy protons. Hence the energy dependent behavior of carrier removal is attributed to the reduction in proton range with decreasing energy.

CONCLUSION

The behavior of the present heteroepitaxial cells, at the lower proton energies, is consistent with previous results obtained for diffused junction InP cells.⁸ The decreased radiation resistance observed at 0.5 MeV can be understood by noting that, compared to the higher energy irradiations, a much larger defect concentration occurs in the active InP cell region. Also, as noted in the previous section, carrier removal increases as proton energy decreases. The effects of dislocations are apparent in the increased radiation resistance of the heteroepitaxial cells, the temperature dependency of V_{oc} , and the increased carrier removal rate observed for the InP/GaAs cells at 10 MeV. Considering that $Ga_xIn_{1-x}As$ is lattice matched to InP, the relatively low efficiency of the present InP/GaAs cells is disappointing. The

high dislocation densities occurring in these cells is probably due to mismatches occurring in the transition layers.⁴ These results highlight the fact that dislocations are the principal barrier to achieving high efficiencies in heteroepitaxial InP cells. Hence future research efforts in this area would do well to focus their efforts toward reducing dislocation densities into the $10^6/\text{cm}^2$ range.

REFERENCES

1. C.J.Keavney, V.E.Haven and S.M.Vernon, "Emitter Structures in MOCVD InP Solar Cells," 21st IEEE Photovoltaic Spec. Conf. 141-147 (1990)
2. M.W.Wanlass, U.S.Patent No. 4,967,949, 1990.
3. M.W.Wanlass, T.J.Coutts, J.S.Ward and K.A.Emery, "High Efficiency Heteroepitaxial InP Solar Cells," 11th Space Photovoltaic Research and Technology Conf., NASA Conf. Publication 3121, 27-1 to 27-5 (1991)
4. C.Keavney, S.Vernon and V.Haven, "Tunnel Junctions for InP-on-Si Solar Cells," 11th Space Photovoltaic Research and Technology Conference, NASA Conf. Pub. 3121, 1-1 to 1-7 (1991)
5. I.Weinberg, C.K.Swartz, D.J.Brinker and D.M.Wilt, "Effects of Radiation on InP Cells Epitaxially Grown on Si and GaAs Substrates," 21st IEEE Photovoltaic Spec. Conf., 1235-1239 (1990)
6. I.Weinberg, C.K.Swartz, H.B.Curtis, D.J.Brinker, P.Jenkins and M.Faur, "Effect of Dislocations on Properties of Heteroepitaxial InP Solar Cells," 11th Space Photovoltaic Research and Technology Conf., NASA Conf. Pub. 3121, 6-1 to 6-9 (1991)
7. I.Weinberg, H.B.Curtis, C.K.Swartz, D.J.Brinker, P.P.Jenkins and M.Faur, "Radiation and Temperature Effects in Heteroepitaxial and Homoepitaxial InP Cells," 22nd IEEE Photovoltaic Spec. Conf., 1445-1451 (1991)
8. M.Yamaguchi et al, "First Space Flight of InP Solar Cells," 22nd IEEE Photovoltaic Spec. Conf., 1198-1202 (1991)
9. I.Weinberg, C.K.Swartz, H.B.Curtis, P.Jenkins and D.J.Brinker, "Carrier Removal, Temperature Dependency and Photoluminescence in Heteroepitaxial InP Solar Cells," 3rd Int'l Conf. on InP and Related Materials, IEEE Piscataway, N.J. 1991, 52-55.

10. John C.C.Fang, "Theoretical Temperature Dependence of Solar Cell Parameters," Solar Cells 17, 309-315 (1986)

Table I : Cell Performance at BOL

Cell	Jsc (mA/cm ²)	Voc (mV)	FF (%)	Eff. (%)
InP/GaAs	27.6±.08	697±4.4	72.8±.25	10.2±.08
InP ^a	33.7	828	81.6	16.6

a M. Yamaguchi et al, 21th PVSC ,p1198(1990)

Table II : Normalized Parameters at High Fluence

InP/GaAs; $\Phi = 10^{13}/\text{cm}^2$

Proton Energy (MeV)	Jsc (mA/cm ²)	Voc (mV)	FF (%)	Eff. (%)
3.0	0.98	0.94	0.95	0.87
0.5	0.13	0.67	0.87	0.08

Table III : Cell Temperature Coefficients at 328 K

Cell	dPm/dT (mW/cm ² K)	dVoc/dT (mV/K)	dJsc/dT (mA/cm ² K)	dFF/dT (%/K)
InP/GaAs ^a	-(5.21±.27)X10 ⁻²	-(2.53±.01)	(1.41±.08)X10 ⁻²	-(6.56±.58)X10 ⁻²
InP/GaAs ^b	-(5.63±.25)X10 ⁻²	-(2.51±.01)	(1.99±.11)X10 ⁻²	-(7.50±1.97)X10 ⁻²
InP/InP ^b	-(5.41±.21)X10 ⁻²	-(2.07±.02)	(2.21±.40)X10 ⁻²	-(5.43±1.56)X10 ⁻²

a Present Work

b I. Weinberg et al , 3rd Int'l. Conf. InP & Related Materials, p52 (1991)

Table IV : Temperature Dependency of Voc

Cell	Voc (mV)	dVoc/dT (mV/K)	
		Measured	Calculated
InP/GaAs ^a	697±4.4	-2.52±.01	-2.82±.02
InP/GaAs ^b	700±6.0	-2.51±.02	-2.84±.03
InP/InP ^b	874±1.0	-2.07±.02	-2.27±.01

a Present Work

b I. Weinberg et al, 3rd Int'l. Conf. InP & Related Materials, p55(1991)

Table V : Carrier Removal Rates

Cell	InP/InP ^b	InP/GaAs ^b	InP/GaAs ^a	
Proton Energy (MeV)	10	10	3	0.5
Carrier Removal Rate (cm ⁻¹)	540	880	1.4x10 ³	8.4x10 ³

a Present Work

b I. Weinberg, et al, 3rd Int'l. Conf. InP & Related Materials, p55(1991)

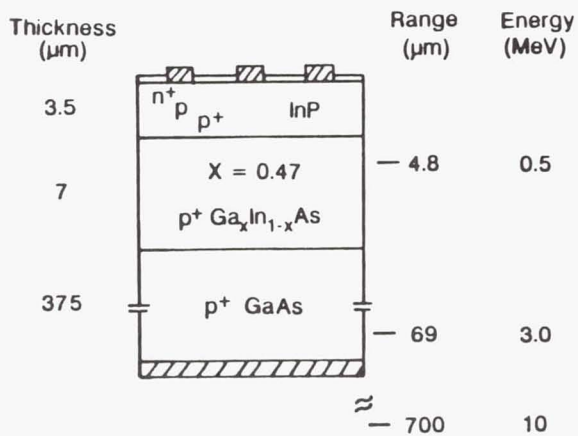


Figure 1 : Cell Details

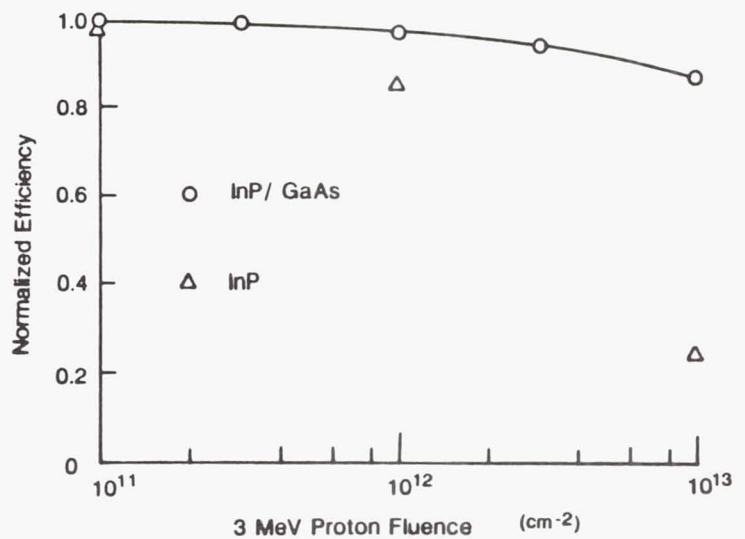


Figure 2 : Normalized Efficiencies at 3 MeV

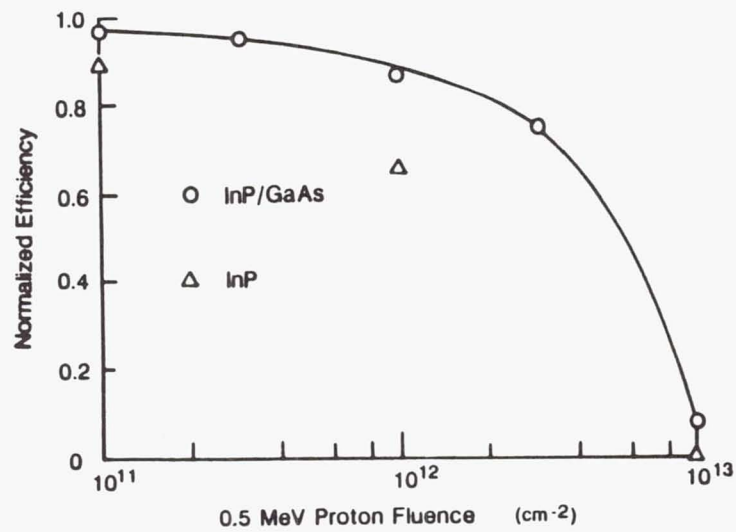


Figure 3 : Normalized Efficiencies at 0.5 MeV

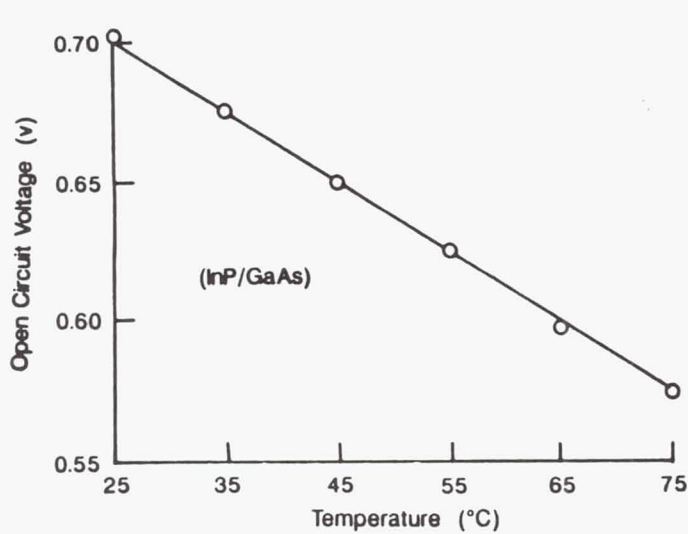


Figure 4 : Temperature Dependency of Voc

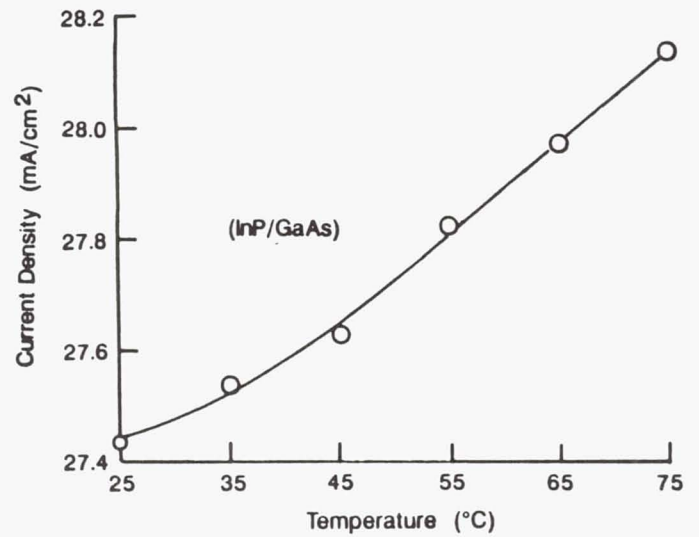


Figure 5 : Temperature Dependency of Jsc

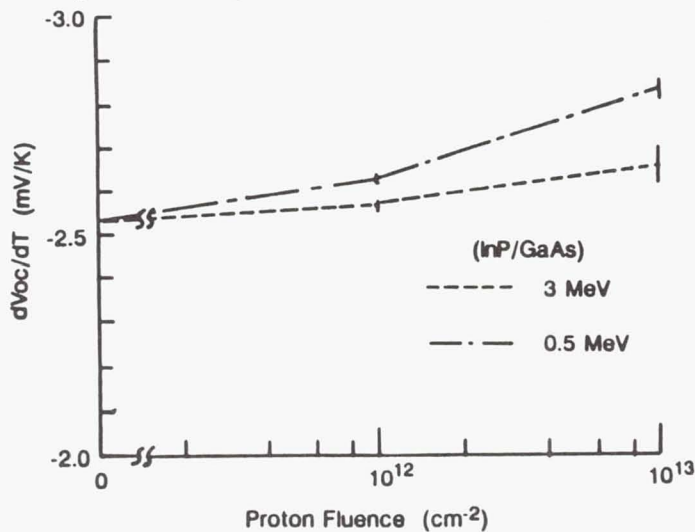


Figure 6 : Fluence Dependency of dVoc/dT

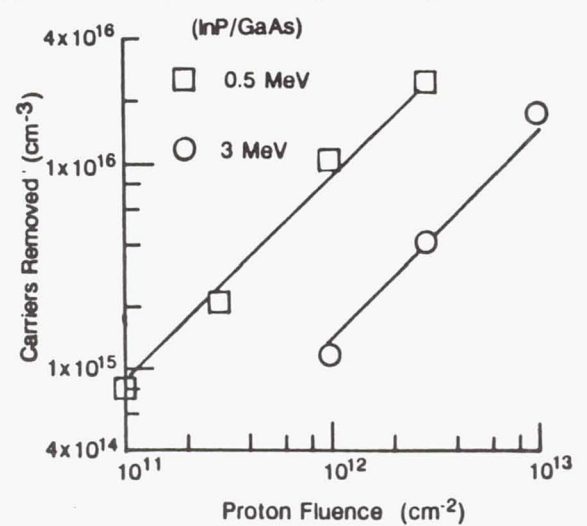


Figure 7 : Carrier Removal at 0.5 and 3.0 MeV

PROGRESS IN p^+n InP SOLAR CELLS FABRICATED BY THERMAL DIFFUSION

Mircea Faur, Maria Faur*, C. Goradia, M. Goradia
Space Photovoltaic Research Center**, Electrical Engineering Department
Cleveland State University, Cleveland, OH 44115

D. J. Flood, D. J. Brinker, I. Weinberg, C. Vargas
NASA Lewis Research Center, Cleveland, OH 44135

N. S. Fatemi
Sverdrup Technology, Inc., Cleveland, OH 44135

ABSTRACT

In this work we present the performance results of our most recently thermally diffused InP solar cells using the p^+n (Cd,S) structures. We have succeeded in fabricating cells with measured AMO, 25°C V_{oc} exceeding 880 mV (bare cells) which to the best of our knowledge is higher than previously reported V_{oc} values for any InP homojunction solar cells. The cells were fabricated by thinning the emitter, after Au-Zn front contacting, from its initial thickness of about 4.5 μm to about 0.6 μm . After thinning, the exposed surface of the emitter was passivated by a thin ($\sim 50\text{\AA}$) P-rich oxide. Based on the measured EQY and J_{sc} - V_{oc} characteristics of our experimental high V_{oc} p^+n InP solar cells, we project that reducing the emitter thickness to 0.3 μm , using an optimized AR coating, maintaining the surface hole concentration of $3 \times 10^{18}\text{cm}^{-3}$, reducing the grid shadowing from actual 10.55% to 6% and reducing the contact resistance will increase the actual measured 12.57% AMO 25°C efficiency to about 20.1%. By using our state-of-the-art p^+n structures which have a surface hole concentration of $4 \times 10^{18}\text{cm}^{-3}$ and slightly improving the front surface passivation, we project an even higher practically achievable AMO, 25°C efficiency of 21.3%.

INTRODUCTION

At the last SPRAT conference we predicted that for homojunction InP solar cells made by thermal diffusion the p^+n configuration has a higher efficiency than the n^+p configuration due especially to an increased V_{oc} (ref 1). The prediction was based on AMO, 25°C V_{oc} values of 860 mV we recorded for p^+n (Cd,S) InP solar cells as compared to experiment-based projected V_{oc} of only 840 mV for n^+p (S,Cd) InP solar cells. This value of V_{oc} for the n^+p (S,Cd) solar cells is in good agreement with previously predicted maximum V_{oc} values for thermally diffused n^+p (S,Zn) InP solar cells (ref 2).

Thermal diffusion is a desirable technique for homojunction InP solar cell fabrication because of its reduced complexity and a lower processing cost due to the possibility of large-scale batch processing of large-area devices. The drawback of this fabrication technique is that a large number of defects are present in the emitter layer after diffusion (ref 3), which makes the solar cell efficiency lower than that of solar cells fabricated by epitaxy, due especially to a lower open circuit voltage V_{oc} . In this paper we show how we have overcome this drawback and have achieved, to our knowledge, the highest V_{oc} for an InP homojunction solar cell.

*National Research Council-Research Associateship Program at NASA LeRC

**Funded by NASA Lewis Research Center, Cleveland, Ohio

A significant improvement in the quality and radiation tolerance of InP structures fabricated by closed-ampoule thermal diffusion was obtained after optimizing the diffusion process using electrochemical (EC) techniques for step-by-step characterization of these structures during fabrication and after irradiation with high energy electrons and protons (ref 4). For our thermally diffused p^+n and n^+p InP structures, we found the ranking in decreasing order of projected maximum efficiency to be: 1) p^+n (Cd,S), 2) n^+p (S,Cd), 3) p^+n (Zn,S) and 4) n^+p (S,Zn). Based on experimental results we have projected a practically achievable AMO, 25°C efficiency of 21.3% for the p^+n (Cd,S) InP solar cell. A preliminary investigation of p^+n (Cd,S), n^+p (S,Cd) and p^+n (Zn,S) thermally diffused InP structures both prior to and after irradiation by high energy electrons and protons indicates that the same ranking holds for these three structures with respect to radiation tolerance as indicated above for maximum efficiency.

EXPERIMENTAL

Cd and Zn diffusions into n-InP:S ($N_D - N_A = 3.5 \times 10^{16} \text{cm}^{-3}$) were performed by a closed ampoule technique using high purity Cd_3P_2 and Zn_3P_2 (ref 5). Diffusion temperatures were from 500 to 550°C for Zn and from 560 to 660°C for Cd diffusion. The substrates were Czochralski LEC grown with an EPD of about $5 \times 10^4 \text{cm}^{-2}$. Diffusions were performed using a thin (40-50Å) phosphorus-rich chemical oxide diffusion cap layer (ref 1). Electrochemical techniques were used for step-by-step characterization of these diffused structures during fabrication and after irradiation with high energy protons (ref 3).

Small area (0.52 cm^2) p^+n InP solar cells were fabricated on diffused structures with net surface acceptor concentration of $3 \times 10^{18} \text{cm}^{-3}$, diffused at 650°C. Au was used for the back contact and Au-Zn-Au (0.25 μm thick) for the front contact. Since Au-Zn front contacts melt as far deep as over 3 μm into the emitter during sintering at 430°C, p^+n structures with 4 to 5 μm thick emitters were fabricated. Therefore, after front contact sintering, the emitters had to be thinned down over the uncontacted areas. Chemical thinning was employed using a new etchant which we call the "PNP" etchant (ref 6). No AR coating was used except for the thin (about 50Å) residual oxide which resulted from the thinning process. The front grid coverage was 10.55%. The 0.52 cm^2 total cell area was defined by mesa etching.

The solar cell performance parameters after thinning the emitter to different depths using this low etch rate PNP etchant were recorded at CSU using an ELH lamp after each thinning step. For selected cells, illuminated I-V measurements were done under AMO, 25°C conditions at NASA-LeRC. For these cells, dark I-V, I_{sc} - V_{oc} , spectral response and temperature variation of performance parameters were also measured.

RESULTS

At the last SPRAT conference we reported an AMO, 25°C, V_{oc} value of 860 mV for a p^+n (Cd,S) InP solar cell fabricated by closed ampoule thermal diffusion (ref 1). For an emitter thickness of about 0.25 μm and using only a thin (~ 50Å thick) P-rich passivating layer as an AR coating, the J_{sc} value was 29.1 mA/cm^2 . From I_{sc} - V_{oc} and spectral response measurements we calculated that by using an optimized ZnS/MgF_2 AR coating the expected V_{oc} and J_{sc} values for this cell would be 872 mV and 36.3 mA/cm^2 , which are higher than previously reported V_{oc} and J_{sc} values for p^+n InP structures fabricated by epitaxy (refs 7,8). However, a low FF of 52% was responsible for the low measured

AMO, 25°C efficiency of only 9.51%. The low FF was due both to a high contact resistance of our Au-Zn-Au front contacts and a large sheet resistance of about $5 \times 10^3 \Omega\text{-cm}^2$ which resulted after thinning the emitter from an initial emitter thickness of about $2 \mu\text{m}$ down to $0.25 \mu\text{m}$. The surface net acceptor concentration of these structures was 1.5 to $2 \times 10^{18} \text{cm}^{-3}$.

In order to reduce the series resistance R_s and therefore increase the FF we have concentrated our efforts on i) increasing the surface hole concentration, without altering the diffused structure quality and ii) find a good alternative for our Au-Zn-Au front contacts fabricated presently by E-beam evaporation such as to be able to deposit ohmic contacts on thin emitters without short-circuiting the junction.

A step-by-step electrochemical characterization of p^+n (Cd,S) structures as a function of processing parameters has enabled us to improve the fabrication process of diffused structures by reducing the structural and electrical-type defect density while increasing the surface net acceptor concentration (ref 4). As an example for structures with a net surface hole concentration of $3 \times 10^{18} \text{cm}^{-3}$ (see Figure 1, curve A) we recorded EPDs as low as $2 \times 10^2 \text{cm}^{-2}$. The surface state density minima determined electrochemically after removing the front contamination layer ($\sim 300 \text{\AA}$) from the surface of the lower surface concentration structure was below our measurable limit of $10^{10} \text{eV}^{-1} \text{cm}^{-2}$, while for the unoptimized higher surface concentration structure (curve B) was about $2 \times 10^{10} \text{eV}^{-1} \text{cm}^{-2}$.

Using these low defect density p^+n InP diffused structures with a net surface acceptor concentration of $3 \times 10^{18} \text{cm}^{-3}$ (curve A, Figure 1) we have been able to fabricate cells with measured AMO, 25°C V_{oc} exceeding 880 mV (see Figure 2), which, to the best of our knowledge, is higher than previously reported V_{oc} values for any InP homojunction solar cell. The cells were fabricated by thinning the emitter from its initial thickness of about $4.5 \mu\text{m}$ to about $0.6 \mu\text{m}$ after Au-Zn front contacting. It was necessary to start with a thick emitter and to thin it down after sinering the front contacts because during sintering, the contact metallization penetrated about $3 \mu\text{m}$ below the front surface. This has the drawback of reducing the surface hole concentration in the thinned emitter, thereby increasing the series resistance and lowering the fill factor. Figure 3 shows the external quantum efficiency (EQY) of this cell with a grid coverage of 10.55% and no AR coating. The low J_{sc} value of 26.8 mA/cm^2 and the low EQY of this cell can be explained by the very large thickness of the emitter, a large grid coverage and the absence of an AR coating. The cell shows a surprisingly good blue response for an emitter as thick as $0.62 \mu\text{m}$, indicating a highly passivated surface with a very low recombination velocity. The cell had a high series resistance R_s of about $3 \Omega\text{-cm}^2$ due to both high contact and sheet resistances, resulting in low fill factor (FF) of 73.1% and efficiency of 12.57%, respectively.

By further thinning the emitter, both V_{oc} and J_{sc} values increased, reaching a maximum of 884.6 mV and 29.95 mA/cm^2 (bare cell) respectively, at an emitter thickness of $0.3 \mu\text{m}$. An increased R_s due to an increased emitter sheet resistivity produced a decrease in FF to 57.7% with a drop in efficiency to about 10.9%.

By using an optimized two layer AR coating, and reducing the grid shadowing to 6% the projected J_{sc} value for a $0.3 \mu\text{m}$ thick emitter is about 37.5 mA/cm^2 . From the I_{sc} - V_{oc} characteristics (not shown) such an increase in J_{sc} will increase the V_{oc} by 10-11 mV, which means that the expected V_{oc} for these cells should be about 895 mV. Figure 4 shows the recorded temperature dependence of V_{oc} and efficiency for a p^+n InP cell after thinning the emitter to a thickness of about $0.7 \mu\text{m}$. An ELH lamp was used for illumination. The AMO V_{oc} and η values for this cell were 875.6 mV and 11.54%, respectively (bare surface). As far as we know, it is the first time a measured $|\Delta V_{oc}/\Delta T|$ value below $2 \text{ mV}/^\circ\text{C}$ is reported for an InP solar cell. This is not surprising since, as known, the theoretical value of $|\Delta V_{oc}/\Delta T|$ decreases as the V_{oc} increases. Should it be possible to deposit ohmic front contacts on thin emitters (i.e. up to $0.5 \mu\text{m}$ thick) without short-circuiting the junction, then the high surface hole concentration in the emitter would be preserved, and the projected FF of these cells should be about 82%

and the projected AMO, 25°C efficiency of 20.1%.

Our preliminary results using Au-Zn co-evaporation are very encouraging. After sintering at 350°C, for 1 minute 0.25 μm thick Au-Zn contacts deposited by co-evaporation on a 0.6 μm thick emitter with a net surface acceptor concentration of only $1.5 \times 10^{18} \text{cm}^{-3}$, gave an R_s value of about $1.6 \Omega\text{-cm}^2$ after thinning the emitter to 0.25 μm . By comparison, using E-beam evaporated Au-Zn-Au of similar thickness, deposited on 3 μm thick emitters with a similar surface concentration, after sintering for 2 minutes at 430°C and thinning the emitter to about 0.25 μm gave an R_s value of $10 \Omega\text{-cm}^2$, using the same photolithographically defined mask with a front contact coverage of 6.5%. The large increase is due especially to an increased sheet resistivity once the surface hole concentration drops below 10^{18}cm^{-3} , which is what happens after thinning down thick emitters. The layered Au-Zn-Au contacts require thick emitters since the sintering temperature for forming ohmic contacts is about 430°C for 2 minutes and which causes after sintering the Au to penetrate the emitter at depths greater than 2 μm .

If well controlled, we feel that co-evaporation, or better still, sputtering using premixed Au-Zn or Au-Cd targets, followed by a low temperature, short time sintering could be used for fabrication of good quality front ohmic contacts using thin emitters without short-circuiting the junction.

DISCUSSION

Although not explicitly shown here, for our thermally diffused p^+n and n^+p InP structures, we found the ranking in decreasing order of projected maximum cell efficiency to be: (1) p^+n (Cd,S); (2) n^+p (S,Cd); (3) p^+n (S,Zn), and (4) n^+p (Zn,S). The performances of solar cells fabricated on these structures have shown that the same ranking holds. Except for the p^+n (Cd,S) cells the principal limiting factor for the other cell structures is V_{oc} . Experiment-based projected maximum achievable V_{oc} for our thermally diffused n^+p cells appears to be 840 mV, while for the p^+n (S,Zn) cell appears to be limited to about 860 mV. The large structural and electric-type defect density found in structures (2), (3) and (4) as compared to (1), namely, the p^+n (Cd,S) structure, explains their V_{oc} limitation. This possibly explains why although a relatively large experimental effort was made by NTT (Japan) to improve the V_{oc} and efficiency of diffused n^+p (S,Zn) cells the maximum reported AMO efficiency for these cells was of only 16.6% (ref 2) as compared to 19.1% reported for n^+p (Si,Zn) InP solar cells fabricated by MOCVD (ref 9).

As seen in Table 1, experiment-based (ref 10) projected maximum practically achievable efficiency for diffused n^+p (S,Cd) InP cells is of about 18.8%. A rather thick emitter of 0.08 μm was considered in this case due to the fact that even at low diffusion temperatures (i.e., 600°C), a front phosphorus depleted dead layer is present at the surface. However, higher diffusion temperatures of 660 to 675°C are needed in order to increase the surface donor concentration. Owing to the graded nature of donor concentration profile, in this case, thinning the emitter below 800 Å will decrease the surface concentration to below $4 \times 10^{18} \text{cm}^{-3}$ which produces a decrease in V_{oc} and FF which upsets the J_{sc} increase.

The achievement of V_{oc} values for our diffused p^+n (Cd,S) bare cells, higher than those reported for epitaxially grown p^+n InP cells with optimized AR coating (refs 7,8) and even higher than that reported for all epitaxially grown $n^+(\text{InGaAs})/n(\text{InP})/p(\text{InP})/p^+(\text{InP})$ solar cell of 876 mV which corresponds to the maximum reported AMO efficiency of 19.1% for an InP solar cell (ref 9), along with a high blue response, indicates that we have succeeded in overcoming the primary drawback of the thermal diffusion process, and we are able to obtain high quality reproducible p^+n diffused junctions with

very low bulk and surface defect densities in the emitter layer. As shown in the previous section, by reducing external losses, the projected AMO efficiency of cells fabricated on diffused p^+n (Cd,S) structures with a net surface concentration of $3 \times 10^{18} \text{cm}^{-3}$ is 20.1%. As seen in Table 1, by using our state-of-the-art p^+n structures with a surface concentration of $4 \times 10^{18} \text{cm}^{-3}$ (see Figure 1, curve B) we project the maximum achievable efficiency to be 21.3%. The relatively large increase in V_{oc} , from our presently projected value of 895 mV to 910 mV, is based not only on a V_{oc} increase with surface concentration but on our latest experimental data which show that further improvement in surface passivation is possible. Even higher V_{oc} values, approaching 930 mV are possible by using better quality substrates (i.e. with EPD below 10^4cm^{-2}), optimizing base doping, further optimizing the diffusion process and the quality of the passivating layer. Preliminary electrochemical investigation of our diffused p^+n (Cd,S), n^+p (S,Cd) and p^+n (Zn,S) InP structures prior to and after irradiating the structures by electrons and protons, included studies of carrier removal and structural and electrical-type defects introduced by irradiation, and appeared to indicate that the same ranking holds for these three structures with respect to radiation tolerance as indicated above for maximum efficiency. As an example, Figure 5 shows the variation in EC-V carrier concentration depth profiles as a result of irradiating p^+n (Cd,S) and p^+n (Zn,S) InP structures at a fluence of 10^{13}cm^{-2} with 3 MeV protons. In this example, the p^+n (Zn,S) and p^+n (Cd,S) structures were diffused at 500 and 540°C and 560 and 650°C, respectively, using small amounts of source materials such that the surface dopant concentration was below the solubility limit of the diffusing species. This was done to decrease the density of diffusion-created defects such as surface and deep Zn_3P_2 or Cd_3P_2 precipitates and interstitial Zn or Cd. As seen, the carrier removal rates of p^+n (Cd,S) structures are significantly smaller than those of their p^+n (Zn,S) counterparts.

Since radiation resistance measurements are meaningful only when done on high efficiency solar cells, we have chosen to do them on our thermally diffused solar cells when we achieve BOL efficiencies of 18% or greater at 1 AMO, 25°C.

CONCLUSIONS

By drastically reducing the defect densities of p^+n InP diffused structures we have succeeded in fabricating thermally diffused p^+n InP solar cells with measured AMO, 25°C V_{oc} exceeding 880 mV (bare cells) which is higher than previously reported V_{oc} values for any InP homojunction solar cells. Experiment-based projected maximum achievable AMO, 25°C efficiency of these cells is 21.3%.

For our thermally diffused structures the ranking in decreasing order of maximum efficiency is: 1) p^+n (Cd,S), 2) n^+p (S,Cd), 3) p^+n (Zn,S) and 4) n^+p (S,Zn). A preliminary investigation of p^+n (Cd,S), n^+p (S,Cd) and p^+n (Zn,S) InP structures both prior to and after irradiating by high energy electrons and protons indicates that the same ranking holds for these three structures with respect to radiation tolerance as indicated above for maximum efficiency. If this is correct, then p^+n (Cd,S) InP solar cells made by thermal diffusion can become very attractive for space applications due to a potential low cost, reduced complexity and adaptability to large scale batch processing.

REFERENCES

1. M. Faur, M. Faur, D. J. Flood, I. Weinberg, D. J. Brinker, C. Goradia, N. S. Fatemi, M. Goradia and W. Thesling, Proc. of the 11th SPRAT Conference, Cleveland, OH, p. 3-1, May 7-9, 1991.

2. H. Okazaki, T. Tokamoto, H. Takamura, T. Kamei, M. Ura, A. Yamamoto and M. Yamaguchi, Proc. of the 20th IEEE PVSC, 886 (1988).
3. M. Faur, M. Faur, C. Goradia, M. Ghalla, and I. Weinberg, Proc. of the 4th Int. Conf. on InP and Related Materials, Newport, RI, p. 322, April 21-24, 1992.
4. M. Faur, M. Faur, M. Goradia, C. Vargas-Aburto, and D. M. Wilt, This Conference.
5. M. Faur, M. Faur, C. Goradia, M. Goradia, and I. Weinberg, Proc. of the 3rd Int. Conf. on InP and Related Materials, Cardiff, Wales, UK, April 8-11, p. 130 (1991).
6. M. Faur, M. Faur, S. Bailey, D. J. Brinker, M. Goradia, I. Weinberg, and N. Fatemi, Proc. of the 22nd IEEE PVSC, 241 (1991).
7. Y. Itoh, M. Yamaguchi and C. Uemura, IEEE Electron Device Lett., EDL-7(2), 127 (1986).
8. K. Y. Choi, C. C. Shen, and B. I. Miller, Proc. of 19th IEEE PVSC, p. 255 (1987).
9. C. J. Keavney, V. E. Haven, and S. M. Vernon, Proc. of the 21st IEEE PVSC, 141 (1990).
10. M. Faur, M. Faur, C. Goradia, M. Goradia, N. Fatemi, D. J. Brinker, and R. D. Thomas, Proc. of the 1st Int. Conf. on InP and Related Materials, Norman, OK, p. 459 (1989).

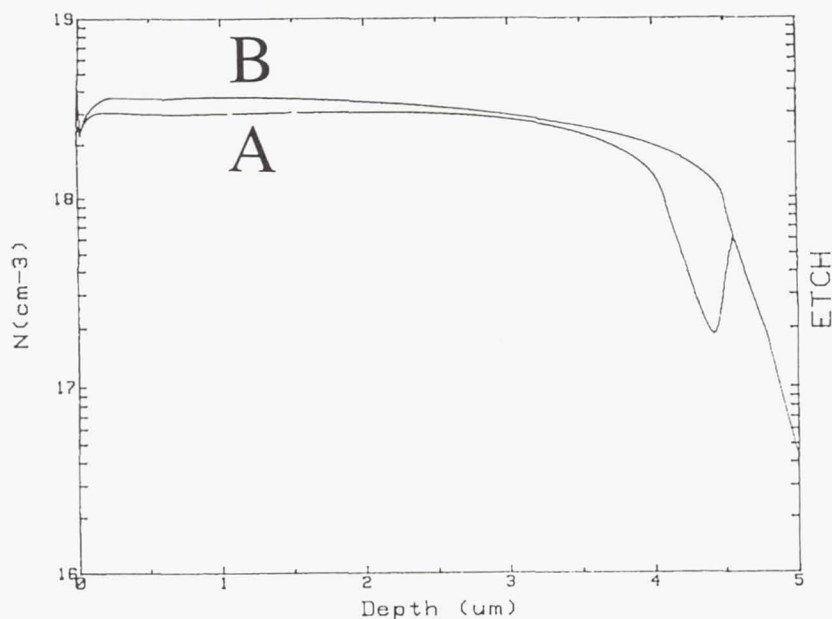


Figure 1. EC-V net acceptor concentration depth profiles of state-of-the-art thermally diffused $p^+n(\text{Cd,S})$ InP structures. (A) Used for fabrication of cell in Fig.2; (B) High acceptor concentration structure to be used for our projected 21.3% efficiency cell (See Table 1).

Cell : 53
Date : 9 Oct 1992
Reference Cell : A-181
Area : .52 cm²
Temperature : 25°C
Air Mass Zero

I_{sc} = 13.943 mA
 V_{oc} = 880.3 mV
 I_{max} = 12.78 mA
 V_{max} = 702.2 mV
 P_{max} = 8.975 mW
F.F. = 73.1
Eff. = 12.57 %

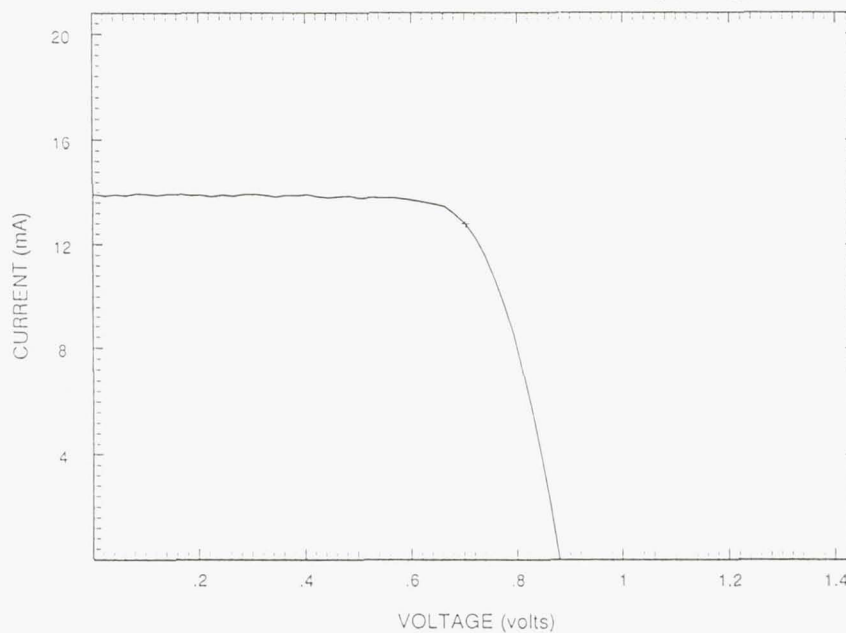


Figure 2. AM0, 25°C I-V characteristic of a p⁺n InP solar cell after thinning down the emitter from 4.5 μm to 0.62 μm . No AR coating; front contact coverage: 10.55%.

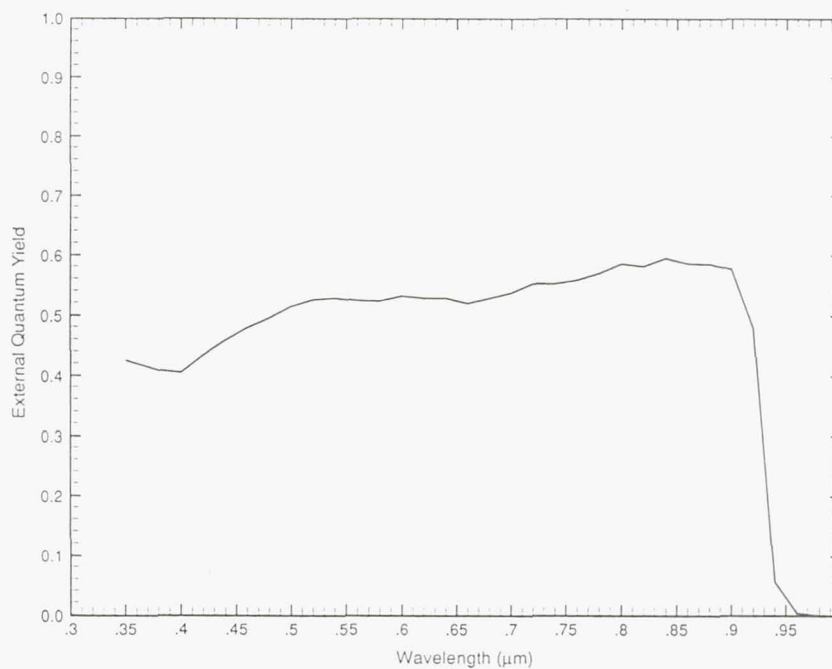


Figure 3. External Quantum Efficiency of cell in Fig. 2.

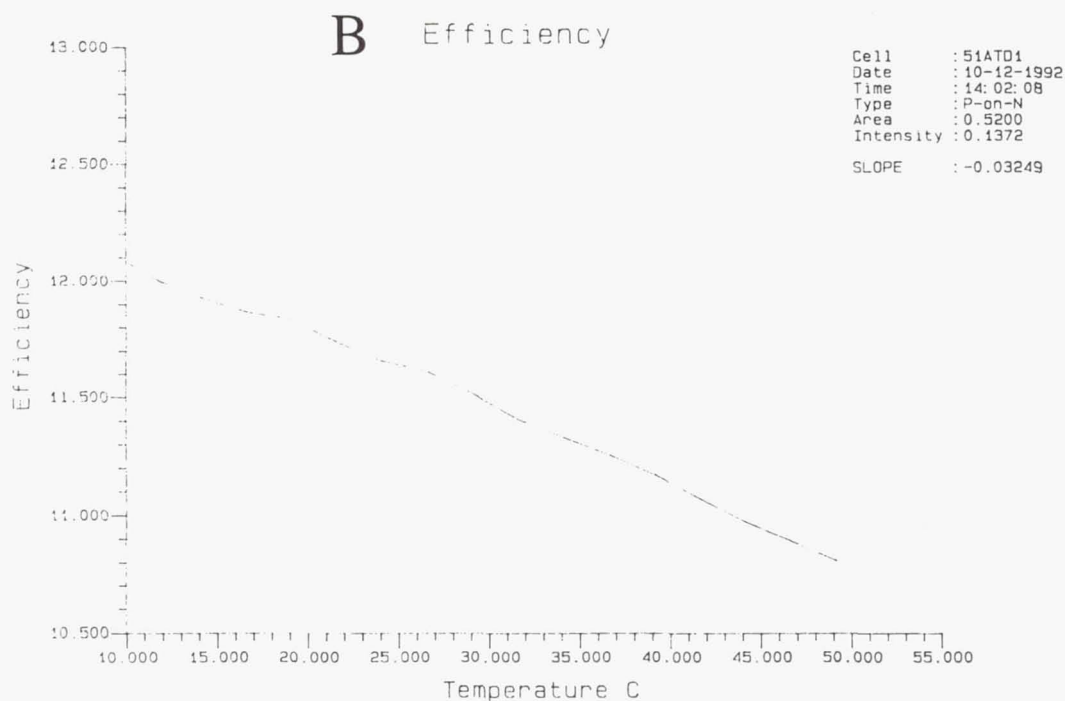
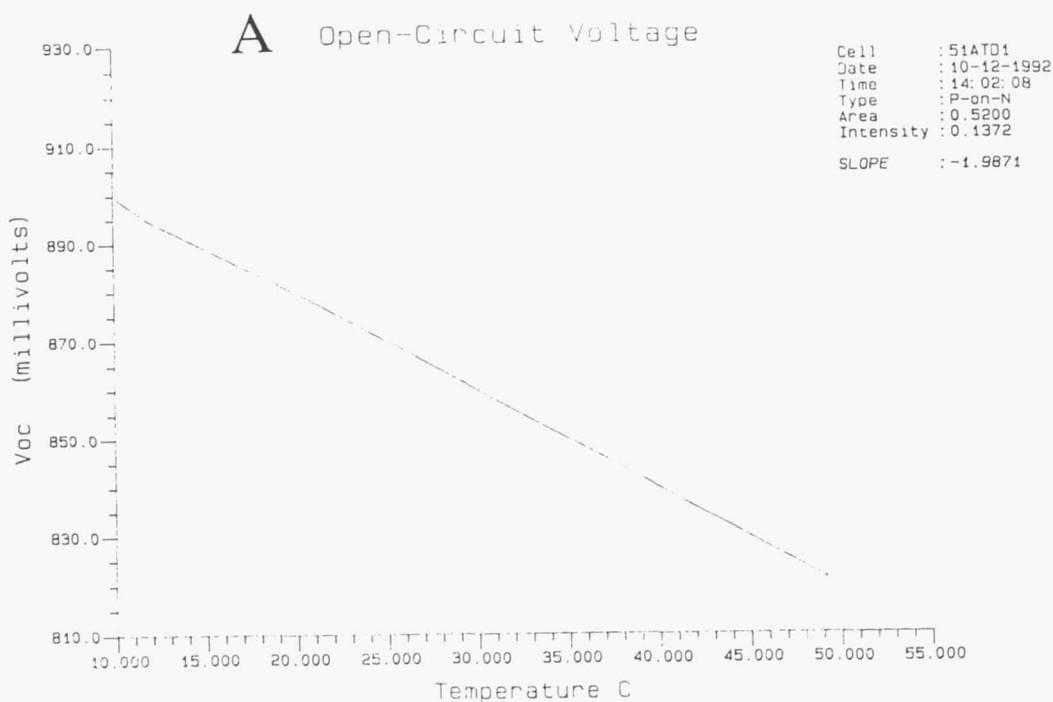


Figure 4. Temperature variation of V_{oc} (A) and efficiency (B) for a p⁺n (Cd,S) InP solar cell with no AR coating and emitter thickness of 0.7 μm .

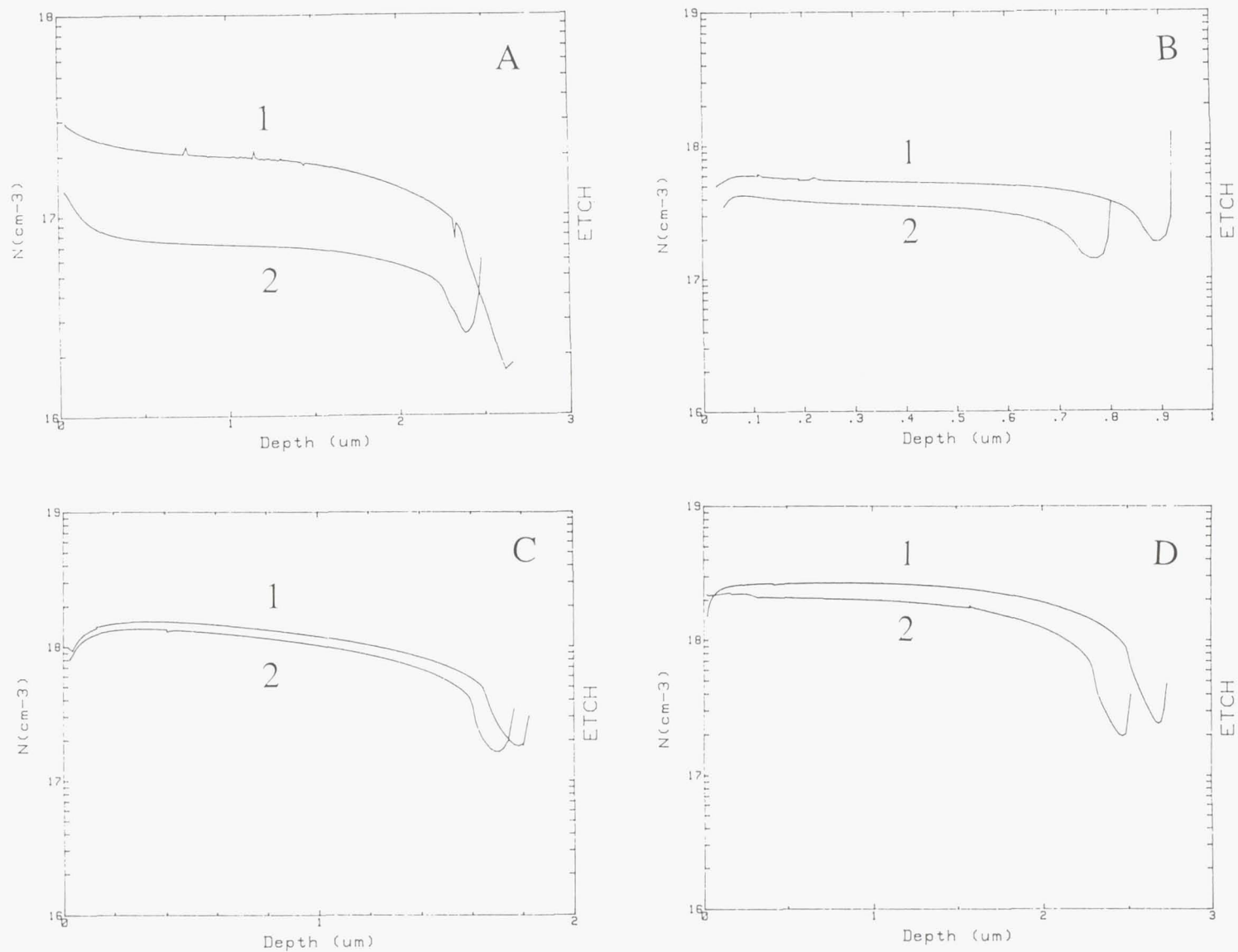


Figure 5. EC-V net acceptor carrier concentration prior to (curves 1) and after (curves 2) irradiating at a fluence of $10^{13}/\text{cm}^2$ with 3 MeV protons of $\text{InP}(\text{Zn},\text{S})$ structures diffused at (A) 500°C and (B) at 540°C , and of $\text{InP}(\text{Cd},\text{S})$ structures diffused at (C) 560°C and (D) at 650°C .

Table 1. Measured or Projected AMO, 25°C n/p and p/n InP Solar Cell Performances

Structure	Junction formation technique	Dopant	Approx Junction depth (μm)	V_{oc} (mV)	J_{sc} (mA/cm ²)	FF (%)	η (%)	Ref.
n ⁺ (InGaAs)/ n(InP)/p(InP)/ p ⁺ (InP)	MOCVD	Si/Zn	0.025	876	36.34	82.4	19.1	[9]
n ⁺ -p	Closed Ampoule	S/Zn	0.2-0.3	828	33.7	81.6	16.6	[2]
n ⁺ -p	Closed Ampoule	S/Cd	0.15 0.08-0.1	806 840	30.5 36.5	80.1 84	14.35 ^(a) 18.8 ^(b)	[10]
p ⁺ -i-n	LPE	Mg/S	0.6	823.7	37.6 (active area)	75.4	17.2	[7]
p ⁺ (InGaAs)/ p ⁺ (InP)/n(InP)	LPE	Zn/S	0.7	866	29.25	81	15	[8]
n ⁺ (InP)	MOCVD			864	32.84	76.7	15.9	
p ⁺ -n	Closed Ampoule	Cd/S	0.25 0.62 0.3 0.25	860 880.3 895 910	29.1 26.8 37.5 38.2	52.2 73.1 82 84	9.52 12.57 ^(c) 20.1 ^(d) 21.3 ^(e)	[1] This work

(a) Measured on cells with unoptimized AR coating, and front contacts; (b) experimental-based projected maximum practically achievable performances; (c) Measured values on bare cell, $R_s \sim 3\Omega \text{ cm}^{-2}$, front grid coverage: 10.55%; (d) Projected parameters of cell above by using an optimized AR coating, reducing the grid shadowing to 6% and reducing R_s to $\sim 0.5\Omega \text{ cm}^{-2}$; and (e) Maximum practically achievable projected parameters using our state-of-the-art diffused structures with a net surface acceptor concentration of $4 \times 10^{18} \text{ cm}^{-3}$.

ELECTROCHEMICAL CHARACTERIZATION OF p^+n and n^+p DIFFUSED InP STRUCTURES

Maria Faur*, Mircea Faur, M. Goradia
Space Photovoltaics Research Center**, Electrical Engineering Department
Cleveland State University, Cleveland, OH 44115

Carlos Vargas-Aburto
Kent State University, Kent, OH 44242

David M. Wilt
NASA Lewis Research Center, Cleveland, OH 44135

The relatively well documented and widely used electrolytes for characterization and processing of Si and GaAs-related materials and structures by electrochemical methods are of little or no use with InP because the electrolytes presently used either dissolve the surface preferentially at the defect areas or form residual oxides and introduce a large density of surface states. Using an electrolyte which we have newly developed for anodic dissolution of InP, and have named the 'FAP' electrolyte, we have performed accurate characterization of InP related structures including nature and density of surface states, defect density and net majority carrier concentration, all as functions of depth. A step-by-step optimization of n^+p and p^+n InP structures made by thermal diffusion was done using the electrochemical techniques, and resulted in high performance homojunction InP structures.

INTRODUCTION

Electrochemical (EC) techniques represent a simple and yet accurate method to characterize InP and related structures. It is known that using solid-state techniques, a large number of uncertainties in the measurements arise from factors such as gas adsorption, the composition and thickness of front oxide and dead layers, carrier concentration, the quality of contacts, etc.. Using EC techniques these uncertainties can be significantly reduced when both a suitable electrolyte is used and the measuring conditions are properly selected. In addition, EC techniques are of reduced complexity, faster, and allow in-situ recording of a large number of semiconductor characteristics at different depths throughout a structure and in a multilayer structure, within each layer and at the interfaces.

Various surface and bulk semiconductor properties can be determined from electrochemical I-V, C-V and G-V characteristics.

Dark and illuminated I-V characteristics are essential in helping to choose the electrolyte and working conditions for anodic dissolution, surface passivation, revealing of structural defects and EC-V net majority carrier concentration depth profiling. They can also be used in determining various surface and bulk semiconductor properties such as the diffusion length and lifetime of minority carriers and the surface recombination velocity. From illuminated I-V characteristics, the maximum J_{sc} and V_{oc} of solar cells fabricated on these structures can be predicted as well.

EC-V characteristics are useful for choosing the electrolyte for which the parasitic components of the total semiconductor/electrolyte interface capacitance, mainly due to residual oxides and surface

*National Research Council - NASA LeRC Research Associateship

**Funded by NASA Lewis Research Center

states at the interface, are minimal.

Two important parameters for the study of semiconductor materials, namely the flat band potential (V_{fb}) and the net majority carrier concentration at a given depth are extracted from the $1/C^2$ -V characteristics of the semiconductor/electrolyte interface, after dissolution to that depth.

If the electrolyte is well chosen, a very accurate method for determining the density and energy distribution of surface states and traps as a function of depth, applicable to anodic dissolution and surface passivation studies, is based on electrochemical G-V characteristics at low frequencies.

In this work we report on the use of photoelectrochemical techniques for characterization of InP and related material structures. The work focuses on both the characterization and step-by-step optimization of n^+p and p^+n InP structures fabricated by thermal diffusion, with application to fabrication of high efficiency, radiation resistant InP solar cells by this method of junction formation. The emitter layer and the junction proximity of the base are characterized as functions of: (a) various surface preparation procedures; (b) diffusion cap; (c) diffusion source, and (d) diffusion conditions (diffusion temperature and time, amount of source material and added phosphorus, and temperature difference between the source and substrates). The EC characteristics of the emitter layer provides: (a) thicknesses of front oxide and damaged layers; (b) density of surface and deep dislocation and precipitates; (c) net majority carrier concentration depth profile, and (d) surface and deep trap level density. The EC characterization was done before and after irradiating the structures with high energy electrons and protons.

In order to maximize the solar cell performances, we also investigated different post-diffusion surface preparation procedures such as removal of the front damaged emitter layer and subsequent surface passivation to obtain smooth, low defect density surfaces with good electrical characteristics.

EXPERIMENTAL

The experimental study was conducted using a large number of n , p , n^+ and p^+ InP substrates and thermally diffused n^+p and p^+n InP structures. The EC techniques were also tested on epitaxially grown n^+p and p^+nn^+ InP structures.

We compared our newly developed FAP electrolyte (ref 3) to a selection of previously recommended electrolytes including 0.5M HCl (ref. 1) and the Pear etch (ref 2).

The quality of InP materials and related material structures after anodic dissolution to different depths was characterized by:

(a) an analysis of dark I-V, illuminated I-V, C-V, $1/C^2$ -V and G-V characteristics using a commercially available Polaron Profiler (Bio-Rad Polaron PN 4200);

(b) inspection of surface topography using Nomarski and SEM microscopy;

(c) Dektak inspection of the craters;

and, (d) on selected samples, EDAX or XPS study of the surface contaminants and oxidation stage after dissolution in different electrolytes.

In order to optimize the post-diffusion surface preparation procedures and maximize the solar cell performances we investigated the effect of removal of the front damaged emitter layer and surface passivation on liquid-junction electrolyte/InP solar cell parameters.

RESULTS AND DISCUSSION

Dark and illuminated I-V characteristics were used to study the electrolyte/InP interface with applications ranging from anodic dissolution and surface passivation to predicting the J_{sc} values of solar cells fabricated on these structures.

From the high values of dark saturation current at the electrolyte/InP liquid junction, using previously recommended electrolytes (i.e., 0.5M HCl and the Pear etch) one can conclude that preferential dissolution of one of the components takes place. Thus, the high dark saturation current densities (J_0) are due to the presence of a large surface state density due to such defects as P or In vacancies. An example is given here in the case of 0.5M HCl. We attribute the high J_0 values seen in Figure 1 to surface states introduced by In vacancies as confirmed by XPS and low frequency electrochemical G-V measurements. By comparison, under similar conditions, that is, after the removal of about 300Å from the p^+ InP surface using the FAP electrolyte, J_0 is zero within the measuring capabilities at a reverse bias of up to 1.5V. Also, the illuminated I-V characteristic in this case shows a near ideal behavior. This confirms our XPS and EG-V results which show a near ideal surface stoichiometry and a very low surface state density after dissolving good quality structures using the FAP electrolyte.

From the illuminated electrochemical I-V characteristics of diffused InP structures we were able to predict the maximum short-circuit current density (J_{sc}) of solid-state solar cells fabricated on these structures, and to estimate the optimal emitter thickness. We found a very good agreement between the J_{sc} values of liquid and solid state solar cells. As an example, the maximum J_{sc} values of a liquid junction p^+n InP/FAP electrolyte cell was found after dissolving about 0.81µm from the surface (initial emitter thickness ~ 1.15µm). Extrapolating the illumination levels in Figure 2 at 130 mW/cm², the calculated J_{sc} value is about 33.2 mA/cm². The J_{sc} value of a solar cell fabricated on a similar structure, prior to AR coating, measured using an ELH lamp at 130mW/cm² was 30.7 mA/cm². Since the front contact coverage was about 6.5%, the active area J_{sc} value becomes 32.8 mA/cm², which within experimental errors is very close to the liquid junction cell J_{sc} value.

In the case of an optimized thermally diffused n^+p (S,Zn) InP structure, the effect of removing the highly damaged front n^+ layer on the quality of the emitter is evident in Figure 3 by the variation of the photoelectrochemical J_{sc} at the FAP electrolyte/ n^+ InP liquid junction under a constant low level illumination (~ 5mW/cm²) under an incandescent lamp. The J_{sc} reaches a maximum of about 1.2 mA/cm² after removal of about 400Å from the surface, corresponding to surface carrier concentration of about 2×10^{18} cm⁻² (ref 4). Interestingly enough, AES profiling has shown that in this case the phosphorous depleted dead layer also extends to about 400Å below the surface (ref 5). The density of phosphorous vacancy related traps with an energy of 0.24 eV above the valence band calculated from electrochemical G-V plots at 0.8 kHz is shown for this structure in Figure 4 (the lower curve). It reaches a minimum of about 10^{11} cm⁻² eV⁻¹ also after removing about 400Å from the surface. The V_p -related hole trap density prior to optimization of the diffusion process was much higher as can be seen in the upper curve. The two structures in this figure were diffused for 3 hours at 660°C using the shown amounts of In₂S₃ and red phosphorus normalized to the ampoule volume. The optimized structure was diffused through a thin phosphorus rich (~ 50Å thick) diffusion cap layer while the high V_p -related defect density structure was diffused through a clean surface.

The J_{sc} value of a solar cell fabricated on the optimized structure, measured using a ELH lamp at 130 mW/cm², was about 31.6 mA/cm² (active area, no AR coating) after removing about 400 Å from the surface which is close to the 32.2 mA/cm² value calculated by extrapolating the liquid junction cell

J_{sc} value of 1.2 mA/cm² mentioned above.

Electrochemical C-V, $1/C^2$ -V and low frequency G-V characteristics are used not only for characterization of InP materials and structures but also for step-by-step optimization of fabrication procedures of thermally diffused p⁺n and n⁺p InP structures.

As an example, in connection with Figure 5 in the case of our initial p⁺n InP structures a large number of surface and deep defects have been revealed. In this example at the surface of a Cd-doped p⁺n InP (S-doped substrates) we found two trap lines; one of 0.6 eV above the valence band which we believe is a phosphorus vacancy (V_p) related defect and another at 0.21 eV below the conduction band which we attributed to interstitial Cd. After removing about 400 Å from the surface the deep acceptor-like defect disappeared, but the donor-like defect could still be found in large concentrations, i.e., about 3×10^{14} cm⁻²eV⁻¹, maximum value at 0.8 KHz. By using a thin phosphorus-rich (~ 50 Å thick) diffusion cap layer and optimized diffusion conditions, the C-V, $1/C^2$ -V and G-V characteristics recorded at 0.8 KHz at the p⁺ InP/FAP electrolyte interface behave normally. The curvatures in $1/C^2$ -V and G-V characteristics seen in Figure 6a are due to impurities present in the front contamination layer. After removing only about 300 Å from the surface, including the front oxide layer (see the decrease in the capacitance), as seen in Figure 6b the three characteristics are quasi-ideal.

The use of FAP electrolyte for EC characterization of diffused and other related InP structures proved to be a very good choice. Although for some applications such as revealing the dislocation density a series of other electrolytes could be used (ref 4), FAP electrolyte is the only good choice we found for mapping the dislocation density (etch pits and precipitates) as a function of depth, which is essential for defect revealing in thin multi-layer InP structures either at a certain depth or at an interface (ref 6).

For other applications such as EC-V profiling, the FAP electrolyte to our knowledge is the only good choice (ref 4). Previously recommended electrolytes such as 0.5M HCl and the Pear etch do not satisfy the criteria of a good electrolyte because of one or more drawbacks such as: dissolving InP preferentially at the defect areas, forming insoluble products on the surfaces, producing rounding at the crater rim, introducing parasitic capacitance components at the electrolyte/InP interface, etc., which result in inaccurate profiles.

Due to its intrinsic qualities (ref 4) the FAP electrolyte appears to be quasi-ideal for performing accurate net majority carrier concentration EC-V profilings. As an example, Figure 7 shows an EC-V profile of an epitaxially grown p⁺nn⁺ InP structure. As seen, after profiling the structure to a depth of 6 μm, the known n⁺ base donor concentration of 2×10^{18} cm⁻³ is very close to the recorded value. Additionally, the crater depth measured using a Dektak profilometer, of about 5.85 μm almost coincide with the calculated EC-V depth.

A step-by-step EC characterization of n⁺p (S,Zn), n⁺p (S,Cd), p⁺n (Zn,S) and p⁺n (Cd,S) InP structures, fabricated by thermal diffusion, as a function of processing parameters has helped us not only to improve the fabrication process of diffused structures but also to predict the J_{sc} and V_{oc} values of solar cells made from these structures.

For performing such an extensive experimental task EC techniques are much faster and could be more reliable as compared to solid-state techniques. They allow one to study not only the global picture of one of the characteristics of interest as is the case with most of the solid-state techniques but also the variation of these characteristics at different depths throughout the structures.

A significant improvement in the quality of n⁺p and p⁺n InP structures fabricated by closed-ampoule thermal diffusion was obtained after optimizing the diffusion processing using EC techniques for step-by-step characterization of these structures. The investigation was designed to establish: (i) a proper surface preparation procedure prior to diffusion for the substrates; (ii) the right dopant for the

substrates and the right diffusant; (iii) the nature and thickness of the diffusion cap layer; (iv) diffusion temperature and amounts of source materials for doping the substrates below the solubility limit of the doping species; (v) diffusion time for obtaining a desired junction depth; (vi) temperature difference between the substrates and source zones; (vii) thickness of the front dead layer, and (viii) the post-diffusion surface preparation procedure for the removal of the front damaged layer of the surface so as to obtain smooth passivated surfaces with good electrical characteristics.

As an example, a significant reduction of structural defect densities of n^+p and p^+n InP structures was obtained after optimizing the diffusion process, as can be seen in Tables 1 and 2 (ref 6). For n^+p structures, the lowest etch pit density (EPD) of $6 \times 10^5 \text{ cm}^{-2}$ was achieved after S diffusion into InP:Cd ($N_A \sim 1.2 \times 10^{16} \text{ cm}^{-3}$) substrates using a thin $\text{In}(\text{PO}_3)_3$ -rich anodic oxide diffusion cap layer at a diffusion temperature of 660°C , while the lowest EPD after S diffusion into InP:Zn ($N_A \sim 2 \times 10^{16} \text{ cm}^{-3}$) under similar diffusion conditions was $8 \times 10^6 \text{ cm}^{-2}$. For p^+n structures, surface EPD values as low as $2 \times 10^2 \text{ cm}^{-2}$ were achieved in the case of Cd diffusion into InP:S ($N_D = 3.5 \times 10^{16} \text{ cm}^{-3}$) substrates at a diffusion temperature of 560°C using a thin $\text{In}(\text{PO}_3)_3$ -rich chemical oxide diffusion cap layer, while the lowest EPD in the case of Zn diffusion was $3 \times 10^5 \text{ cm}^{-2}$. The differences are explained by the large number of In_2S_3 , InS and Zn_3P_2 surface and deep precipitates detected in the case of n^+p (S,Zn) and p^+n (Zn,S) InP structures.

From the EC characteristics for our diffused structures, we found the ranking in decreasing order of projected maximum efficiency to be: (1) p^+n (Cd,S), (2) n^+p (S,Cd), (3) p^+n (Zn,S), (4) n^+p (S,Zn). The AMO, 25°C efficiency of solar cells fabricated on these structures have confirmed that the maximum efficiency could be obtained in the case of p^+n (Cd,S) solar cells while the worst performances were recorded in the case of n^+p (S,Zn) cells. A preliminary EC investigation of p^+n (Cd,S), n^+p (S,Cd) and p^+n (Zn,S) structures both prior to and after irradiation with 10^{13} cm^{-2} of 3 MeV protons, which includes studies of electrical and structural defect densities and net majority carrier concentration variations in the emitter and the immediate junction proximity of the base, seems to indicate that the same ranking as above holds for radiation tolerance. Therefore, we have lately concentrated our efforts on optimizing the p^+n InP (Cd,S) diffused structures so as to achieve high-efficiency, radiation resistant InP solar cells by this method of junction formation. As a result, the maximum AMO, 25°C open circuit voltage (V_{oc}) values of bare solar cells have reached 880 mV which as far as we know is the highest value reported to date for any InP solar cell (ref 7).

CONCLUSIONS

As a process control tool, EC techniques are faster and of reduced complexity compared to solid-state techniques. In addition, the use of EC techniques allows in-situ recording of a large number of semiconductor characteristics at different depths throughout the structure and, in a multilayer structure, within each layer and at the interfaces.

It is our opinion that EC techniques are or could become more accurate than any known solid-state techniques for performing majority and possibly minority doping concentration depth profilings, as well as for the mapping of structural and electrical type defect densities as functions of depth.

Using improved EC characterization techniques for step-by-step optimization of n^+p and p^+n InP diffused structures has made it possible to fabricate high performance homojunction InP structures.

REFERENCES

- [1]. T. Ambridge and D. J. Ashen, Electron Lett. 15, 674 (1979).
- [2]. R. T. Green, D. K. Walker and C. M. Wolfe, J. Electrochem. Soc. 133(11), 2278 (1986).
- [3]. Maria Faur, Mircea Faur, Patent pending (1992).
- [4]. Maria Faur, Mircea Faur, I. Weinberg, M. Goradia, and C. Vargas, Proceedings of the 11th SPRAT Conference, May 7-9, 1991, p. 7-1.
- [5]. Mircea Faur, Maria Faur, F. Honey, C. Goradia, M. Goradia, D. Jayne and R. Clark, J. Vac. Sci. Technol. B10 (4), 1277 (1992).
- [6]. Mircea Faur, Maria Faur, C. Goradia, M. Goradia, and I. Weinberg, Proceedings of the 4th Int. Conf. on InP and Related Materials, Newport, Rhode Island, April 20-24, 1992, p. 322.
- [7]. Mircea Faur, Maria Faur, C. Goradia, M. Goradia, D. J. Flood, D. J. Brinker, I. Weinberg, C. Vargas, and N. S. Fatemi, this Conference.

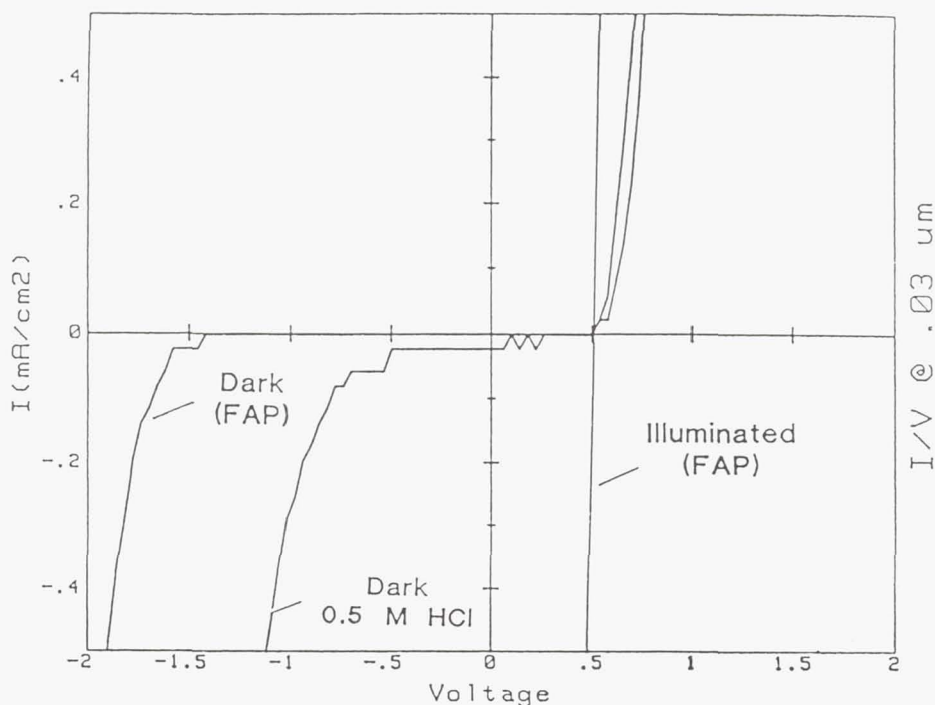


Figure 1. I-V characteristics of p⁺n InP/electrolyte after removing 0.03 μm from the surface using 0.5M HCl and the FAP electrolytes.

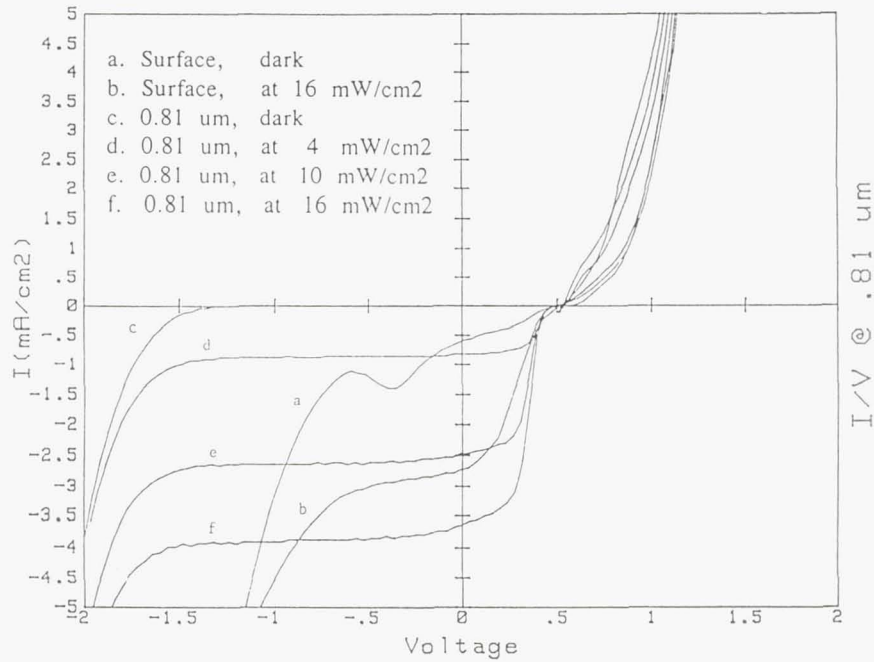


Figure 2. Dark and illuminated I-V characteristics of $p^+n(\text{Cd,S})$ InP/FAP electrolyte junction prior to and after the removal of $0.81 \mu\text{m}$ from the surface.

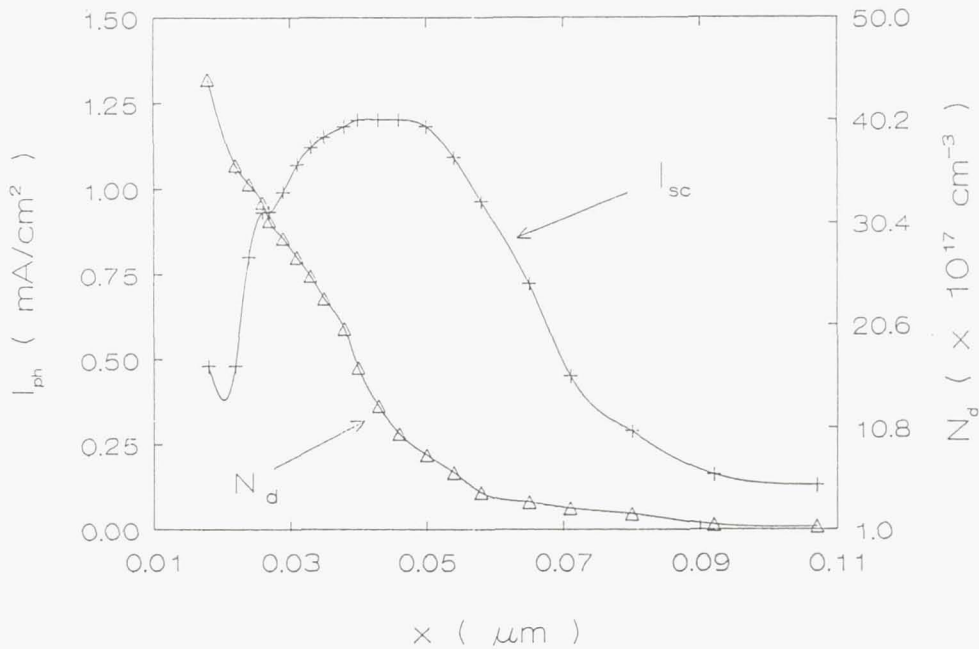


Figure 3. Variation of J_{sc} and net majority carrier concentration (N_D) as a function of dissolution depth of an optimized $n^+p(\text{S,Zn})$ InP structure. Diffusion temperature: 600°C ; Diffusion time: 3 hours. Normalized amounts of source and red P: $200 \mu\text{g In}_2\text{S}_3/\text{cm}^3$ and $75 \mu\text{g P}/\text{cm}^3$.

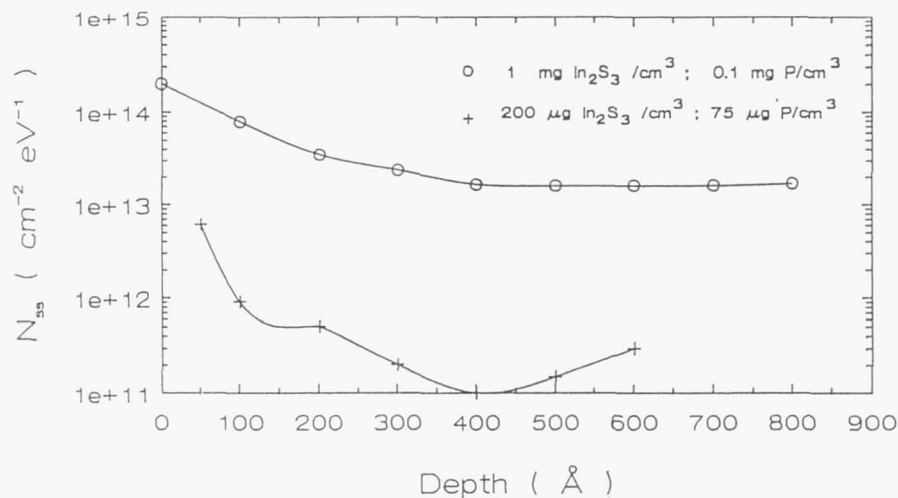


Figure 4. Surface state density (N_{ss}) after anodic dissolution of n^+p InP structures made by S-diffusion into Zn-doped ($N_A = 8 \times 10^{15} \text{ cm}^{-3}$) substrates. Diffusion temperature: 660°C ; Diffusion time: 3 hours.

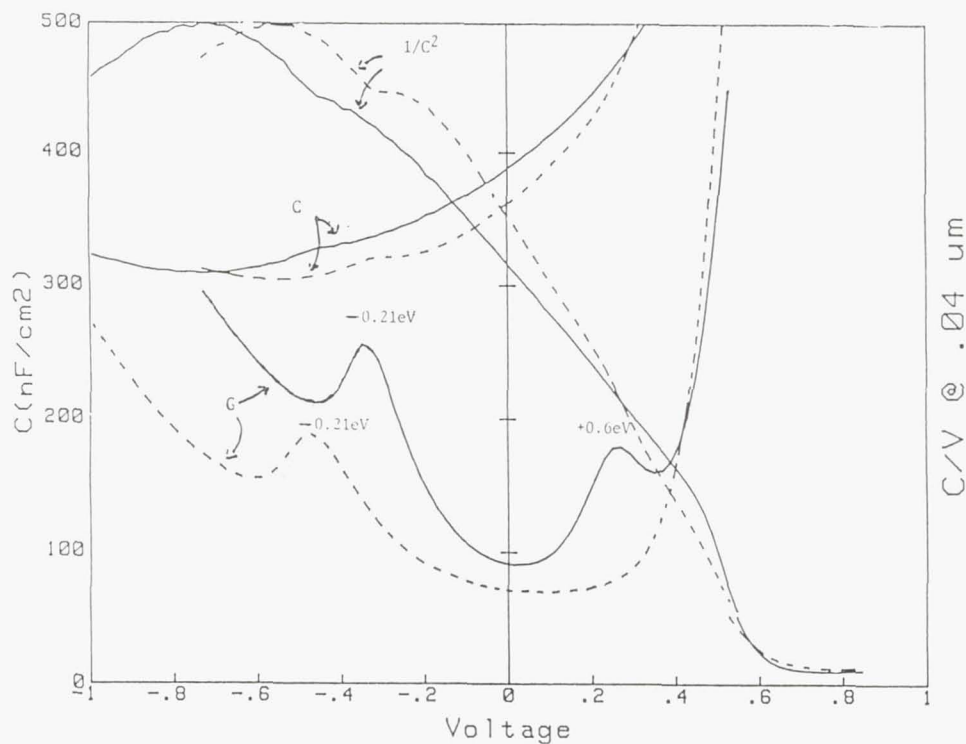


Figure 5. Electrochemical C-V, G-V, and $1/C^2$ -V plots before (solid line) and after (dashed line) removal of $0.04 \mu\text{m}$ from the surface of a $p^+n(\text{Cd,S})$ InP thermally diffused structure.

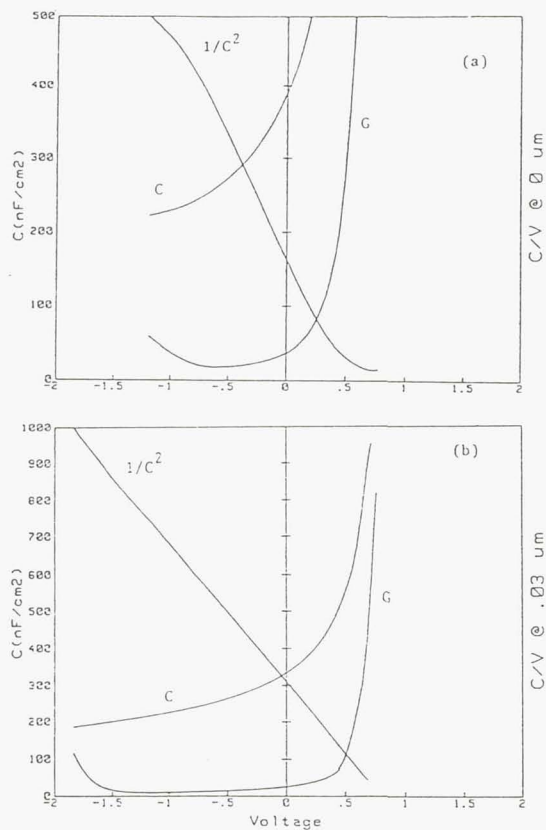


Figure 6. Electrochemical C-V, G-V, and $1/C^2$ -V plots: (a) prior to and after removing $0.03 \mu\text{m}$ from the surface of an optimized $p^+n(\text{Cd,S})$ InP structure.

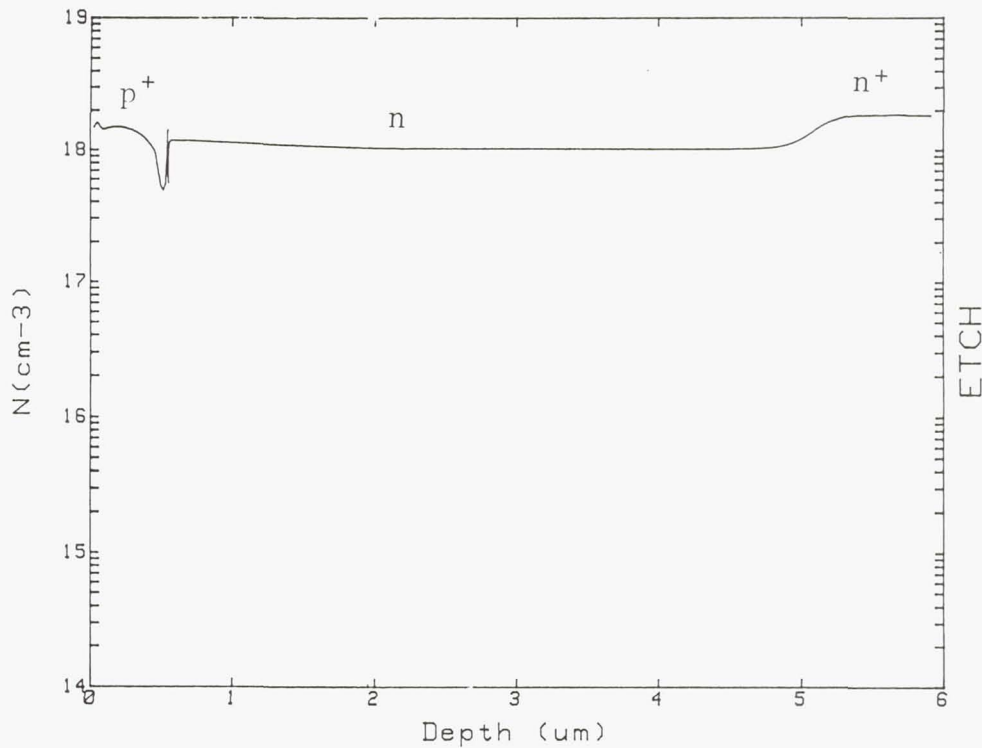


Figure 7. EC-V net carrier concentration depth profile of an epitaxially grown p^+nn^+ InP structure.

Table 1. Surface EPD and precipitates of n^+p InP structures diffused at 660°C through bare and capped surfaces.

Structure	Diffusion Cap	Surface EPD (cm^{-2})	Surface Precipitates	Deep
n^+p (S,Zn)	Bare	6×10^8	In_2S_3	ZnS
n^+p (S,Cd)	Surface	3×10^7	In_2S_3	--
n^+p (S,Zn)	$\text{In}(\text{PO}_3)_3$	8×10^6	In_2S_3	--
n^+p (S,Cd)	($\approx 50\text{\AA}$)	6×10^5	In_2S_3	--

Table 2. Surface EPD and precipitates in p^+n InP structures.

Structure	Diffusion Cap	Diffusion Temp ($^\circ\text{C}$)	Surface EPD (cm^{-2})	Surface Precipitates	Deep
p^+n (Zn,S)	Bare	520	5×10^7	Zn_3P_2	Zn_3P_2
p^+n (Cd,S)	Surface	560	7×10^5	Cd_3P_2	--
p^+n (Zn,S)	$\text{In}(\text{PO}_3)_3$	520	3×10^5	Zn_3P_2	Zn_3P_2
p^+n (Cd,S)	($\approx 40\text{\AA}$)	560	2×10^2	--	--

ACTIVATION ENERGY AND CAPTURE CROSS SECTION OF MAJORITY CARRIER TRAPS IN Zn DOPED InP

GEORGE RYBICKI# AND WENDELL WILLIAMS*

PHOTOVOLTAICS BRANCH NASA LEWIS RESEARCH CENTER

* DEPARTMENT OF MATERIALS SCIENCE AND ENGINEERING
CASE WESTERN RESERVE UNIVERSITY

Schottky barrier diodes were fabricated on Zn doped InP Wafers. The diodes were radiation damaged with 2 MeV protons to a dose of $2 \times 10^{12} \text{cm}^{-2}$. The damage was analyzed by DLTS (deep level transient spectroscopy) using the double correlation technique. Capture cross sections were measured directly. Two major defects were observed in the DLTS spectra. The first defect, was H4 at $E_v + 0.29 \text{ eV}$, with capture cross section $1.1 \times 10^{-17} \text{cm}^2$. The second defect, was H5 at $E_v + 0.53 \text{ eV}$. Its capture cross section varied with temperature as described by the relationship $\sigma = \sigma_0 \exp^{-E/kT}$ where $\sigma_0 = 1.3 \times 10^{-19} \text{cm}^2$ and $E = .08 \text{ eV}$. This relationship yields a σ of $5.9 \times 10^{-21} \text{cm}^2$ at room temperature. The surprisingly small capture cross section of H5 and its temperature dependence are discussed in terms of the multiphonon emission process for carrier capture at the defect. The advantages of the improved experimental techniques used are also discussed.

INTRODUCTION

Deep Level Transient Spectroscopy (DLTS) has been widely used in studies of electrically active defects in semiconductors. A DLTS analysis can tell whether a defect is a majority or minority carrier trap, the defect energy level, its capture cross section and the trap concentration. However DLTS has some limitations. A suitable diode sample is required for the analysis. High quality ohmic and or Schottky contacts are required. The sample must be of limited capacitance and low resistance (1), the junction or barrier must have very small leakage current (2), and the concentration of electrically active defects must be limited (3).

A DLTS analysis is performed using a diode sample, pulse generator, DC power supply and capacitance meter. The sample is reverse biased to deplete the region below the contact of carriers. A pulse generator is used to inject carriers into the depletion region. At the end of the injection pulse the sample capacitance returns to its quiescent value rapidly if no traps are present. If there are traps in the depletion region, they will capture carriers during the injection pulse and then emit the trapped carriers in a thermally activated process at its end. This causes a slow return to the quiescent capacitance or a capacitance transient. The analysis of this transient yields the defect parameters.

The magnitude of the capacitance transient is related to the charge trapped and thus the concentration of the defect. The following relationship was derived by Lang (4).

$$N_t / N_d = 2 \Delta C / C_0 ,$$

where N_t is the trap concentration, N_d is the doping concentration, C_0 is the quiescent capacitance and ΔC is the magnitude of the capacitance transient.

The carriers trapped at the defect are thermally excited from the defect level. The emission rate of carriers is described by the following relation (4).

$$\varepsilon = (\sigma v N/g) \exp^{-E/kT},$$

where ε is the emission rate, σ is the capture cross section, N is the density of states, v is the thermal velocity, g is the degeneracy of the level, E is the activation energy, k is Boltzman's constant and T the absolute temperature.

The capacitance transient decays exponentially as the carriers are emitted, and the time constant of the decay is analyzed to determine the trap parameters. The transient is normally monitored by correlators which respond to the time constant with which the transient decays. The analysis is carried out by varying the temperature from liquid nitrogen or helium temperature to room temperature with 3 or more different correlator time constants. This allows the fixing of an emission rate and temperature at which it is occurring. A plot of $\ln \varepsilon / T^2$ versus $1/T$ has a slope of E/k and from the intercept the apparent capture cross section can be extracted.

The speed, sensitivity and simplicity of DLTS have led to its application to a large number of systems. A large number of DLTS articles are available in the literature. Unfortunately many of the results may have been compromised by poor technique and by some of the intrinsic assumptions made in the analysis.

The limitations of the technique are associated with the characteristics of the depletion region near the contacts. Figure 1 shows the depletion region in the area below the contact. The conduction band and valence bands, Fermi level and defect levels are shown. It is apparent that the occupancy of some of the traps cannot be changed. These traps will always be above the Fermi level due to the band bending. The deeper the trap the larger the fraction of traps affected. A correction must be applied to the defect concentration calculation or the trap concentration will not be accurately measured (5).

A second effect involves the carrier concentration near the edge of the depletion region. Near the edge of the depletion region band bending results in a carrier concentration that varies and is less than that in the bulk. The change in carrier concentration affects the carrier capture properties in that region. This phenomenon is called the Debye tail effect (6). The strong electric field near the junction may also affect capture and emission (7). The electric field is a maximum at the contact or junction. The high field may result in tunneling of carriers out of deep levels in addition to the expected thermally activated emission. The magnitude of the field varies across the depletion region and may cause a variation in emission rates across the depletion region. Both of these phenomena may result in non-exponential capacitance transients.

The above mentioned complications may affect both the measured activation energy of a defect and its apparent capture cross section. The method of estimating the capture cross section from the intercept of an activation energy plot can be compromised if the capture cross section varies with temperature, and the values thus obtained should be treated with caution unless verified by direct measurements.

A direct measurement of the capture cross section can be made by varying the injection pulse width at a fixed temperature during a DLTS measurement (8). A plot of the variation of the magnitude of the capacitance transient versus injection pulse width will have a slope equal to

$$M = \sigma v N_d,$$

where M is the slope, σ is the capture cross section, v is the thermal velocity of the carriers and N_d is the dopant concentration. A plot of $\ln \sigma$ versus $1/T$ will reveal the true capture cross section and, if measurements are made over a range of temperatures, any activation energy associated with it.

Both activation energy and capture cross section measurements can be influenced by non-exponentiality in carrier capture and emission phenomena. In most cases this is associated with the extremes of the depletion region. These regions can be avoided by using Double Correlation Deep Level Transient Spectroscopy (DDLTS) (9). In DDLTS two pulse generators are used to generate two fill pulses

of different magnitudes, but neither completely collapses the depletion region. The transients are analyzed using two correlators whose outputs are subtracted. The resulting signal is due only to traps in the center of the depletion region. This technique thus avoids the Debye tail region and minimizes the effect of a varying electric field across the depletion region. In the present case the improved DDLTS technique was used to study proton radiation damage in p-type Zn doped InP.

EXPERIMENTAL

Schottky barrier diodes were fabricated on Zn doped p-type Inp wafers. The wafers were grown by the CZ process and had a carrier concentration of $2.5 \times 10^{16} \text{cm}^{-3}$. Contacts were electron beam evaporated, Au for the Schottky contact and Au-Zn alloy with a subsequent heat treatment for the ohmic contact. The diodes were characterized by IV, CV and DLTS; no traps were present in the as processed diodes. The diodes were radiation damaged, at room temperature, using 2 MeV protons to a dose of $2 \times 10^{12} \text{cm}^{-3}$. Current was limited to 2 nA to limit sample heating. The diodes were then analyzed by CV, DLTS and DDLTS techniques. DLTS spectra were taken at -4 volt bias with a 4 volt fill pulse. DDLTS spectra were taken at -6 volt bias with 2 volt and 4 volt fill pulses. The values obtained for trap concentration, activation energy and capture cross sections are contained in Table 1.

RESULTS

Analysis of the diodes after radiation revealed significant carrier loss. Before radiation the mean carrier concentration was $N_d = 2.6 \times 10^{16} \text{cm}^{-3}$, post radiation carrier concentration was $N_d = 1.3 \times 10^{16} \text{cm}^{-3}$. The loss was then $1.3 \times 10^{16} \text{cm}^{-3}$ or 6500 cm^{-1} . This result falls somewhere between that for 500 KeV protons, 8400 cm^{-1} , and 3 MeV protons, 1400 cm^{-1} , as reported by Weinberg et al (10). The values however, must be compared carefully, due to the different diode structures used in the experiments.

Figure 2 is a typical spectrum taken during DLTS analysis. Spectra obtained during both DLTS and DDLTS were analyzed and the data appears in Table 1. Two traps were present in the spectra. The peak appearing at lower temperature had an activation energy of $E_v + 0.33 \text{ eV}$ as determined by DLTS and $E_v + 0.29 \text{ eV}$ as determined by DDLTS. This energy level is consistent with the trap H4 at $E_v + 0.37 \text{ eV}$, as obtained by standard DLTS, in the literature (11). The defect H4 was present at an average concentration of $4.5 \times 10^{14} \text{cm}^{-3}$ as determined by DDLTS.

The apparent capture cross section of the defect H4 has been reported to be $8 \times 10^{-16} \text{cm}^2$ as determined by the intercept method. The capture cross section determined from the activation energy plot intercept was $6.3 \times 10^{-16} \text{cm}^2$ using DLTS and $1.1 \times 10^{-16} \text{cm}^2$ using DDLTS. The data however varied considerably from sample to sample and much more so than the activation energies.

Direct measurements of the capture cross section of H4 were not attempted previously due to the limited pulse width generation ability of most DLTS equipment (12,13). This limitation has been overcome in this case by interfacing a high speed external pulse generator to the DLTS equipment. Pulses as narrow as 50 nS could be generated by this method. Using this technique the majority carrier capture cross section of the defect H4 was directly measured to be $1.1 \times 10^{-17} \text{cm}^2$. Capture cross section measurements made at various temperatures showed the capture cross section of H4 to be independent of temperature, as shown by Figure 3.

The peak appearing at higher temperatures in the DLTS spectra was determined to have an energy level at $E_v + 0.60 \text{ eV}$ by DLTS and $E_v + 0.53 \text{ eV}$ by DDLTS. This level is consistent with the defect H5 at $E_v + 0.52 \text{ eV}$ as reported in the literature (11). The defect H5 was present at an average concentration of $3.3 \times 10^{14} \text{cm}^{-3}$.

The apparent capture cross section of the defect H5 has been reported to be $5.5 \times 10^{-15} \text{cm}^2$ (11). The capture cross sections determined by the intercept method were $8.5 \times 10^{-14} \text{cm}^2$ using DLTS and $1.6 \times 10^{-14} \text{cm}^2$ using DDLTS, both with significant variation from sample to sample.

Direct measurements of the capture cross section of H5 have been performed. These measurements differ widely from the apparent cross section. Bretagnon et al have measured a thermally activated majority carrier capture cross section described by the relation

$$\sigma = \sigma_0 \exp^{-\Delta E_0/kT}$$

with $\sigma_0 = 1 \times 10^{-13} \text{cm}^2$ and $\Delta E_0 = 0.27 \text{ eV}$, where σ_0 is the intercept of the $\ln \sigma$ vs $1/T$ plot and ΔE_0 is the activation energy associated with the capture cross section (13). Walters and Summers found a similar temperature dependence with $\Delta E_0 = 0.13 \text{ eV}$ (14). In the present work the capture cross section of H5 was found to be temperature dependent, as seen in Figure 3, with $\sigma_0 = 1.3 \times 10^{-19} \text{cm}^2$ and $\Delta E = 0.08 \text{ eV}$.

DISCUSSION

The defect H4 has been suggested to be a primary defect occurring in the P sublattice of InP. These observations were made after demonstrating an anisotropy in the defect introduction rate when radiation damage was introduced in the crystal along a direction favoring P displacement (15). The activation energy measured by DLTS is in reasonable agreement with the literature value. The value measured by DDLTS is somewhat less. The difference is due to the more favorable carrier capture and emission observed in the center of the depletion region, an advantage of the DDLTS technique.

The directly measured capture cross section was substantially less than the value obtained the intercept method, but in other systems the directly measured values are often an order of magnitude less than those from the intercept method (16).

The defect H5 has been suggested to be a complex of a simple defect and a doping atom, due to the dependence of its observed concentration on the doping level (17). The activation energy of H5 as determined by DLTS is in good agreement with the literature value, the value obtained by DDLTS is again somewhat less. The value obtained by DDLTS is different because is obtained only from traps favorably situated in the center of the depletion region.

The activation energy associated with capture is the cause of the difference between the values of H5 from the indirect intercept technique and direct measurements. The intercept method assumes a capture cross section independent of temperature. The value of σ_0 obtained from the activation energy plot intercept, $5.5 \times 10^{-15} \text{cm}^2$ is vastly different from the intercept of the plot of the $\ln \sigma$, the directly measured values vs $1/T$, $1.3 \times 10^{-19} \text{cm}^2$. In addition, the activation energy associated with capture reduces the capture cross section to $5.9 \times 10^{-21} \text{cm}^2$ at room temperature. Use of the value obtained by the indirect method would lead to an error of six orders of magnitude!

An activation energy associated with capture cross section may also cause errors in the measurement of the trap energy level. The activation energy for capture must be subtracted from the ΔE value obtained for the trap level. The resultant trap level for H5 is $E_v + 0.45 \text{ eV}$.

The difference in the present results of direct measurements of the capture cross section and those of previous authors are a result of limitations associated with the measurement technique. The trap H5 at $E_v + 0.53 \text{ eV}$ is a very deep trap. When attempting to measure the capture cross section of H5 in DLTS a significant region near the contact is affected by the Debye tail effect. Traps near the interface will not be able to capture carriers during the measurement period, or will fill at a rate different than those in the bulk. This can produce a non-exponential transient. These effects are more significant for a deeper traps like H5. In this work the surface region was avoided by measuring the capture cross section of H5 by pulse width variation technique using DDLTS. With this technique capture and emission are more ideally exponential and better values for the extracted parameters are obtained.

The value obtained for the capture cross section of H4 is consistent with the size of a simple atomic defect or πr^2 where r is an atomic radius or 10^{-9} cm . The small value for the capture cross section of H5

and the variation of cross section with temperature shows that carrier capture at H5 is obviously more complicated than at a simple defect.

Henry and Lang have observed small values of capture cross section that vary with temperature in GaP and GaAs and developed the multiphonon emission model (MPE) to explain the results (18). In the multiphonon emission model it is theorized that a large lattice relaxation is associated with capture of a carrier at the defect. This relaxation and the subsequent shift of the defect and energy band minima gives rise to a barrier associated with capture of a carrier at a defect, as shown schematically in Figure 4. The temperature dependence of the capture cross section is related exponentially to this barrier.

$$\sigma = \sigma_0 \exp^{-E_a/kT}$$

The presence of the activation energy barrier reduces the capture cross section below that which would be expected for a simple trap. The energy associated with the capture causes a violent lattice vibration at the defect and is emitted as phonons into the lattice during the damping of this vibration; this feature gives the model its name. This violent lattice vibration may cause defect motion or recombination enhanced defect reactions. These reactions have been observed in InP, GaAs and GaP (19,20).

CONCLUSIONS

By using the DDLTS technique improvements in the measured values of activation energy and capture cross section can be realized. The values for the activation energy of H4 and H5 obtained by DDLTS were less than those obtained by DLTS but in reasonable agreement with the literature values. The DDLTS method is preferable as it minimizes the effect of the Debye tail and junction electric field. The values obtained for capture cross sections however were not in good agreement with the literature. This was partially due to the fact that few direct measurements of cross sections are made and in many studies apparent cross sections are reported. The assumption that the actual capture cross section of a defect is equal to the apparent capture cross section, determined by the intercept of an activation energy plot, is not generally valid. An activation energy associated with capture may cause the capture cross section to be very much different. In addition the activation energy associated with capture cross section must be applied to the activation energy for trap emission or the reported defect energy level will be in error. Direct measurements of capture cross section also displayed much less variation from sample to sample than values from the intercept method. The values of capture cross section for the trap H5 were much smaller than those for the trap H4 and varied with temperature. The properties of the trap H5 are consistent with carrier capture by multiphonon emission.

REFERENCES

1. A.Broniatowski, A.Blosse, P.Srivasta and J.Bourgoin.,J.Appl.Phys.,54,2907(1983)
2. M.Chen, D.Lang, W.Smith, A.Sergent, J.Harbison, Appl.Phys.Lett.,44,790(1984)
3. D.Stievenaard, M.Lannoo and J.C.Bourgoin, Solid State Elec.,28,482(1985)
4. D.Lang, J.Appl.Phys.,45,3023(1974)
5. J.Bourgoin and M.Lannoo, Point Defects in Semiconductors II, Springer-Verlag, NY, NY, (1983)p.167.
6. Y.Zohta and M.Watanabe, J.Appl.Phys.,53,1809(1982)
7. G.Vincent, A.Chantre and D.Bois, J.Appl.Phys.,50,5484(1979)
8. A.Telia, B.Lepely and C.Michel, J.Appl.Phys.,69,7159(1991)
9. H.Lefeverre and M.Schulz, Appl.Phys.,12,45(1977)
10. I.Weinberg, Proc. XII Space Photovoltaic Research And Technology Conf.,Cleveland,Ohio,1992
11. I.Weinberg, Solar Cells,31,331(1991)
12. M.Levinson, H.Tempkin and W.Bonner, J.Elec.Mater.,12,423(1983)
13. T.Bretagnon, G.Bastide and M.Rouzeyre, Phys.Rev.B,41,1028(1990)
14. R.Walters and G.Summers, J.Appl.Phys.,69,6491(1991)
15. A.Sibile, J.Suski and G. Le Roux, Phys.Rev.B.,30,1119(1984)
16. Lang, Ann.Rev.Mater.Sci.,377(1977)
17. M.Yamaguchi and K.Ando, J.Appl.Phys.,60,935(1986)
18. C.Henry and D.Lang, Phys.Rev.B,15,989(1977)
19. D.Lang and L.Kimmerling, Phys.Rev.Lett.,33,489(1974)
20. K.Ando,M.Yamaguchi and C.Umera, Phys.Rev.B,34,3041(1986)

TRAP	Nt cm ⁻³	DLTS ▲E eV	σ_a cm ²	DDLTS ▲E eV	σ_a cm ²	σ_d cm ²	▲E _n eV
H4	4.5 x 10 ¹⁴	0.33	6.3 x 10 ⁻¹⁶	0.29	1.1 x 10 ⁻¹⁶	1.1 x 10 ⁻¹⁷	0
	±0.45	±.04	±7 x 10 ⁻¹⁶	±0.03	±2 x 10 ⁻¹⁶	±3 x 10 ⁻¹⁸	
Lit.		0.37	8 x 10 ⁻¹⁶				
H5	3.3 x 10 ¹⁴	0.60	8.5 x 10 ⁻¹⁴	0.53	1.6 x 10 ⁻¹⁴	1.3 x 10 ⁻¹⁹	.08
	±0.98	±0.03	±9 x 10 ⁻¹⁴	±0.05	±2 x 10 ⁻¹⁴	±2 x 10 ⁻²⁰	±0.01
Lit.		0.52	5.5 x 10 ⁻¹⁵				

Table I: Summary of DLTS, DDLTS, and Capture Cross Section Measurements, σ_a is the apparent cross section and σ_d is the directly measured cross section.

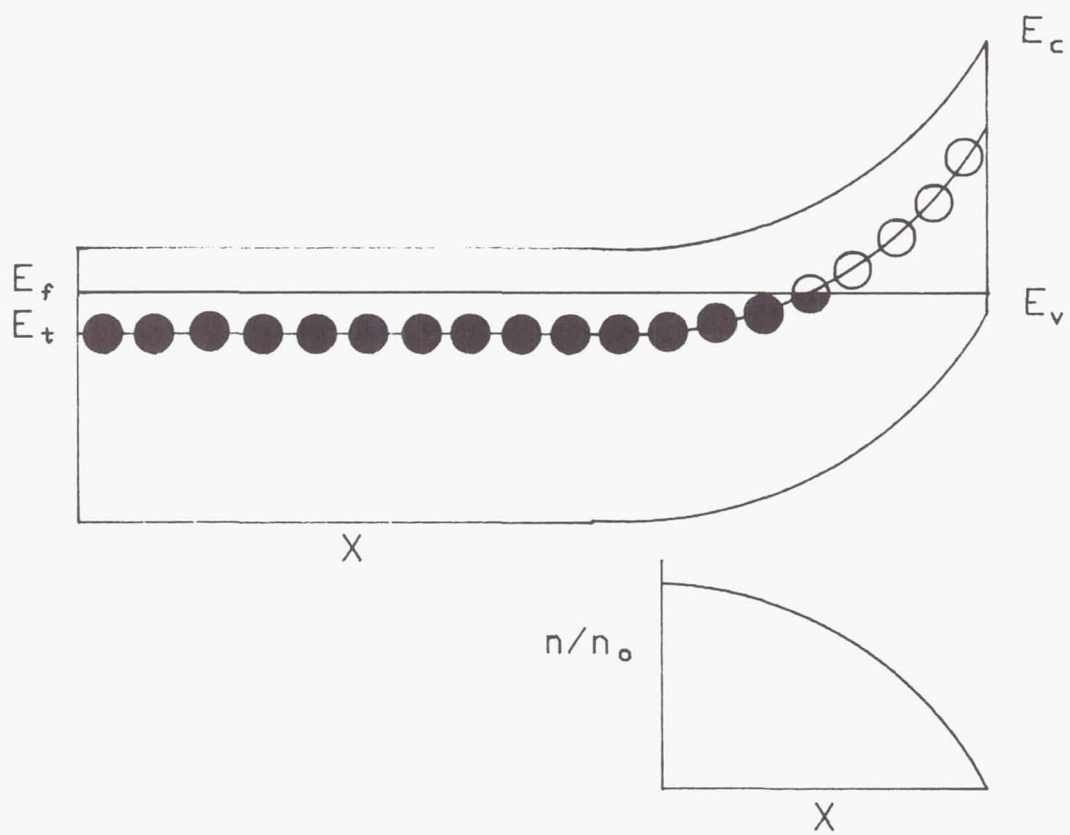


FIGURE 1: DEPLETION REGION AND DEBYE TAIL EFFECT

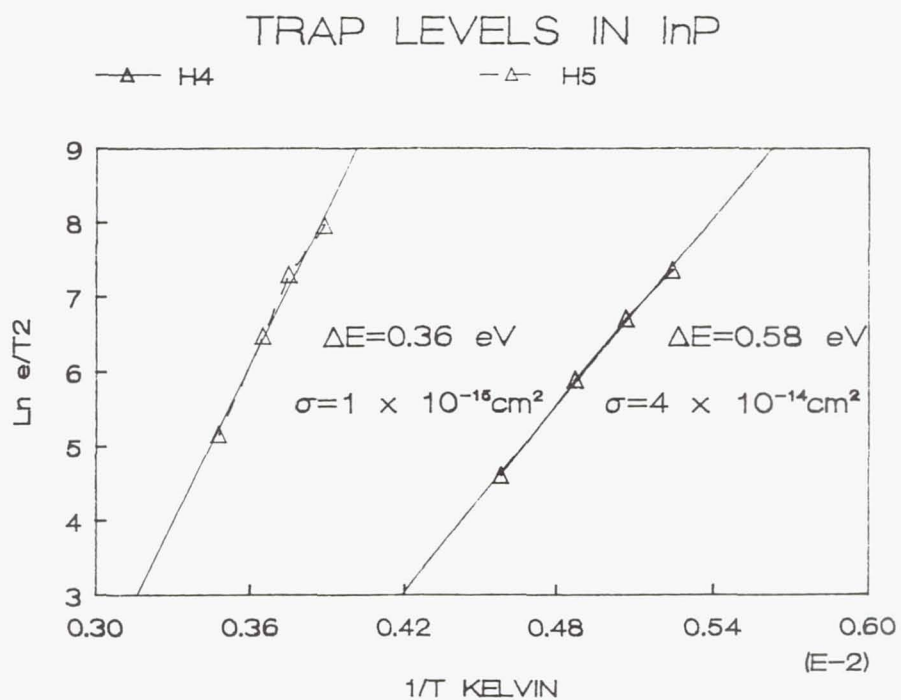
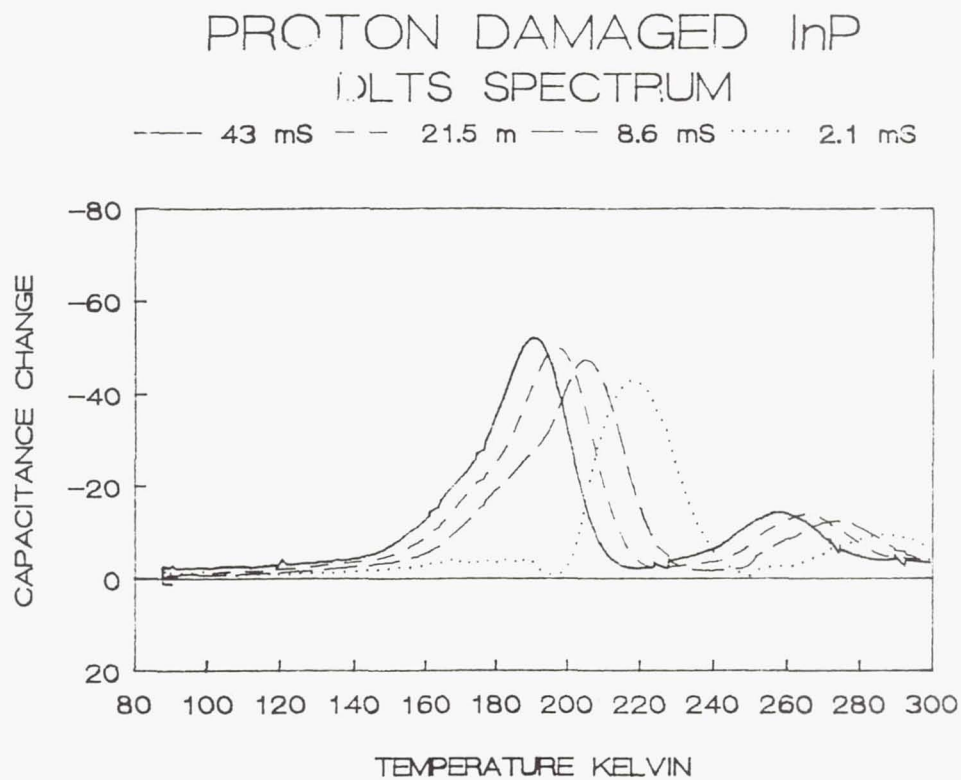
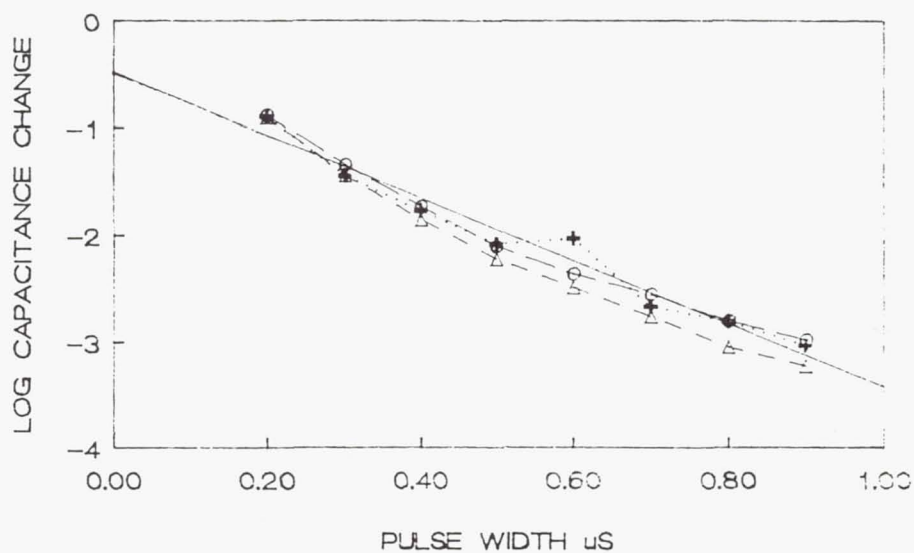


FIGURE 2: DLTS SPECTRUM AND ANALYSIS

CAPTURE CROSS SECTION

H4 IN InP

Δ 21 mS 197 K \circ 8.6 mS 205 K $+$ 2.1 mS 218 K



CAPTURE CROSS SECTION

H5 IN InP

∇ 43 mS 260 K Δ 8.6 mS 275 K \circ 2.1 mS 287 K

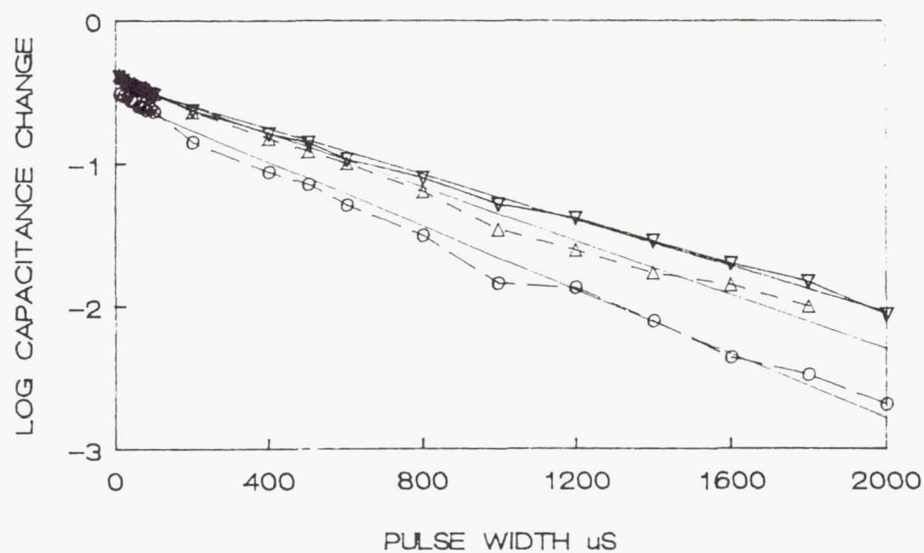


FIGURE 3: CAPTURE CROSS SECTION AND ANALYSIS

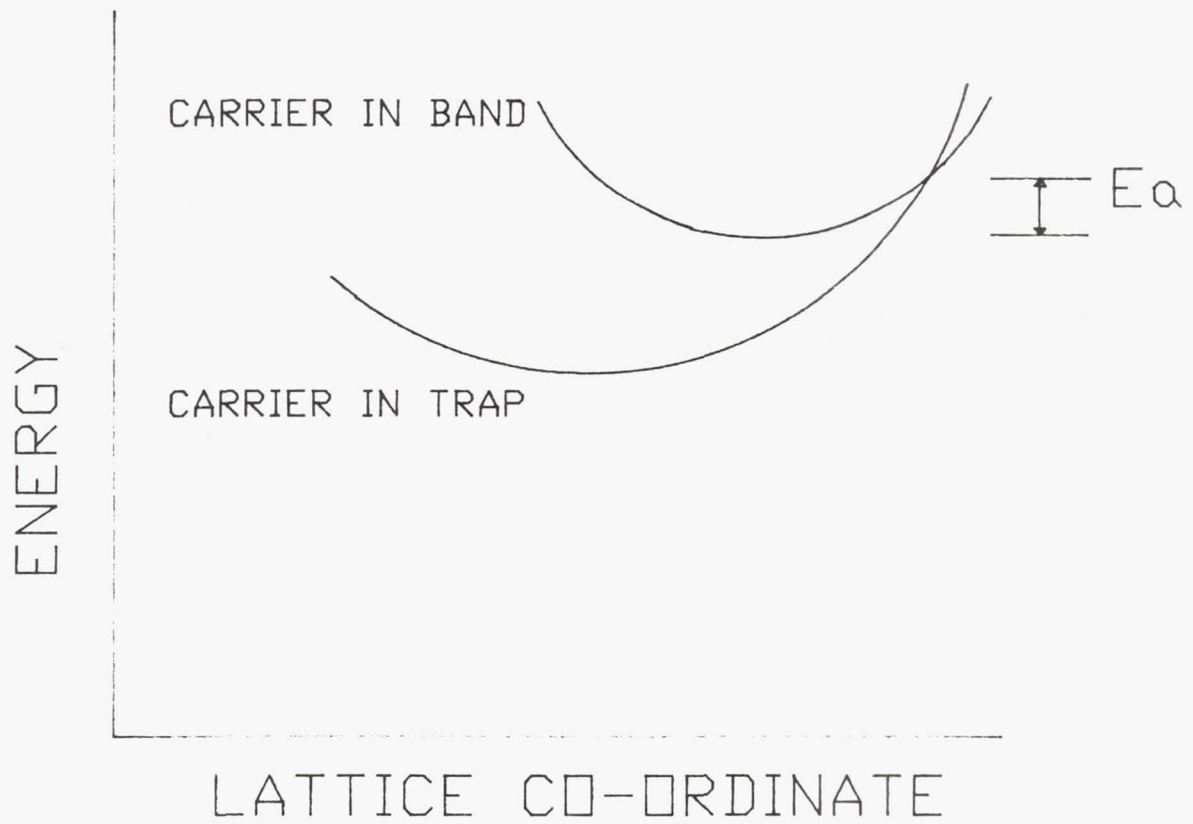


FIGURE 4: SCHEMATIC DIAGRAM OF MPE PROCESS

EFFECTS OF SOLAR CELL ENVIRONMENT ON CONTACT INTEGRITY

Navid S. Fatemi[†] and Victor G. Weizer[‡]

[†]Sverdrup Technology, Inc.

[‡]NASA Lewis Research Center

The III-V semiconductors react extremely rapidly with most commonly used contact metallizations. This precludes the use of elevated temperatures in the contact formation process for solar cells and other shallow junction devices. These devices must rely upon contact metallizations that are sufficiently conductive in their "as-fabricated" state. However, while there are a number of non-sintered metallizations that have acceptable characteristics, the lack of a sintering step makes them vulnerable to a variety of environmentally induced degradation processes. This paper describes the degrading effects resulting from the exposure of unsintered devices to a humid environment and to a vacuum (space) environment. It is shown, further, that these effects are magnified by the presence of mechanical damage in the contact metallization. The means to avoid or prevent these degrading interactions are presented.

INTRODUCTION

It is generally accepted that in forming contacts on shallow junction III-V devices, processing at elevated temperatures should be avoided if at all possible. The benefits attendant to unsintered contacts are an undegraded emitter and a smooth and well defined contact topology. The main drawback to the use of as-fabricated contacts is a higher-than-optimum value of the specific contact resistivity ρ_c . A second disadvantage that is incurred if sintering is avoided is that the unsintered contacts are susceptible to several environmentally induced degradation processes.

Before discussing these, however, let us consider the range of as-fabricated contact resistivities that have been achieved for contacts to n-type InP. Fig. 1 shows the values we have found for various metal combinations on (100) oriented n-type InP, Si doped to $1.7 \times 10^{18} \text{ cm}^{-3}$. The resistivity measurements were made on unsintered devices using the transmission line method (TLM).

As can be seen, the lowest R_c values (in the high 10^{-6} ohm cm^2 range) were found for Au contacts in which a thin (20 Å) layer of Au_2P_3 had been introduced at the InP-Au interface (ref.1). Unfortunately these and other unsintered Au-based contacts are subject to several environmentally induced degradation mechanisms. The first involves a significant increase in the metal-semiconductor interaction rate when the contacts are exposed to a vacuum (space) environment. This phenomenon is common to all Au-contacted III-V semiconductors in which the metal-semiconductor reaction rate is controlled by the vacancy generation rate at the free surface of the contact metallization. Both InP and GaAs are included in this group.

The second degradation process that we will discuss concerns the reaction of ambient humidity with the contact metallization and, ultimately, with the semiconductor substrate. Although both InP and GaAs are affected by this process, there is a fundamental difference between the reactions in these two systems. Let us first discuss the effects of a vacuum environment and then consider the effects of ambient humidity.

VACUUM INDUCED DEGRADATION

A vacuum environment greatly increases the sensitivity of Au-based contacts on both InP and GaAs to thermal excursions. Fig. 2, for example, shows the difference in the degree of pitting in the GaAs surface for two Au-contacted GaAs samples after being heated to 300°C for 8 minutes, one in vacuum and one in a nitrogen ambient. While there is only a hint of activity on the sample annealed in nitrogen, the vacuum-annealed sample is severely pitted. It is estimated that the metal-semiconductor reaction rate was increased between three and four orders of magnitude by performing the heat treatment in a vacuum environment rather than in a gaseous ambient.

The mechanism believed to be responsible for the enhanced reaction rate is based on the fact that, in the early stages of these metal-semiconductor interactions, the group III element (i.e., Ga or In) leaves the semiconductor and enters the Au contact metallization interstitially (ref. 2,3). These interstitial metal atoms then diffuse through the metal until encountering vacant lattice sites on the metal lattice, at which point they enter the vacant sites and take substitutional sites on the metal lattice. The vacancies needed for this reaction are generated at the free surface of the metallization, and it has been shown that both the Au-GaAs and the Au-InP interaction rates are controlled by the rate at which these vacancies are generated (ref. 2,3).

It should be recalled, furthermore, that the generation of a vacancy at the surface of the metallization requires the removal of a near-surface atom from the metallization (thus creating a vacancy) and the placement of that atom on the metal surface. It has been postulated that the continuous kinetic impact of ambient gas molecules on the Au surface inhibits the rate of thermal ejection of these near-surface Au atoms out of the lattice to high energy sites on the surface (vacancy generation) (ref. 2). In this way the vacancy generation rate is enhanced when the impinging ambient gas atoms are removed by placing the sample in a vacuum. The greater the vacancy generation rate, the greater the rate of In (and P) entry into the metallization, and the greater the rate of emitter dissolution/ degradation.

While the metal-semiconductor interaction rate increases significantly when heat treatment takes place in a vacuum environment, the situation is made even worse if, in addition, the free surface of the Au metallization is mechanically disordered. Fig. 3, for instance, shows the drastic increase in GaAs surface pitting that occurred beneath several small scratches that had been made in the Au surface prior to heat treatment (in vacuum) at 300°C for several minutes. Since regions of lattice disorder would be expected to be regions of enhanced vacancy generation, the increased reaction rate is without doubt due to an increase in the vacancy supply in the scratched regions.

It is estimated that if the Au surface contains mechanical damage, thermal excursions (in vacuum) of a few seconds at 300°C or a few tens of minutes at 200°C would seriously degrade devices with junction depths of 0.2 μm or less. Both GaAs and InP would be equally affected.

HUMIDITY INDUCED DEGRADATION

A humid ambient atmosphere also has a detrimental effect on unsintered Au-based contacts on both InP and GaAs (ref. 4,5). After aging for a matter of months in a humid environment, islands have been observed to grow on the metal surfaces of Au contacted InP and GaAs. Figures 4 and 5 are micrographs of the growths observed on Au contacted InP and GaAs, respectively, after prolonged room temperature aging. In both cases the volume of the growths has been shown to be a direct function of the aging time and the humidity level of the ambient atmosphere.

In both cases the islands have a liquid-like consistency as the result of water accumulation by deliquescent compounds that form on the metal surface. It has been determined that the compound that forms on the Au/InP

surface is an indium (group III) based compound, $\text{In}(\text{NO}_3)_3 \cdot x\text{H}_2\text{O}$ (ref. 5). In the case of the Au-GaAs system, on the other hand, the growths have been identified as the group V related compound As_2O_3 (ref. 4). This difference is very important when one considers the potential harm that these phenomena might cause. Let us first discuss the Au-InP system.

The Au-InP System.

As mentioned, the islands on Au/InP have an as-grown liquid-like consistency (Fig. 4). When put in a vacuum, however, as is done for observation in the scanning electron microscope, they become desiccated and revert to the solid $\text{In}(\text{NO}_3)_3$ (Fig. 6). The process by which this compound forms can be understood by considering the details of the Au-InP interaction.

As has been mentioned, the room temperature reaction of Au with InP consists of the entry of both In and P into the contacting metallization. The In atoms enter the Au lattice as interstitials and diffuse rapidly until encountering vacant sites in the Au lattice, at which point they enter the vacant sites and take substitutional positions in the Au lattice. Since the vacant lattice sites are generated only at the free surface of the metallization, the probability of the vacancy-interstitial encounter is greatest there. The resulting In concentration profile therefore reaches a maximum at the free surface of the contact metallization (ref. 3).

Because of this profile, a large number of In atoms are in a position to react with atmospheric oxygen and nitrogen to form the nitrate at the metal-ambient interface. Once formed, the nitrate, because of its deliquescent nature, attracts and adsorbs large quantities of atmospheric water. The water then removes the nitrate from the metal surface by taking it into solution. The action of the water is thus to clear the metal surface so that the process can be repeated over and over again. The entire process is envisioned to continue as long as O_2 , N_2 , and water vapor are available to the Au surface, leading to extensive decomposition of the semiconductor substrate. Fig. 7 illustrates the pitting observed in the surface of an InP sample (Au removed) after eight months at room temperature under normal humidity conditions.

If the above considerations are correct, the rate at which the islands grow should depend on the rate at which In is transported from the InP substrate to the metal-ambient interface, which, in turn, should be dependent on the vacancy generation rate at that interface. We should thus expect to see an enhancement in the rate of nitrate formation if the vacancy generation rate at the Au surface is increased. Evidence that the island growth rate is sensitive to the vacancy generation rate is given in Fig. 8. The free surface of the Au contact metal on the sample shown in the figure had been mechanically damaged (scratched) prior to room temperature aging (increasing the vacancy generation rate in those regions). As can be seen, after several months at room temperature, island growth on the scratched Au surface is substantially greater than on the undamaged portion of the Au surface. Thus both the vacuum induced degradation process and the humidity induced degradation process are affected by the condition of the free surface of the contact metallization.

The Au-GaAs System.

Similar appearing islands have been observed to grow on aged Au-contacted GaAs (Fig. 5). Although the growths appear to be quite similar to those observed in the Au-InP system, even to the extent that they are deliquescent, they are fundamentally different. Compositional analysis indicates that, rather than containing the group III element (Ga), the islands are composed of the group V compound As_2O_3 (ref. 4). The major difference between this system and the Au-InP system, therefore, is that the present reaction does not result in the removal of the group III element from the metallization. Because of this, island growth in the Au-GaAs system should be self limiting. This follows from the fact that in both the Au-InP system and in the Au-GaAs system, the entry of the group III element into the Au contact metallization always precedes the entry of the group V element (ref. 2,3). When

group III atoms stop entering the metallization, the entire reaction stops. In both the Au-InP system and the Au-GaAs system the group III elements diffuse into the metallization until solid solubility limits are reached. At this point the Au lattice can hold no more group III atoms and the reaction stops. In both cases the group V atoms entering with the group III atoms slowly leave the system without reacting (ref. 2,3).

During the humidity induced island growth in the Au-InP system, In atoms are removed from the Au lattice, permitting the entry of additional In atoms from the InP substrate. During island growth in the Au-GaAs system, on the other hand, group V, not group III, atoms are removed from the Au. Since the Au lattice remains saturated with group III atoms, no further dissolution of the GaAs substrate takes place. The only group V atoms that are available to take part in island formation are those liberated before the Au becomes saturated with group III atoms. Thus, in contrast with the Au-InP system, island growth in the Au-GaAs system stops when the Ga content in the Au lattice reaches its solid solubility limit.

ENVIRONMENTALLY STABLE CONTACTS

Vacuum Induced Degradation.

According to the preceding analysis the vacuum induced degradation process operates by enhancing the vacancy generation rate at the free surface of the contact metallization. The metal-semiconductor systems that are susceptible to this type of degradation are those in which the metal-semiconductor interdiffusion rate is controlled by the vacancy generation rate at that surface. If it were possible to alter these systems in such away as to eliminate their vacancy generation rate dependency, the degradation problem would vanish. It appears that this should be possible without too much trouble in both the Au-InP and the Au-GaAs systems.

Studies of both of these systems have shown that the metal-semiconductor interaction rates are vacancy generation rate dependent only if the group III concentrations in the Au contact metallization are less than the solid solubility limits (ref. 2,3). It follows, therefore, that by adding sufficient Ga or In to the Au contact metallization in the Au-GaAs and the Au-InP systems, respectively, to raise the concentrations to their respective limits, the systems will no longer be vacancy generation rate dependent and vacuum degradation will no longer be a problem.

Humidity Induced Degradation.

As we have shown, the humidity problem fortunately only has severe effects on the Au-InP system. It causes a continual flow of In atoms from the InP, through the metallization, to the surface of the metallization where they chemically combine with species in the ambient. The obvious preventative approach would be to stop In entry into the metallization. The use of a saturated solid solution of In in Au (as we did to prevent vacuum degradation) would be effective in preventing more In from entering the Au if it were not for the fact that the In level would continually be lowered below the saturation level as In is leached out by the growing nitrate islands.

Another approach that does hold promise involves the addition of Ga to the Au metallization in amounts that exceed the solubility limit for Ga in Au (~1 at% at 20°C). It has been shown that when Ga is added, a portion of the Ga enters and saturates the interstices of the Au lattice so that no other interstitial species can enter (ref. 1). The addition of Ga, therefore, would prevent In entry into the Au lattice and thus prevent the destructive growth of indium nitrate islands on the surface of the contact metallization. Fig.9 shows a comparison of Auger electron spectroscopy (AES) depth profiles of Au-only and Au-1%Ga on InP heat treated for 40 minutes at 355°C. As shown, even at elevated temperatures, the presence of 1 at% Ga in Au completely suppresses the In out-diffusion from the InP substrate to the Au surface.

Resistivity Improvements.

In the preceding we have suggested ways of eliminating both the vacuum- and the humidity-induced degradation phenomena by adding various amounts of In or Ga to the Au contact metallization. In addition to preventing device degradation, we have found that these additions actually lower the unsintered contact resistivity values. Figures 10 and 11, for example, show the reductions in Au-only and Au-on-Au₂P₃ contact resistivities that are obtained with the addition of various amounts of In or Ga to the Au metallization. As can be seen, order of magnitude reductions are effected.

It is suggested that the cause of the observed resistivity reductions is a change in the In-to-P ratio at the metal-semiconductor interface. When In and P leave the InP and enter the Au metallization, the In atoms rapidly diffuse (interstitially) away from the InP-metal interface. The P atoms, on the other hand, dissipate much more slowly. The result is an interface that is relatively phosphorus rich. There is ample evidence in the literature correlating a P-rich interface with elevated contact resistivity. When In or Ga are added, their main effect is to slow down the rate of In entry, giving the newly entering P atoms time to dissipate. The result is an increase in the In-to-P ratio and thus a reduction in the contact resistivity.

SUMMARY

The major conclusions that can be drawn from the preceding analysis can be summarized as follows:

1. As-fabricated contacts to III-V semiconductors are susceptible to several environmentally induced degradation processes. The degradation is caused by an increase in the metal-semiconductor reaction rate when the cells are placed in a vacuum (space) or humid environment.
2. The increased rate of metal-semiconductor interactions in a humid ambient is self-limiting for contacts to GaAs. In contrast, this reaction rate is not self-limiting, and therefore catastrophic, for contacts to InP.
3. This metal-semiconductor reaction rate is further increased if the surface of the metallization is mechanically damaged.
4. The introduction of small amounts of Ga or In (1-10 at%) into the Au metallization stops the metal-semiconductor interactions, even if the cell is placed in a vacuum or a humid environment or the surface of the metallization is mechanically damaged.
5. Furthermore, The addition of Ga or In to Au effects an order of magnitude reduction in the metal-InP contact resistance.

REFERENCES

1. V. G. Weizer and N. S. Fatemi, "The influence of interstitial Ga and interfacial Au_2P_3 on the electrical and metallurgical behavior of Au-contacted III-V semiconductors," J. Appl. Phys. **6 9**, 8253 (1991).
2. V. G. Weizer and N. S. Fatemi, "The interaction of Au with GaAs," J. Appl. Phys. **6 4**, 4618 (1988).
3. N. S. Fatemi and V. G. Weizer, "The effect of metal surface passivation on the Au-InP interaction," J. Appl. Phys. **6 5**, 2111 (1989).
4. H. Goronkin and D. Convey, "Arsenic polyps on contacts to GaAs," IEEE Trans. Electron. Dev. **ED-36**, 600 (1989).
5. N. S. Fatemi and V. G. Weizer, "Humidity-induced room-temperature decomposition of Au contacted InP," Appl. Phys. Lett. **5 7**, 500 (1990).

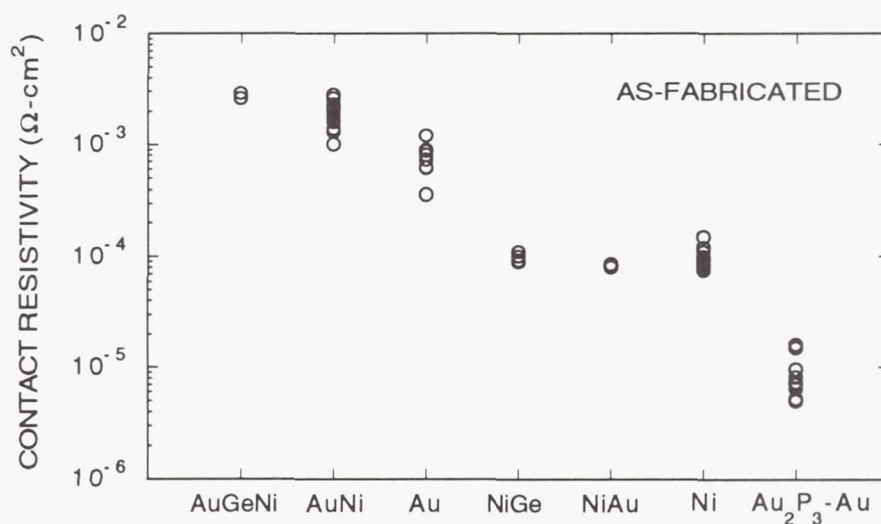


Fig. 1 As-fabricated contact resistivities for various contact systems.

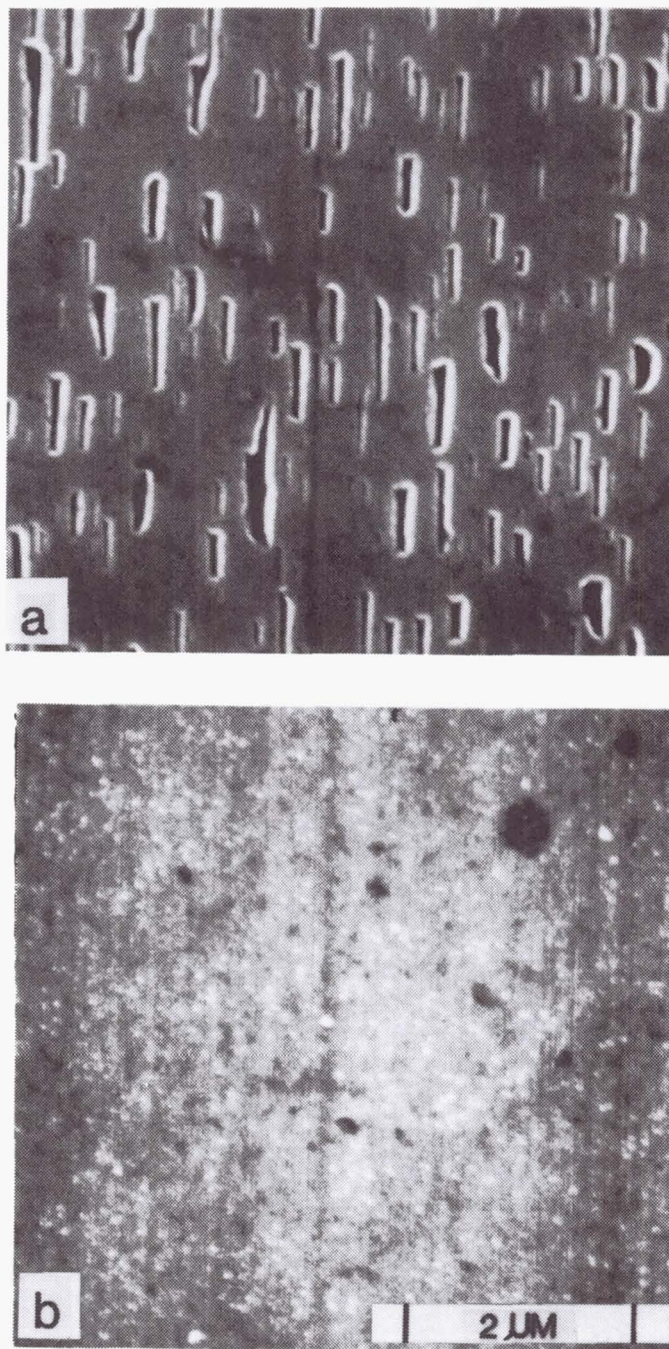


Fig. 2 GaAs surface pitting (Au metallization removed) after 8 min., 300°C heat treatment: (a) in vacuum, (b) in nitrogen.

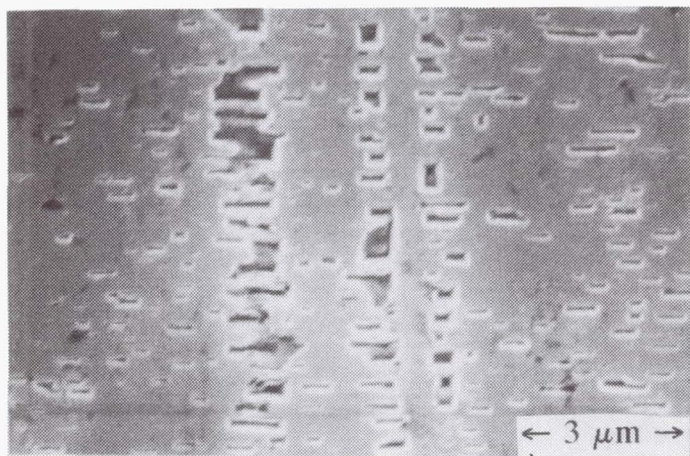


Fig. 3 GaAs surface pitting under three scratches made on Au surface prior to heat treatment at 300°C (8 min.) in vacuum.

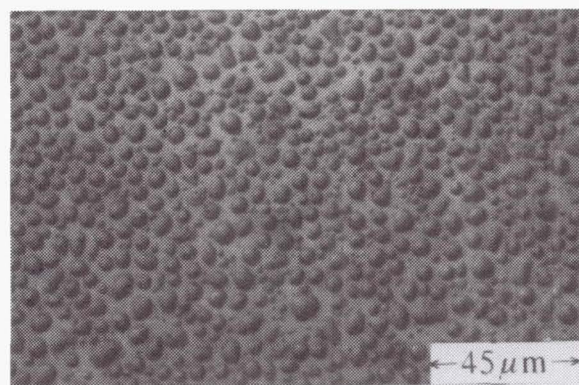


Fig. 4 Light micrograph of growths on Au surface on InP aged at room temperature for 12 mo.

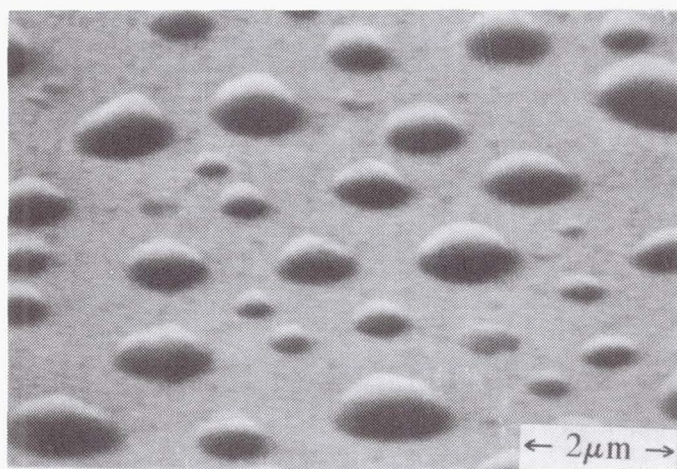


Fig. 5 SEM micrograph of growths on Au surface on GaAs aged at room temperature for 2 yrs.

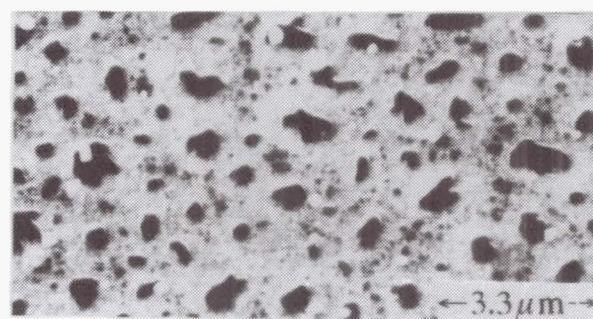
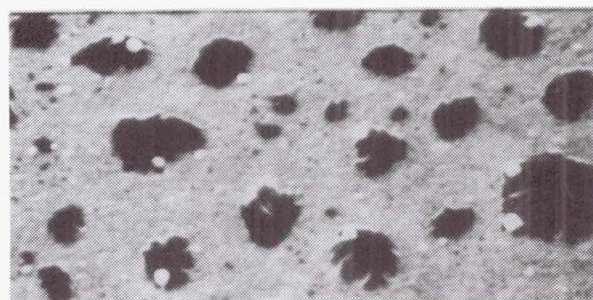


Fig. 6 SEM micrograph of growths on Au surface. Lower: aged for 4 months in ambient humidity. Upper: aged as in lower plus 22 hrs. at 100% humidity.

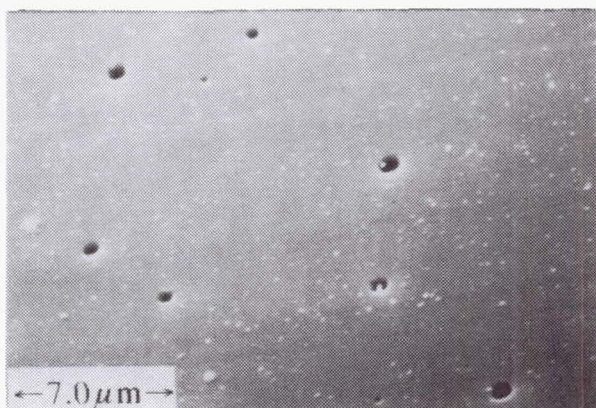


Fig. 7 Pitting in InP surface (Au removed) after aging for 4 months at room temperature in ambient humidity.

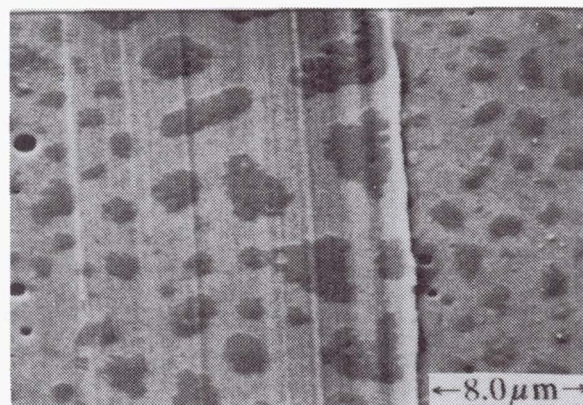


Fig. 8 Effect of mechanically damaged (scratched) Au surface on InP on the rate of island growth.

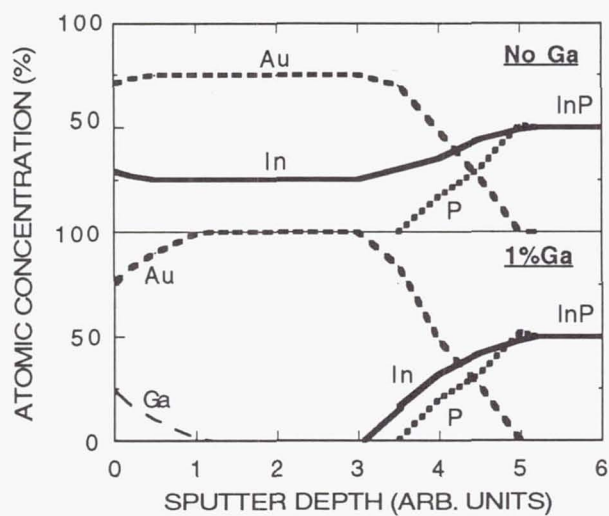


Fig. 9 XPS concentration depth profiles for Au-only (upper) and Au-1 at% Ga (lower) contacts on InP heat treated at 355°C for 40 min.

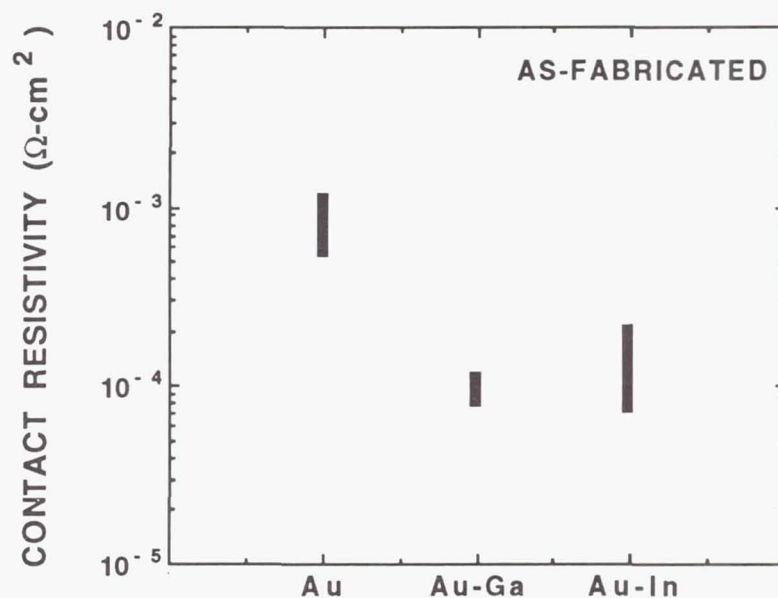


Fig. 10 Measured as-fabricated range of contact resistivities for Au-only, Au-Ga, and Au-In contacts on n-InP.

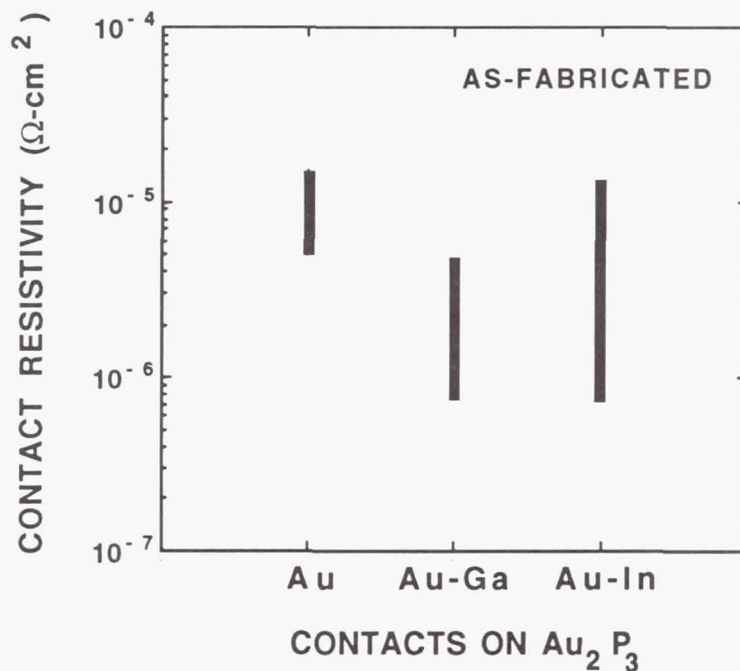


Fig. 11 Measured as-fabricated range of contact resistivities for Au, Au-Ga, and Au-In on Au_2P_3 on n-InP.

MEASUREMENT OF THE MINORITY CARRIER DIFFUSION LENGTH AND EDGE SURFACE-RECOMBINATION VELOCITY IN InP

Roshanak Hakimzadeh^{1,2} and Sheila G. Bailey³

¹Sverdrup Technology, Inc., Lewis Research Center Group, Brook Park, Ohio 44142

²Case Western Reserve University, Cleveland, Ohio 44106

³NASA Lewis Research Center, Cleveland, Ohio 44135

A scanning electron microscope (SEM) was used to measure the electron (minority carrier) diffusion length (L_n) and the edge surface-recombination velocity (V_s) in zinc-doped Czochralski-grown InP wafers. Electron-beam-induced current (EBIC) profiles were obtained in specimens containing a Schottky barrier perpendicular to the scanned (edge) surface. An independent technique was used to measure V_s , and these values were used in a theoretical expression (Donolato, Ref. 12) for normalized EBIC. A fit of the experimental data with this expression enabled us to determine L_n .

I. INTRODUCTION

The minority carrier diffusion length (L) is an important parameter in determining the performance of minority carrier devices, such as solar cells. In the past many different techniques have been used to determine L . Some rely on the measurement of the minority lifetime by means of photoluminescence [1,2]. The scanning electron microscope (SEM) is widely used for the measurement of L . With the SEM a high energy electron beam can be used in a line scan mode to generate a volume of charge carriers within the sample. The advantage of using an electron beam as opposed to other sources of excitation, such as optical [3], is that the volume and depth of generation can be accurately controlled by varying the beam voltage.

In the "normal collector geometry" the p-n junction or Schottky barrier is viewed edge-on. With the SEM in a line scan mode, the electron beam scans the semiconductor perpendicular to the potential barrier (Figure 1). The generated charge carriers can then diffuse to the potential barrier where the electrons and holes are separated and a current, $I(x,z)$, is generated in the external circuit. This current, referred to as electron-beam-induced current (EBIC), reflects the

amount of excess carriers generated. The surface on which the beam impinges acts as a surface recombination path into which the generated minority carriers diffuse and are annihilated. We will refer to the recombination velocity of this surface as the edge-surface recombination velocity, V_s (cm/sec).

If we make the assumption that the electric field outside the junction space charge region is negligible, the transport of the generated minority carriers is purely diffusive. Under this condition, and if $V_s=0$, the EBIC will decrease exponentially with increasing distance, x , from the junction as follows:

$$I(x, z) = I(0) \exp\left(-\frac{x}{L}\right) \Big|_{z=\text{const.}} \quad (1)$$

(For a definition of the coordinate system refer to Figure 1.) A plot of $\log[I(x, z)]$ versus x , therefore, would result in a straight line from which L can be found. If the diffusion length is different on either side of the junction, the slopes will also be different. The plot will go through a peak which occurs at the metallurgical junction, as shown in Figure 2 [4]. In practice, however, V_s cannot be neglected and the plot of $\log[I(x, z)]$ versus x is no longer linear but appears concave upward near the junction, becoming steeper with increasing V_s .

Increasing the electron beam accelerating voltage, V_0 , increases the depth at which the carriers are generated, thereby minimizing the effect of V_s . However, for large beam voltages the electron range, R , may become comparable to the value of L , diminishing the resolution of the technique [5]. Figure 3 shows a plot of R as a function of the beam voltage, V_0 . Throughout this work V_0 was limited to 15 KV.

Several theoretical expressions have been derived for the induced current profile which incorporate the effects of V_s . The first such expression was derived by Van Roosbroeck [6] from the solution of the diffusion problem for a point source of minority carriers at a depth, z , in a semi-infinite specimen. Other papers have been published which refer to Van Roosbroeck [7]. Expressions based on more realistic generation schemes, such as the uniform sphere or the spherically symmetric Gaussian, have also been derived [8-12]. These expressions give the induced current profile in terms of integrals of a modified Bessel function. In limiting cases ($V_s \rightarrow 0$, $V_s \rightarrow \infty$) these lead to analytical expressions of $I(x, z)$ which have exact solutions. However, for arbitrary V_s , these have to be solved numerically.

Donolato derived a simpler expression for $I(x, z)$ through the use of the Fourier transform method [13]. The simplification results from the consideration of a two-dimensional study of the diffusion problem. Hakimzadeh et al. [14] have measured the minority carrier diffusion length in GaAs solar cells by fitting experimentally obtained EBIC

profiles to Donolato's equation. In their study, an independent technique was used for the measurement of V_s as a function of x [15].

In this work we have applied the experimental technique described in [14] to measure electron diffusion length, L_n , in Zn-doped InP materials. A review of the theoretical approach is given in Section II.

II. REVIEW OF THE THEORY

The expression derived by Donolato is shown in Equation 2.

$$\frac{I(x, z)}{I(0, z)} = \frac{2}{\pi} \int_0^{\infty} \frac{K}{\mu^2} \left\{ \exp\left(-\frac{K^2 \sigma^2}{2}\right) - 0.57 \exp\left(\frac{\lambda^2 \sigma^2}{2} - \mu Z_0\right) \right. \\ \left. \times \frac{s}{\mu + s} \operatorname{erfc}\left[\frac{\sigma}{\sqrt{2}} \left(\mu - \frac{Z_0}{\sigma^2}\right)\right] \right\} \sin(Kx) dK \quad (2)$$

where:

$$\lambda = \frac{1}{L} \quad (3)$$

$$\mu = (K^2 + \lambda^2)^{\frac{1}{2}} \quad (4)$$

$$\lambda = \frac{R}{\sqrt{15}} \quad (5)$$

$$s = \frac{V_s}{D} \quad (6)$$

where R is the range of the generation volume in μm , K is the wave-number, D is the minority carrier diffusion coefficient in cm^2/sec , and $I(0, z)$ is the maximum EBIC collected at the junction in amperes. If we assume the generation volume to be a three-dimensional Gaussian, the

range, R , will be given by [16]:

$$R = \frac{0.0276 A V_o^{1.67}}{(Z^{0.889} \rho)} \quad \mu m \quad (7)$$

where V_o is in KV, A is the atomic weight in g/mole, Z is the atomic number of the target, and ρ is the density of the semiconductor in g/cm³. It can be seen that the two unknowns in Equation 2 are L and s .

The technique developed by Watanabe et al. [15] was used to measure s as a function of x . Their Equation is repeated here in our notation:

$$s = \frac{V_s}{D} = \frac{\partial}{\partial Z_o} \ln I(x, z) \Big|_{z_o=0} \quad (8)$$

EBIC profiles were obtained along the same line scan for a number of accelerating voltages, from 4 KV to 15 KV. For each point, x , s was obtained from the slope of the $\ln[I(x, z)]$ versus Z_o plot using Equation 8. A typical plot is shown in Figure 4. The s values obtained in this manner were stored in an ASCII data file. The advantage of working with s rather than V_s is that D need not be known. This eliminates errors resulting from a calculated value of D .

To obtain L_n , EBIC profiles for a 15 KV accelerating voltage were used. A program was written in FORTRAN to perform the integration in Equation 2 by approximating the generation volume by a Gaussian. The accuracy of this program has been checked previously [14]. When running the FORTRAN program the user is prompted for V_o , $I(0, z)$, the names of the ASCII data files containing experimentally obtained $I(x, z)$ and the s values. $I(0, z)$ was calculated by extrapolating the experimental plots of $\log[I(x, z)]$ versus x back to the junction, as described in [14]. The program calculates values of L_n for different points, x , and outputs these to an ASCII data file.

III. EXPERIMENTAL DETAILS

The aim of this work was to measure L_n in InP materials. For this reason Schottky barriers were formed to minimize the effect of processing which may result from junction formation. We used Czochochalski-grown zinc-doped InP wafers with reported carrier densities of $2 \times 10^{16} \text{ cm}^{-3}$ and $1 \times 10^{18} \text{ cm}^{-3}$, purchased from Crystacom. All wafers were of (100) surface orientation with an uncertainty of 2° off axis towards (110). Ohmic contacts were evaporated on the back (unpolished) surface. Gold Schottky contacts (2000 Å thick) were evaporated on the front

(polished) surface in the form of 2.5 mm-diameter dots. The specimens were cleaved to expose the rectifying junction, as shown in Figure 5. SEM sample holders held these specimens in place and made electrical contacts to the front and back of the specimens. EBIC profiles were obtained by scanning the electron-beam along this cleaved edge, and the analysis was carried out as described in Section II.

We observed an unexpected effect which prevented us from measuring L_n in the lower doped materials. This effect and other results will be discussed in Section IV.

IV. RESULTS AND DISCUSSION

We found that in the lower doped specimens EBIC profiles did not decay very much with increasing x implying that charge collection occurs with approximate unity efficiency up to hundreds of micrometers from the Schottky barrier. An example is shown in Figure 6. This effect has been observed before in Si [17] and is thought to be due to an inversion layer which forms as a result of the interaction of the electron beam with the native oxide at the surface. The charge introduced by the electron beam on this surface is annihilated by the nearby holes and results in a negatively charged layer close to the surface. This inversion layer created near the surface results in the collection of the beam-generated minority carriers along the entire length of the scan.

In Si [17] it has been shown that after about 20 successive scans the charge collection efficiency at large distances from the junction is progressively reduced [17], and finally normal behavior is re-established. This was not observed here for InP, even after many more scans.

To alleviate this problem, we attempted to remove the native oxide prior to the SEM characterization by etching the edge surface in a solution of 10% HF [18]. However, even in the vacuum chamber of the SEM (which is $\sim 10^{-5}$ or 10^{-6} Torr) we were unable to keep the oxide layer from building up long enough to make the necessary measurements.

This surface inversion effect was not observed in the higher-doped specimens since they require much more charge at the surface to create an inversion layer. EBIC profiles in these higher-doped specimens decayed with increasing x , as expected. The analysis described in Section II was applied to measure L_n and s as a function of x in these specimens. Typical results are shown in Figure 7.

Figure 7 illustrates that L_n increases sharply as the junction is approached. This is due to the fact that the lateral extension of the generation volume is $\epsilon = 2\sigma = R/2$ [13], therefore Donolato's equation is only applicable for $x \geq R/2$. For $x < R/2$ the effect seen is an artifact since Donolato's equation no longer holds in this region. At large distances, x , L_n is seen to increase again. In these regions the

EBIC measured is very small and comparable in magnitude to the beam current. This results in a large error in the measured values of L_n . We therefore concentrate only in the middle regions where L_n appears to be constant. In these regions the measured values of L_n and s were as shown in Table I. These results are in the right ballpark as compared to previously published results which indicate that for p-type InP with a carrier concentration of $1 \times 10^{18} \text{ cm}^{-3}$ L_n is about $3 \mu\text{m}$ [19]. If we assume that D is a constant in these specimens and is approximately equal to $104 \text{ cm}^2/\text{sec}$, the measured V_n values ranged from 40.86 to $1.80 \times 10^3 \text{ cm/sec}$.

The aim of this work was to measure the L_n values in the bulk. Therefore, it was necessary to ensure that the measured values were not in any way affected by surface defects. The edge surface of some typical samples were etched in concentrated HCl acid for about 15 seconds. This created a uniformly "pitted" surface as shown in Figure 8. It has been shown that etching in concentrated HCl for this length of time removes about $3 \mu\text{m}$ from this edge surface [20].

EBIC analysis was carried out on such treated samples, and L_n and s values were determined as described in Sections II and III. Figure 9 shows the results before and after treatment for a typical sample. It can be seen that although the s values have increased in the treated samples, L_n appears to remain constant.

REFERENCES

1. C.H. Wang, IEEE Trans. Electron Devices, **38** (9), 2169 (1991).
2. P. Jenkins, G.A. Landis, I. Weinberg and K. Lneisel, Proceedings of the 22nd Photovoltaic Spec. Conference (IEEE, New York, 1991), p. 177.
3. F.S. Goucher, G.L. Pearson, M. Sparks, G.K. Teal, and W. Schockley, Phys. Rev., **81**, 637 (1951).
4. D.E. Newbury, D.C. Joy, P. Echlin, C.E. Fiori and J.I. Goldstein, Advanced Scanning Electron Microscopy and X-Ray Microanalysis (Plenum, New York, 1986), p. 65.
5. R.P. Leon, Proceedings of the 19th Photovoltaic Spec. Conference (IEEE, New York, 1987), p. 808.
6. W. van Roosbroeck, J. Appl. Phys., **26**, 380 (1955).
7. C. Hu and C. Drowley, Solid State Electron., **21**, 965 (1978).

8. J.F. Bresse, in Proceedings of the 5th Ann. SEM Symposium IITRI, edited by O. Johary and I. Corvin (IIT Research Institute, Chicago, 1972), pp. 105-112.
9. F. Berz and H.K. Kuiken, Solid State Electron., 19, 437 (1976).
10. C. van Opdorp, Phillips Res. Rept., 32, 192 (1977).
11. T. Fuyuki, H. Matsunami and T. Tanaka, J. Phys. D:Appl. Phys., 13, 1093 (1980); ibid 13, 1503 (1980).
12. G. Oelgart, J. Fiddicke and R. Reulke, Phys. Status Solidi A, 66, 283 (1981).
13. C. Donolato, Solid State Electron., 25, 1077 (1982).
14. R. Hakimzadeh, H.J. Möller and S. Bailey, Proceedings of the 22nd Photovoltaic Spec. Conference (IEEE, New York, 1991), p. 335.
15. M. Watanabe, H.C. Gatos and G. Actor, in Proceedings of the International Symp. on Solar Energy, edited by J.B. Berkowitz and I.A Lesk (Electrochem. Soc. 1976), pp. 283-289.
16. J.I. Goldstein, D.E. Newbury, P. Echlin, D.C. Joy, C. Fiori, and E. Lifshin, Scanning Electron Microscopy and X-Ray Microanalysis (Plenum, New York, 1981), p. 1080.
17. G.A. Hungerfold and D.B. Holt, Microscopy of Semiconducting Materials, Conf. Series Nov. 87, eds A.G. Cullis and P. Augustus, Institute of Physics, Bristol, pp. 721-726.
18. M. Faur, M. Faur, P. Jenkins, M. Goradia, S. Bailey, D. Jayne, I. Weinberg and C. Goradia, Surface and Interface Analysis, 15, 745 (1990).
19. C.L. Chiang, S. Wagner and A.A. Ballman, Mater. Lett. 1, 145 (1983).
20. S. Adachi and H. Kawaguchi, J. Electrochem. Soc., 128, 1342 (1981).

TABLE I. Measured values of L_n and s .

Wafer Number	Sample Number	L_n (μm)	Range of s ($\times 10^3 \text{ cm}^{-1}$)
3	1	0.64	37.42 - 47.71
3	2	1.36	8.86 - 64.87
3	5	0.78	4.25 - 19.28
3	7	0.39	5.74 - 33.61
3	8	0.45	87.25 - 108.33
3	13	0.44	52.73 - 135.03
3	14	0.77	149.52 - 183.08
2	19	0.26	88.71 - 347.23
2	20	0.38	154.08 - 171.57
2	21	0.36	136.76 - 164.21
2	23	0.26	33.17 - 51.47
2	25	0.39	8.50 - 52.12
2	26	0.73	17.16 - 36.93
2	28	0.34	36.18 - 109.68
2	30	0.50	53.43 - 71.73
2	31	0.39	91.50 - 143.46
2	32	0.50	116.02 - 186.98
2	33	0.78	137.09 - 149.02

All wafers had the following specifications:
 Crystacomm crystal #4420, zinc-doped with a carrier concentration of
 $1 \times 10^{18} \text{ cm}^{-3}$.

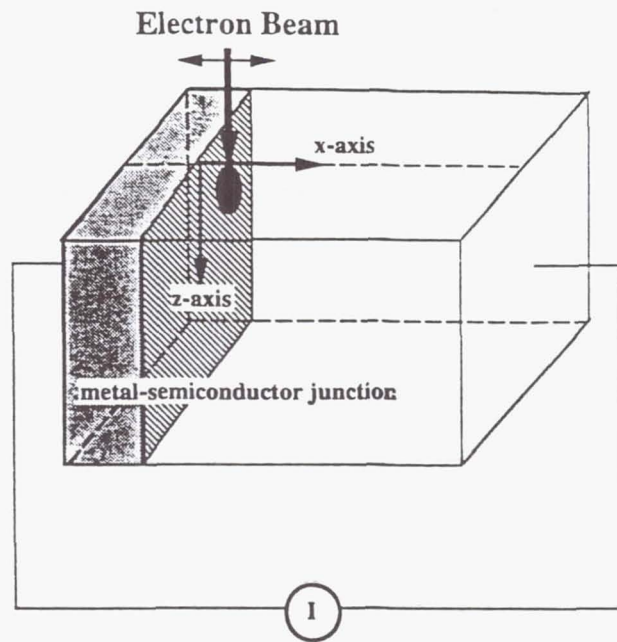


Figure 1. Schematic diagram of the beam-specimen interaction (normal collector geometry).

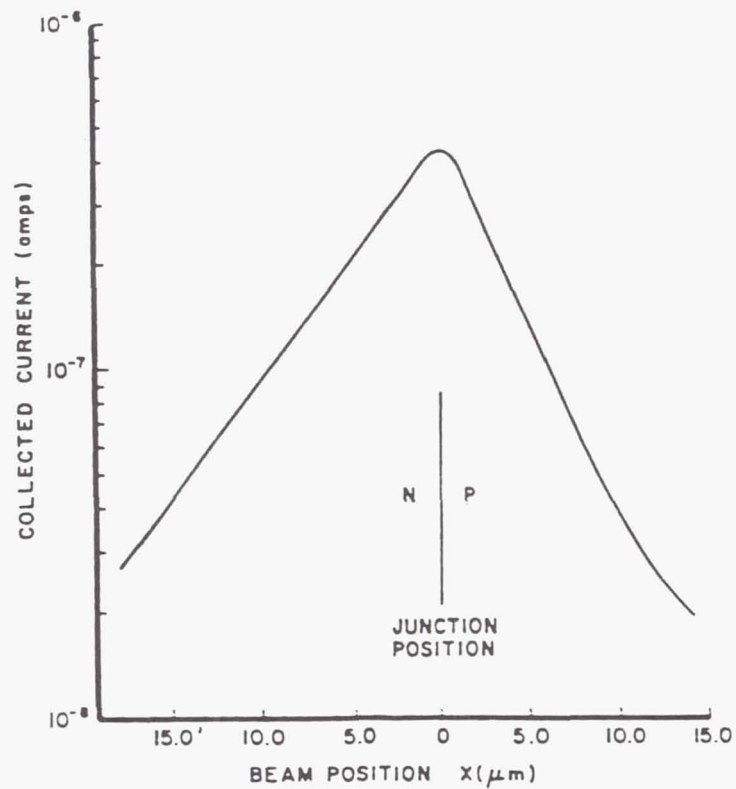


Figure 2. EBIC signal variations around a vertical p-n junction. (Reproduced from [4]).

Dependence of R on V_0

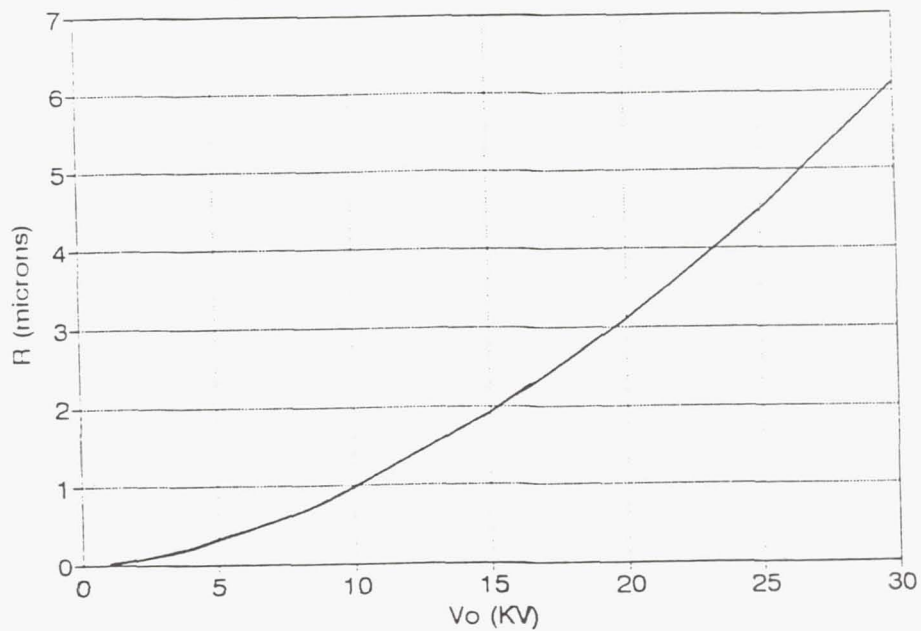


Figure 3. Plot of R as a function of V_0 .

(CRYSTACOMM 4420, SAMPLE #7)

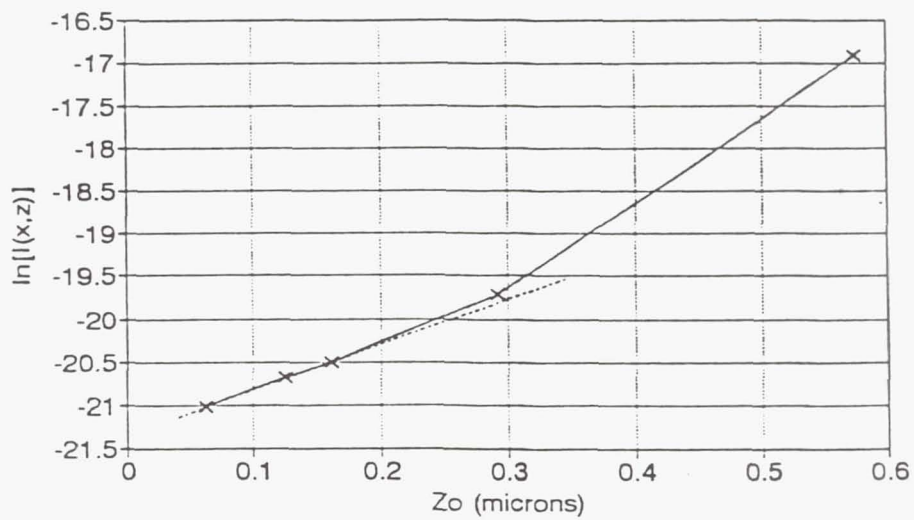


Figure 4. Plot of $\ln[I(x,z)]$ versus Z_0 for a typical sample and for $x = 0.52 \mu\text{m}$.

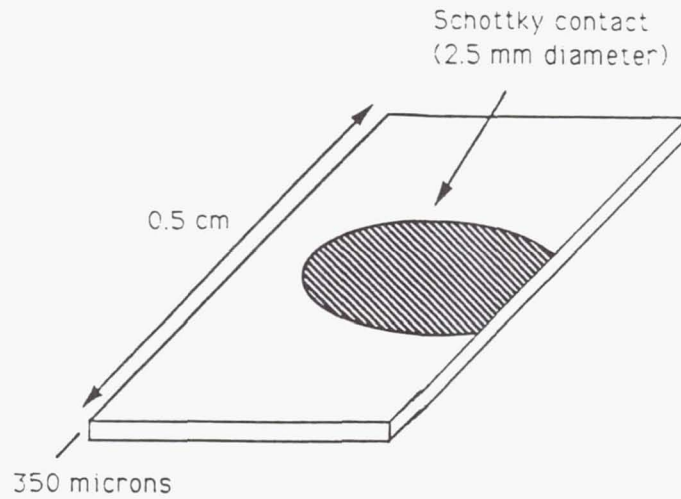


Figure 5. Schematic diagram of a cleaved InP Schottky specimen.

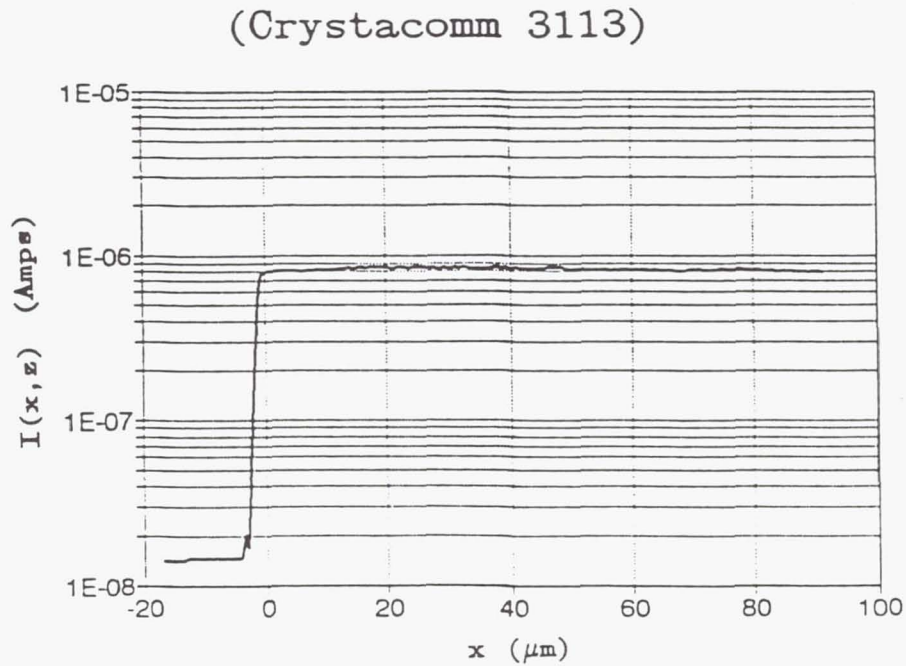


Figure 6. Typical EBIC profile of a specimen with dopant density $= 2 \times 10^{16} \text{ cm}^{-3}$.

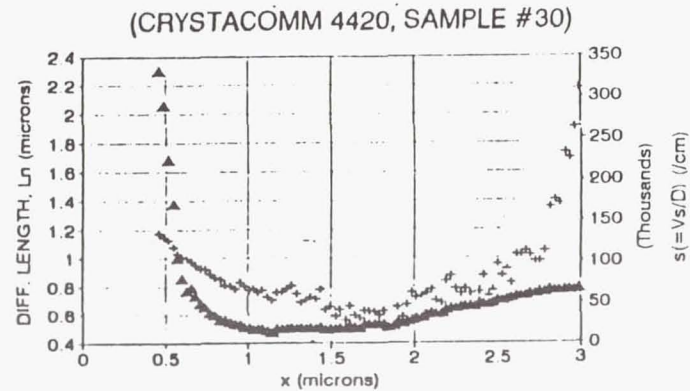
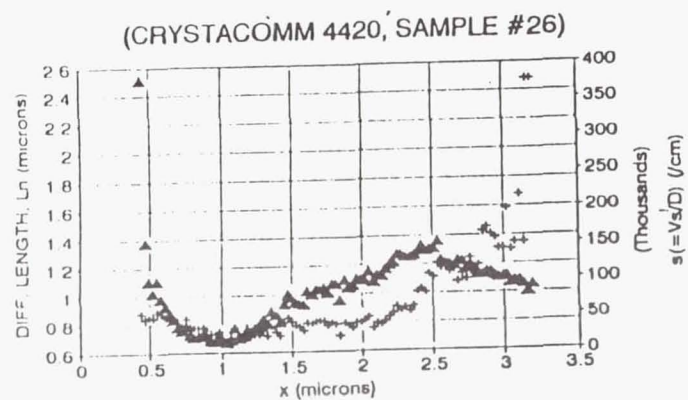
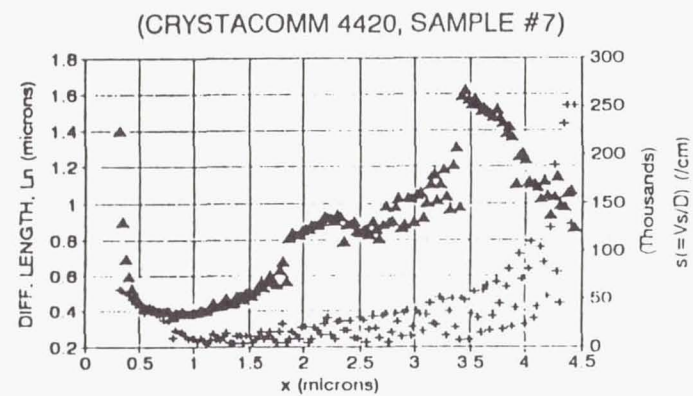
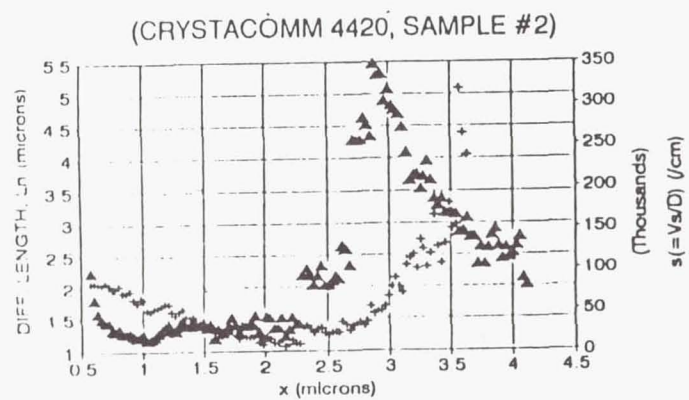


Figure 7. Results obtained for four typical samples. $\Delta = L_n$, $+$ = s .

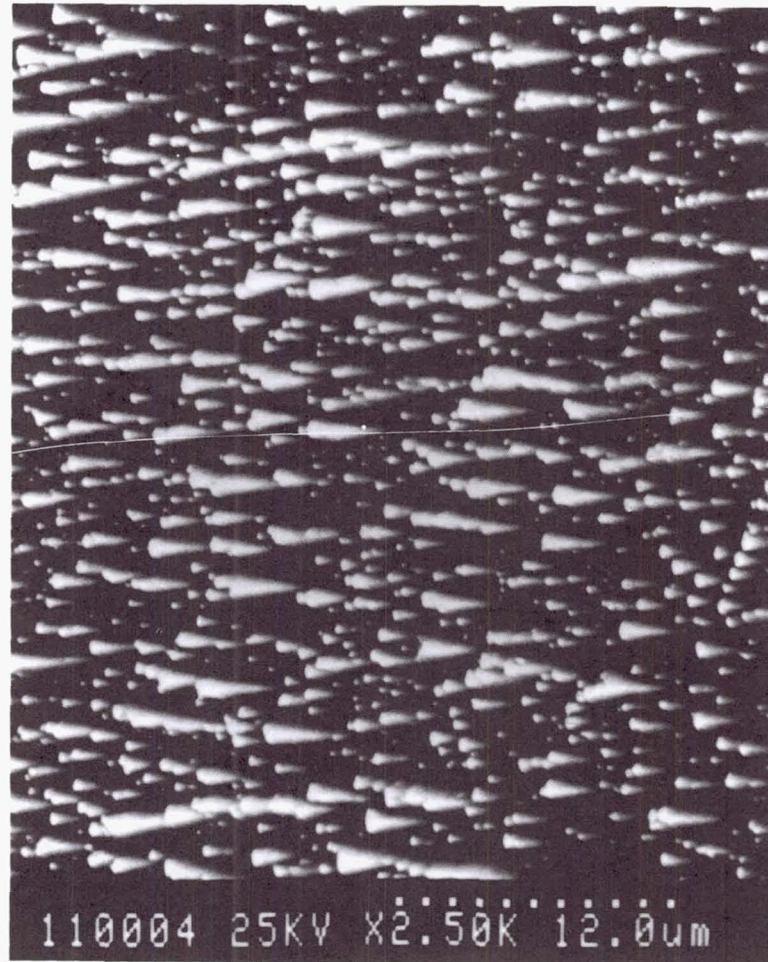
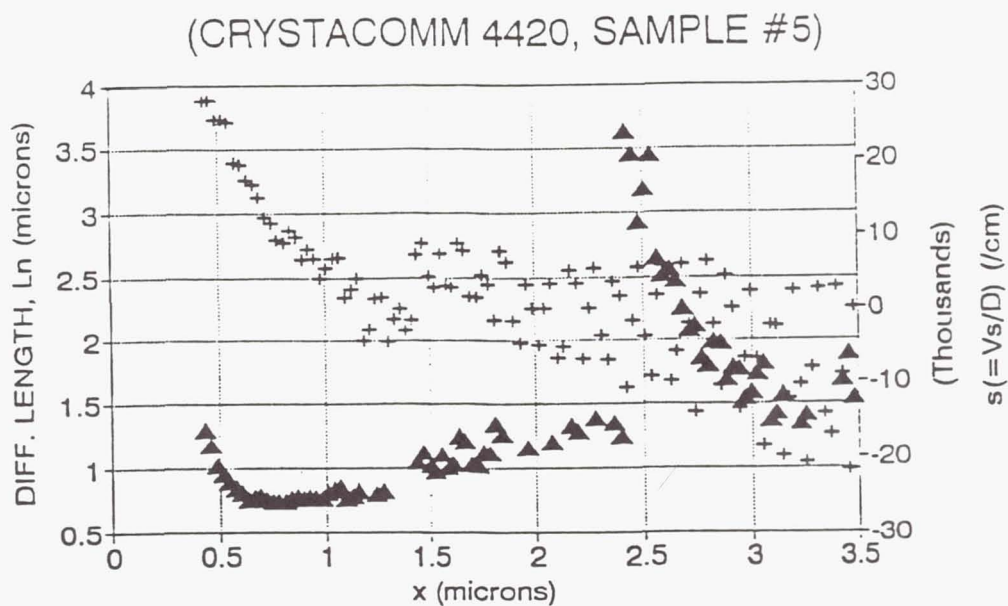
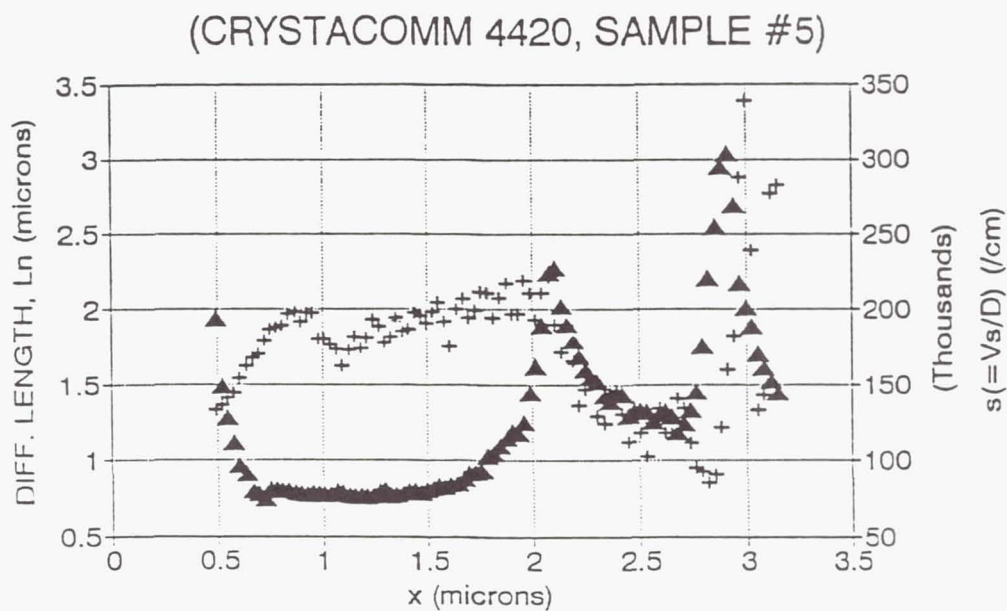


Figure 8. Photograph of a pitted surface, created by etching the edge surface in HCl.



(a)



(b)

Figure 9. Results obtained in a typical specimen (a) before etching in HCl, (b) after etching in HCl.

SURFACE PASSIVATION OF InP SOLAR CELLS WITH InAlAs LAYERS

Raj K. Jain¹, Geoffrey A. Landis* and Dennis J. Flood
NASA Lewis Research Center, Cleveland, OH 44135
* Sverdrup Technology Inc., Brookpark, OH 44142

The efficiency of indium phosphide solar cells is limited by high values of surface recombination. This work investigates the effect of a lattice-matched $\text{In}_{0.52}\text{Al}_{0.48}\text{As}$ window layer material for InP solar cells, using the numerical code PC-1D. We have found that the use of InAlAs layer significantly enhances the p^+n cell efficiency, while no appreciable improvement is seen for n^+p cells. The conduction band energy discontinuity at the heterojunction helps in improving the surface recombination. An optimally designed InP cell efficiency improves from 15.4% to 23% AM0 for a 10 nm thick InAlAs layer. The efficiency improvement reduces with increase in InAlAs layer thickness, due to light absorption in the window layer.

INTRODUCTION

Indium phosphide solar cells have great potential for space photovoltaic power applications due to their superior radiation resistance (refs. 1,2). However, experimental cell efficiencies are limited by high surface recombination (refs. 3,4). This work investigates the effect of a wide-bandgap lattice-matched $\text{In}_{0.52}\text{Al}_{0.48}\text{As}$ window layer on InP solar cells, using a numerical code PC-1D (ref. 5). PC-1D is a quasi-one-dimensional program operated on a personal computer for investigating the transport of electrons and holes in semiconductor devices. The semiconductor device transport equations are solved by a finite-element approach. We have found that the use of InAlAs as a window layer significantly enhances the p^+n InP cell efficiency, while no appreciable improvement is seen for n^+p cells. The performance enhancement in p^+n cells is due to the energy discontinuity at the heterojunction, as shown in Fig. 1. The InAlAs window layer acts as a minority carrier mirror and confines the minority carrier electrons in the cell emitter region.

Preliminary calculations on the effect of the window layer on performance of a baseline (unoptimized) p^+n cell are available elsewhere (ref. 6). This paper discusses the effects of the window layer on an optimally designed p^+n InP cell.

¹This work was done while the author held a National Research Council - NASA Lewis Research Center Associateship.

NUMERICAL APPROACH AND RESULTS

The previously presented results ("baseline cell") used materials parameters estimated to be of typical of solar cells currently fabricated. In this work we use parameters which we believe are achievable in InP. This is referred to as the "optimized" cell. The minority carrier lifetimes, diffusion lengths, and mobilities are shown in Table I. As can be seen, an improvement of 2 - 5 times in minority carrier diffusion length from the "baseline" to the "optimized" cell is required. The optimized p^+n InP cell model has been reported elsewhere (refs. 4,7). The InP solar cell structure is shown in Fig. 2. The front surface recombination velocity (SRV) has been assumed equal to 10^7 cm/s. Using PC-1D, we obtain an efficiency for the p^+n optimized InP cell with no window layer of 15.4% AM0. This cell efficiency is limited by front SRV, and could be increased to over 24% if the SRV could be reduced from 10^7 to 10^4 cm/s (ref. 4). The reduction in SRV could be effectively accomplished by the use of window layer, similar to improved results obtained on gallium arsenide (ref. 8) and silicon (ref. 9) solar cells.

Data on minority carrier lifetime in p^+ InP is sparse. Lifetime at concentrations up to 4×10^{17} cm^{-3} were measured (ref. 10). At 4×10^{17} cm^{-3} , the lifetime was slightly greater than 1 nS. Since the curve shows that the lifetime decreases with concentration, a lifetime under 1 nS is expected for concentration of 10^{18} cm^{-3} . A recent paper (ref. 11) however, indicates a lifetime over 3 nS at 10^{18} cm^{-3} . This work also suggests that in the range of 10^{15} cm^{-3} to 10^{17} cm^{-3} , minority carrier lifetime in p -type InP increases as doping increases, which is unexpected behavior. Until better lifetime data is available, the assumed value of 0.73 nS at 10^{18} cm^{-3} is a reasonable estimate lying between the two measured values.

In the present work we have considered the use of wide-bandgap lattice-matched $\text{In}_{0.52}\text{Al}_{0.48}\text{As}$ as a window layer. The p^+n InP solar cell structure with InAlAs window layer is shown in Fig. 2. An InAlAs doping of 10^{18} cm^{-3} was assumed, equal to the emitter doping. Moderate doping levels were considered to avoid heavy doping effects such as band gap narrowing. The minority carrier diffusion length was assumed to be 2 μm in the window layer. The InAlAs window layer thickness was varied from 10 nm to 200 nm. The InAlAs material parameters available in the literature were used and others (n_i , α) were extrapolated from values appropriate to InP as described in reference 6.

Figure 3 shows the calculated I-V characteristics of the p^+n InP cell with no window layer, and with window layer thicknesses of 10, 50, 100, and 150 nm. All results are calculated under AM0 illumination at 137.2 mW/cm^2 and 25°C . The optimized InP cell efficiency without InAlAs layer is 15.4% AM0. Efficiency is significantly enhanced by the window layer. For a 10 nm thick window layer the calculated efficiency improves to 23% AM0. Efficiency decreases as the InAlAs layer thickness increases, due to increased light absorption in the window layer. Figure 4 shows the calculated p^+n InP cell efficiency as a function of window layer thickness. The optimized InP cell has a higher minority carrier diffusion lengths than the baseline cell, and the cell efficiency improvement due to the window layer is higher because the effect of surface recombination is more important as the other recombination is decreased. For comparison, calculated results for the baseline cell are also plotted. Compared to n^+p cells, p^+n cells have relatively thicker emitters and are more sensitive to surface recombination than n^+p structures [see calculated results (ref. 12), shown in Fig. 5]. The window layer improves the short circuit current as well as the open circuit voltage as seen in Fig. 3. The open circuit voltage changes little (975 to 970 mV) with the increase in window layer thickness from 10 nm to 150 nm. The short circuit current decreases with window layer thickness, and for a 150 nm thick window layer, the current is even lower than that of the optimized cell without a window layer (27.8 mA/cm^2).

The previous calculations have assumed that the doping of the window layer is identical to that of the emitter, 10^{18} cm^{-3} . As seen in Fig. 1, there is a discontinuity ΔE_c of about 179 mV in the valence band edge. The requirement that the Fermi level must be constant across the heterojunction forces the bands to bend, forming a positive energy spike (i.e., hole accumulation) in the valence band on the InAlAs side of the heterojunction, and a corresponding negative energy dip (i.e., hole depletion) on the InP side of the heterojunction. Correspondingly, the spike and dip result in electron depletion and accumulation on the InAlAs and InP sides of the heterojunction respectively.

If the doping is increased by a factor of $\exp(\Delta E_c/kT) = 10^3$ from the InP to the InAlAs, the spike and dip in the energy bands will vanish. This would require the doping of the p^+ emitter to be reduced to 10^{15} cm^{-3} if the window layer doping is held constant at 10^{18} cm^{-3} , or increasing the window doping to 10^{21} cm^{-3} if the emitter doping is held constant at 10^{18} cm^{-3} .

Reducing the emitter doping would decrease the cell voltage and increase the emitter sheet resistance. Because of the high sheet resistance of the emitter in p/n cells, this is not practical.

While increasing the window layer doping would be advantageous, there are two difficulties: (1) there is little or no information about the growth and properties of heavily doped p-type InAlAs, (2) doping above 10^{18} cm^{-3} will require heavy-doping corrections (particularly bandgap narrowing) to the InAlAs parameters, which will reduce the performance. Experimental information on heavy doping effects in p-type InAlAs is to date lacking.

Figure 6 shows the effect of the window layer doping on cell performance, where heavy doping effects have not been included. This curve shows that higher doping levels in the window layer result in increased performance. However, heavy doping effects will cause this curve to turn down at the high doping side of the scale.

The enhanced cell performance clearly demonstrate that the wide-bandgap lattice matched $\text{In}_{0.52}\text{Al}_{0.48}\text{As}$ is effectively reducing the surface recombination. The conduction band discontinuity at the heterojunction (InAlAs/InP), shown in Fig. 1, helps in confining the electrons in the cell emitter region, resulting in lower recombination.

The effect of an InAlAs window layer on an n^+p InP cell was also modeled, but resulted in no appreciable improvements in efficiency. Table II describes the calculated efficiency results for no window layer, 10nm and 50 nm InAlAs layers for n^+p baseline and optimized InP cells. Table I also describes the assumed n^+p indium phosphide solar cell parameters. The baseline cell represents approximately the current state-of-art technology (ref. 3). Figure 7 shows the calculated current-voltage characteristics of an n^+p baseline solar cell (ref. 13). A 10 nm window layer offers a slight improvement in efficiency but calculated cell efficiency reduces for thicker window layers. For all calculations a front SRV of 10^7 cm/s was assumed. The use of InAlAs on optimized n^+p InP cell offers slightly better improvement for 10 nm thick window layer, but still not significant. We were not able to calculate cell performance for window layers less than 10 nm thick using PC-1D. It may be possible to achieve improved results for window layers thinner than 10 nm. Quantum well structures with $\text{In}_{0.52}\text{Al}_{0.48}\text{As}$ layers around 5 nm thick have been fabricated successfully. To understand the performance of very-thin windows on solar cells will require a better understanding of the effects of the interface and surface and their interactions.

CONCLUSIONS

In summary, calculations have shown that significant efficiency improvements could be achieved by using $\text{In}_{0.52}\text{Al}_{0.48}\text{As}$ as a window layer material in p^+n indium phosphide solar cells. Cell efficiencies as high as 23% could be achieved with a 10 nm thick window layer. No appreciable improvement on n^+p InP cells has been seen with InAlAs window layer. The performance improvement is caused by the effective reduction in the surface recombination velocity due to minority carrier confinement by the conduction band energy discontinuity. The hetero-interface acts as a minority carrier mirror.

REFERENCES

- [1] M. Yamaguchi, K. Ando, A. Yamamoto and C. Uemura, "Minority-Carrier Injection Annealing of Electron Irradiation-Induced Defects in InP Solar Cells," *Appl. Phys. Lett.*, vol. 44, p. 432, 1984.
- [2] I. Weinberg, C. K. Swartz and R. E. Hart, "Potential for Use of InP Solar Cells in the Space Radiation Environment," *Conf. Rec. 18th IEEE Photovoltaic Specialists Conf.* (Las Vegas, NV), Oct. 1985, pp. 1722-1724.
- [3] C. J. Keavney, V. E. Haven and S. M. Vernon, "Surface Recombination and High Efficiency in InP Solar Cells," *Proc. 2nd Int. Conf. Indium Phosphide and Related Materials* (Denver, CO), April 1990, pp. 435-438.
- [4] R. K. Jain and D. J. Flood, "Design Modeling of High Efficiency p^+n Indium Phosphide Solar Cells," *IEEE Trans. on Electron Devices*, vol. 40, p. 224, 1993.
- [5] P. A. Basore, PC-1D Installation Manual and User's Guide Version 3, Oct. 1991.
- [6] R. K. Jain and G. A. Landis, "Calculated Performance of p^+n InP Solar Cells with $\text{In}_{0.52}\text{Al}_{0.48}\text{As}$ Window Layers," *Appl. Phys. Lett.*, vol. 59, p. 2555, 1991.
- [7] R. K. Jain, I. Weinberg and D. J. Flood, "Comparative Modeling of InP Solar Cell Structures," in *Proc. Space Photovoltaic Research and Technology Conf.* (Cleveland, OH), May 1991, pp. 29/1-29/9.
- [8] H. J. Hovel, *Semiconductors and Semimetals*, Vol. 11, "Solar Cells," Academic Press Inc., 1975, pp.195.
- [9] G. A. Landis, J. J. Loferski, R. Beaulieu, P. A. Sekula-Moise, S. M. Vernon, M. B. Spitzer and C. J. Keavney, "Wide-Bandgap Epitaxial Heterojunction Windows for Silicon Solar Cells," *IEEE Trans. on Electron Devices*, vol. 37, p. 372, 1990.
- [10] P. Jenkins, G. A. Landis, I. Weinberg and K. Kneisel, "Minority Carrier Lifetime in Indium Phosphide," *Conf. Rec. 22nd IEEE Photovoltaic Specialists Conf.* (Las Vegas, NV), Oct. 1991, pp. 177-181.
- [11] Y. Rosenwaks, Y. Shapira and D. Huppert, "Picosecond Time-Resolved Luminescence Studies of Surface and Bulk Recombination Processes in InP," *Phys. Rev. B*, vol. 45, p. 9108, 1992.
- [12] R. K. Jain and D. J. Flood, "Effect of Surface Recombination Velocity and Minority Carrier Diffusion Length in p^+n Indium Phosphide Solar Cells," unpublished.
- [13] R. K. Jain and D. J. Flood, unpublished.

TABLE I. Assumed baseline and optimized p^+n and n^+p indium phosphide solar cell parameters.

	E M I T T E R				B A S E			
InP Solar Cell	Doping (cm^{-3})	Lifetime (nS)	Mobility ($\text{cm}^2/\text{V-S}$)	Diff.Length (μm)	Doping (cm^{-3})	Lifetime (nS)	Mobility ($\text{cm}^2/\text{V-S}$)	Diff. Length (μm)
Baseline	$10^{18} p$	0.046	2100	0.5	$10^{17} n$	25	65	2
Optimized	$10^{18} p$	0.733	2100	2	$10^{17} n$	151	65	5
Baseline	$10^{18} n$	0.025	40	0.05	$10^{17} p$	3.5	2800	5
Optimized	$10^{18} n$	0.1	40	0.1	$10^{17} p$	56	2800	20

TABLE II. Effect of InAlAs window layer on the performance of n^+p InP solar cell.

InAlAs Window Layer Thickness, nm	Baseline n^+p InP Cell Efficiency, %	Optimized n^+p InP Cell Efficiency, %
no window layer	19.5	21.5
10	19.6	22.6
50	16.3	19.8

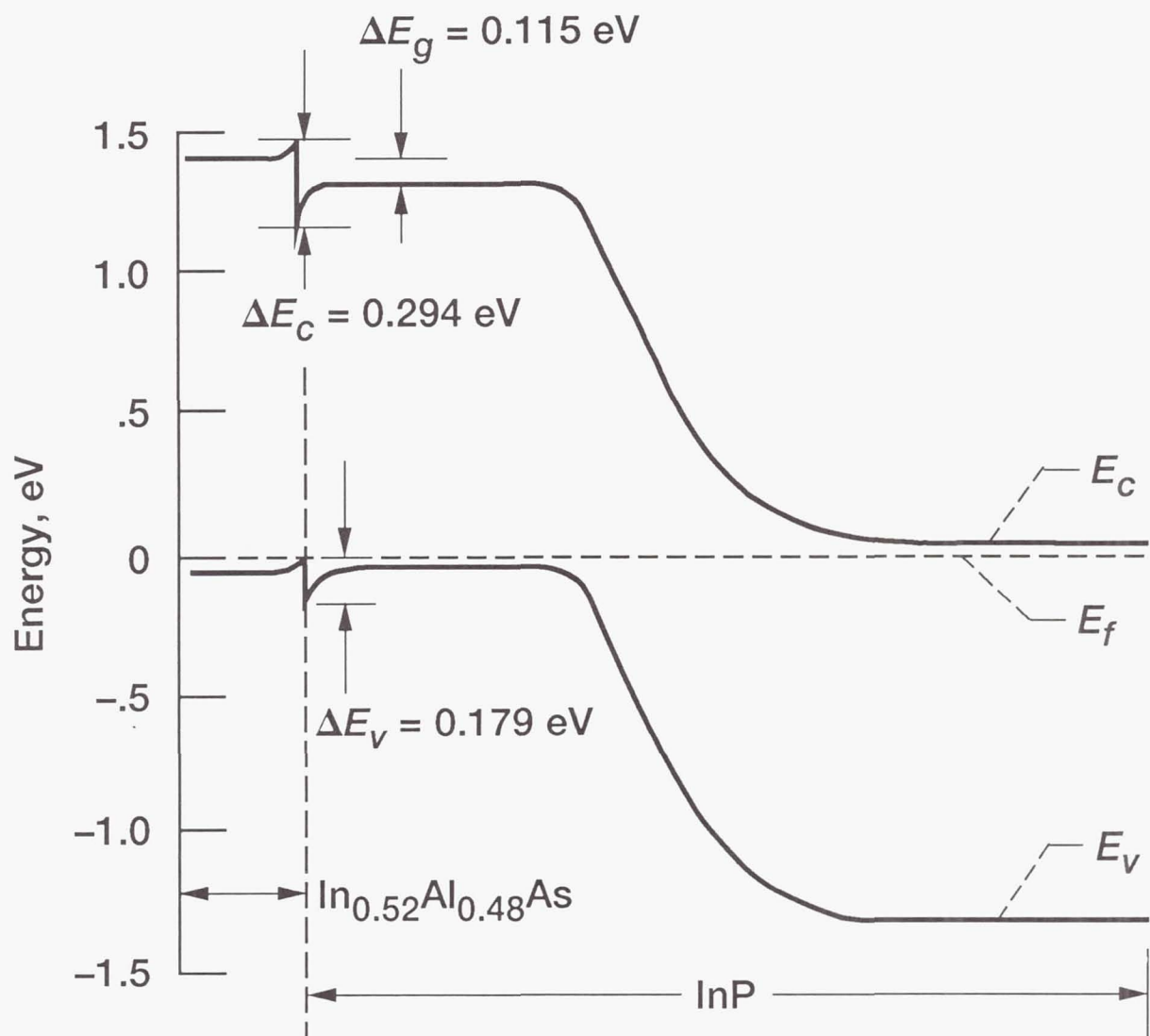


Fig. 1 Energy band diagram of a $p^+ \text{InAlAs}/p^+ \text{InP}/n \text{InP}$ solar cell.

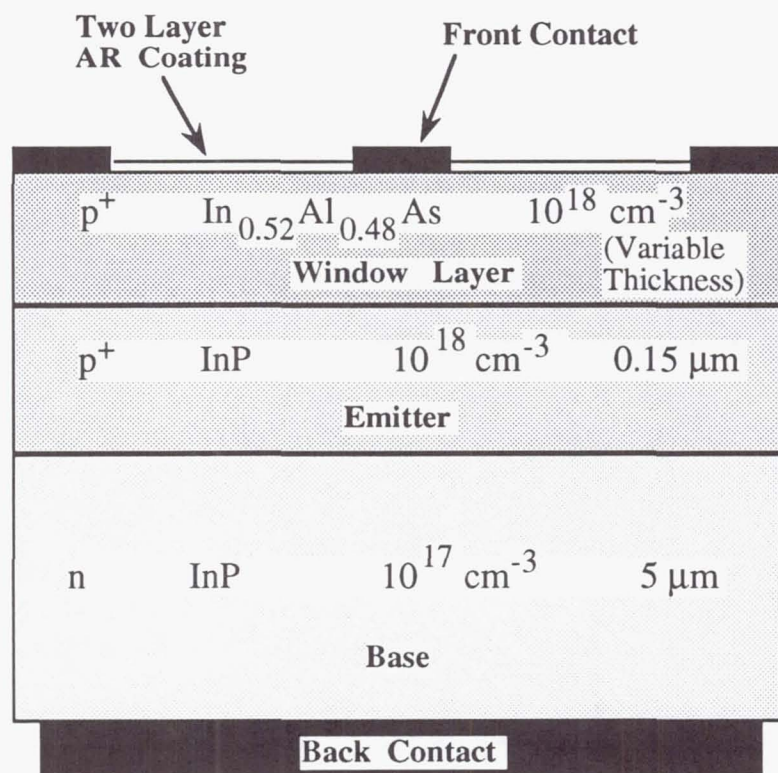


Fig. 2 Structure of a p^+n InP solar cell with an InAlAs window layer.

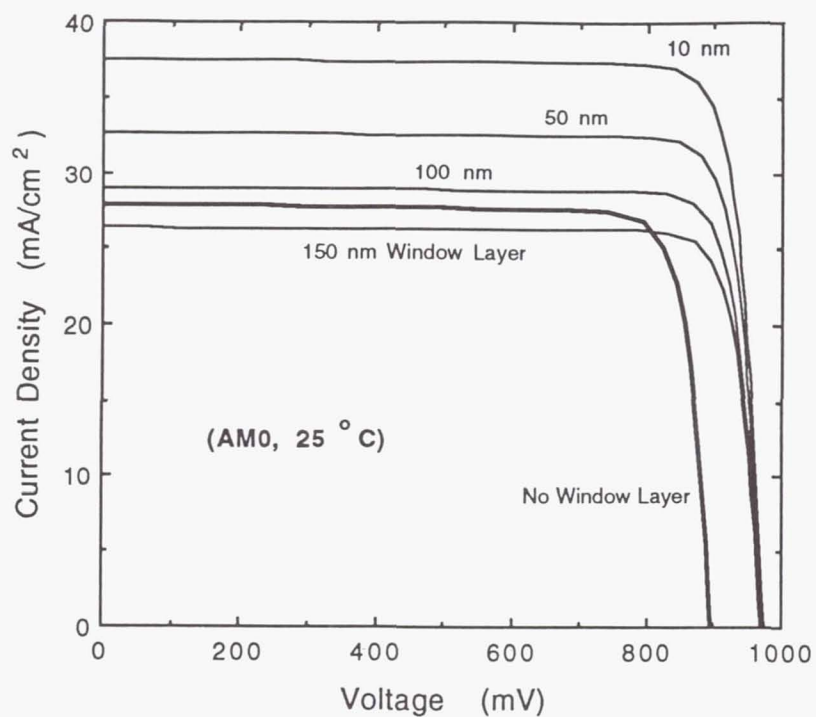


Fig. 3 Calculated I-V characteristics of a p^+n InP solar cell with and without InAlAs window layer.

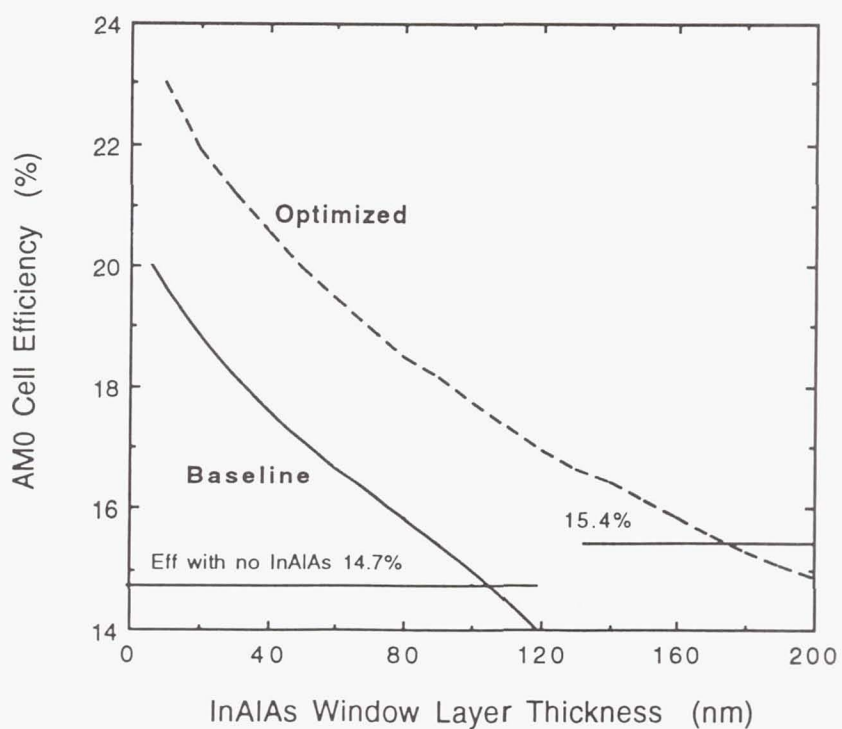


Fig. 4 Variation of p^+n InP solar cell efficiency with InAlAs window layer thickness.

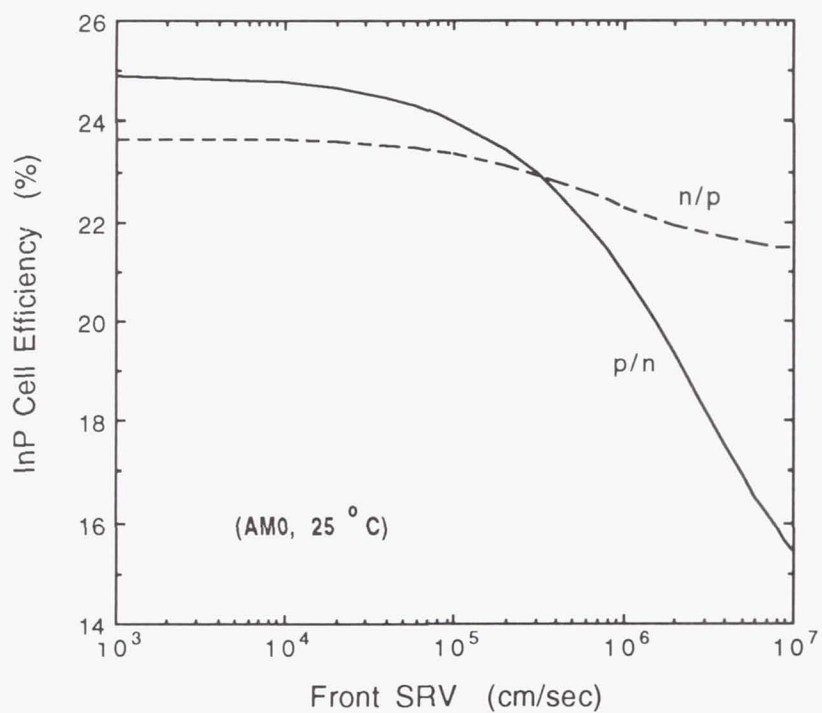
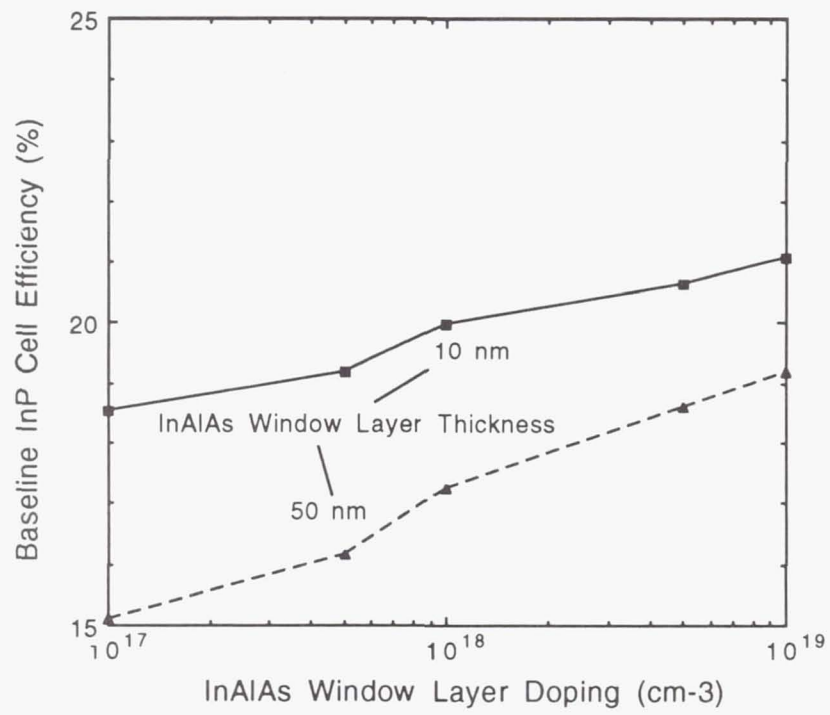
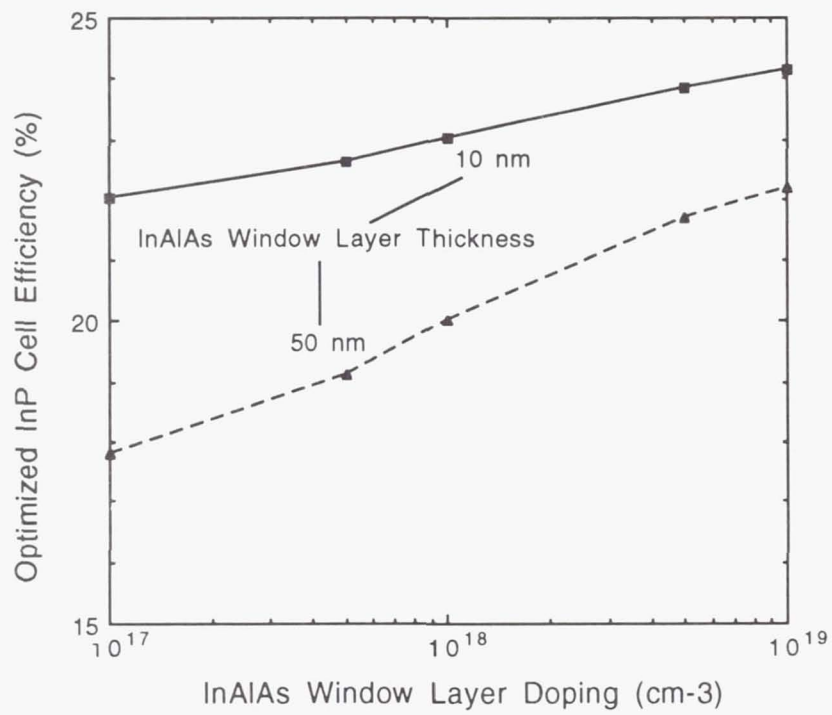


Fig. 5 Effect of the front surface recombination velocity on the calculated efficiency of the optimized n^+p and p^+n InP solar cells (ref. 12).



(a)



(b)

Fig. 6 Variation of p^+n InP solar cell efficiency with InAlAs window layer doping.

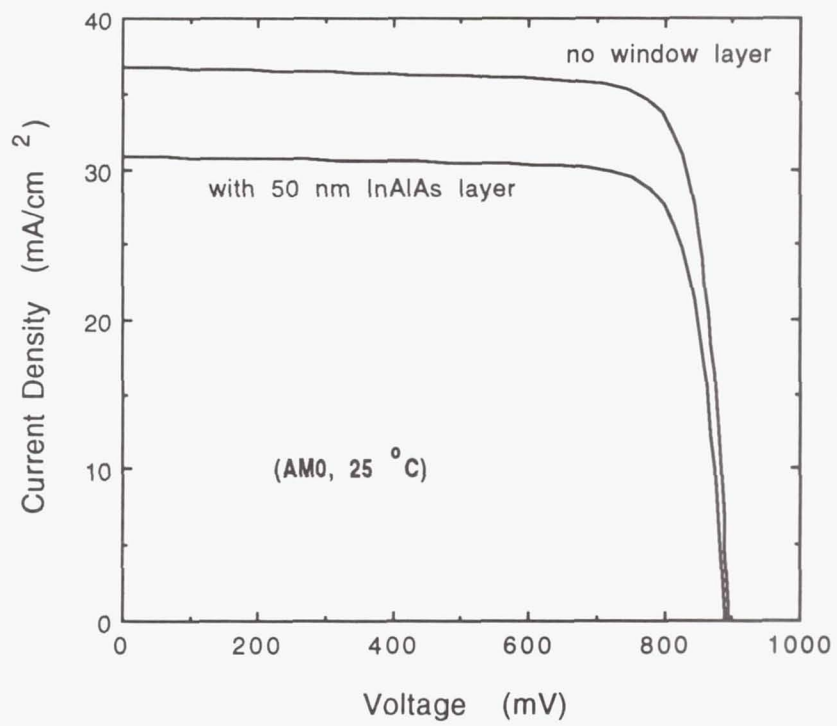


Fig. 7 Calculated I-V characteristics of an n⁺p InP baseline solar cell with and without InAlAs.

POLYIMIDE BASED AMORPHOUS SILICON SOLAR MODULES ¹

Frank R. Jeffrey, Derrick P. Grimmer, Steven A. Martens,
Khaled Abudagga, Michael L. Thomas, and Max Noak²
Iowa Thin Film Technologies
Ames, Iowa, 50010

Requirements for space power are increasingly emphasizing lower costs and higher specific powers. This results from new fiscal constraints, higher power requirements for larger applications and the evolution toward longer distance missions such as a Lunar or Mars base. The polyimide based a-Si modules described in this paper are being developed to meet these needs. The modules consist of tandem a-Si solar cell material deposited directly on a roll of polyimide. A laser scribing/printing process subdivides the deposition into discrete cell strips which are series connected to produce the required voltage without cutting the polymer backing. The result is a large, monolithic, blanket type module approximately 30 cm wide and variable in length depending on demand. Current production modules have a specific power slightly over 500 W/Kg with room for significant improvement. Costs for the full blanket modules range from \$30/Watt to \$150/Watt depending on quantity and engineering requirements. Work to date has focussed on the modules themselves and adjusting them for the AMO spectrum. Work is needed yet to insure that the modules are suitable for the space environment.

Introduction

This project, initiated in 1990, is designed to simultaneously develop a lightweight flexible PV technology suitable for space application and the process for producing large arrays from that technology. The product is a monolithically integrated amorphous silicon module, fabricated directly on a polyimide blanket.

Benefits of this technology include extremely high power to weight ratios and low potential costs. The high specific power results from the ability to deposit the thin film cells directly on a polyimide substrate. The low potential costs are due to the low material costs of the thin film approach and the economic benefits of full roll-to-roll processing. Attainment of low costs is predicated on high volume production (>1MW/yr) which will require piggybacking manufacturing if space cells on manufacturing for terrestrial applications.

Another group of benefits relate to the basic nature of the product. The material comes already integrated into large area modules. This greatly simplifies full system assembly and thus reduces full system costs. The flexible nature of the material provides a wide range of stowage and deployment options which may translate into improved costs and reliability. The combination of amorphous material and polymer substrate make a robust module which will not be easily damaged by launch shocks or impacts. This feature improves reliability and can reduce launch weight by eliminating some of the protective measures required for more fragile type cells.

¹ This work is partially sponsored by NASA Lewis Research Center under contract # NAS3-26244

² Member of technical staff: Microelectronics Research Center, Iowa State University

The principal price paid for these benefits is conversion efficiency. While the weight and cost per watt are significantly lower than for other technologies, the area required for an application will be increased. This shortcoming will limit the applications of the product. Use in lower orbits, where drag is significant, will probably have to be limited to back-up power or to short duration flights.

The benefits of this material will become more significant as mission distance increases and power demands increase. In these cases, weight and cost will become the stronger driving factors.

Device Structure

Currently, the tandem a-Si device structure shown in figure 1 is being deposited on 2 mil thick polyimide substrate. Both i layers in this structure are a-Si:H material while all doped layers are microcrystalline.

The key features in maximizing performance of this structure, outside of basic material quality are: 1) maximizing transmission through the TCO and P+ top layers. 2) Insuring the adequacy of doped layers to provide full voltage. 3) Providing high recombination rates in the tunnel junction to minimize resistance and voltage loss. 4) Maximizing reflectance and scattering of red light off the back metal contact. 5) Balancing the thicknesses of the two i layers to insure current matching under the AM 0 spectrum.

Minimizing absorption in the top p+ layer and insuring adequate thickness and doping to achieve full voltage are competing elements. Thicker and more heavily boron doped layers absorb more of the incoming blue and near UV light. We have chosen a microcrystalline p+ layer to minimize this absorption. Achieving a good microcrystalline layer is very sensitive to many system design and deposition parameters. Figure 2 demonstrates this, showing Quantum Efficiency (Q.E.) curves for two single junction samples with slightly different p+ deposition conditions. A significant difference is seen in the blue response of these devices which correlates with a 10 % difference in device current. Neither curve shows a very good blue response. Calculations indicate that further work in this areas could yield another 20% improvement in current.

The tunnel junction must provide for recombination of the electrons injected from the top device and holes coming from the bottom device. The recombination rate must be fast enough that no reverse voltage is generated at the p+ n+ interface. To achieve this, highly degenerate layers are required and must have adequate thickness. Figure 3a shows an I-V curve for a single junction device with an n+ layer on top to form a tunnel junction. The double-back curve is a signature of a reverse junction at the p+ n+ interface indicating inadequate doping or thickness of one of the layers. It was determined in this case that the p+ layer was inadequate. Figure 3b shows the I-V curve of a later cell with adequate doping.

Optimum utilization of the red end of the spectrum can be achieved by maximizing reflection and scattering off the back metal contact. Scattering provides the longest path length within the semiconductor material while high reflectance reduces the energy lost to absorption in the back metal. Figure 4 shows Q.E. curves for a device on specular metal and on our current textured back metal contact. This figure also shows a Q.E. curve for optimized light trapping for a superstrate cell with silver/SnO₂ back contact from Solarex. (1) Current texturing is clearly having an effect, however there is still improvement to be made. Calculations show another 20 % improvement in current over our current devices appears achievable.

Balancing the thicknesses of the i layers to match currents under an AM 0 spectrum is required for maximum cell output. This process must be redone after any of the cell improvement modifications discussed above. Table 1 demonstrates the dependence of optimum layer thicknesses on spectral distribution. The table gives the short circuit currents under ELH and LAPPS illumination for three tandem samples with different thickness top i layers. The ELH spectrum is heavy in the red end while the LAPSS spectrum is heavier in the blue and UV, more closely simulating AM0. The optimum thickness for the ELH spectrum appears to be in the range of 850 Å to 900 Å, while the optimum for the LAPSS spectrum is closer to 670 Å. From this data, the optimum for LAPPS may even be significantly less than 670 Å. Improvement in the blue response of the device will call for reducing the top i layer thickness, while improvement in the red response will call for a thicker layer.

Module Structure

To achieve the large area modules, cells are subdivided without cutting the polyimide substrate and interconnected as shown in figure 5. The first laser scribing step defines individual cells by cutting the combined back metal contact and a-Si device layers. Two insulating ink lines are then printed to protect against shorting in the first scribe cut and to act as a beam stop for next laser scribe. The TCO is next deposited over the a-Si device layer and the ink lines. Next, conductive ink grid lines are printed over the TCO. To finish the interconnect system, the laser is used to cut the TCO over the second ink line and to weld between the top and bottom layers in the interconnect area.

Currently, maximum substrate width is 13" and maximum web length is 500 ft. This could be configured into a single module 13" wide by 500 ft long, but would, in most cases, be cut into smaller strips. Our typical interconnect results in a module voltage of 10 Volts per linear ft so that a 1 ft wide by 10 ft long module would operate at 0.5 Amps and 100 Volts. Interconnects can easily be varied by changing the print patterns and the laser scribing program. This allows modules with a wide range of currents and voltages to be produced.

As a result of the fabrication process, the basic unit of this technology is not a single cell, but a large area module blanket. It is important to recognize that all cell parameters are applicable to full blankets or wings (minus support structures) and should be compared to full blanket arrays of competing technologies rather than to individual cell parameters. This applies to \$/Watt, Watts/ Kg and Watts/ M².

Performance

Figure 6 show and I-V curve for the current level of device coming off the manufacturing line. Table 2 shows performance parameters for the full modules. The first column give the current parameters. The second column give the parameters expected within the next few years. The third column gives an estimate of the potential of the technology.

Future Work

There is considerable work yet to be done to make this product ready for space use. This includes device processing development and space qualification work.

Significant efficiency improvement is possible by improving materials and processing. Short circuit current can be improved by improving the p+ layer transmission, the back metal contact reflectance, deposition of an index matching layer on top of the TCO, and reducing the interconnect areas though tighter alignment. Open circuit voltage and fill factor can be increased by improving the p+/i interfaces and the tunnel junction.

Space qualification tests are yet to be started. Of particular need are thermal shock tests, radiation resistance and light induced degradation under space conditions.

Conclusions

The capability has been developed for fabricating large area arrays of tandem a-Si devices on polyimide substrates. Performance of material currently being manufactured provides very high specific power ratios and low cost per watt, but is limited by relatively low power per unit area. Performance in all areas is expected to improve significantly.

References

1. Catalano, A. et. al. " Solarex Annual Subcontractors Report", NREL/TP-411-4995 Aug. 1989

Sample #	1	2	3
Top i Layer Thickness	670 Å	840 Å	1000 Å
Short Circuit Current Under ELH	49.0 mA	54.4 mA	53.8 mA
Short Circuit Current Under LAPSS	44.1 mA	41.4 mA	37.4mA

Table 1. Short circuit currents for a series of samples under ELH and LAPSS illumination. The samples are identical tandem devices except for the thickness of the top i layer.

PARAMETERS @ 100mW/cm (@ 140mW/cm)	CURRENT PERFORMANCE LEVELS	EXPECTED PERFORMANCE LEVELS (2YRS)	POTENTIAL PERFORMANCE LEVELS
POWER/WEIGHT RATIO (W/KG)	550 W/KG (770 W/KG)	1760 W/KG (2460 W/KG)	2200 W/KG (3080 W/KG)
POWER/AREA RATIO (W/M ²)	50 W/M ² (70 W/M ²)	80 W/M ² (112 W/M ²)	100W/M ² (140W/M ²)
COST/POWER \$/W	\$20/W (\$14.5/W)	\$10/W (\$7/W)	\$5/W (\$3.60/W)
PROCESS CONTROL	LOW YIELD	HIGH YIELD	HIGH YIELD

Table 2. Performance parameters for arrays showing current performance, performance expected in 1 to 2 years, and potential performance in the longer term. Parameters are based on 100 mW/cm. Data in parenthesis are for 140mW/cm to allow crude extension to AM0.

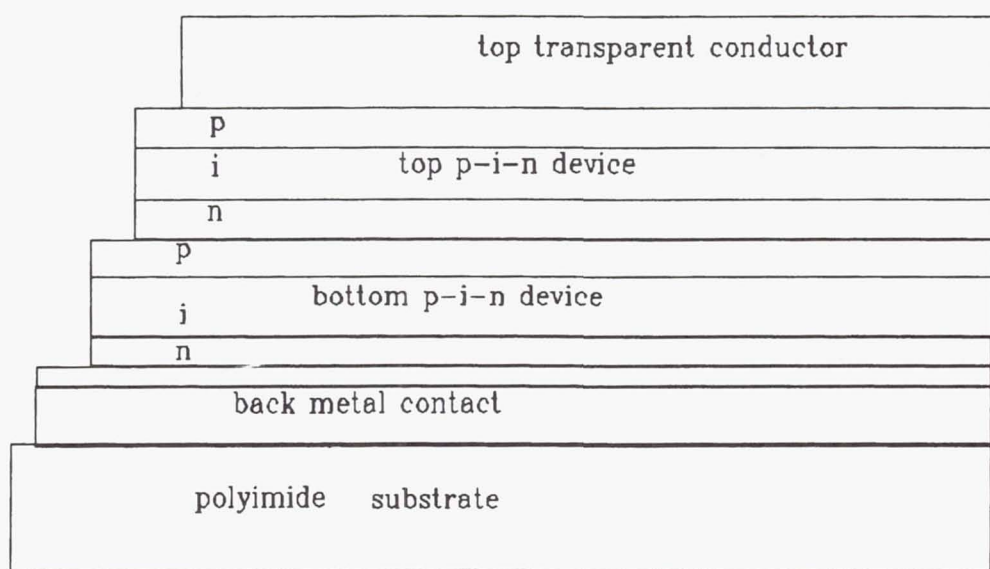


Figure 1. Diagram of the tandem a-Si device on polyimide substrate.

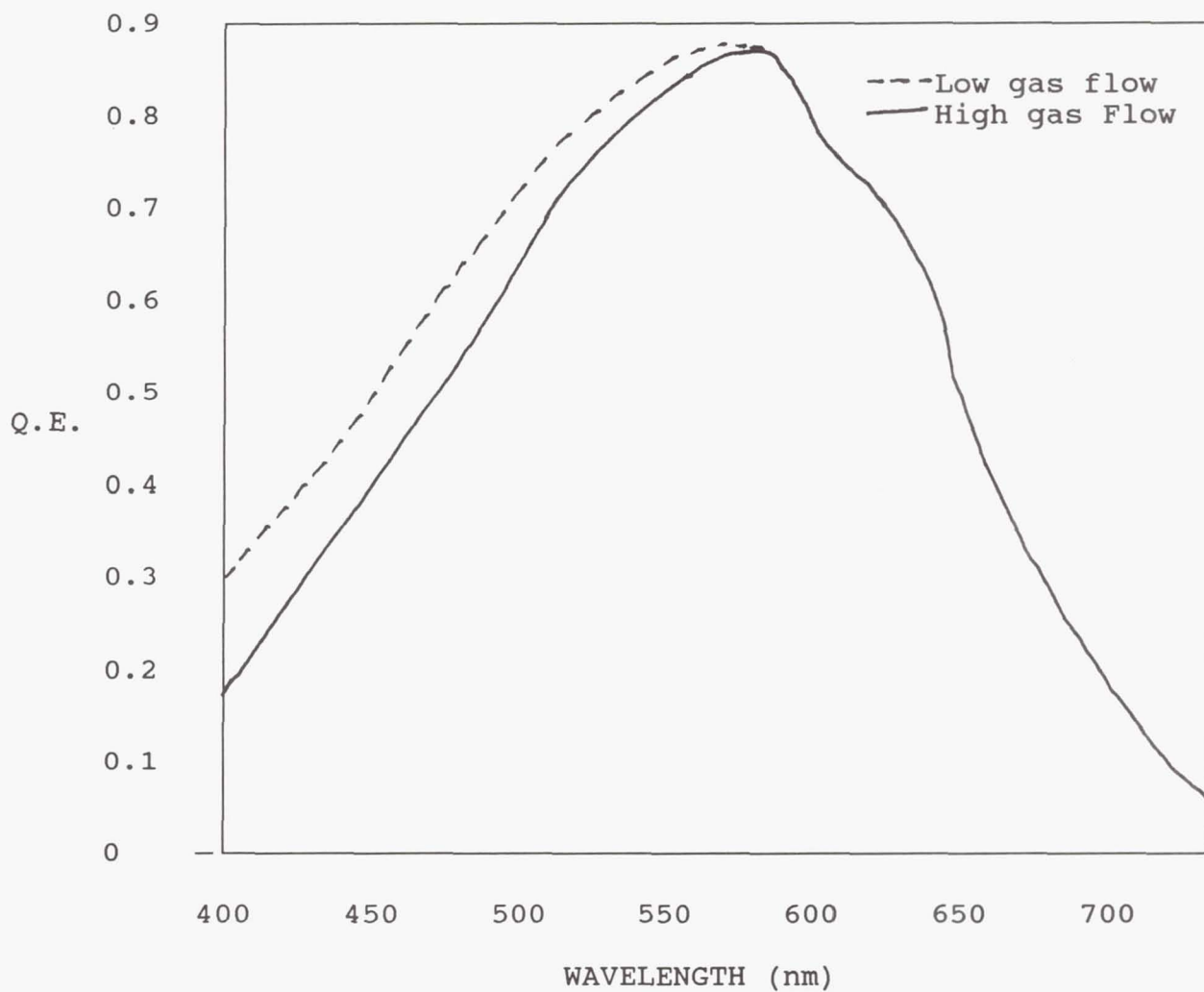


Figure 2. Quantum Efficiency data on two samples with p+ layers deposited under slightly different conditions. Gas ratios during p+ deposition were the same, but sample 2 had a higher total gas flow resulting in a higher deposition rate.

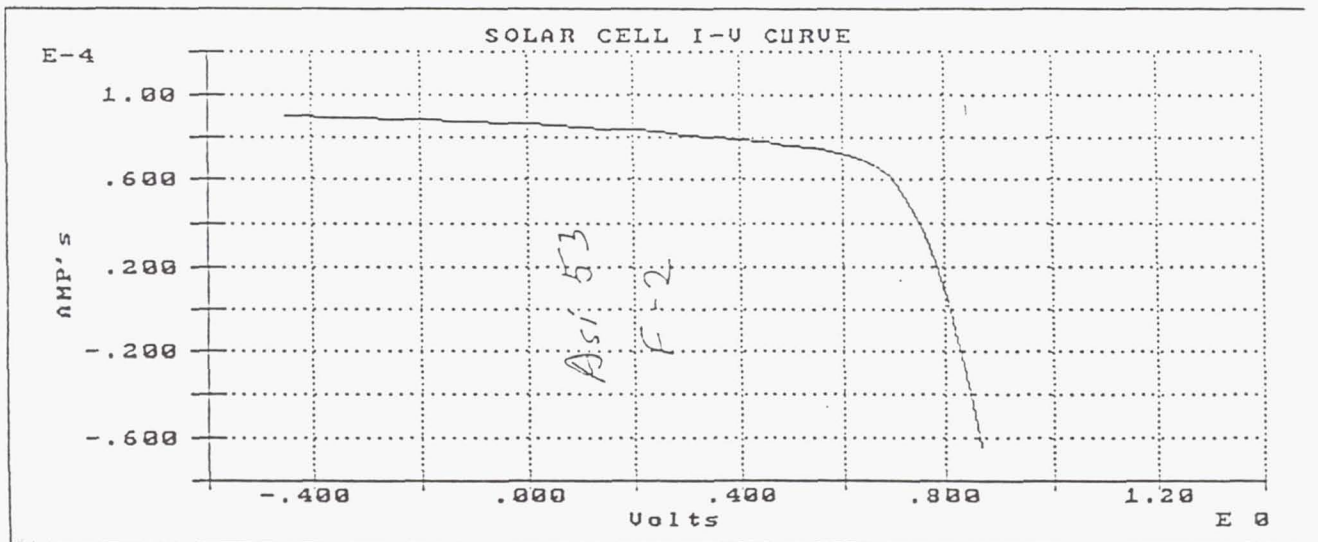
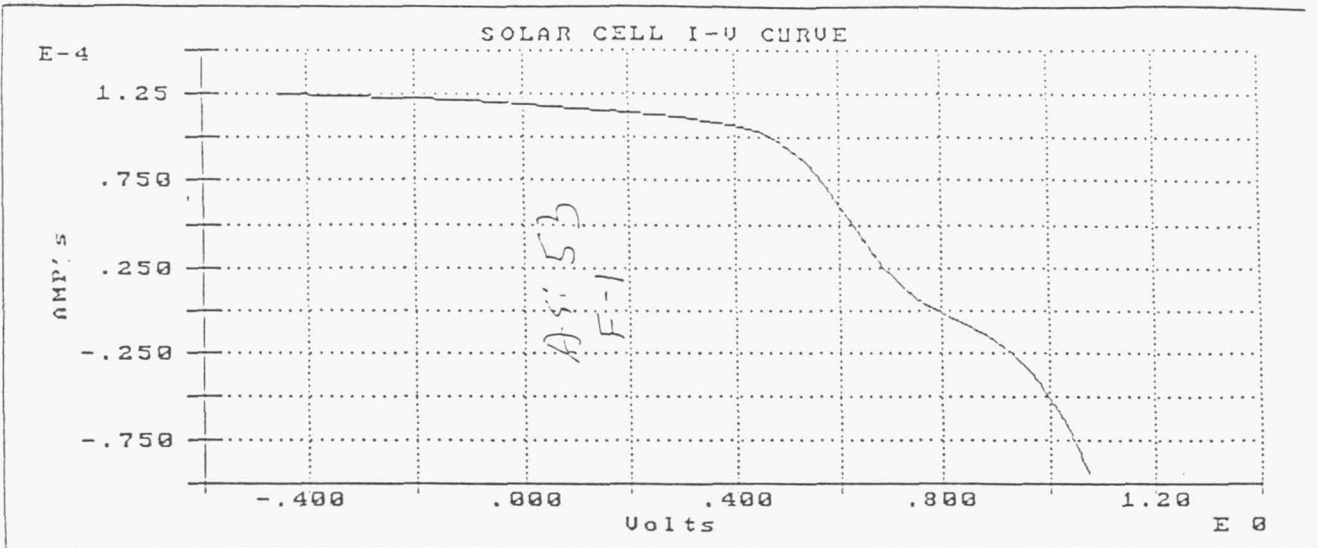


Figure 3. I-V curves for two n/p/i/n devices fabricated during the same run with 300 Watt (a) and 500 Watt (b) p⁺ layers. The 300 Watt p⁺ layer junction shows a reverse barrier at the tunnel junction while the 500 W p⁺ layer junction shows excellent conduction.

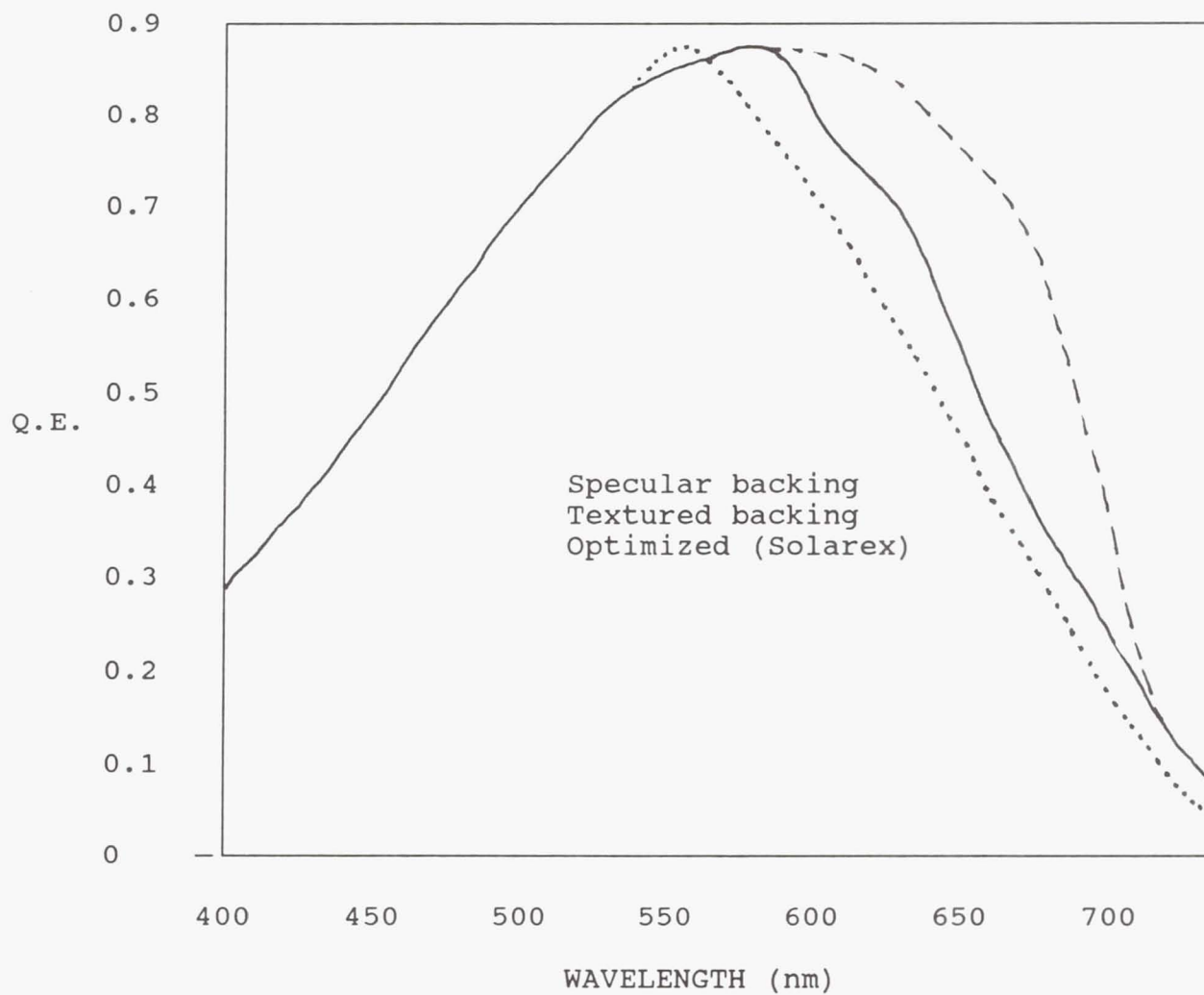


Figure 4. Quantum Efficiency data showing red response of devices with a specular back contact, our current textured back contact, and an optimized scattering and reflecting back contact from a Solarex superstrate device (ref 1).

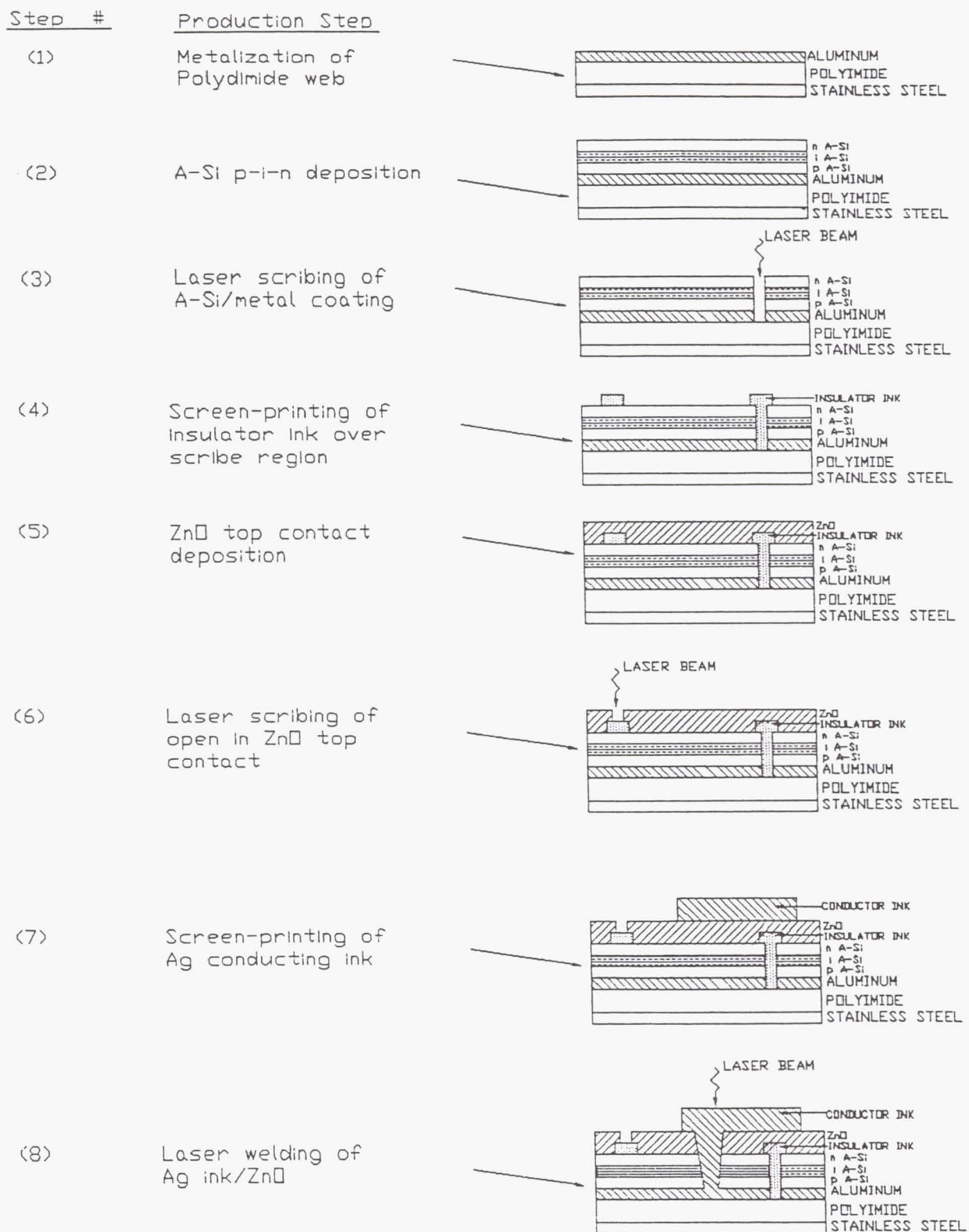
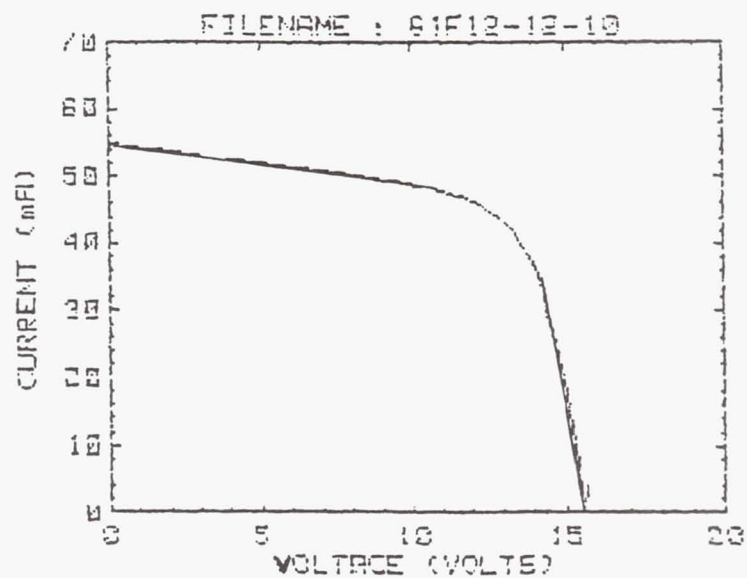


Figure 5. Structure of the monolithic interconnects used in the modules and the sequence of process steps needed to fabricate them.



Post V_{oc} = 15.607 volts
 I_{sc} = -.054959 A
 Fill Fctr = .660143
 V_{maxpwr} = 12.818 volts
 I_{maxpwr} = -.044176 A

Figure 6. I-V curve of a module demonstrating performance of devices coming from the current manufacturing level.

INVESTIGATION OF THE RADIATION RESISTANCE OF TRIPLE-JUNCTION a-Si:H ALLOY SOLAR CELLS IRRADIATED WITH 1.00 MeV PROTONS¹

Kenneth R. Lord II, Michael R. Walters and James R. Woodyard
Institute for Manufacturing Research

and
Department of Electrical and Computer Engineering
Wayne State University, Detroit, MI 48202

SUMMARY

The effect of 1.00 MeV proton irradiation on hydrogenated amorphous silicon alloy triple-junction solar cells is reported for the first time. The cells were designed for radiation resistance studies and included 0.35 cm² active areas on 1.0 by 2.0 cm² glass superstrates. Three cells were irradiated through the bottom contact at each of six fluences between 5.10E12 and 1.46E15 cm⁻². The effect of the irradiations was determined with light current-voltage measurements. Proton irradiation degraded the cell power densities from 8.0 to 98% for the fluences investigated. Annealing irradiated cells at 200 °C for two hours restored the power densities to better than 90%. The cells exhibited radiation resistances which are superior to cells reported in the literature for fluences less than 1E14 cm⁻².

INTRODUCTION

The Thin-Film Cell Development Workshop, conducted in conjunction with the XI Space Photovoltaic Research and Technology Conference, concluded that thin-film solar cells offer the potential for high specific power density, low cost, flexible arrays, monolithic structures and high EOL performance (ref. 1). The workshop report concludes low cost is possible if thin-film solar cell technology feeds off terrestrial photovoltaic programs, and suggested that CdTe, CuInSe₂ and a-Si:H alloys are potential materials for thin-film cells. The workshop report stresses more research is needed in order to understand the effects of radiation with particle energies as low as 50 keV.

Engineers are considering array designs which take advantage of the high specific power densities of thin-film cells. The designs do not include cover glasses and require cells which may be deposited on ultralight materials. The arrays must provide high EOL performance for applications of ten years duration in space environments ranging from LEO through GEO. Integrated ten-year fluences for 0.10 to 200 MeV protons range between about 1E11 and 3E15 cm⁻² for these applications; ten-year fluences for 0.05 to 10 MeV electrons are between about 4E8 and 2E16 cm⁻² (ref. 1). While there are preliminary results on the radiation resistance of thin-film cells (ref. 2), a great deal more work needs to be done to provide performance data for array engineers as well as to understand the fundamental defect generation and passivation mechanisms in thin-film solar cells.

The goals of our research program are two-fold. The first is to measure and model the radiation resistance of thin-film cells to be used in various space environments. The second is to understand the

¹ Supported by TRW Engineering & Test Division and NASA Grant 3-833.

details of both proton and electron defect generation, stability and passivation. This work reports preliminary results of our investigations of 1.00 MeV proton radiation resistance of triple-tandem solar cells fabricated from a-Si:H alloys.

Our past work served as a basis for the design of experiments reported in this work (ref. 3). It has become clear that it is important to develop experimental techniques for making large numbers of measurements to provide a statistical basis for the results. There is a potential for drawing erroneous conclusions when a single measurement is made with an irradiating particle at a given energy and fluence. It is desirable to use a number of cells for each fluence, energy and irradiating particle. Three cells is the smallest number which can be used in a study which purports to have a statistical basis. The limited resources available for studies of this type are not adequate for using three cells for each fluence, energy and irradiating particle. The basis for this statement is illustrated by considering the number of cells required for an investigation of fluences in the $1\text{E}11$ to $1\text{E}16\text{ cm}^{-2}$ range and energies from 50 keV to 5.0 MeV using both protons and electrons. If three cells are used per fluence and energy measurement, and ten measurements are made per fluence and energy decade, then 3000 cells are required for each particle type. Adding control and calibration samples increases the number to about 3200 cells for each irradiating particle type. It is our experience that obtaining a total of between 10 to 100 cells for an investigation is reasonable with available resources. Other constraints involve obtaining the resources for instrumentation designed to measure and irradiate a large number of samples.

Clearly, approaches must be considered to reduce the number of cells used in investigations of the radiation resistance of solar cells which provide results with a statistical basis. The objectives of this work are two fold. The first objective is to explore the possibility of using a small number of cells in a statistical investigation based on multiple irradiation and annealing cycles. The first step in accomplishing the objective is to evaluate the effect of multiple annealing cycles on cell parameters. The next step is to study the effect of multiple cycles, including irradiations and subsequent anneals, on the cell parameters. If the original cell parameters can be demonstrated to be restored, then a small set of cells can be used in a statistical study of the radiation resistance of thin-film solar cells. The second objective is to evaluate the cell design, uniformity of the various layers and the effect of existing variations in layer thicknesses.

EXPERIMENTAL

The support level for this work enabled us to obtain a-Si:H alloy triple-junction cells from the Thin Film Division of Solarex, Inc., for proton irradiation studies. Solarex has developed technology for producing 12 by 13 in² modules for terrestrial applications with efficiencies of about 10% under AM1.5 global illumination; the modules employ a superstrate structure (ref. 4). We were able to collaborate with Solarex on the cell design for our experiments.² The design criteria for the cells used for this work were developed considering the proton beam area, cell mounting, proton energy loss and electrical contacting requirements.

The area of the irradiating beam must be larger than the active area of the cells; we are able to produce a uniform proton beam 1.0 by 1.0 cm² without resorting to scanning or foil scattering techniques. The design must take into consideration the mounting of cells on the sample manipulator in the accelerator target vacuum chamber; both the chamber dimensions and the number of cells to be irradiated during a single loading must be considered. The dimensions of the chamber and sample manipulator dictated an area 1.0 by 2.0 cm² to permit mounting 23 cells on the manipulator. Twenty-three cells makes it possible to irradiate at seven fluence levels with three cells per fluence. The remaining two cells may be used for control purposes.

² We are grateful to Dr. Robert D'Aiello, Thin Film Division, Solarex, Inc., for the design and fabrication of the cells.

Investigations of irradiation-induced defect generation mechanisms requires the proton energy in the active layers of the device to be well characterized. It is desirable for the protons to lose only a small fraction of their energy in passing through either the contacts or superstrate. The thickness of the superstrate used in this work, 0.51 mm, precludes irradiating the active layers through the superstrate. TRIM calculations (ref. 5) were carried out to determine the contact thickness which would result in a negligible energy loss of a 1.00 MeV proton energy passing through the contact layers; the calculations show the contact thickness should be less than about 200 nm (nanometers).

The electrical contacts must be reliable under several contacting cycles and withstand temperatures of 200 °C; these requirements eliminate solder-contact methods from consideration. Laser scribing was used to isolate 0.35 by 1.0 cm² cell active areas. The active areas were contacted to two probe pads which were outside the active areas; the pads measured about 0.30 by 0.35 cm² and were defined by laser scribing during the fabrication process.

The cells were deposited on 5.0 by 5.0 cm² OCLI 0213 Ce doped glass sheets 0.51 mm thick. Ce doped OCLI 0213 glass was chosen by Solarex for the superstrate because of its superior radiation resistance; while thinner and larger area glass sheets would have been more desirable for this work, the glass sheets were selected because they were readily available. Cells measuring 1.0 by 2.0 cm² were cut by Solarex from the glass sheets by mechanical scribing following fabrication and laser scribing.

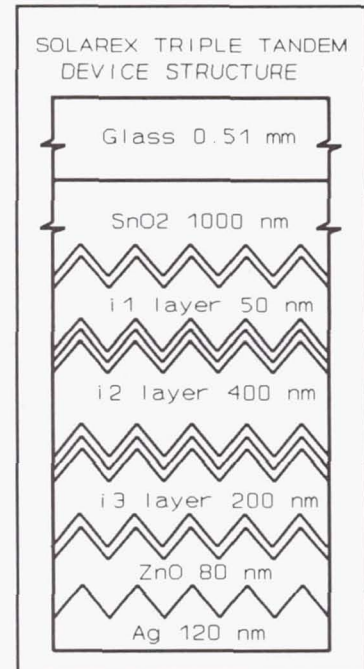


Figure 1. Solarex triple-tandem device structure.

The a-Si:H alloy triple-tandem device structure used in this work has been discussed by Carlson in reference 4 and is shown in Figure 1. The layer thicknesses shown in Figure 1 were communicated by Solarex and based on processing parameters. The SnO₂ layer was deposited on the 0.51 mm thick glass superstrate using a chemical vapor deposition method; it is 1000 nm thick with a RMS roughness of about 30 nm; saw-tooth lines are used in Figure 1 to illustrate the SnO₂ surface layer roughness and its effect on the topography of the active layers of the cells. The three a-Si:H alloy junctions which make up the active layers of the cell were deposited using plasma enhanced chemical vapor deposition. The top p-i-n junction illustrated in Figure 1 has an a-Si:H intrinsic layer, i1, with an average thickness of 50 nm and a band gap of 1.72 eV. The middle p-i-n has an a-Si:H layer, i2, about 400 nm thick with a 1.72 eV band gap. The bottom p-i-n junction has an a-Si_{1-x}Ge_x:H layer, i3, with an average thickness of 200 nm and a band gap of 1.42 eV. The p layers of the three junctions are about 10 nm thick while the n layers range between 10 and 25 nm. The bottom contact was made by first sputter depositing an 80 nm thick ZnO layer and then a 120 nm thick Ag layer. TRIM calculations show 1.00 MeV protons lose an average of 22 keV traversing the 200 nm thick bottom contact. Hence, the cells were irradiated with 1.022 MeV protons through the bottom contact in order for protons to enter the bottom junction with an average energy of 1.00 MeV. The electronic stopping power for 1.00 MeV protons in a-Si:H is about 40 eV/nm; the nuclear stopping power is about 3.0E-2 eV/nm (ref. 5). The average energy loss of a 1.00 MeV proton in the active volume of the cell structure illustrated in Figure 1 is about 29 keV, and the stopping powers are approximately constant as the proton traverses the active layers. Most of the proton energy is deposited in the SnO₂ layer and glass superstrate.

The cells were illuminated using an Optical Radiation Corporation model SS1000 solar simulator equipped with a model 1522B intensity feedback controller. The solar simulator intensity was adjusted to produce the short-circuit current density, J_{sc}, of triple-junction cells calibrated by Solarex with their dual source AM1.5 global solar simulator (ref. 6). The spectral irradiance of our simulator was not measured; it was used with the filter provided by the manufacturer in the AM0 position. The cells were mounted on an air-cooled stage and contacted with probes. The cell temperature was monitored using the open

circuit voltage, V_{oc} , which was measured at the start and end of J-V measurements. The air flow was adjusted to insure the cell temperature was within one degree Celsius of the stage temperature during the measurements.

RESULTS AND DISCUSSION

Thirty-seven a-Si:H alloy triple-tandem cells were received from Solarex for our proton radiation resistance studies. J-V measurements under illuminated conditions were used to evaluate the "as-received" cells. The cells were then annealed at 200 °C for two hours in a vacuum of about 1E-6 Torr; this anneal is referred to as anneal 1 in the discussion which follows. Following anneal 1 the J-V measurements were repeated; a fill-factor, FF, criterion of $FF > 0.60$ was used to select cells for the investigations; 27 cells met the $FF > 0.60$ criterion and were used in the investigations discussed in this work.

Figure 2 shows the J-V characteristics for a typical cell, ST007, following anneal 1; the J-V measurement shows the cell parameters following anneal 1 are $FF = 0.680$, $V_{oc} = 2.24$ V and $J_{sc} = -5.46$ mA/cm²; the cell efficiencies are about 8.0%. The cell efficiencies are believed to be less than the 10% possible with Solarex technology for two reasons. First, the optical absorption in the OCLI 0213 glass superstrate and SnO₂ layer degrades the cell performance. Secondly, Solarex designed the active layers in order to spectrally match the cells to an AM0 spectrum. However, the efficiencies were measured by Solarex under an AM1.5 global spectrum. The precision of our J-V measurements was limited to about 2% because of probe contacting and solar simulator instability. The laboratory temperature ranged between 19 and 28 °C during the measurements. The effect of variations in laboratory temperature on cell parameters was investigated. Variations in FF and J_{sc} were found to be insignificant at the 1% level; V_{oc} values were found to vary by about 10 mV/°C and were corrected to values at 24 °C.

The effect of multiple annealing cycles on cell parameters was investigated. Six cells were investigated and the number of anneal cycles was between 10 and 12. The anneal cycle included soaking the cells at 200 °C for two hours in a vacuum of about 1E-6 Torr. Most of the cells were annealed at the same time; following each anneal cycle, the cells were removed from the anneal apparatus and the J-V characteristics measured. The cell parameters were determined from the J-V characteristics and the ratio of the standard deviation to the average cell parame-

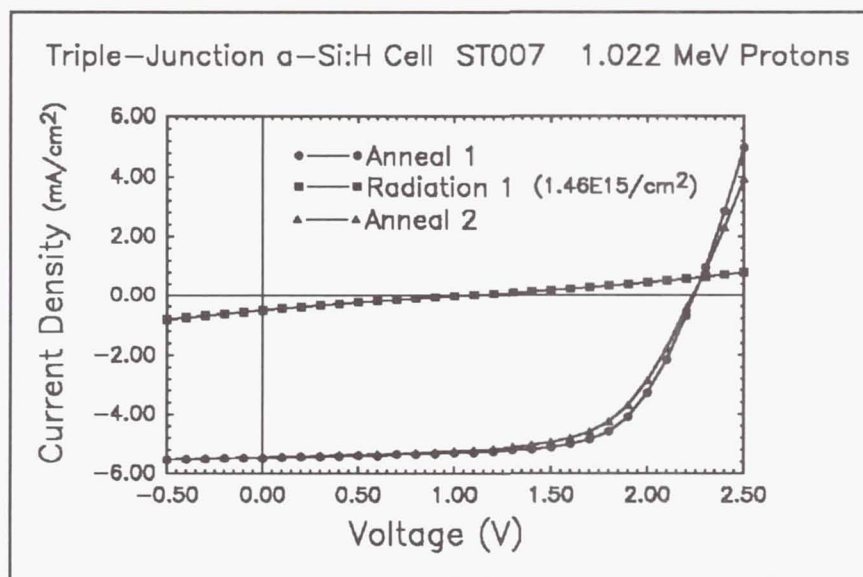


Figure 2. Cell ST007 J-V measurements following anneal 1, irradiation and anneal 2.

Table I. The effect of annealing cycles on the ratio of the standard deviation to the average value for the FF, V_{oc} and I_{sc} .

Cell	FF (%)	V_{oc} (%)	I_{sc} (%)	Cycles (number)
ST024	1.06	0.47	1.87	12
ST026	3.06	0.70	2.19	12
ST037	1.81	0.70	2.20	10
ST038	3.32	0.98	1.95	10
ST039	1.05	0.68	2.69	10
ST040	1.21	1.00	2.69	11
Avg.	1.81	0.70	2.20	

ter was calculated. The results of multiple anneal cycles on the cells are shown in Table I. The averages of the ratios for the FF, V_{oc} and I_{sc} range between 0.70 and 3.32%. The data show the changes in intrinsic cell parameters produced by 10 to 12 annealing cycles are less than 4% and at the level of the precision of the measurements. It is concluded the cell parameters are stable to within a few percent following multiple anneals. The finding supports the position that the effect of annealing on irradiated cells is to anneal defects produced by irradiation, instead of changing intrinsic cell parameters. Annealing studies of irradiated cells should be useful in clarifying the nature of radiation-induced defects.

Our earlier work shows device thickness plays an important role in radiation resistance (ref. 7). Three cells with $FF < 0.60$ which had been excluded from the proton irradiation studies were analyzed using Rutherford Backscattering Spectrometry, RBS, (ref. 8). Cells with $FF < 0.60$ were used because the radiation damage produced by 2.00 MeV He^+ RBS fluences is much greater than the radiation damage produced by the largest 1.022 MeV proton fluences used. RUMP simulations (ref. 9) were carried out to determine the thicknesses of the a-Si:H alloy layers, and the contact and SnO_2 layers. The resolution of the RBS measurements is about 20 nm for the active layers of the cells; the RUMP simulations produced

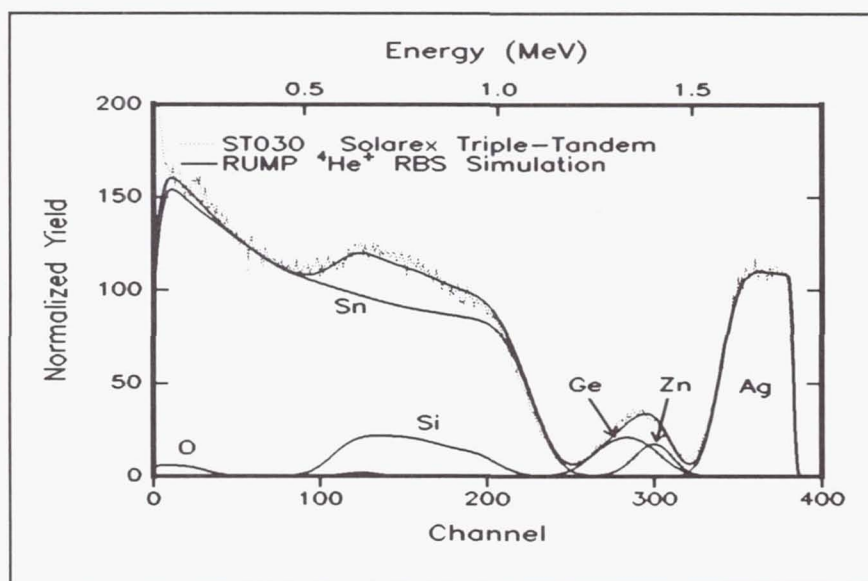


Figure 3. Cell ST030 2.00 MeV RBS measurements and RUMP simulation.

active layer thicknesses of cells irradiated with 1.022 MeV protons; protons backscattered during 1.022 MeV irradiations were used for RBS measurements. The measurements show the variation in thickness of the active layers of the cells is less than 20%.

Twenty-one cells were mounted on a sample holder attached to a stepper-motor controlled sample manipulator in the accelerator target chamber; the chamber pressure was about $1E-6$ Torr during the irradiations. Eighteen triple-tandem cells were irradiated with 1.022 MeV proton fluences. Three cells were irradiated with each of the following six fluences: $5.10E12$, $1.46E13$, $5.10E13$, $1.46E14$, $5.10E14$ and $1.46E15$ cm^{-2} . Three cells used for control purposes were mounted on the sample holder. Control cells were carried through the same steps as irradiated cells with the exception of irradiation; they were mounted between cells irradiated with the highest fluences. No radiation induced changes were measured in the control cells; this shows the beam collimation insured adjacent cells were not exposed to fluences detectable with J-V measurements. The cells were irradiated in the dark with the contact pads shorted to the sample holder. Proton beam currents between 2.5 and 50 nA were used. Cells were

visually monitored during irradiation with the aid of a video system; on one occasion a spark was observed suggesting problems with the method of shorting the cells to the sample holder. The effect of sparking on the cells is of great concern and will be investigated in our future work. Efforts will be made to improve the electrical contacting of cell contact pads to the sample holder.

Reciprocity of current and time was tested at two fluences, namely, $5.10\text{E}13\text{ cm}^{-2}$ using currents of 10, 23 and 50 nA, and $5.10\text{E}12\text{ cm}^{-2}$ with currents of 2.5, 5.0 and 9.0 nA. No differences in the parameters of six cells used in the reciprocity tests could be correlated with the failure of reciprocity. It is concluded that reciprocity of beam current and irradiation time holds for this work.

Following proton irradiation the cells were placed in copper ampules and transported to the device characterization laboratory. The cells were stored for 29 days in a refrigerator maintained at $-10\text{ }^{\circ}\text{C}$ and under dark conditions. The cells were stored at $-10\text{ }^{\circ}\text{C}$ because our earlier work demonstrated annealing of irradiated a-Si:H alloy cells occurs when cells are stored at $0\text{ }^{\circ}\text{C}$ (ref. 3). Prior to measuring the J-V characteristics of a cell, the cell and copper ampule were removed from the refrigerator and placed in a desiccator, and warmed to

Table II. Maximum and normalized power densities (shown in parentheses) measured pre-irradiation, A1, and post-irradiation, R1 CYCLE 1 and R1 CYCLE 2.

Cell	Fluence (cm^{-2})	Maximum and Normalized Power Densities (mW/cm^2)				
		A1	R1 CYCLE 1	(1.01)	R1 CYCLE 2	(1.02)
ST008	Control	8.36	8.41	(1.01)	8.53	(1.02)
ST033	$5.10\text{E}12$	8.44	7.79	(0.92)	7.88	(0.93)
ST028	$1.46\text{E}13$	8.03	6.82	(0.85)	6.99	(0.87)
ST021	$5.10\text{E}13$	8.64	4.76	(0.55)	4.92	(0.57)
ST020	$1.46\text{E}14$	7.75	1.96	(0.25)	2.07	(0.27)
ST019	$1.46\text{E}14$	8.06	1.66	(0.21)	1.74	(0.22)
ST017	$5.10\text{E}14$	8.61	0.20	(0.02)	0.23	(0.03)
ST009	$1.46\text{E}15$	8.31	0.03	(0.00)	0.04	(0.00)
ST001	$1.46\text{E}15$	8.23	0.21	(0.03)	0.21	(0.03)

room temperature in about 30 minutes. The cell was removed from the copper ampule, mounted in the solar simulator sample stage and probes affixed to the cell contact pads. Cell mounting and dark and light J-V measurements were completed in less than 30 minutes. Following J-V measurements, the cell was returned to the copper ampule and stored in the refrigerator. The total time elapsed during a measurement cycle, namely, the time required to remove a cell from the refrigerator, carry out the measurements, and return it to the refrigerator was less than one hour. The effect of the J-V measurement cycle on cell parameters was evaluated by repeating the measurement cycle six days later, 35 days following the irradiations. Nine cells were measured with at least one cell irradiated at each of the six fluences investigated. Results of measurements of the power density evaluated at the maximum power point on the J-V characteristic are shown in Table II. Anneal 1 data in the column labelled A1 were measured pre-irradiation; columns labelled R1 CYCLE 1 and R1 CYCLE 2 contain the data measured 29 and 35 days post-irradiation, respectively. The first measurement cycle, R1 CYCLE 1, was carried out 29 days after the irradiations with the cells stored at $-10\text{ }^{\circ}\text{C}$; the second measurement cycle, R1 CYCLE 2, was carried out six days later with the cells stored at $-10\text{ }^{\circ}\text{C}$ following the R1 CYCLE 1 measurement. The results in Table II are presented two ways. The maximum power densities are shown for the A1, R1 CYCLE 1 and R1 CYCLE 2 measurements; the R1 CYCLE 1 and R1 CYCLE 2 measurements are normalized to A1 measurements and shown in parentheses. Table II shows a 2% change in the power density of the control cell over a 35 day period. The change in control cell power density is representative of the long-term stability in the solar simulator spectral irradiance. This shows the precision of our measurements, including stability of the simulator, is about 2% for this work. Power densities decrease with increasing fluence, as do the normalized values, but the differences between the R1 CYCLE 1 and R1 CYCLE 2 measurements are less than or equal to 2%. It is concluded the measurements show no differences in power density which can be attributed to the measurement cycle. The differences between the power densities of cells irradiated with the same fluences are about 4%; this difference is larger than the precision of the measurements.

The results of 1.022 MeV proton irradiations on a-Si:H alloy triple-tandem cells are shown in Figure 2 and Table III. Figure 2 shows the J-V characteristics for one of the cells, ST007, which was irradiated to a fluence of $1.46\text{E}15\text{ cm}^{-2}$. Following irradiation the cell parameters are: $\text{FF}=0.227$; $V_{\text{oc}}=1.10\text{ V}$; $J_{\text{sc}}=-0.53\text{ mA/cm}^2$; and $P_{\text{max}}=0.13\text{ mW/cm}^2$. The values correspond to degradation in normalized cell parameters to: $\text{FF}=33\%$; $V_{\text{oc}}=49\%$; $J_{\text{sc}}=10\%$; and $P_{\text{max}}=1.6\%$. Annealing cell ST007 at $200\text{ }^{\circ}\text{C}$ for two hours resulted in the recovery of the J-V characteristic as shown in Figure 2. The normalized cell parameters recovered to the following percentages of the pre-irradiation values: $\text{FF}=94\%$; $V_{\text{oc}}=99\%$; $J_{\text{sc}}=100\%$; and $P_{\text{max}}=93\%$. The J-V characteristic observed for cell ST007 is characteristic of the other irradiated cells with the exception that there is less degradation and better recovery for lower fluences. Table III shows the variation in the average maximum and normalized power densities. The power densities were measured at the maximum power point and the average power densities are for three cells irradiated to the fluences indicated. The average power densities in column A1 were measured on cells annealed at $200\text{ }^{\circ}\text{C}$ for two hours prior to proton irradiation. Column R1 shows the average power densities measured 29 days after irradiation with the cells stored in the dark at $-10\text{ }^{\circ}\text{C}$. Column (R1/A1) contains the average post-irradiation power densities normalized to the A1 values. The cells were annealed at $200\text{ }^{\circ}\text{C}$ for two hours following R1 measurements. The average power densities under these conditions are in column A2; the A2 power densities normalized to the A1 values are shown in column (A2/A1). Table III shows 1.022 MeV protons degrade the normalized average power density to 0.92 at the lowest fluence used in this work, namely, $5.10\text{E}12\text{ cm}^{-2}$. Increasing the fluence to $1.46\text{E}15\text{ cm}^{-2}$ degrades the normalized average power density to about 0.02. Annealing the cells restored the average power densities to the pre-irradiation values for fluences less than and equal to $5.10\text{E}13\text{ cm}^{-2}$. For fluences above this value, a two-hour anneal at $200\text{ }^{\circ}\text{C}$ restores the average power densities to within 90% of the pre-irradiation values. We expect that annealing for longer times will restore the average power densities for these higher fluences.

The normalized average power densities for the triple-tandem a-Si:H alloy solar cells following irradiation are compared to different types of solar cells in Figure 4. Smooth curves are plotted through the normalized power densities measured following irradiation of the cells with

Table III. Maximum and normalized average power densities under pre-irradiation, A1, post-irradiation, R1, and post-irradiation annealed, A2, conditions.

Fluence (cm^{-2})	Maximum and Normalized Average Power Densities (mW/cm^2)				
	A1	R1	(R1/A1)	A2	(A2/A1)
Control	8.18	8.26	(1.01)	8.32	(1.02)
$5.10\text{E}12$	8.26	7.60	(0.92)	8.42	(1.02)
$1.46\text{E}13$	8.27	6.74	(0.82)	8.52	(1.03)
$5.10\text{E}13$	8.04	4.24	(0.53)	8.20	(1.02)
$1.46\text{E}14$	8.16	1.84	(0.23)	7.66	(0.94)
$5.10\text{E}14$	8.31	0.39	(0.05)	8.10	(0.98)
$1.46\text{E}15$	8.31	0.13	(0.02)	7.55	(0.91)

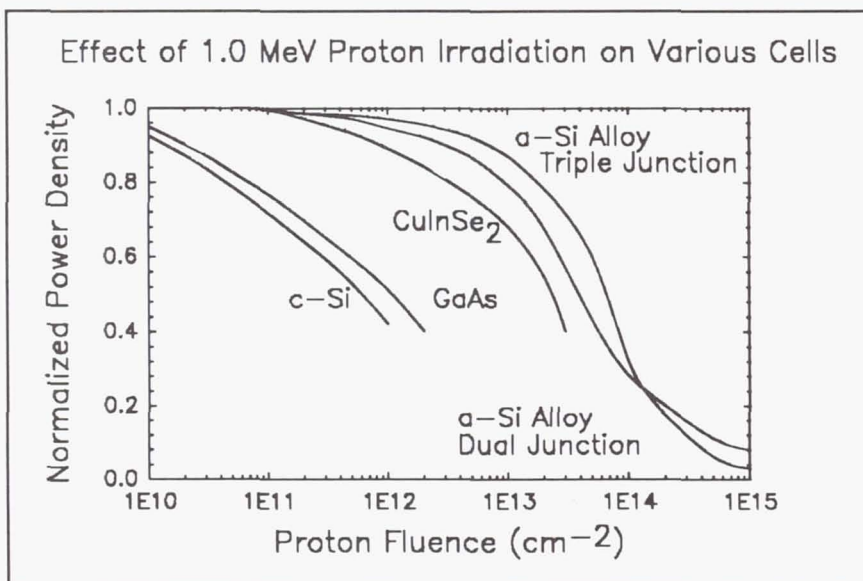


Figure 4. Normalized cell power for crystalline Si and GaAs, CuInSe₂ and a-Si:H solar cells irradiated with 1.00 MeV protons.

various proton fluences. One MeV proton irradiation of crystalline Si and GaAs cells (ref. 10), and CuInSe₂ cells (ref. 11) are shown along with dual-junction a-Si:H alloy cells (ref. 12). Data for 1.00 MeV proton irradiation of InP have not been published; 10 MeV proton data for fluences below 5E12 cm⁻² have been published (ref. 13); the data are not shown in Figure 4 but would fall between the dual-junction tandem a-Si:H alloy and CuInSe₂ curves. The stopping power of 10 MeV protons in InP is less at 1.00 MeV. InP data resulting from 1.00 MeV proton irradiation will be shifted to lower normalized cell powers. Figure 4 shows triple-junction a-Si:H alloy cells have a 1.00 MeV proton radiation resistance superior to other cells for fluences less than about 1E14 cm⁻²; dual junction a-Si:H alloy cells have better radiation resistance for fluences above 1E14 cm⁻².

The degradation in the average value of parameters for cells irradiated with 1.00 MeV protons is shown in Figure 5. The percent of the pre-irradiation average values of FF, V_{oc} and J_{sc} are shown versus fluence; the average values of the cell parameters were determined using the data from three cells irradiated to the same fluence. The decrease in average cell power density is dominated by FF for fluences up to about 5E13 cm⁻²; above this fluence, J_{sc} dominates the degradation in the power density.

Figure 6 shows the manner in which FF varied for all irradiated cells along with the average values; the figure also shows FF following one anneal of each cell at 200 °C for two hours. The scatter in post-irradiation FF at each fluence and the corresponding FF following annealing is within the scatter of the pre-irradiation values except for cell ST020 which was irradiated with a fluence of 1.46E14 cm⁻²; the reason for this is not understood. With the exception of cell ST020, cells irradiated with fluences less than 5.10E14cm⁻² are restored to within 4% of the pre-irradiation FF values with annealing; cells irradiated with fluences greater than or equal to 5.10E14cm⁻² annealed within 7% of pre-irradi-

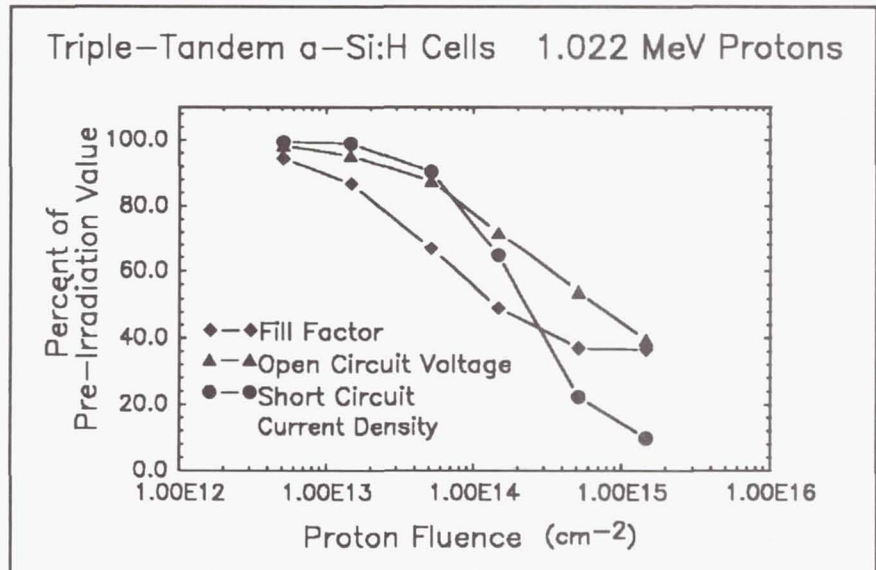


Figure 5. Changes in the FF, V_{oc} and J_{sc} of triple-junction a-Si:H alloy solar cells produced by 1.022 MeV proton irradiation.

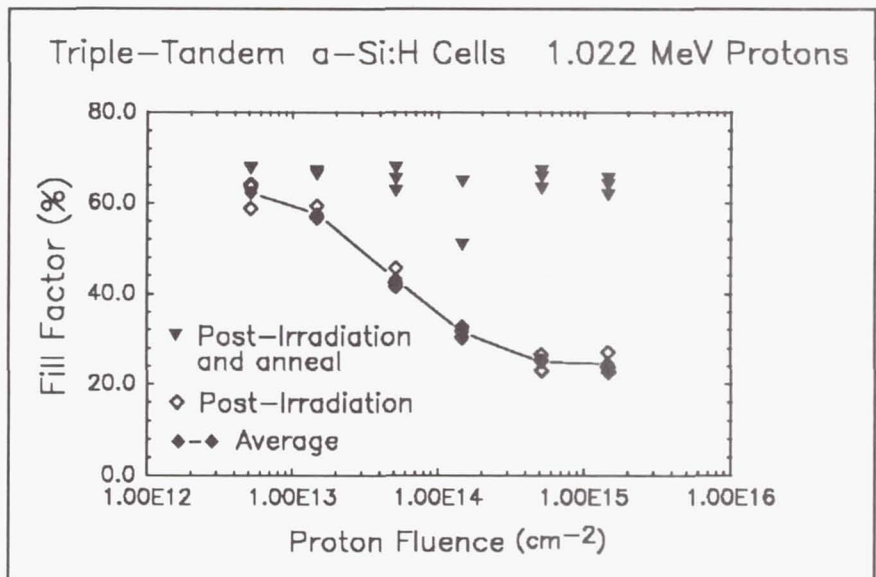


Figure 6. Percent change in FF of triple-junction a-Si:H alloy solar cells following 1.022 MeV proton irradiation and annealing.

ation FF values. Cell ST020 has an annealed post-irradiation FF value which differs from the pre-irradiation value by 20%.

The behavior of V_{oc} with irradiation and post-irradiation annealing is shown in Figure 7. V_{oc} shows scatter at each fluence following irradiation which exceeds the scatter both in the pre-irradiation and the annealed post-irradiation values. With the exception of cell ST020, annealed post-irradiation V_{oc} values are within 3% of the pre-irradiation values. Cell ST020 has an annealed post-irradiation which is 5% less than the pre-irradiation V_{oc} . Figure 7 shows the lowest post-irradiation value of V_{oc} was measured on cell ST009 which was irradiated to a fluence of $1.46E15 \text{ cm}^{-2}$. Sparking was observed during irradiation of cell ST009. The role of sparking on the post-irradiation V_{oc} values and the scatter in V_{oc} values of cells irradiated to the same fluence will be the subject of future investigations.

The correlation of scatter in V_{oc} with active layer thickness was explored. RBS measurements and RUMP simulations show 14 cells have active layer thicknesses ranging between 680 and 760 nm. Four cells had active layer thicknesses ranging between 620 and 630 nm. V_{oc} differences between cells of the same thickness are about the same as the cells different thicknesses. We are unable to correlate the scatter in V_{oc} with cell active layer thickness.

The effect of 1.022 MeV proton irradiation on J_{sc} is shown in Figure 8. The scatter in the post-irradiation values exceeds the scatter in both the pre-irradiation and annealed post-irradiation values of J_{sc} ; the annealed post-irradiation values recovered to within 2% of the pre-irradiation values. The exception is cell ST009 which annealed to within 8% of the pre-irradiation value. The active layer thickness appears to contribute to the

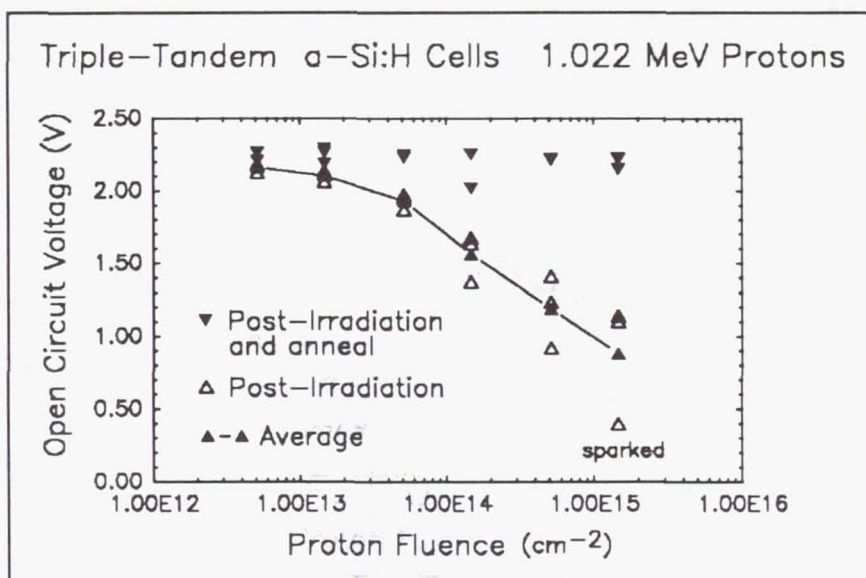


Figure 7. V_{oc} for triple-junction a-Si:H solar cells following 1.022 MeV proton irradiation and annealing.

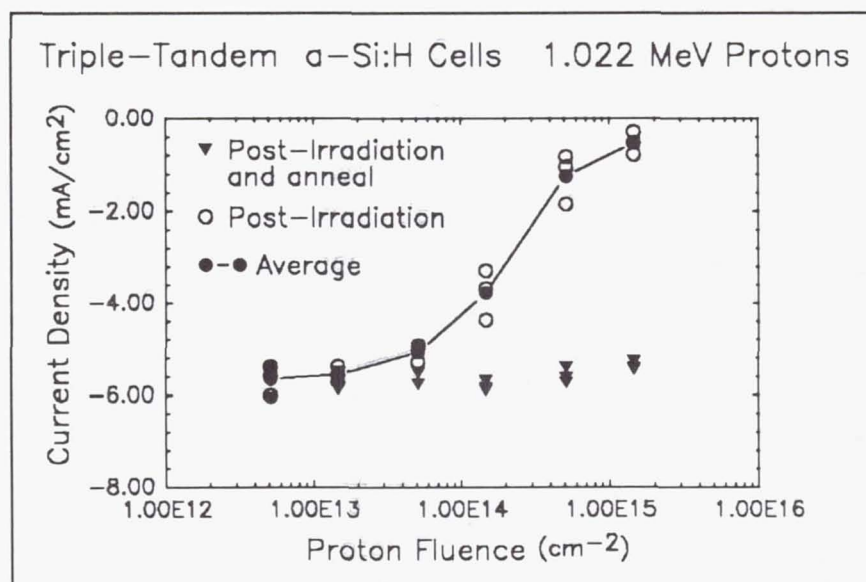


Figure 8. J_{sc} for triple-junction a-Si:H alloy solar cells following 1.022 MeV proton irradiation and annealing.

scatter in J_{sc} . Cells irradiated to the same fluence with thinner active layers exhibited less degradation in J_{sc} than the thicker cells.

CONCLUSIONS

Investigations of twenty-seven triple-junction a-Si:H alloy cells for use in radiation resistance studies show the cells are stable when annealed for up to 12 cycles. The average cell power degrades from a pre-irradiation value of 8.18 to 0.13 mW/cm² following irradiation with a 1.022 MeV proton fluence of 1.46E15 cm⁻². Reciprocity between irradiating beam current and time appears to hold for these studies. The cells have a 1.00 MeV proton radiation resistance which is superior to the other cells for fluences less than about 1E14 cm⁻²; dual junction a-Si:H alloy cells have better radiation resistance for fluences above 1E14 cm⁻². A two-hour 200 °C anneal restores the power to better than 90% of the pre-irradiation value. If the two cells which produced anomalous results are eliminated from the averages, the power density recovers at the 98% level with annealing at 200 °C for two hours. Power density measurements on irradiated cells show no differences which can be attributed to the measurement cycle itself. Variations in V_{oc} at the 20% and J_{sc} at the 10% level were observed for cells irradiated with the same fluence. While some of the variations in J_{sc} correlate with the differences in cell active layer thickness, the variations in V_{oc} cannot be correlated to cell thickness. The source of the variations will be the subject of future studies. RBS measurements and RUMP simulations show the active layer thickness of the cells ranges between 620 and 760 nm; the thicknesses are within 15% of the values determined from the deposition parameters. There is a discrepancy in the SnO₂ layer thickness; the processing parameters suggest the layer is 1000 nm thick while RBS measurements indicate a thickness of 2000 nm. The discrepancy will be explored using other measurement techniques. The cell design developed by Solarex appears to be excellent for radiation resistance research. More research is required to determine if a set of about 25 cells can be used in radiation resistance studies employing multiple irradiation and annealing cycles. The development of experimental techniques will be continued in order to accomplish our goal of reproducing all measurements at the 1% percent level.

REFERENCES

1. James R. Woodyard, Eleventh Space Photovoltaic Research and Technology Conference-1991, NASA Conference Publication 3121, 1991, p. 48-1.
2. James R. Woodyard and Geoffrey A. Landis, Solar Cells **31**, 1991, p. 297
3. Salman Abdulaziz, J. Scott Payson, Yang Li and James R. Woodyard, 21st IEEE Photovoltaic Specialists Conference Proceedings, 1990, p. 1510.
4. D.E. Carlson, 22st IEEE Photovoltaic Specialists Conference Proceedings, 1991, p. 1207.
5. J.F. Ziegler and W. K. Chu, IBM Report RC 4288, 1973.
6. M. S. Bennett and R. Podlesny, 21st IEEE Photovoltaic Specialists Conference Proceedings, 1990, p. 1438.
7. James R. Woodyard, Amorphous Silicon Technology-1992, Materials Research Society Symposium Proceedings, Edited by M. J. Thompson, P. G. LeComber, Y. Hamakawa, A. Madan and E. Schiff, 1992, p. 1151.
8. Backscattering Spectrometry, W. K. Chu, J. W. Mayer, and M. A. Nicolet, Academic Press, NY, 1978.
9. L. R. Doolittle, Nucl. Inst. Meth. **B15**, 1986, 227.
10. B. E. Anspaugh and R. G. Downing, 17st IEEE Photovoltaic Specialists Conference Proceedings, 1984, p. 23.
11. H. Dursch, W. Chen and D. Russel, Proc. of the Space Photovoltaic Research and Technology Conference, NASA Conference Publication 2408, 1985, p. 165.
12. J.J. Hanak, A. Myatt, P. Nath and J.R. Woodyard, Proc. of the 18th IEEE Photovoltaic Specialists Conference, 1985, p. 1718.
13. I. Weinberg, C.K. Swartz and R.E. Hart Jr., Proc. of the 20th IEEE Photovoltaic Specialist Conference, 1988, p.893.

RESULTS OF SOME INITIAL SPACE QUALIFICATION TESTING ON TRIPLE JUNCTION a-Si and CuInSe₂ THIN FILM SOLAR CELLS¹

Robert L. Mueller, Bruce E. Anspaugh
California Institute of Technology, Jet Propulsion Laboratory
Pasadena, California 91109

ABSTRACT

A series of environmental tests have been completed on one type of triple junction a-Si and two types of CuInSe₂ thin film solar cells. The environmental tests include electron irradiation at energies of 0.7, 1.0 and 2.0 MeV, proton irradiation at energies of 0.115, 0.24, 0.3, 0.5, 1.0 and 3.0 MeV, post-irradiation annealing at temperatures between 20°C and 60°C, long term exposure to air mass zero (AM0) photons, measurement of the cells as a function of temperature and illumination intensity, and contact pull strength tests. As expected, the cells are very resistant to electron and proton irradiation. However, when a selected cell type is exposed to low energy protons designed to penetrate to the junction region, there is evidence of more significant damage. A significant amount of recovery was observed after annealing in several of the cells. However, it is not permanent and durable, but merely a temporary restoration, later nullified with additional irradiation. Contact pull strengths measured on the triple junction a-Si cells averaged 667 grams, and pull strengths measured on the Boeing CuInSe₂ cells averaged 880 grams. Significant degradation of all cell types was observed after exposure to a 580 hour photon degradation test, regardless of whether the cells had been unirradiated or irradiated (electrons or protons). Although one cell from one manufacturer lost $\approx 60\%$ of its power after the photon test, several other cells from this manufacturer did not degrade at all.

INTRODUCTION

Thin film solar cells have been developed over the past few years primarily for terrestrial applications. Recently developed cells are exhibiting efficiencies that approach the efficiencies of silicon solar cells currently in use on space solar arrays. The most promising thin film solar cells are made of copper indium di-selenide (CIS) and amorphous silicon (a-Si). Preliminary results (refs. 1-4) have also shown that both cell types are very resistant to electron and proton radiation. These attributes of light weight, moderately high efficiencies, and radiation resistance are whetting the interest of many space solar array designers. The purpose of the work reported here was to test and evaluate CIS and a-Si solar cell technology for potential application to space missions.

SOLAR CELLS

The solar cells tested were purchased from three vendors, Boeing and ISET for the CuInSe₂ cells and Solarex for the triple junction a-Si cells. The Boeing cells were made by a physical vapor deposition of the CIS film from multiple elemental sources in a vacuum (refs. 5,6). The ISET cells were made by the selenization of electron-beam-evaporated Cu-In films in a H₂Se atmosphere, followed by deposition of thin

¹ The research described in this paper was carried out by the Jet Propulsion Laboratory, California Institute of Technology, and was sponsored by the U.S. Air Force Phillips Laboratory.

Reference herein to any specific commercial product, process, or service by trade name, trademark, manufacturer, or otherwise, does not constitute or imply its endorsement by the United States Government, or the Jet Propulsion Laboratory, California Institute of Technology.

CdS and ZnO window layers (ref. 7). The Solarex cells were made by the DC plasma assisted CVD technique (ref. 8). The cell structures of all three cell types are diagrammed in Figure 1. The CIS cells were all made on 500 μm -thick glass substrates and were constructed so that both the n and the p contacts were accessible from the front cell surface. The Solarex cell was made with a 500 μm -thick glass superstrate. It was made of OCLI 0213 Ce-doped coverglass material so that radiation darkening of the glass would not obscure the results of the cell's radiation testing. The Solarex cell contacts were both accessible from the rear cell surface.

Since most of the cells used in these tests were manufactured primarily for terrestrial use, an initial purchase was made of a few cells from each vendor in order to see if there would be any problems with the way the cells would interact with our test probes and procedures. Contact structure modifications were found necessary on the ISET and Solarex cells, and the manufacturers were very cooperative in modifying the contacts for us. A second batch of modified cells was purchased with the contacts compatible with space testing procedures. The cells procured for these tests were quite expensive because they are not available in production quantities. However, we were able to purchase a sufficient quantity of cells so that a sample size of at least three was used in nearly all the experiments.

SOLAR CELL ELECTRICAL TESTS

All solar cells were electrically characterized before and after any of the tests reported here by measuring their I-V characteristics and their spectral responses. The I-V measurements were performed using a Spectrolab X-25 Mark II solar simulator as the light source. Its illumination level was set to air mass zero (AM0) intensity (136.7 mW/cm^2) using an appropriate balloon flight standard. Special fixtures were constructed for measuring each cell type. The fixtures used spring loaded probes to contact the cells. During the measurements, the cells were held at 28°C . The computer program and electronics ordinarily used for measuring the I-V characteristics of crystalline Si and GaAs cells was used for these measurements without modification.

I-V measurements were obtained on thirty Boeing CIS cells, twenty-nine ISET CIS cells, thirty-one Lot I Solarex triple junction a-Si cells and twenty Lot II Solarex triple junction a-Si cells (The Solarex cells were divided into two lots because they had noticeably different I-V and spectral response characteristics). The averaged values for the initial AM0 electrical parameters are summarized in Table I. Conversion efficiencies were computed by using the active areas listed in the table. Active areas were used in the calculations for comparison purposes because some cells had very large contact pads outside the cell area and would be much smaller in production cells.

The JPL spectral response apparatus was modified for measurements of the triple-junction a-Si cells. As reported in ref. 9, this involved the measurement of each cell three times. During each measurement the dc bias light was filtered in such a manner that first junctions 2 and 3 were turned on by the filtered light so that only junction 1 responded to the chopped light from the monochromator. Then the filter was replaced by a second filter which turned on junctions 1 and 3, while junction 2 was measured, and so on. The overall spectral response of the cell is then computed by summing the three curves measured in this manner.

CONTACT STRENGTH TEST RESULTS

Cell contact pull strength tests were completed on the Boeing CIS and the Solarex Triple Junction a-Si cells. No attempt was made to solder or weld to the aluminum contacts on the ISET CIS cells. L-shaped leads consisting of pure silver ribbon ($0.1\text{mm} \times 0.5\text{mm}$) were soldered to the cell contacts using Sn62 (2% Silver) eutectic solder. Care was taken to minimize soldering iron temperature and soldering time (≈ 2 seconds). The 5mm length of the "L" was soldered to the cell contact. The 15mm length of the "L" was used to pull the contact at a 90 degree angle from the cell surface. The pull rate was $\approx 3\text{cm/minute}$ and

the temperature of the pull samples was 20 ± 2 degrees C. The results, shown in Table II, reveal that the contact pull strengths of the cells test was satisfactory.

PROTON IRRADIATION TEST RESULTS

The proton irradiations were performed on the CalTech tandem Van de Graaff accelerator. The beams were spread laterally by passing the proton beams through appropriate chromium or gold scattering foils to produce a beam uniformity of better than $\pm 5\%$ over a 10-cm diameter circle at the target plane. A small Faraday cup at the center of the target plane was used for measuring flux and fluence. The target plane remained at room temperature with no need for active thermal control at the low flux rates used. The cells were attached to the target plane with double-backed adhesive tape. Immediately after irradiation, the cells were removed from the target area and packed in dry ice until electrical measurements began.

Four sets of thin film cells were selected for proton testing. Each set consisted of three of the Boeing, ISET and Solarex Lot I and two of the Solarex Lot II cells. Each set was exposed to a specific proton energy to a schedule of fluences ranging between 1×10^9 and 2×10^{12} p/cm². The proton energies were 0.5, 1.0, and 3.0 MeV for all cell types plus a specific low energy for each cell type. In the case of the CIS cells, these energies were 300 keV for the Boeing cells and 240 keV for the ISET cells. These energies were chosen so that they would stop after penetrating most of the way through the topmost semiconductor layer, at which point they are expected to produce the maximum amount of damage in the cell. The specific energy chosen for the Solarex cells was 115 keV. This proton energy was calculated to stop in the center of the topmost junction of these cells when the protons were incident from the rear. The analysis of the energy absorption of the cell materials was based upon material and thickness information obtained from the cell manufacturers, and the errors made in the calculation will vary as the thickness tolerances and material densities vary. It was found that 500 keV protons would just penetrate all the semiconductor layers of both CIS cell types, and would penetrate all the layers and stop in the superstrate glass in the Solarex cell.

The normalized P_{\max} curves of Figures 2 through 5 summarize the results of the proton irradiations prior to annealing. It is clear that the lowest energy protons which stopped in the top layer of the CIS cells produced very little, if any, damage to the cells. But as the energy was increased to the value that just completely penetrated the CIS cells, 500 keV, the damage was substantial. As the energy was increased to 1 MeV, the damage decreased, and as the energy was increased to 3 MeV, the damage decreased even further. The Solarex cells appear to degrade significantly after bombardment with only one energy, 115 keV. These protons stop in a vulnerable part of the cell while the higher energies pass on through mostly without stopping anywhere in the active part of the cell. While the data for all three cells is too sparse for a precise determination, it may be that the cells are all degrading in accordance with the energy dependence for proton-induced displacement damage of $\ln E/E$ (ref. 10). This line of reasoning also tells us that proton energies between 300 and 500 keV may cause a great deal of damage in the ISET and Boeing cells, and energies between 46 keV (the energy required to penetrate to the third junction) to 500 keV may also cause a lot of damage in these a-Si cells.

After the cells had been irradiated to a fluence of 1×10^{12} p/cm², and characterized electrically, they were annealed at $\approx 20^\circ\text{C}$ for 14 days, then remeasured. They were then placed in a 60°C air oven for 18 hours, and again measured. At this point the cells were irradiated with an additional 1×10^{12} p/cm², and the annealing process repeated (here a 35 day anneal at 20°C was used).

The results of the annealing experiments are summarized in the normalized P_{\max} curves shown in Figures 6 through 9, which show the power remaining after the final 60°C anneals. The total amount of annealing can be computed by a comparison with the matching unannealed curves of Figures 2 through 5. We can make some observations about the annealing behavior. It is possible to anneal out a great deal of the damage produced by low energy protons in all the cells, but the damage produced by the higher energies of 1 and 3 MeV anneals very little. The annealing at 20°C is responsible for the major share of the

recovery. In general, the additional improvement due to the 60°C anneal was only about half the recovery achieved by the 20°C treatment.

ELECTRON IRRADIATION TEST RESULTS

The electron irradiations were performed on the JPL Dynamitron accelerator with the samples held at 28°C during the irradiations. The electron beams were spread laterally with appropriate aluminum or copper scattering foils to give a beam uniformity of better than $\pm 5\%$ over the target plane. The cells were held in thermal contact with the temperature controlled target plane by a thin layer of Apiezon H vacuum grease. In most cases, the cells were measured electrically within a few minutes after irradiation, but in those cases where it would be several hours before measurements could be initiated, the cells were placed in a freezer to minimize annealing.

Three sets of cells consisting of three of the Boeing, ISET and Solarex Lot I and two of the Solarex Lot II cells were exposed to 0.7, 1.0, and 2.0 MeV electrons. Each set of cells was individually exposed to cumulative fluences between 3×10^{13} and 1×10^{16} e/cm² in \approx half order of magnitude steps. The Boeing and ISET cells were exposed to the electrons through their front surfaces, but the Solarex cells were exposed through their rear surfaces so the electrons would not have to first penetrate the superstrate glass. Since the thickness of the actual cell structure is less than 1/100 of the range of 700 keV electrons, the incidence direction matters very little as long as we avoid irradiating through the relatively thick glass supports. I-V measurements were taken after each radiation exposure. Observed changes in normalized maximum power ($P_{\max}/P_{\max 0}$), before annealing, are shown in Figures 10, 11, 12 and 13. A plot of the normalized power behavior of a crystalline silicon cell (ASEC 10 Ω -cm, BSR, dual AR) irradiated with 1 MeV electrons is included in the figures for comparison.

All cells were annealed at low temperatures after they reached fluences of 1×10^{15} e/cm². The first anneal was at room temperature (20°C), and the second anneal was at 60°C in an air oven for \approx 18 hours. I-V measurements were made after each annealing step. The cells were then irradiated to a cumulative fluence of 3×10^{15} e/cm² and the annealing steps were repeated. The cells were then irradiated to a cumulative fluence of 1×10^{16} e/cm², measured, annealed at room temperature for three to five days, and finally annealed at 60°C again for 20 hours. The results of the annealing experiments following the 1×10^{15} , 3×10^{15} and 1×10^{16} e/cm² fluences are shown in the normalized P_{\max} plots of Figures 14, 15, 16 and 17, along with a comparison curve for the ASEC Si cell.

Under electron irradiation, conventional Si and GaAs cells degrade more as the energy is increased. This is in agreement with displacement damage theory as predicted by displacement damage theory. This was also true for CIS cells irradiated to fluences less than $\approx 1 \times 10^{15}$ e/cm², but at higher fluences the 700 keV and 2 MeV electrons were both more damaging than 1 MeV electrons. In contrast, the a-Si cells degraded less with increasing electron energy, indicating that displacement damage is not the only mechanism which is degrading these cells.

It is also clear from the plots of both annealed and unannealed P_{\max} data that the crystalline Si cells begin degrading at low fluences, while the thin film cells exhibit very little degradation until they have been exposed to $\approx 1 \times 10^{15}$ e/cm², at which point their degradation rate increases markedly. The losses in all the cells appear to be about equally shared between losses in V_{oc} and I_{sc} .

All the thin film cells tested here exhibit a much greater recovery of their damage when annealed at low temperatures than the crystalline Si cells. In most cases it was observed that the more the cell was damaged by radiation, the more it will anneal. Examples are the Solarex and ISET cells, heavily degraded after receiving fluences of 1×10^{16} e/cm², which all recovered from 10 to 25% of their pre-irradiation power after the 20° and 60°C anneals. The Boeing cells, less severely damaged, all recovered to within at least 97% of their pre-irradiation values. All cells showed significant recovery after the 2 to 5 day 20°C anneal. The CIS cells all annealed at least as much at room temperature as they did at 60°C, and in some cells the 60°C anneal did not induce any additional recovery at all. The behavior of the cells after irradiation and

annealing, followed by additional irradiation is worthy of comment. It was observed in all cases, that the annealed cells upon receiving their next electron dose, appeared to immediately revert to the state they had been in prior to the annealing, then proceeded to follow an unannealed degradation curve from there on. However, at the moment this observation is rather speculative and would have to be confirmed by performing additional experimentation.

PHOTON DEGRADATION TEST RESULTS

Samples of the three types of cells also underwent long term exposure to air mass zero (AM0) photons for a period of 580 hours. A Spectrolab X-25L was used as the light source. The cells were tested in atmosphere under open circuit condition, and were temperature controlled to 20°C. Proton irradiated, electron irradiated and non-irradiated samples from all three manufacturers were tested. The cells were removed from the exposure fixture for electrical characterization after exposures of 21, 90, 158, 275, 443, and 580 hours.

The proton irradiated cell group consisted of eight cells (two Boeing, two ISET, two Solarex Lot I and two Solarex Lot II) which had been heavily damaged by protons then subjected to the annealing schedules discussed previously. The electron irradiated cell group also consisted of eight typical, 60°C annealed cells that had all been irradiated to 1×10^{18} e/cm². This included one cell each of the four types that had been irradiated with 0.7 MeV electrons, and one cell of each type that had been irradiated with 1 MeV electrons. Eight non-irradiated cells were also included in the test, two from each cell type.

There are some inconsistencies in the results of this test in that it gave poor agreement with a similar test run earlier at JPL. However, some observations may be made. All cell types were observed to degrade with photons, but it takes about 40 hours of exposure to produce a noticeable degradation in most cells. In general, the cells which had been irradiated heavily with either electrons or protons did not degrade as much as unirradiated cells. The degradation of the Solarex cells matched previously observed results at both Solarex and JPL wherein the maximum power dropped $\approx 20\%$ after 500 hours of photon exposure. The CIS cells degraded significantly differently than in previous experiments. Some cells did not degrade at all, and some types that had not degraded at all or only slightly in earlier experiments were seen to degrade a great deal. The reason for these discrepant results is still under investigation.

CONCLUSIONS

Although the thin film cells measured here are very promising, they are probably not yet ready for space use. On the plus side, their radiation resistance to both protons and electrons is generally superior to crystalline Si and GaAs solar cells and the heavy radiation damage induced in thin film cells by both electrons and protons can be mitigated by annealing at fairly low temperatures. All the thin film cells examined here are easily damaged by low energy protons which stop in the active areas of the cells, but the cells can easily be shielded from these protons. The efficiencies are low in comparison with crystalline Si and GaAs cells (the highest efficiency cell measured here was 9.5%), but the potential for making very light weight cells is very good. Photon degradation remains a problem, not only for the a-Si cells, but for the CIS cells as well. Contacts continue to be a problem with some of the thin film cells. Although the contact pull strengths on the cells tested were found to be satisfactory, making contact with the cells was quite difficult and in some cases impossible. The cells we procured for this task were purchased from research laboratories, and the cells experienced an amount of variability in their characteristics that might be expected from cells made in that environment. We are left with the nagging feeling that some of the conclusions drawn here are the result of manufacturing variability. We believe the next step in examining the readiness of these cells for space, will have to involve homing in on a promising manufacturing process, setting up a pilot line, then producing a large quantity of test cells using that process.

REFERENCES

1. Gay, C.F.; Potter, R.R.; Tanner, D.P.; Anspaugh, B.E.: "Radiation Effects on Thin Film Solar Cells," Proc. of the 17th IEEE Photovoltaic Specialists Conf., Kissimmee, FL, 1984, p. 151.
2. Byvik, C.E.; Slomp, W.S.; Smith, B.T.; Buoncristiani, A.M.: "Radiation Damage and Annealing of Amorphous Silicon Solar Cells," Proc. of the 17th IEEE Photovoltaic Specialists Conf., Kissimmee, FL, 1984, p. 155.
3. Schwarz, R.; Kolodzey, J.; Aljishi, S.; Wagner, S.; Kouzes, R.T.: "Radiation Damage by 12 MeV Protons and Annealing of Hydrogenated Amorphous Silicon," Proc. of the 18th IEEE Photovoltaic Specialists Conf., Las Vegas, NV, 1985, p. 903.
4. Burgess, R.M.; Chen, W.S.; Devaney, W.E.; Doyle, D.H.; Kim, N.P.; Stanbery, B.J.: "Electron and Proton Radiation Effects on GaAs and CuInSe₂ Thin Film Solar Cells," Proc. of the 20th IEEE Photovoltaic Specialists Conf., Las Vegas, NV, 1988, p. 909.
5. Kim, N.P.; and Devaney, W.E.: "Low Cost CuInSe₂ Solar Cells for Space Applications," 26 IECEC Conf., San Diego, CA, 1992, Vol. 2, p 314.
6. Mickelsen, R.A.; and Chen, W.S.: "Development of a 9.4% Efficient Thin-Film CuInSe₂/CdS Solar Cell," Proc. of the 15th IEEE Photovoltaics Specialists Conf., Kissimmee, FL, 1981, p. 800.
7. Basol, B.M.; Kapur, V.K.; and Halani, A.: "Advances in High Efficiency CuInSe₂ Solar Cells Prepared by the Selenization Technique," Proc. of the 22nd IEEE Photovoltaics Specialists Conf., Las Vegas, NV, 1991.
8. Carlson, D.E.: "Markets, Manufacturing and Technical Progress in Amorphous Silicon Photovoltaics in the U.S.," Proc. of the 22nd IEEE Photovoltaics Specialists Conf., Las Vegas, NV, 1991, p. 1207.
9. Mueller, R.L.: "Spectral Response Measurements of Two-Terminal Triple-Junction a-Si Solar Cells," to be published.
10. Tada, H.Y.; Carter, Jr., J.R.; Anspaugh, B.E.; and Downing, R.G.: Solar Cell Radiation Handbook, 3rd Edition, JPL Publication 82-69, Jet Propulsion Lab, Pasadena, CA, 1982.

Table I. Initial Electrical Parameters for Tested Thin Film Cells

Manufacturer	I _{sc} (mA)	V _{oc} (mV)	P _{max} (mW)	Active Area (cm ²)	Eff. (%)
Boeing	171.6	408.9	45.25	4.0	8.28
ISET	144.6	452.3	38.73	3.62	7.83
Solarex Lot 1	50.0	2242.9	67.91	7.0	7.10
Solarex Lot 2	45.7	2244.8	51.80	7.0	5.41

Table II. Results of 90 Degree Angle Cell Contact Pull Strength Tests

Cell Mfg	Pull Strength	Std. Dev.	Failure Mode
Boeing	880 grams	± 65 grams	50% Solder 50% Pull Wire
Solarex	667 grams	± 144 grams	Cell Metallization

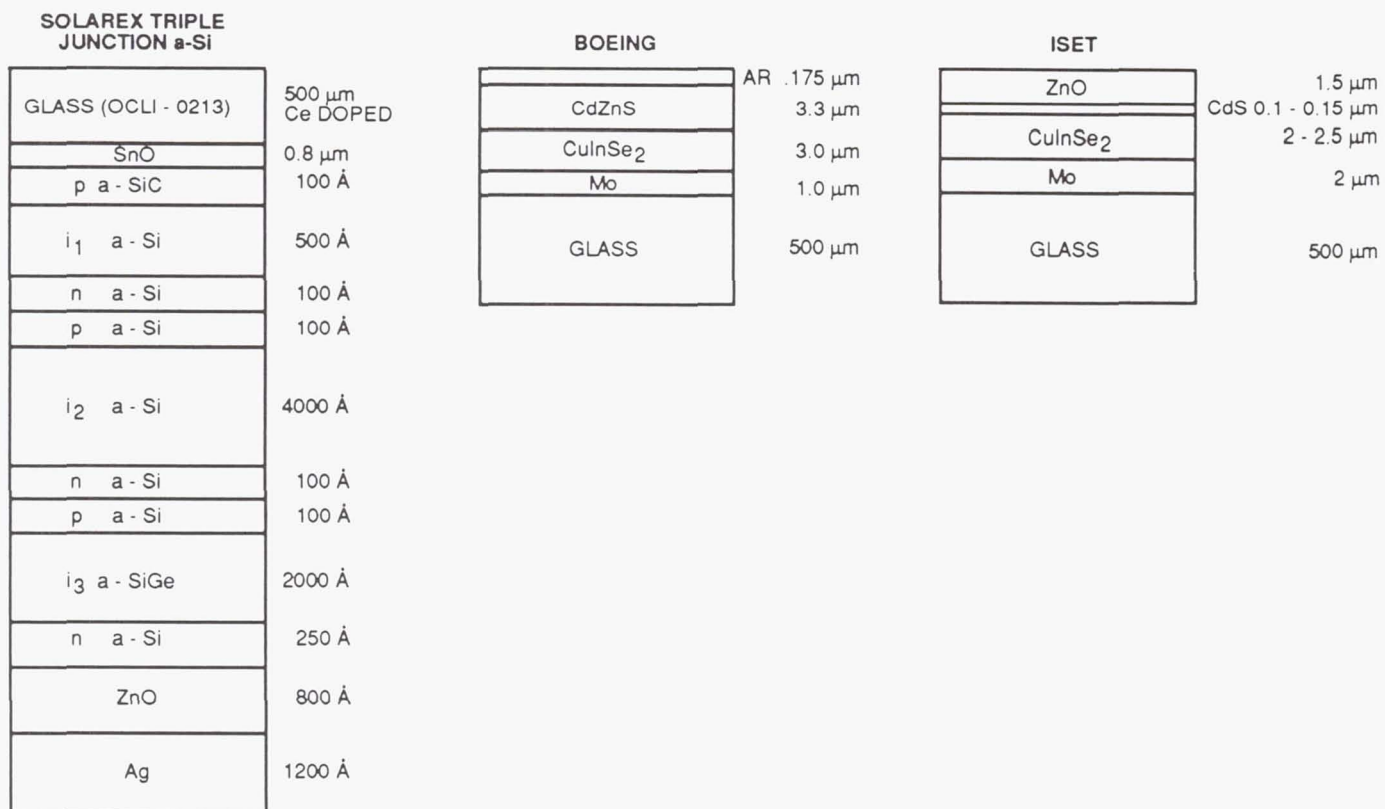


Figure 1 Cross-sections of the Thin Film Solar Cells

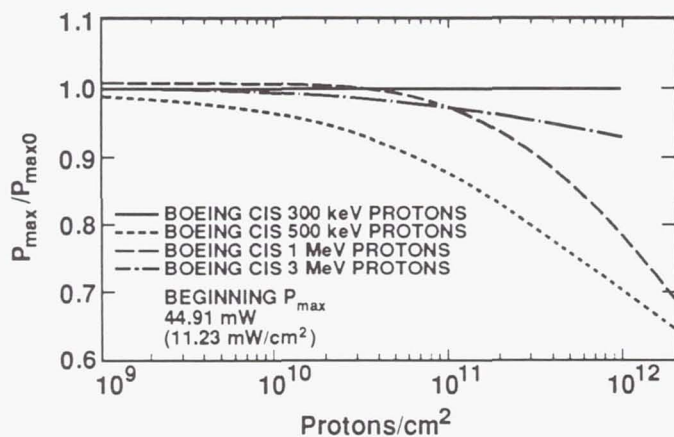


Figure 2 Proton Irradiation Results for Non-annealed Boeing CIS Cells

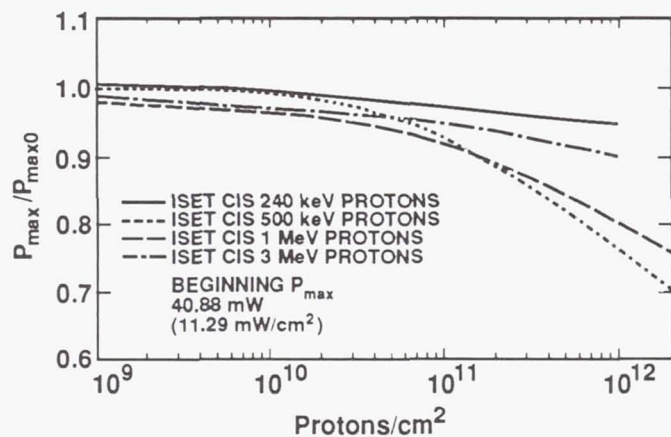


Figure 3 Proton Irradiation Results for Non-annealed ISET CIS Cells

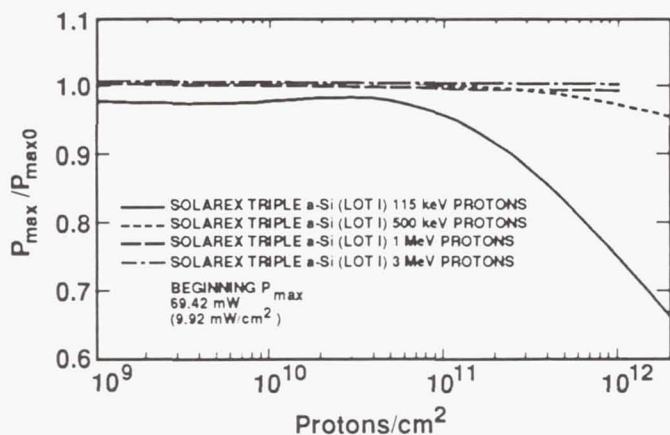


Figure 4 Proton Irradiation Results for Non-annealed Solarex Lot I Triple Junction a-Si Cells

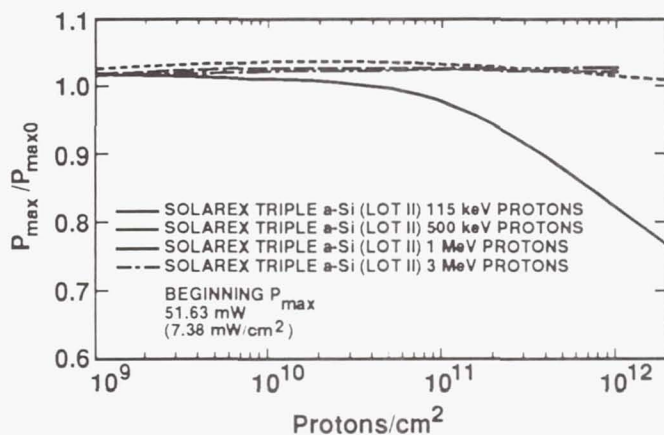


Figure 5 Proton Irradiation Results for Non-annealed Solarex Lot II Triple Junction a-Si Cells

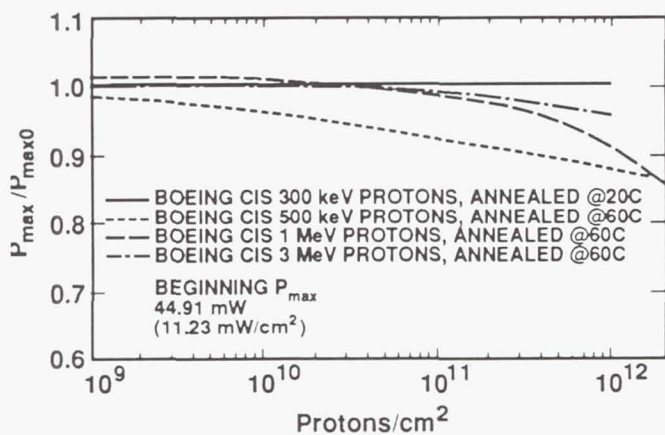


Figure 6 Proton Irradiation Results for 60°C Annealed Boeing CIS Cells

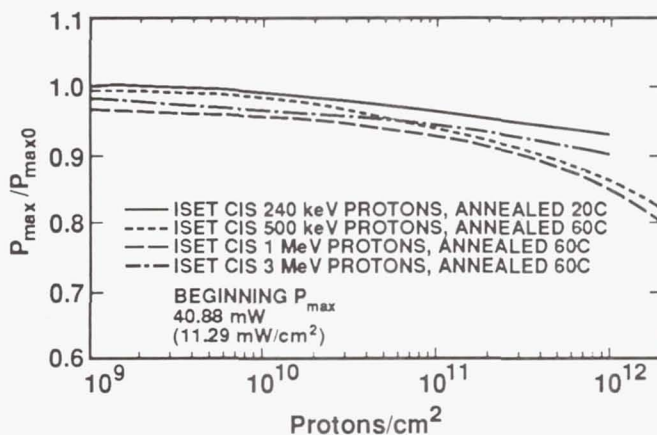


Figure 7 Proton Irradiation Results for 60°C Annealed ISET CIS Cells

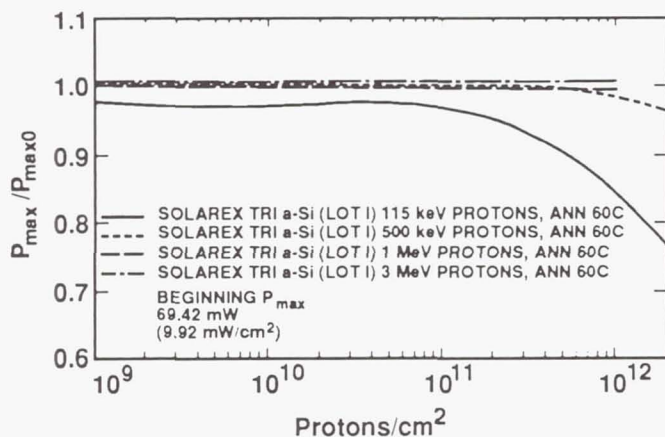


Figure 8 Proton Irradiation Results for 60°C Annealed Solarex Lot I Triple Junction a-Si Cells

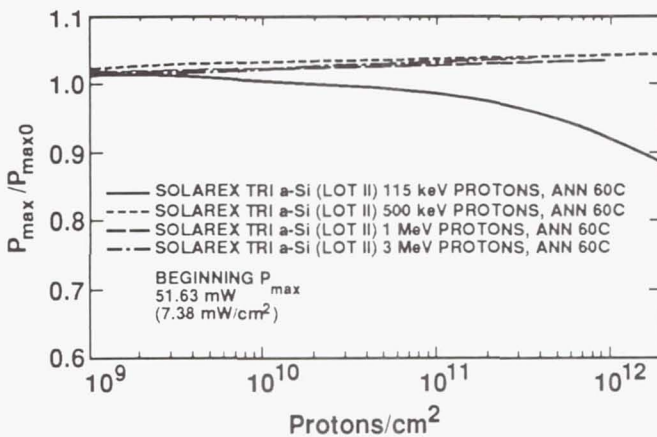


Figure 9 Proton Irradiation Results for 60°C Annealed Solarex Lot II Triple Junction a-Si Cells

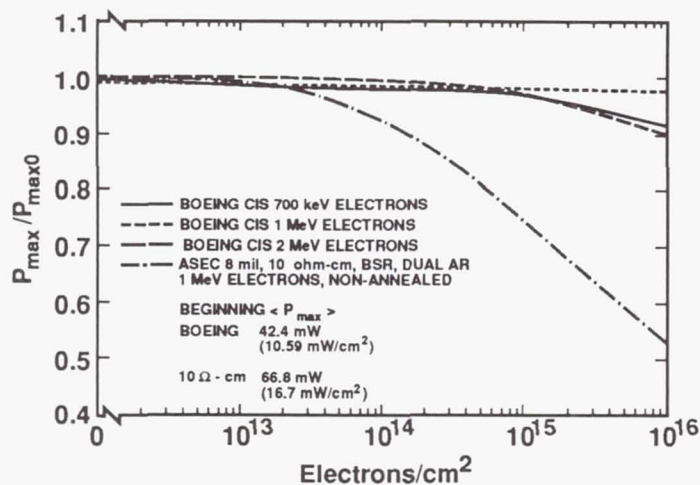


Figure 10 Electron Irradiation Results for Non-annealed Boeing CIS Cells

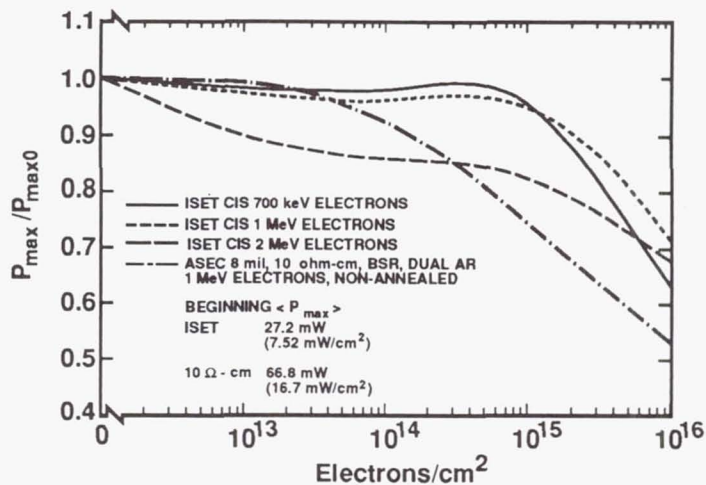


Figure 11 Electron Irradiation Results for Non-annealed ISET CIS Cells

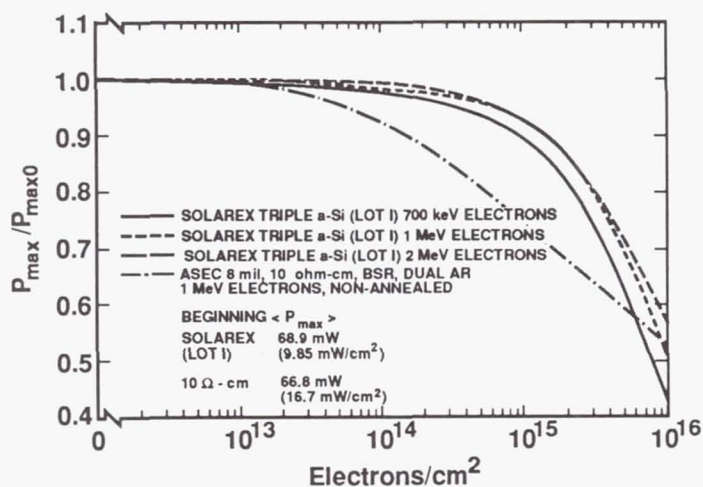


Figure 12 Electron Irradiation Results for Non-annealed Solarex Lot I Triple Junction a-Si Cells

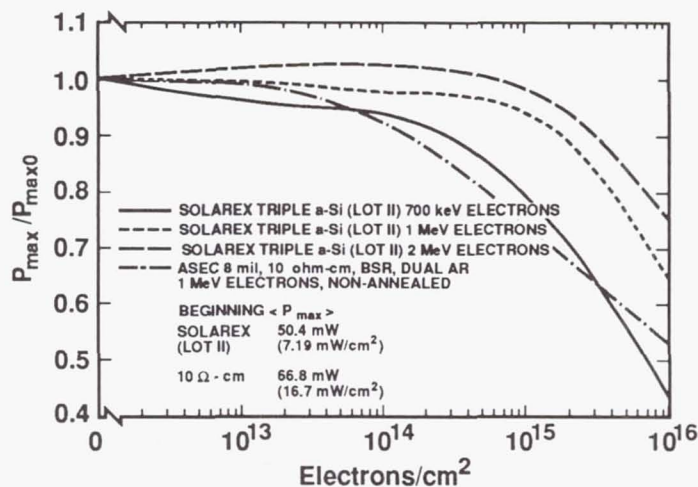


Figure 13 Electron Irradiation Results for Non-annealed Solarex Lot II Triple Junction a-Si Cells

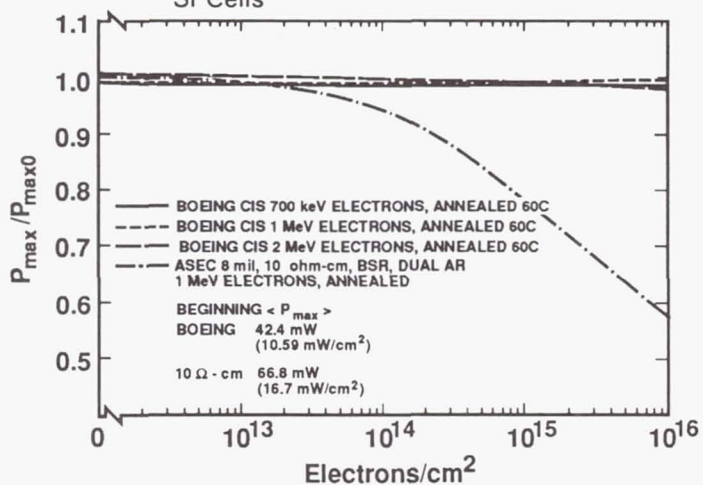


Figure 14 Electron Irradiation Results for 60°C Annealed Boeing CIS Cells

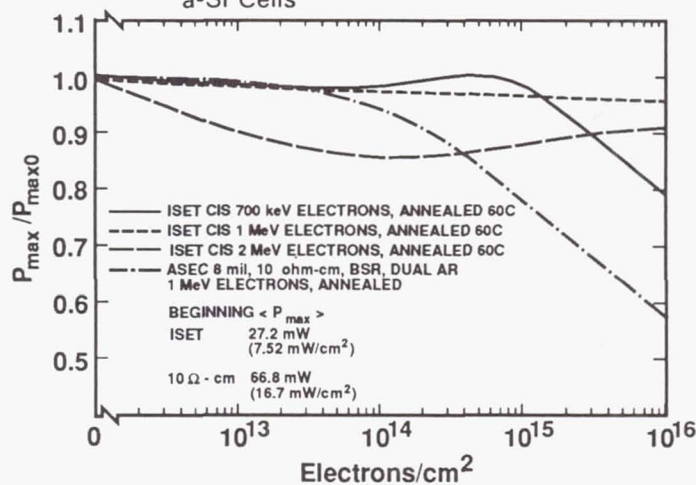


Figure 15 Electron Irradiation Results for 60°C Annealed ISET CIS Cells

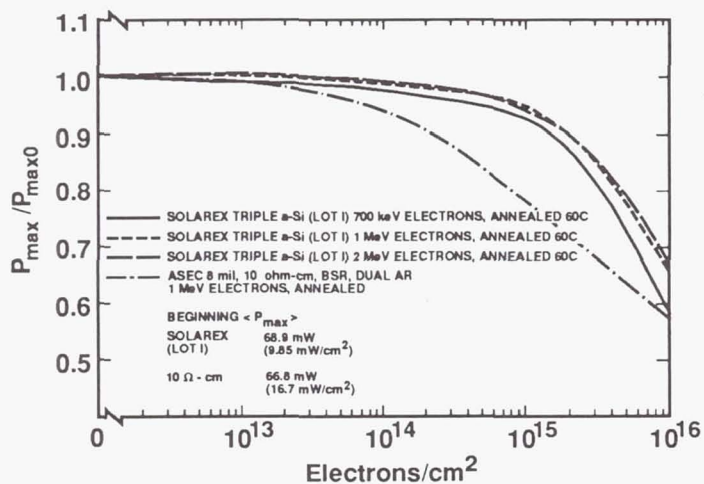


Figure 16 Electron Irradiation Results for 60°C Annealed Solarex Lot I Triple Junction a-Si Cells

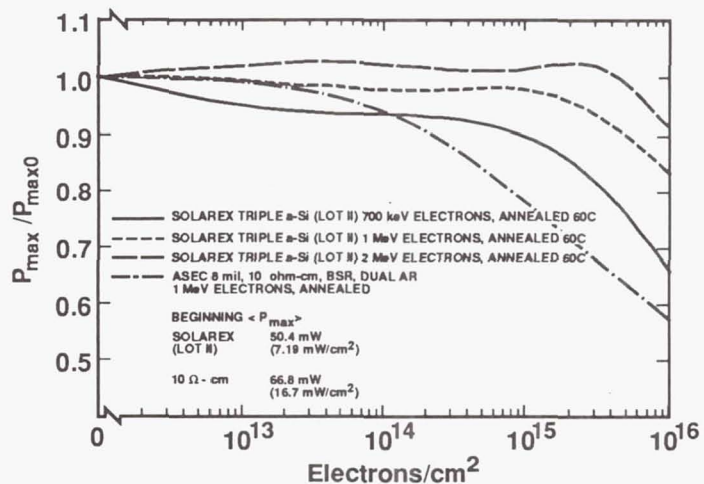


Figure 17 Electron Irradiation Results for 60°C Annealed Solarex Lot II Triple Junction a-Si Cells

Flexible Polycrystalline Thin-Film Photovoltaics for Space Applications*

J.H. Armstrong, B.R. Lanning, M.S. Misra
Martin Marietta Astronautics Group
Denver, Colorado

V.K. Kapur, B.M. Basol
International Solar Electric Technology, Inc.
Inglewood, California

Polycrystalline thin-film photovoltaics (PV), such as CIS and CdTe, have received considerable attention recently with respect to space power applications. Their combination of stability, efficiency, and economy from large-scale monolithic integration of modules can have significant impact on cost and weight of PV arrays for spacecraft and planetary experiments. An added advantage, due to their minimal thickness ($\approx 6 \mu\text{m}$ sans substrate), is the ability to manufacture lightweight, flexible devices ($\approx 2000 \text{ W/kg}$) using large-volume manufacturing techniques. In this paper, the photovoltaic effort at Martin Marietta and ISET will be discussed, including large-area, large-volume thin-film deposition techniques such as electrodeposition and rotating cylindrical magnetron sputtering. Progress in the development of flexible polycrystalline thin-film PV will be presented, including evaluation of flexible CIS cells. In addition, progress on flexible CdTe cells will be presented. Finally, examples of lightweight, flexible arrays and their potential cost and weight impact will be discussed.

This work performed under Martin Marietta IR&D D-17R, "Photovoltaic Technologies"

InGaAs CONCENTRATOR CELLS FOR LASER POWER CONVERTERS AND TANDEM CELLS¹

S. Wojtczuk, S. Vernon and E. Gagnon
Spire Corporation, Bedford, MA 01730-2396

Abstract

$\text{In}_{0.53}\text{Ga}_{0.47}\text{As}$ N-on-P concentrator cells were made as part of an effort to develop 1.315 μm laser power converters. The 1.315 μm laser power conversion efficiency was estimated as 29.4% (at 5.57 W/cm²) based on an 86% measured external quantum efficiency at 1.315 μm , and a measured open circuit voltage (484mV), and fill-factor (67%) at the equivalent AM0 short-circuit photocurrent (5.07 A/cm²). A 13.5% AM0 efficiency was achieved at 89 suns and 25C. Measured one-sun and 100-sun AM0 efficiency, log I-V analysis, and quantum efficiency are presented for InGaAs cells with and without InP windows to passivate the front surface. Windowed cells performed better at concentration than windowless cells. Lattice mismatch between InGaAs epilayers and InP substrate was <800 ppm. Theoretical efficiency is estimated for 1.315 μm laser power converters versus the bandgap energy. Adding aluminum to InGaAs to form $\text{In}_x\text{Al}_y\text{Ga}_{1-x-y}\text{As}$ is presented as a way to achieve an optimal bandgap for 1.315 μm laser power conversion.

Introduction

Solar cells are often used as power for space missions where sunlight is available. However, some applications (ref.1) such as satellites in eclipse, moon bases in lunar night, orbital transfer vehicles, and planetary rovers need power when sunlight is unavailable or require a higher power than the sun provides. Laser beams directed onto the solar cells can provide high power in these instances. In laser power conversion, the cell is optimized for the single laser wavelength and has a higher efficiency ($\approx 30\text{-}60\%$) than cells designed for sunlight ($\approx 15\text{-}25\%$), where compromises are made in design in order to extract the most power from the multiple-wavelength solar spectrum. Achieving the best overall power conversion efficiency involves optimizing both source (laser) and receiver (solar cell) power efficiency. We present data on solar cells useful for converting 1.315 μm laser radiation. This wavelength is of interest because of the existence of high-efficiency 1.315 μm iodine lasers and power conversion systems explored by Walker et al. (ref.2).

Indium gallium arsenide ($\text{In}_{0.53}\text{Ga}_{0.47}\text{As}$) single-junction N-on-P cells used as laser power converters (LPCs) are investigated. The $\text{In}_{0.53}\text{Ga}_{0.47}\text{As}$ ("InGaAs" henceforth) is lattice-matched to indium phosphide (InP) substrates. Measured AM0 and quantum efficiency data are used to estimate the laser power converter (LPC) efficiency at 1.315 μm (29.4%). The 0.75eV bandgap of InGaAs is slightly sub-optimal for 1.315 μm laser power conversion. Adding aluminum to InGaAs to form $\text{In}_x\text{Al}_y\text{Ga}_{1-x-y}\text{As}$ is suggested to increase the bandgap towards the optimal 0.9eV energy, while maintaining InP lattice match. Theoretical efficiency limits for 1.315 μm LPCs versus the bandgap are presented. These single-junction LPCs can use laser powers of $\approx 5\text{ W/cm}^2$ (about 100 AM0 suns). For higher power (e.g. 100 W/cm²), a single junction LPC has excessive I²R loss. Spire plans to eventually series-connect (boosting voltage) many small junctions over the same area as the larger single junction, to lower photocurrent and I²R loss, similar to how a generating station transmits power to consumers at high-voltage to avoid I²R loss through miles of copper. Multijunction LPCs have been implemented in GaAs technology (ref.3,4). Finally, the cells and data reported are also of interest as bottom cells of high efficiency InP/InGaAs two-junction tandems (ref. 5,6).

¹This work performed under NASA contracts NAS-19258 and NAS1-19592.

Laser Power Converter Material Growth and Device Fabrication

The InGaAs layers (Table I) used were grown in a Spire 100S single-wafer metal organic chemical vapor deposition (MOCVD) epitaxial reactor under conditions summarized in Table II on P⁺ InP substrates. Two structures were used, one with the window and cap, and the other omitting those two layers.

Table I InGaAs LPC Epilayer Structures.

Thickness (μm)	Doping Type	Doping (cm ⁻³)	Material	Purpose
0.3	N	10 ¹⁹	InGaAs	Contact Cap
0.5	N	10 ¹⁸	InP	Window
0.3	N	10 ¹⁸	InGaAs	Emitter
2.7	P	10 ¹⁷	InGaAs	Base
0.3	P	10 ¹⁹	InP	Back Surface Field
300	P	10 ¹⁸	InP	Substrate

Table II InGaAs Growth Parameters in a Spire 100S MOCVD Reactor.

Growth Pressure	76 torr
Growth Temperature	600 °C
Wafer Rotation	15 rpm
Hydrogen Mainflow	2 slpm
Indium Source, Bubblers Temperature	Ethylindium, +10° C
Gallium Source, Bubblers Temperature	Trimethylgallium, -10° C
Arsenic Source	100% Arsine
V to III Ratio	≈400:1
Growth Rate	≈7Å/s or 2.5μm/hr
P-type Dopant	Dimethylzinc, 1000ppm diluted in H ₂
N-type Dopant	Silane, 500ppm diluted in H ₂

The N⁺ InGaAs contact cap allows a lower resistance ohmic contact to be made to the low bandgap InGaAs (0.75eV) than could be made to the high bandgap InP (1.34eV) window. The cap is later etched off everywhere but underneath the front metal contacts, since InGaAs absorbs 1.3μm light strongly, and carriers generated in the cap cannot diffuse through the InP window and are lost to recombination. The N⁺ InP window lowers the recombination velocity at the N⁺ InGaAs emitter front surface, and should decrease dark current and increase quantum efficiency at 1.3μm. The thick 0.5μm InP window is not best for AM0 power conversion, since the visible sunlight with energy above the InP bandgap is absorbed. However, the thick InP window lowers series resistance without appreciably absorbing 1.3μm light, an important design point for these high current 1.315μm converters. The absorption length of In_{0.53}Ga_{0.47}As at 1.3μm is ≈0.8μm, so the 3μm InGaAs emitter and base regions absorb ≈98% of 1.3μm light.

Figure 1 is an outline of the fabrication process for cells with windows. Cells without windows are made using a similar, simpler process. Figure 2 shows a picture of a completed cell.

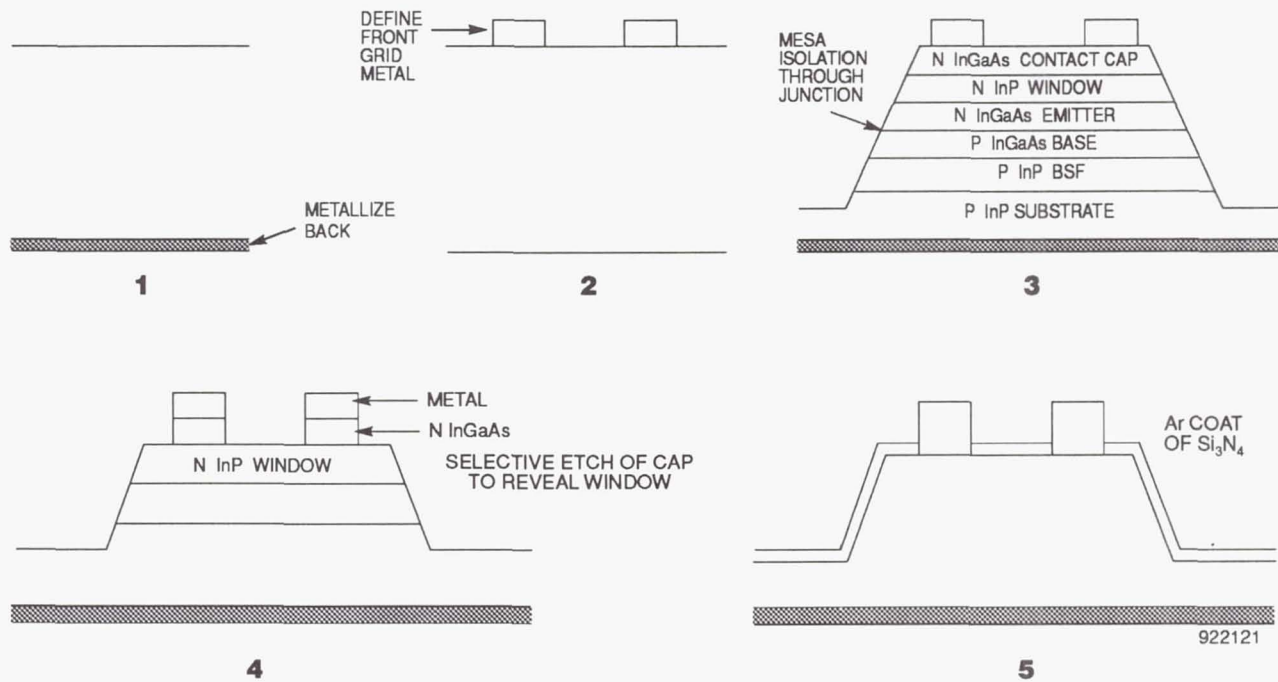


Figure 1 Simplified converter fabrication process. 1) Metallize backs. 2) Define front contact grid. 3) Isolate devices. 4) Strip InGaAs contact cap from photoarea. 5) Anti-reflection coating.

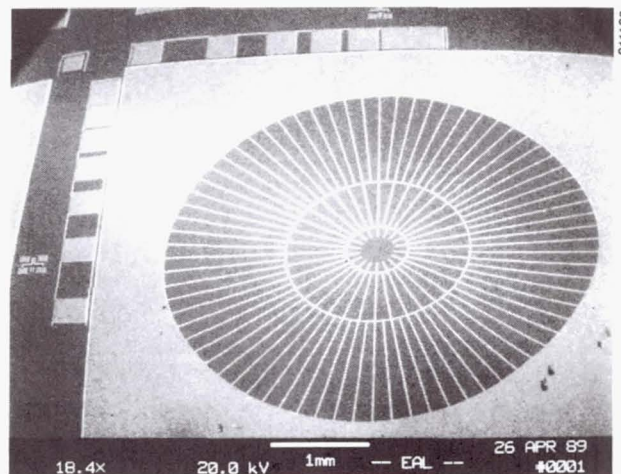


Figure 2 Scanning electron micrograph of an LPC. Photoarea is 0.136 cm^2 , $\approx 4 \text{ mm}$ in diameter. P-N junction area is 5 mm^2 (0.25 cm^2). Grid lines are $3 \mu\text{m}$ wide and $3 \mu\text{m}$ high.

The process used is briefly described below:

- 1) (BACK METALLIZATION) Protect epilayers with Si_3N_4 . Clean InP wafer backs by HCL etching. Metallize backs of the P^+ InP wafers with thermally evaporated AuZn and vacuum anneal.
- 2) (FRONT METALLIZATION) Photolithographically define front contact grids in photoresist using image reversal process, clean surface with $\text{NH}_4\text{OH}:\text{H}_2\text{O}$, plasma etch in O_2 to remove any resist residue, clean oxides in openings with a buffered HF dip, electron-beam evaporate Cr/Ag/Au front grid metal. Liftoff excess metal with an acetone soak, leaving the front contact grid metal.
- 3) (DEVICE ISOLATION) Photolithographically cover device area with photoresist. Selectively etch off $0.3\mu\text{m}$ InGaAs cap from exposed areas with $1\text{H}_3\text{PO}_4:1\text{H}_2\text{O}_2:8\text{H}_2\text{O}$. Selectively etch $0.5\mu\text{m}$ InP window off in HCL. Selectively etch InGaAs layers using 1:1:8 etch. Dektak wafers to determine actual thickness of etched material to insure junctions are isolated between devices.
- 4) (CAP STRIP FROM PHOTOACTIVE AREA) Selectively etch off the $1.3\mu\text{m}$ light-absorbing InGaAs contact cap from the active device area with the 1:1:8 etch, using the front-grid metal as a self-aligned mask. No photolithography needed.
- 5) (ANTI-REFLECTION COATING) Plasma deposit Si_3N_4 for a quarter wave AR coat optimized at $1.3\mu\text{m}$. Final photolithography step removes silicon nitride off the front contact busbar.

$\text{In}_{0.53}\text{Ga}_{0.47}\text{As}$ Laser Power Converter Cell Test Data

The $1.315\mu\text{m}$ laser power conversion efficiency was estimated at 29.4% (at 5.57 W/cm^2). We assumed an incident $1.315\mu\text{m}$ laser power density of 5.57 W/cm^2 because the measured external quantum efficiency of 86% at $1.315\mu\text{m}$ gives a short-circuit photocurrent of 5.07 A/cm^2 with 5.57 W/cm^2 of $1.315\mu\text{m}$ laser power. Measured AM0 concentration data at this same current density (Table III) should accurately give the open-circuit voltage (484mV) and fill-factor (66.8%) the cell would exhibit if operated as a converter under this laser illumination. These values were used to estimate the efficiency, as described later. Table III summarizes AM0 efficiencies, open-circuit voltages (V_{OC}), short circuit currents (I_{SC}), short-circuit current densities (J_{SC}), and fill-factors (FF) measured at Spire. Cells were made on 2-inch InP P^+ wafers; there were 29 cells on each wafer as well as several diagnostic test patterns. Both one-sun data for the best cell and average data for all 29 cells is reported. This AM0 data is useful in evaluating the performance of these devices as bottom cells of InP/InGaAs high efficiency two-junction tandems cells. Also, as explained above, the AM0 concentration tests allow measurements of V_{OC} , FF, and series resistance effects at the high photocurrents which would occur under laser testing. The antireflection coating and InP windows were optimized for $1.315\mu\text{m}$ and not for the broad AM0 spectrum.

The InGaAs cells with InP windows had higher AM0 efficiencies at concentration, since they had better quantum efficiency, and because the thick InP window lowers the emitter sheet series resistance (higher FF). In contrast, windowless cells had their FF drop at concentration, implying a series resistance problem in the thin emitter at high currents. Photocurrents of windowless cells were less than windowed cells, which was somewhat surprising since the InP window absorbs visible AM0 light. Presumably, high surface recombination at the exposed InGaAs emitter surface lowered the minority lifetimes in the emitter more than we expected, reducing the photocurrent. This surface is passivated when the InP window is added, which is the probable reason why the cells with windows had higher photocurrents, although there could be some photocurrent collection from the InP window itself. InGaAs cells without windows had slightly better one-sun efficiencies, despite the lower photocurrent, because of higher photovoltages at one-sun, which is probably due to their lower dark current in the one-sun bias region. The lower generation-recombination space charge current of the windowless cells may be due to the excellent lattice matching ($<280\text{ppm}$) achieved in this cell run.

Table III Spire AM0 Efficiency Tests.

Converter ID	Voc V	Isc mA	Jsc mA/cm ²	AM0 Suns	Fill %	Eff %	Comments
InGaAs n/p Cell with InP Window - lattice mismatch 790ppm							
5501-1425-21	0.287	7.781	57.21	1	57.1	6.83	Best cell
5501-1425-21	0.484	690.2	5074.80	88.7	66.8	13.5	Best cell
average	0.279	7.773	57.16	1	56.6	6.58	Average of all 29 cells
average	0.483	701.6	5158.73	90	65.3	13.2	Average of 6 cells
InGaAs n/p Cell with No Window - lattice mismatch 280ppm							
5501-1419-18	0.305	6.174	45.40	1	70.8	7.14	Best cell
5501-1419-18	0.439	656.2	4825.0	106	65.8	9.57	Best cell
average	0.298	6.078	44.69	1	67.4	6.57	Average of 29 cells
average	0.436	620.7	4564.06	102	62.4	8.91	Average of 6 cells

The measured external quantum efficiency and reflectance is shown in Figure 3 for a typical InGaAs converter with and without InP windows.

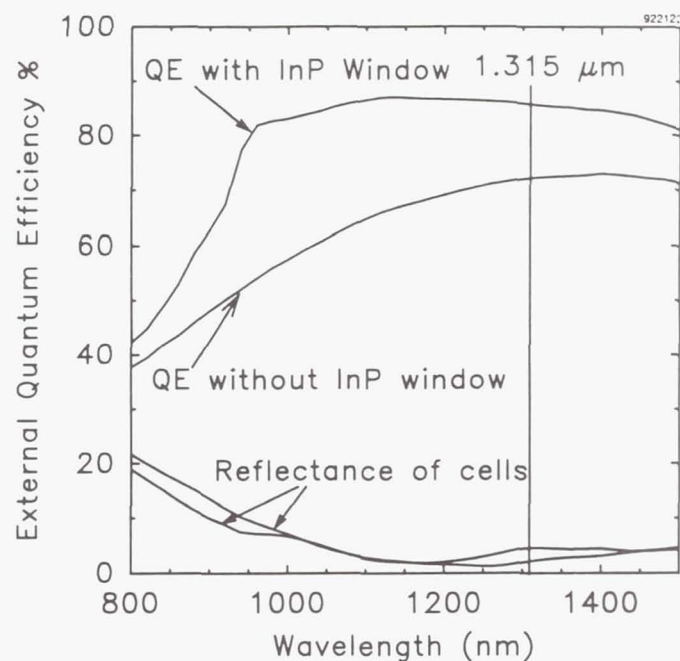


Figure 3 External quantum efficiency and reflectance measured for InGaAs LPCs.

InGaAs has a cutoff wavelength of 1.65 μ m, which is off the plot in Figure 3. The quantum efficiency roll-off in the InGaAs LPCs without InP windows below 1200nm is probably due to the high surface recombination at the unpassivated InGaAs emitter front surface. For the InGaAs LPCs with an InP window, the quantum efficiency is strikingly improved above 900nm, due to the InP window (minority carrier mirror) separating the photogenerated carriers in the InGaAs from the surface. Below 920nm, the InP window is itself absorbing, and the photogenerated carriers created in the InP window due to this light are again lost to surface recombination. The InP/InGaAs interface recombination is clearly low enough so that we gain an appreciable advantage in quantum efficiency using windowed structures.

Converter I-V data are shown in Figure 4. Windowless InGaAs junctions had lower lattice mismatch (280ppm, measured by X-ray diffraction) and lower dark current. The windowless junctions are diffusion current limited; the cells with windows are dominated by space-charge recombination current. Table IV shows the I-V least-squares fit to a simple diode model to extract the relative contributions of the diffusion current versus the space-charge region recombination current.

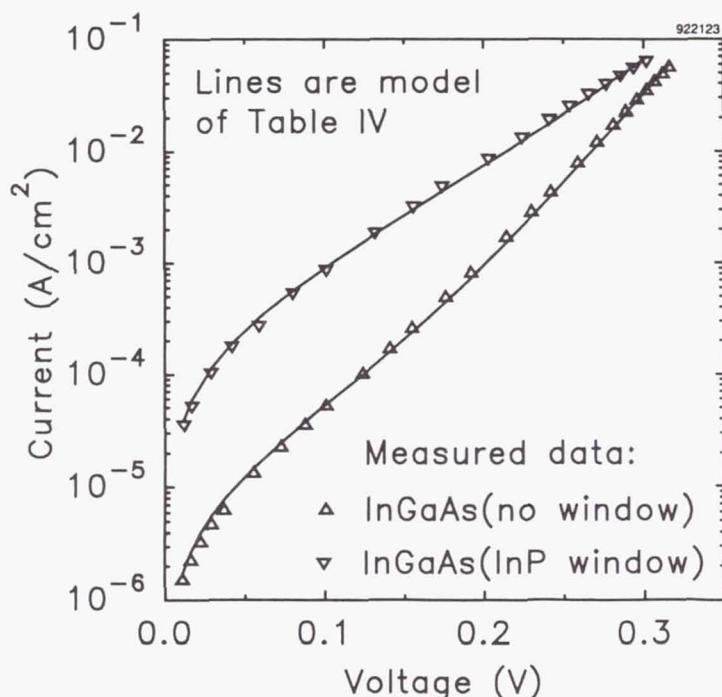


Figure 4 Log I-V curves of InGaAs junction with (ID#1419) and without (ID# 1425) InP window.

Table IV Diffusion and Space Charge Recombination Current Components Fit to Measured InGaAs LPC IVs.

ID #	Diffusion Current Jo1 (A/cm ²)	Space-charge Current Jo2 (A/cm ²)	Comments
1419-24	2.7x10 ⁻⁷	6.6x10 ⁻⁶	no window, 280 ppm mismatch
1425-14	1.4x10 ⁻⁷	1.5x10 ⁻⁴	InP window, 790 ppm mismatch
$J = Jo1 [\exp (qV/kT - 1)] + Jo2 [\exp (qV/2kT - 1)]$			

Theoretical Laser Power Converter Efficiency versus Bandgap

In this section, laser power converter efficiency versus semiconductor bandgap is modeled, with the goal of estimating the increase in 1.315 μ m converter efficiency if a bandgap higher than In_{0.53}Ga_{0.47}As (0.75eV) is used. The short-circuit photocurrent J_{sc} (units: A/cm²) for monochromatic light is:

$$J_{sc} = \frac{q(QE)P\lambda}{hc} \quad \text{or} \quad \frac{J_{sc}}{P} = 1.06 \text{ QE (A/W at 1.315 } \mu\text{m)} \quad (1)$$

Here "q" is the electron charge (C), "QE" the external quantum efficiency at the laser wavelength " λ " (m), "P" the incident laser power (W/cm²), "h" Planck's constant (J-s), and "c" the velocity of light (m/s). J_{sc} is to first-order independent of bandgap since "QE" is to first order also independent of bandgap. The dark current limit J_o (A/cm²) versus direct bandgap energy can be estimated simply as (ref.7):

$$J_o = \frac{2\pi kTq^3(n^2+1)E_G^2}{10,000h^3c^2} \exp\left(-\frac{qE_G}{kT}\right) \approx 6,960 E_G^2 \exp\left(-\frac{E_G}{0.026}\right) \quad (2)$$

This is "perfect" dark current assuming radiative-limited lifetimes and no surface recombination, derived from detailed balance equations for photon absorption and radiative recombination. As a check, the formula predicts about half the diffusion current of very good GaAs cells. "k" is Boltzmann's constant (J/K), "T" is the temperature (K), "n" is the refractive index at the laser wavelength, and "E_G" is the bandgap voltage (V). The above approximation uses an "n" of 4 and a 300K "T". The open-circuit voltage V_{oc} is then:

$$V_{oc} = \frac{kT}{q} \ln\left(\frac{J_{sc}}{J_o} + 1\right) \quad (3)$$

The fill-factor (FF) was calculated numerically for the theoretical data presented below. However, for a single-junction cell with no series resistance, excellent agreement (to three places) exists between the numerical calculations for the fill-factor and an analytical formula by Green (ref.8):

$$FF = \frac{v - \ln(v + 0.72)}{v + 1} \quad (4)$$

"v" is the normalized voltage variable (qV_{oc}/kT). The laser power conversion efficiency η is then:

$$\eta = \frac{V_{oc} J_{sc} FF}{P} \quad (5)$$

Using the above formulae, upper theoretical efficiency limits for 1.315 μ m laser power converters as a function of bandgap are shown in Figure 5, ranging from the 0.75eV bandgap energy of In_{0.53}Ga_{0.47}As to near the 0.94eV photon energy of the 1.315 μ m wavelength laser light. The assumptions are:

- 1) 100% external quantum efficiency at 1.315 μ m
- 2) "perfect" radiative-lifetime-limited dark current as in the approximate equality of equation (2)
- 3) room temperature operation
- 4) no series resistance
- 5) 5 W/cm² incident 1.315 μ m laser power density

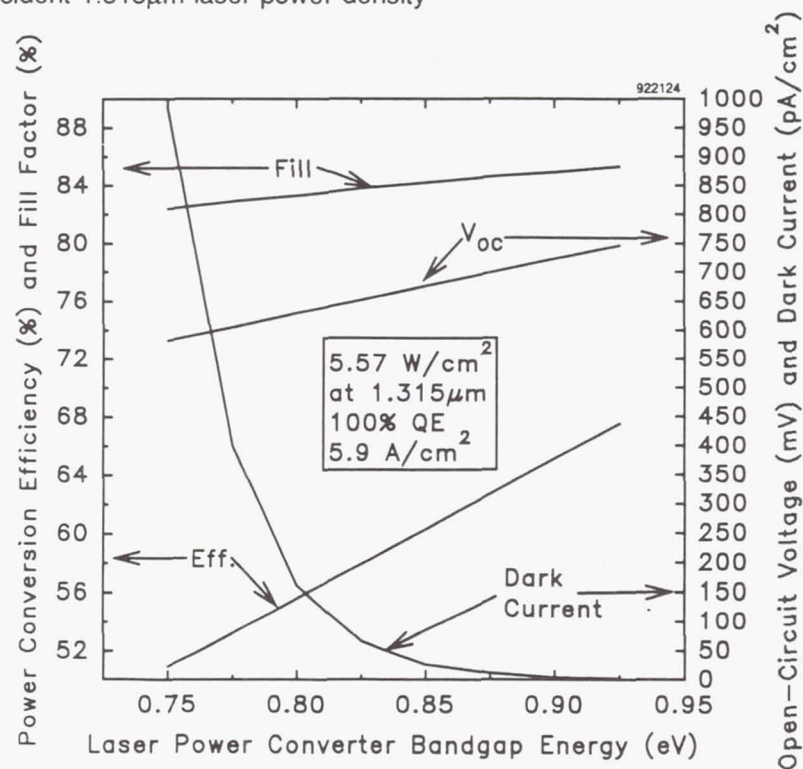


Figure 5 Upper theoretical efficiency limits for a 1.315 μ m laser power converter as a function of the semiconductor bandgap of the converter material.

Table V compares theoretical predictions versus measured data achieved in this work. Of the parameters, we believe it is relatively easy to improve J_{sc} (i.e. approach 100% external quantum efficiency at the single 1.315 μ m wavelength), and to reduce the series resistance further to improve FF somewhat. However, to improve V_{oc} and FF toward their theoretical limits, dark currents will have to be reduced substantially by lowering surface/interface recombination velocities and space-charge dark currents, and increasing material lifetime toward the radiative limit, a very challenging task.

Table V Upper Theoretical Limits versus Achieved Data for 0.75eV InGaAs 1.315 μ m Converters.

	V_{oc} (mV)	J_{sc} (A/cm ²)	FF (%)	Eff. (%)
Theory (Figure V)	582	5.9	82	50
Achieved (Table III)	484	5.1	67	29
Theoretical/Achieved	83%	86%	82%	58%

InGaAs converters are not optimum for 1.315 μ m laser power conversion due to the 190meV energy difference between the 0.75eV bandgap and 0.94eV photon energies, which is wasted as heat. This lost power can be recovered if a higher bandgap converter is used, as Figure 5 illustrates. Lower indium composition $\text{In}_x\text{Ga}_{1-x}\text{As}$ ($x < 0.53$) has a higher bandgap, but the grown film is no longer lattice matched to the InP wafer, which generates stress-relieving dislocations in the material that act as recombination centers, decreasing minority carrier lifetimes and lowering efficiency. However, some compositions of $\text{In}_x\text{Al}_y\text{Ga}_{1-x-y}\text{As}$ (Figure 6) can be grown with bandgaps approaching the 0.9eV optimum, while maintaining lattice match to InP. InAlGaAs is of great interest since it may be easier to grow by MOCVD than InGaAsP, which covers about the same bandgap and wavelength range. InAlGaAs is a III-III-III-V quaternary material, with only one group V element. It is relatively easy to grow, since the material composition is adjusted by controlling the gas flows of similar group III's, which incorporate into the material similarly. In contrast, InGaAsP, a III-III-V-V quaternary, needs to control not only the group III ratio, but the group V ratio as well. The arsine and phosphine gases used to supply the group V's work best at quite different material growth temperatures, making InGaAsP growth inherently more difficult.

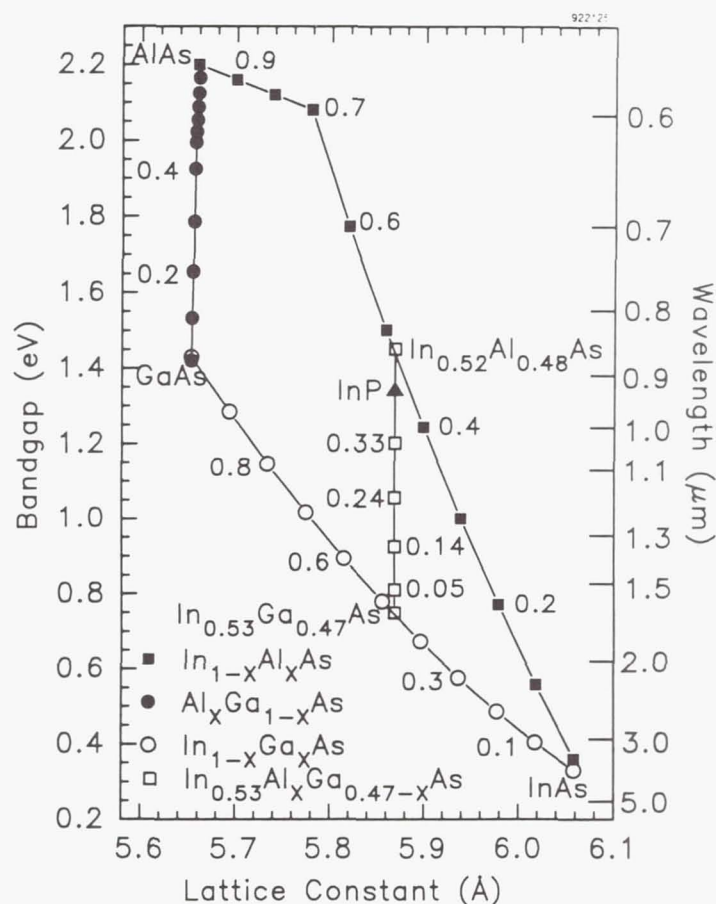


Figure 6 Bandgap vs. lattice-constant for $\text{In}_x\text{Al}_y\text{Ga}_{1-x-y}\text{As}$ quaternary. Vertical line is the composition of $\text{In}_x\text{Al}_y\text{Ga}_{1-x-y}\text{As}$ lattice matched to InP. Raw data from Madelung (ref.9).

Conclusions

In this work, we describe the epitaxial growth, fabrication, and test results of single-junction 0.75eV $\text{In}_{0.53}\text{Ga}_{0.47}\text{As}$ laser power converters. Although we lacked a high power laser to do direct measurements, we estimate the 1.315 μm laser power conversion efficiency as 29.4% (at 5.57 W/cm²) based on an 86% measured external quantum efficiency at 1.315 μm , and a measured open circuit voltage (484mV), and fill-factor (67%) at the equivalent AM0 short-circuit photocurrent (5.07 A/cm²). Absolute external quantum efficiency and reflectance, IV data, and AM0 one-sun and concentration efficiencies were measured for InGaAs cells without and with InP windows to passivate the front surface of the emitter layer. Cells with InP windows had the highest external quantum efficiency (86% at 1.315 μm), as well as the highest AM0 efficiencies under concentration (13.5%, 89 suns). Theoretical efficiency estimates were made for 1.315 μm laser power converters versus the cell bandgap energy. Adding aluminum to InGaAs to form $\text{In}_x\text{Al}_y\text{Ga}_{1-x-y}\text{As}$ is presented as a way to achieve an optimal bandgap for 1.315 μm laser power conversion, and efficiencies over 60%.

References

1. Landis, G.A.: "Photovoltaic Receivers for Laser Beamed Power in Space," Proc. of 22nd IEEE PVSC, pp.1494-1502, (1991).
2. Walker, G.H. and Heinbockel, J.H.: "Mathematical Modeling of a Photovoltaic-Laser Energy Converter for Iodine Laser Radiation," NASA Tech. Memo. 100482, (1987).
3. Borden, P.G.: "A Monolithic Series-Connected AlGaAs/GaAs Solar Cell Array", Proc. of 14th IEEE PVSC, pp.554-562., (1980).
4. Spitzer, M.B.; McClelland, R.W.; Dingle, B.D.; Dingle, J.E.; Hill, D.S.; and Rose, B.H.: "Monolithic Series-Connected Gallium Arsenide Converter Development", Proc. of 22nd IEEE PVSC, pp.142-146, (1991).
5. Osterwald, C.R.; Wanlass, M.W.; Ward, J.S.; Keyes, B.M.; Emery, K.A.; and Coutts, T.J.: "Modeled Performance of Monolithic, 3-Terminal InP/InGaAs Concentrator Solar Cells as a Function of Temperature and Concentration Ratio", Proc. of 22nd IEEE PVSC, pp.216-219, (1991).
6. M.W. Wanlass, T.J. Coutts, J.S. Ward, K.A. Emery, T.A. Gessert, and C.R. Osterwald, "Advanced High-Efficiency Concentrator Tandem Solar Cells", Proc. of 22nd IEEE PVSC, pp. 38-45, (1991).
7. Henry, C.H.: "Limiting efficiencies of ideal single and multiple energy gap terrestrial solar cells", J. Appl. Phys. 51(8), pp.4494-4500., (1980).
8. Green, M.A.: "Solar Cells", Prentice-Hall, p.80, (1982).
9. Madelung, O. (Ed.): "Semiconductors - Group IV Elements and III-V Compounds", Springer-Verlag, (1991).

The Efficiency of Photovoltaic Cells Exposed to Pulsed Laser Light

R. A. Lowe, Cleveland State University, and G. A. Landis,
P. Jenkins, Sverdrup Technology, Inc.

Future space missions may use laser power beaming systems with a free electron laser (FEL) to transmit light to a photovoltaic array receiver. To investigate the efficiency of solar cells with pulsed laser light, several types of GaAs, Si, CuInSe₂, and GaSb cells were tested with the simulated pulse format of the induction and radio frequency (RF) FEL. The induction pulse format was simulated with an 800-watt average power copper vapor laser and the RF format with a frequency-doubled mode-locked Nd:YAG laser. Averaged current vs bias voltage measurements for each cell were taken at various optical power levels and the efficiency measured at the maximum power point.

Experimental results show that the conversion efficiency for the cells tested is highly dependent on cell minority carrier lifetime, the width and frequency of the pulses, load impedance, and the average incident power. Three main effects were found to decrease the efficiency of solar cells exposed to simulated FEL illumination: cell series resistance, LC "ringing", and output inductance. Improvements in efficiency were achieved by modifying the frequency response of the cell to match the spectral energy content of the laser pulse with external passive components.

Introduction

It is possible to send power over long distances by using a laser beam to transmit power to a receiving photovoltaic array [1,2]. Many potential space applications for beamed power systems have been identified. For example, satellites operating in Geosynchronous Earth orbit (GEO) are currently powered by solar arrays. Half of the mass of a satellite power system consists of batteries and other components performing regulating and charging functions of the batteries, with the sole function of providing power for less than 1% of the time. Laser light beamed from the ground could provide power during the eclipse period and reduce the mass of the satellite by eliminating or reducing the need for energy storage, or could be used to supplement solar power for satellites with degraded solar arrays [2]. For a photovoltaic-power system for a lunar base, power storage capability is required to supply power during the 354-hr. lunar night. A laser used to illuminate an array during the night would substantially reduce the storage mass [3,4]. For an orbital transfer vehicle, electric rocket engines (ion engines, plasmadynamic thrusters) have high specific impulse but require large amounts of power. For a vehicle configured with such engines the amount of fuel required could be reduced with a beamed power/PV array system. Such a vehicle would provide an efficient LEO to GEO or LEO to lunar orbit shuttle [5].

A beamed power system would consist of one or more ground-based lasers, an adaptive optics system to compensate for atmospheric distortion, a large optical element at each laser site to shape and direct the beam, and photovoltaic (PV) arrays as receivers [2]. Several types of lasers have been investigated for space power transmission. The free-electron laser (FEL) is especially

attractive because of its potentially high efficiency, tunability over a wide wavelength range, and potential for high average power operation [6]. Lasers used for power beaming must operate in the portion of the visible or NIR spectrum which efficiently penetrates the atmosphere. While a RF-FEL has demonstrated operation at wavelengths as short as 550 nm [7], a FEL has not yet been demonstrated combining both the high average power required for power beaming and the short wavelength operation required for Si and GaAs solar cells.

Previous studies have investigated the efficiency of solar cells with continuous-wave lasers [1,8,9]. However, FEL lasers are by nature pulsed. Pulsed operation of photovoltaic cells at high average power has significant differences from operation under continuous illumination [10]. Until this work, operation of cells in this regime has not been tested.

There are two main designs of free-electron laser, differing in the type of accelerator used to produce the electron beam: the induction FEL and the radio-frequency FEL. The pulse formats produced by the two accelerator types are significantly different.

The induction FEL will have characteristically 10-50 nanosecond wide pulses at maximum repetition frequencies on the order of ten kilohertz. The induction FEL considered for power beaming [11] will produce pulses 50 nS wide, separated by 100 μ S (10 kHz), producing a duty factor of 1:2000. This is a somewhat optimistic projection of future improvements in efficiency for induction accelerators.

A RF FEL, on the other hand, will produce pulses with a width of 5-10 picoseconds (referred to as "micropulses"), at a repetition rate of tens of megahertz. In some designs of RF FEL, the series of RF micropulses will then be repetitively pulsed, for a "macropulse".

The proposed RF FEL for quasi-CW operation (i.e., a continuous string of micropulses), has a pulse width of 15 to 20 pS, with 27 nS between pulses (repetition rate 36 MHz, the 12th harmonic of the RF frequency of 433 MHz). This gives a duty factor for the micropulse of about 1:1500 [12]. An alternative variation is a pulsed laser. A pulsed RF FEL may be more efficient to operate at lower power levels. The RF FEL [13] also modulates the micropulses with a 5 μ S macropulse at a 1 kHz repetition rate, for a macropulse duty factor of 1:200.

Near the maximum power bias point of a solar cell, the output from the cell is expected to stretch the input pulse by an amount comparable to the minority-carrier lifetime of the semiconductor (more properly, by a weighted average of the emitter and base minority-carrier lifetimes). The response to pulsed illumination will thus depend on whether the spacing between pulses is significantly greater than, or significantly less than, the minority carrier lifetime in the semiconductor [8]. For direct bandgap materials such as GaAs, the minority carrier lifetimes are typically on the order of nanoseconds [14]. Since the spacing between pulses for the induction laser is significantly larger than the lifetime, it is expected that the output of the GaAs cells will not significantly stretch the pulse, and hence the cells will respond to the peak incident power. For indirect bandgap materials such as Si, the minority carrier lifetimes are typically on the order of microseconds [15]. Since this is on the order of the spacing between pulses for the induction laser, it is expected that the output from silicon cells will significantly stretch the pulse, and hence the cell will tend to average the pulses.

For the RF FEL, the minority carrier lifetime is comparable or longer than the spacing between micropulses for all the materials, and hence the output pulse from the solar cell is expected to be stretched nearly to CW. However, the spacing between macropulses (for the pulsed RF FEL) is significantly longer than the minority carrier lifetime for either GaAs or Si, and hence the cell output should follow the macropulse.

In an effort to understand the issues involved in using PV cells to convert power transmitted by a free electron laser, a study was undertaken to measure the efficiency of a wide variety of PV cells

with rapidly pulsed lasers. The main purpose of this experiment was to test the response of cells to the induction FEL pulse format, however, for comparison, several of the cells were also tested using a laser which simulated the pulsed RF FEL pulses.

Cells Tested

Several different types of cell, made from four different semiconductor materials, were tested. Table 1 lists the types of cells tested. Silicon, an indirect bandgap material, has long minority carrier lifetime. GaAs, GaSb, and CuInSe₂ were tested as examples of direct bandgap, and hence short minority carrier lifetime, materials.

Before testing, the cells efficiencies and current-voltage (I-V) characteristics were measured under the simulated air-mass zero (AM0) spectrum (25°C, 137 mW/cm²), the dark diode characteristics were measured, and the cell internal series resistances were calculated by comparison of the dark diode characteristic with the V_{OC} - I_{SC} characteristic using the method of Rajkanan [16]. Representative cells were also measured for capacitance at zero bias.

Silicon cells: Silicon (Si) cells are used for primary power for almost all satellites currently in orbit. Several types of silicon cells were measured. Cells typical of satellites currently in orbit were studied, including a cell with radiation damage of 5×10^{14} electrons/cm², typical of the conditions encountered after ~20 years in geosynchronous orbit. In addition, several cells of more advanced design were measured, including concentrator cell types designed for high peak currents. The highest efficiency Si cell tested was a low resistivity (0.15 Ω -cm base) cell manufactured using the high-efficiency, low resistance laser-grooved process [17].

GaAs cells. Gallium arsenide (GaAs) cells have higher efficiency than silicon cells, and will be used for missions where high efficiency is critical. Cells from several manufacturers were tested. Two general configurations were measured: flat-panel cells and concentrator cells. The flat-panel cells are typical of existing satellite solar array designs, but are poorly designed for the high peak current output expected for the peak of the laser pulse. The concentrator cell designs [15,16] are small area cells with low series resistance, and are designed to have much better response to high peak currents.

GaSb cells. Gallium antimonide (GaSb) cells are not currently used on satellites; however, for some applications, it has been suggested that it may be desirable to use an "eyesafe" laser wavelength greater than 1400 nm, a wavelength range to which neither silicon nor GaAs cells will respond. GaSb cells were tested as typical of cell types which may operate in this wavelength regime.

CuInSe₂ cells. Copper indium diselenide (CuInSe₂) cells are also not currently used on satellites. Such cells currently have much lower efficiencies than silicon or GaAs cells and are not made in versions acceptable for space operation, however, it has been suggested that future thin-film arrays may use CuInSe₂ cells.

In addition to the tests of the solar cells alone, one GaAs cell was also tested with capacitors of 500 nF and 4.4 μ F added directly to the cell to smooth the peak current transients and thus reduce inductive effects.

Laser Systems

The laser wavelengths used for the test were 521 ± 11 nm. Three laser systems were employed to simulate the FEL pulse formats. Efficiency under CW laser illumination was measured using an Argon-ion laser operating at a wavelength of 514.5 nm, at an intensity of 165 mW/cm^2 .

The induction FEL pulse format was simulated using a 800-watt average power copper vapor laser (CVL) with associated optics to provide beam attenuation and uniformity. The pulse width, shown in fig. 1a, is 38 ns (FWHM) with a PRF (pulse repetition frequency) of 8.6 KHz. The 572 nm component of the CVL light was dichroically separated from the beam, leaving the 511 nm collimated beam incident on the PV cells.

Finally, for some of the cells, the pulse format of a pulsed RF FEL was simulated with a frequency doubled mode-locked Nd:YAG laser operating at 532 nm. The micropulse structure consisted of a 100 picosecond FWHM pulse with a spacing of 10 ns. These micropulses were modulated by an approximately rectangular macropulse with a duration of 4 μs and a PRF of 10 Hz. The laser pulse format is shown in fig. 1b. While a 100 pS micropulse is considerably longer than the 15 pS pulses expected from a RF FEL operating at 840 nm, both the 100 pS pulses simulated and the 15 pS expected are both significantly less than the minority carrier lifetimes, and hence little difference is expected.

The laser wavelengths were chosen for the availability of high-power lasers with the pulse format required. For power beaming operation, however, it is expected that the laser wavelength will be chosen at a value near the wavelength of peak monochromatic efficiency of the solar cell. This wavelength is in the range of 840 nm for typical GaAs cells, 950-1000 nm for silicon cells (without radiation damage), and about 1600 nm for GaSb cells. Radiation damage will shift the monochromatic efficiency peak to shorter wavelengths.

Efficiencies measured at the test wavelength must be corrected to the desired operating wavelength. This is done by a wavelength correction factor

$$\frac{\text{Efficiency at } \lambda(1)}{\text{Efficiency at } \lambda(2)} = \frac{\lambda(1)}{\lambda(2)} [\text{QE}(\lambda(1))/\text{QE}(\lambda(2))] \quad (1)$$

The wavelength term accounts for the fact that for constant photon flux, the incident power is inversely proportional to the wavelength. The quantum efficiency term accounts for the fact that the probability of collection of an electron-hole pair created by absorption of a photon will have some dependence on the depth of penetration of the light, and hence the wavelength. For the high-efficiency cells tested, the quantum efficiency (QE(λ)) is not strongly dependent on the wavelength at the wavelengths of interest below the band edge. To within the measurement accuracy, the correction factor may be estimated as equal to the ratio of the wavelengths (except for the radiation-damaged silicon cell, where the long-wavelength quantum efficiency is preferentially damaged.)

The correction factors shown in table 2 are used to translate data from the test wavelength to the desired operating wavelength. The efficiency is multiplied by the correction factor. The effective laser power must be divided by the correction factor, thus keeping the photon flux constant.

Use of this correction factor implicitly assumes that the time dependence of the output response of the solar cell is independent of the wavelength of the incident light. This is not strictly correct. Short wavelength light is absorbed near the junction, and the generated electron-hole pairs are collected quickly. Since longer wavelength light is absorbed deeper in the material, however, the response to the long wavelength light will be slightly slower. This will result in a slightly different output waveform for the response to light near the band edge of the material due to the additional time for carriers to be collected by the junction. However, the amount by which the output pulse can be stretched is at most equal to the minority carrier lifetime in the cell base. This is small enough that the difference will not alter the main conclusions of the experiment.

Measurement Apparatus

The experimental apparatus is shown in fig. 2. The apparatus was designed to measure both the average power output of the cell, which is important to operation of a power system, and also to measure the instantaneous current and voltage as a function of time. The cell is mounted on an electrically isolated stage with a large heatsink and a thermocouple to measure cell temperature. Temperature did not rise significantly during the test.

A 11,000 μfd capacitor mounted near the cell integrates the AC current pulse generated by the cell. The average DC output current through the load is measured with a DC milliammeter. The lead length and parasitic inductance between the cell and capacitor is minimized to reduce the induced voltage generated by the large current transient during the pulse. A minimum wire length of 3 cm was required for the current pick-up; additional wiring in the system added 2-3 cm. A digital sampling oscilloscope with a 200 Mhz inductive current pickup and a 3.5 Ghz high-impedance sampling head were utilized to obtain the current and voltage waveforms out of the cell, and 16 to 128 waveforms were averaged to reduce noise.

The conversion efficiency value for the inductive FEL is calculated from the bias applied to the cell (V_{bias}), the average current delivered by the cell (I_{out}), and the energy incident on the cell using

$$\eta = \frac{P_{\text{out}}}{P_{\text{in}} A} \quad (2)$$

where $P_{\text{out}} = I_{\text{out}} \times V_{\text{bias}}$ is the electrical power output of the cell at the maximum power point, P_{in} is the radiant energy input in mW/cm^2 , and A is the area of the cell in cm^2 . The cell bias voltage was varied to find the maximum power point. I_{out} and V_{bias} here are DC values. This is thus the average efficiency over the laser cycle, including both the illuminated and dark periods of the cycle. While the instantaneous efficiency during one particular instant of the pulse may be higher, this DC efficiency is a good measure of power obtainable in an operational situation. As a check, these efficiency values were verified by comparison with the power dissipated by use of a purely resistive load.

A bias voltage was provided with a variable bipolar power supply, allowing various points on the cell operating I-V curve to be measured. For pulsed operation, there is a significant difference in efficiency that depends on whether a resistive or a constant voltage bias is used. The source used provided an approximation to a constant-voltage bias; this is typical of a satellite power bus. While a constant voltage bias provides a better match to the maximum power point of the cell during intensity variation, the cell dark current adds a constant power loss during both the illuminated and the dark portion of the pulse. Use of a blocking diode can nearly eliminate this dark current loss, at the cost of the diode voltage drop.

For the RF FEL simulation, a slightly different data acquisition system was used to allow measurements at the low pulse repetition rate. Voltage and current waveform acquisition over the macropulse were made with a 400 Mhz digitizing sampling oscilloscope.

Efficiency measured for the RF FEL was done by averaging the energy output during a macropulse, divided by the incident energy measured with a radiometer. The cell bias voltage was varied to find the maximum power point. This was then averaged over 32 pulses to reduce the noise. Again, $P_{out} = I_{avg} \times V_{bias}$; however, for this measurement I_{avg} was measured from the output current waveform measured by the oscilloscope, rather than from an independent ammeter.

As a comparison, the measured current $V(t)$ and voltage $I(t)$ were multiplied to find the time dependent output power $P(t)$ which was integrated to find the total energy:

$$P_{out} = \int_0^{t_0} v(t)i(t)dt \quad (3)$$

where t_0 is the duration of the pulse.

Results

Table 3 shows the efficiency of PV cells tested under CW laser illumination, compared with pulsed laser illumination with the induction laser format. The power listed is the average power. For the inductive format the pulse duty cycle (at FWHM) is approximately 1:3200. The maximum power in the pulse is 3200 times the average power. Measurements were made at an incident average power level of 253 mW/cm^2 (1.85 suns, where one sun intensity is 137 mW/cm^2), and then at reduced intensities of 25 and 2.5 mW/cm^2 (0.185 and 0.019 suns respectively). These intensities correspond to peak powers of 5920, 592, and 59 suns. Table 4 shows the wavelength corrected efficiencies of Si, GaAs, and GaSb cells using the correction factors from table 2 for the induction FEL.

Three cells were also tested using the RF laser format. The efficiency calculated by the current times the bias was compared with efficiency based on the total energy produced from the time-dependant power curve, equation (3). This data is shown in table 5. For the RF FEL, the power is the average power delivered over the duration of one macropulse (4 μs). The cells tested with the RF FEL format are exposed to a lower average power. Since the PRF of the Nd:YAG laser was very

low, 10Hz, the duty cycle of the laser is only 1:25000. The laser power for this test was set to simulate the same peak power as an RF-FEL with a repetitive (macro) pulse rate of 1 kHz. The average power delivered during the 4 μ S macropulse was thus about 16.7 W/cm² (122 suns).

As discussed, the average efficiency measured with the RF laser simulation included only the efficiency during the macropulse. If the efficiency over the entire pulse string is to be considered, the power loss due to dark reverse current between macropulses must be subtracted from the power. Table 6 shows the DC bias voltage at maximum power and the measured dark reverse current at the bias voltage for the GaAs and Si cells for both lasers.

Discussion:

Illumination of the solar cells with the induction FEL pulse format resulted in significant decreases in efficiency of the solar cells measured, compared to the continuous-wave laser. At all except the lowest intensities, the silicon cells outperformed the GaAs cells. This is as expected from the longer minority carrier lifetimes.

Three main effects decrease the efficiency of the solar cells for the induction-FEL format pulsed illumination:

1. Series Resistance. For the laser format used, the peak power during the pulse (8.6 kHz, 38 nS FWHM) is 3200 times the average power. Thus, for short lifetime cells, the peak output current must be 3200 times the average current for the cell to respond. I^2R losses due to the series resistance of the cell reduce the performance severely.

For example, the lowest resistance cell measured had a series resistance designed for operation at 850 times solar concentration, well below the 3200x in the experiment. In addition, the series resistance limits the peak current to

$$I < V_{OC}/R$$

2. L-C "Ringing." A solar cell is essentially a large-area p-n junction, and thus has a large junction capacitance. This, in conjunction with the necessary inductance of the output wiring, results in LC oscillations. Such oscillations result in operation of the cell at a bias different from the peak power point, and hence reduce the power.

3. Output inductance. The inductance L of the output wiring results in a maximum rate of increase in current:

$$dI/dt \leq V_{OC}/L$$

and hence, the cell is held at open-circuit voltage for a time

$$t \approx (LI_{SC})/V_{OC}$$

during which it produces little power.

Note that this experiment used wire lengths on the order of 3 cm, far shorter (and hence, far lower inductance) than would be found in any real-life solar array. These effects are discussed below.

At the highest intensity level, 5600 suns peak (approx. 2 suns avg.), of the induction-format pulse, the efficiency is the lowest for each cell. This is due to series-resistance limiting of internal cell

voltage by high current. Fig. 3 shows the effect of series resistance limiting on Si, GaAs, CuInSe₂, and GaSb cells at 5600 suns peak (253 mW/cm²). At the next lower intensity, 560 suns peak, the efficiency of all cells improve. The effect on the peak output current is minimal with a 10x reduction in the input power causing the efficiency to increase significantly. At 56 suns peak intensity the efficiency for the Si cells has leveled off or dropped slightly, with the exception of the radiation-damaged cell, where the minority carrier lifetime has been degraded and the series resistance increased. The efficiency is improved at the lowest intensity because of the high series resistance of 1.9 ohms.

An LRC circuit is formed by the junction capacitance of the cell and the parasitic resistance and inductance in the leads and capacitors. Where insufficient resistance is present for damping a characteristic "ringing" is present in the voltage and current. For a purely resistive load attached to the cell the power delivered depends on

$$p(t) = \frac{1}{T} \int_0^T v(t)i(t)dt \quad (5)$$

where $V(t)$ and $I(t)$ are periodic signals with period T . Reactive elements in the circuit cause a difference in phase angle between the output current and voltage. The power delivered to a resistive load is proportional to $\cos(f)$, where f is the phase angle difference between $V(t)$ and $I(t)$. Resistance in the circuit decreases the phase angle but causes a loss in efficiency by forcing cell output voltage to V_{oc} . Phase angle may also be reduced by limiting inductance in the circuit. This approach is impractical because at very high frequencies the induced voltages generated by parasitic inductance in short leads, capacitors, and resistors are unavoidable.

An integrating capacitor across the cell converts the AC pulsed output to DC, a form more suitable for distribution. The energy delivered to the capacitor from the cell is a function of voltage and is independent of phase angle. Energy losses in a capacitive load are confined to leakage current, parasitic resistance, and dielectric loss. Additional circuit losses are the cell dark diode current and, similar for a resistive load, resistive dissipation within the cell-circuit during oscillation. A significant improvement in efficiency for cells with oscillating transients can be achieved by mounting a small capacitor (100 nF-500 nF) across the cell contacts. The small capacitor reduces the effect of the induced EMF when the cell discharges current into the inductance of the integrating capacitor leads. As a result, a larger portion of the energy is transferred to the integrating capacitor and less energy is dissipated in the cell. For example, the output voltage and current of the VS 850x GaAs concentrator cell at 253 mW/cm² is shown in fig. 4a,b. Fig. 4c,d is the output voltage and current with a 500 nF capacitor across the cell terminals. The efficiency with a 500 nF capacitor was measured at 4.5 % as compared to 2.0 % for the uncompensated cell. The improvement in cell efficiency with the addition of passive devices will be addressed more completely in a future paper.

Induced voltage caused by the interaction of large current transients with the parasitic inductance in the cell interconnects and series resistance losses in the cell are the major causes of efficiency loss. Voltage developed across the cell during the onset of the laser pulse is due to the electric field generated by charged carrier separation and the induced voltage

$$V_i = L \frac{dI}{dt} \quad (4)$$

where V_i is the induced voltage, L is the parasitic inductance in the cell leads, and dI/dt is the time rate of change of the current waveform. Fig. 5 shows the current and voltage response of a 2x2 cm GaAs cell to a CVL (induction FEL format) pulse at I_{sc} . The initial slope of the current waveform with $\Delta I = .88$ A and $\Delta t = 40$ ns is 2.2×10^7 amps/sec. Using an estimate of $L = 35$ nH for the cell lead/integrating cap. inductance, V_i is 770 mv. This is the significant factor forcing the cell output to V_{oc} in the first 20 ns. During the next 100 ns cell output voltage is held at V_{oc} and large amounts of current are dissipated in the cell contributing to a loss in efficiency. Minimizing this effect using short leads and high frequency capacitors is possible, however, even short leads (3 cm) possess enough parasitic inductance to produce prohibitively large induced voltages.

Minority carrier lifetime affects the falltime of the cell output current and voltage. Fig. 6 shows the current and voltage response of a long lifetime Si cell such as the ASEC 10 ohm cm. The time for the voltage to decay to 10 % of its maximum value differs by a factor of 13 (8 ms for Si vs .6 ms for GaAs in fig. 4). As minority carrier lifetime increases carriers diffuse to the depletion region for a longer duration of time and are collected as current. A high carrier mobility will tend to offset this effect in a short minority carrier lifetime material such as GaAs.

Cell voltage bias affects the shape of the output waveform by reducing ringing. The load, consisting of a voltage supply that can sink current, presents a constantly varying impedance $\hat{Z}_{load} = V_{bias} / \hat{I}_{cell}$ to the cell. Figure 7 a,b show the voltage output waveform of a GaAs concentrator cell biased at 0V and .520V (P_{max}) respectively. At P_{max} the impedance is larger due

to increased V_{bias} , reduced \hat{I}_{cell} , and the cell output oscillations are damped. For other cells, fig.

7 c,d, damping was evident but the effect was not as pronounced. Reducing oscillation and eliminating the phase angle difference between \hat{V}_{cell} and \hat{I}_{cell} increases the power delivered to a resistive load and improves the efficiency of the cell.

Conclusion

Experimental results show the conversion efficiency of photovoltaic cells to pulsed laser light, for existing cell designs tested, is highly dependent on the cell minority carrier lifetime, the width and frequency of the pulses, and average incident power. Factors such as matching source wavelength to the bandgap energy of the PV material and minimizing series resistance are critical in designing efficient PV cells for a laser power beaming system. For cells with short minority carrier lifetimes, resistance and high-frequency electrical effects caused by short laser pulses prohibit efficient operation of the cell and transfer of power to a load. Future cell designs for a pulsed laser system would need to address the AC response of the cell and interconnects and reducing series resistance for efficient operation at high power levels. Modification of the cell's AC response utilizing external passive components may also prove effective in improving efficiency.

Acknowledgements: Peter Iles, ASEC; Mark Spitzer, Kopin; VS, Boeing, Herbert Friedman, Livermore; Rocketdyne, Bruce Anspaugh and Bob Mueller; NASA JPL

References

1. C.E. Backus, Conf. Record 9th IEEE Photovoltaic Specialists Conf., Silver Spring, MD, May 1972, 61-65.
2. G. A. Landis, 26th Intersociety Energy Conversion Engineering Conference, Boston, MA, Aug. 1991; reprinted in IEEE AES Systems Magazine., pp. 3-7, Nov. 1991
3. G. A. Landis, 9th Princeton/SSI Conference on Space Manufacturing, Princeton NJ, May 10-13 1989; paper published in Space Manufacturing 7 290 (AIAA, 1989). Also available as NASA Technical Memorandum TM-102127 (1989)
4. G. A. Landis, J. Propulsion and Power, Vol. 8, No. 1, 251-254 (1992).
5. S. Oleson, G.A. Landis, M. Stavens and J. Bozek, paper AIAA-92-3213. 28th Joint Propulsion Conf., Nashville, TN, July 1992, .
6. N. Bloembergen et al., Lasers. Science and Technology of Directed Energy Weapons, Report of the American Physical Society Study Group, Chap 3, pp. 51-139, (1987) [see also Rev. Modern Phys. 59, No. 3, part II (1987)]
7. Boeing HAP laser. Results reported in G. Emanuel et al., Aerospace Am. 28, No. 12, 28 (1990)
8. P.A. Iles, Conf. Record 21st IEEE Photovoltaic Specialists Conf., Kissimmee, FL, May. 1990, Vol. I, 420-423.
9. L.C. Olsen et al., Conf. Record 22nd IEEE Photovoltaic Specialists Conf., Las Vegas NV, Oct. 1991, Vol. I, 419-424.
10. G.A. Landis, Conf. Record 22nd IEEE Photovoltaic Specialists Conf., Las Vegas NV, Oct. 1991, Vol. II, 1494-1502; available as NASA Contractor Report 189075 (1991).
11. D. Goodman, Review of SELENE 91 Program Results and FY 92 Program Kickoff, Dec. 10-11, 1991, NASA Marshall Spaceflight Center, p. IV-47; also Technology Workshop on Laser Beamed Power, NASA Lewis Research Center, Feb. 5 1991, p. C-15
12. APLE laser scaled to 840 nm operation. R. L. Lamb, Boeing Corporation, private communication, March 1992.
13. R. Burke, SELENE Laser Power Beaming Applications Workshop, Mar. 24, 1992, NASA Marshall Space Flight Center, AL.
14. R.K. Ahrenkiel, D.J. Dunlavy and T. Hanak, Solar Cells, Vol. 24, 339-352 (1988).
15. G.A. Landis and H. Stoddart, Conf. Record 19th IEEE Photovoltaic Specialists Conf., Kissimmee, New Orleans LA, May 1987, 761-763.
16. K. Rajkanan and J. Shewchun, Solid State Electronics Vol. 22, 193-197 (1979)
17. S.R. Wenham, F. Zhang, C.M. Chong and M.A. Green, Conf. Record. 21st IEEE Photovoltaic Specialists Conf., Kissimmee, FL, May 1990, 323-326.
18. H.F. MacMillan et al., Conf. Record. 20th IEEE Photovoltaic Specialists Conf., Las Vegas, NV, 1988, 462-468.
19. M.B. Spitzer et al., Conf. Record. 20th IEEE Photovoltaic Specialists Conf., Las Vegas, NV, 1988, 930-933.

Cell	Type	Material	Area cm ²	R _{series} (Ω) ¹	I _{sc} (A)
ASEC 10 ohm-cm	planar	Si	4	.068	.47
ASEC .2 ohm-cm	"	"	4	.159	.16
ASEC 10 ohm-cm	planar (radiation damaged)	"	4	1.904	.29
ASEC 10 ohm-cm	concentrator	"	1	.182	.45
ASEC .15 ohm-cm	"	"	1	.050	.067
VARIAN	planar	GaAs	4	.093	.15
KOPIN	concentrator	"	.59	.162	.23
VS x850	"	"	.196	.100	.13
ASEC #16	planar	GaAs/Ge	4	.208	.25
BOEING A096A	planar	CIS	4	.879	.165
BOEING #6701	concentrator	GaSb	.238	.212	.09

¹ by comparison of V_{oc} vs I_{sc} against dark diode curve

Table 1 Cell Types tested under RF and Inductive FEL and CW Formats

<u>Laser type</u>	<u>wavelength (nm)</u>	<u>correction factor</u>
<i>Correcting to 840 nm (GaAs cells):</i>		
Copper Vapor Laser	511	1.64
Ar Ion Laser	514.5	1.63
Doubled YAG Laser	532	1.58
<i>Correcting to 950 nm (Si cells)</i>		
Copper Vapor Laser	511	1.86
Ar Ion Laser	514.5	1.85
Doubled YAG Laser	532	1.79
<i>Correction to 1600 nm (GaSb cells)</i>		
Copper Vapor Laser	511	3.13
Ar Ion Laser	514.5	3.11
Doubled YAG Laser	532	3.01

Table 2. Correction factor to translate efficiencies measured at test wavelength to efficiencies at longer operating wavelength, assuming equal quantum efficiency at both wavelengths.

Cells	intensity (mw/cm) ²	Efficiency (%)				
		AM0	CW laser	induction FEL		
		137	170	253	25	2.5
Silicon						
ASEC .15 ohm-cm concentrator		15.0	15.3	12.1	13.8	13.8
ASEC .2 ohm-cm		15.5	19.0	7.2	11.9	11.3
ASEC 10 ohm-cm		11.9	14.5	5.6	10.1	9.1
ASEC 10 ohm-cm(rad. damaged)		10.5	13.9	1.9	5.5	7.5
ASEC 10 ohm-cm concentrator		12.9	13.7	7.6	10.4	8.6
GaAs						
VARIAN		16.9	29.0	.15	1.5	12.0
Kopin		20.7	26.6	1.3	7.3	20.7
VS x850		19.4	21.7	2.0		
VS x850 with .5uf cap				4.5		
VS x850 with 4.4 uf cap				3.4	10.2	13.2
GaAs/Ge						
ASEC #16		17.9	26.0			
CuInSe ₂						
Boeing A096A		8.4	5.5	.01		.5
GaSb						
Boeing #6701		5.7	1.26		.25	.26

¹ Power levels of 253, 25, and 2.5 mw/cm² represent the average of all individual power measurements. The exact power, measured for each cell, is used to calculate the efficiency for that cell.

Table 3 Cell Efficiency (%) with AM0, CW, and Inductive FEL Format

Cells	Efficiency (%) @ 253 mW/cm ²
Silicon	
ASEC .15 ohm-cm	22.5
ASEC 10 ohm-cm	10.4
ASEC 10 ohm-cm (rad. damaged)	3.5
GaAs	
VARIAN	.25
KOPIN	2.1
GaSb	
Boeing #6701	.81 [†]

[†] Incident power for the GaSb cell is 25.3 mW/cm

Table 4 Wavelength Corrected Efficiencies of Si, GaAs, and GaSb Cells for induction FEL

Cell	Power W/cm ²	Efficiency, %	
		$I_{avg} \times V_{bias}$	$\int_0^{t_0} v(t)i(t)dt$
<u>GaAs/Ge</u> ASEC #16	16.7	3.4	5.0
<u>GaAs</u> Varian x850	16.7	1.15	.2
Varian x850 w/4.4uf cap.	16.7	24.1	30.1
<u>Si</u> ASEC .15 ohm-cm	15.0	11.1	11.8

Table 5 Comparison of cell efficiency using $I_{avg} \times V_{bias}$ and the total area under the curve for P_{avg} at 530nm for the RF pulse format

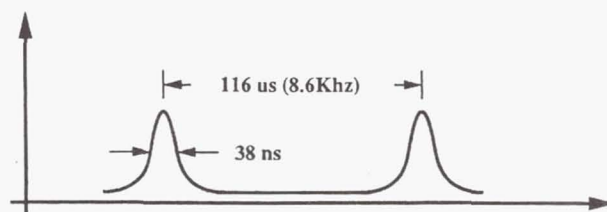
Cell	V_{mp} (mV)	I_{mp} (mA) ¹	I_{dark} (mA) ²
Induction Laser Format, 253 mW/cm ²			
Si: ASEC 10 ohm-cm	400	148	0.87
ASEC Rad. damaged	350	52	0.27
ASEC .15 ohm conc.	550	58	0.53
ASEC conc.#1 (10 Ω)	425	50	1.1
GaAs: VARIAN	650	2.0	0.028
Kopin	700	3.2	0.013
VS x850 (no cap)	725	1.33	0.030
(500 nF)	725	2.9	0.030
(4.4 uF)	650	2.45	0.012
RF Laser Format			
Si: ASEC .15 ohm conc.	600	1763	3.0
GaAs: ASEC Mantec GaAs/Ge	500	2370	0.04
VS x850 (no cap)	500	43	0.0022
(with cap)	780	596	0.064

¹ Current at maximum power point for the RF laser format is the average current over the duration of the pulse.

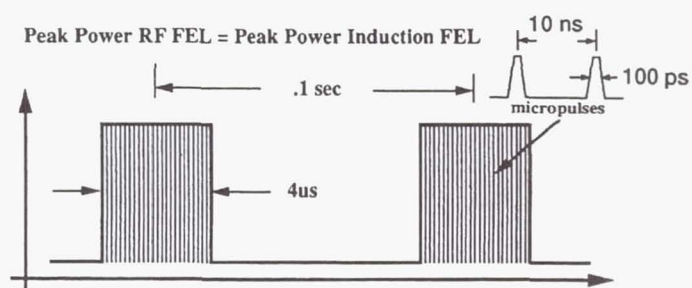
² Dark current is taken from $V_{oc} - I_{sc}$ measurement.

Table 6: Bias voltage and current at maximum power point and dark forward current at bias voltage for Si and GaAs cells under pulsed illumination.

Peak Power $\approx 3200 \times$ average power



(a) Induction FEL pulse format.



(b) RF FEL pulse format.

Figure 1.—Induction and RF FEL pulse formats.

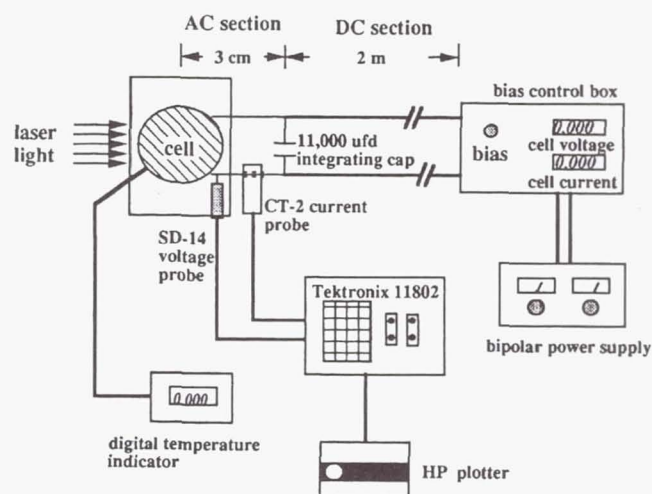


Figure 2.—Schematic of measuring circuit.

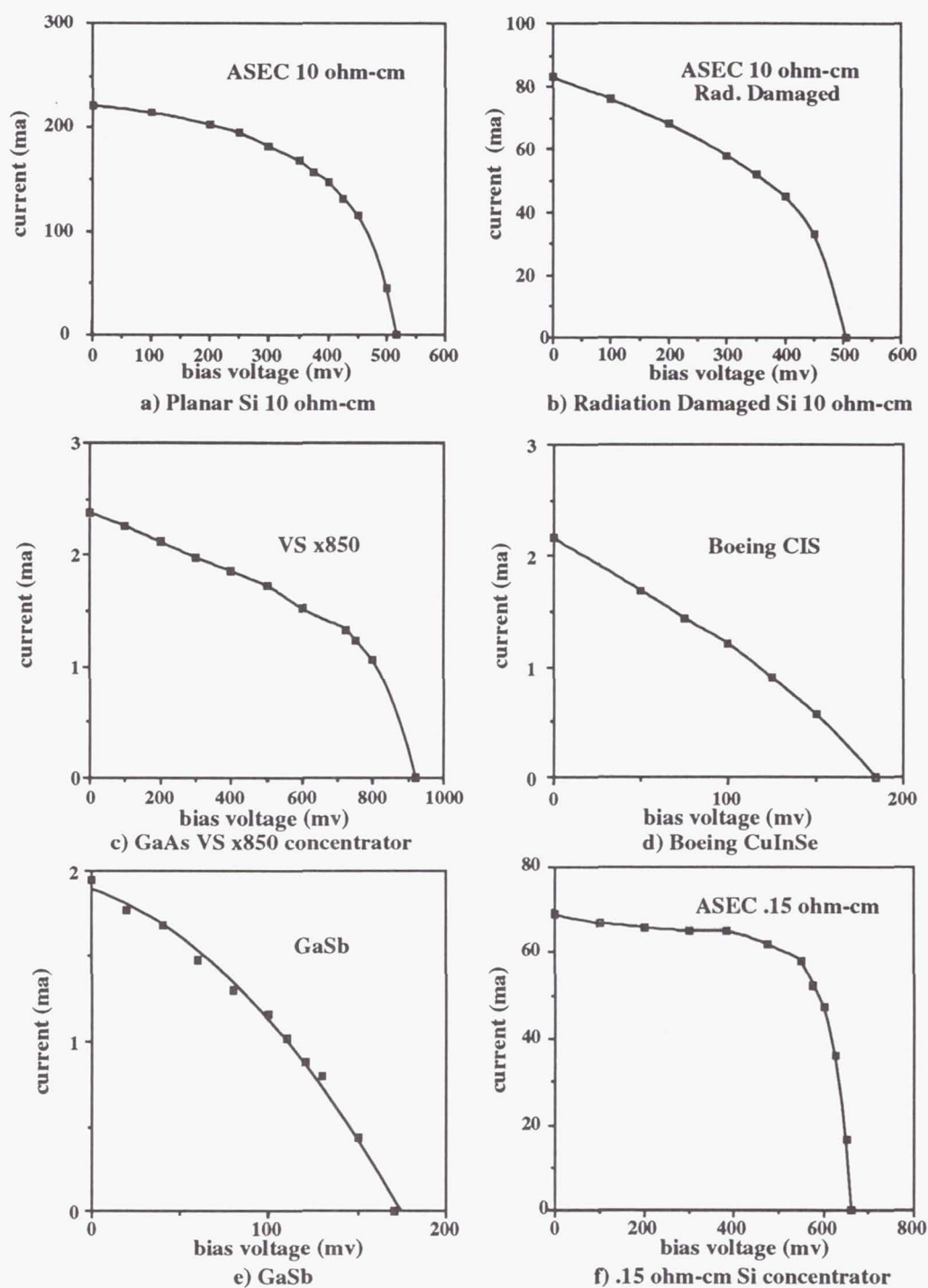
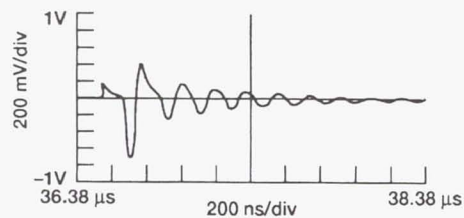
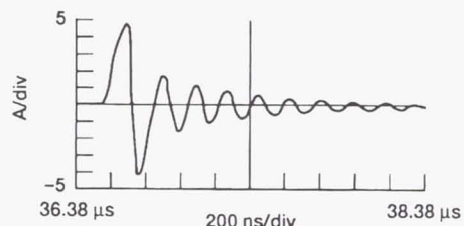


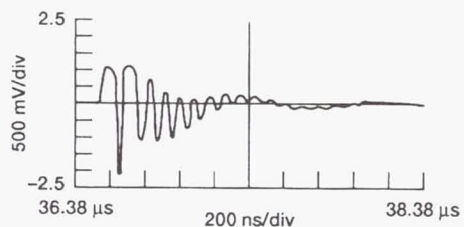
Figure 3 IV characteristics of Si, GaAs, CuInSe₂ and GaSb cells at 253 mW/cm² illumination



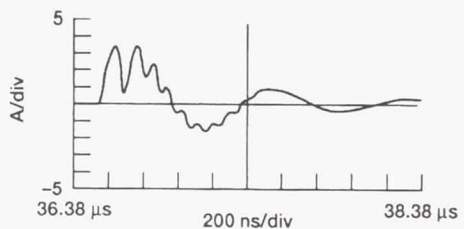
(a) Voltage response of VSx850 GaAs concentrator cell at 0V bias.



(b) Current response of VSx850 GaAs concentrator cell at 0V bias.

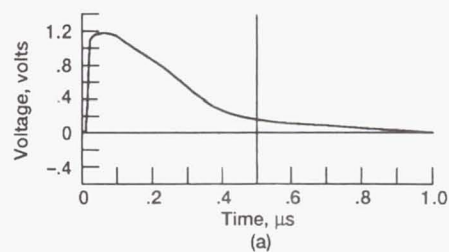


(c) Voltage response of VSx850 GaAs concentrator cell with 500 nF capacitor at 0V bias.

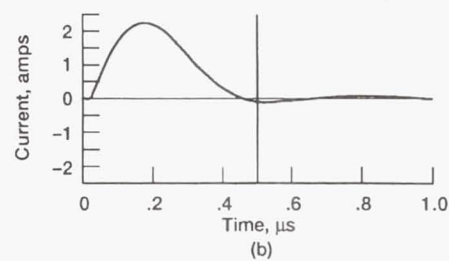


(d) Current response of VSx850 GaAs concentrator cell with 500 nF capacitor at 0V bias.

Figure 4.—Response of VSx850 GaAs concentrator cell with and without 500 nF capacitor.



(a)



(b)

Figure 5.—Voltage and current response of GaAs planar cell to CVL (induction FEL) pulse at 0V bias.

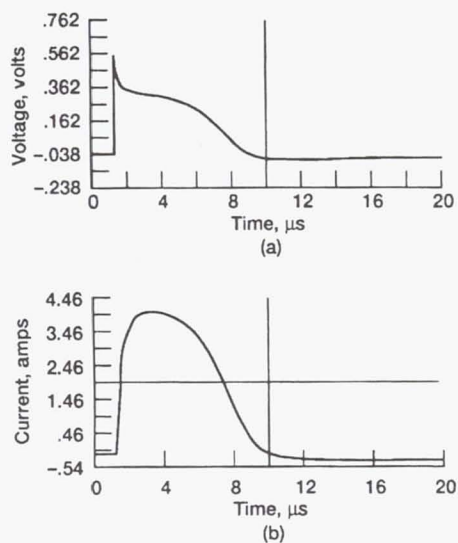
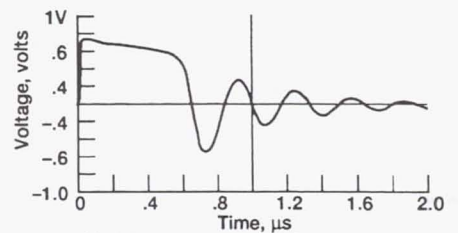
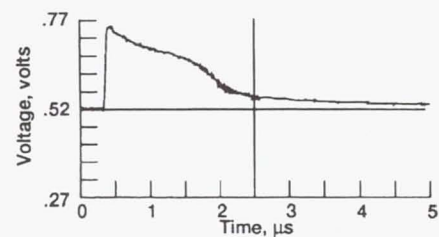


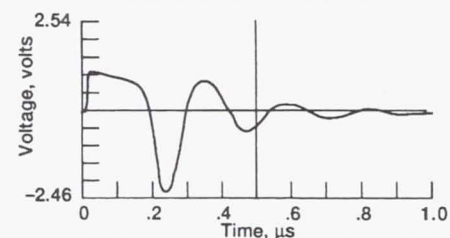
Figure 6.—Voltage and current response of ASEC 10 ohm-cm Si cell to CVL (induction FEL) pulse at 0V bias.



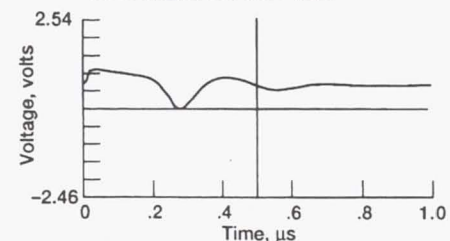
(a) Voltage response of GaAs concentrator cell biased at 0V to CVL pulse.



(b) Voltage response of GaAs concentrator cell biased at .52 V to CVL pulse.



(c) Voltage response of "Kopin Super" GaAs concentrator cell at 0V bias.



(d) Voltage response of "Kopin Super" GaAs concentrator cell at .700 V bias.

Figure 7.—Voltage response of GaAs concentrator cells showing effect of bias voltage on ringing.

RESPONSE OF SILICON SOLAR CELL TO PULSED LASER ILLUMINATION

D. Willowby, D. Alexander, T. Edge, K. Herren
National Aeronautics and Space Administration
George C. Marshall Space Flight Center
Information and Electronic Systems Laboratory
Marshall Space Flight Center, AL 35812

This paper deals with the response of silicon solar cell(s) to pulsed laser illumination. The motivation for this work was due to the interest of Earth to space/Moon power beaming applications. When this work began, it was not known if solar cells would respond to laser light with pulse lengths in the nanosecond range and a repetition frequency in the kHz range. This is because the laser pulse would be shorter than the minority carrier lifetime of silicon. A 20-nanosecond (ns) full width half max (FWHM) pulse from an aluminum-gallium/arsenide (Al-Ga-As) diode laser was used to illuminate silicon solar cells at a wavelength of 885 nanometers (nm). Using a high-speed digital oscilloscope, the response of the solar cells to individual pulses across various resistive loads was observed and recorded.

INTRODUCTION

The SpacE Laser ENERGY program (SELENE) has proposed using an Earth-based induction linac free electron laser (FEL) to provide energy to users in space. This relatively cheap laser energy from Earth would then be converted back into electrical energy by solar cells. Battelle Pacific Northwest Laboratory and Washington State University have already done research with gallium arsenide (Ga-As) cells and continuous wave laser at 806 nm and demonstrated 53-percent efficiency.¹ The induction linac FEL proposed would have a high-intensity pulse lasting 20 ns with a peak-to-peak spacing of 50 microseconds (ms), a rep rate of 20,000 Hz (fig. 1).

When this was put forth, there was some uncertainty whether silicon or Ga-As solar cells would respond to the laser pulse train. The minority carrier lifetime of silicon ranges from 10 to 100 ms and 10 to 100 ns for Ga-As, which is shorter than the pulse separation of the induction FEL. It was not clear whether the solar cells would respond to individual pulses, average the pulses, or respond at all. This experiment was conducted to determine what the response would be.

EXPERIMENT

The test setup is shown in figure 2. A Tektronix high-speed digital oscilloscope was used to measure the output of the solar cell. A converging lens was used to focus the laser light into a circle and the distance to the solar cell adjusted so that the entire cell would be illuminated. An Al-Ga-As diode laser with a wavelength of 0.885 microns was used for this experiment. The laser produced eighty 20-ns FWHM pulses at a 10-kHz rate.

Figure 3 shows the output of the Al-Ga-As laser with the characteristic "tail" of diode lasers as seen by an Antel Optronics model AR-S2 ultra-high-speed photodetector. The laser had a very low intensity, with the majority of the energy in the peak of the pulse.

Several attempts were made with 2- by 4-cm Ga-As solar cells. We believe we did not get a response from the Ga-As solar cells due to the low energy and the wavelength of the laser being close to the cutoff (0.9 microns) of Ga-As. Several 2- by 2-cm silicon Apollo telescope mount (ATM) cells were used in this test. The current-voltage (I-V) curve of the 2- by 2-cm ATM silicon solar cell is shown in figure 4.

In addition to verifying that a silicon cell would respond to pulsed laser illumination, we wanted to develop an I-V curve for the cell under laser light. To accomplish this, resistors of varying values were used. Wire-wound resistors were avoided so as to minimize problems with inductance.

RESULTS

Measurements were taken from short-circuit to open-circuit conditions. In each case, a resistor was used and it was soldered in place. The laser pulses were displayed, and the last pulse was recorded by the oscilloscope and printed. Figure 5 shows the response of the ATM cell in open circuit as measured by a current probe. An important thing to note about these plots is the time scale of the response curves compared to the laser pulse. As can be seen here, the silicon cell integrated a nanosecond laser pulse into a several microsecond response.

Figure 6 shows the cell's response across a 0.53-ohm wire-wound resistor. This is still close to open circuit and shows a pronounced secondary response which is due to the increased induction brought about by the wire-wound resistor.

Figure 7 shows the response of the cell across a 5.3-ohm load. Here, both an exponential and a capacitance decay can be seen.

In figure 8, the cell is loaded with a 10-ohm load. The cell's response has greatly increased, and it should be noted that the time scale has been increased.

Figure 9 shows the response of a silicon cell to 20-ns FWHM pulses at a 10-kHz rep rate. The sample rate of the oscilloscope at this time scale is such that not all the cell response is captured.

Figure 10 puts the laser pulse, silicon cell response to multiple pulses, and the response across a 4.3-ohm load together for comparison. Note that the time scales are all different.

An I-V curve was constructed from the data collected which shows high series resistance in the silicon cell's response to laser illumination (fig. 11). The I-V curve also shows the response of the cell under one-Sun conditions.

The efficiency of the silicon cell under illumination was difficult to determine due to uncertainty of the total amount of laser energy on the cell. However, the efficiency did seem to increase with increasing load value. The cell losses appear to be due to high series resistance, cell capacitance and inductance, and inductance in the circuit.

CONCLUSIONS

This experiment verified that silicon solar cells will respond to light pulses shorter than silicon's minority carrier lifetime. For silicon cells to operate under pulsed laser illumination where the pulse separation is greater than the minority carrier lifetime, the cells will need to have low series resistance, to have minimum inductance, and to be designed to respond to peak pulse power, as well as have protection from dark reverse current flow when the cell is not illuminated. The power system will have to minimize inductance as well as be designed to handle power pulses.

REFERENCES

1. Olsen, L.C.; Dunham, G.; Huber, D.A.; Addis, F.W.; Annheier, N.; and Coomes, E.P.: "GaAs Solar Cells for Laser Power Beaming," Proc. of the 11th Space Photovoltaic Research and Technology Conference, Cleveland, OH, 1991, p. 26-1.

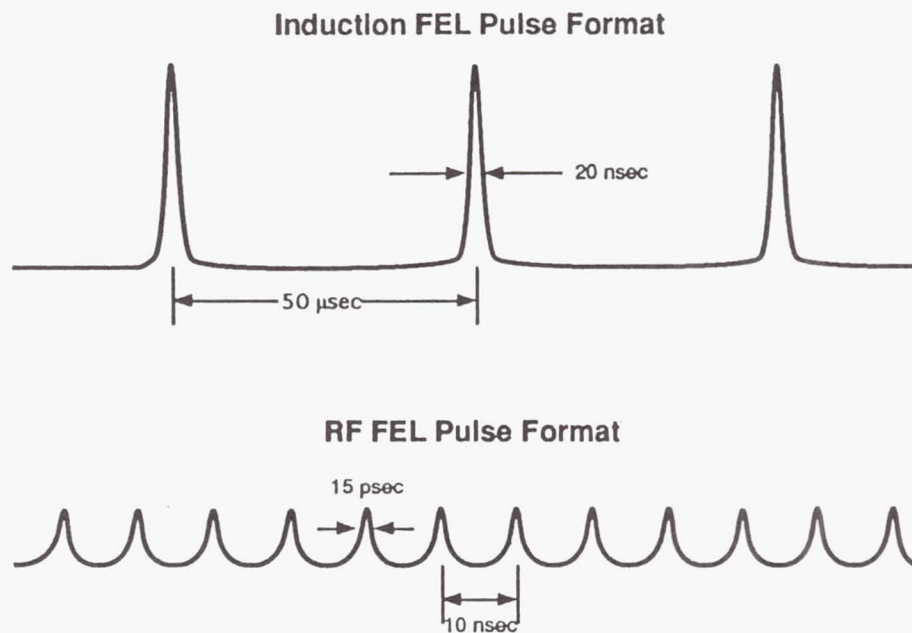


Figure 1. Typical optical pulse train formats for FEL's.

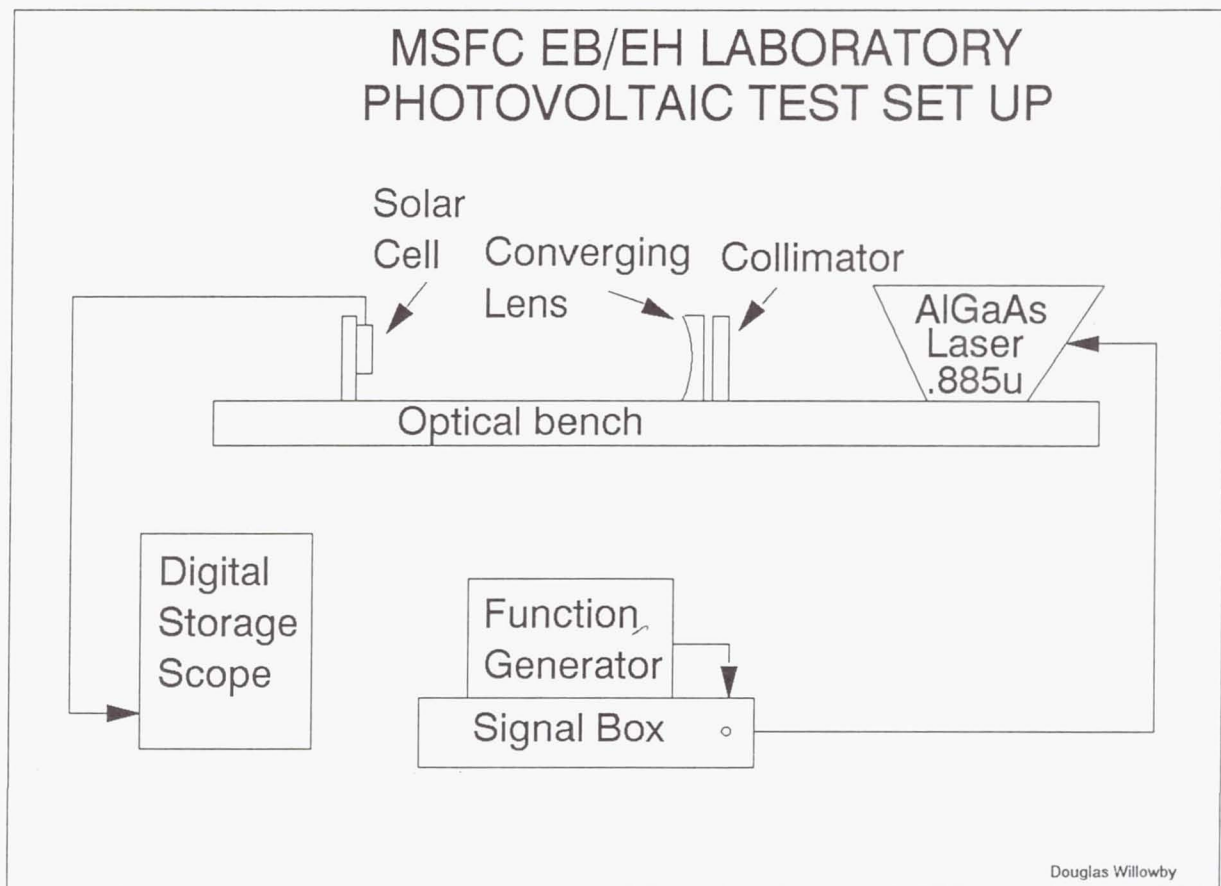


Figure 2. MSFC test setup.

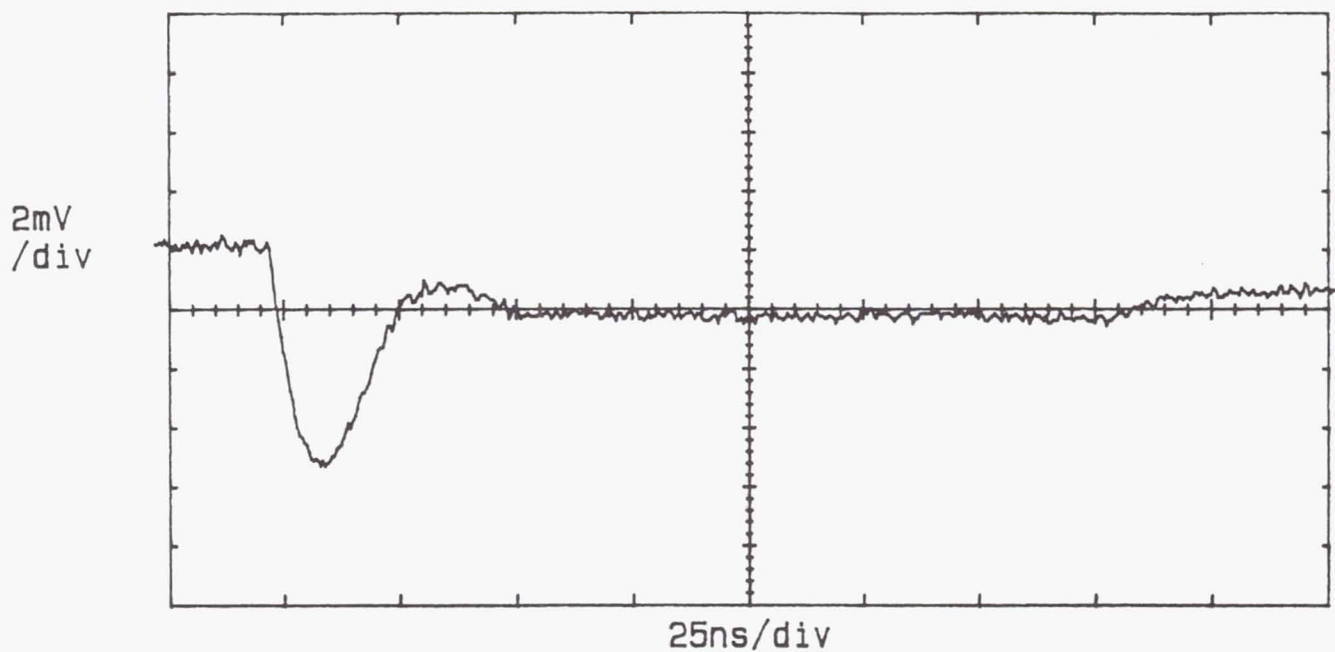


Figure 3. Al-Ga-As laser pulse.

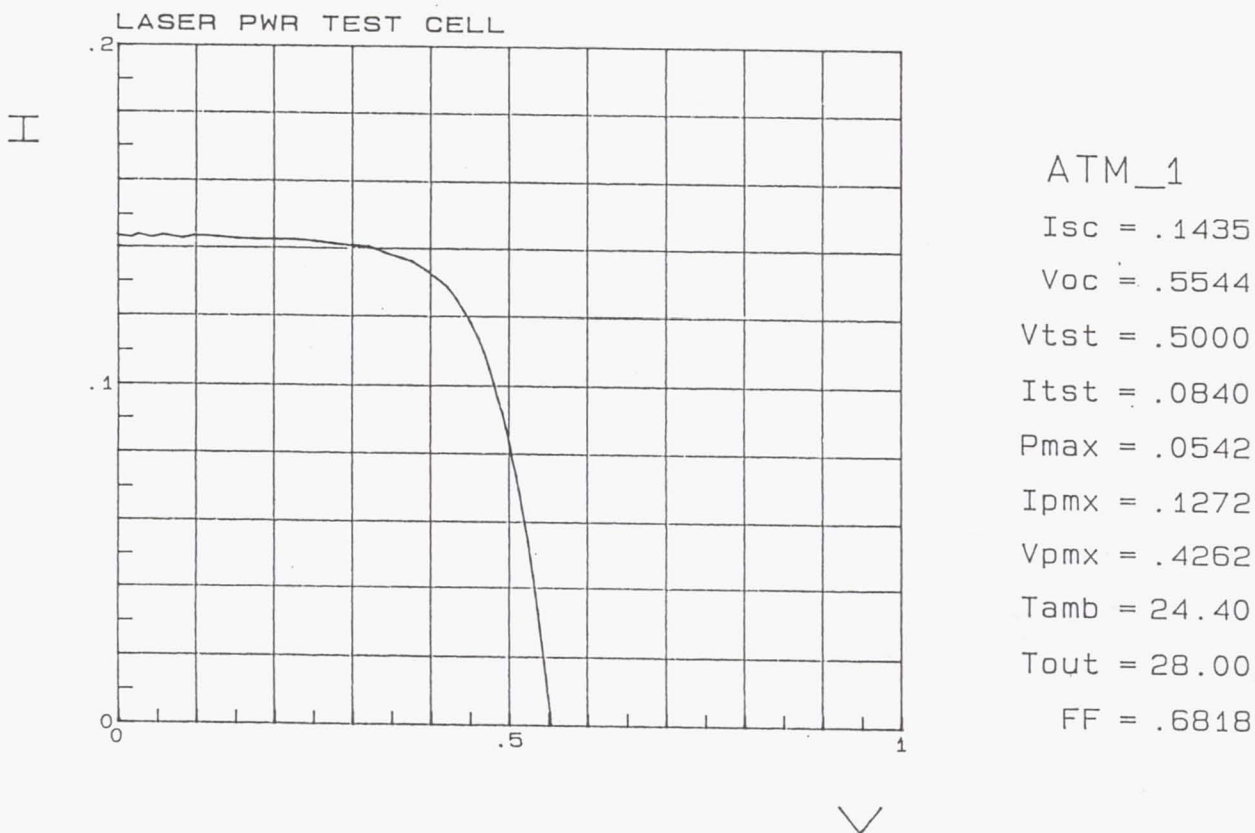


Figure 4. AM0 I-V curve of 2- by 2-cm ATM cell.

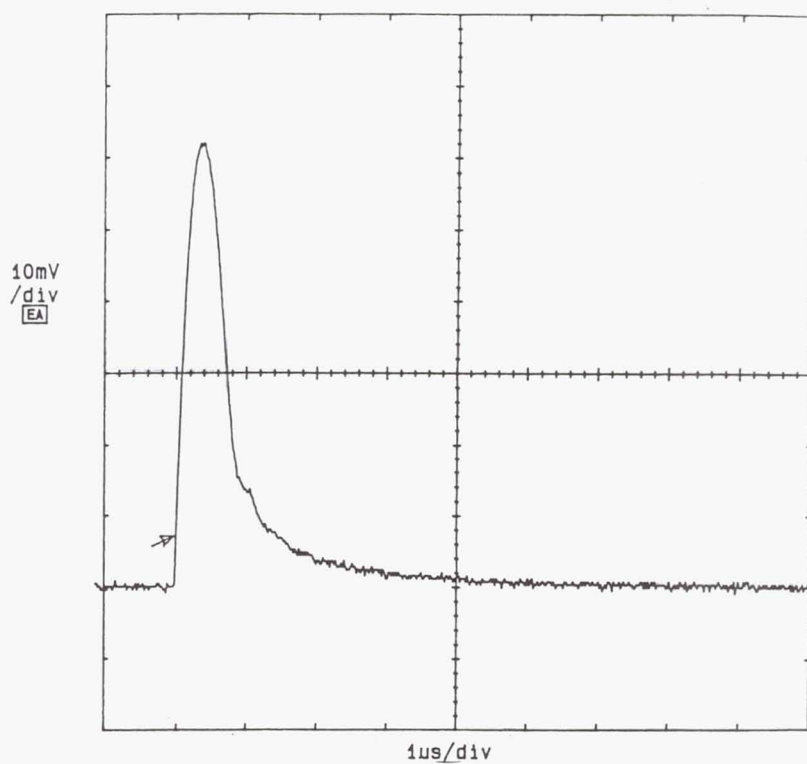


Figure 5. ATM cells current.

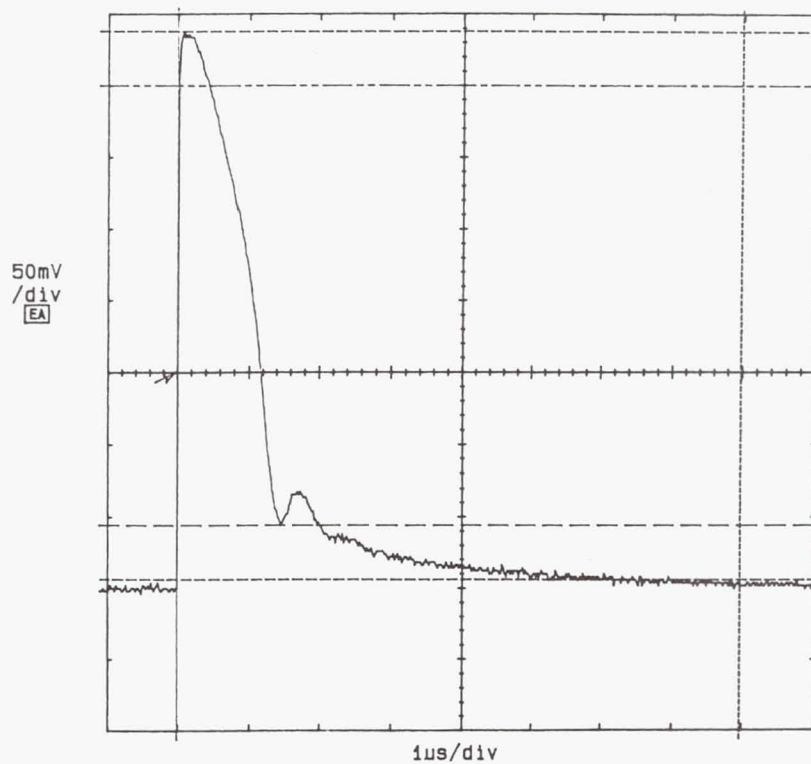


Figure 6. 0.53-ohm response.

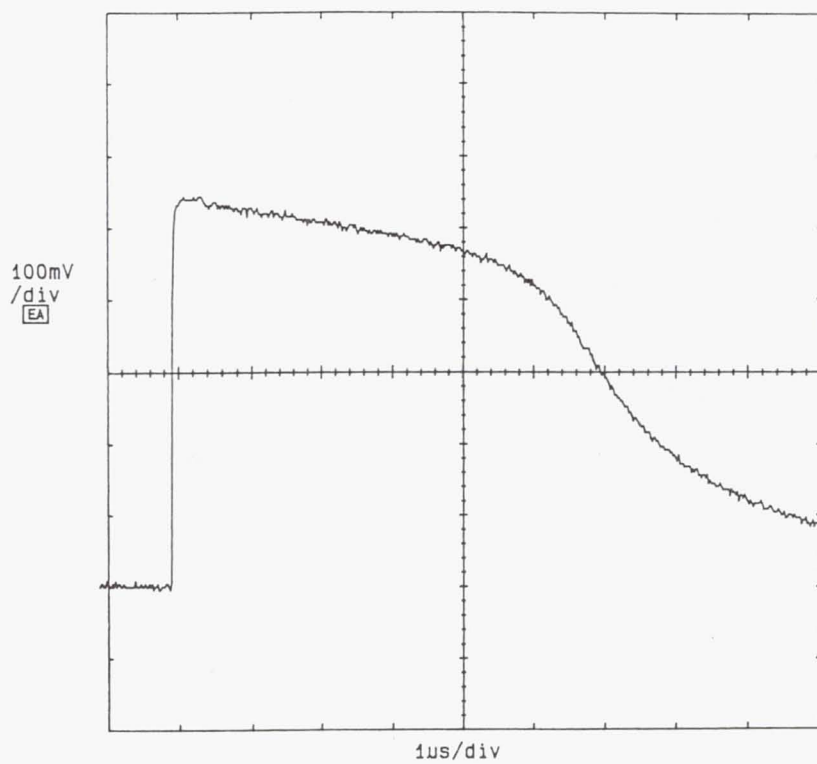


Figure 7. 5.3-ohm response.

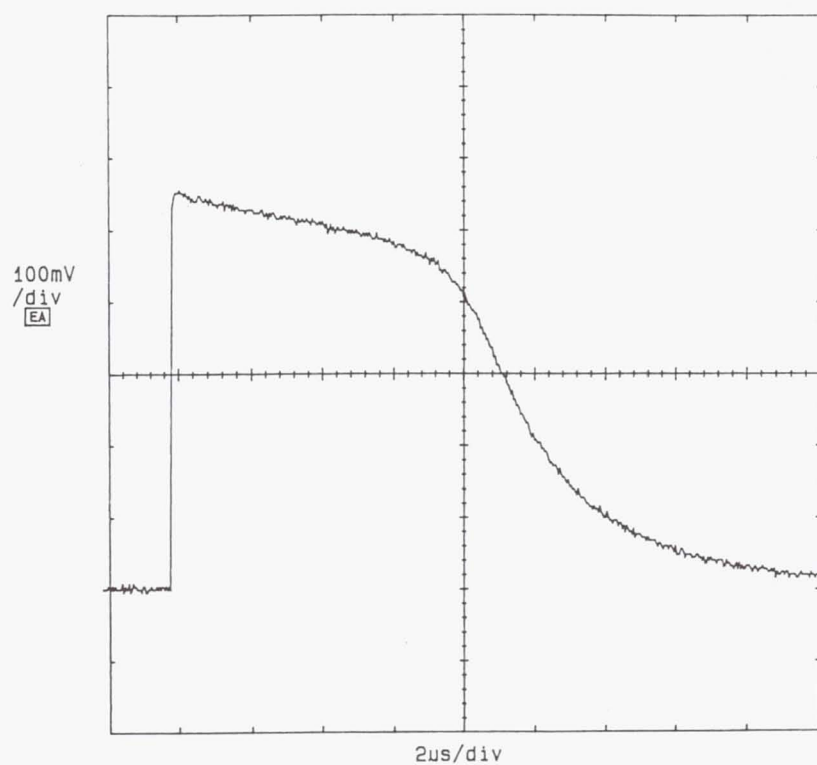
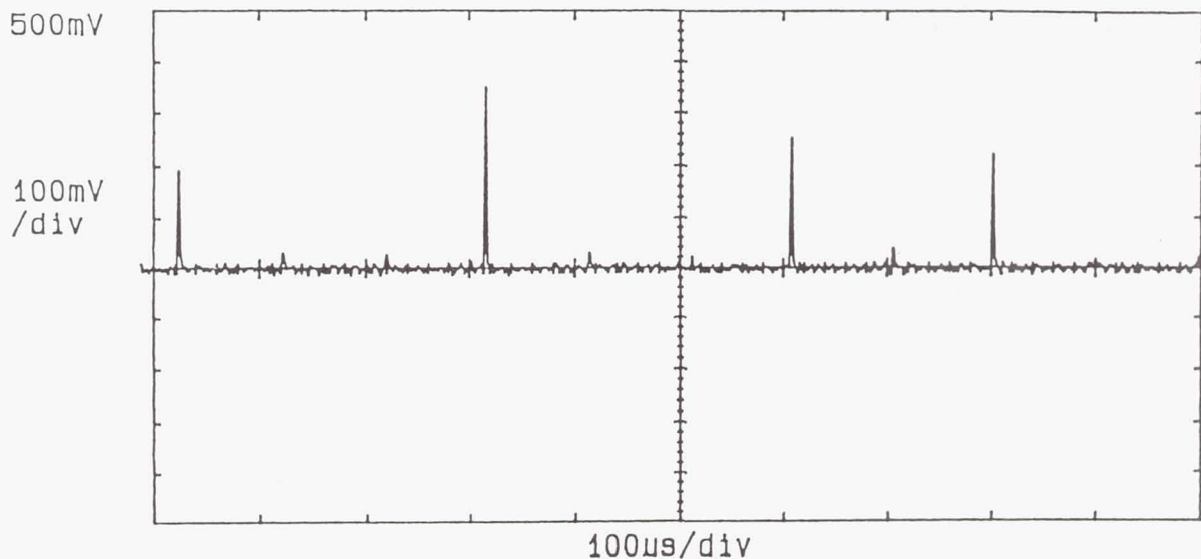


Figure 8. 10-ohm response.



Silicon solar cell being pulsed by laser at a rep rate of 10 KHz
Low sample rate does not always catch peak power

Figure 9. Response to pulse train.

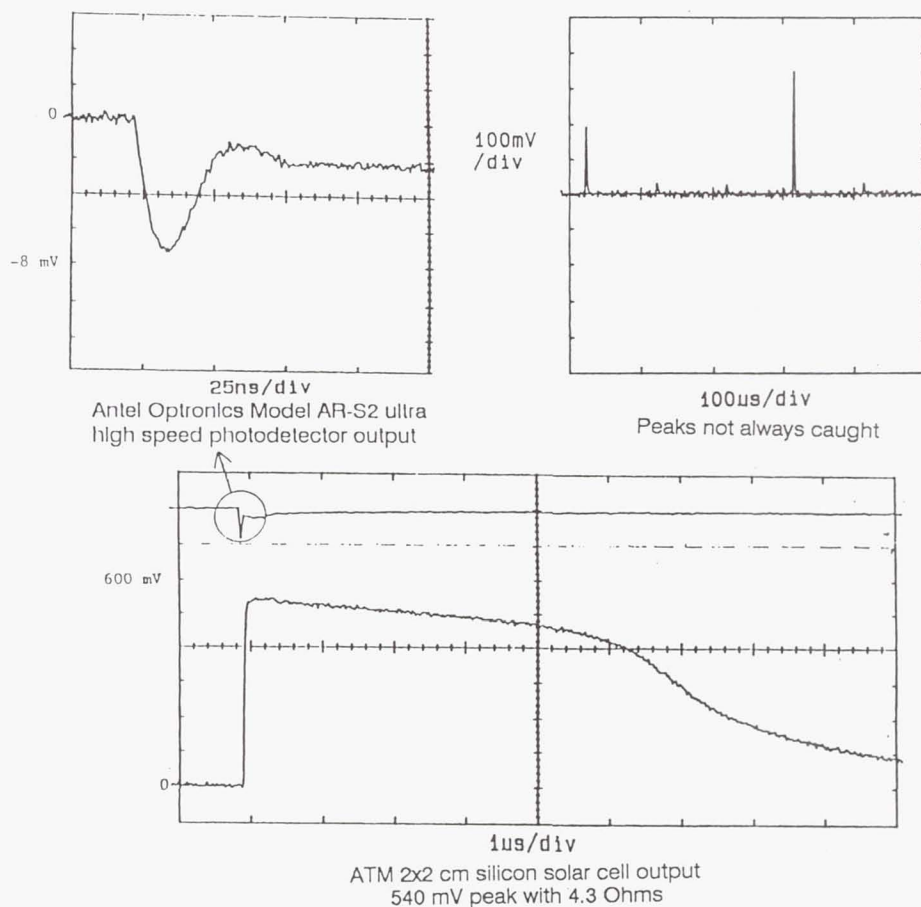


Figure 10. Laser pulse and cell response comparison.

2x2 cm ATM Silicon Solar Cell

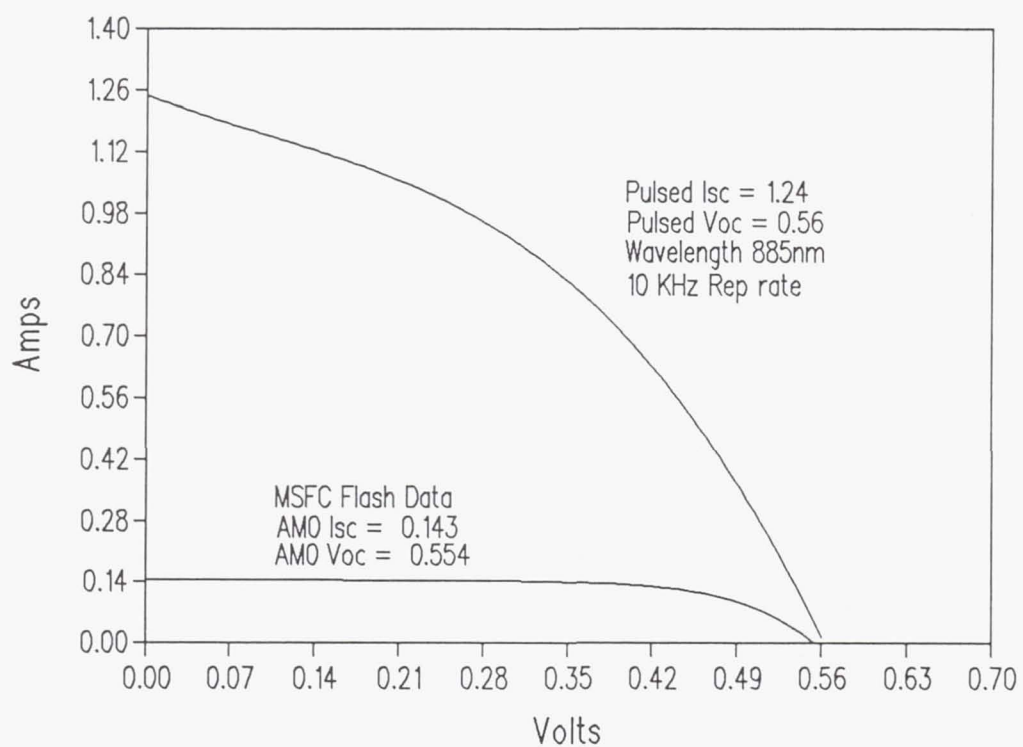


Figure 11. ATM pulse and AM0 I-V curves.

Approaches to Solar Cell Design for Pulsed Laser Power Receivers

Geoffrey A. Landis* and Raj K. Jain†

NASA Lewis Research Center
Photovoltaics Branch, 302-1
21000 Brookpark Rd.,
Cleveland, OH 44135

Abstract

Using a laser to beam power from Earth to a photovoltaic receiver in space could be a technology with applications to many space missions. Extremely high average-power lasers would be required in a wavelength range of 700-1000 nm. However, high-power lasers inherently operate in a pulsed format. Existing solar cells are not well designed to respond to pulsed incident power.

To better understand cell response to pulsed illumination at high intensity, the PC-1D finite-element computer model was used to analyze the response of solar cells to continuous and pulsed laser illumination. Over 50% efficiency was calculated for both InP and GaAs cells under steady-state illumination near the optimum wavelength. The time-dependent response of a high-efficiency GaAs concentrator cell to a laser pulse was modeled, and the effect of laser intensity, wavelength, and bias point was studied.

Three main effects decrease the efficiency of a solar cell under pulsed laser illumination: series resistance, L-C "ringing" with the output circuit, and current limiting due to the output inductance.

The problems can be solved either by changing the pulse shape or designing a solar cell to accept the pulsed input. Cell design possibilities discussed are a high-efficiency, light-trapping silicon cell, and a monolithic, low-inductance GaAs cell.

1. Introduction

Laser beaming of power from Earth to space using a photovoltaic array as a laser power converter could be an extremely useful technology, with applications to space missions from low Earth orbit to a lunar base [1-3]. Extremely high average-power lasers would be required, with laser power ranging from hundreds of kilowatts to several megawatts, in a wavelength range of ~700-1000 nm. The high-power laser proposed for this purpose by the NASA SELENE project is the induction free-electron laser (FEL), with a proposed operating wavelength of 840 nm.

Free electron lasers inherently operate in a pulsed format. The output of the proposed induction FEL, for example, consists of a continuous string of pulses approximately fifty nanoseconds wide with 50 μ s between pulses, resulting in a duty factor of approximately 1:1000. Other high-power lasers currently available, such as copper-vapor lasers and frequency-doubled Nd:YAG lasers, have similarly pulsed output.

Another type of FEL, the Radio Frequency (RF) FEL, has typically 10-20 pS pulse width and 30-50 nS spacing between pulses. This pulse format is significantly different from the induction laser, and will not be discussed in detail.

*Sverdrup Technology Inc., Brook Park, OH 44142. Work supported under NASA contract 33-25266

†NRC Resident Research Associate at NASA Lewis Research Center

Existing solar cells are not well designed to respond to pulsed incident power. An overview of issues involved in using photovoltaic cells for laser conversion can be found in references [4, 5].

In an experiment to test the response of solar cells to the induction free-electron laser pulse, a copper-vapor laser pulse was used. For this experiment the pulse width was 38 nS, with 115 μ S spacing between pulses. The wavelength used was 511 nm. The details of this experiment are discussed elsewhere [6,7] and will not be repeated here.

2. Modeling Response of Cells

The PC-1D finite-element computer model was used to model the output of solar cells under laser illumination. Over 50% efficiency was calculated for both InP and GaAs cells under steady-state illumination near the optimum wavelength [8]. For GaAs, this compares well to results measured under laser illumination.

In order to understand the response of a cell to pulsed illumination at high intensity, a high-efficiency GaAs concentrator cell similar to the ones tested in the copper-vapor experiment was modeled. This cell is shown in figure 1. Use of a computer model allows us to observe the output of the cell separated from the circuit interactions which dominate the experimental output; the cell output can then be used as input to the circuit model to understand the array interaction with pulsed incident light.

The response to a single monochromatic light pulse was calculated at 1 nS time intervals. Figure 2 shows the pulse format of the experiment compared to the modeled pulse. A rectangular (step function) illumination pulse was chosen for the model, compared to the slightly rounded pulse of the actual laser. From the response to a rectangular pulse, the response to an arbitrary pulse shape can be found. Some difficulty was found in reaching convergence of the PC-1D algorithm at the abrupt change in current; this problem could usually be resolved by restarting the simulation without reinitializing the conditions.

Figure 3 shows the current output of the cell biased at zero voltage (short circuit), during and after the pulse. The wavelength is 840 nm. The result is shown for four values of peak intensity. At these levels the output does not significantly depend on intensity. Two regimes are visible in the decay of the current after the pulse. There is an initial drop in current which is abrupt on the 1 nS time scale, immediately at the end of the light pulse. This drop comes from current generated in the emitter and space charge region of the cell. Following the immediate drop is a slow decay, with a time constant equal to half the minority carrier lifetime. This decay is quite exponential, as is shown by the straightness of the plot on the semi-log scale.

Since intensity was not seen to be a significant factor in the shape of the decay, a peak intensity of 50 W/cm² was used for further simulations.

Figure 4 shows the effect of the incident wavelength. 840 nm is near the GaAs efficiency peak; 511 nm is the wavelength of a copper-vapor laser, and 870 nm is close to the band edge of GaAs. The amount of decrease in current at the end of the pulse depends significantly on the absorption depth of the light, and hence, on the wavelength. Table 1 shows the absorption depths assumed.

The slope of the decay after the initial drop depends only on the minority carrier lifetime and is independent of the wavelength. The slope of this decay is also almost independent of the bias voltage, as shown in figure 5. Here the current axis shows the change in current from the steady-state (dark) conditions. At the peak intensity, the maximum power bias point is about 1 V. Decay at maximum power is almost identical to the short-circuit current decay.

Table 1: Absorption Depth in GaAs

Wavelength λ (nm)	Absorption Depth α^{-1} (μ)
511	0.103
840	0.968
870	1.96

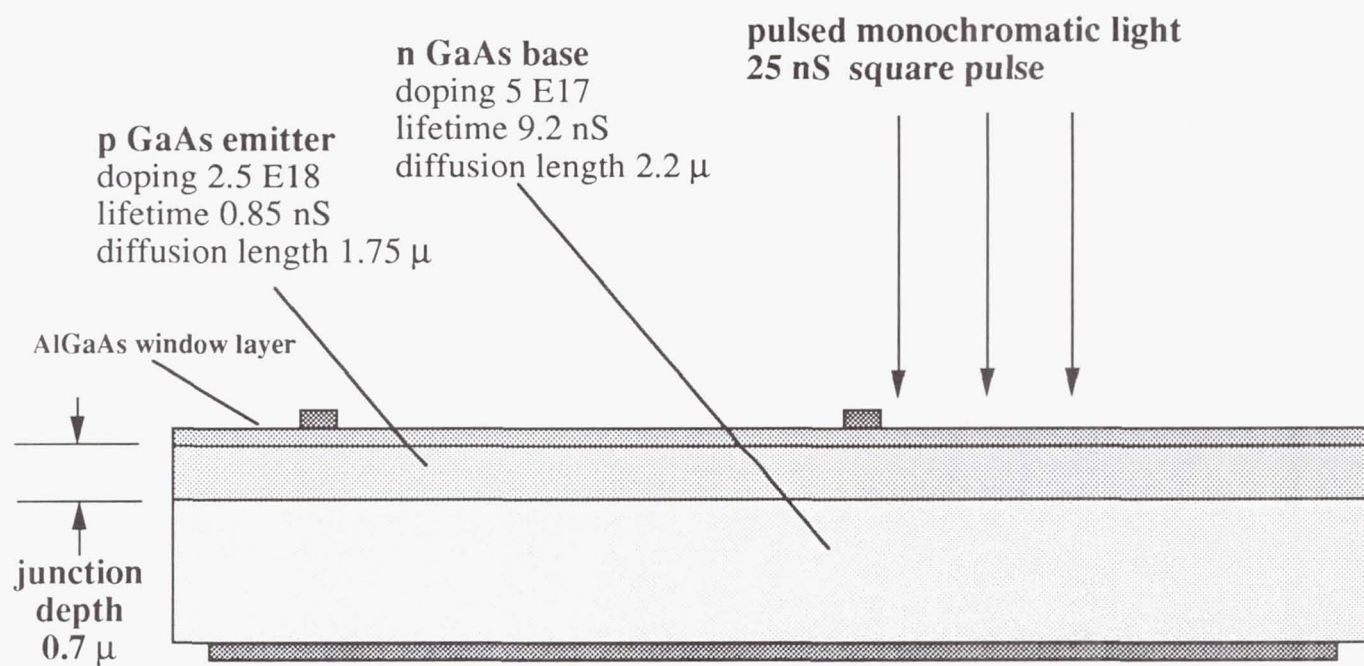


Figure 1. GaAs solar cell model used for computer simulations.

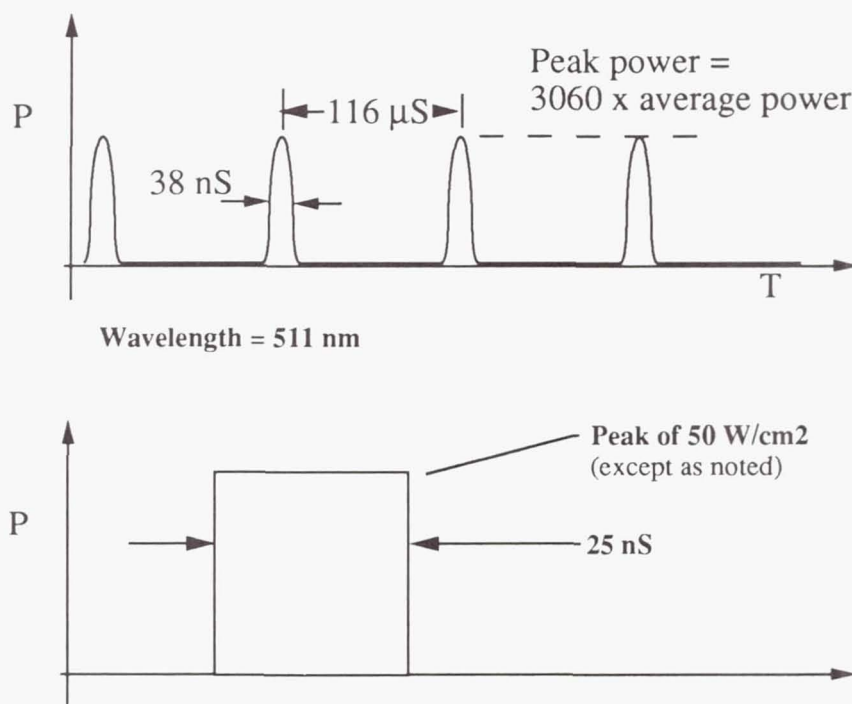


Figure 2. Pulse format of copper-vapor laser (top) and pulse used in computer model (bottom)

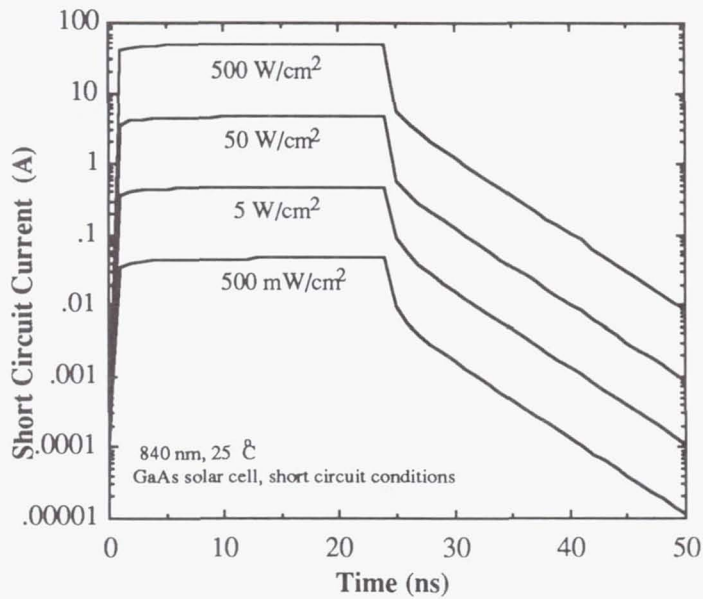


Figure 3. Short circuit current of GaAs cell during laser pulse (semi-log scale) as a function of time, with peak intensity as parameter.

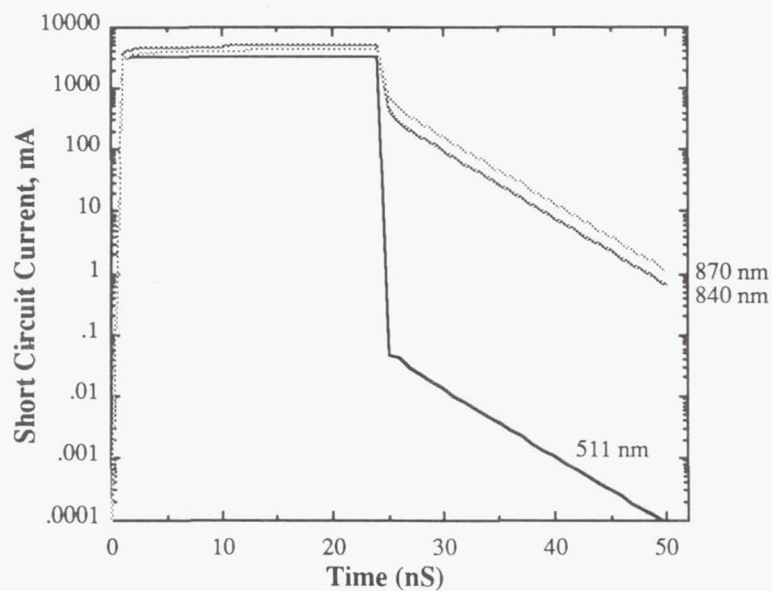


Figure 4. Short circuit current of cell during laser pulse with incident wavelength as parameter. Peak intensity 50 W/cm².

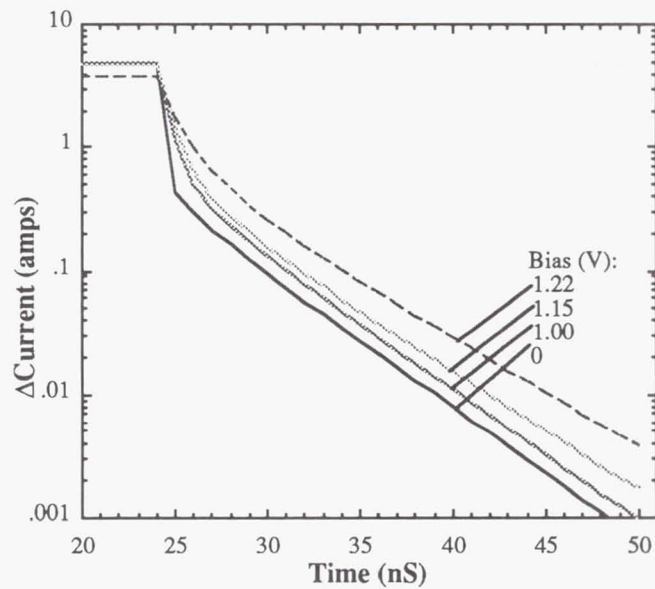


Figure 5. Current output of GaAs cell during laser pulse with cell bias as parameter. Incident pulse 50 W/cm², 840 nm.

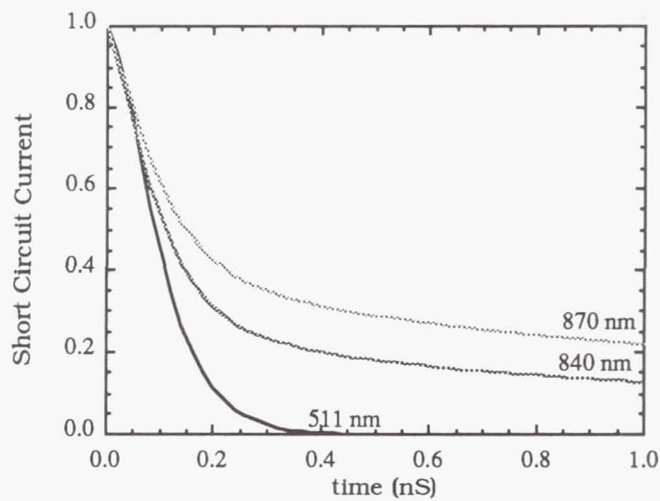


Figure 6. Normalized short circuit current decay in first nanosecond after pulse (linear scale), for 511 nm, 840 nm and 870 nm light pulse.

To examine the initial fast drop in current in more detail, a step-function decrease from steady-state illumination of 50 W/cm^2 to zero was examined in 20 pS time steps. Figure 6 shows this decay for the GaAs cell biased at short circuit. Figure 7 shows the effect of bias voltage. Since the time constant of this decay does not depend significantly on the minority carrier lifetime, but varies on the minority carrier mobility, this decay is apparently driven by the transit time rather than recombination.

At time scales of many nS characteristic of the induction laser and the copper-vapor laser pulse, it is reasonable to approximate these results for the circuit simulations [7] as showing that the GaAs cell response follows the laser pulse shape. For the copper vapor laser at 511 nm, the pulse broadening is less than 1 nS, which is insignificant considering that the copper-vapor laser pulse itself has a nearly Gaussian decay with constant considerably greater than 1 nS.

3. Circuit Effects on Pulse Illuminated Solar Cells

Three main effects decrease the efficiency of the solar cell in the tests using the pulsed copper-vapor laser:

1. Series Resistance

For the laser format used in the experimental test, the peak power during the pulse (8.6 kHz, 36 nS effective pulse width) is 3200 times the average power. Thus, for short lifetime cells, the peak output current must be 3200 times the average current for the cell to respond. I^2R losses due to the series resistance of the cell reduces the performance severely. For example, the lowest resistance cell measured had a series resistance designed for operation at 800 times solar concentration, well below the 3200x in the experiment.

In addition, the series resistance limits the peak current to:

$$I < V_{oc}/R \quad (1)$$

For the 0.5 cm diameter GaAs concentrator cells tested, the measured series resistance was about $100 \text{ m}\Omega$. At this resistance, series resistance limits the peak current output at a peak intensity of 75 W/cm^2 , corresponding to an average power of 75 mW/cm^2 at a peak/average ratio of 1000. At this intensity the current does not significantly increase with further increases in intensity.

2. L-C "Ringing"

Any p-n junction (*i.e.*, solar cell) has a junction capacitance. This, in conjunction with the necessary inductance of the output wiring, results in LC oscillations in the output. Oscillations result in the cell being operated at a bias point away from the peak power point.

3. Output inductance.

The inductance L of the output wiring results in a maximum rate of increase in current:

$$dI/dt \leq V_{oc}/L \quad (2)$$

and hence, the cell is held at open-circuit voltage for a time

$$t \approx (L I_{sc})/V_{oc} \quad (3)$$

during which it produces little power.

Note that the experiment used wire lengths on the order of 3 cm, far shorter (and hence, far lower inductance) than would be found in an actual flight solar array.

4. Approaches to Solution

The possible solutions to the problem are to either change the light source, or to redesign the photovoltaic receivers:

LASER SOLUTIONS

1. Change the laser to one with a more favorable pulse format
2. Stretch the length of the light pulse

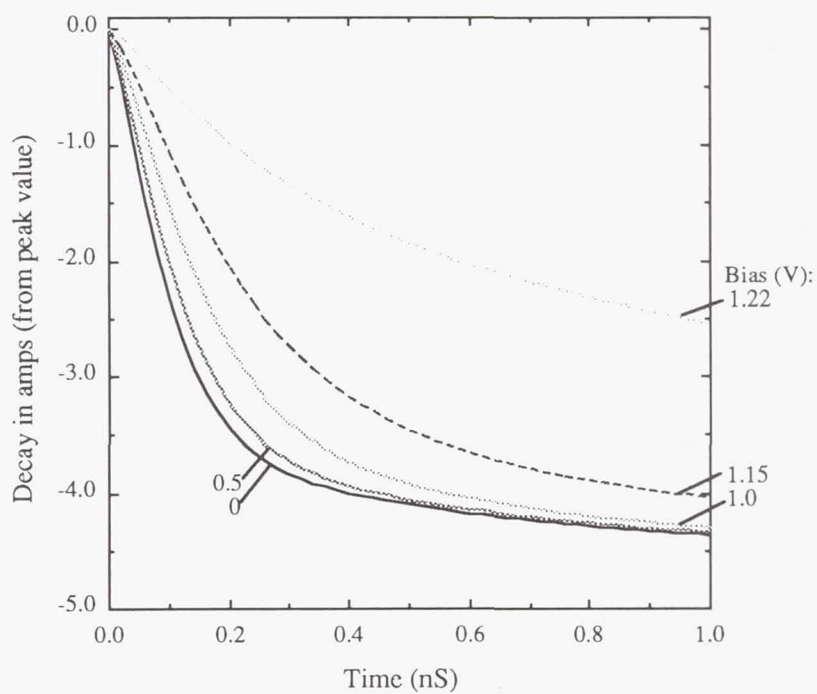


Figure 7. Current decay in first nanosecond of pulse as a function of bias (linear scale; current measured a decrease from illuminated value. Wavelength 840 nm; intensity 50 W/cm².

PHOTOVOLTAIC SOLUTIONS

3. Redesign existing array and cells to maximize performance with existing output pulse, including reduction of induction and ringing effects and minimization of losses due to series resistance.

4. Design a new cell type to stretch the output and hence, by averaging the output current over a longer period, reduce the peak current value. Three approaches are possible:

a. Improve the minority carrier lifetime on GaAs cell

While low doping, low defects, photon recycling could improve lifetime, it is unlikely that lifetimes could be improved into the microsecond and longer time scales required to average the induction laser pulses. It will also be necessary to reduce the fast portion of the decay curve.

b. Switch to Si cell

Si has an inherently longer lifetime due to the indirect bandgap. The long lifetime means cell output will stretch pulse, making induction effects and series resistance less important.

c. Other techniques to stretch pulse.

Possible methods to stretch the pulse are to use an intermediate phosphor with a long luminescence lifetime, or to collect the radiation to heat an absorber and use thermophotovoltaic cells for conversion.

In this paper, changes to the light source will not be considered. Two approaches will be considered in depth: designing a silicon cell for high response to the laser, and redesigning a GaAs cell for high pulse response.

4.1. High-Efficiency Silicon Solar Cell For Laser Conversion

Silicon is an under-appreciated material for space applications. Existing silicon cells used in space use reliable, but old (circa 1978) technology. The efficiency of currently used silicon cells (for example, SSF cells) is about 13%. However, as shown in table 2, over 20% efficiency has been achieved in several different laboratories across the world.

Table 2: Advanced Silicon Cell Efficiencies Achieved
Solar Efficiency (AM1.5 measurements)

21.3%, (12 cm ² cell)
University of New South Wales laser-grooved PERL cell [10]
22.3%
Stanford Point Contact Cell (SunPower Corporation) [11]
23.0%
University of New South Wales PERL Cell [12].

Laser Efficiency
(4cm² cell)

0.80 μm	34.9%
1.02 μm	45.1%
1.06 μm	39.4%
University of New South Wales PERL Cell. [9].	

Silicon, with an indirect bandgap, has minority carrier lifetime on the order of a thousand times longer than that of GaAs. Lifetimes as high as many milliseconds have been achieved. The long minority carrier lifetime of silicon means that the pulse may be stretched, reducing the peak current to a value where series resistance is much less important. Development of a high-efficiency Si cell for laser power beaming will have many potential advantages:

- Efficiency potentially comparable to GaAs
- Light weight (half the density of GaAs)
- Peak monochromatic efficiency at 1.06 μ
- Expected to have good radiation tolerance (if thin)
- Long minority carrier lifetime will average pulsed input into CW output
- High efficiency Si cell will have other applications:
 - As high-efficiency solar cell for ultra-lightweight space solar arrays
 - As low bandgap element of a high-efficiency tandem cell

Existing high-efficiency silicon cells have been measured with over 45% laser efficiency [9]. The requirements, then, are to improve the efficiency another 5% to meet the efficiency goals of the project, and to maintain high performance under expected space radiation conditions.

Silicon is an indirect bandgap semiconductor. This results in a high minority carrier lifetime, which is desirable; however, it also means that the optical absorption coefficient is low ($\alpha^{-1} \sim 100$ microns at 1.06 μ). Low optical absorption means that silicon becomes nearly transparent to light near the bandgap, precisely the wavelengths where monochromatic conversion efficiency ought to be highest. The solution is to increase the optical pathlength within the cell to increase the absorption, without increasing the physical thickness, since the diffusion length decreases with radiation damage. Use of a light trapping structure allows the solar cell to be made thin without loss of light-generated current. Thin Si cells are expected to be extremely radiation tolerant [11].

Long-pathlength light trapping technology has been analyzed in depth [13-15], but has not been used for single-crystal silicon cells to date because there is little motivation to make cells for terrestrial applications thin. One such light trapping design, which increases the average pathlength by more than a factor of 50, is shown in figure 8. Manufacturability of such ultra-thin cells has been discussed in [13].

Using light-trapping, the peak response of a silicon solar cell is expected to shift from 900 nm to slightly over 1 μ m. This is not a problem; in fact, the baseline laser wavelength of 840 nm represents a compromise between the long wavelengths desired by the laser designers and the wavelength under 850 nm required by the performance of the GaAs cell. As discussed by Parenti and Primmerman [16], the change of wavelength from the initial baseline of 1.06 μ m [17] to the requested 840 nm (which was originally done in order to allow GaAs cells to be used) has increased the difficulty and risk of the adaptive optics design, and it is not known if the optical performance required will even be possible at the shorter wavelength. A return to the 1.06 μ m baseline would simplify the adaptive optics design considerably.

An analysis of the response of thin light-trapping Si cells to pulsed laser illumination remains to be done. It is reasonable to expect, but has not yet been demonstrated, that the proposed thin, light-trapping Si cell will retain the desirable pulse-response properties.

4.2 Monolithic Voltage-Adding GaAs Cell Design

An alternative approach is to use a gallium arsenide cell, with the cell and circuit designed to accept the fact that the output will include extremely high current spikes. This requires a redesigned cell structure which has low inductance and series resistance, as well as an output circuit with low inductance and a power management circuit which can accept high peak currents.

One way to accomplish the cell portion of such a design is with a monolithic series structure, as shown in schematic in figure 9.

A monolithic series, or voltage-adding, solar cell is one in which each wafer has many individual sub-cells connected electrically in series. This results in a much larger voltage (N times the voltage of a single cell, where N is the number of subcells connected in series), and a correspondingly lower current. Such a cell may be used, for example, where a voltage higher than a single junction voltage is desired on a single small-area substrate. Monolithic series cells are currently used, for example, as power converters for fiber optic laser illumination [18,19]. Monolithic series interconnection is also useful for operation at high intensity [20], since the electrical series resistance losses are reduced substantially.

Since the subcells are physically small, the distance over which current must flow is reduced, and hence the resistance can decrease. The fractional loss due to series resistance is proportional to the area of the subcell, and hence decreases proportional to N (assuming constant metal coverage and thickness).

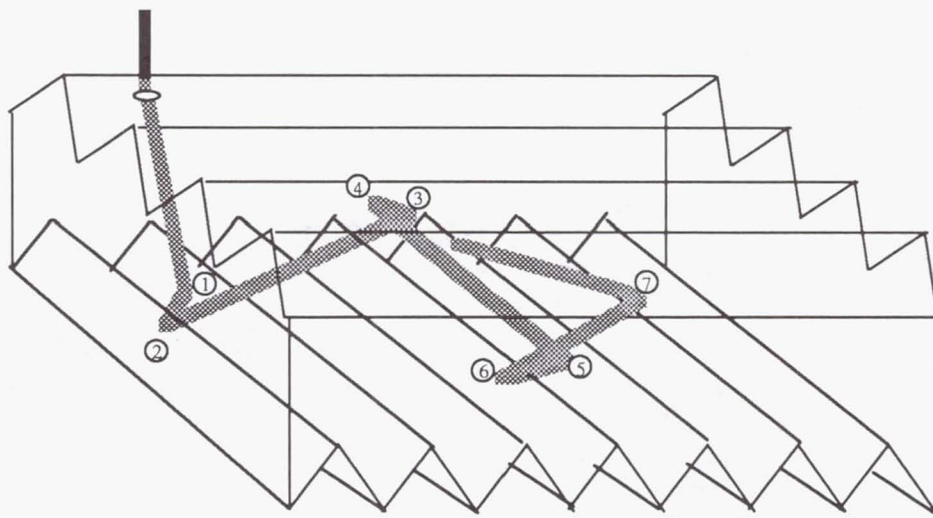


Figure 8. Schematic of cross-grooved light-trapping structure for a thin silicon solar cell, showing typical light path for first two light passages

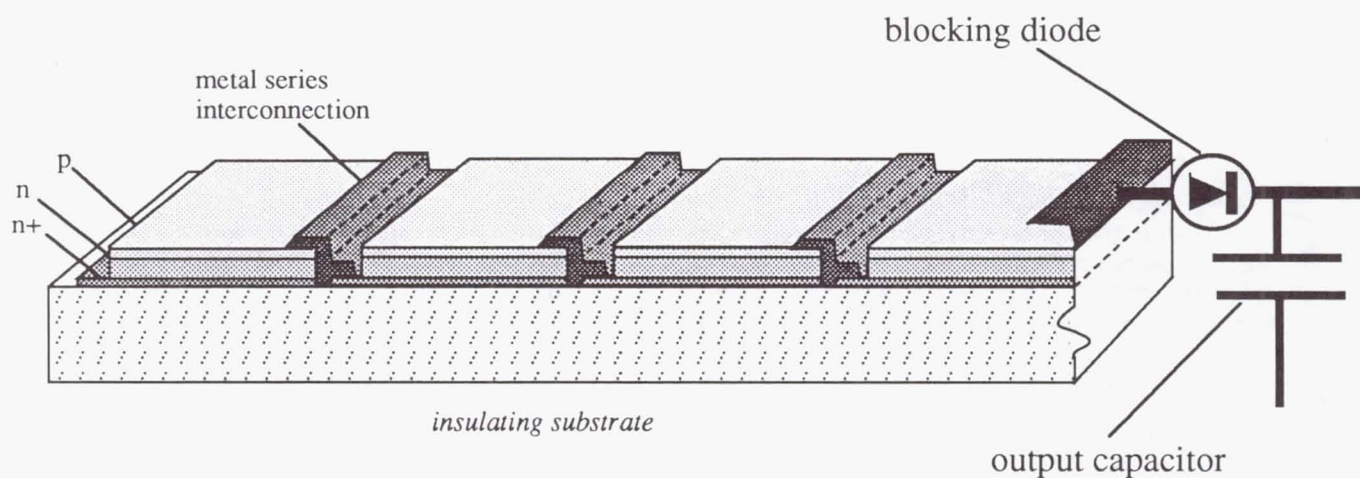


Figure 9. Monolithic voltage-adding GaAs solar cell structure

For pulsed laser illumination, the voltage-adding design has several advantages, as was discussed at the recent workshop on photovoltaics for laser power beaming [21]:

(1) The lower series resistance is an advantage for pulsed laser applications, since the high peak to average intensity ratio results in high peak currents. I^2R losses are especially high if the goal is to operate at the equivalent of many suns of laser intensity, where low series resistance is a major design goal.

(2) Series connected cells allow use of a blocking diode across a high-voltage substring.

An integral diode will reduce dark current. This is important when the duty cycle of the laser is small, since the dark current represents a constant loss when the cell is biased away from zero volts. The diode voltage drop in forward bias is shared among the N subcells, and thus by increasing N the loss due to the blocking diode turn-on voltage drop can be minimized. Such a blocking diode will eliminate the losses associated with the reverse current during the unilluminated portion of the cycle.

Further, by clipping the reverse-current portion of the oscillation, a blocking diode damps the following oscillations.

(3) The series-connected cell has a lower junction capacitance than a single cell of the same area. If N subcell p-n junctions are added electrically in series, the area of each junction is divided by N , and the total capacitance is reduced by a factor of $1/N^2$. This will reduce the LC oscillations.

(4) The series-connected cell allows faster current rise. The current rise in a solar cell with an associated output inductance is limited by the open circuit voltage, $dI/dT \leq L/V_{oc}$ (eq. 2). By connecting N subcells in series, the open circuit voltage is increased by N , and hence the current rise time is faster by a factor of N .

(5) If an output capacitor can be placed at the electrical connections of the cell, or of a group of series interconnected cells, most of the losses due to the electrical pulse interaction with the output wiring can be reduced, since the capacitor will integrate the pulses. By increasing the voltage and decreasing the current compared to a single junction cell, the interconnected cell allows a smaller capacitance and hence lower associated inductance.

Figure 9 shows the important elements of a monolithic voltage-adding design for a GaAs cell, including a blocking diode and integral capacitor. Details common to conventional cell designs, such as an antireflective coating, are not shown. Layer thicknesses are chosen to maximize response at the wavelength of operation. The thickness and doping will also be affected by the need to design for minimum series resistance. A feature not shown is a sawtooth ("prismatic") coverglass to divert light away from the gaps between the cells. Either the p-on-n structure shown, or a n-on-p structure could be used. The distance between subcell elements is set by the maximum allowable resistive loss due to sheet resistance. If larger subcell elements are needed, then a metallization finger pattern running perpendicular to the inter-subcell metallization could be used.

Many monolithic series designs have been proposed [18-26]. The design shown is similar to that of Borden [21].

In addition to cell design, unless all of the current spikes can be integrated by an integral output capacitor, the output wiring must also be designed for low inductance. This requirement leads to short wires, wide and flat conductors, and low magnetic-field design with balanced out and return current paths. A pulse-tolerant power management circuit must also be used, designed using RF design rules. In particular, the shunt regulation circuit must be designed to not dump high transient currents into the shunt.

5. Conclusions

High peak intensities are characteristic of the pulsed output of an induction free-electron laser or a copper-vapor laser. These high intensities presents unique difficulties for photovoltaic receivers, especially for solar cells made from direct-bandgap materials such as GaAs, in which the output of the cell follows the illumination profile on a nanosecond time scale. However, these difficulties do not seem to be insurmountable, and several approaches to design of cells which will accept the high peak intensity pulsed input have been suggested.

6. References

1. G.A. Landis, *IEEE Aerospace and Electronic Systems Magazine*, Vol. 6, No. 6, pp. 3-7 (1991); presented at 26th Intersociety Energy Conversion Engineering Conference, Boston MA, Aug. 1991.
2. C.E. Backus, *Conference Record of the 9th IEEE Photovoltaic Specialists Conference*, Silver Spring MD, pp. 61-65 (1972).
3. G.A. Landis, *Journal of Propulsion and Power*, Vol. 8, No. 1, pp. 251-254 (1992).
4. G.A. Landis, *Photovoltaic Receivers for Laser Beamed Power in Space*, NASA Contractor Report 189075 (1991); published in *Conference Record of the 22nd IEEE Photovoltaic Specialists Conference*, Vol. 2, pp. 1494-1502 (1991).
5. L.C. Olsen et al., *Space Photovoltaic Research and Technology 1991*, NASA Conference Publication 3121, pp. 26-1 to 26-9 (1991).
6. B. Anspaugh, R. Mueller, R. Lowe and G. Landis, *Results of Illuminating Various Solar Cells with Pulsed Laser Beams*, NASA Jet Propulsion Laboratory, JPL Publication 92-25, November 1, 1992.
7. R. Lowe, P. Jenkins and G. Landis, *Space Photovoltaic Research and Technology 1992*, NASA Lewis Research Center, Cleveland, OH (1992).
8. R.K. Jain and G.A. Landis, paper 929121, *Proceedings of the 27th Intersociety Energy Conversion Engineering Conference*, Vol. 1, P-259, pp. 1.303-1.307 (1992).
9. J. Zhao, A. Wang, X. Dai, M.A. Green, and S.R. Wenham, *Conference Record of the 22nd IEEE Photovoltaic Specialists Conference*, Vol. 1, pp. 399-402 (1991).
10. R.R. King, R.A. Sinton and R.M. Swanson, *Conference Record of the 20th IEEE Photovoltaic Specialists Conference*, Vol. 1, pp. 538-544 (1988).
11. M.A. Green, *Proceedings of the 10th European Photovoltaics Conference*, pp. 250-253 (1991).
12. M.A. Green, J. Zhao, A. Wang, and S.R. Wenham, *IEEE Electron Device Letters*, Vol. 13, No. 6, pp. 317-318 (1992).
13. G.A. Landis, "A Process Sequence for Manufacture of Ultra-Thin, Light-Trapping Silicon Solar Cells," *Solar Cells*, Vol. 29, pp. 257-266 (1990).
14. P. Campbell and M.A. Green, *Journal of Applied Physics*, Vol. 62, No. 1, pp. 243-249 (1987).
15. G.A. Landis, *Wide Bandgap Heterojunction Window Layers and Optical Confinement for High Efficiency Silicon Solar Cells*, PhD. Thesis, Department of Physics, Brown University (1988).
16. R. Parenti and C. Primmerman, "Power Beaming System Analysis Update," MIT Lincoln Laboratories PBP Memorandum No. 54PM-PBP-001 (15 May 1992).
17. R. Parenti, "Technology Concept Definition for a Ground-Based Power Beaming System," MIT Lincoln Laboratories Report PBP-1 (22 April 1992).
18. M.B. Spitzer et al., "Monolithic Series-Connected GaAs Converter Development," *Conference Record 22nd IEEE Photovoltaic Specialists Conference*, Vol. 1, pp. 142-146 (1991).
19. B. Beaumont et al., "High Efficiency Conversion of Laser Energy and Its Application to Optical Power Transmission," *Conference Record of the 22nd IEEE Photovoltaic Specialists Conference*, pp. 1503-1508 (1991).
20. B. Sater and C. Goradia, "The High Intensity Solar Cell - Key to Low Cost Photovoltaic Power," *Conference Record of the 11th IEEE Photovoltaic Specialists Conference*, pp. 356-363 (1975).
21. SELENE Laser Power Beaming Photovoltaics/FEL Interactions Workshop, NASA Marshall Space Flight Center, Alabama, March 25, 1992.
22. P.G. Borden, *Applied Physics Letters*, Vol. 35, No. 7, pp. 553-554 (1979).
23. B.L. Sater, H.W. Brandhorst, T.J. Riley and R.E. Hart, *Conference Record of the 10th IEEE Photovoltaic Specialists Conference*, pp. 188-193 (1973).
24. A. Gover and P. Stella, *IEEE Transactions Electron Devices*, Vol. ED-21, No. 6, p. 351-356 (1974).
25. R.M. Warner, E.M. Murray, and W.K. Smith, *Applied Physics Letters*, Vol. 31, No. 12, pp. 838-839 (1978).
26. J.C. Evans, A-T. Chai, and C. Goradia, *Conference Record of the 14th IEEE Photovoltaic Specialists Conference*, pp. 194-196 (1980).

EOL PERFORMANCE COMPARISON OF GaAs/Ge AND Si BSF/R SOLAR ARRAYS

Thomas W. Woike
Applied Solar Energy Corporation
City of Industry, CA 91749

EOL power estimates for solar array designs are significantly influenced by the predicted degradation due to charged-particle radiation. This paper presents new radiation-induced power degradation data for GaAs/Ge solar arrays applicable to missions ranging from low earth orbit (LEO) to geosynchronous earth orbit (GEO) and compares these results to silicon BSF/R arrays. These results are based on recently published radiation damage coefficients for GaAs/Ge cells (ref. 1). The power density ratio (GaAs/Ge to Si BSF/R) has been found to be as high as 1.83 for the proton-dominated worst-case altitude of 7408 km (MEO). Based on the EOL GaAs/Ge solar array power density results for MEO, missions which were previously considered infeasible may be reviewed based on these more favorable results. The additional life afforded by using GaAs/Ge cells is an important factor in system-level trade studies when selecting a solar cell technology for a mission and needs to be considered. The data presented in this paper supports this decision since the selected orbits have characteristics similar to most orbits of interest.

INTRODUCTION

Since the 1980s, production quantities of GaAs solar cells have been available. Within the last few years, MOCVD growth of high-quality GaAs films on Ge substrates has enabled these high-efficiency cells to be manufactured in large volume at a lower cost.

GaAs/Ge solar cells have significant advantages over silicon cells for space-based solar arrays:

The efficiency (BOL, AM0, 28°C) of space-qualified, production-grade, MOCVD-grown GaAs/Ge cells is greater than 18%, compared to less than 15% for conventional silicon cells and less than 16% for textured silicon cells.

The Pmax temperature coefficient for GaAs/Ge is more favorable than the value for silicon.

For almost all missions, GaAs/Ge cells are more resistant to radiation-induced power degradation than silicon cells.

This degradation is typically established by first converting the proton and electron spectra associated with an orbit to an equivalent fluence of 1 MeV electrons and then assigning a degradation value based on 1 MeV electron radiation data for the cell type of interest. This methodology is used to determine the radiation-induced power degradation results presented in this paper.

ANALYSIS

Nineteen orbits of general interest were selected for this study. These orbits were chosen to provide results across the broadest spectrum possible:

Low Earth Orbit (LEO)
Altitudes 300 km, 500 km, 926 km (500 n.mi.)
Inclinations 0° (926 km only), 30° (28.5° for 300 and 500 km), 60°, 90°

Medium Earth Orbit (MEO)
Altitude 7408 km (4000 n.mi.)
Inclinations 0°, 30°, 60°, 90°

High Earth Orbit (HEO)
Altitude 20372 km (11000 n.mi.)
Inclinations 0°, 30°, 60°, 90°

Geosynchronous Earth Orbit (GEO)
Altitude 35794 km (19327 n.mi.)
Inclination 0°

Equivalent annual 1 MeV electron fluences for these orbits were determined by multiplying the electron and proton spectra for these orbits and the damage coefficients established for the solar cell material, and converting the proton results to equivalent 1 MeV electrons. This was done for both Si BSF/R and GaAs/Ge solar cells. The equivalent fluence data for all listed orbits except 300 km and 500 km altitudes were provided by B. Anspaugh of JPL. The 300 km and 500 km values were obtained by using the electron and proton spectra for these orbits (ref. 2) as input to the EQFLUX algorithm. The AEI7LO and AP8MAX radiation models were used for electrons and protons respectively for all orbits except 300 km and 500 km which used the AE8MIN and AP8MIN models. Six fluences were determined for each orbit, representing 3, 6, 12, 20, 30, and 60 mil coverglass thicknesses. The AP8MIN proton fluences for the 300 km and 500 km orbits were reduced by a factor of 1.4 to be consistent with the AP8MAX model. The reduced values for these orbits are the ones reported in this paper.

These equivalent annual fluences were then used to determine total mission equivalent fluence for mission lengths from 0.5 to 10 years. Based on these total exposures, power degradation factors were then determined from published degradation characteristics for GaAs/Ge (ref. 1) and Si BSF/R (ref. 3) solar cells.

These degradation factors were then applied to BOL power densities for GaAs/Ge and Si BSF/R solar arrays to determine the EOL power density characteristics presented in the next section.

The BOL power densities were established by assuming AM0 illumination at normal incidence, 100% packing factor, no assembly losses, no environmental losses except for radiation degradation, and infinite backshielding for both array types. Even though some of these characteristics may not be achievable in practice, these assumptions allow for simpler analysis without invalidating the GaAs/Ge and Si BSF/R comparison. Operating temperature is assumed to be 55°C and 50°C for GaAs/Ge and Si BSF/R cells respectively, while their BOL AM0 28°C efficiencies are assumed to be 18.3% and 14.7%.

Finally solar flare protons are assumed to be negligible. This assumption holds for LEO and MEO. In HEO and GEO, solar flare protons comprise about 10% - 30% of total equivalent fluence. Since GaAs/Ge cells are more resistant to protons (as reported in the next section) than Si BSF/R cells, the inclusion of solar flare protons would improve the relative performance of GaAs/Ge cells beyond the results reported in this paper.

RESULTS

Annual Equivalent Fluence Data

Tables I - IV show that the annual equivalent fluences for GaAs/Ge and Si BSF/R arrays are about the same for the electron-dominated HEO and GEO orbits, while Si BSF/R is subjected to about a factor of 3 higher equivalent fluence than GaAs/Ge in the proton-dominated LEO and MEO orbits.

Low Earth Orbit (LEO) Power Predictions, 300 km - 926 km

Figures 1 through 4 demonstrate the worst case (926 km) for the LEO orbits studied. The GaAs/Ge solar array power density is greater than 216 W/m^2 for a ten year design life using a 3 mil or thicker coverglass over all inclinations of the LEO orbits studied. Figures 5 - 8 demonstrate that for a 926 km altitude, the EOL power advantage of GaAs/Ge over Si BSF/R increases with increasing mission duration and decreasing coverglass thickness, with 60° being approximately the optimum inclination. For a ten year design life, GaAs/Ge provides between 48% to 70% higher EOL power than Si BSF/R when a 3 mil coverglass is used. This range is 48% to 62% for a 6 mil coverglass. The power density ratio does not increase as much from the BOL value of 1.33 for the lower LEO orbits.

Medium Earth Orbit (MEO) Power Predictions, 7408 km (4000 n.mi.)

Figure 9 shows that even at this nearly worst-case radiation altitude, the GaAs/Ge solar array power density exceeds 180 W/m^2 after five years at the worst-case inclination of 0° , provided that a 60 mil coverglass is used. The 180 W/m^2 value serves as an important benchmark because this slightly exceeds the BOL Si BSF/R solar array power density. Figure 10 indicates that for 30° inclination the GaAs/Ge solar array power density will not degrade to the BOL Si BSF/R solar array power density value until 3.5 years when a thinner 30 mil coverglass is used. Figure 11 shows that the same can be said at 60° inclination after 1.9 and 6.5 years when using a 20 mil and 30 mil coverglass respectively. Figure 12 demonstrates that a polar orbit (90° inclination) improves the aforementioned values to 2.1 and 7.5 years.

As evidenced by Figures 13 - 16, the comparison between GaAs/Ge and Si BSF/R solar array power density is incomplete for this altitude. Since the highest radiation exposure on JPL's test cells is $10^{16} \text{ 1 MeV electrons/cm}^2$, no EOL power densities are calculated when total mission fluence exceeds this value. Notwithstanding, the use of GaAs/Ge is particularly beneficial at this altitude since EOL power densities as high as 83% above those of Si BSF/R can be attained.

High Earth Orbit (HEO) Power Predictions, 20372 km (11000 n.mi.)

Figures 17 - 20 demonstrate that at this altitude the GaAs/Ge solar array power density after nine years of life exceeds the BOL Si BSF/R solar array power density value for all inclinations studied when a standard 6 mil coverglass is used. Figures 21 - 24 indicate that the EOL GaAs/Ge solar array power density is generally at least 50% higher than for Si BSF/R for most design lives.

Geosynchronous Earth Orbit (GEO) Power Predictions, 35794 km (19327 n.mi.)

Figure 25 shows that in GEO the GaAs/Ge solar array power density after ten years of life is about 210 W/m^2 (6 mil coverglass) compared to the BOL Si BSF/R solar array power density of almost 180 W/m^2 . Figure 26 demonstrates that throughout the design life, GaAs/Ge typically affords a 40% to 50% power density improvement over Si BSF/R.

CONCLUSIONS

Recently published damage coefficients for GaAs/Ge solar cells and updated normalized power degradation characteristics (ref. 1) were used to predict EOL power for 19 selected orbits of general interest.

The equivalent fluences for GaAs/Ge and Si BSF/R arrays are about the same for the electron-dominated HEO and GEO orbits, while Si BSF/R is subjected to about a factor of 3 higher equivalent fluence than GaAs/Ge in the proton-dominated LEO and MEO orbits.

At the beginning of life (BOL), the GaAs/Ge solar array power density is about 240 W/m^2 , compared to nearly 180

W/m^2 for Si BSF/R. This 33% advantage is entirely due to higher initial efficiency (18.3% versus 14.7%) and a more favorable temperature coefficient. This power density ratio then initially increases with mission life. In all but 16 of the 114 cases studied, the power density ratio continues to increase out to a ten year design life. For the other cases, the ratio peaks and then decreases slightly, but never below 1.5 (50% EOL power advantage for GaAs/Ge).

The power density ratio has been found to be as high as 1.83 for the proton-dominated worst-case altitude of 7408 km (MEO). Based on the EOL GaAs/Ge solar array power density results for MEO, missions which were previously considered infeasible may be reviewed based on these more favorable results.

The additional life afforded by using GaAs/Ge is an important factor in system-level trade studies when selecting a solar cell technology for a mission and needs to be considered. The higher EOL/BOL power ratio of a GaAs/Ge array translates into more relaxed requirements for power conditioning equipment and reduces the need for dissipative components to remove the additional BOL power for an array designed for EOL operation, thereby reducing system costs. The advantage in operating life also supports a favorable EOL power to weight ratio for a GaAs/Ge array.

REFERENCES

1. Anspaugh, B., "Proton and Electron Damage Coefficients for GaAs/Ge Solar Cells," 22nd IEEE Photovoltaic Specialists Conference, p.1593, 1991.
2. Stassinopoulos, E., and Raymond, J., "The Space Radiation Environment for Electronics," Space Photovoltaic Research and Technology Conference XI, NASA Conference Publication 3121, p.46-1, 1991.
3. Anspaugh, B., "Solar Cell Radiation Handbook, Addendum 1: 1982-1988," JPL Publication 82-69, Addendum 1, 1989.

Table I
Total Annual Pmax Equivalent Fluence for 0° Inclination

Total Annual Fluence for Pmax 1 MeV equivalent electrons/cm ² 0° Inclination						
Altitude (km)	Coverglass thickness (mils)					
	3	6	12	20	30	60
GaAs/Ge						
926	2.05e+12	1.93e+12	1.79e+12	1.67e+12	1.54e+12	1.38e+12
7408	1.39e+17	4.50e+16	9.46e+15	3.32e+15	9.38e+14	2.32e+14
20372	1.82e+14	1.41e+14	1.14e+14	8.97e+13	6.88e+13	3.36e+13
35794	3.12e+13	2.49e+13	1.73e+13	1.16e+13	7.47e+12	2.38e+12
Si BSF/R						
926	5.86e+12	5.48e+12	4.99e+12	4.48e+12	4.14e+12	3.61e+12
7408	4.12e+17	1.47e+17	3.52e+16	1.03e+16	3.96e+15	8.21e+14
20372	2.08e+14	1.61e+14	1.29e+14	1.01e+14	7.75e+13	3.78e+13
35794	3.10e+13	2.48e+13	1.72e+13	1.15e+13	7.36e+12	2.34e+12

Table II
Total Annual Pmax Equivalent Fluence for 30° Inclination

Total Annual Fluence for Pmax 1 MeV equivalent electrons/cm ² 30° Inclination						
Altitude (km)	Coverglass thickness (mils)					
	3	6	12	20	30	60
	GaAs/Ge					
300	5.82e+10	5.40e+10	4.93e+10	4.55e+10	4.20e+10	3.83e+10
500	7.95e+11	7.22e+11	6.42e+11	5.80e+11	5.18e+11	4.50e+11
926	1.09e+13	9.23e+12	7.52e+12	6.31e+12	5.22e+12	4.20e+12
7408	6.11e+16	1.85e+16	3.66e+15	1.28e+15	3.61e+14	9.00e+13
20372	1.18e+14	9.51e+13	7.62e+13	5.94e+13	4.50e+13	2.13e+13
	Si BSF/R					
300	1.70e+11	1.56e+11	1.39e+11	1.23e+11	1.14e+11	1.02e+11
500	2.43e+12	2.19e+12	1.91e+12	1.65e+12	1.48e+12	1.25e+12
926	3.50e+13	2.97e+13	2.38e+13	1.87e+13	1.58e+13	1.19e+13
7408	1.77e+17	5.99e+16	1.36e+16	3.95e+15	1.51e+15	3.16e+14
20372	1.33e+14	1.06e+14	8.52e+13	6.62e+13	4.99e+13	2.36e+13

Table III
Total Annual Pmax Equivalent Fluence for 60° Inclination

Total Annual Fluence for Pmax 1 MeV equivalent electrons/cm ² 60° Inclination						
Altitude (km)	Coverglass thickness (mils)					
	3	6	12	20	30	60
	GaAs/Ge					
300	2.52e+12	1.05e+12	3.80e+11	2.24e+11	1.38e+11	8.93e+10
500	6.12e+12	2.68e+12	1.13e+12	7.34e+11	5.05e+11	3.64e+11
926	1.72e+13	9.56e+12	5.60e+12	4.14e+12	3.10e+12	2.29e+12
7408	3.13e+16	9.60e+15	1.92e+15	6.75e+14	1.92e+14	4.86e+13
20372	5.97e+13	4.71e+13	3.76e+13	2.93e+13	2.21e+13	1.04e+13
	Si BSF/R					
300	7.82e+12	3.51e+12	1.33e+12	6.78e+11	4.47e+11	2.65e+11
500	1.89e+13	8.96e+12	3.86e+12	2.21e+12	1.59e+12	1.06e+12
926	5.35e+13	3.13e+13	1.82e+13	1.21e+13	9.37e+12	6.51e+12
7408	9.10e+16	3.10e+16	7.13e+15	2.08e+15	7.98e+14	1.66e+14
20372	6.78e+13	5.28e+13	4.20e+13	3.26e+13	2.45e+13	1.16e+13

Table IV
Total Annual Pmax Equivalent Fluence for 90° Inclination

Total Annual Fluence for Pmax 1 MeV equivalent electrons/cm ² 90° Inclination						
Altitude (km)	Coverglass thickness (mils)					
	3	6	12	20	30	60
GaAs/Ge						
300	1.88e+12	7.97e+11	2.96e+11	1.76e+11	1.10e+11	7.14e+10
500	4.32e+12	1.96e+12	8.63e+11	5.76e+11	4.04e+11	2.93e+11
926	1.25e+13	7.17e+12	4.34e+12	3.27e+12	2.50e+12	1.86e+12
7408	2.70e+16	8.27e+15	1.66e+15	5.81e+14	1.65e+14	4.15e+13
20372	5.04e+13	3.94e+13	3.15e+13	2.45e+13	1.85e+13	8.74e+12
Si BSF/R						
300	5.83e+12	2.65e+12	1.02e+12	5.23e+11	3.47e+11	2.08e+11
500	1.34e+13	6.53e+12	2.92e+12	1.72e+12	1.26e+12	8.46e+11
926	3.87e+13	2.31e+13	1.38e+13	9.46e+12	7.44e+12	5.24e+12
7408	7.83e+16	2.68e+16	6.15e+15	1.80e+15	6.87e+14	1.44e+14
20372	5.75e+13	4.42e+13	3.52e+13	2.73e+13	2.06e+13	9.71e+12

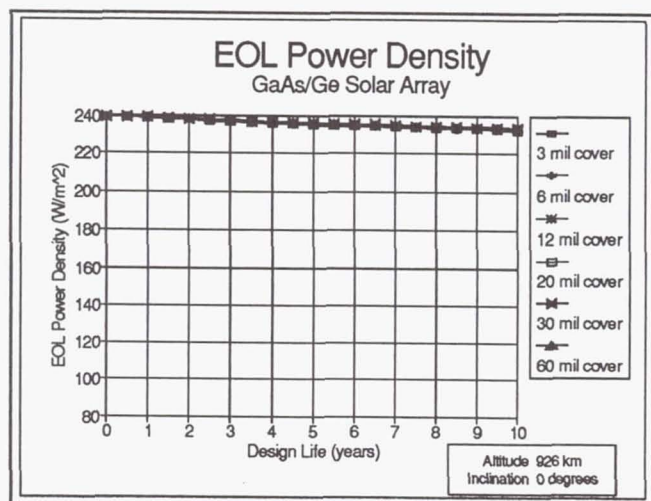


Figure 1

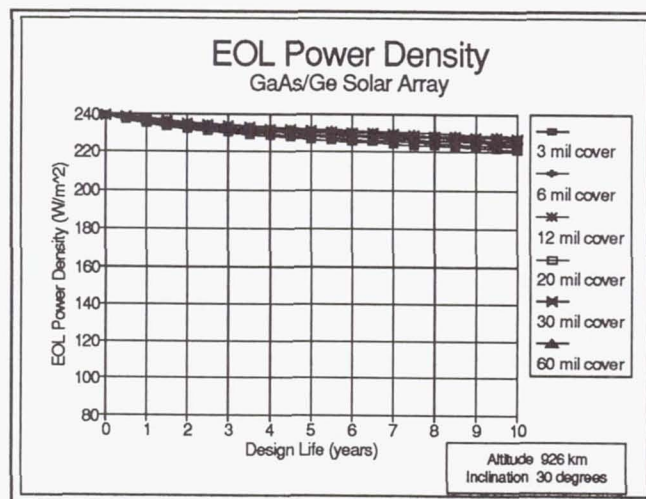


Figure 2

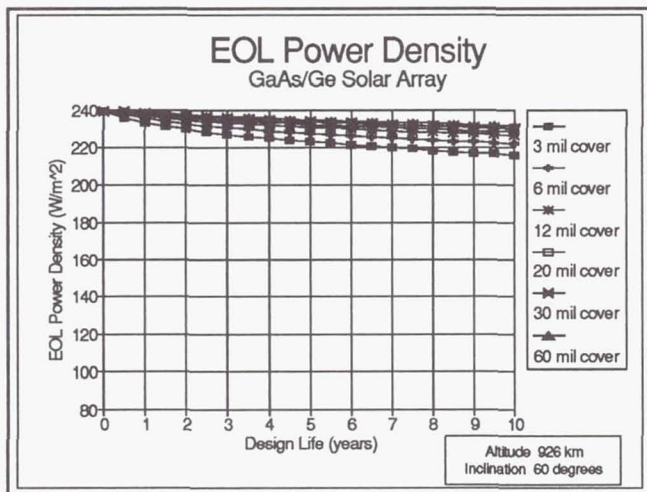


Figure 3

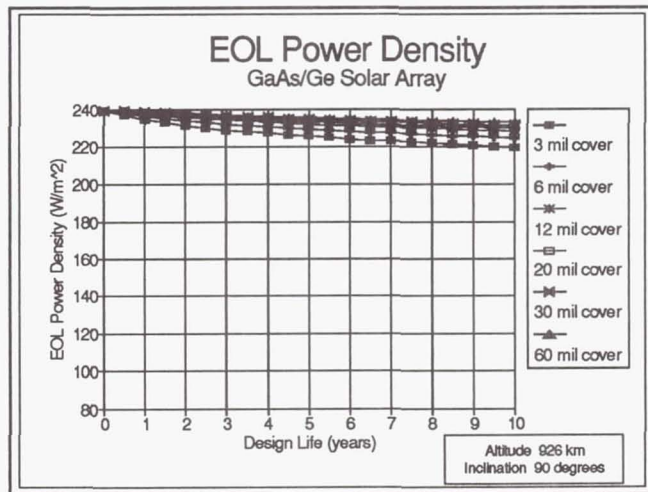


Figure 4

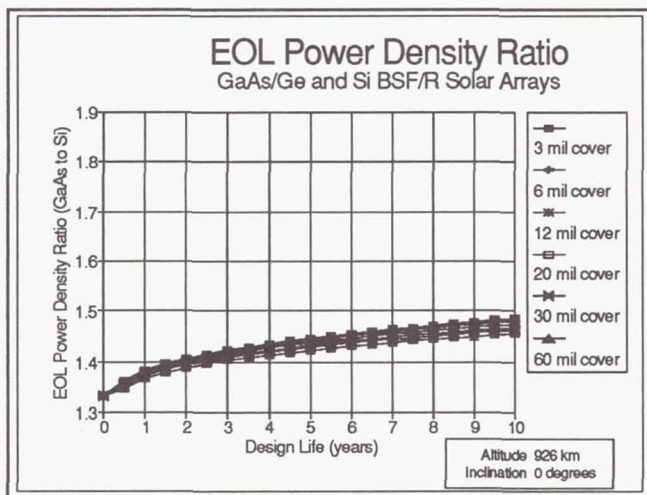


Figure 5

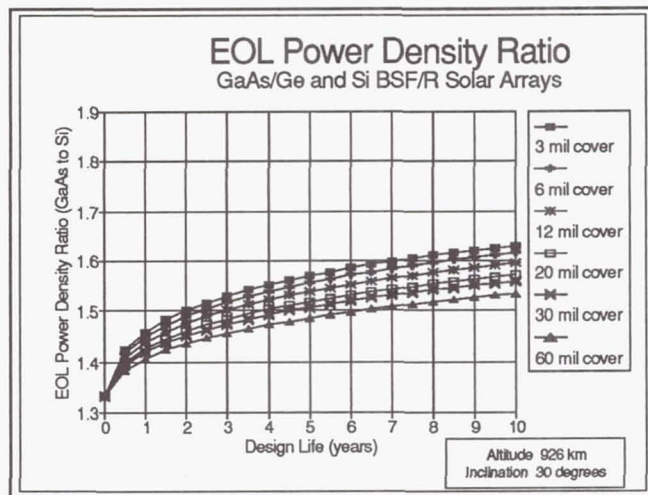


Figure 6

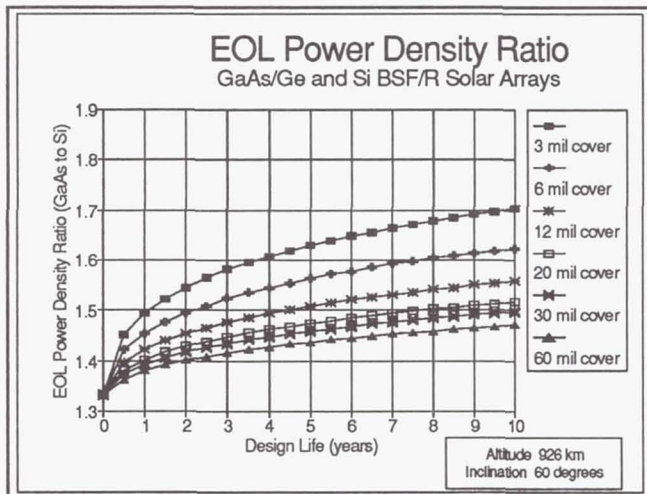


Figure 7

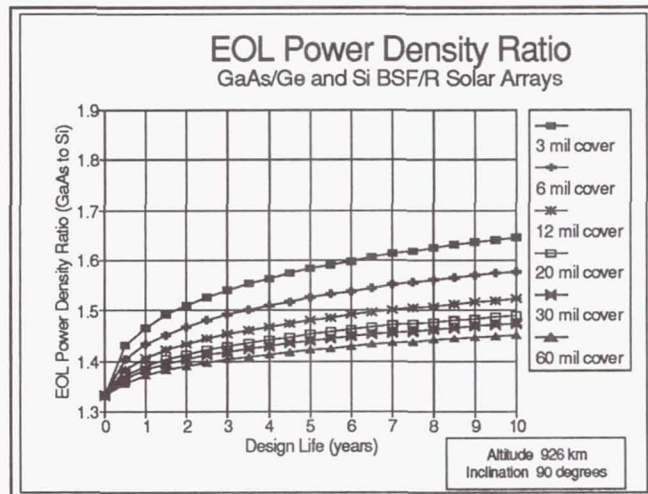


Figure 8

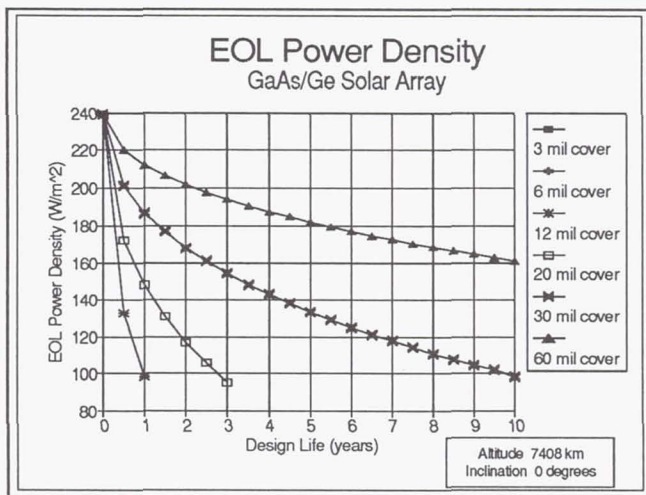


Figure 9

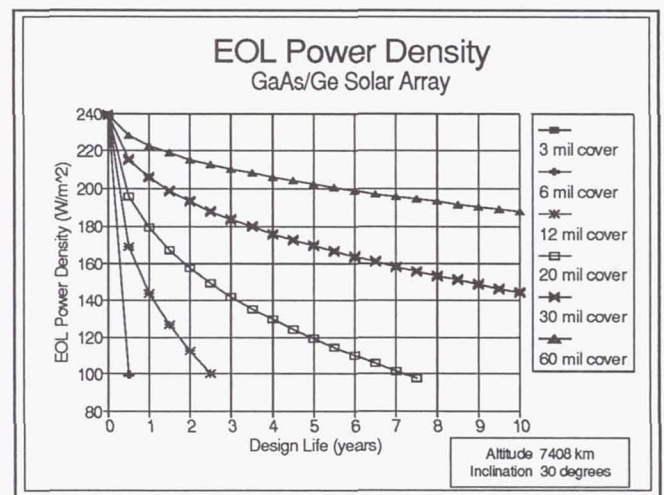


Figure 10

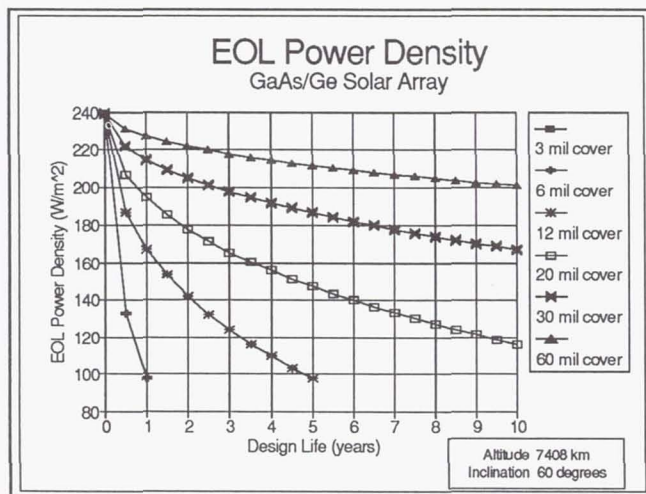


Figure 11

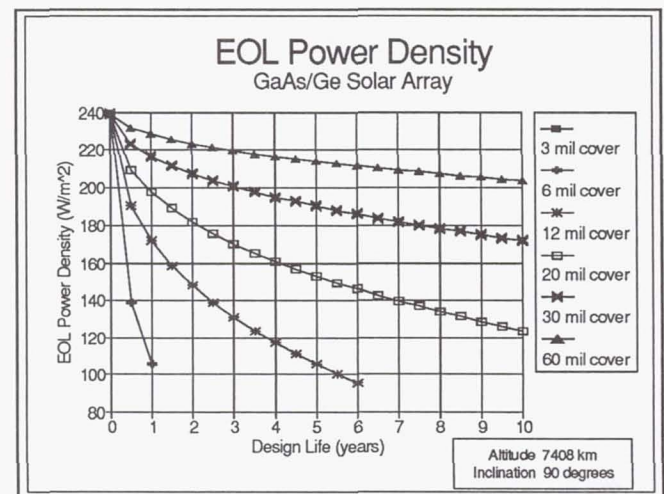


Figure 12

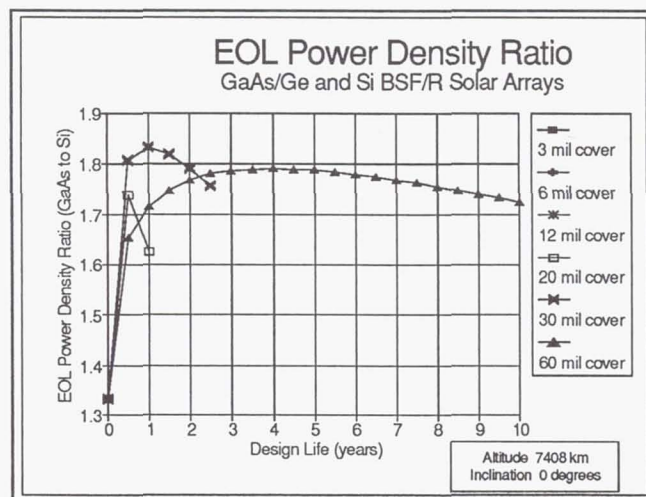


Figure 13

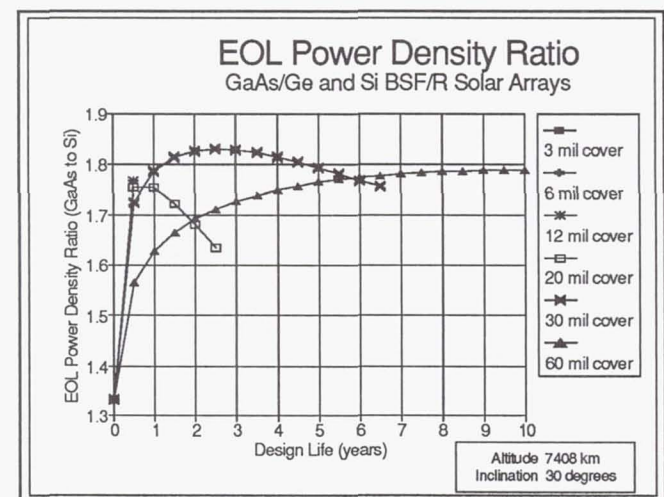


Figure 14

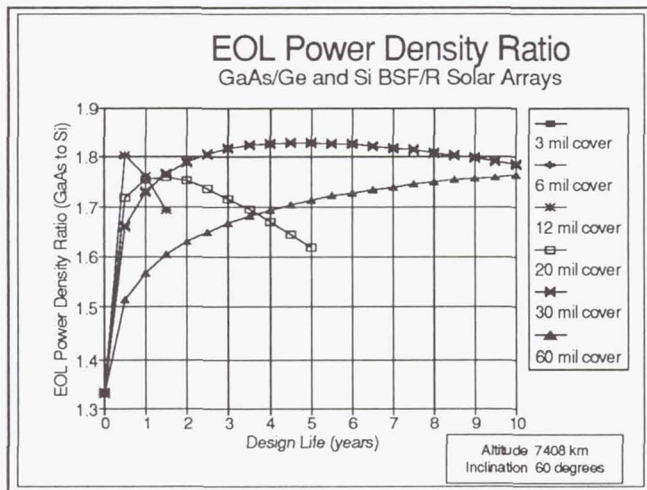


Figure 15

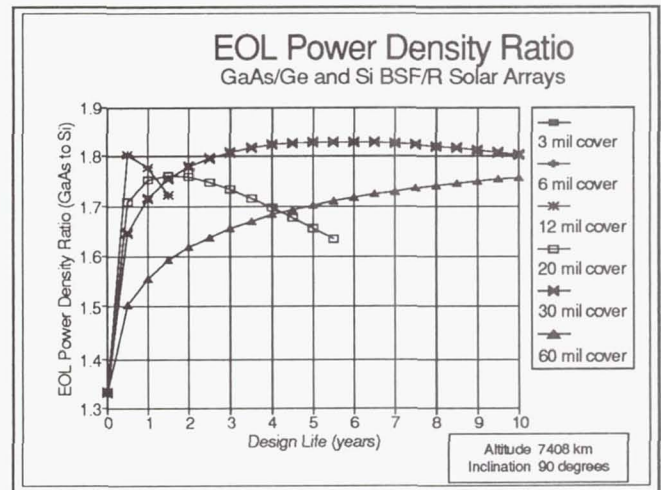


Figure 16

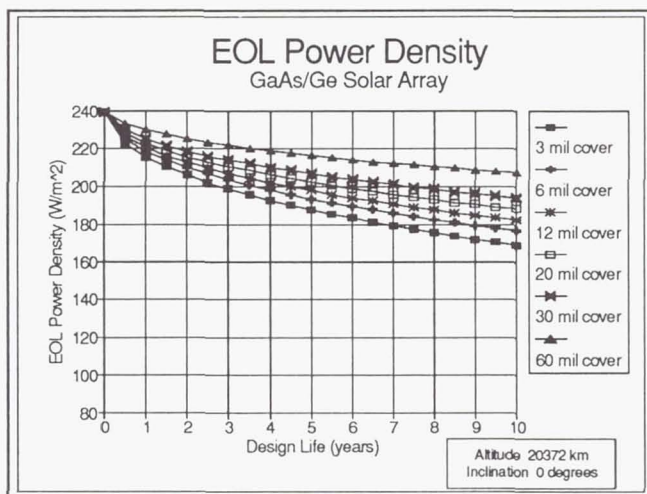


Figure 17

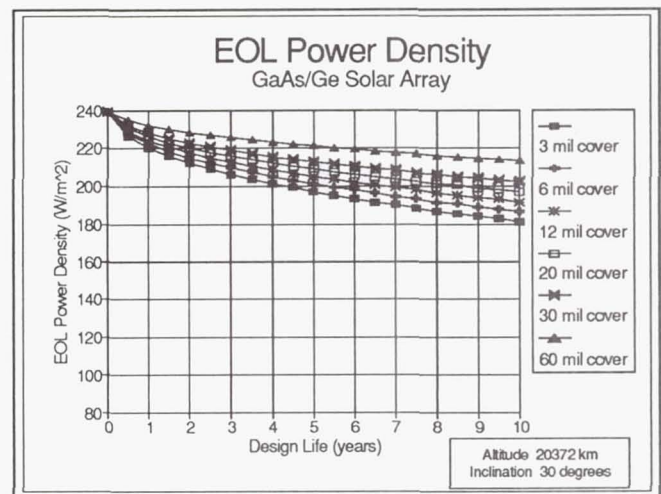


Figure 18

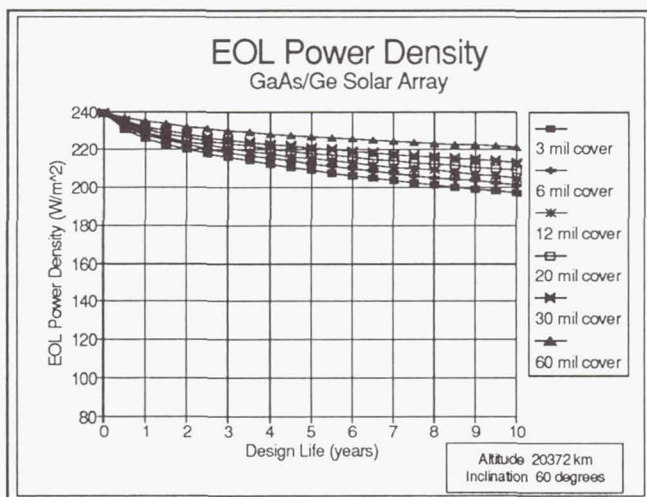


Figure 19

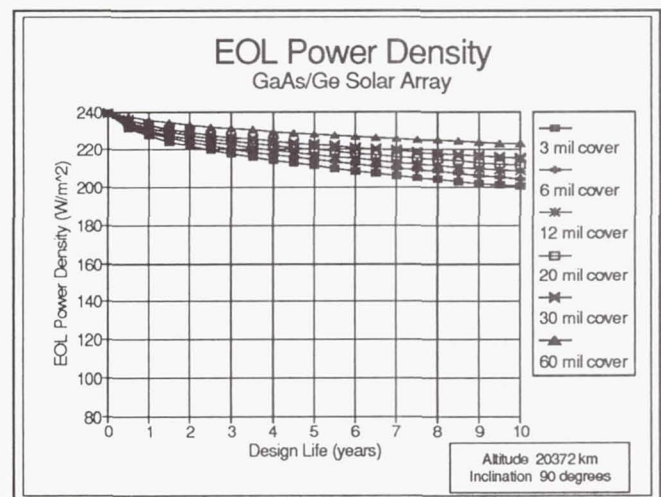


Figure 20

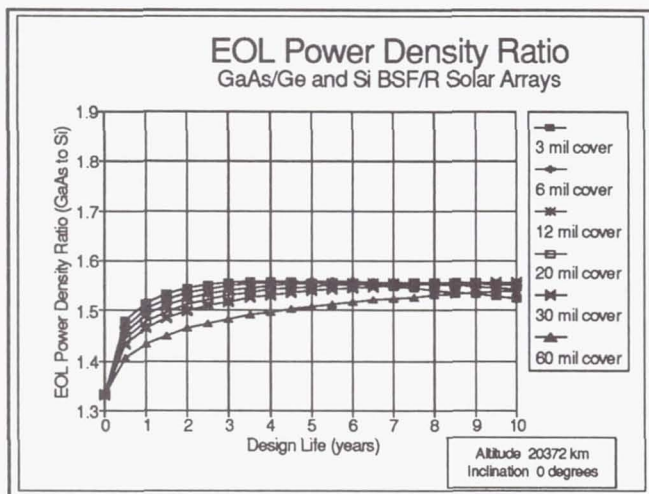


Figure 21

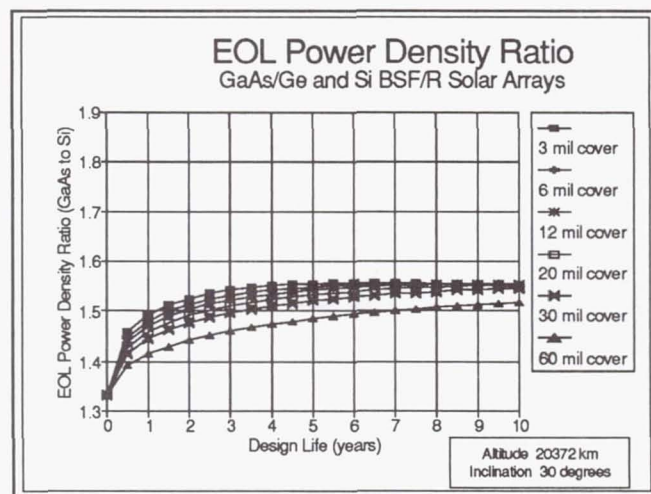


Figure 22

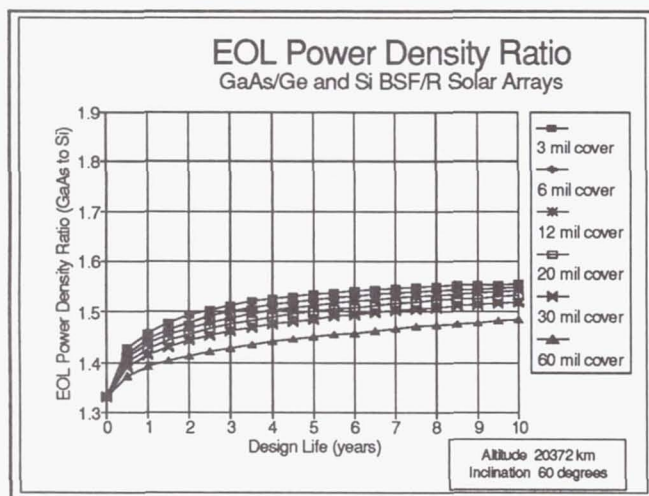


Figure 23

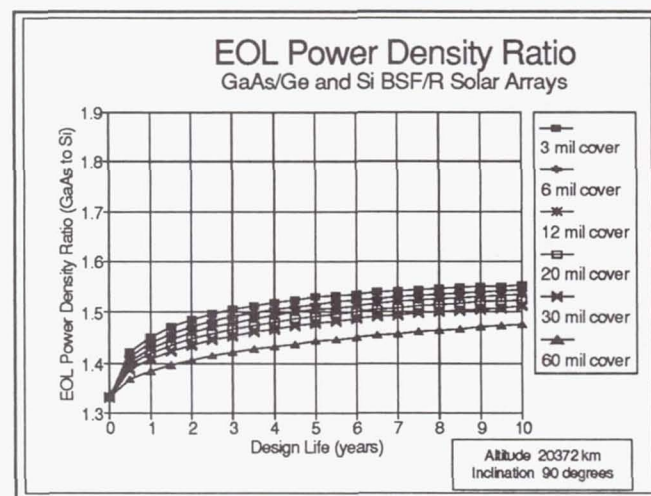


Figure 24

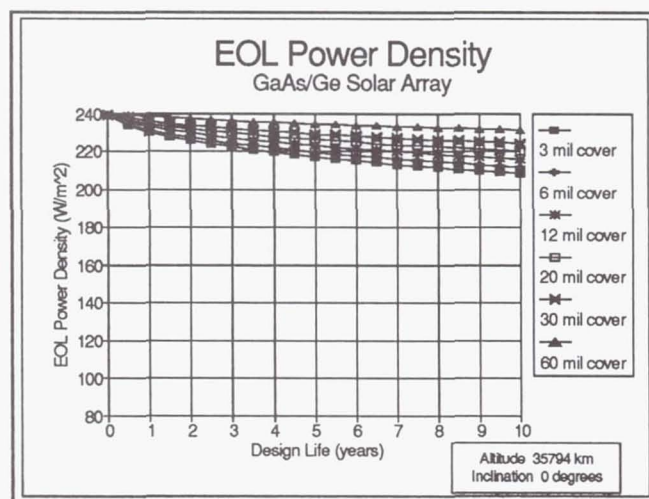


Figure 25

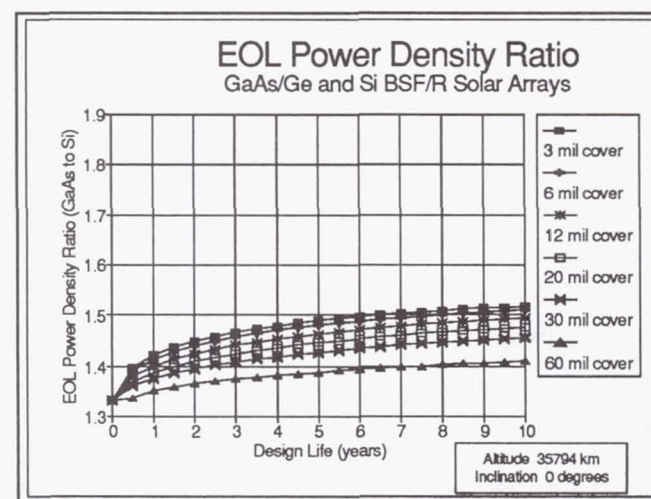


Figure 26

A HIGH SPECIFIC POWER SOLAR ARRAY FOR LOW TO MID-POWER SPACECRAFT

P. Alan Jones, Stephen F. White and T. Jeffery Harvey
AEC-Able Engineering Company, Inc.
Goleta, California 93117

Brian S. Smith
Spectrolab, Inc.
Sylmar, California 91342-5373

UltraFlex is the generic term for a solar array system which delivers on-orbit power in the 400 to 6,000 watt per wing sizes with end-of-life specific power performance ranging to 150 watts-per-kilogram. Such performance is accomplished with off-the-shelf solar cells and state-of the-art materials and processes.

Much of the recent work in photovoltaics is centered on advanced solar cell development. Successful as such work has been, no integrated solar array system has emerged which meets NASA's stated goals of "increasing the end-of-life performance of space solar cells and arrays while minimizing their mass and cost." Here we address this issue; namely, is there an array design that satisfies the usual requirements for space-rated hardware and that is inherently reliable, inexpensive, easily manufactured and simple, which can be used with both advanced cells currently in development and with inexpensive silicon cells? The answer is yes.

The UltraFlex array described below incorporates use of a blanket substrate which is thermally compatible with silicon and other materials typical of advanced multi-junction devices. The blanket materials are intrinsically insensitive to atomic oxygen degradation, are space rated, and are compatible with standard cell bonding processes. The deployment mechanism is simple and reliable and the structure is inherently stiff (high natural frequency). Mechanical vibration modes are also readily damped.

The basic design is presented as well as supporting analysis and development tests.

INTRODUCTION

To obtain program funding in today's political-economic environment it is a practical necessity for spacecraft programs to either maximize return through increased operational payloads or reduce launch costs with a less massive spacecraft. Dual motivations exist for reducing spacecraft mass: The increasing costs for existing launch systems and the introduction of new low-cost, low-payload launch vehicles (Pegasus, Taurus, Connestoga, etc.). A low-cost, lightweight spacecraft power source can contribute towards this end.

The preferred power source for most spacecraft launched today is a solar cell array [1]. Solar cell arrays provide clean, long-term spacecraft power at a reasonable cost. Great benefits to the spacecraft mission can be realized with any significant increase in solar array specific power. The resultant reduced solar array mass allows for the allocation of more mass to other spacecraft features. These can be additional communication transponders or scientific instruments, or additional station-keeping fuel to allow longer on-station life. In addition, overall spacecraft mass may be reduced, rather than reallocated, to allow for the use of a smaller, more economical launch vehicle or, perhaps, a more profitable mission orbit. However this performance dividend is actually realized, increased solar array specific power can provide large cost/performance benefits to the spacecraft designer.

While increased array specific power is a very attractive goal, its benefits must not be mitigated by an increase in solar array subsystem cost. Recent solar cell technological advances have the potential to improve specific power however, the issues of environmental durability, large-scale manufacturability, and cost cloud their potential. Spacecraft designers in the near future must therefore rely on well established solar cell technologies to meet the coupled goal of increased specific power at a reasonable cost.

Such a solar array system which is currently under development by AEC-Able Engineering in collaboration with Spectrolab. Present development progress to-date indicates an end-of-life (EOL) specific power of 125 W/kg for a 634-watt 7-year low-earth-orbit (LEO) mission with silicon cells. A larger 3986 watt version produces 140 W/kg. Gallium-cell-based UltraFlex arrays will produce on the order of 153 W/kg at the 3131 watt scale. These values greatly exceed typical rigid array specific powers in the range of 35 to 40 W/kg. Conventional silicon or gallium solar cells coupled with a unique mechanical/structural system enable the UltraFlex solar array to provide superior performance with today's established technologies.

BACKGROUND

The specific power performance data for several rigid and flexible solar arrays have been compiled in Figure 1. Since the various arrays are designed to varied requirements and environments the data in Figure 1 should be interpreted as a general historic overview rather than as a point-to-point comparison. Considerable effort, by various authors, has been extended on estimating the break-point in total array power below which a rigid array is more advantageous versus a flexible array. Total array power values from 4 to 10 kW have been offered [2] as break points above which rigid arrays are less desirable due to cost, reliability, and performance.

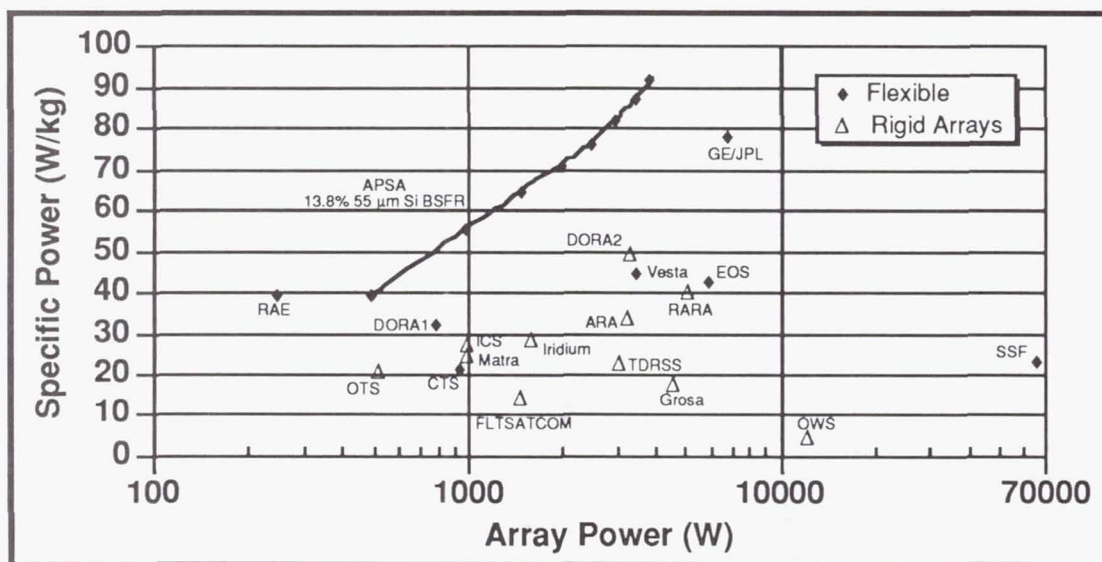


Figure 1
Solar Array Specific Power versus Array Power

The performance break-point can be illustrated by the JPL-developed Advanced Photovoltaic Solar Array (APSA) data shown above. While the APSA system produces 92.5 W/kg at 3.9 kW, mass efficiency drops to 40 W/kg at 0.5 kW [3]. This drop is due to the non-linear mass scaling of its structural components. Most notable are the deployment mast system and the blanket containment structures. The curve of APSA specific power versus power data crosses the typical rigid array specific power (40 W/kg) at approximately 1/2 kW. The performance break-point will occur at higher power levels for less-optimized array designs (EOS and SSF).

The APSA program was very successful in meeting its general goal: the development of a high performance photovoltaic solar array. The program laid a solid foundation of work in the areas of ultra-thin solar cell usage, lightweight substrates, and optimized structures. The APSA program currently reports the highest specific array power of any tested solar array. It is evident, from the data in Figure 1, that very high specific power solar arrays (150 W/kg) in the 0.5 to 2.0 kW power range do not exist in any deployable form. This is the performance niche that UltraFlex targets.

DESIGN CONFIGURATION

An initial study indicated that only flexible substrate solar arrays could produce the desired 150 W/kg specific power performance at low power levels. ABLE initiated a design effort to produce a solar array that satisfied the structural requirements displayed in Table 1 and delivered superior specific power performance.

Table 1 STRUCTURAL REQUIREMENTS	
Stowed First Mode	30 Hz, Minimum
Deployed First Mode	0.1 Hz, Minimum
Stowed Maximum G's	25 g normal, 30 g lateral
Deployed Maximum G's	0.1 g (all axes)
Launch Acoustic Vibration	146 dB Overall

The result is the UltraFlex solar array*, shown isometrically and in plan view in Figure 2. It is a departure from the standard rectangular shape typically seen in rigid or flexible arrays. The UltraFlex deploys a flexible cell blanket into a multisided polygon using a fan-like deployment, shown schematically in Figure 3. The individual gore assemblies have flexure hingelines at the gore centerline. During deployment the system flexes into a tensioned, complex paraboloid. The pre-stressed shape acts to stiffen the deployed structure enabling reasonably high natural frequencies. A mockup was constructed which depicts the deployed shape (Figure 4).

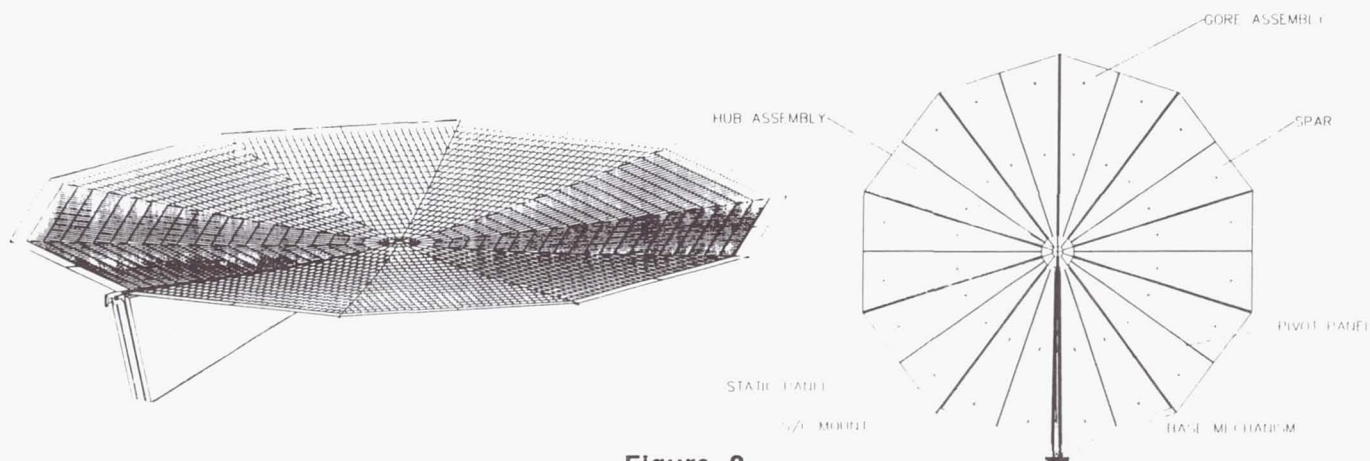


Figure 2
UltraFlex Deployed Configuration



Figure 3
UltraFlex Deployment Sequence

* Patent Pending

Prior to deployment the array is sandwiched between two structural panels which, through the use of a compressed polyimide foam, maintain sufficient areal pressure on the solar cells to survive launch vibratory loads. This established approach is the baseline on the APSA and Space Station solar array systems [3,4]. The two structural panels (denoted pivot panel and static panel) are hinged together at one end by a hub mechanism.

Two pyrotechnically released tiedown mechanisms are used to secure the system to the spacecraft for launch. In addition to the two active launch restraints mentioned, three other passive cup-cone assemblies complete the launch restraint system. After launch tiedown release, deployment is accomplished by the rotation of the pivot panel about the central hub away from the static panel. Deployment torque is provided by a DC motor system. The pivot panel rotates a full 360° pulling and tensioning the hinged-together blanket subassemblies into their deployed configuration. After this rotation the pivot panel is latched to the static panel with a passive latch mechanism.

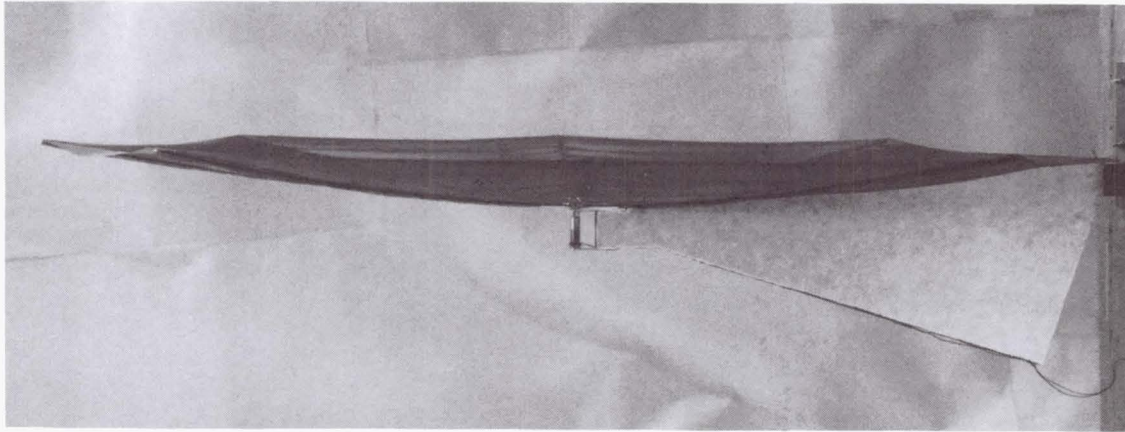


Figure 4
UltraFlex Mockup

Substrate

Though Kapton has had excellent flight history, its use as a blanket substrate is marred by two problems: it degrades in the presence of atomic oxygen and it readily tears once a flaw is introduced. Due to these concerns ABLE developed a new substrate for the UltraFlex array.

First, the material should be 100% compatible with the space environment, both low earth and geostationary. Secondly, the material should lend itself to established cell laydown and attachment practices to minimize the extent and cost of requalification. Lastly, the material should have good dielectric, low mass, and low cost characteristics. During the initial UltraFlex conceptualization a re-evaluation of flexible blanket material options offered some interesting possibilities. To satisfy the above requirements a flexible composite substrate* has been developed which combines an inorganic open-weave fabric with an inorganic binder resin. The inorganic nature of both materials should preclude their corrosion in the atomic oxygen environment.

Solar cell to substrate compatibility is, to a large measure, dictated by their relative coefficients of thermal expansion (CTE). The effective CTE of the UltraFlex substrate is estimated to be $0.51 \mu\text{in/in}/^\circ\text{F}$. The resultant substrate-to-silicon cell CTE mismatch is estimated to be less than $0.93 \mu\text{in/in}/^\circ\text{F}$. For GaAs/Ge solar cells the mismatch is $2.7 \mu\text{in/in}/^\circ\text{F}$. These low CTE mismatch values are desired to assure good thermal cycle capability. By comparison, the CTE mismatch of Kapton H with silicon cells is about $26.5 \mu\text{in/in}/^\circ\text{F}$.

The choice of an open-scrim material was intended to reduce areal mass and provide for good cell heat rejection. The substrate openings, approximately 60%, allow for the direct emission from the rear surface of the solar cell. Typically, the rearside heat loss must first be conducted from the cell through the substrate to finally be emitted from the rearside. Solar cells currently have a low rearside emissivity, on the order of 0.12. Coatings on the cell backside to improve emission have been attempted in the past [1]. If implemented, these coatings will improve UltraFlex performance through reduced cell operating temperature.

* Patent Pending

Gore Subassembly

The gore subassembly consists of the substrate material, edge spars, solar cells, and a flex-circuit harness section. The subassembly is assembled in its deployed, tensioned shape to assure proper distribution of membrane preload forces. To maintain low recurring costs, a primary substrate requirement was for good compatibility with established solar cell attachment techniques. This has been established through bonding trials at Spectrolab and subsequent thermal cycle testing at ABLE.

The triangular shape of the gore subassembly (Figure 5) unfortunately inhibits efficient cell packing. To maximize packing factor the number of cells per string are reduced one-per-row. Thus, the geometry of the gores are directly linked to the aspect ratio of the solar cell. Since there are only integer choices for array geometry (e.g., 8, 9, or 10 gores per wing) solar cell aspect ratios are limited to discrete values.

Electrical power is collected from the solar cell strings and routed to the base of the deployed wing with a Kapton insulated custom flex circuit. For LEO applications the Kapton is coated an $\text{SiO}_{1.9-2.0}$ coating. The multi-fingered flex circuit harnesses are bonded to the gore rearsides during the assembly process. The ends of these fingers have redundant bared solder pads for direct interface with the cell circuits. These harnesses lead into a central collection harness which runs around the central hub. This central multi-layer circuit employs specialized pin connectors to interface with the individual gore harnesses.

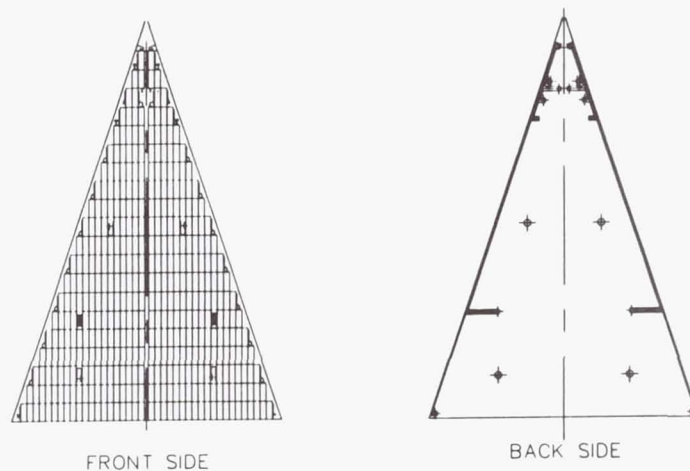


Figure 5
Gore Subassembly

Mechanisms

The UltraFlex obtains its high specific performance by minimizing the quantity and scale of non-power-producing mechanical and structural components required to deploy and support a given area of solar cells. Reliability is also enhanced over typical rigid arrays by the use of a single deployment mechanism and a single latch mechanism rather than two or three hinge/latch mechanisms at each of three to six hingelines. Current reliability estimates indicate a probability of successful deployment to be 0.9975.

The single deployment mechanism consists of an electrically redundant DC brushless motor coupled via a spur geartrain to a lanyard-reel system. Tension is created in the Elgiloy lanyard which, in turn, produces a deploying moment around the center hub. As the system nears full deployment the lanyard serves to pull the pivot panel directly to the latch probe. The latch mechanism, mounted on the static panel, utilizes a spring-loaded male probe to engage the receptacle on the pivot panel. The deploy motor system remains activated until full latching is reached.

DEVELOPMENT TESTS

Cell-to-Substrate Bond Strength

The main concerns over the compatibility of the material with standard solar cell array bonding techniques lay in whether the silicone adhesive used for bonding the cells would adhere to the substrate and whether the contact area of substrate to cells was sufficient to provide adequate bond strength. In addition, the completed assembly of cells to substrate was to meet stringent low weight goals. A series of tests were performed to address these concerns prior to coupon assembly.

Cell-substrate bonding tests were conducted for two bonding approaches. In the first approach adhesive was applied to the cell surface only. In the second approach adhesive was applied to the substrate only. The bonded samples were then pulled apart to obtain pull strength information. These comparative tests showed that applying adhesive only to the weave gave pull strengths of the order 150 gm while applying adhesive only to the cells gave pull strengths of the order 250 gm. To minimize substrate areal mass and despite its lower strength, the former bonding method was selected.

During additional testing, 0.5 in. wide by 2 in. long strips of the open weave material were bonded to the rearside of solar cells. Control samples of Kapton of the same dimensions were similarly bonded. After curing the adhesive, all samples were pulled. The open weave material had an average over ten samples of 96 gm, while the Kapton control specimens (3) had an average of 176 gm. These values reflected the area of contact of the two materials. The open weave has an approximate bond fill factor of 50%.

Thermal Cycle Testing

A primary concern with the use of a developmental blanket material is its ability to form a strong, fatigue-resistant joint with solar cells. As noted above, the material selected produces a low CTE mismatch between cell and substrate which is a central contributor to thermal cycle fatigue capability. To demonstrate the applicability of the UltraFlex open weave material as a solar array blanket substrate, a small coupon (approx. 8 x 7 in.) was assembled with 10 large area (3.2 x 6.7 cm) silicon BSR cells of 7 mil thickness (Figure 6). The coupon was electrically tested and subjected to various thermal cycles. The test phases are given in Table 2.

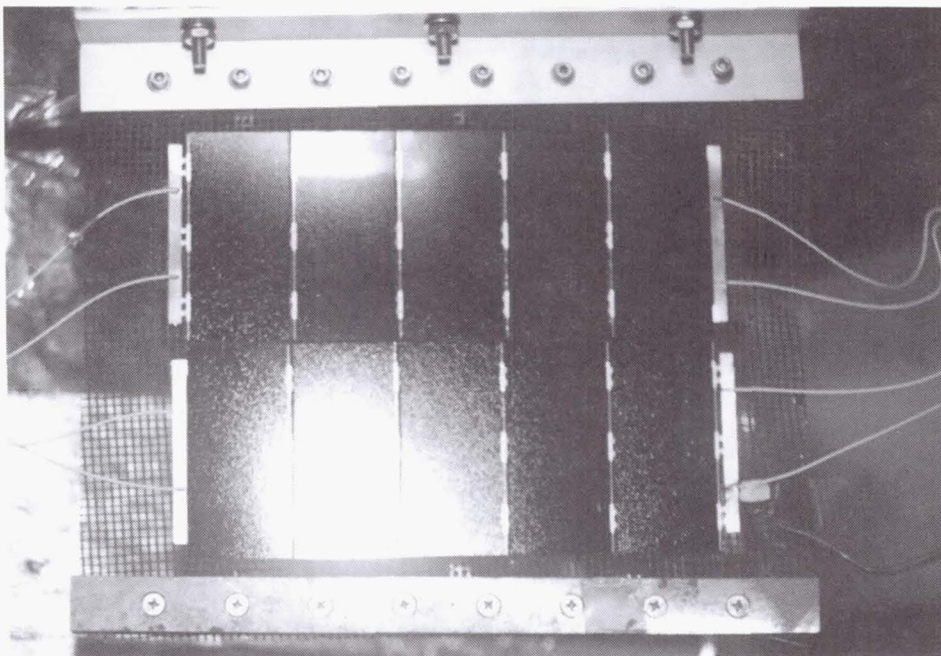


Figure 6
UltraFlex Substrate Coupon

Table 2 Thermal Cycle Testing Parameters and Results			
Test Phase	Cold Temperature (°C)	Hot Temperature (°C)	Number of Cycles
1	+ 55	- 61	5808
2	+ 70	- 70	1004
3	+ 100	- 150	In Progress 4 Completed 50 Planned

Test results through phase 2 were quite successful with no cell-substrate delaminations, cracked cells or coverslides, or interconnect failures observed. The coupon was then electrically tested to ensure no electrical degradation had occurred. The electrical test data before and after thermal cycling is shown in Table 3. The degradation observed was within the limits of test error. The UltraFlex substrate thus demonstrated bondability, bond strength and the ability to survive environmental testing with negligible mechanical or electrical degradation. It is therefore an excellent candidate material for solar array blanket substrates.

Table 3 Thermal Cycling Cell Degradation			
	Pre-Test	Post-Test	Change (%)
ISC	0.818	0.811	-0.86
Voc	5.442	5.435	-0.13
I _{mp}	0.771	0.767	-0.52
V _{mp}	4.523	4.515	-0.18

ANALYTICAL PERFORMANCE

Thermal Analysis

To estimate on-orbit solar array power production the cell operating temperature must be determined. For this purpose a one-dimensional thermal model was constructed. However, the rearside of the substrate is an open mesh with distinct two-dimensional properties. To maintain the simplicity of the one-dimensional model the substrate radiative properties were approximated with an exposed area weighting method (Figure 7).

$$\Phi_{a,cell} = (\Phi_{a, total}) (A_{cell}) (\alpha_{cell})$$

and

$$\Phi_{a,sub} = (\Phi_{a, total}) (A_{sub}) (\alpha_{sub})$$

Where:

- $\Phi_{a, total}$ = Total albedo input flux.
- $\Phi_{a,cell}$ = Cell albedo input flux.
- $\Phi_{a,sub}$ = Substrate albedo input flux.
- A_{cell} = Cell rearside area ratio.
- A_{sub} = Substrate rearside area ratio.
- α_{cell} = Cell rearside solar absorptivity.
- α_{sub} = Substrate rearside solar absorptivity.

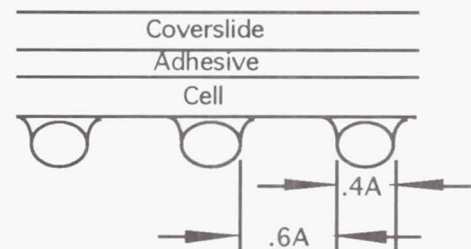


Figure 7
One-Dimensional Thermal Model

A similar formulation was used for rearside earth infrared (IR) flux input but with IR absorptivities. The rearside cell emission was also approximated with the above technique but to account for the increased emissive area of the fabric mesh bundles, an additional area factor term was included.

$$\epsilon_{a,sub} = (\pi/2) (A_{sub}) (\epsilon_{sub})$$

Where: $\pi/2$ = Area multiplier to account for 2-D shape of fabric emissive surface. (See Figure 7)
 ϵ_{sub} = Cell rearside emissivity.

The thermal model was run and cell operational temperatures were collected for multiple orbits and seasons. The results are given in Table 4.

Table 4 Thermal Analysis Results								
Orbit	Silicon Cells				GaAs/Ge Cells			
	Low Earth		Geostationary		Low Earth		Geostationary	
	BOL	EOL	BOL	EOL	BOL	EOL	BOL	EOL
Equinox	77.6 °C	81.5 °C	50.0 °C	55.2 °C	85.9 °C	89.3 °C	60.4 °C	65.8 °C
Summer Solstice	67.4 °C	78.5 °C	38.8 °C	44.9 °C	75.3 °C	78.7 °C	50.2 °C	55.5 °C
Winter Solstice	72.2 °C	78.4 °C	44.2 °C	50.6 °C	80.1 °C	83.7 °C	55.8 °C	61.2 °C

Power Analysis

On-orbit power production analyses were performed for the UltraFlex prototype wing currently under construction. The current prototype design specifies the use of 3960 2.4 mil BSFR cells (13.70%, 21.8 mg/cm²) with 4 mil CMX coverslides assembled into 99 cell strings. The analysis was also performed for an array based on 3.5 mil GaAs/Ge solar cells (18.33%, 55 mg/cm²) with 4 mil CMX coverslides. The analysis was done for both LEO (555 km, i=60°, 7-year) and GEO (10-year) applications. Two axis solar tracking was assumed. The resultant power predictions are presented in Table 5.

Table 5 Power Production Analysis Results								
Orbit	Silicon Cells				GaAs/Ge Cells			
	Low Earth		Geostationary		Low Earth		Geostationary	
	BOL	EOL	BOL	EOL	BOL	EOL	BOL	EOL
Equinox	778 W	645 W	888 W	660 W	1184 W	1011 W	1235 W	939 W
Summer Solstice	791 W	634 W	823 W	612 W	1166 W	996 W	1114 W	848 W
Winter Solstice	826 W	678 W	860 W	639 W	1237 W	1056 W	1181 W	898 W

Mass Properties

A mass properties analysis was performed for the prototype unit based on volumetric calculations of piece part weights. The masses of the major contributors, the solar cells and the substrate, have been confirmed by test. A 5% contingency is also carried for conservatism. The mass breakdown is given in Table 6.

Table 6 Prototype Mass Breakdown		
Subassemblies	2.4 mil Silicon Version	3.5 mil GaAs/Ge Version
Substrates and Adhesives	546	546
Cells	3163	4982
Spars	282	282
Harnesses	101	101
Pivot Panel	350	350
Static Panel	285	285
Center Hub	90	90
Deploy Mechanism	217	217
Subtotal	5177	6996
Contingency (5%)	259	350
Total (grams)	5436	7346

The above results were combined with Table 5 to produce array specific power performance estimates. This data is given in Table 7 and again in Figure 8 as an overlay on the previous specific power efficiencies given in Figure 1.

Table 7 Specific Power Results								
Orbit	Silicon Cells				GaAs/Ge Cells			
	Low Earth		Geostationary		Low Earth		Geostationary	
	BOL	EOL	BOL	EOL	BOL	EOL	BOL	EOL
Equinox	143 W/kg	119 W/kg	163 W/kg	121 W/kg	161 W/kg	138 W/kg	168 W/kg	128 W/kg
Summer Solstice	145 W/kg	117 W/kg	151 W/kg	113 W/kg	159 W/kg	136 W/kg	152 W/kg	115 W/kg
Winter Solstice	152 W/kg	125 W/kg	158 W/kg	118 W/kg	168 W/kg	144 W/kg	161 W/kg	122 W/kg

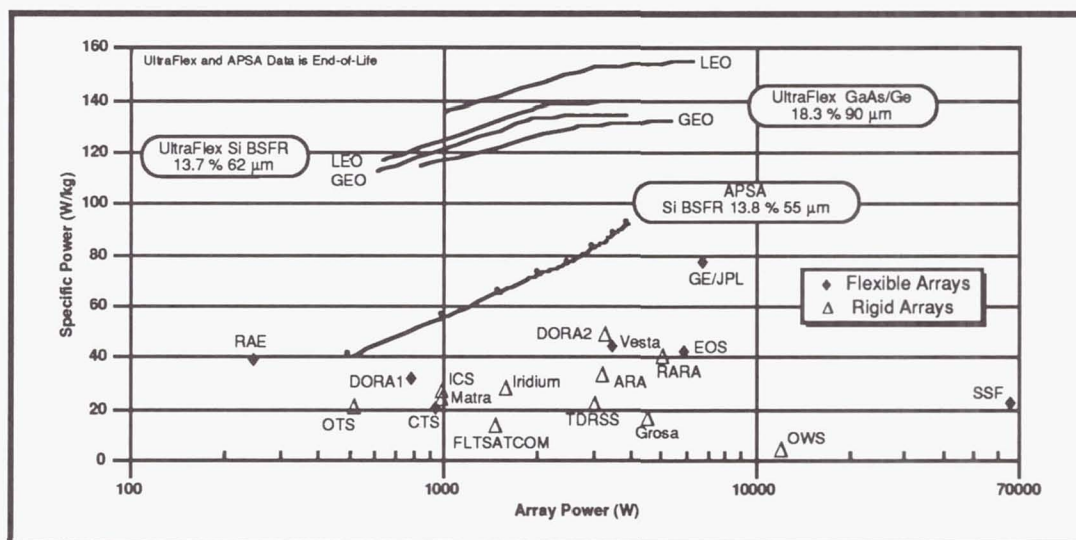


Figure 8
UltraFlex End-of-Life Specific Power

Deployed Structural Analysis

An ANSYS finite element model of the deployed UltraFlex array was developed to verify that the wing's performance fulfilled the structural requirements defined in Table 1. The stiffening effect of the prestressed gores and spars, which results from the pretensioned nature of the deployed system, needed to be accounted for in the analysis. The model consisted of shell elements that represented the tensioned gore sections and beam elements that represented the spars. The modeling approach employed material properties that were tailored such that a single gore section would have the same fundamental frequency (i.e., mass and stiffness matrix terms) as would a similar model of that was pretensioned by directly applied in-plane circumferential loads. With this technique successive loading steps were avoided. The array "cupping" was introduced directly into the model geometry. This modeling approach gave reasonable results for deployed acceleration and frequency calculations.

Using this model, a modal analysis was performed to determine the frequencies and mode shapes of the deployed UltraFlex array. The first fundamental mode for the prototype array design is a torsional motion of the gore sections about the support panel axis, as shown in Figure 9. A parametric study was then performed to assess the effect of gore tension variations (and corresponding "cup" deflections) on deployed frequencies. Preliminary results of this analysis indicate that the frequency will increase in an approximately linear fashion as gore tension is increased up to about 0.10 lb/in. after which the frequency changes are minimal. Since the baseline pretensions are in excess of 0.10 lb/in. slight preload variations due to tolerance build-ups or thermally induced deflections will have minimal effects on the deployed characteristics.

The deployed model was subjected to accelerations about each of the orthogonal array axes to determine maximum allowable acceleration loads. The critical limiting load is an out-of-plane acceleration of 0.4 g's, which causes the gore to "snap through" to an equilibrium state where the gore is cupped in the other direction. This "snap-through," while not advised, is not considered to be catastrophic to the operation of the array.

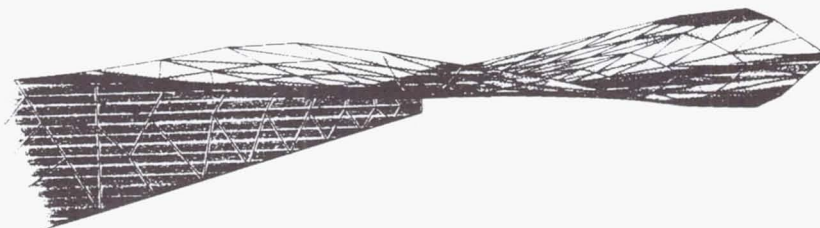


Figure 9
Deployed Minimum Mode Frequency

CONCLUSION

The UltraFlex solar array design has been presented as a viable advanced photovoltaic candidate for consideration as a power source for near or far term spacecraft. Any of the UltraFlex's superior performance characteristics, extremely low array mass, low deployed inertia, reduced center-of-pressure offset, or intrinsic damping capability, can potentially be mission enabling.

The underlying tenant of the UltraFlex concept is the use of superior performance to reduce program costs. As noted above program cost savings can be realized many ways. With today's launch costs averaging around [5] \$7,302 per pound, for a LEO, and about \$54,307 per pound for a GEO insertion, a two kilowatt UltraFlex wing's low mass can save about 685 k\$ and 5,251 k\$, respectively. However, in a more realistic scenario, a launch vehicle will be selected and funded for a given mission and, in due course, the vehicle's payload will be fully allocated. In this case, the solar array weight savings will be reallocated for additional payloads such as experiments, communication transponders, or maneuvering fuel in an effort to maximize mission "payoff." This payoff will be realized as additional scientific data or additional operational capability. In some extreme cases the weight savings afforded by the use of the UltraFlex array will allow use of a smaller class of launch vehicle. The step-wise cost savings realized

in this situation can be significant. There may also be some cases where the reduced spacecraft mass does not allow a down-scaled launcher but does allow the spacecraft to be inserted into an orbit which may be more desirable. Additionally, the reduced UltraFlex inertia will require less station-keeping fuel to stabilize over the course of a mission. The unneeded fuel may be used for a longer mission life or its mass may be used for additional payload.

To date significant design, analytical, and material studies have been performed by the ABLE/Spectrolab team and a prototype model is currently under construction. A qualification test unit is currently planned with testing to be completed in late 1993. Upon initial examination the concept satisfies the standard criteria for spacecraft solar array systems. These include superior specific power performance, small stowed volume requirement, high reliability, sufficient structural and environmental capability, and an established technology basis.

REFERENCES

1. Solar Cell Array Design Handbook Volume 1 and 2, JPL Publication No. SP 43-48, October 1986.
 2. *Retractable Advanced Rigid Array*, DeKam, 1988, IEEE.
 3. *Advanced Photovoltaic Solar Array Prototype Development and Testing, Final Review Data Package, Phase III*, NASA JPL Contract 957990, 12 August 1991.
 4. The Advanced Photovoltaic Solar Array Program, R. Kurland, P.M. Stella, ESA SP-294, August 1989.
 5. NASA, Pentagon Chart Ambitious Unmanned Launch Vehicle Program, E.H. Kolcum, Aviation Week and Space Technology, Vol. 136, No. 11, March 16, 1992.
-

TAB INTERCONNECTS FOR SPACE CONCENTRATOR SOLAR CELL ARRAYS

J. Avery, J. S. Bauman, P. Gallagher and J. W. Yerkes
Boeing Defense and Space Group, Seattle, WA. 98124

ABSTRACT

The Boeing Company has evaluated the use of Tape Automated Bonding (TAB) and Surface Mount Technology (SMT) for a highly reliable, low cost interconnect for concentrator solar cell arrays. TAB and SMT are currently used in the electronics industry for chip interconnects and printed circuit board assembly.

TAB tape consists of sixty-four 3-mil/1-oz tin-plated copper leads on 8-mil centers. The leads are thermocompression gang bonded to GaAs concentrator solar cell with silver contacts. This bond, known as an Inner Lead Bond (ILB), allows for pretesting and sorting capability via nondestruct wire bond pull and flash testing. Destructive wire pull tests have resulted in preferred mid-span failures. Improvements in fill factor have been attributed to decreased contact resistance on TAB bonded cells.

Preliminary thermal cycling and aging tests have shown excellent bond strength and metallurgical results. Auger scans of bond sites reveals an Ag-Cu-Tin composition. Improper bonds are identified through flash testing as a performance degradation. On going testing of cells are underway at Lewis Research Center.

SMT techniques are utilized to excise and form TAB leads post ILB. The formed leads' shape isolates thermal mismatches between the cells and the flex circuit they are mounted on. TABed cells are picked and placed with a gantry x-y-z positioning system with pattern recognition. Adhesives are selected to avoid thermal expansion mismatch and promote thermal transfer to the flex circuit. TAB outer lead bonds are parallel gap welded (PGW) to the flex circuit to finish the concentrator solar cell subassembly.

HISTORY

Three methods are available today for chip level inter-connects. Wirebonding, soldering, and TAB. Wirebonding is the most common chip-bonding technology utilized in the defense industry. This technology requires the chip to be bonded to be first attached with adhesives to the substrate or printed wiring board. Wirebonds are then placed one at a time from chip to substrate. Several bonds per second can be made by wire bonding. Soldering, also known as "flip chip", requires solder bumps to be attached to the chip. The chip is then flipped over and bonded to its substrate. TAB allows for many leads to be bonded simultaneously to the chip. General Electric first introduced TAB in the late 1960s as a possible replacement for wire bonding technology. It wasn't until the 1980s that TAB became of interest as a natural extension of SMT. The greatest percentage of TAB used today is for liquid crystal displays, watches, cameras, memory cards, smart cards, thermal printer heads, pocket televisions and calculators, notebook computers and office equipment. TAB is also use in high reliable applications such as personnel and mainframe computers.

Boeing first purchased a thermal compression gang bonder from Jade in 1985 for evaluating TAB bonding. Boeing's High Technology Group (HTC), concentrated on developing the substrate, while the Advanced Packaging Group focused on producing the TAB memory component using an IC memory device. Their experience concluded that the semiconductor design needed thicker metalization to accommodate TAB. This meant that all components that were to be use would needed to be custom. Add to this the low volume need, cost became prohibited.

During the first quarter of 1992, the Prototype Development Group at HTC, began evaluating the use of TAB bonding on their concentrator GaAs solar cell. TAB bonding studies using a laser were conducted at MCC by Doug Pietilla, assignee from Boeing. Although successful, this process was eliminated due to the cost of the capital equipment. Thermal compression single point bonding with 1- by 3-mil ribbon was also evaluated. The success of single point thermal compression bonding, led to evaluating thermal compression gang bonding as a baseline. A Jade thermal compression gang bonder was liberated from surplus status and move to the Prototype Development Group for further evaluation.

TAB TAPE DESIGN

Fatigue resistance and current carrying capability constitute the most important issues in the functional design requirements for the concentrator solar cell interconnect. Two distinct types of fatigue plague electrical connections in earth orbit: lead bending and joint shear. Lead bending stress is minimized by maximizing the lead length, limiting the lead thickness and providing a strain relief to eliminate pure tensile loading.

Lead length is limited by manufacturing considerations in that long leads are easily damaged during handling. This may occur between operations in ILB, lead form and excise and outer lead bonding. Unsupported beam length should not exceed ten times the width of the beam according to 3M. Lead thickness is a function of manufacturing preference since all other variables can be manipulated after a choice is made. TAB tape producers have made 1 oz (1.4 mil) copper the standard. Their tooling and processes are aligned with this choice.

Cyclic thermally induced strains in the TAB lead occur in orbit. The lead must be shaped in such a way that the preferred bending mode is across the thinnest dimension of the beam. This will minimize strains, stress and in turn improve fatigue life. The thinner the beam the smaller the strain, the lower the stress and longer life. According to the above constraints 1.4-mil thick copper was the obvious choice.

Strain relief is provided inherently when a lead traverses planes ie. from the top of the cell down to the base flex circuit. A special case exists where the TAB is bonded to the bottom of the cell and to the circuit which all occurs in one plane. For this situation a pipeline type (omega shape) strain relief must be formed in the TAB lead.

Handling joint fatigue is less a matter of TAB design than the metallurgy of the joint, covered later. A joint no larger in any dimension than the width of the lead is required to minimize the shear stress induced due to mismatched coefficients of thermal expansion at the bond interface.

Current carrying capability must be maximized to avoid significant loss of power in the system. The space available on the cell for bonding leads from each TAB is 0.265" less side margins. Using 3-mil wide leads on 8-mil pitch, 32 leads can be bonded comfortably on the cell. This gives a collective resistance of 4.5×10^{-4} ohms per buss. Previously, gold wires were used which had a total resistance of 3.4×10^{-4} ohms per buss.

ILB METALLURGY

Boeing concentrator solar cells utilized gold contacts for inner lead bonding. This was ok for R&D quantities, however cost prohibitive for production. Boeing contracted Spectrolab to make 200 each Boeing GaAs concentrator solar cells with silver contacts. In the mean time sample Spectrolab one sun cells with silver contacts were obtained for evaluation of TAB thermal compression gang bonding. The cells had only 4 microns of silver, were GaAs on germanium, and had no dielectric layer under the contact area. In short the silver was too thin and the cell wafer was different. These one-sun cells were diced to 0.265 by 0.305 inches to begin to evaluate TAB bonds to silver. The silver contact areas to be bonded had an anti-reflective coating on them which made TAB bonding difficult. It was removed with a pencil eraser to expose the silver contact area and sample TAB bonds were made.

The metallurgy of the ILB is expected to be described by a ternary system consisting of 5 to 10 percent tin with equal remaining parts of copper and silver. A diagram representing this system can be found in ("Ternary Alloys: A comprehensive Compendium of Evaluated Constitutional Data and Phase Diagrams, Vol 2", edited by G. Petzow and G. Effenberg, Published by Verlagsgesellschaft, 1988). Considerable information should be available on this ternary as it forms the basis for dental amalgams. Intermetallic compounds (IMC) growth in this ternary system is also expected. The equation for IMC thickness versus time and temperature have been described by (D. Frear, W. Jones and K.

Kinnsman, "Solder Mechanics: A State of the Art Assessment, Chapter 2, Trans Metallurgical Society 1990"). They show that a .5um thick tin plate on the copper leads will be consumed in a relatively short period of time at 60 degrees C in the formation of Ag-Sn and Cu-Sn intermetallic compounds (even if IMC formation during bonding is not considered). The compounds expected to form are Ag_3Sn , Cu_6Sn_5 , and Cu_3Sn . This bond may not necessarily be weaker.

ILB PROCESS DEVELOPMENT

The tool that is used to make a thermal compression bond is known as a thermode. The thermode used in this experiment was made from tungsten carbide with the Prototype Development's wire EDM machine. The bonding footprint was 0.005 x 0.300 inches. Right angled edges on the first designed thermode caused the TAB leads to be coined and partially sheared at the bond site. Bonding however proved to be encouraging with good pull strengths of greater than 40 grams per lead. The first thermode was chipped during process development. This led to a revised design eliminating sharp thermode edges with radii. The coining was reduced to an acceptable level. Lead failures during pull testing resulted at places other than the coined edge.

One-sun cells were gang bonded and flash tested. These cells degraded up to 5 percent in fill factor and voltage. Auger scans of the metallurgy revealed copper in the junction below the ILB. About 50% of the ILBs that were sampled showed a good contact. The copper in these bonds did not diffuse into the junction. The gang bonded cells were then thermal cycled 250 times from -70 to +96°C and flash tested again. Further degradation was observed and attributed to the lack of a dielectric layer to impede copper migration into the solar cell junction. Boeing cells with gold contacts were then bonded. They showed no degradation from bonding due to the dielectric layer under the contact area impeding copper migration. However the thinness of the gold contact made for a weak bond.

ILB PROCESS

Critical bonding parameters for successful ILB include thermode planarity, thermode temperature, stage temperature, bond time, bond force, and solar cell TAB tape alignment. In September of '92, we received our Boeing/Spectrolab transparent GaAs concentrator solar cells. Several cells were bonded and pull tested. Pull testing helped correct process parameters. Thermode planarity could be identified by uniform pull strength of the 32 tabs being bonded. If the thermode was off, weak bonds of around 30 grams would be on one side while strong bonds with cratering would be on the other side of the solar cell. Once thermode planetary was adjusted the other parameters were evaluated until favorable mid span lead breakages were made while pull testing. Pull test strengths were optimized at 45 ± 5 grams per lead. General process parameters that were successful were as follows:

Thermode Temperature	550 to 600°C	Bond Time	3 seconds
Stage Temperature	150°C	Bond Force	8 psi

With the ILB process established 45 each Boeing/Spectrolab cells were flash tested and bonded then flash tested again (see figures 1, 2 and 3). Two out of the 45 were eliminated from the data due to silver metal damage from prior dicing. The rest of the cells proved to be undamaged by the bonding process. Shifts in fill factor, voltage, and current averaged less than 1 percent, (see table 1).

Table 1. Boeing/Spectrolab Silver Contractor Solar Cells

	Before TAB			After TAB		
	FF	Voc	Isc	FF	Voc	Isc
Average	0.7628	1.0808	0.3648	0.7608	1.0830	0.3608
Standard Deviation	0.0397	0.0149	0.0092	0.0433	0.0168	0.0088
Range	0.16	0.057	0.0409	0.191	0.074	0.0438
Average Shift	0.27%	0.20%	1.09%			

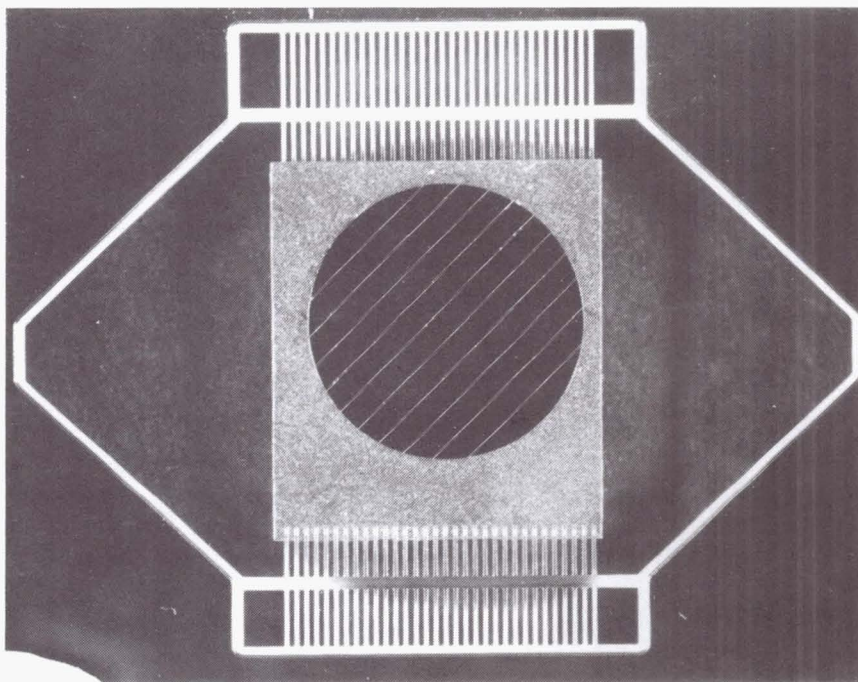


Figure 1. TABed Boeing/Spectrolab GaAs Concentrator Solar Cell

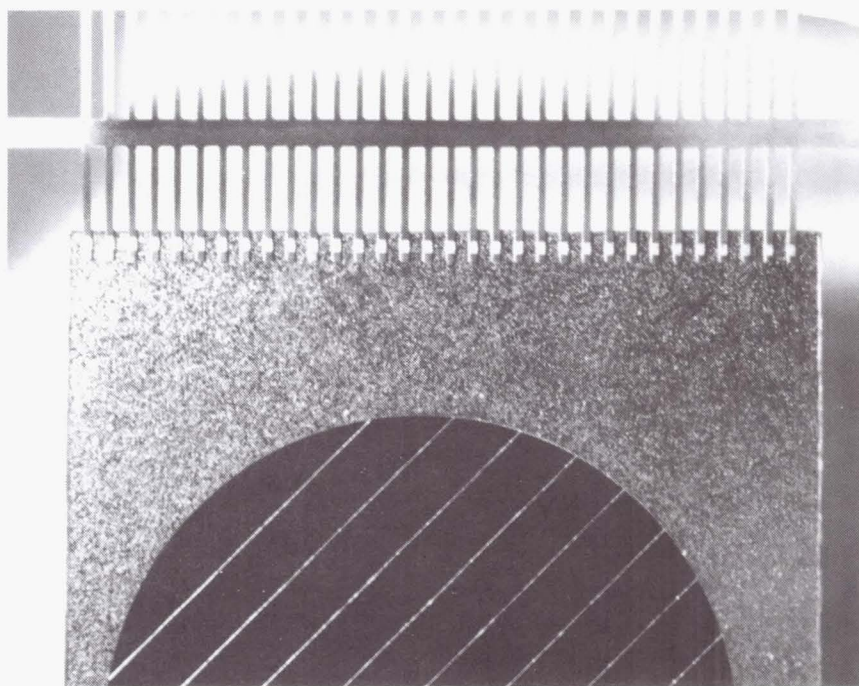


Figure 2. Closeup of ILBs and TAB Tie Bar

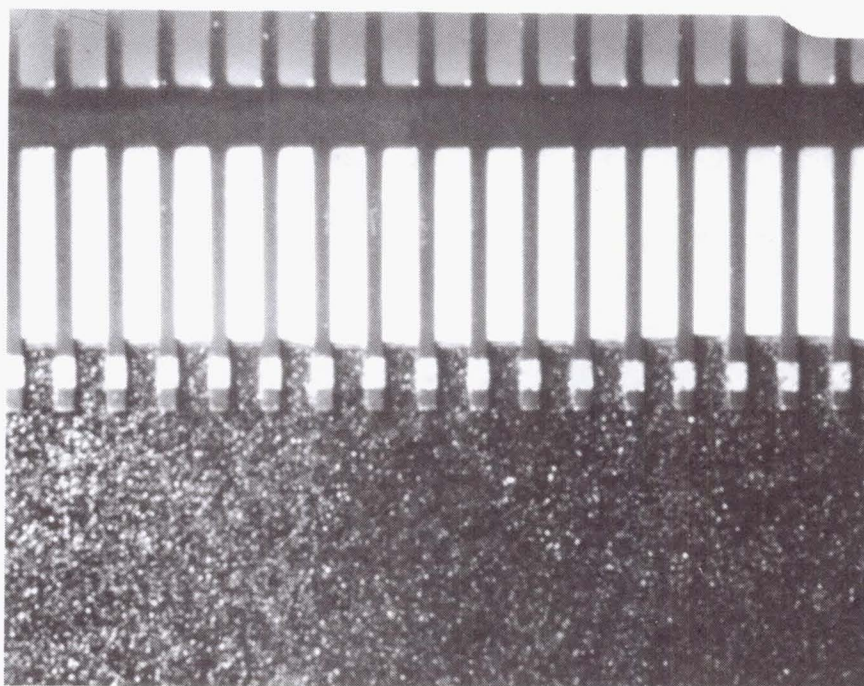


Figure 3. TABed Lead 3-Mil Wide on 8-Mil Centers

PRODUCTION IDEAS

Slide carriers offer a method of handling one TAB frame at a time, (see figure 4). This allows sorting the cell after flash testing, prior to lead forming. The disadvantage to the slide carrier is its added cost. The cost to load single TAB frame into the carrier, the carrier itself and extra capital equipment for sorting TABed Cells. The alternative method is to work with a group of TAB frames. For example; cut off group of ten from a TAB tape reel, ILB all ten fronts first, flip and push cell through, then bond all ILB backs. All ten then could be flash tested at once. The problems with this method are first, TAB tape is not a 100% yield product. Each strip of ten TAB frames could have a couple of bad frames. In addition post ILB flash testing may reject additional cells. Inventory of cells according to efficiency could be a problem.

EXCISE & FORMING

Post ILB, the concentrator solar cell needs to be excised from the TAB tape and the leads be formed for stress requirements. A single die was designed by the Prototype Development Lab and machined using wire EDM to do both excising and forming in one operation, (see figures 5, 6 and 7). This operation although manual can be automated with common SMT tooling and equipment.

After the die for excise and forming was made it had to be functionally tested. First, the shear was tested using cigarette paper instead of copper. Once quality shearing in the paper was achieved, copper strips were used. Paper can also indicate incorrect clearances in the forming feature relationships. The paper will be torn if the die is pinching. Next a dummy cell with a bonded tape was tested in the die set. After successful excise and forming was indicated, a real cell with correct bonds was tried. Minor adjustments were needed along with some shimming under the die to acquire consistent shearing. Generally, most difficulty was encountered in the shear function; the forming feature worked well from the onset.

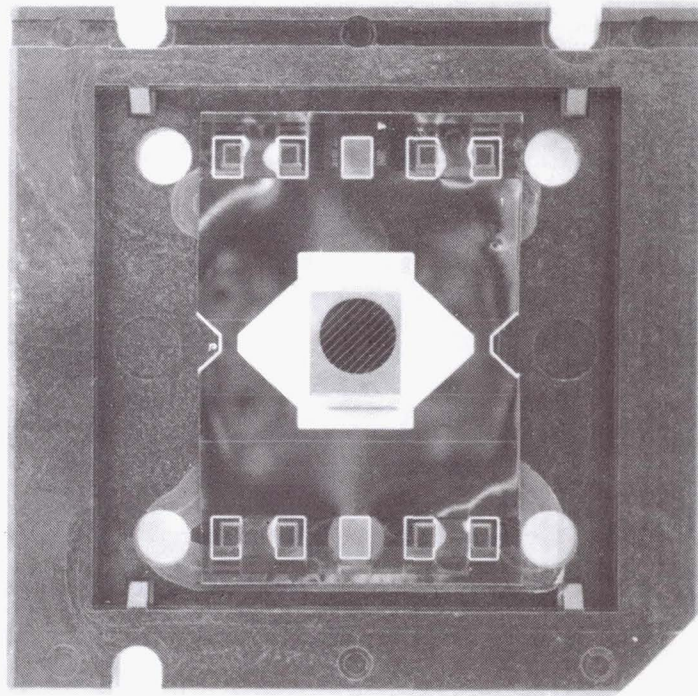


Figure 4. TAB Slide Carrier With Concentrator GaAs Solar Cell

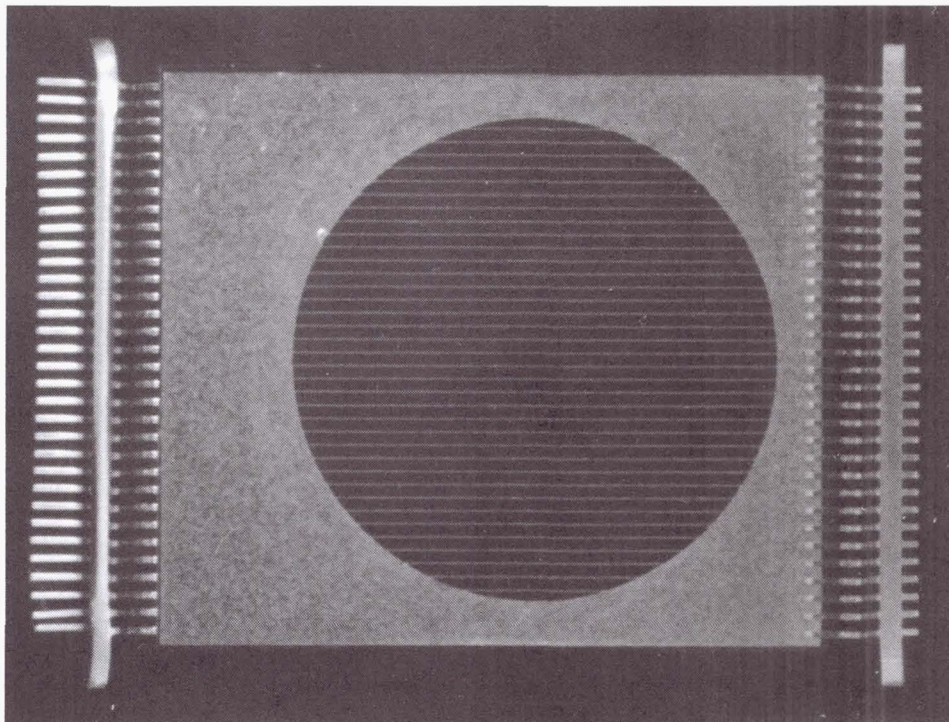


Figure 5. Top View of Cell After Excise and Forming Operation

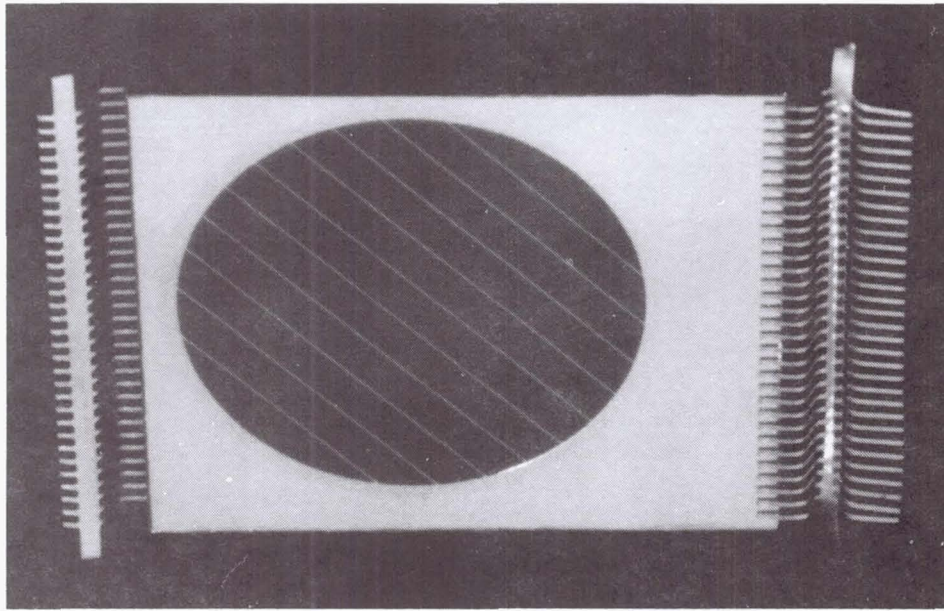


Figure 6. Excised and Formed Rotated For View of Stress Loop

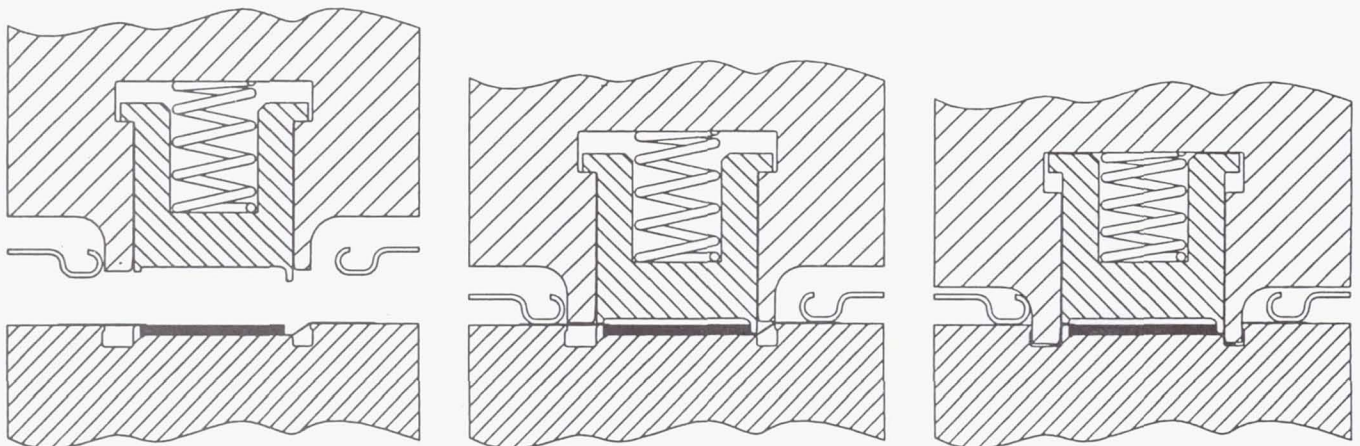


Figure 7. Excise and Form Tooling Sequence

PICK & PLACE

Once the solar cell leads are excised and formed, they need to be picked and placed to their respective locations on a flex circuit. At first this was done with a tooling microscope. This was fine for prototypes however it was time to evaluate automation. The concentrator solar cell placement required placement accuracies of ± 0.005 inches in order to maintain alignment with the focusing lenses.

A 12 cell flex circuit was fabricated at Boeing's flex circuit facility. It consisted of a 3-mil aluminum backing sheet, laminated with polyimide and copper. The copper was nickel flashed and gold plated. This circuit was placed on an EPE 20/20i gantry style x-y-z-theta pick and place machine with pattern recognition. The Boeing EPE 20/20i is capable of ± 0.001 " accuracy for alignment of top and bottom tandem cells on the flex circuit. The pick and place system was taught

were to find low e epoxy preforms and TABed solar cells in a waffle pack and to look for fiduciaries on the flex circuit. Epoxy TABed preforms were first picked, aligned and placed on a preheated flex circuit. the solar cells were then picked, aligned and placed atop the epoxy. Parallel gap welding the outer lead bonds completed the 12 cell solar cell circuit (see figure 8).

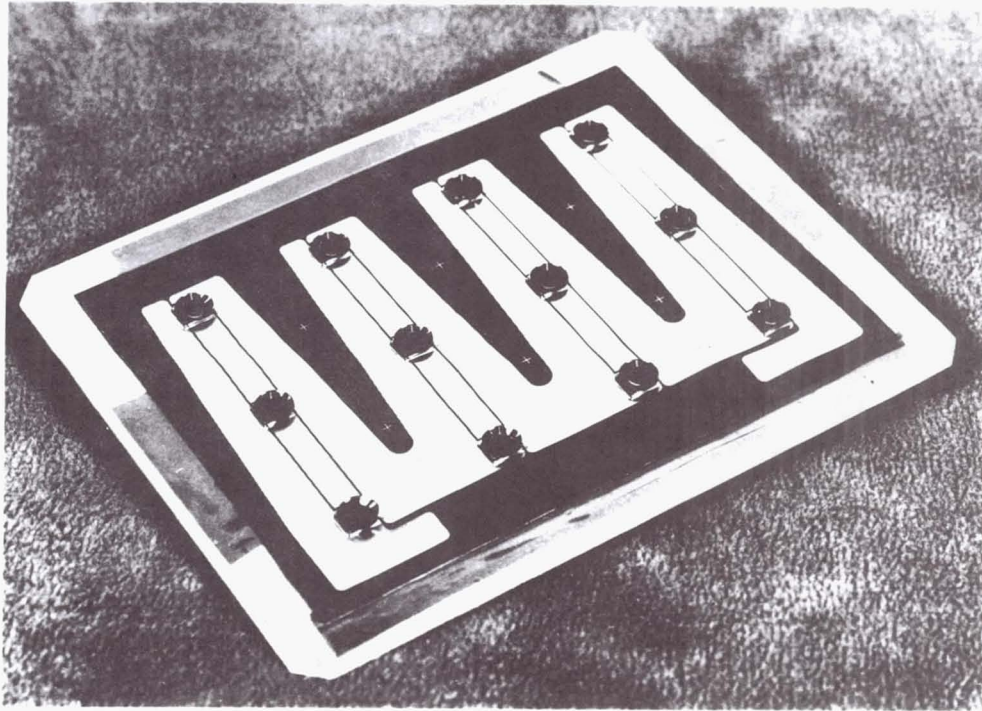


Figure 8. TAB Concentrator Solar Cells, Assembled on Flex Circuit, Topped With Optical Secondaries

CONCLUSIONS

The results of the flash testing on Boeing/Spectrolab concentrator solar cells are encouraging. No degradation has been observed on the new cells post ILB. Thermal cycle results on former 1 sun cells with silver contacts indicate a need for a barrier layer under the bond site to inhibit copper migration into the junction. Thermal cycle studies of silver-copper-tin ILBs will begin to evaluate the new Boeing/Spectrolab cells.

Preliminary evaluations of utilizing SMT pick and place technology for concentrator solar cell placement is encouraging. This technology is also being considered for placement of optical secondaries on production spacecraft contracts. One advantage of the EPE 20/20i machine is the ability to make a video record of each cell bond & placement for later review and record keeping.

SPACE STATION FREEDOM ADVANCED PHOTOVOLTAICS AND BATTERY TECHNOLOGY DEVELOPMENT PLANNING¹

Spruce M. Cox, Boeing Defense & Space Group, Huntsville, AL 35824
Mark T. Gates, Scott A. Verzwylt, Boeing Defense & Space Group, Seattle, WA 98124
Karen D. Brender, NASA Langley Research Center, Hampton, VA 23665

1.0 Introduction

Space Station Freedom (SSF) usable electrical power is planned to be built up incrementally during assembly phase to a peak of 75 kW end-of-life (EOL) shortly after Permanently Manned Capability (PMC) is achieved in 1999. This power will be provided by planar silicon (Si) arrays and nickel-hydrogen (NiH₂) batteries. The need for power is expected to grow from 75 kW to as much as 150 kW EOL during the evolutionary phase of SSF, with initial increases beginning as early as 2002. Providing this additional power with current technology may not be as cost effective as using advanced technology arrays and batteries expected to develop prior to this evolutionary phase. A six-month study sponsored by NASA Langley Research Center and conducted by Boeing Defense and Space Group was initiated in August, 1991 (ref. 1). The purpose of the study was to prepare technology development plans for cost effective advanced photovoltaic (PV) and battery technologies with application to SSF growth, SSF upgrade after its arrays and batteries reach the end of their design lives, and other low Earth orbit (LEO) platforms. Study scope was limited to information available in the literature, informal industry contacts, and key representatives from NASA and Boeing involved in PV and battery research and development. The authors wish to thank all study contributors.

Ten battery and 32 PV technologies were examined and their performance estimated for SSF application. Promising technologies were identified based on performance and development risk. Rough order of magnitude cost estimates were prepared for development, fabrication, launch, and operation. Roadmaps were generated describing key issues and development paths for maturing these technologies with focus on SSF application.

2.0 Technology Goals

SSF Si arrays and NiH₂ batteries were defined as the state-of-the-art (SOA) for this study. The technology goal for advanced PV was to double areal performance of the SOA arrays, from a blanket-level value of 95 W/sq m to 190 W/sq m or greater, while maintaining a 15 year design life. The battery technology goal was a 50% increase in operational specific energy of the SOA batteries, from 16 Whr/kg to 24 Whr/kg (cell level) or greater while maintaining a five year design life. Operational Whr/kg is defined as the nameplate Whr/kg rating of a battery multiplied by the depth of discharge (DoD), a more representative measure of merit than the nameplate rating alone. In both cases, the first increment of increased capability was to be available around the time of the first envisioned SSF growth increment, approximately 2002. This date was not a hard requirement. It was used to identify technologies that would mature approximately in time to support SSF growth.

3.0 Advanced Batteries

3.1 Technology Readiness Assessment

Table I summarizes the technology readiness assessment of the 10 battery systems evaluated in this study. Readiness and risk values are estimated from standard definitions (readiness levels 1 [basic principles observed] to 7 [engineering model tested in space] and risk levels 10 [unknown materials/processes] to 1 [off-the-shelf]). Readiness levels were estimated based on the probability of a battery system demonstrating the study performance goal by the year 1996. This 1996 date would allow five years (battery design life used in this study) of real time battery/mission relevant testing prior to flight to confirm capability.

¹ This work was sponsored by the NASA Langley Research Center under contract #NAS1-19247.

Table I - Advanced Battery Technology Assessment

System Concept	Cell Performance [Whr/kg, oper Whr/kg*, Whr/liter]	Readiness Level	Risk Level
SOA			
• NiH2-Large IPV (HST)	45, 5, 70	7	2
• NiH2-Larger IPV (SSF)	46, 16, 74	6	4
Advanced			
• NiH2-Improved Mgmt**	48, 24, 74	5	4
• NiH2-Largest IPV	55, ?, 80	5	4
• NiH2-CPV	60, ?, 70	5	6
• NiH2-Bipolar/ CPV	75, ?, ?	4	7
• NiMH	45, 15, 160	5	5
• NaS-Tubular Electrolyte	110, 33, ?	4	7
• NaMCl2	140, ?, ?	3	8
• NaS-Thin Flat Electrolyte	220, ?, ?	3	8
* Operational Whr/kg---Nominal cell Whr/kg times depth of discharge (normalized to 30,000 cycles) ** Improved battery management/component to increase average depth of discharge vs life cycle function NiH2---Nickel Hydrogen, NiMH---Nickel Metal Hydride, NaS---Sodium Sulfur, NaMCl2---Sodium Metal Chloride, IPV---Individual pressure vessel, CPV---Common pressure vessel			

Prediction of cell level operational specific energy to obtain 30,000 LEO cycles (five year life) was central to this assessment. Operational specific energy was determined by derating the cell nameplate by the percent DoD that would achieve 30,000 cycles. At least five years of calendar life and the capability of high temperature systems to meet freeze/thaw requirements were assumed. Cell level specific energies were readily available in the literature, but DoD versus cycle life functions for most of these advanced systems were not. The baseline SSF NiH2 system was projected to support 35% DoD at 30,000 cycles by data available in the literature, but verification cell testing is currently only at the two-thirds point (ref. 2). Air Force qualification of NiH2 individual pressure vessel (IPV) for LEO is also short of the five year point (ref. 3). Extrapolation of performance data between NiH2 cell designs (for example IPV to common pressure vessel-CPV) was not attempted because of interaction of battery system operating parameters including LEO charge/discharge rates, electrolyte management, and thermal cycles.

3.2 Screening Results

The central screening criteria of candidate battery systems was its capability to meet or exceed the technology goal when the technology was incorporated into a flight system. Battery producibility must have been demonstrated. The system also had to have single point failure tolerance (cell short and open circuit).

A key screening analysis parameter was the DoD value that enabled a five year design life. There is sufficient evidence to suggest that the inherent DoD versus cycle life function of NiH2 IPV systems could be significantly improved (ref. 4,5). The Improved NiH2 IPV battery incorporated improvements in cell components and battery management to realize a DoD of 50%. Low development risk and minimal design impact on the baseline SSF system made the Improved NiH2 IPV a viable candidate. Modifications of the Improved NiH2 battery could be embodied in more advanced packaging designs. However, name plate specific energy gains attained through improved packaging of CPVs or larger IPV designs may not be realized operationally. Thermal path length at LEO charge/discharge rates and electrolyte and oxygen management issues may negate minor weight advantages by reduction of the DoD versus cycle life function.

Nickel metal hydride (NiMH) offers significant energy density improvement over the baseline NiH2. Effects of long term LEO cycling on metal hydride alloys need to be established, but reported results are encouraging (ref. 6). A cycle life improvement over NiH2 IPV is not anticipated. NiMH was evaluated at 30% DoD for a five year mission life.

Sodium sulfur (NaS) with tubular electrolyte is the most technically ready of the high temperature systems and offers significant improvement in name plate specific energy over the rechargeable nickel systems. Operational specific

energy prediction for the SSF application is difficult because of the very limited cycle life database. NaS with tubular electrolyte was evaluated at 30% DoD for a five year mission life.

3.3 Cost/Benefit Analysis

Relative costs that discriminated between technologies were estimated. These costs consist of technology development, hardware production, and launch. Calculations were performed at the battery level and did not include heat pipe/radiators, interconnects, and other structural elements associated with a battery ORU. Batteries were sized to provide the total SSF load during a 36 minute shadow at EOL. This would be a 45 kWhr load for a 75 kW station (90 kWhr for a 150 kW station). A 22% packaging weight penalty was applied to account for effects of integration of cells into batteries. A 10% spare cell count was included in the cost of production, but not for launch. A Space Shuttle launch cost factor of \$4620/kg was used (ref. 1). Table II summarizes DoD predicted to support a five year life in LEO, battery production costs based on name plate kWhr from reference 7 and data supplied by Eagle-Picher Industries, and ROM development costs of each system analyzed.

Table II - Battery Production Costs

System	DoD	\$K/kWhr	Develop Cost (\$M)
• SOA NiH2	35%	140	0
• Improved NiH2	50%	140	6

System	DoD	\$K/kWhr	Develop Cost (\$M)
• NiMH	30%	70	10
• NaS (Tubular)	30%	90	22

It was assumed that Improved NiH2 would be a refinement of the SOA NiH2, and hardware development costs were expected to be small. The NiMH development cost assumed that nickel cadmium (NiCd) and NiH2 cell components and integration elements are applicable. NiMH performance and its DoD versus cycle life function must be established. We assumed that the Air Force NaS tubular design has potential to achieve a 30,000 cycle life, but development costs would be high and must address major issues including consistency, DoD versus cycle life function, battery management/charge control, ORU structure, and thermal control materials and processes.

Cost/benefit analysis results are shown in Figures 1 and 2 for 75 kW and 150 kW battery complements, respectively. The 75 kW analysis applies to an increase in SSF capability from 75 kW to 150 kW. However, if the initial SSF battery complement is flown during initial SSF assembly planned for 1995-1996, its design life will be reached when the first complement of growth batteries are delivered around 2002. Replacement of the initial battery complement with new technology and addition of the growth batteries are included in the 150 kW analysis.

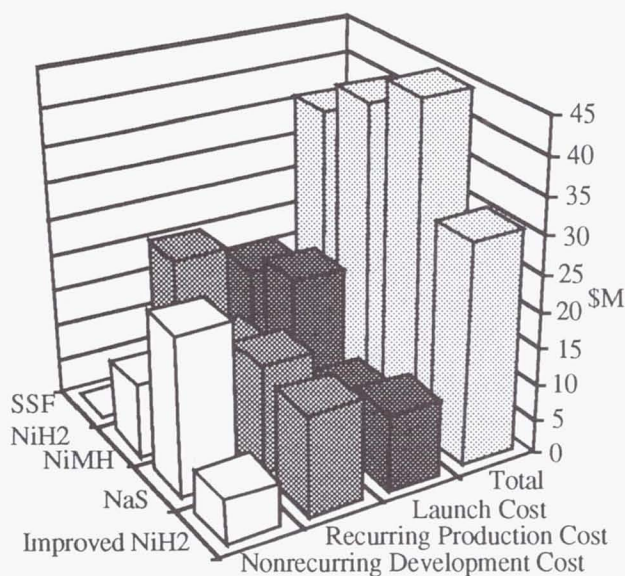


Figure 1 - Relative Cost of Batteries (75 kW)

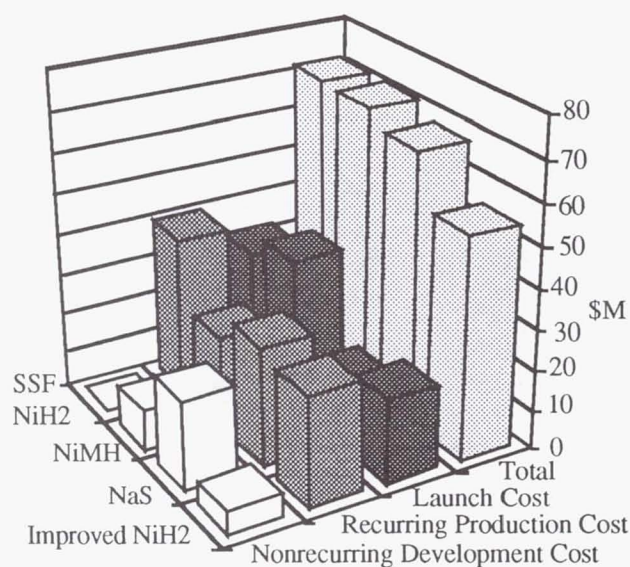


Figure 2 - Relative Cost of Batteries (150 kW)

Results showed that Improved NiH2 met the performance goal at the least cost for both 75 kW and 150 kW battery complements. At the 75 kW level, baseline NiH2 came in second to Improved NiH2. NiMH and NaS were both more costly. In the 150 kW analysis, NaS came in second to Improved NiH2. This was primarily because low NaS weight resulted in reduced launch cost. Over the 30 year life of SSF, a five year battery life would require launching as many as five replacement sets of 150 kW battery complements. Low NaS weight resulted in comparable savings to Improved NiH2 toward the end of this period.

Analysis showed that Improved NiH2 technology offers the best performance for the cost of battery technologies considered. Improved NiH2 batteries should be developed for SSF growth and for initial battery replacement at the end of their design life. NaS batteries show promise for savings towards the end of SSF design life. An investigation should be undertaken to establish the NaS depth of discharge versus cycle life relationship. Once this has been established, a better assessment between NaS and Improved NiH2 technologies can be made.

3.4 Roadmap Analysis

Roadmaps were generated for promising battery technologies to describe the development required to achieve readiness level 6 (engineering model tested in relevant environment). In emerging technologies this process is speculative. The roadmaps include our assessment of all tasks required to mature each technology, some of which are already underway. At a readiness level 6 milestone, if a decision to incorporate that technology into a real program were made, that technology would follow a Phase C/D development process to launch. A conservative value of six years was estimated for this process (ref. 1).

Roadmaps for Improved NiH2 and NaS battery technology were generated from historical battery technology roadmaps tailored for specific development issues and tasks. ROM costs of each phase of development were also predicted. Launch of flight hardware was shown no sooner than five years after battery readiness level 6 was achieved. This five year period was provided to allow battery level real-time mission simulation to confirm capability. Confirmation is required because of the complex interaction of battery cell design, thermal design, charge control, and applied charge/discharge rates on mission life and performance.

Technology roadmap for Improved NiH2 appears in Figure 3. A key issue to be resolved is the isolation of charged active material on discharge by a nonconducting discharge crystal phase form. Testing of 26% aqueous potassium hydroxide electrolyte, sponsored by NASA LeRC, has demonstrated significant cycle life improvement at higher DoD's by limiting isolation of active material at the prototype cell level. Improving conductivity through the discharge crystal phase form by additives and limiting corrosion of the nickel current collector may also limit charged active material isolation. At the battery level, charge control and thermal management are critical to the formation of the bimodal charged crystal phase mix. Precision of charge control in flight batteries is critical to reducing battery stress and prolonging battery life. Implementation of charge control via hydrogen pressure may limit overcharge, limit charge material isolation, and offer improved autonomy as a state of charge indicator. Reduction of current density at the nickel electrode, improved oxygen gas management, and improved manufacturing quality may improve the DoD versus cycle life relationship. Developments proven at the component, cell, and battery levels will be integrated into a real-time model cell cycle life test to prove 30,000 cycle (5 year) capability. Later a similar real-time battery test under simulated flight conditions would be undertaken.

A similar technology roadmap for tubular electrolyte NaS was prepared. Demonstration of the intrinsic capability of the cell design to perform for the LEO high cycle requirement has priority. The issues of micro-crack formation and cantilever suspension design of the alumina solid electrolyte need to be examined. Micro-gravity effects on cell operation, corrosion of cell seals, and accelerated corrosion beyond 60% DoD are also issues. Elements of battery charge control have to be established. Methods of operational cell balancing and cell open-circuit bypass hardware may be needed. NaS battery thermal management requires new approaches such as high temperature heat pipes or louver thermal windows, new thermal blanket technology, and cold launch scenarios.

3.5 Battery Conclusions

Improved NiH2 offers the most attractive cost benefit analysis results, least technical risk, and least potential impact to SSF. It is recommended that the development of Improved NiH2 proceed for the SSF growth and upgrade application. Tubular electrolyte NaS has the advantage of low material cost and very high name plate specific energy resulting in potentially low weight. This may result in cost savings for the SSF application towards the end of its

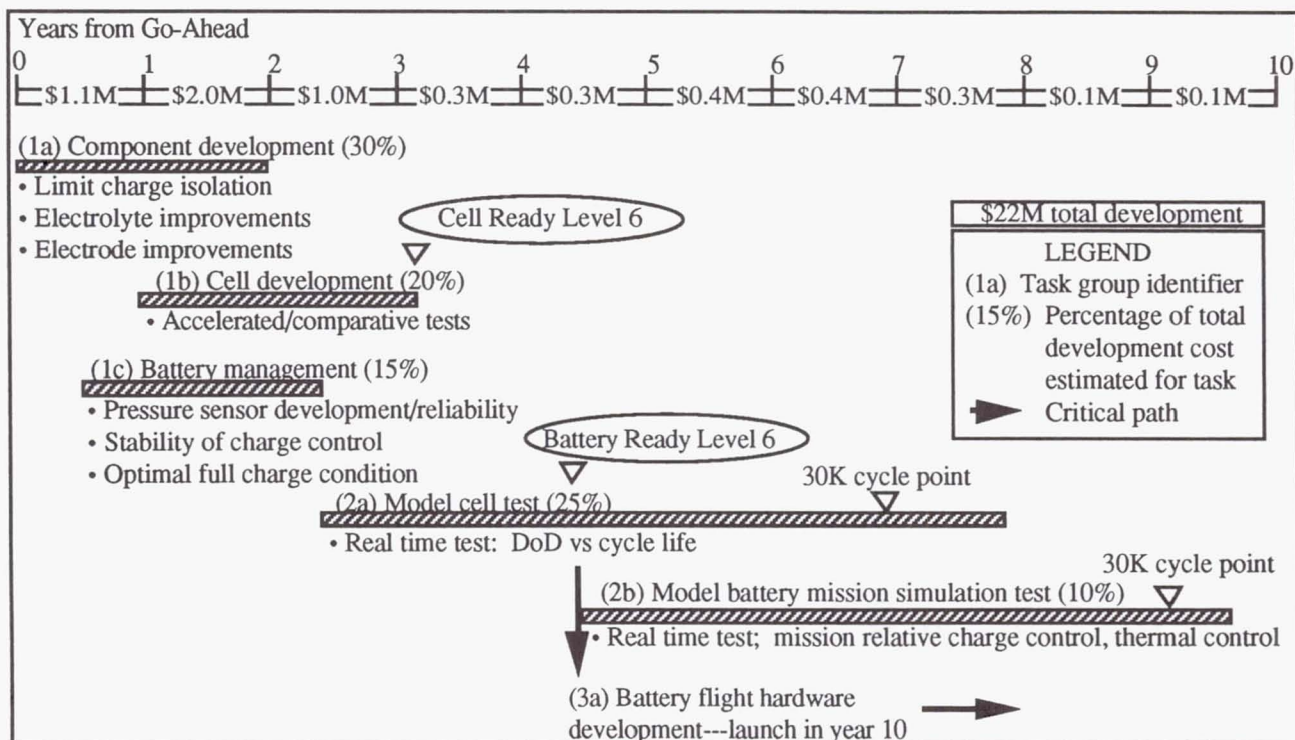


Figure 3 - Improved NiH2 Battery Roadmap

design life. It is recommended that the intrinsic NaS cycle life be established to determine the operational specific energy and actual weight savings. NaS battery and thermal management investigations should not proceed until intrinsic cell cycle life has been demonstrated.

4.0 Advanced Photovoltaics

4.1 Technical Readiness Assessment

Technical readiness of the 32 solar cell/array designs evaluated in this study is shown in Table III. The assessment was based on technology maturity and capability of large scale production startup in 1996-1997. Array technology was either based on the present SSF solar array design (ref. 8) (adapted to a study baseline planar array) or one of three concentrator array designs; General Dynamics Solar Low Aperture Troughs (SLATS), TRW Mini-Cassegrainian (ref. 9), or Boeing Minidome (ref. 10). The study baseline planar array design was used to simplify cell-to-cell comparisons and minimize development cost of new planar array structure. The technology performance goal was to double the SSF array areal power of 95 W/sq m while maintaining a power density over 80 W/kg. Areal performance was viewed as most critical due to array contribution to SSF atmospheric drag. Estimates of NASA readiness and risk level (defined in 3.1) were assigned on the basis of flight experience, cell production, and published papers.

Planar Array Technology. To compare planar solar cells, on-orbit expected BOL efficiencies were computed for each cell from its specified standard condition electrical efficiency and the expected panel operating temperature. Projected efficiencies for immature cell designs were derated to reduce risk. Array BOL areal power for the comparison cells were given by the ratio of the comparison cell efficiency over the baseline 8 mil Si cell efficiency multiplied by the SSF array areal power, 95 W/sq m (ref. 8). The BOL cell efficiencies and resulting areal powers are shown in Table III. By using this ratio method, common array design factors such as harness loss and tracking error were included.

Concentrator Array Technology. Data for SLATS and Mini-Cassegrainian, taken from the literature, and Minidome, taken from Boeing, indicated these arrays exceeded the performance goal. The concentrator designs all used a GaAs/GaSb tandem cell or equivalent (31% efficient at 100 AM0, 25°C).

Table III - Advanced Photovoltaics Technology Assessment

System Concept	Cell BOL % Efficiency	BOL Perf W/kg, W/sqm*	Readiness Level	Risk Level	System Concept	Cell BOL % Efficiency	BOL Perf W/kg, W/sqm*	Readiness Level	Risk Level
SOA					• CLEFT AlGaAs/CIS Tandem	26.0	85, 179	4	5
• Si WTC 8mil (SSF)	14.6	43, 95	7	1	• AlGaAs/active Ge	25.0	81, 170	4	5
Advanced					• AlGaAs/Si Tandem	32.0	111, 222	2	7
• "K7" Si, 2 mil	13.5	46, 87	7	2	• AlGaAs/InGaAsP	32.0	100, 220	2	7
• GaAs/inactive Ge, 3.5 mil	20.0	56, 135	5	3	• AlGaAs/active GaAs	24.0	59, 169	3	6
• AlGaAs/inactive GaAs	16.0	38, 108	3	5	• Epitaxial GaAs/Si	21.0	77, 146	2	6
• GaAs/Ge WTC, 7 mil	16.0	44, 135	5	4	• InAlAs/GaAs	26.0	64, 177	2	6
• GaAs/Ge IDC, 3.5 mil	16.0	56, 135	5	4	• GaInP2 Top Cell/Si	30.3	98, 212	3	6
• InP	20.0	49, 131	6	4	• GaInAs&GaInAsP Bottom Cell	25.0	82, 172	3	6
• GaAs/Ge, 7 mil	16.0	44, 135	6	2	• Amorphous Si	13.0	49, 86	3	5
• CLEFT GaAs/CIS	21.0	67, 142	6	4	• AlGaAs/GaAs/InGaAs	26.0	64, 177	3	6
• GaAs/GaSb SLATS	31.0	66, 200	6	5	• AlGaAs/GaAs/InGaAsP	26.0	64, 177	3	6
• GaAs/GaSb Minidome	31.0	100, 300	6	5	• InP/GaInAs Concentrator	28.0	94, 230	3	6
• APSA	13.5	100, 117	6	3	• GaAs/GaSb Mini-Cassegrainian	31.0	82, 257	6	5
• Silicon PERL	20.8	69, 135	4	6	• GaAs/GaInAs(P)/inactive Ge	25.0	81, 170	4	5
• Front Contact PIN Si	21.0	72, 141	4	6	• GaInP2/GaAs/inactive Ge	25.0	81, 170	4	5
• CLEFT InP	20.0	68, 135	2	7					
• CLEFT GaAs	21.0	73, 146	6	4					

* Blanket-level performance estimates. Planar arrays assume use of modified SSF array structure. Each concentrator uses unique array structure.

4.2 Screening Results

The key screening criteria was performance. Areal powers in Table III were divided into three groups. The first group included most of the single junction cells with performance near 140-150 W/sq m. The second group at 170-180 W/sq m included most of the mature multijunction and tandem cells. The last group, over 200 W/sq m, included concentrators and advanced multijunction and tandem cells. With the increased array packing factor discussed above, performance of the three groups shifted to 160-179, 195-205, and over 220. The second and third groups then passed the performance goal. Other screening criteria were producibility cost and ease of array fabrication.

Planar Array Technology. Four planar cells were selected for further analysis; CLEFT AlGaAs/CIS tandem, AlGaAs/Si tandem, AlGaAs/active Ge multijunction (or variants GaAs/GaInAs/inactive Ge, GaAs/GaInAsP/inactive Ge), and GaInP2/GaAs/inactive Ge multijunction. These cells offered promising performance versus risk. Other cells may also be suitable but should not be substantially different than these.

Concentrator Array Technology. The Minidome and SLATS concentrators were selected for further analysis. A high SSF contamination environment was a concern for EOL array performance, especially for the SLATS and Mini-Cassegrainian designs. The baseline SSF planar array has a 15% contamination loss factor after 15 years. With a planar array or the Minidome design, light makes only one pass through the contamination layer. SLATS requires incoming light to pass through the contamination layer three times (in and out of one optical surface and then into cell). Mini-Cassegrainian requires the incoming light to pass through the contamination layer five times (in and out of two optical surfaces and then into cell). These designs may require more than a 15% contamination loss factor.

Mini-Cassegrainian was eliminated because of this potentially large contamination loss and its optical complexity. The design should not be completely eliminated from consideration until it is shown that contamination is a problem.

4.3 Cost/Benefit Analysis

Relative array costs over a 15 year period were computed for the screened array designs. Only costs that discriminated between technologies were estimated. These costs consisted of technology development, hardware production, launch, and reboost (\$/sq m drag area). Reboost cost is the cost of launching propellant to SSF to reboost it back to a higher orbit to make up for atmospheric drag.

In order to proceed to a cost estimate, a total array size had to be estimated for each candidate. It was determined that 75 kW of useable power required a 218 kW array based on the following factors; 0.80 battery charge efficiency, 42 minute full charge, 36 minute eclipse, and the following loss factors: 0.98 UV, 0.95 thermal cycle, 0.85 contamination, 0.98 meteoroid/debris, and 0.92 radiation. Since radiation degradation of the selected cell types was expected to be lower than the baseline Si but was unknown for most of the cells, a constant 8% radiation loss was assumed for all arrays. The 8% radiation loss was a simplification that favored the baseline Si array but was probably over-conservative for the concentrators. Another change to reduce planar array area was to increase the packing factor to 79% from the SSF array value of approximately 69% (ref. 8). This was accomplished by filling in empty panels (2%), eliminating the space where transverse panel longerons used to be (3%), and decreasing interpanel hinge spacing (5%). Resulting array areas and masses were calculated.

Estimated cell and array fabrication costs are shown in Table IV. Three specific cell costs were used as a cell point of departure: GaAs/GaSb estimate, GaAs/inactive Ge estimate, and baseline SSF Si cost (ref. 1). The cost of the other advanced cells were scaled from these. SSF array costs were used as an array point of departure. Total cost of the SSF arrays was given as approximately \$400,000,000, half non-recurring and half recurring, for 246.4 kW (75 kW useable power from four PV power modules) (ref. 1). In Table IV, the cost of baseline SSF Si arrays for the second 75 kW (for a total of 150 kW) was just the recurring cost stated above. The cost for advanced planar arrays was the

Table IV - Relative Fabrication Cost of Solar Arrays for SSF Upgrade/Growth

CELL COSTS (DOLLARS)

Start with ~\$300/5.5 X 6 cm GaAs/inactive Ge cell,~10,000 cells.

Scale up to 8 x 8 cm (x1.93), very large quantities (x0.86), yields \$500/8 x 8 cell.

Now add complexity factors for other cells compared to GaAs/Ge:

Cell Type	Factor	Rationale	Cell Cost (8x8 cm equiv cell area)
AlGaAs/Silicon	1.75	Two cells, somewhat fragile silicon substrate	\$875
AlGaAs/CIS	1.5	Two cells, CIS is rugged	\$750
AlGaAs/Ge	1.1	Almost the same as GaAs/inactive Ge	\$550
GaAs/GaSb mini	0.54	Small, complex cells, 1/50 the area of planar	\$269
GaAs/GaSb SLATS	0.75	Small, complex cells, 1/20 the area of planar	\$375
Baseline Silicon	0.35		\$175

ARRAY COSTS (\$ MILLIONS)

Cell Type	Nonrecurring Cell Costs	Recurring Cell Costs	Labor Costs	Structure Non-Recurring	Structure Recurring	Test	Total Fabrication
AlGaAs/Silicon	\$20	\$138	\$52	\$5	\$28	\$19	\$262
AlGaAs/CIS	\$20	\$124	\$54	\$5	\$29	\$19	\$251
AlGaAs/Ge	\$20	\$95	\$57	\$5	\$30	\$19	\$226
GaAs/GaSb mini	\$8	\$30	\$94	\$45	\$50	\$35	\$262
GaAs/GaSb SLATS	\$11	\$58	\$88	\$35	\$47	\$33	\$272
Baseline Silicon	\$0	\$50	\$91	\$0	\$49	\$10	\$200

sum of modifying the existing SSF array to accept new cells plus recurring costs. Minidome and SLATS concentrator array costs included the total cost of cells and structure, assuming no benefit from SSF array development because of the large differences between concentrator and planar arrays. This assumption may have over-penalized the concentrators. Minidome costs were based on estimates from the Boeing array developers. SLATS costs were scaled from Minidome costs. Advanced array fabrication costs were all comparable in Table IV.

Launch and reboost costs were based on a Space Shuttle launch cost factor of \$4620/kg, and a SSF reboost cost factor of \$26,900 per drag square meter per year (ref. 1). Other costs such as EVA activity were assumed to be the same for all array types and were not included. Figure 4 indicates that relative array costs for all advanced arrays were much lower than the baseline array, primarily because of reduced reboost costs. In order to reduce anticipated high reboost costs, we assumed that arrays would be feathered during eclipse to reduce drag, an option that is not presently planned for SSF. If the present SSF no-feathering operational scenario had been assumed, reboost costs would have been approximately 40% higher than shown. Figure 4 shows that the Minidome concentrator had the lowest relative cost, followed closely by the planar arrays. The winning arrays were all about equal in cost when uncertainties in the estimates were considered.

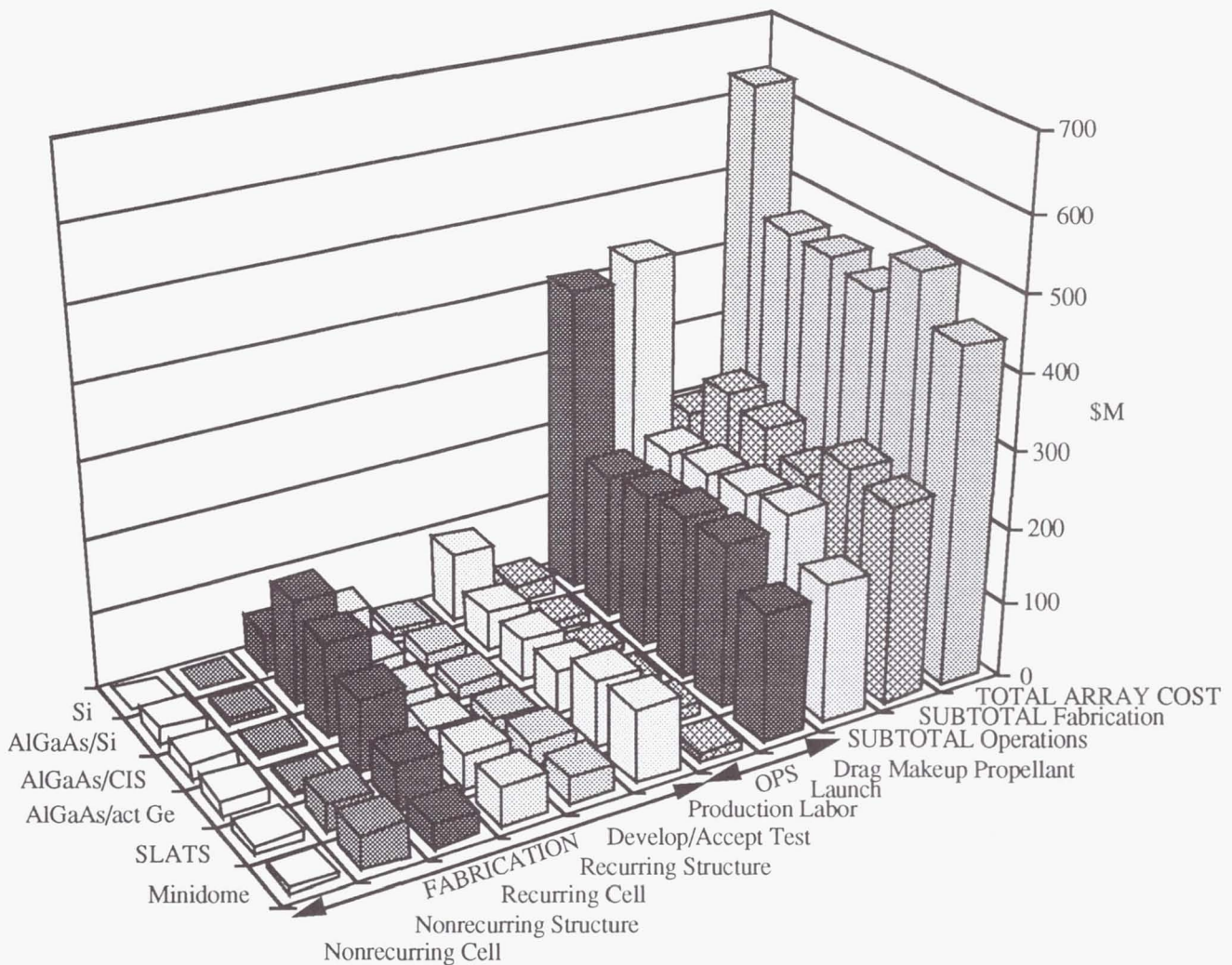


Figure 4 - Relative Cost of Solar Arrays for SSF Upgrade/Growth

4.4 Roadmap Analysis

Roadmaps were generated for selected advanced arrays in the same manner as that described for batteries above. We identified initial technology development steps that were similar for all advanced planar arrays considered. The steps include: development of electrical efficiency and cell process in small cells, increase in cell size while controlling cost, and modification of existing array blankets and circuitry to accept new cell types.

A key development issue that applies to all advanced arrays in a SSF application is the determination of an accurate contamination loss factor. Front surface concentrator optics are especially vulnerable to contamination, and multijunction cells may also be at risk. Series interconnection makes multijunction cells susceptible to current limiting losses beyond the normal 15% if the contamination is spectrally selective. It is possible that contamination will cause one or more of the selected array concepts to drop out before an initial development effort is undertaken.

Minidome technology development roadmap is shown in Figure 5. Other roadmaps for SLATS, tandem cell (AlGaAs/CIS or AlGaAs/Si), and multijunction cell (AlGaAs/active Ge, GaInP2/GaAs/ inactive Ge, or GaAs/GaInAs(P)/ inactive Ge) arrays were prepared. Both SLATS and Minidome will need structure development. Concentrator pointing requirements must be accounted for with possible design impacts in the joints and main structure. Initial cell development and module demonstration for Minidome have been accomplished. Finalization of optics design with regard to cost and pointing requirements is continuing. Latest optical designs allow for an increase in pointing tolerance from 3° to 4°, but there will still probably be design impacts on the present SSF tracking mechanisms.

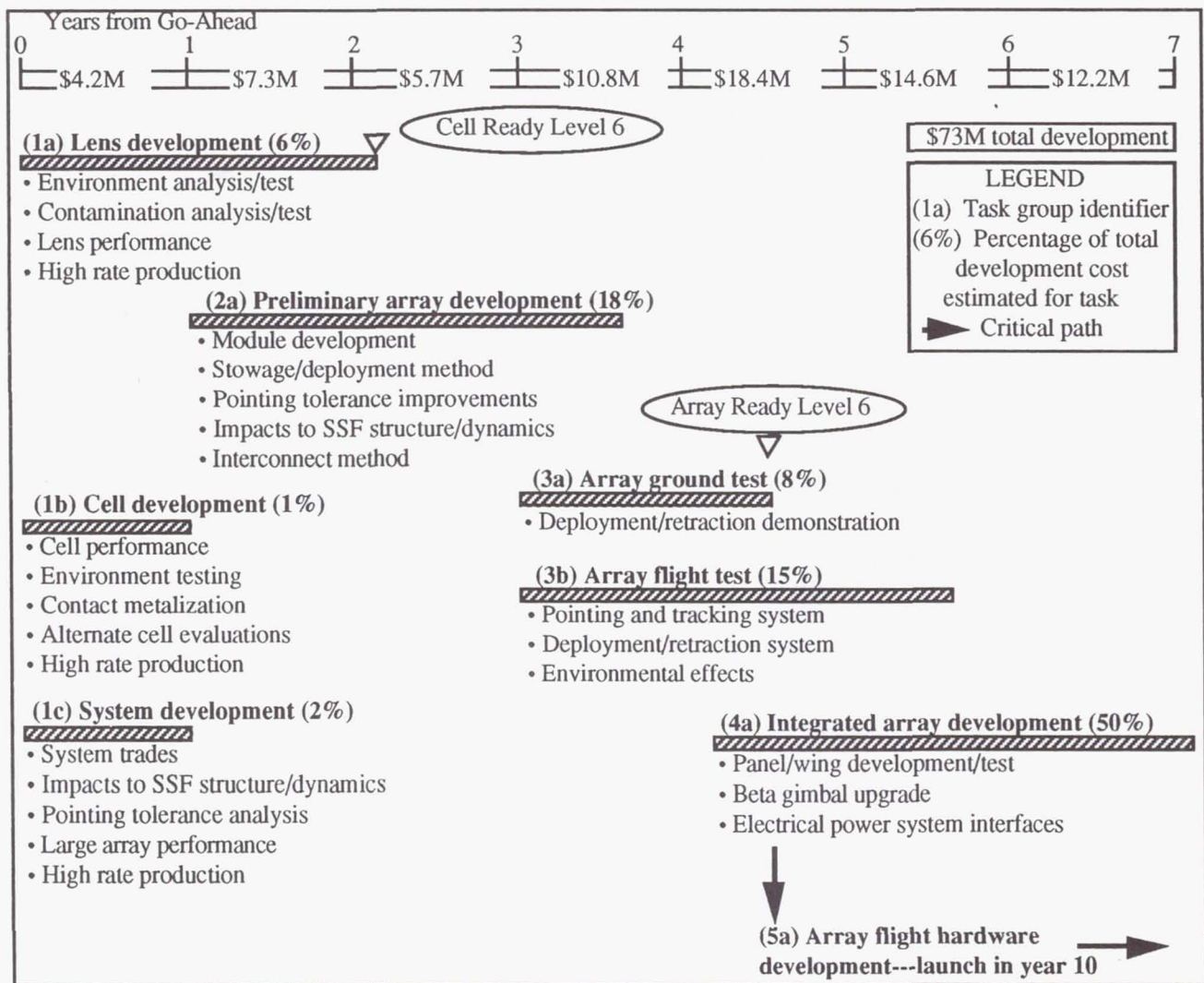


Figure 5 - Minidome Concentrator Array Roadmap

The SLATS concentrator array has been developed in a threat hardened form for the 10 kW Survivable Power Subsystem Demonstration (SUPER) array effort. It was assumed that this design was relatively mature for a concentrator and that much of the development could be used for a SSF application. If this is not valid, larger development costs would result. Contamination may be a problem, and the effect of the meteoroid/debris environment on optical efficiency needs to be determined.

4.5 PV Conclusions

This study identified several promising advanced PV concepts for SSF growth or upgrade. The concepts are only moderately complex and offer significant performance improvements and substantial cost savings. It is recommended that an early assessment of the expected SSF contamination environment and its impact on these technologies be undertaken. In parallel, initial development tasks should be performed for Minidome and SLATS concentrator arrays, and tandem cell (AlGaAs/CIS or AlGaAs/Si) and multijunction cell (AlGaAs/active Ge, GaInP2/GaAs/inactive Ge, or GaAs/GaInAs(P)/inactive Ge) arrays. After these initial tasks are accomplished, more accurate estimates of future array performance for SSF application can be made. Downselection to the most promising technology could then be accomplished.

5.0 Study Conclusions

Roadmaps generated for the most promising advanced battery and PV technologies provide focused development toward SSF growth, SSF upgrade, and LEO space platform applications. Funding of technology development steps described in these roadmaps, and resolution of associated development issues, will accelerate technology readiness and give hardware programs earlier access to cost effective advanced technologies for their application.

6.0 References

1. Cox, S.M., Gates, M.T., Verzwylt, S.A., Advanced SSF High Efficiency Power Systems Technology Development Planning, Boeing Defense & Space Group, D567-32000-1, March 31, 1992
2. Frate, D.T., Nickel-Hydrogen Cell Low-Earth-Orbit Life Test Update, 1991 IECEC Proceedings, Vol. 3, pp 263-266.
3. Hill, C.H., Matsumoto, J.M., Poston, T.M., Prater, A., Brown, H., Hall, S., and House, S., Air Force Nickel Hydrogen Cell Low Earth Orbit Life Test-Update, 1992 IECEC Proceedings, Vol. 1, pp.131-139.
4. Lim, H.S., Verzwylt, S.A., KOH Concentration Effect on the Cycle Life of Nickel-Hydrogen Cells, III. Cycle Life Test, Journal of Power Sources, 1988, Vol. 22, pp. 213-220.
5. Smithrick J.J. and Hall, S., Validation Test of Advanced Technology for IPV Nickel-Hydrogen Flight Cells - Update, 1992 IECEC Proceedings, Vol. 1, pp. 215-225.
6. Otzinger, B., Accelerated Cycle Life Performance for Ovonic Nickel-Metal Hydride Cells, 1990 NASA Aerospace Battery Workshop, pp. 547-557.
7. Sernka, R.P., Sodium-Sulfur- An Advanced Battery for Space, IAAA/DARPA Meeting on Light Weight Satellite Systems, 1987, p35-38.
8. Barona, C., Status of the SSF Solar Array, Space Photovoltaic Research and Technology Conference, Lewis Research Center, Nov 9,1989.
9. Solar Concentrator Array Development Final Technical Report, NASA 37439, Sept 30,1991.
10. O'Neill, M.J., Piszczor, M.F., Fraas, L.M., Key Results of the Mini-Dome Fresnel Lens Concentrator Array Development Program Under Recently Completed NASA & SDIO SBIR Reports, Space Photovoltaic Research and Technology Conference, 1991, pp 20-1 to 20-12.

Recent Developments in Refractive Concentrators for Space Photovoltaic Power Systems

Michael F. Piszczor
NASA Lewis Research Center
Cleveland, OH 44135

&

Mark J. O'Neill
ENTECH, Inc.
DFW Airport, TX 75261

Since SPRAT XI, significant progress has been made in the development of refractive concentrator elements and components designed specifically for space applications. This paper will discuss the status of the mini-dome Fresnel lens concentrator array and then summarize the results of work recently completed in the area of prismatic cell covers for concentrator systems. This will be followed by a brief discussion of some work just starting in the area of line-focus refractive concentrators for space.

INTRODUCTION

Since 1986 NASA Lewis and ENTECH, Inc. have been working on developing high efficiency, light weight refractive concentrator optics and components for use with space photovoltaic (PV) power systems. Since that time, considerable progress has been made in the development of the mini-dome Fresnel lens photovoltaic concentrator system (refs. 1,2). Within the past year, a number of new developments have been made, particularly in the area of prismatic cell covers. This paper will address four main areas:

1. Mini-Dome Fresnel Lens Concentrators
2. All-Glass Prismatic Cell Covers
3. Silicone Prismatic Cell Covers
4. Line-Focus Fresnel Lens Concentrators

The first area will cover the current status of the mini-dome concentrator program, which has been the focus of NASA's photovoltaic concentrator program over the past number of years. The next two areas will discuss new developments in the area of prismatic cell covers for both space and terrestrial applications. As will be discussed further, the new developments in terrestrial-based silicone prismatic cell cover technology could have a significant impact on the manufacturability and cost of future space refractive concentrator systems. The last topic will address the development of a linear refractive concentrator element under a program that has just started.

MINI-DOME FRESNEL LENS CONCENTRATORS

The mini-dome Fresnel lens concentrator is a unique point-focus refractive concentrator lens that was originally developed under the NASA and SDIO Small Business Innovation Research (SBIR) Programs by ENTECH, Inc.

Since 1989 the Boeing High Tech Center and the Boeing Defense & Space Group have pursued the development of this technology, expending a considerable amount of resources to bring this technology from a conceptual design and prototype component hardware stage to a point where the feasibility of assembling manufacturable concentrator array modules into a high efficiency, light weight power system has been demonstrated. These developments, along with a more detailed description of the hardware, have been discussed in previous papers (refs. 2,3) and will not be reviewed at this point.

Currently, the mini-dome concentrator program, both within NASA Lewis and at Boeing, emphasizes the large-scale manufacturability and assembly of array components as well as environmental and performance testing at the component and module level. The thermal cycling of various tandem cell interconnect patterns and prototype modules (ref. 4) has been performed. There are also a number of shuttle-based flight experiments planned that will evaluate the environmental stability of lens materials. Lens and cell material samples were recently flown on the EOIM-3 shuttle experiment. The results from this experiment are currently being analyzed will be reported once the post-flight data analysis is complete.

The key experiment for the mini-dome technology at this point is the Photovoltaic Array Space Power Plus Diagnostics (PASP Plus) Flight Experiment. PASP Plus is an Air Force-sponsored experiment that will test twelve different types of photovoltaic cell/array configurations in space (ref. 5). The Pegasus-launched experiment will have a highly elliptical orbit (190 n.m. by 1050 n.m., 70 degree inclination) that will expose the test modules to a variety of space environmental conditions (radiation, atomic oxygen, space plasma, etc.). An important feature of the PASP Plus experiment is that a number of the test modules will be biased to voltages up to ± 500 V in order to investigate array interaction with the space plasma under simulated high voltage array operating conditions.

One of the twelve individual experiments on PASP Plus is a NASA Lewis/Boeing mini-dome Fresnel lens concentrator module. The experimental module, built by Boeing, is 7.5 by 4.4 inches in size and consists of 12 lens-cell elements. A photograph of the flight hardware is shown in Figure 1. The concentrator lenses are made from silicone (DC 93500) and coated with a proprietary coating for protection against atomic oxygen and UV degradation. The cells are gallium arsenide/gallium antimonide (GaAs/GaSb) tandem cells made by Boeing. Each cell operates under a concentration of approximately 50 suns and has a pointing requirement of ± 2 degrees.

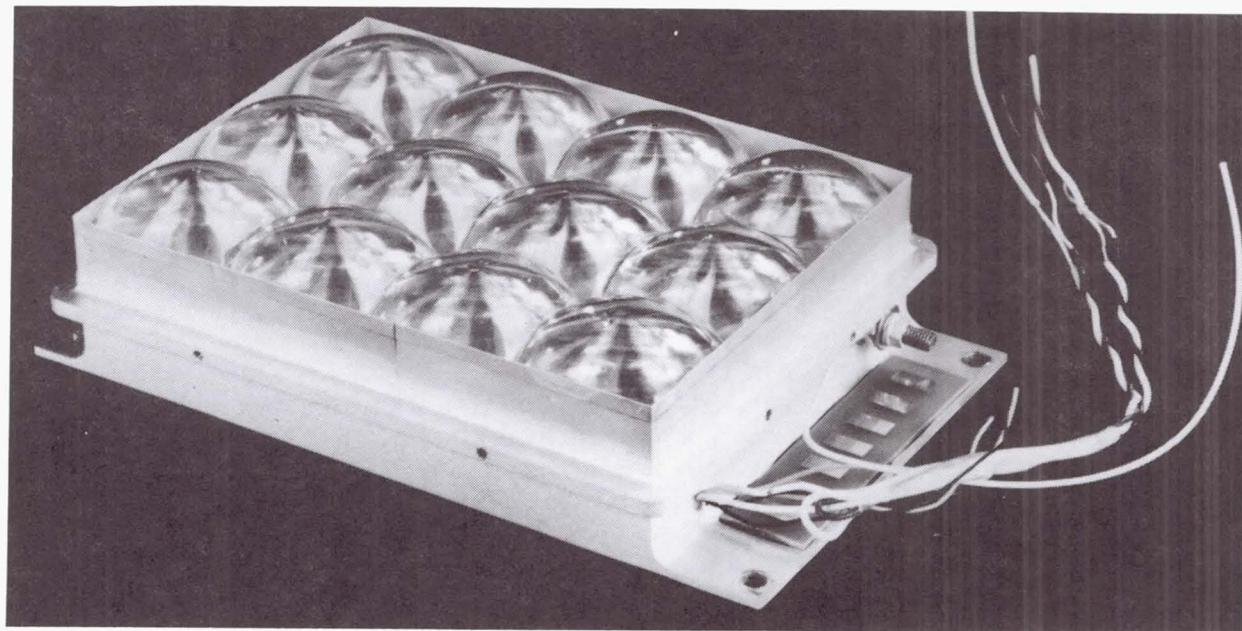


Figure 1. Photo of the mini-dome Fresnel lens concentrator test module being flown on the Photovoltaic Array Space Power Plus Diagnostics (PASP Plus) Flight Experiment.

Each set of three tandem cells is wired in a triplet configuration (ref. 6) which consists of three GaAs cells each in parallel with a series string of three GaSb cells. The four triplets are then wired in series to provide a two terminal output for the test module.

The PASP Plus experiment will be the first space flight test of the mini-dome concentrator lens and GaAs/GaSb cell technologies. In addition to the normal performance and long-term stability test data expected from this experiment, the mini-dome concentrator module will also participate in the high voltage plasma interaction part of PASP Plus. Ground-based testing on an earlier prototype module has shown minimal interaction with the space plasma at voltages up to ± 500 V. It is anticipated that the flight data from PASP Plus will confirm the expectation, based on previous ground-based testing, that concentrator arrays are less susceptible to plasma interaction effects than normal planar arrays at high operating voltages. This is due primarily to the inherent shielding of the cell from the space plasma that is provided by the concentrator array structure. The scheduled launch date for the PASP Plus experiment is the summer of 1993, with an expected operational lifetime of from 1 to 3 years.

ALL-GLASS PRISMATIC CELL COVERS

The concept of the prismatic cell cover has been around for a number of years. Projected applications have ranged from use on cells in planar arrays to ENTECH's patented concept of using the prismatic cover in conjunction with a concentrator element. The basic concept of the prismatic cell cover is shown in Figure 2. Utilizing the refractive optics of the prism cover, light is redirected away from the top metal gridlines toward the active area of the cell below. This translates into an increase in the amount of current produced by the cell and, if properly designed, is directly proportional to the amount of metallization covering the front surface.

ENTECH has had considerable experience using prismatic covers on their terrestrial concentrator systems. These prism covers are made from silicone. While silicone materials have been used extensively in space, specifically as an adhesive for bonding coverglasses to photovoltaic cells, there are a number of anticipated applications where all-glass prism covers would be desirable.

For space applications, a glass prismatic cell cover has a number of advantages. Glass is resistant to ultraviolet radiation, impermeable to monatomic oxygen, and provides excellent and well known resistance to particulate radiation. In addition, glass is very stable, even at extremely high temperatures. Thus if a glass prismatic cover were electrostatically bonded to a solar cell, the cell assembly could tolerate extremely high temperatures. Unfortunately, glass is very difficult, if not impossible, to form into the intricate prismatic cover shape with normal glass-forming technology. Under Phase I of an SDIO-sponsored SBIR contract, ENTECH and GELTECH, Inc., a small company with significant experience in forming small, high quality glass products, have successfully developed an all-glass prismatic cover via the sol-gel casting process (ref. 7). In sol-gel processing, very small colloidal particles are first formed in a solution. In sufficient concentration, these very small particles link together in chains, and then, in turn, into three-dimensional networks. Using a multi-step processing sequence, the gels can be molded exactly or very close to a final desired shape. The characteristics and properties of the pure silica made by sol-gel technology are equal to or better than those of other commercially available silicas.

A schematic of the prototype cover produced under the SBIR contract is shown in Figure 3. To cast the silica prismatic cell covers using the sol-gel process, a polystyrene mold was used. Polystyrene was selected as the best material for making the expendable molds due to its known compatibility with the sol-gel material and the casting process. The polystyrene molds were made from an existing diamond-cut master prism cover tool which was available to ENTECH.

An important point to note is that during sol-gel processing an enormous amount of shrinkage takes place. Shrinkage in all three dimensions must be accounted for when designing the sol-gel casting mold in order to achieve a final part with the desired dimensions. Despite the enormous amount of shrinkage inherent in the sol-gel process (equivalent to a 94% reduction in volume), the replication accuracy was outstanding. Figures 4 and 5 are photographs of the polystyrene mold and the silica prism cover respectively. (Note that the change in the magnification in the two photographs is due to shrinkage of the silica part after sol-gel processing). To further

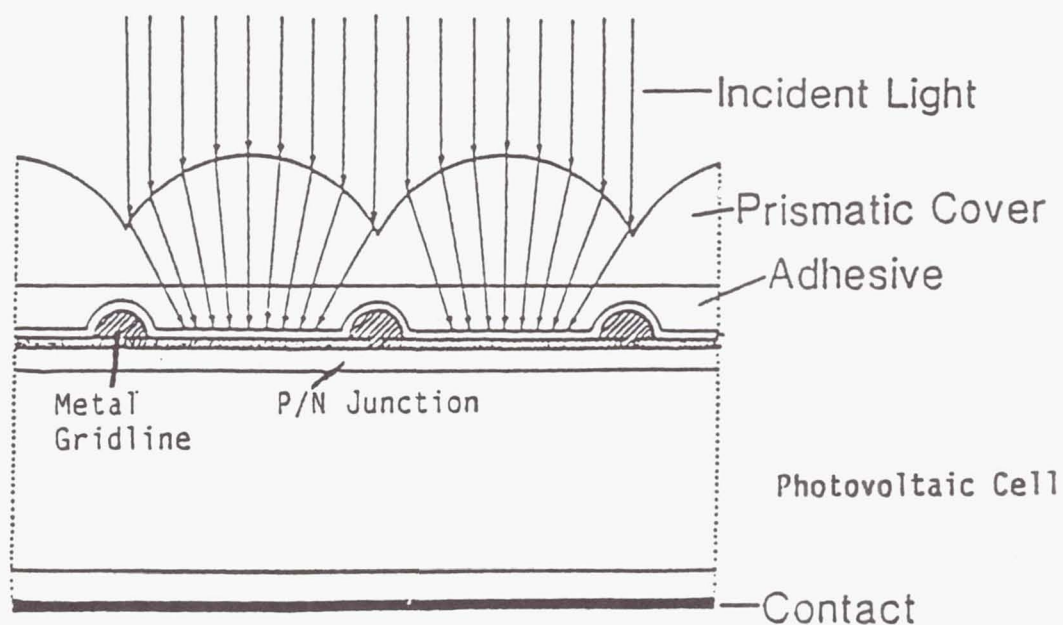
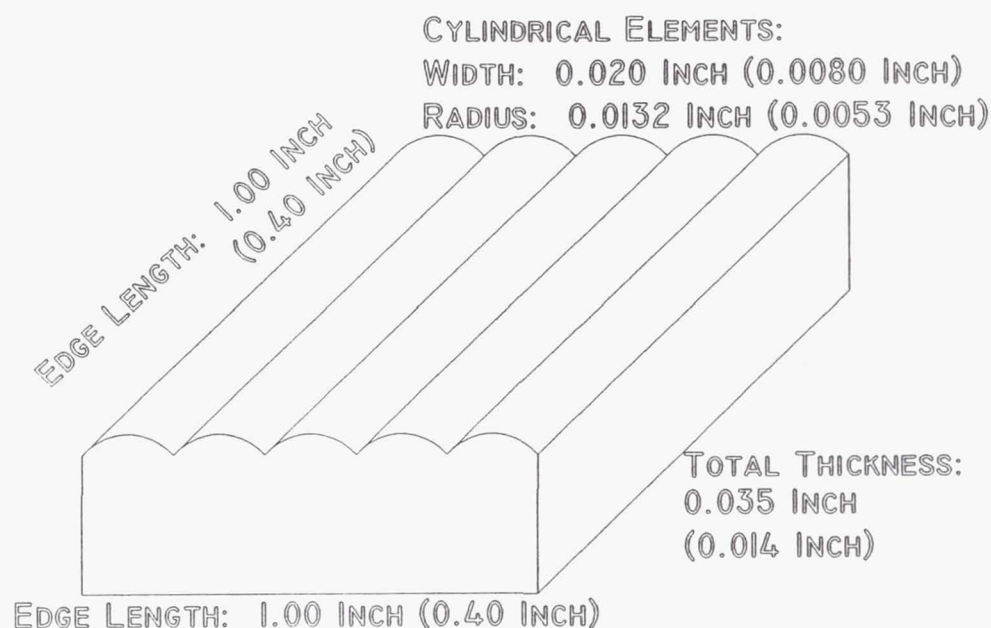


Figure 2. Cross-section of ENTECH's patented prismatic cell cover.



NOTE: INITIAL (MOLD) DIMENSIONS WITHOUT PARENTHESES
 FINAL (PART) DIMENSIONS AFTER SHRINKAGE SHOWN IN PARENTHESES

Figure 3. Schematic of selected sol-gel prismatic cell cover design. (Optical elements greatly exaggerated in size. Only 5 elements of the 50 elements are shown.)

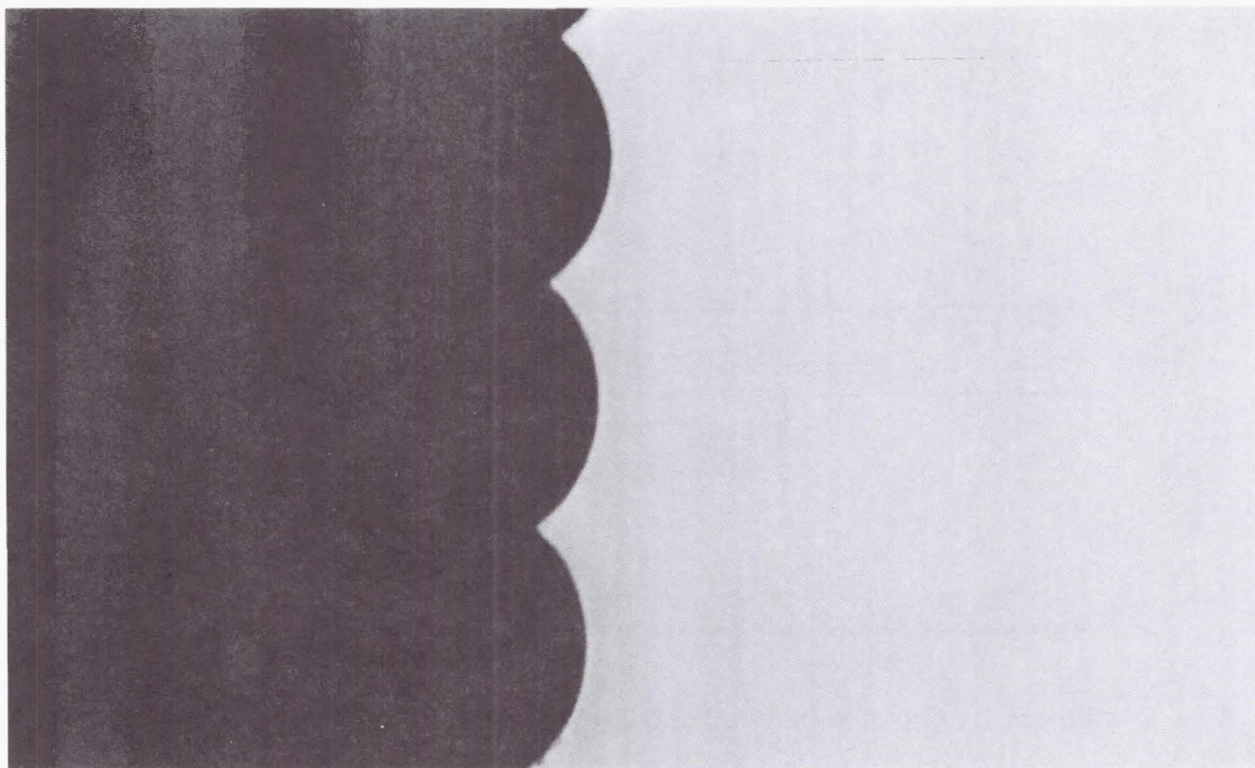


Figure 4. Silicone rubber impression of polystyrene mold at 50X magnification. (White color on right represents polystyrene mold cross-section).

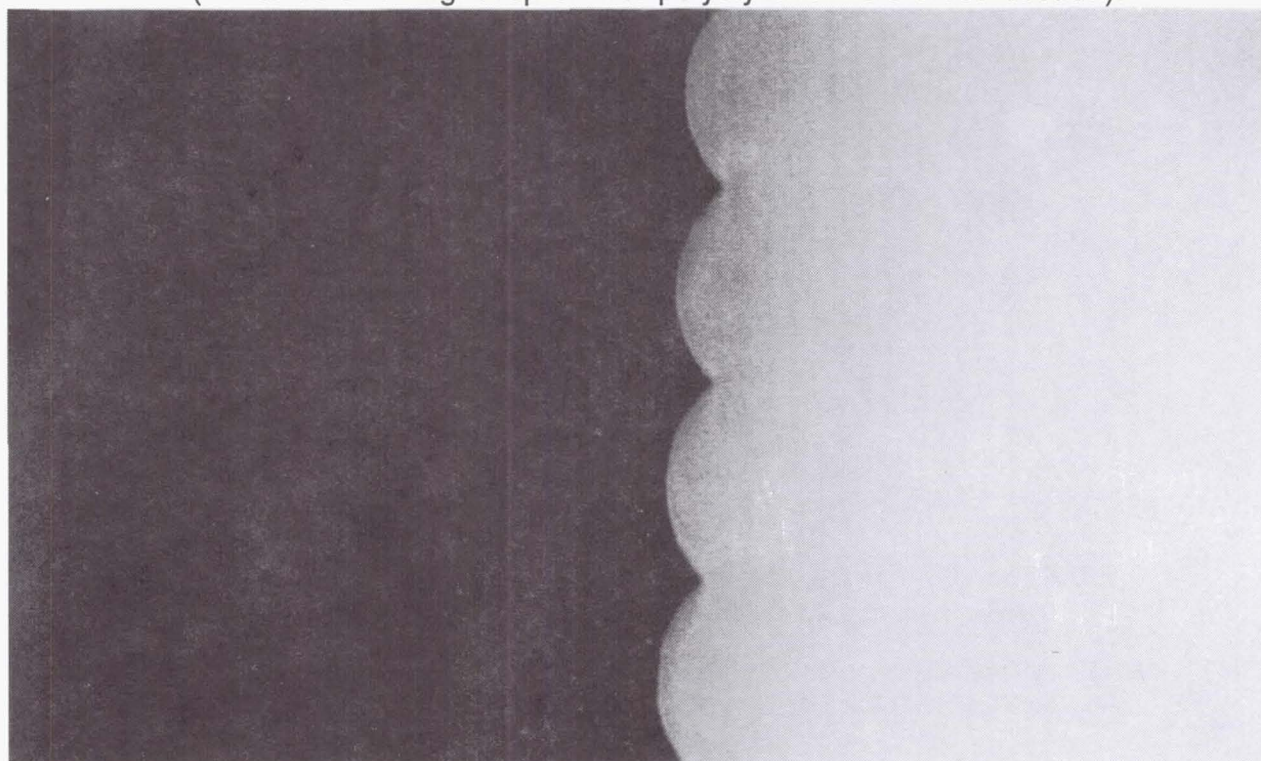


Figure 5. Silicone rubber impression of prismatic cell cover at 100X magnification. (White color on right represents silica cell cover cross-section).

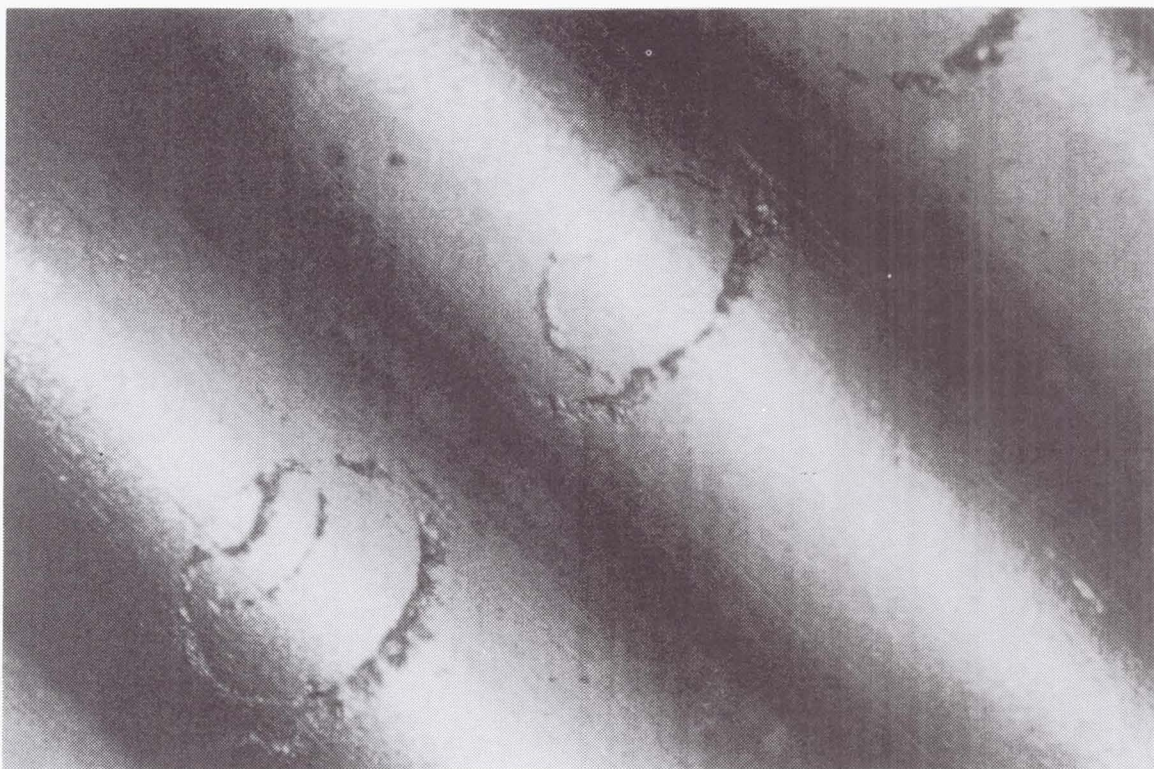


Figure 6. Polystyrene mold surface at 100X magnification.

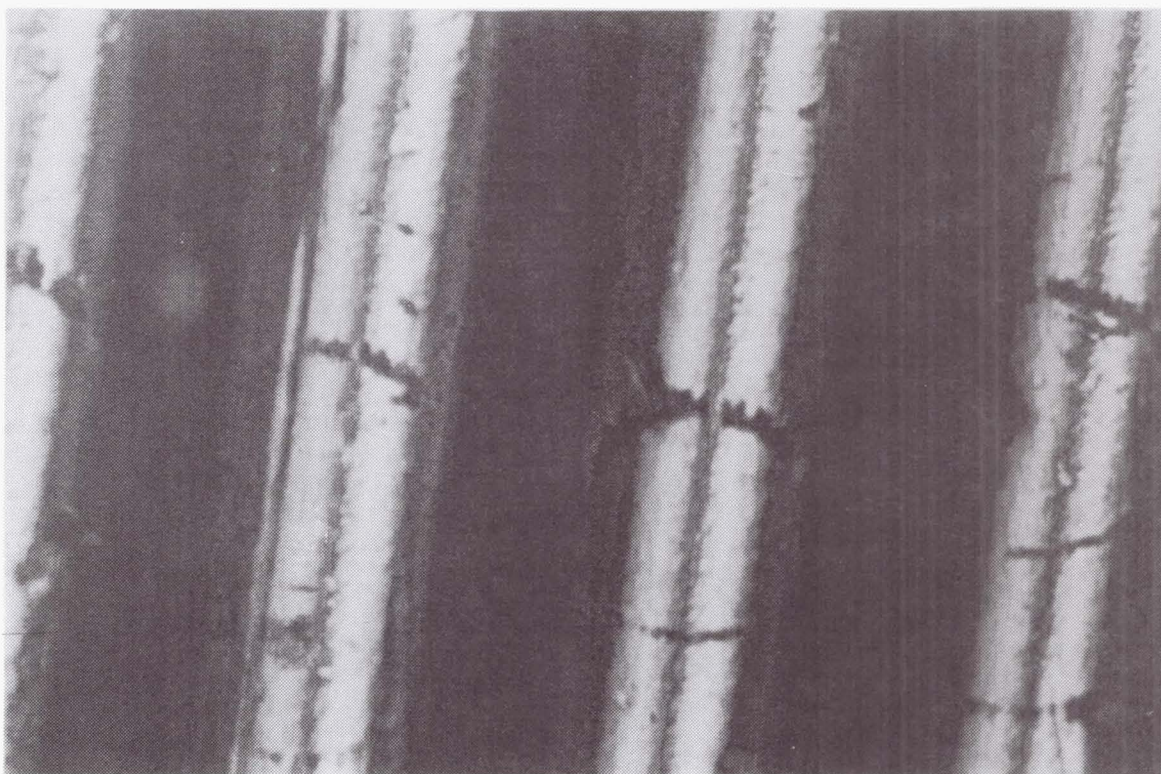
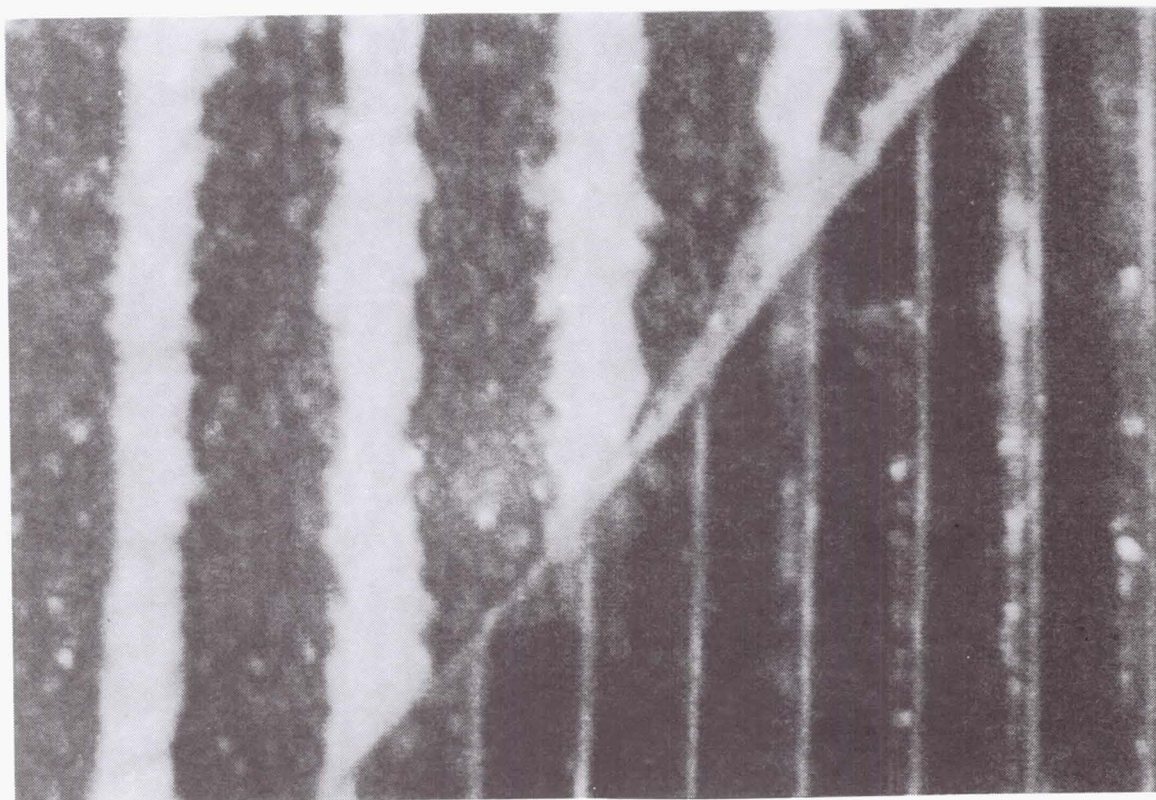


Figure 7. Silica cell cover surface at 200X magnification.



NOTES: - BARE "CELL" UPPER LEFT, COVERED "CELL" LOWER RIGHT
 - WHITE SIMULATED "GRIDLINES" ARE ON 0.016 INCH CENTERS

Figure 8. Photograph of sol-gel glass prismatic cell cover over a linear pattern simulating solar cell gridlines.

illustrate the excellent replication accuracy of the sol-gel technique, a photograph of the surface of the polystyrene mold is shown in Figure 6. Groove marks, created during fabrication of the master prism cover tool and transmitted to the polystyrene mold, are clearly visible. As seen in Figure 7, the same machining grooves present in the polystyrene mold were translated through the sol-gel processing and are also visible in the finished silica part.

Since the molds were made from an existing master tool, which was not designed to account for sol-gel processing shrinkage, photovoltaic cells with the proper front metallization pattern were not readily available. Thus a direct measure of current gain achieved by using the sol-gel prism cover could not be obtained at that time. In an effort to simulate the visible effects of the prism cover, a finished glass prismatic cover was placed over a pattern of alternating white and black parallel lines (simulating the gridlines on a concentrator cell). The results of this experiment are shown in Figure 8. The glass prism cover performed as expected, optically eliminating the white "gridlines" from view.

While the work in this area was limited to a single Phase I SBIR contract, a number of significant results were achieved under this effort. The replication capabilities of the sol-gel casting process were clearly demonstrated and two all-glass prismatic cell covers were made. While the progress was notable, a number of other issues such as final part thickness, sol-gel processing time, large-scale manufacturability, etc. will need to be addressed in future efforts.

SILICONE PRISMATIC CELL COVERS

As mentioned previously, prismatic cell covers have been used extensively in ENTECH's commercially-available terrestrial concentrator systems. The ENTECH concentrator is a linear design that uses a silicon concentrator cell approximately 1.5 by 3.5 inches in size. The cell operates at a nominal concentration of 22 suns and has about 25% front metallization grid coverage. Until recently, the silicone prism covers were made by a labor-intensive cast-and-cure process. While this process is very repeatable and produces high quality covers, it does not readily lend itself to a large quantity, low cost manufacturing approach.

During the past year, under the U.S. Department of Energy's Photovoltaic Manufacturing Technology (PVMaT) Initiative, ENTECH and 3M have successfully demonstrated a continuous production process for making silicone prismatic cell cover "tape". A photograph of a 200 ft. roll of the new prism cover "tape" is shown in Figure 9. This new product is made by a proprietary 3M process and results in excellent optical quality at a low manufacturing cost. The optical quality of the cell covers produced by this process is better than that of the covers made by the previous cast-and-cure process. The new "tape" not only reduces the cost of the prismatic cover by an order of magnitude, but also makes its application to the solar cell much easier and quicker. The "tape" comes with a relatively stiff transparent liner on the prismatic surface. The semi-rigid transparent liner supports the flexible silicone cover during alignment and during the rapid thermal curing of the adhesive layer between cover and cell. A cross-section of the new prism cover "tape," after it has been applied to a photovoltaic cell, is shown in Figure 10.

While this new process applies primarily to the terrestrial photovoltaic market, it has been discussed here because of the significant potential it offers for space applications. The process could not only be used to make prismatic covers for space photovoltaic devices, but it also could be applied to the fabrication of linear Fresnel lenses. The prismatic cell cover pattern on the current roll-to-roll process could easily be changed to a linear Fresnel lens concentrator pattern. This could significantly affect the ease of manufacturability, and cost, of future refractive concentrator optics. The development of the line-focus refractive concentrator is discussed further in the next section.

LINE-FOCUS FRESNEL LENS CONCENTRATORS

The mini-dome Fresnel lens concentrator system offers a number of distinct performance advantages over state-of-the-art planar arrays (ref. 8). However, these performance gains come with the added requirement of two-axis tracking for the point-focus concentrator system. While the performance improvements of advanced space concentrator systems are substantial at the array level, the ultimate benefit, and eventual use of such systems, will be dependent upon "system" implications and performance. This means that the array must not be viewed as a separate entity, but as an integral part of the spacecraft. Under this viewpoint, tracking requirements, stowability, structural dynamics, etc. become as important as the panel efficiency, specific power and radiation hardness of the array.

Keeping these "system" aspects in mind, there may be a number of space missions where single-axis tracking requirements have a distinct benefit over double-axis tracking. Thus, NASA Lewis has decided to initiate a small program to investigate linear refractive concentrator systems for use in space. Under a SBIR Phase I contract, ENTECH will develop a line-focus Fresnel lens concentrator element. The line-focus lens will be made in a flat form, and then mechanically contoured to the desired aspheric shape. A sketch of the linear concentrator element is shown in Figure 11. The prototype elements will be fabricated with various rim angles and focal plane irradiance profiles to allow for the experimental verification of various lens design parameters.

While the program has just started, there already seem to be a number of inherent advantages to the linear concentrator element. Besides the reduction in tracking requirements to a single axis, linear lenses seem to offer substantial benefits in ease of manufacturability and cost over refractive point-focus elements. Indeed, the new continuous silicone prism cover "tape" process, discussed above, could be directly applicable to linear Fresnel lens production. These benefits still need to be quantified, as do the effects of reduced concentration ratio and increased cell area on system performance and cost. This program will address these issues and, in doing so, try to determine the usefulness of linear Fresnel lens concentrator systems for various space missions.

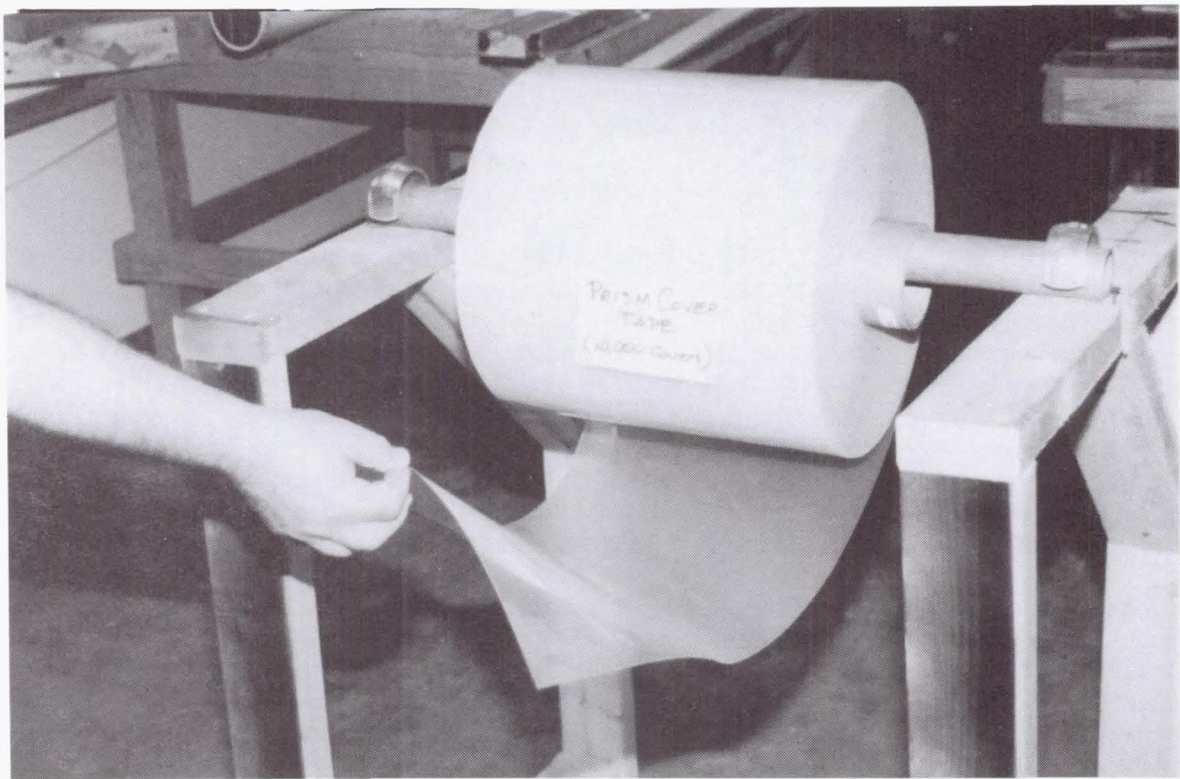


Figure 9. Photograph of 200 ft. roll of prismatic cell cover "tape" developed under PVMaT Program.

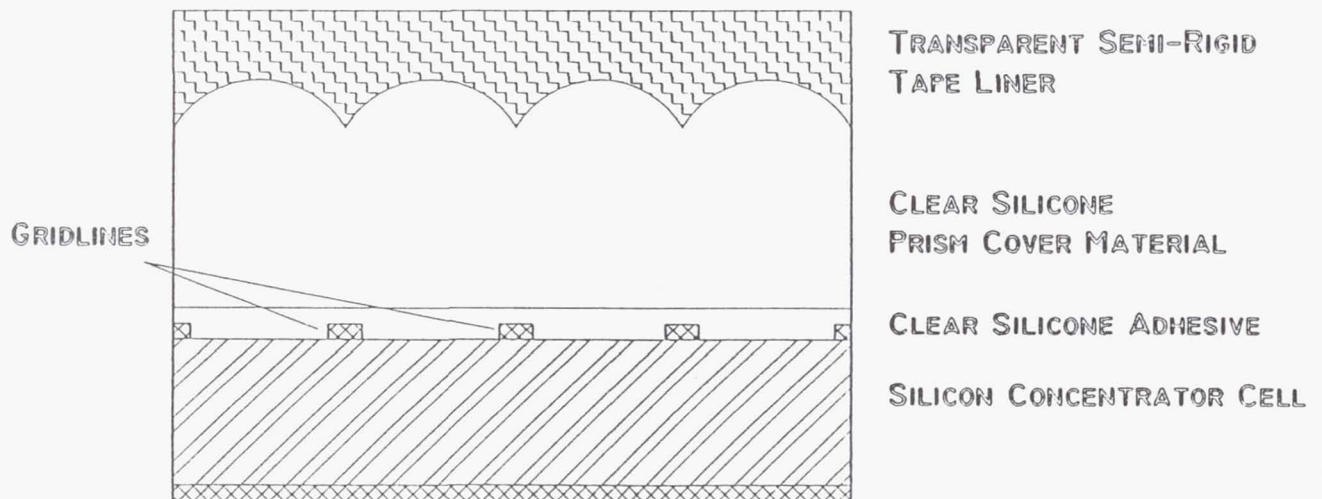


Figure 10. Schematic of new prismatic cell cover "tape" material applied to a terrestrial silicon concentrator cell.

Laminated Ceria Microglass/Silicone RTV Line Focus Fresnel Lens

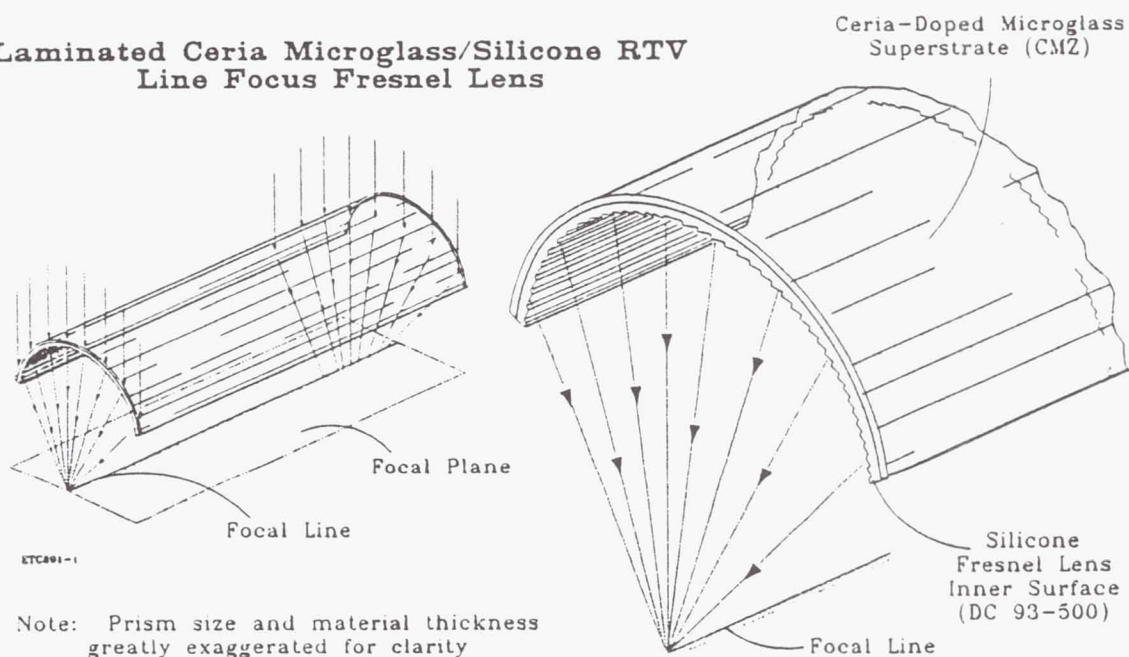


Figure 11. Proposed Linear Fresnel Lens Photovoltaic Concentrator Element for Space

SUMMARY

A number of recent achievements have been made in the development of space-based refractive concentrator systems and components. The mini-dome Fresnel lens concentrator program continues to grow, currently emphasizing the areas of manufacturability and environmental durability. The program is now awaiting critical flight data from a variety of space experiments. All-glass prismatic cell covers have been made, demonstrating the ability of the sol-gel process to fabricate the intricate designs necessary for good prismatic cell cover performance. Advances have been made in the manufacturability of silicone prism covers for terrestrial photovoltaic concentrator systems under the Department of Energy's PVMat Initiative. This new roll-to-roll prism cover "tape" process may have direct applicability to a variety of space refractive concentrator systems, significantly influencing the manufacturability and cost of these advanced systems. As a supplement to the current refractive concentrator program, work has also started on the development of a line-focus Fresnel lens concentrator element. These developments, along with similar improvements in the efficiency photovoltaic concentrator cells, could have a dramatic impact on the performance of future spacecraft power systems.

REFERENCES

1. M.F. Piszczor and M.J. O'Neill, "Development of a Dome Fresnel Lens/Gallium Arsenide Photovoltaic Concentrator for Space Applications," Proc. of 19th IEEE Photovoltaic Specialist Conf., New Orleans, LA, May 1987, pp. 479-484.
2. M.F. Piszczor et al, "A High-Performance Photovoltaic Concentrator Array: The Mini-Dome Fresnel Lens Concentrator with 30% Efficient GaAs/GaSb Tandem Cells," Proc. of 22nd IEEE Photovoltaic Specialist Conf., Las Vegas, NV, October 1991, pp. 1485-1490.

3. J. Avery, J.S. Bauman, P. Gallagher and J.W. Yerkes, "TAB Interconnects for Space Concentrator Solar Cell Arrays," Proc. of 12th NASA Space Photovoltaic Research and Technology Conf., Cleveland, OH, October 1992, to be published.
4. H.B. Curtis, D.A. Guidice, P.S. Severance and M.F. Piszczor, "Results of Thermal Vacuum Tests for the PASP+ Flight Modules," Proc. of 12th NASA Space Photovoltaic Research and Technology Conf., Cleveland, OH, October 1992, to be published.
5. D.A. Guidice, P.S. Severance and K.C. Reinhardt, "Measurement of High-Voltage and Radiation-Damage Limitations to Advanced Solar Array Performance," Proc. of 11th NASA Space Photovoltaic Research and Technology Conf., Cleveland, OH, May 1991, p. 33-1.
6. J.E. Avery et al, "Lightweight Concentrator Module with 30% AM0 Efficient GaAs/GaSb Tandem Cells," Proc. of 21st IEEE Photovoltaic Specialist Conf., Kissimmee, FL, May 1990, pp. 1277-1281.
7. J.L. Noguez and A.J. LaPaglia, "Processing, Properties, and Applications of Sol-Gel Silica Optics," Proc. of SPIE's 33rd Annual International Technical Symposium on Optical and Optoelectronic Applied Science and Engineering, San Diego, CA, 1989.
8. R. Kraus, "Mass Properties Survey of Solar Array Technologies," Proc. of 11th NASA Space Photovoltaic Research and Technology Conf., Cleveland, OH, May 1991, p. 23-1.

NEW EXPERIMENTAL TECHNIQUES FOR SOLAR CELLS

R. Lenk
Space Systems/Loral
Palo Alto, CA 94303

Solar cell capacitance has special importance for an array controlled by shunting. Experimental measurements of solar cell capacitance in the past have shown disagreements of orders of magnitude. Correct measurement technique depends on maintaining the excitation voltage less than the thermal voltage. Two different experimental methods are shown to match theory well, and two effective capacitances are defined for quantifying the effect of the solar cell capacitance on the shunting system.

INTRODUCTION

New orbital platforms will control the power delivery of their solar arrays by pulse-width modulation shunting, for example at 20kHz. Figure 1 shows a block diagram of the shunt for an array. Each time the shunt turns on, it must not only shunt the short-circuit current of the array, it must also discharge an effective capacitance associated with the cells. Conversely, when the shunt turns off, the array does not instantaneously rise to its operating point on its I-V curve, it must charge up this effective capacitance to the operational voltage before it can deliver power.

There are two major consequences. The first is that there will be extra currents flowing in the wires connecting the array and the shunt, due to the capacitance, beyond those anticipated by naive inspection of the I-V curve, generating additional electromagnetic interference (EMI). The design must provide filtering to suppress this EMI. The capacitance also means there will be higher peak currents in the shunt than the array short-circuit current, which can lead to failure of the shunt. Second, the shunt, being non-ideal, has losses dependent on the current and voltage; discharging a capacitance will mean additional losses in the shunt, which must then be designed to withstand the additional power dissipation.

THEORY

As is well known from semiconductor theory (ref. 1), a p-n junction has two types of capacitance, transition capacitance and diffusion capacitance. Transition capacitance is due to the space-charge region of the junction, and depends on the temperature and external bias. It is a "real" capacitance in the sense that there is a real displacement current corresponding to it.

The diffusion capacitance expresses a variation in stored charge with excess carrier density. It too depends on junction temperature and external bias. In the sense that it is a differential effect, depending on changes in stored charge rather than a displacement current, it might be called a "pseudo-capacitance"; but for the purposes of measurements, as well as for the issues raised in the introduction, it is just as real as the transition capacitance.

For most bias conditions of a cell, the diffusion capacitance is much larger than the transition capacitance, and a good first approximation will be to ignore the transition capacitance. Diffusion capacitance is given by:

$$C_D = \frac{q^2 A n_i^2 L_e}{k T N_A} e^{q V / k T} \quad (1)$$

where n_i , the intrinsic carrier density, is given by:

$$n_i = \text{constant} * T^{3/2} e^{-q E_g / 2 k T} \quad (2)$$

Here, q is the electron charge, A is the cell area, k is Boltzmann's constant, T is the absolute temperature in Kelvin, and V is the cell voltage. N_A is the dopant concentration, L_e is the electron diffusion length, with a $T^{1/2}$ temperature dependence, and E_g is the band gap, which may be represented as a constant minus a term linear in the temperature.

Combining all these terms, we find that the diffusion capacitance has the form:

$$C_D = \text{constant} * T^{5/2} e^{q(V - E_g) / k T} \quad (3)$$

with all temperature dependencies explicitly shown, except for E_g . E_g 's term linear in the temperature, when divided by kT becomes another constant, that could be absorbed into the leading constant of C_D .

EXPERIMENT

The cell capacitance thus has an exponential dependence on the cell voltage. It will be measured by exciting the cell with an ac voltage, as shown in Figure 2. Expanding equation (3) into a Taylor series,

$$C_D = \text{constant} * T^{5/2} [1 + q(V - E_{gap}) / k T + \dots] \quad (4)$$

we see that the condition for the capacitance to be approximately constant during the measurement at some fixed temperature is that V , the excitation voltage, must be smaller than kT/q , the thermal voltage, approximately 26mV at room temperature. For these experiments, the signal-to-noise ratio improves with the excitation voltage, and so 10mV was selected as a reasonable compromise.

Figure 2 shows a block diagram of the experimental setup. The cell is illuminated by a one sun source, and is kept at a fixed temperature by a circulating water system in its mounting fixture. The cell is loaded by a power supply in series with an inductor, the power supply sinking current to maintain the cell at a particular point on the I-V curve, and the inductor buffering the ac drive. A sweepable AC signal is coupled into the cell via a capacitor, and the impedance is deduced by dividing the AC voltage on the cell by the AC current into the cell. The inductor is necessary to prevent the AC signal from trying to drive the power supply.

A typical result is shown in Figure 3, for a cell at 65C, 150mV and 619mA. The low frequency impedance, though noisy up to approximately 10kHz, is essentially a constant, dV/dI (not V/I !); the noise is due to the low excitation level. At somewhat higher frequencies (10kHz to 300kHz), the impedance rolls off at 6dB/octave, corresponding to a capacitor. At 300kHz, there is a resonance between the capacitance of the cell and the inductance of the wires attached to it. Finally, at frequencies above 300kHz, the impedance increases at 6dB/octave, corresponding to the wiring inductance.

RESULTS

Two separate methods were used to calculate cell capacitance from the data of Figure 3, and similar plots at other temperatures and points on the I-V curve. In the first, the capacitance was calculated by using the well-known impedance characteristic of a capacitor,

$$|Z| = 1 / (2 \pi f C) \quad (5)$$

at a particular frequency f (20kHz here), and deducing the capacitance from the measured impedance. In a second method, the wiring inductance was found from the high-frequency impedance; it is of course independent of temperature or operating point. Given this and the resonant frequency from the impedance measurement, the capacitance can be calculated from the well-known condition for resonance:

$$f = 1 / [2 \pi \sqrt{L C}] \quad (6)$$

Both independent methods of calculating capacitance yielded results that were the same to within experimental uncertainty. Close to open-circuit conditions, both methods tended to fail, because the capacitance was so large that it became comparable in impedance with the series resistance of the cell. This makes the impedance curve look essentially flat until it reaches the inductance portion. This failure was considered unimportant because it occurs at voltages above the maximum intended operating voltage of the cell; it could be remedied by placing n cells in series, which would reduce the capacitance by n and increase the resistance by n .

The capacitances so measured were then fitted to the expected form of the capacitance, as given in equation (3) above, using a least-squares method. The constant was determined to be $0.8 \text{ F-K}^{(-5/2)}$, using $E_g = 1.222 - 0.0004 * T$ volts. A plot of the capacitance so determined, at $T = 353\text{K}$ ($=80\text{C}$) is shown in Figure 4 as the top curve, "Apparent Capacitance", extrapolated from a quarter cell (which was actually measured) to a string of 400 cells in series. An offset of 5nF was added at short-circuit to account for the transition capacitance not included in equation (3). As can be seen, the capacitance reaches almost $5\mu\text{F}$ at 180V ($=450\text{mV}/\text{cell}$, with an open circuit voltage at this temperature of 484mV). This is a very significant size capacitance, justifying the concerns cited in the Introduction. The shunt must be designed to take into account this capacitance, plus some margin due to uncertainties in lot-to-lot variation of the cells.

DISCUSSION

The Introduction discussed two major areas wherein the cell capacitance would have a major effect on performance of the shunt power control system: EMI and peak currents; and increased power dissipation in the shunt. The effects were grouped this way because they depend on two separate aspects of the capacitance, which, though equivalent for linear capacitors, have a complex relationship for the type of non-linear capacitance manifested by solar cells. These aspects are : 1) The amount of stored charge in the capacitance; and 2) The amount of stored energy in the capacitance. The stored charge will determine aspects of cell operation which depend on currents, such as EMI, which is specified in terms of allowable currents at various frequencies, and peak currents. The stored energy will determine aspects of cell operation which depend on both current and voltage, such as the shunting element being used to control the array power output.

For a linear capacitor, the stored charge and stored energy are simply related:

$$Q = C V \quad (7)$$

and

$$E = 1/2 C V^2 \quad (8)$$

with V the voltage, C the capacitance and Q and E the stored charge and stored energy, respectively.

For a non-linear capacitor, these relationships could not be expected to hold; for example, if in equation (7) the voltage is doubled, the stored charge would double. If on the other hand, the voltage on a non-linear capacitor were doubled, and at the same time the capacitance doubled due to its dependence on voltage, the stored charge would quadruple. Such changes leave unclear how to calculate current, or power for equation (8).

Equations (7) and (8) can be rewritten in such a way as to make them applicable to all capacitors, whether linear or non-linear:

$$Q = \int C dV \quad (7a)$$

and

$$E = \int C * V dV \quad (8a)$$

Clearly, these reproduce equations (7) and (8) when C is independent of V . They will also work for non-linear capacitors, since C may now be an explicit function of V . In particular, current, defined as $I = dQ/dt$, with equation (7a) explicitly recognizes the change in both capacitance and voltage as a function of time. A similar description holds for power, defined as $P = dE/dt$, in equation (8a).

For many purposes, including modelling, what is desired is not an analytic expression for a non-linear capacitance, plus integrals describing charge and energy, but rather a single number (or a couple of numbers) that somehow characterizes the non-linearity as it is applicable to the particular circuit being designed. In the case of a shunt, the voltage is swinging from an output voltage, V_{out} , to 0, or else from 0 to V_{out} . What is desired, then, is an effective linear capacitance that for some particular V_{out} will deliver the same current, or the same power, as the actual non-linear capacitor does in the same circuit.

To accomplish this, two new capacitances can be defined, based on equation (7a) and (8a) above. A charge-effective capacitance, C_Q , will be defined to be a linear capacitor that has the same total charge in it as the non-linear capacitor does at the same voltage; it is of course, necessarily a function of voltage:

$$C_Q = \frac{1}{V_{out}} \int_0^{V_{out}} C(V) dV \quad (9)$$

That is, the total charge stored in the non-linear capacitance at a particular voltage may be calculated by inserting the voltage and C_Q into equation (7). When C is independent of V , equation (9) is an identity, stating that the charge-effective capacitance is equal to the capacitance, as it must. For C a function of V , C_Q is less than $C(V)$ for any given voltage, as is to be expected: part of the voltage "goes into increasing the capacitance" rather than "charging up the capacitor".

Similarly, an energy-effective capacitance, C_E , can be defined, which will be a linear capacitor containing the same energy as the original non-linear capacitance does at a given voltage. Total energy stored in the non-linear capacitance may be calculated by inserting the voltage and C_E into equation (8).

$$C_E = \frac{2}{V_{out}^2} \int_0^{V_{out}} C(V) * V dV \quad (10)$$

Again, the equation states the identity of C_E and C for C independent of V ; and for C a function of V , C_E is less than $C(V)$ for any given voltage, again based on an heuristic argument concerning conservation of energy.

Figure 4 shows these three capacitances. The measured capacitance is the top curve, labelled "C(apparent)", the energy-effective capacitance is the middle curve, labelled "C(energy)", and the charge-effective capacitance is the bottom curve, labelled "C(charge)". As expected (see the Appendix for a mathematical derivation), the capacitances are ordered: Measured $C > C_E > C_Q$. These curves can now be used for modelling the solar arrays used on an orbital platform, and for designing the shunt circuit used to control power delivery from this array.

As a final note, it may be observed that for purposes of EMI, the charge-effective capacitance does not tell the whole story. A linear capacitor (with no ESR) could form a resonant tank with (say) a cable inductance, yielding an infinite Q . The actual non-linear capacitance of the cells swings with voltage, which has the effect of de-Qing such a tank circuit, and thus reducing EMI at such a resonant frequency. Work is ongoing to describe this reduction in Q in a form compatible with the linear equivalent circuits introduced here.

APPENDIX

I will demonstrate that the two newly defined capacitances and the measured cell capacitance are ordered, $C \geq C_E \geq C_Q$, subject to the conditions that $V_{out} \geq 0$, and that $C(V)$ is a monotonically non-decreasing function of V : $dC/dV \geq 0 \forall V$.

The first inequality puts a bound on C_E . It is easily established by considering that since $dC/dV \geq 0$, $C(V_{out}) \geq C(V) \forall V \leq V_{out}$. Therefore,

$$C_E = \frac{2}{V_{out}^2} \int_0^{V_{out}} C(V) * V dV \leq \frac{2}{V_{out}^2} C(V_{out}) \int_0^{V_{out}} V dV = C(V_{out}), \quad (A1)$$

QED. The inequality $C_E \geq C_Q$ may be demonstrated by first observing that both C_E and C_Q are functions of V_{out} . Since $V_{out} \geq 0$, both can be multiplied by V_{out}^2 :

$$2 \int_0^{V_{out}} C(V) * V dV \stackrel{?}{\geq} V_{out} \int_0^{V_{out}} C(V) dV. \quad (A2)$$

Now, both sides of this inequality can be seen to be = 0 when $V_{out} = 0$; further, since $C(V)$ is monotonically non-decreasing, both sides of the inequality are also. Therefore, the inequality will still be valid if differentiated with respect to the variable, V_{out} :

$$2 C(V_{out}) V_{out} \stackrel{?}{\geq} V_{out} C(V_{out}) + \int_0^{V_{out}} C(V) dV \quad (A3)$$

or

$$V_{out} C(V_{out}) \stackrel{?}{\geq} \int_0^{V_{out}} C(V) dV. \quad (A4)$$

But this is again apparent because $C(V_{out})$ is an upper bound for $C(V)$ for $0 \leq V \leq V_{out}$. Therefore the original inequality, $C_E \geq C_Q$ is also true, and the proposition is demonstrated.

REFERENCES

1. Greiner, R.A.: "Semiconductor Devices and Applications," McGraw-Hill (1961).

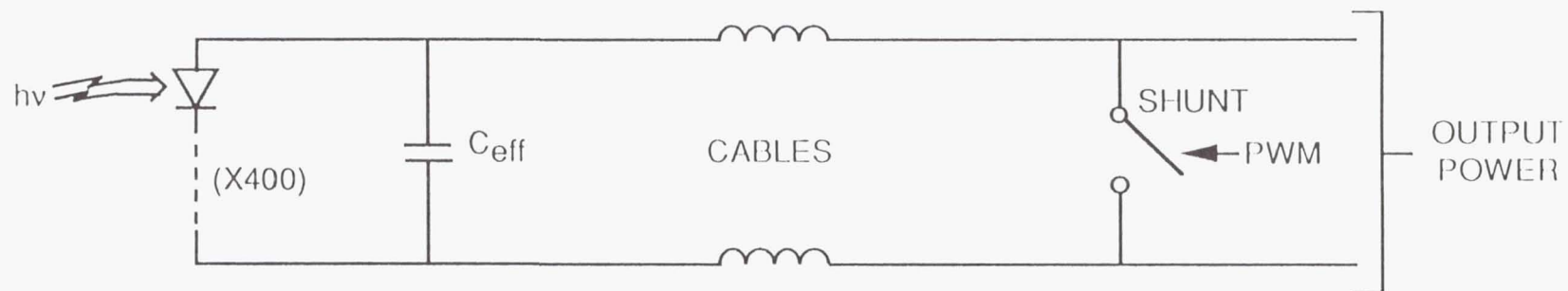


FIGURE 1. BLOCK DIAGRAM OF SHUNT POWER CONTROL SYSTEM FOR ARRAY. OUTPUT POWER IS DETERMINED BY PERCENTAGE OF TIME THE SHUNT IS OFF.

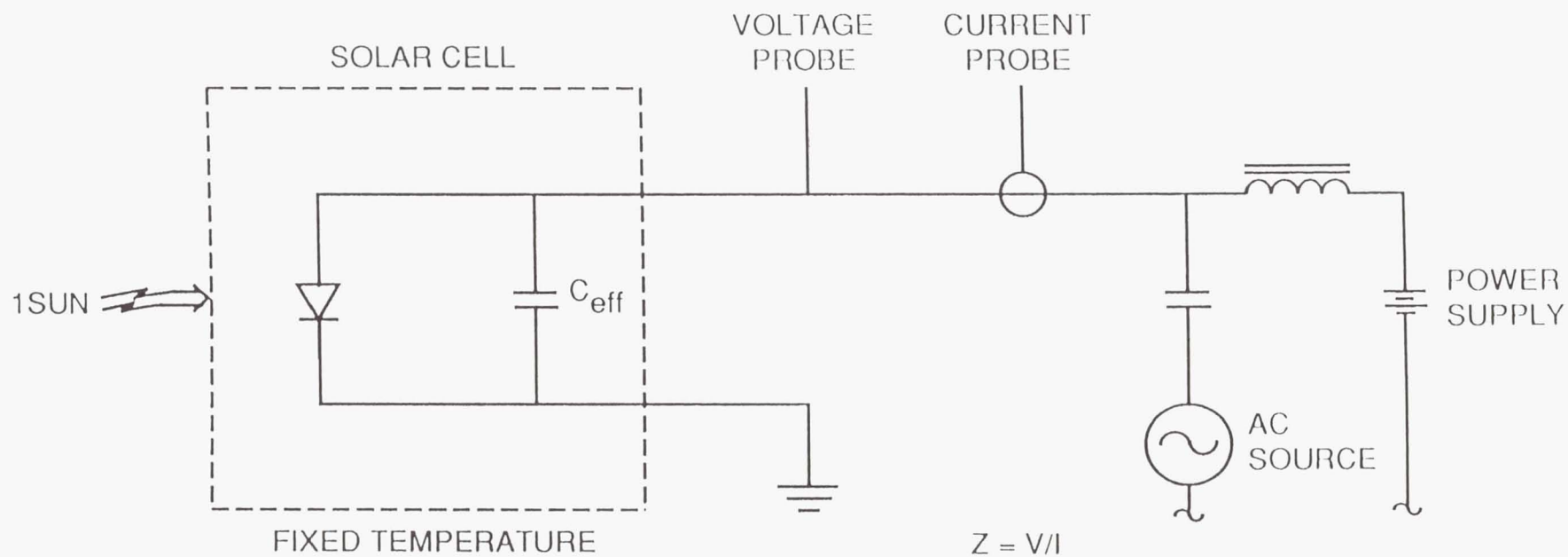
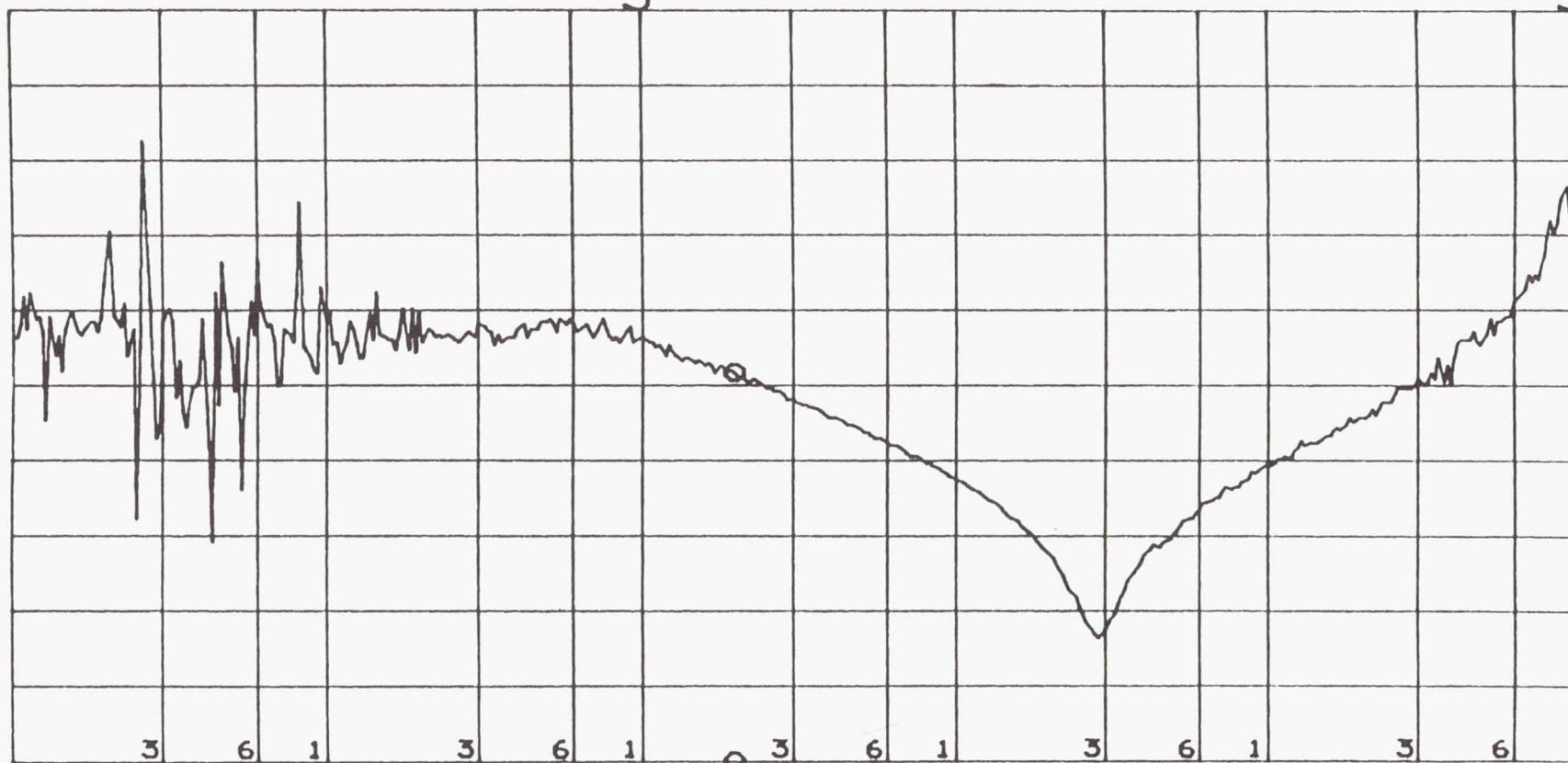


FIGURE 2. EXPERIMENTAL SETUP FOR MEASURING CELL CAPACITANCE.
THE PROBES ARE PHASE-LOCKED TO THE AC SOURCE TO IMPROVE
SIGNAL-TO-NOISE RATIO.

A: T/R (dB) B: θ o MKR 19 952.623 Hz
 A MAX 90.00 dB GAIN 41.6633 dB
 B MAX 180.0 deg PHASE deg



A/DIV 10.00 dB START 100.000 Hz
 B MIN -180.0 deg STOP 10 000 000.000 Hz
 OSC= 1.00E-02 V

Figure 3. Cell impedance vs. frequency, Y-axis in db-ohms.

CAPACITANCE FOR 400 SERIES CELLS

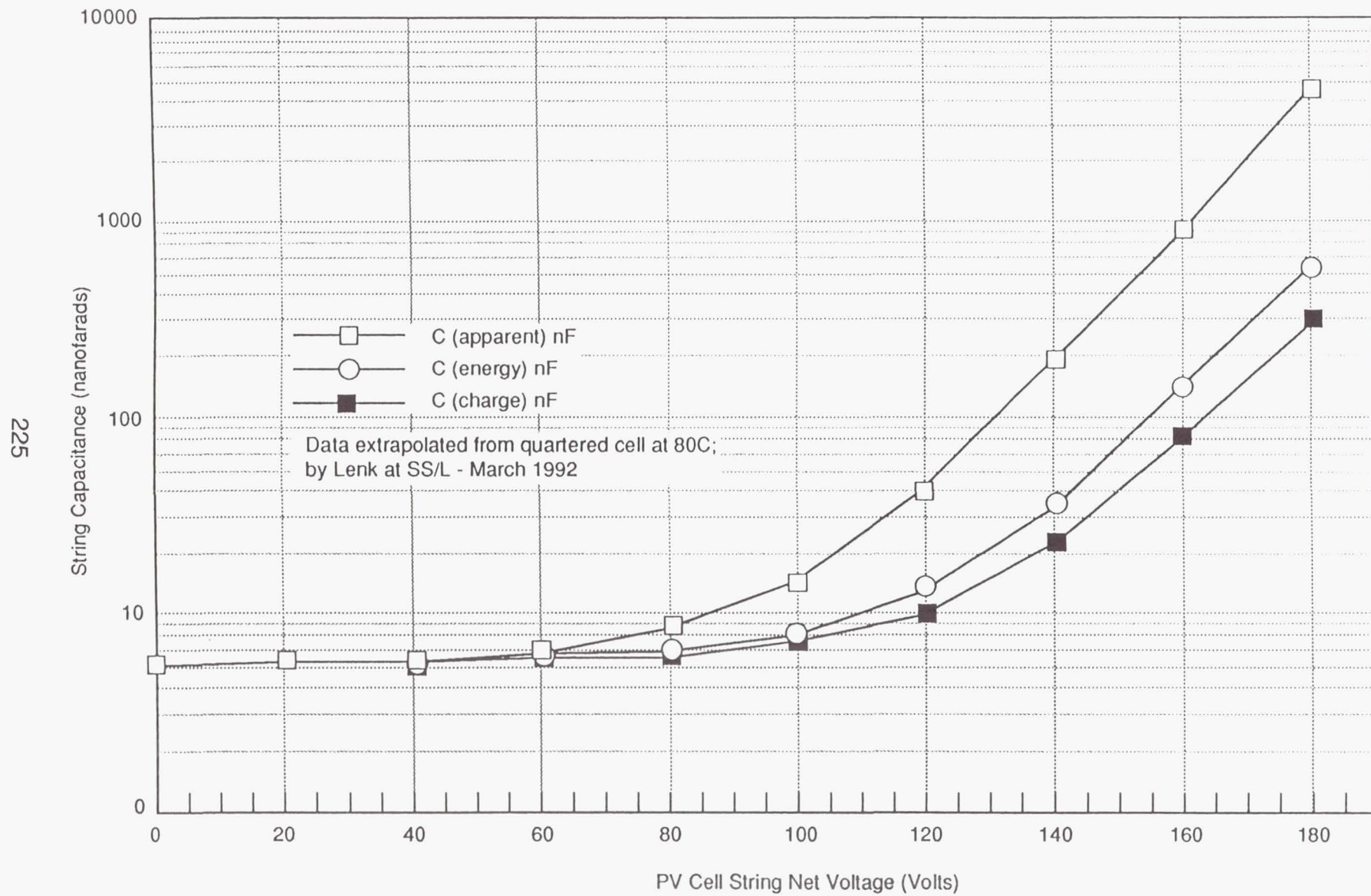


Figure 4

Radiation Effects in $\text{Ga}_{0.47}\text{In}_{0.53}\text{As}$ Solar Cells

R.J. Walters, G.J. Shaw*, and G.P. Summers

Naval Research Laboratory, Washington, DC 20375

* G.J. Shaw is supported by the ONT post doctoral fellowship program

S.R. Messenger

SFA, Inc., Landover, MD 20785

ABSTRACT

The effects of irradiating $\text{Ga}_{0.47}\text{In}_{0.53}\text{As}$ p-i-n junctions with 1 MeV electrons have been measured using Deep Level Transient Spectroscopy, (DLTS) and both dark and illuminated (1 sun, air mass zero (AM0)) current-voltage (I-V) measurements. The I-V measurements were made over the range $100\text{K} < T < 350\text{K}$. Temperature coefficients of the $\text{Ga}_{0.47}\text{In}_{0.53}\text{As}$ photovoltaic parameters are presented which follow the same general behavior as other solar cell materials (e.g. Si and GaAs). Fits of the dark I-V data to the two term diode equation before irradiation were satisfactory, yielding an estimated band-gap energy of 0.79 eV. The recombination component of the dark current was found to increase linearly with fluence. DLTS detected two radiation-induced defect levels, one shallow ($E_c - 0.10$ eV) and one near mid-gap ($E_c - 0.29$ eV), and it is the near mid-gap level which is expected to be the cause of the dark current increase. The radiation-induced degradation of the open circuit voltage is shown to be accurately predicted from the dark I-V measurements. The degradation of the open circuit voltage dominated the radiation response of the photovoltaic parameters while the short circuit current was only moderately degraded. This behavior is qualitatively explained in terms of the base thickness and dopant level. Appropriate changes in the device structure are suggested which should increase the radiation resistance. Isochronal thermal annealing induced recovery in the photovoltaic parameters at ≈ 400 K, coinciding with an annealing stage of the near mid-gap defect level.

INTRODUCTION

The radiation resistance of InP solar cells is well known to this community. Equally well known are the rapid advance made by the National Renewable Energy Laboratory (NREL) in growing a high efficiency, monolithic InP/ $\text{Ga}_{0.47}\text{In}_{0.53}\text{As}$ tandem solar cell [ref 1-3] (figure 1). This cell has achieved efficiencies of 31.8% under 50 suns concentration (direct, 25°C) which was the first time that a monolithic tandem had exceeded 30% efficiency. Under 1 sun, AM0 conditions, this cell has achieved efficiencies of 23.9% (25°C). It has been generally accepted that a multi-band-gap cell with efficiencies of 24% is a viable technology for space power. Clearly, this proves the InP/ $\text{Ga}_{0.47}\text{In}_{0.53}\text{As}$ tandem cell to be one of the most efficient photovoltaic power sources available. Because of this, the Naval Research Laboratory (NRL) is participating in an interagency research contract with NREL to develop the InP/ $\text{Ga}_{0.47}\text{In}_{0.53}\text{As}$ tandem into a radiation resistant, high efficiency space power source. The financial support for this research is provided in part by the Office of Naval Research.

While the InP/ $\text{Ga}_{0.47}\text{In}_{0.53}\text{As}$ tandem cell has demonstrated a beginning of life (BOL) power output which is satisfactory for a space power system, its radiation resistance must be optimized to fully space qualify the cell. The NRL research is designed to do this. As shown at the last InP and Related Materials Conference (April 1992), the top cell of the InP/ $\text{Ga}_{0.47}\text{In}_{0.53}\text{As}$ tandem displays a radiation resistance as high as that of the Spire InP homojunctions [4]. However, the radiation response of the $\text{Ga}_{0.47}\text{In}_{0.53}\text{As}$ bottom cell still needs investigation. This paper reports continuing results of 1 MeV electron irradiation of $\text{Ga}_{0.47}\text{In}_{0.53}\text{As}$.

While this study concerns the $\text{Ga}_{0.47}\text{In}_{0.53}\text{As}$ bottom cell, not enough of these devices were immediately available to conduct a full radiation study. Therefore, commercially available $\text{Ga}_{0.47}\text{In}_{0.53}\text{As}$ photodetectors were used as solar cells (fig. 2). It is the radiation response of these devices which is presented here. It is important to note that while the photodetectors are reasonable representations of a $\text{Ga}_{0.47}\text{In}_{0.53}\text{As}$ solar cell, they represent only a single

possible device structure. In particular, the dopant density in the base is an order of magnitude less than the present design of the tandem cell. In this way, the present data is providing information on the dependence of the radiation response on the device structure. This data will be used ultimately to design the $\text{Ga}_{0.47}\text{In}_{0.53}\text{As}$ bottom cell for maximum radiation tolerance. Therefore, the radiation resistance of the $\text{Ga}_{0.47}\text{In}_{0.53}\text{As}$ bottom cell will be higher than that of the photodetectors measured presently.

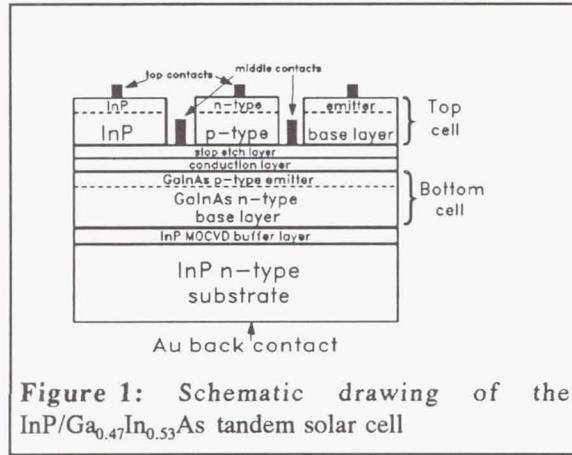


Figure 1: Schematic drawing of the $\text{InP}/\text{Ga}_{0.47}\text{In}_{0.53}\text{As}$ tandem solar cell

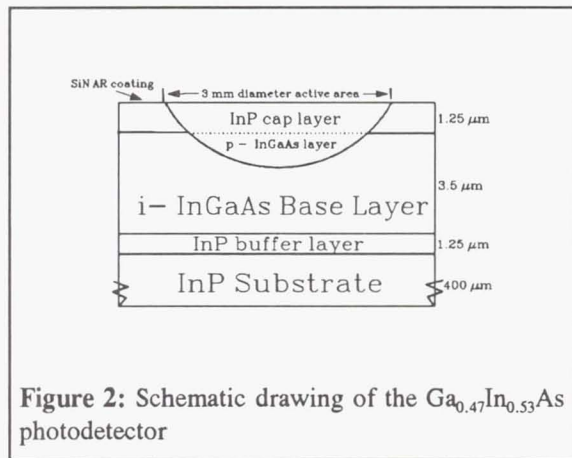


Figure 2: Schematic drawing of the $\text{Ga}_{0.47}\text{In}_{0.53}\text{As}$ photodetector

voltage measurements). The concentration ranged from $2 \times 10^{15} \text{ cm}^{-3}$ at the junction to about $6 \times 10^{15} \text{ cm}^{-3}$ at the substrate. The entire device was capped by $1.25 \mu\text{m}$ InP layer. The p^+ emitter was formed by thermally diffusing Zn through the InP cap into the $\text{Ga}_{0.47}\text{In}_{0.53}\text{As}$ base. The active area was 7.07 mm^2 . A SiN antireflective coating was applied.

RESULTS

A. Dark I-V Measurements

Dark I-V measurements were performed before and after each irradiation step. These measurements were used to determine the initial quality of the junctions and to investigate the important contributions to the junction current. The forward bias dark I-V behavior of a semiconductor junction can be described by [ref 5]

$$I_F = I_{01} (e^{qV/k_B T} - 1) + I_{02} (e^{qV/2k_B T} - 1) + \frac{V}{R_{sh}} \quad (1)$$

where R_{sh} is the diode shunt resistance. The first term on the right hand side describes the diffusion current while

EXPERIMENTAL NOTES

Results of three different types of measurements are presented- deep level transient spectroscopy (DLTS), current-voltage (I-V) measurements in the dark, and I-V measurements under simulated solar illumination. The DLTS measurements were made using a Bio-Rad DL4600 spectrometer with both liquid nitrogen and liquid helium cooled cryostats. The temperature ranged from 30 to 300 K. A 1 ms fill pulse was used for the DLTS measurements, which was sufficient to saturate the DLTS signal. A reverse bias of -2 V was used. The forward bias was zero volts. Attempts to detect minority charge carrier trapping centers were made by applying a positive fill pulse and by using laser excitation, but no minority carrier traps were detected.

I-V measurements were made with the sample mounted in the DLTS cryostat which allowed measurements throughout the temperature range 100 to 350 K. The liquid nitrogen cryostat is equipped with a sapphire window to allow for illumination of the sample. To simulate space conditions, an AM0 filter was used on the solar simulator adjusted to 1 sun intensity using a standard $\text{InP}/\text{Ga}_{0.47}\text{In}_{0.53}\text{As}$ tandem cell calibrated by the NREL. The simulator is an Oriel, 1000 W, xenon arc lamp, portable solar simulator.

The $\text{Ga}_{0.47}\text{In}_{0.53}\text{As}$ photodetectors (fig 2) were grown by Epitaxx Inc. part number EPX-3000CR. The devices were p-i-n structures grown by metalorganic vapor deposition (MOCVD) on n-type InP wafers. The $\text{Ga}_{0.47}\text{In}_{0.53}\text{As}$ base layer had a graded carrier concentration profile (determined here by capacitance-

the second term describes the recombination current. For an abrupt p⁺n junction containing a single level recombination center located near the middle of the bandgap, the parameters I_{01} and I_{02} have the values [ref 6]:

$$I_{01} = qA \sqrt{\frac{D_p}{\tau_p}} \frac{n_i^2}{N_D} \quad (2)$$

$$I_{02} = \frac{qWA}{2} \sigma v_{th} N_t n_i \quad (3)$$

In the expression for I_{01} (eq.(2)) D_p and τ_p are the diffusion coefficient and the minority carrier lifetime in the n-type material, respectively. The quantities n_i and N_D are the intrinsic carrier concentration and the doping level, respectively. The expression for I_{02} contains the characteristics of the recombination centers in the junction region. In this equation σ , v_{th} and N_t are the trap capture cross section, the carrier thermal velocity and the trap density, respectively. W is the width of the depletion region and A is the junction area.

Eq.(1) was found to give a good description of the dark I-V data. The terms I_{01} , I_{02} and R_{sh} were obtained from a modified linear regression to the data following the treatment of [ref 5] and the values obtained in this manner are determined to about 15 %. In most cases, the shunt resistance term was found have a negligible contribution to the current compared to the contribution from the I_{01} and I_{02} terms.

Figure 3 shows dark I-V curves measured at several temperatures for a $\text{Ga}_{0.47}\text{In}_{0.53}\text{As}$ photodiode. These measurements were made over the temperature range 200 to 300 K. The solid lines are fits to Eq.(1) and the agreement can be seen to be good. The current is dominated by the diffusion term for this sample, and the slopes of the lines are essentially $q/k_B T$ except at low voltages. The recombination current was found to be small. Most of the photodiodes studied displayed similar behavior and the absence of a significant recombination current implies that the diodes have few effective recombination centers prior to irradiation, as was confirmed by the DLTS measurements described below.

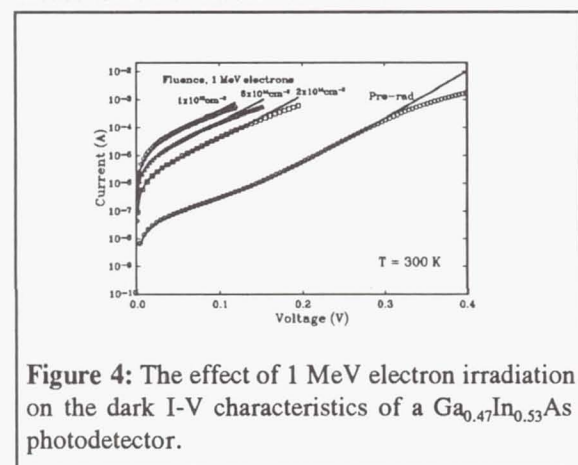


Figure 4: The effect of 1 MeV electron irradiation on the dark I-V characteristics of a $\text{Ga}_{0.47}\text{In}_{0.53}\text{As}$ photodiode.

The temperature dependence of the diffusion current was obtained from the fits, and an estimate for the gap energy was obtained from such data. The approximate T dependence of I_{01} is given by [ref 6]:

$$I_{01}(T) \sim n_i^2(T) \sim T^3 e^{-E_g/k_B T} \quad (4)$$

In Eq.(4), the weak temperature dependence of D_p and τ_p have been neglected. Inclusion of this would introduce only a few percent change, which is well within the present error bars [ref 7]. A value of 0.79 eV was obtained for E_g from fitting the data to Eq.(4). All of the photodiodes studied have been fitted in this fashion and the calculated E_g values range from 0.75 - 0.79 eV. Over the temperature range studied, the accepted band-gap value ranges from

0.75 eV to 0.78 eV [ref 8], in good agreement with the calculated values. Considering I_{01} is known to about 15%, this is further evidence of the good quality of these photodiodes prior to irradiation and lends credence to the use of Eq.(1) to describe the current.

Figure 4 shows the change in the room temperature dark I-V behavior due to irradiation with 1 MeV electrons. The dark I-V fits are shown as the solid lines and the description is reasonable for $I < 10^{-4}$ A. For $I > 10^{-4}$ A, the current tends to "roll-off" with increasing voltage. This most likely marks the onset of the high injection

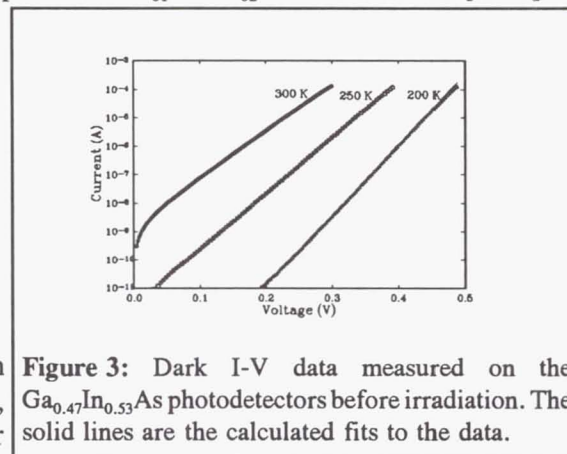


Figure 3: Dark I-V data measured on the $\text{Ga}_{0.47}\text{In}_{0.53}\text{As}$ photodetectors before irradiation. The solid lines are the calculated fits to the data.

region in which the minority carrier concentration becomes comparable to the majority carrier density. Rough calculations of the minority carrier density in this voltage range confirmed this to be the case. Since the junction is not well defined under these conditions, the dark I-V fits were made only for $I < 10^{-4}$ A. The "roll-off" for $I > 10^{-4}$ A might also be attributed to the series resistance of the sample; however, this does not appear to be the case since its inclusion did not describe the "roll-off" region well. Furthermore, the magnitude of the series resistance necessary to account for the "roll-off" would be so large that it would affect the current output throughout the entire voltage range which was not seen.

From the fits, I_{01} and I_{02} were determined following each incremental electron fluence. These values are listed in Table I. Figure 5 plots the recombination term vs. fluence. The data, although sparse, are consistent with I_{02} increasing linearly with fluence. In addition, it was determined that I_{01} (i.e. the diffusion current) dominated the diode current for voltages above ≈ 0.1 V throughout the fluence range studied.

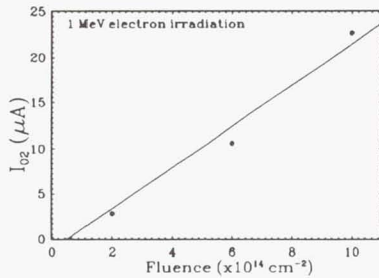


Figure 5: The increase in the recombination term, I_{02} due to 1 MeV electron irradiation. The solid line is a linear least square fit to the data.

B. Illuminated I-V Measurements

The response of the $\text{Ga}_{0.47}\text{In}_{0.53}\text{As}$ devices to 1 sun, AM0 illumination was characterized as a function of temperature and electron fluence. Figure 6 displays a typical photovoltaic (PV) I-V curve of the $\text{Ga}_{0.47}\text{In}_{0.53}\text{As}$ photodetectors measured at room temperature. Table II lists typical values of the PV parameters. The photodetectors appear to suffer from a series resistance which decreases the fill factor (FF). This is due to a lack of metal contact to the top of the sample. A photodetector is not critically dependent on the charge collection efficiency as is a solar cell; therefore, these devices have only a thin circle of metal surrounding the active region instead of a full metal grid of a solar cell. This is the major

difference between these devices and a solar cell. Nevertheless, this difference will have no significant effect on the analysis of the radiation response of the $\text{Ga}_{0.47}\text{In}_{0.53}\text{As}$.

Table I
Calculated Dark I-V Parameters

$\phi \times 10^{14} \text{cm}^{-2}$	I_{01} (nA)	I_{02} (μA)
0	1.86	0.0209
2	558	2.76
6	2190	10.6
10	6000	22.6

Figure 7 displays the variation of the PV parameters of the photodetectors with temperature. The results are similar to those measured on InP homojunction cells [ref 9]. Since the variation of each parameter can be fit to a reasonably good straight line, the temperature coefficients were determined as the slope of the best fit line. The results are given in table III. V_{oc} follows the expected linear decrease with temperature, but the coefficient is less than 2 mV/K measured on InP and Si due to the smaller band-gap of $\text{Ga}_{0.47}\text{In}_{0.53}\text{As}$. The coefficient for J_{sc} is very similar to that of InP.

Figures 8 and 9 show the radiation-induced degradation of the PV response of the $\text{Ga}_{0.47}\text{In}_{0.53}\text{As}$ photodetectors. The data was measured at room temperature. All of the PV parameters show some degradation; however, figure 9 shows that V_{oc} is the parameter most affected. I_{sc} , on the other hand, shows only

moderate degradation. Thus, it is the degradation in V_{oc} which is mainly responsible for the decrease in the cell output under irradiation.

The dark I-V parameters were used to predict the radiation-induced degradation of V_{oc} . V_{oc} can be calculated by the following expression [ref 10] where I_0 represents the dominant term between I_{01} and I_{02} :

$$V_{oc} = \frac{kT}{q} \ln \left(\frac{I_{sc}}{I_0} + 1 \right) \quad (5)$$

The dark I-V data showed I_{01} to dominate in the voltage range near V_{oc} ; therefore, V_{oc} was calculated from the

values of I_{sc} and I_{01} . The results of these calculations are shown in Table IV. It can be seen that the agreement of the predicted V_{oc} values and those measured is quite good.

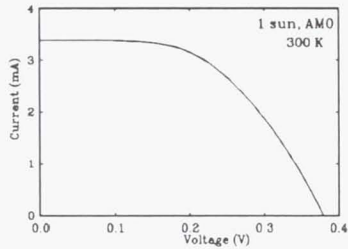


Figure 6: Typical IV curve for the $\text{Ga}_{0.47}\text{In}_{0.53}\text{As}$ photodetectors. The FF is low due to series resistance caused by lack of top metal contact to the photodetectors.

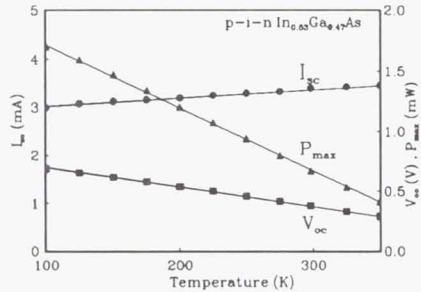


Figure 7: The effect of temperature on the PV parameters of a $\text{Ga}_{0.47}\text{In}_{0.53}\text{As}$ photodetector.

Table II
Typical Room Temperature $\text{Ga}_{0.47}\text{In}_{0.53}\text{As}$ PV Parameters

J_{sc} (mA/cm ²)	48
V_{oc} (V)	0.379
FF	0.521
P_{max} (mW/cm ²)	9.5
Eff (%)	6.9

Table III
Temperature Coefficients for $\text{Ga}_{0.47}\text{In}_{0.53}\text{As}$

dI_{sc}/dT $\mu\text{A}/\text{cm}^2 \cdot \text{K}$	dV_{oc}/dT mV/K	$d\text{Eff}/dT$ %/K
25.6	1.65	0.055

C. DLTS Measurements

Before irradiation, no DLTS signal was detected. The DLTS spectrum measured after 1 MeV electron irradiation is shown in figure 10. The two radiation-induced peaks are majority carrier trapping centers and have been labeled E1 and E2 as shown. Despite extensive experiments to detect minority carrier trapping centers, none were found. The activation energy (E_a) and the capture cross-section obtained from the y-intercept of the Arrhenius plots (σ_∞) for E1 and E2 are given in Table 5. Since these centers capture electrons, E_a is measured from the conduction band as indicated in figure 10. At each fluence level, the defect concentration was estimated from the DLTS peak height by the usual approximation [ref 11]:

$$N_t = 2 \times \left(\frac{\Delta C}{C} \right) \times N_D \quad (6)$$

where ΔC is the DLTS peak height, C is the quiescent capacitance, and N_D is the carrier concentration of the device. The introduction rate of E2 was found to be $0.07 \pm 0.01 \text{ cm}^{-1}$.

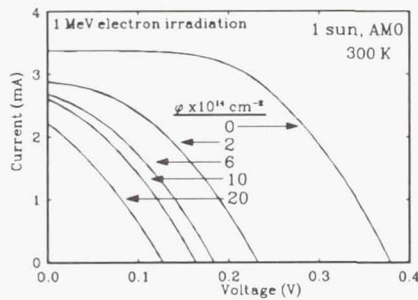


Figure 8: The degradation of the $\text{Ga}_{0.47}\text{In}_{0.53}\text{As}$ IV curves under 1 MeV electron irradiation.

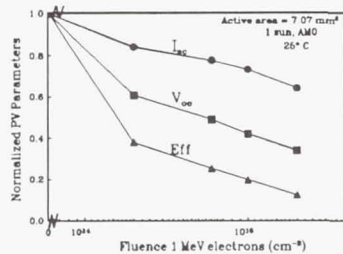


Figure 9: The degradation of the PV parameters. Normalized parameters are plotted to highlight that V_{oc} shows the most degradation while I_{sc} is only moderately degraded.

The sample was then held at 450 K for three successive 30 min periods. This experiment was carried out in the liquid nitrogen cryostat of the DLTS system; therefore, it was not possible to measure the E1 defect during the annealing because the E1 peak occurs at too low of a temperature.

The results of the annealing experiment are presented in figure 11. Note that the abscissa of figure 11 breaks at 450 K from temperature to time. All PV parameters were measured at room temperature. The PV parameters are normalized to their pre-irradiation values while the E2 defect concentration is normalized to its maximum value. An annealing stage for the PV parameters is observed to begin at temperatures as low as 375 K. A large recovery in the PV parameters coinciding with a reduction in the E2 defect concentration occurs at 425 K. A further annealing stage is seen at 450 K. When the sample was held at 450 K for 90 minutes, the V_{oc} and maximum power appear to continue recovering while I_{sc} remains unchanged. The E2 defect concentration seems to follow an exponential decay as would be expected for a first order thermally activated annealing process; however, not enough data yet exists to draw any definitive conclusions about the annealing kinetics. It is also noteworthy that while significant recovery is seen in all the PV parameters, they are still far from full recovery even though the E2 defect concentration has decreased by nearly 90% after 90 minutes at 450 K.

Table IV
Prediction of V_{oc} From the Dark I-V Data

$\phi \times 10^{14} \text{ cm}^{-2}$	I_{01} (nA)	$V_{oc}(\text{V})$ pred.	$V_{oc}(\text{V})$ meas.
0	1.86	0.373	0.380
2	558	0.222	0.231
6	2190	0.184	0.186
10	6000	0.156	0.160

D. Annealing

An isochronal annealing experiment was performed on a photodiode after being irradiated with 2×10^{15} 1 MeV electrons cm^{-2} . The sample was held at elevated temperatures for 10 minutes at each temperature beginning at 325 K and increasing by 25 K at each step. The samples were annealed open circuit in the dark. The samples studied could not withstand temperatures above 450 K, so after 10 minutes at 450 K, the experiment was changed to isothermal annealing.

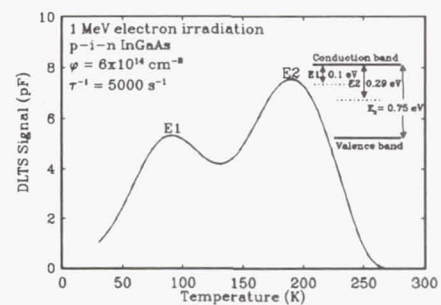


Figure 10: Typical DLTS spectrum measured on the $\text{Ga}_{0.47}\text{In}_{0.53}\text{As}$ material after 1 MeV electron irradiation.

Table V
Measured DLTS Parameters

	E_a eV	σ_∞ cm ²
E1	0.101	6.45×10^{-17}
E2	0.293	2.65×10^{-15}

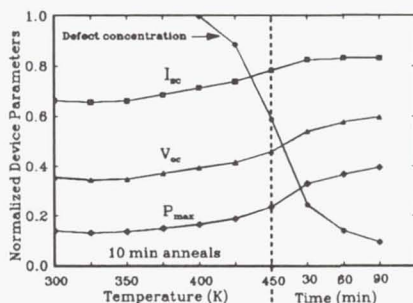


Figure 11: The results of thermally annealing an irradiated Ga_{0.47}In_{0.53}As photodetector.

DISCUSSION

It is clear from the present study that 1 MeV electron irradiation decreases the photovoltaic response of the Ga_{0.47}In_{0.53}As photodetectors by increasing the junction dark current. Since the dark current is most sensitive to defect levels nearest mid-band-gap, the increase is tentatively associated with the introduction of the E2 defect level. The increase in dark current was directly shown to decrease the PV response of the Ga_{0.47}In_{0.53}As devices. Also, the recovery of the PV parameters during thermal annealing seems to be correlated with the decrease of the E2 defect concentration. Therefore, it seems that the E2 defect strongly controls the PV response of these Ga_{0.47}In_{0.53}As photodetectors. Although the E1 defect concentration was not monitored during the annealing, it is not expected to have a large effect on the device performance since it is relatively far from mid-gap and thus will not be an efficient recombination center. Also, some of the experimental results obtained in this research suggests that E1 and E2 are caused by a single defect center, but this is still uncertain. From what is known about radiation-induced defects in GaAs, the most likely defect center which would give rise to this type

of DLTS spectrum would be expected to be associated with an As vacancy. However, DLTS alone is not sufficient to determine the nature of the defect.

It is interesting to note that the V_{oc} of these devices is the parameter most degraded by irradiation. The increased sensitivity of V_{oc} can be explained in terms of the device structure. It was seen in InP homojunction cells that a decrease in the base dopant level caused a decrease in the radiation resistance of V_{oc} but an increase in the resistance of I_{sc} [ref 12,13]. This is thought to be due to the increase in W in the more lightly doped samples. With a wide depletion region, the radiation-induced defects are more likely to act as recombination centers and thus increase the recombination current and decrease V_{oc} . Also with a wide depletion layer, charge collection occurs more by drift through the depleted layer than by diffusion through the bulk. This makes charge collection in lightly doped samples very insensitive to changes in the minority carrier lifetime, thus I_{sc} is little affected by irradiation in such devices.

The present radiation degradation seems to fit this model. The samples are very lightly doped ($N_d \approx 4 \times 10^{15}$ cm⁻³), and as they are irradiated, the recombination current increases which seems to be correlated with the introduction of the E2 defect. This increase was directly shown to decrease V_{oc} . However, I_{sc} is not degraded nearly as much as V_{oc} . The InP research also showed that by increasing the dopant level, the sensitivity of V_{oc} is decreased since less of the base region will be depleted. Since the present results show V_{oc} to be the major cause of the device degradation, a more heavily doped base seems to be in order to improve the radiation hardness.

By the converse of the arguments presented above, an increase in the dopant concentration, while decreasing the sensitivity of V_{oc} to irradiation, will increase the sensitivity of I_{sc} . This is an important consideration since the data indicates a significant degradation of I_{sc} even in the present device geometry. It was seen with the InP homojunctions that a decreased base thickness will offset this increased sensitivity of I_{sc} . A thinner base is also expected to increase the resistance of V_{oc} . Therefore, a more heavily doped, thinner Ga_{0.47}In_{0.53}As bottom cell may be the most radiation resistant configuration for the tandem.

If the trend described above is generally evident in Ga_{0.47}In_{0.53}As as it seems to be in InP, the result will be a tremendous flexibility in the design of the tandem cell. In particular, it would be expected that by adjusting the

base thicknesses and dopant levels of the component cells, the currents can be matched in the tandem, and moreover, the current can be made to be virtually insensitive to particle irradiation up to fluences of 10^{16} 1 MeV electrons cm^{-2} . However, it is stressed that these are currently only speculations. The next stage in the NRL research will be to irradiate $\text{Ga}_{0.47}\text{In}_{0.53}\text{As}$ solar cells of various dopant levels and thickness to determine the relative degradation rates of I_{sc} and V_{oc} .

CONCLUSIONS

This study has presented a preliminary characterization $\text{Ga}_{0.47}\text{In}_{0.53}\text{As}$ as a space solar cell material. The temperature coefficients of the PV parameters have been presented which follow the expected general trends. One MeV electron irradiation have been shown to introduce two majority charge carrier trapping centers, labeled E1 and E2, which have been characterized by DLTS. The preliminary indication is that the E2 defect causes an increase in the junction dark current which has been shown to decrease V_{oc} . It is the degradation of V_{oc} which dominates the degradation of the device output. The degradation seems to fit the model presented for InP solar cells, and a thinner, more heavily doped (i.e. $N_a > 4 \times 10^{15} \text{ cm}^{-3}$) $\text{Ga}_{0.47}\text{In}_{0.53}\text{As}$ bottom cell is expected to show an increased radiation resistance. By also adjusting the structure of the InP top cell in a similar manner, a current matched, radiation resistant tandem solar cell with efficiencies $> 23\%$ (AM0,1 sun) are realistically achievable.

REFERENCES

- [1] M.W. Wanlass, J.S. Ward, T.J. Coutts, K.A. Emery, T.A. Gessert, and C.A. Osterwald. "Monolithic InP/ $\text{Ga}_{0.47}\text{In}_{0.53}\text{As}$ Tandem Solar Cells for Space", Proc. of the Space Photovoltaic Research and Technology Conf., NASA Lewis Research Center, Cleveland Ohio, May 7-9, 1991. NASA Pub. #3121.
- [2] M.W. Wanlass, J.S. Ward, T.J. Coutts, K.A. Emery, T.A. Gessert, and C.A. Osterwald. "Advanced High-Efficiency Concentrator Tandem Solar Cells", (Plenary paper) Proc. 22nd IEEE Photovoltaic Specialist Conf., Las Vegas, NV, Oct. 7-11, 1991.
- [3] M.W. Wanlass, J.S. Ward, K.A. Emery, T.A. Gessert, C.A. Osterwald, and T.J. Coutts, "High-Performance Concentrator Tandem Solar Cells Based on IR-Sensitive Bottom Cells", Solar Cells, **30**, 363 (1991)
- [4] R.J. Walters, G.J. Shaw, G.P. Summers, M.W. Wanlass, and S.J. Ward, "Irradiation of Monolithic InP/ $\text{Ga}_{0.47}\text{In}_{0.53}\text{As}$ Tandem Solar Cells", Fourth International Conf. on InP and Related Materials, April 21-24, Newport, RI. 1992
- [5] G.L. Araujo, E. Sanchez and M. Marti, Solar Cells, **5** (1982) 1990
- [6] S.M. Sze, Physics of Semiconductor Devices, (Wiley, New York, 1981).
- [7] T.P. Pearsall, G. Beuchet, J.P. Hirtz, N. Visentin, and M. Bonnet, "Electron and Hole Mobilities in $\text{Ga}_{0.47}\text{In}_{0.53}\text{As}$ ". Gallium Arsenide and Related Compounds Vienna, 1980 (Bristol, Inst. of Phys.) 639-649
- [8] S.R. Forrest, R.F. Leheny, R.E. Nahory, and M.A. Pollack, " $\text{Ga}_{0.47}\text{In}_{0.53}\text{As}$ Photodiodes With Dark Current Limited by Generation-Recombination and Tunneling", Appl. Phys. Lett., **37**, 322, Aug. 1980

- [9] R.J. Walters, R.L. Statler, and G.P. Summers, "Temperature Coefficients and Radiation Induced DLTS Spectra of MOCVD Grown n⁺p InP Solar Cells", Proceedings of the Space Photovoltaic Research and Technology, NASA Conference Publication 3121, NASA Lewis Research Center, Cleveland, Ohio May 7-9, 1991.
- [10] M.A. Green, Solar Cells: Operating Principles, Technology, and System Applications, (Prentice Hall, Englewood Cliffs: New Jersey, 1982)
- [11] D.V. Lang. "Fast Capacitance Transient Apparatus: Application to ZnO and O centers in GaP p-n junctions", J. Appl. Phys., **45**, 3014, July 1974
- [12] R.J. Walters, C.J. Keavney, S.R. Messenger, G.P. Summers, and E.A. Burke, "The Effect of Dopant Density on the Radiation Resistance of MOCVD InP Solar Cells", Proceedings of the Photovoltaic Specialists Conference, Las Vegas, NV, October 1991.
- [13] C.J. Keavney, R.J. Walters, and P.J. Drevinsky, "Optimizing the Radiation Resistance of InP Solar Cells: The Effect of Dopant Density and Cell Thickness", J. Appl. Phys., **73**, Jan. 1 (1993)

INVESTIGATION OF ZnSe-COATED SILICON SUBSTRATES FOR GaAs SOLAR CELLS¹

Daniel A. Huber, Larry C. Olsen, Glen Dunham, and F. William Addis

Washington State University / Tri-Cities
100 Sprout Road
Richland, WA 99352

Studies are being carried out to determine the feasibility of using ZnSe as a buffer layer for GaAs solar cells grown on silicon. This study was motivated by reports in the literature indicating ZnSe films had been grown by MOCVD onto silicon with EPD values of $2 \times 10^5 \text{ cm}^{-2}$, even though the lattice mismatch between silicon and ZnSe is 4.16 %. These results combined with the fact that ZnSe and GaAs are lattice matched to within 0.24 % suggest that the prospects for growing high efficiency GaAs solar cells onto ZnSe-coated silicon are very good. Work to date has emphasized development of procedures for MOCVD growth of (100) ZnSe onto (100) silicon wafers, and subsequent growth of GaAs films on ZnSe/Si substrates. In order to grow high quality single crystal GaAs with a (100) orientation, which is desirable for solar cells, one must grow single crystal (100) ZnSe onto silicon substrates. A process for growth of (100) ZnSe has been developed involving a two-step growth procedure at 450°C. Single crystal, (100) GaAs films have been grown onto the (100) ZnSe/Si substrates at 610°C that are adherent and specular. Minority carrier diffusion lengths for the GaAs films grown on ZnSe/Si substrates have been determined from photoresponse properties of Al/GaAs Schottky barriers. Diffusion lengths for n-type GaAs films are currently on the order of 0.3 μm compared to 2.0 μm for GaAs films grown simultaneously by homoepitaxy.

INTRODUCTION

This paper concerns investigations of ZnSe as a buffer layer for Single crystal GaAs solar cells grown on silicon. Single crystal silicon is considered a low cost substrate for GaAs solar cells. Since silicon has a lower density than GaAs and can be thinned to less than 2 mils, GaAs cells grown on silicon could lead to high efficiency cells at reduced cost and weight. Significant progress has been made regarding the growth of efficient GaAs cells directly on silicon. However, investigations of GaAs cells on single crystal silicon have not resulted in the high efficiencies that are possible with GaAs substrates. The major problem that must be overcome is related to the high dislocation or other defect density in the GaAs. Although Si has a diamond structure and GaAs a zinc-blende crystal structure, their lattice constants differ

¹This work is funded by the Space Power Division, Phillips Laboratory, Kirtland Air Force Base.

by 4%. As a result, when GaAs films are grown on silicon, the films are characterized by large defect densities. In particular, if a simple two-step growth technique is carried out, dislocation densities $> 10^8 \text{ cm}^{-2}$ are observed for GaAs films grown directly on silicon. Using a thermal-cycle-growth (TCG) process, the dislocation density in GaAs films grown on silicon has been reduced below 10^7 cm^{-2} , which allowed the fabrication of GaAs cells (on silicon) with an AM1.5 efficiency of 18% (ref. 1). Other researchers have utilized a strained layer superlattice (SLS) to reduce dislocation densities. These procedures are relatively complicated and produce only marginal decreases in defect density over thermal-cycle-growth.

The potential use of a strain relieving ZnSe buffer layer to reduce the dislocation density in GaAs films grown on silicon presents the possibility of a much simpler process for growth of high efficiency GaAs cells on silicon. Figure 1 describes the basic approach to cell design using a ZnSe buffer. There is experimental evidence that deposited crystalline films of ZnSe provide strain relief both in the ZnSe film itself and in crystalline films grown on a ZnSe film. Mino, et al., observed that ZnSe films grown by MBE on silicon substrates were characterized by an EPD density of $3 \times 10^5 \text{ cm}^{-2}$ (ref. 2). Lee, et al., have grown GaAs films on silicon substrates with ZnSe buffer layers that were characterized by an EPD count of $2 \times 10^5 \text{ cm}^{-2}$ (ref. 3). Additionally, Lee, et. al., have grown InP films on ZnSe-coated silicon that exhibited a PL spectrum very similar to that measured for InP films grown on InP substrates (ref. 4). Whereas ZnSe and GaAs are lattice matched to within 0.24%, ZnSe and InP are lattice mismatched by 3.4%, and silicon and InP are lattice mismatched by 7.46%. Thus, there is clearly evidence that ZnSe can act as an effective buffer layer between lattice mismatched systems. It appears that the weaker bond strength in ZnSe relative to Si and the III-V compounds allows the ZnSe layer to provide strain relief, which can lead to the misfit dislocations being produced in the ZnSe layer. Table 1 gives some properties of, Si, GaAs and ZnSe. Note that ZnSe is a much softer material than Si and GaAs as evidenced by the Knoop hardness value. Thus, one may consider the softness of ZnSe as the reason for it being an effective buffer layer.

Investigations reported here are in the early stages of the planned effort. To date, studies have focused on the development of MOCVD growth of ZnSe on silicon, and MOCVD growth of GaAs films on ZnSe-coated silicon. Solar cell studies have just recently begun. Discussions of results in these areas follow. Ultimately, the objective of this work is to grow a GaAs cell structure as described in Figure 2. The ZnSe buffer layer would be doped n-type and since the electron affinity is essentially the same as that for silicon and GaAs there should be no significant resistance at the n-GaAs/n-ZnSe and n-ZnSe/n-Si interfaces.

MOCVD GROWTH OF ZnSe ON SILICON

ZnSe is grown by MOCVD in a SPIRE 500XT reactor by reacting a zinc adduct and H_2Se . The zinc adduct was formed by reacting dimethylzinc (DMZn) and triethylamine (TEN). The adduct (DMZn/TEN) source provides a large molecule with zinc at the center and does not react so readily with H_2Se . The use of the adduct has allowed MOCVD growth of ZnSe with minimal prereaction. The optimum substrate temperature for growth of ZnSe on silicon appears to be in the range of 400°C to 450°C . Although some effort has been devoted to

investigating approaches to MOCVD growth of conductive ZnSe, the primary focus has been placed on determining a procedure for growing (100) oriented ZnSe on (100) Si, and the deposition of (100) GaAs on (100) oriented ZnSe/Si substrates. We have found that Al, In and iodine will dope ZnSe n-type. The exact approach to be use for doping ZnSe will be determined after processes for growing the complete solar cell structure are selected.

MOCVD growth of ZnSe at 400°C to 450°C on (100) silicon at a single deposition rate will typically lead to either polycrystalline or crystalline films with a preferred (111) orientation. Growth of GaAs on such ZnSe films would yield low quality GaAs for solar cell fabrication. In order to grow single crystal (100) GaAs, it is necessary that the ZnSe film on the ZnSe/Si substrate have a (100) orientation. One growth procedure that yields (100) ZnSe films on (100) silicon involves a two-step process, namely, nucleation and growth steps. The nucleation step involves MOCVD growth of a few hundred angstroms of ZnSe at 1 Å/s, followed by growth of the remainder of the film at a rate of 5-10 Å/sec. Results of XRD analyses for a ZnSe film grown with a single rate and for a film grown with a two-step procedure are given in Figures 3 and 4, respectively. Figure 3A shows XRD results for polycrystalline ZnSe film with a strong (111) orientation, and Figure 3B shows results for a GaAs film grown on this ZnSe film. The GaAs film was clearly of poor quality. Figure 4A gives results for a single crystal (100) ZnSe film grown with a two-step procedure, while Figure 4B shows the improved quality from the XRD spectrum for a growth relative after growing GaAs at 620°C.

Additional studies are required in order to optimize the growth process for ZnSe on silicon. Two aspects are being pursued, namely, optimization of the process with respect to the impact on the properties of GaAs films grown on ZnSe/Si substrates and identification of procedures compatible with doping the ZnSe film.

MOCVD GROWTH OF GaAs ON ZnSe/SI SUBSTRATES

Once procedures were developed for growth of (100) ZnSe on silicon, progress was made in the growth of GaAs on ZnSe/Si substrates. Initially, polycrystalline GaAs films were grown because the ZnSe films were polycrystalline. The two-step process in growing ZnSe allowed the growth of single crystal (100) GaAs films. Scanning electron micrographs of three GaAs films are shown in Figure 5A, 5B and 5C. Figure 5A shows a polycrystalline GaAs film grown on a ZnSe/Si substrate for which the ZnSe was grown at 450°C with a one-step process. Figure 5B shows a SEM of sample 92GZS165, a structure consisting of GaAs grown on a ZnSe/Si substrate for which the ZnSe film was grown with a two-step process. Although the GaAs film on sample 92GZS165 is single crystal, it is very defective. An improvement in the GaAs film was achieved in the case of sample 92GZS190 which is described by Figure 5C. Note that the magnification is 5 kX for these micrographs. In this case, the ZnSe film was capped with a thin GaAs layer before removing it from the MOCVD system. Refinement of these processes is underway. As illustrated by these scanning electron micrographs, however, improvement in GaAs film quality has been accomplished. As

discussed in a subsequent section improvements in minority carrier diffusion length are also occurring.

In addition to examination by a scanning electron microscope, TEM studies and charged ion concentration profiles taken with a electrochemical C-V profiler are being done for physical characterization. TEM studies are underway and will be reported at a later date. Electrochemical C-V profiles (Polaron profiles) are shown for two n-type GaAs films in Figure 6A and 6B. The profile for sample 92GZS190 (Figure 6A) shows a high charged ion density at a depth $\geq 1 \mu\text{m}$. We interpret these results as indicating there is a large density of defects that are charged and can be detected by the C-V measurement. Figure 6B shows a profile for sample 92GZS204, a GaAs film grown on a ZnSe/Si substrate for which the ZnSe film growth process had been further optimized.

Single crystal GaAs films have been grown on ZnSe on GaAs substrates for comparison. This system is pertinent since the same concerns exist for nucleation of high-quality GaAs on ZnSe but without the strain caused by the silicon substrate. Figure 6C shows the electrochemical C-V profile for sample 92GZG262, a GaAs film grown on a ZnSe/GaAs substrate. Absent is the high charge concentration found in samples grown on silicon substrates. This indicates that the increasing charge density in the samples on ZnSe/Si may be due to a large density of defects rather than interdiffusion. It is reasonable to assume that the large defect density in the films grown on silicon substrates could provide "pipelines" for diffusion transport from the ZnSe. A small increase in charged impurity concentration occurs in sample 92GZG262 close to the GaAs/ZnSe interface. It is not clear whether this indicates interdiffusion or an artifact of the C-V measurement at the heterojunction.

MINORITY CARRIER PROPERTIES

Minority carrier diffusion lengths of GaAs films have been measured by analyzing the photoresponse of Al/n-GaAs Schottky barriers as depicted in Figure 7. We have found that Al will consistently form a Schottky barrier on n-type GaAs if the Al is vacuum deposited at a relatively fast rate, say $\geq 15 \text{ \AA/s}$, at pressures around 2×10^{-6} . Al thicknesses between 80 and 100 \AA are utilized so that the aluminum layer is thin enough to pass a significant fraction of an incident flux of photons into the GaAs region. If photons of energy $h\nu \geq E_g$ are incident on a sample and each photon creates one electron-hole pair, the maximum possible photocurrent density is given by:

$$J_{\text{max}} = q \cdot F \quad (1)$$

where F is the incident photon flux. The two major contributions to the photocurrent of the Schottky barrier are due to current collected from the depletion region and from the bulk. The photocurrent can be written as:

$$J_{\text{ph}} = J(\text{Depletion Region}) + J(\text{Bulk}) \quad (2)$$

where

$$J(\text{Depletion Region}) = q T F f [1 - \exp(-\alpha W)] \quad (3)$$

and

$$J(\text{Bulk}) = q T F \exp(-\alpha W) [\alpha L / (1 + \alpha L)] \quad (4)$$

where T is the transmittance of photons through the metal film, F is the incident photon flux at a specific wavelength of light, f is a collection factor for the depletion region, α is the absorption coefficient, W is the depletion region width, and L is the minority carrier diffusion length. We have introduced a "collection factor" for the depletion region. Thus, although a high field may exist in this region, we assume that the probability of a carrier being swept out of the region may be less than 1.0. Such an assumption allows one to fit data for defective material. It is being assumed, however, that carriers diffusing from the bulk have sufficient velocity to escape with a probability of 1.0. This model is clearly a simplification of a rather complex problem, but provides an approach for evaluating material. As the material improves in quality, the " f " factor should approach 1.0 and diffusion lengths should increase in value. In high-quality material one must also account for the bending of the bands near the metal-semiconductor interface by an image force. The band bending occurs over 50 Å and thus decreases the response to UV light. Finally, it should be noted that the reflection of light from the metal surface and adsorption in the metal film are accounted for in T .

The collection of current from the bulk of the Schottky barrier device is essentially the same as from the base of a p-n junction device with a modification due to the transmittance being less than 100%. Collection of carriers from the bulk is dependent upon the minority carriers having sufficient lifetime (diffusion length) to diffuse to the depletion region. The above expression for $J(\text{Bulk})$ is based on the assumption that the back contact (contact other than the Schottky barrier) is ohmic and that the device thickness is much greater than the minority carrier diffusion length.

We define the external photoresponse of a Schottky barrier by the relationship

$$J_{ph} = Q_{ext} \cdot J_{max} \quad (5)$$

From the above results, we have

$$Q_{ext} = T \cdot \{ f [1 - \exp(-\alpha W)] + \exp(\alpha W) \cdot [\alpha L / (1 + \alpha L)] \} \quad (6)$$

The internal photoresponse (Q_{int}) is given by Q_{ext} / T . Q_{int} is independent of the film transmittance, and thus only depends on the GaAs film properties. To determine the internal photoresponse, the transmittance $T(\lambda)$ must be obtained for the wavelength range of interest.

Calculation of the transmittance T requires knowledge of the optical constants n and k of the Al film. The optical properties of thin aluminum films can vary greatly with deposition conditions. The optical constants are determined from measured values of transmittance (T) and reflectance (R) for Al films deposited on quartz witnesses. The optical constants, n and k , of Al films are calculated with a computer-aided analysis that utilizes values of T and R for each photon wavelength and the optical constants of the quartz substrate. Figure 8 demonstrates the results of modeling the reflection and transmission from an Al Schottky barrier film on GaAs. After determining the optical properties of the Al film and measuring the photoresponse and reflectance of the Schottky barrier device, a data file is constructed that contained the n and k values of the Al film at each photon wavelength, the n and k values from literature of the GaAs at each photon wavelength, the GaAs layer thickness, the depletion width, and assumed values for f and L . Values of the two fitting parameters, collection factor f and diffusion length, are then varied until the best fit to Q_{ext} is attained.

Figure 9 shows results for n-type GaAs films grown on ZnSe/Si substrates. Table 2 summarizes results of photoresponse analysis. Analysis of data for a n-type GaAs film grown simultaneously on GaAs indicates a diffusion length of 2.0 μm , and establishes a reference value with which to compare results obtained for films grown on ZnSe/Si substrates. As the quality of the GaAs films has improved, the internal photoresponse has improved, which is interpreted in terms of an increasing minority carrier diffusion length.

CONCLUSIONS

The objective of these studies is to determine the feasibility of ZnSe buffer layers for growth of GaAs solar cells on silicon substrates. Work to date has primarily involved the development of procedures for MOCVD growth of (100) ZnSe on (100) silicon, and growth of GaAs films on ZnSe/Si substrates. Progress has been made in both areas. A process for growth of single crystal (100) ZnSe on (100) silicon at 450°C has been developed. Films are very specular and uniform. Single crystal GaAs films with (100) orientation have been grown at 620 °C that exhibit finite minority carrier diffusion lengths. Specifically, n-type GaAs films have been grown that have minority carrier diffusion lengths of approximately 0.3 μm . N-type GaAs films grown on GaAs substrates at 620°C were characterized as having a diffusion length of 2 μm . It is expected that improved understanding of film nucleation at the Si-ZnSe and ZnSe-GaAs interfaces will lead to growth of n-type GaAs films with diffusion lengths greater than 1.0 μm and p-type films with diffusion lengths significantly greater than 1.0 μm . Such results would allow the fabrication of high efficiency GaAs cells on ZnSe/Si substrates.

REFERENCES

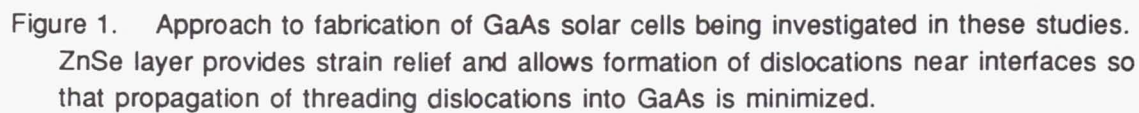
- [1] S. M. Vernon, et al., "Efficiency Improvements in GaAs on Si Solar Cells," 20th IEEE Photovoltaic Specialists Conference (1988), p. 481.
- [2] Naoki Mino, et al., "Epitaxial Growth of High Quality ZnSe on Si Substrates by Molecular Beam Epitaxy and Application to dc Electroluminescent Cells," Journal of Applied Physics 58, 793 (1985).
- [3] M. K. Lee et. al., "Improvements in the heteroepitaxy of GaAs on Si by incorporating a ZnSe buffer layer," Applied Physics Letters 59, 207 (1991).
- [4] M. K. Lee, et al., "Growth and Characterization of InP Epilayers on ZnSe-Coated Si Substrates by Low-Pressure Metalorganic Chemical Vapor Deposition," Applied Physics Letters 53, 107 (1988).

Table 1. Material Parameters for Si, GaAs and ZnSe

Material	Si	GaAs	ZnSe
Lattice Constant (Å)	5.43095	5.6534	5.6686
Coefficient of Expansion ($^{\circ}\text{C}^{-1}$)	2.32×10^{-6}	5.75×10^{-6}	7.0×10^{-6}
Bandgap(eV)	1.12	1.42	2.67
Electron Affinity (eV)	4.05	4.07	4.09
Crystal Structure	Diamond Cubic	Zinc-blend	Zinc-blend
Density (g/cm^3)	2.33	5.32	5.32
Knoop Hardness	1150	780	150

Table 2. Minority Carrier Properties Of GaAs Films Grown On ZnSe/Si Substrates

Device	Depletion Width (μm)	Collection Factor	Carrier Concentration (cm^{-3})	Diffusion Length (μm)
92GZS171	0.05	0.02	1×10^{17}	0.1
92GZS190	0.05	0.30	1×10^{17}	0.1
92GZS204	0.10	0.75	2×10^{17}	0.3
92GG825	0.10	1.00	4×10^{17}	2.0



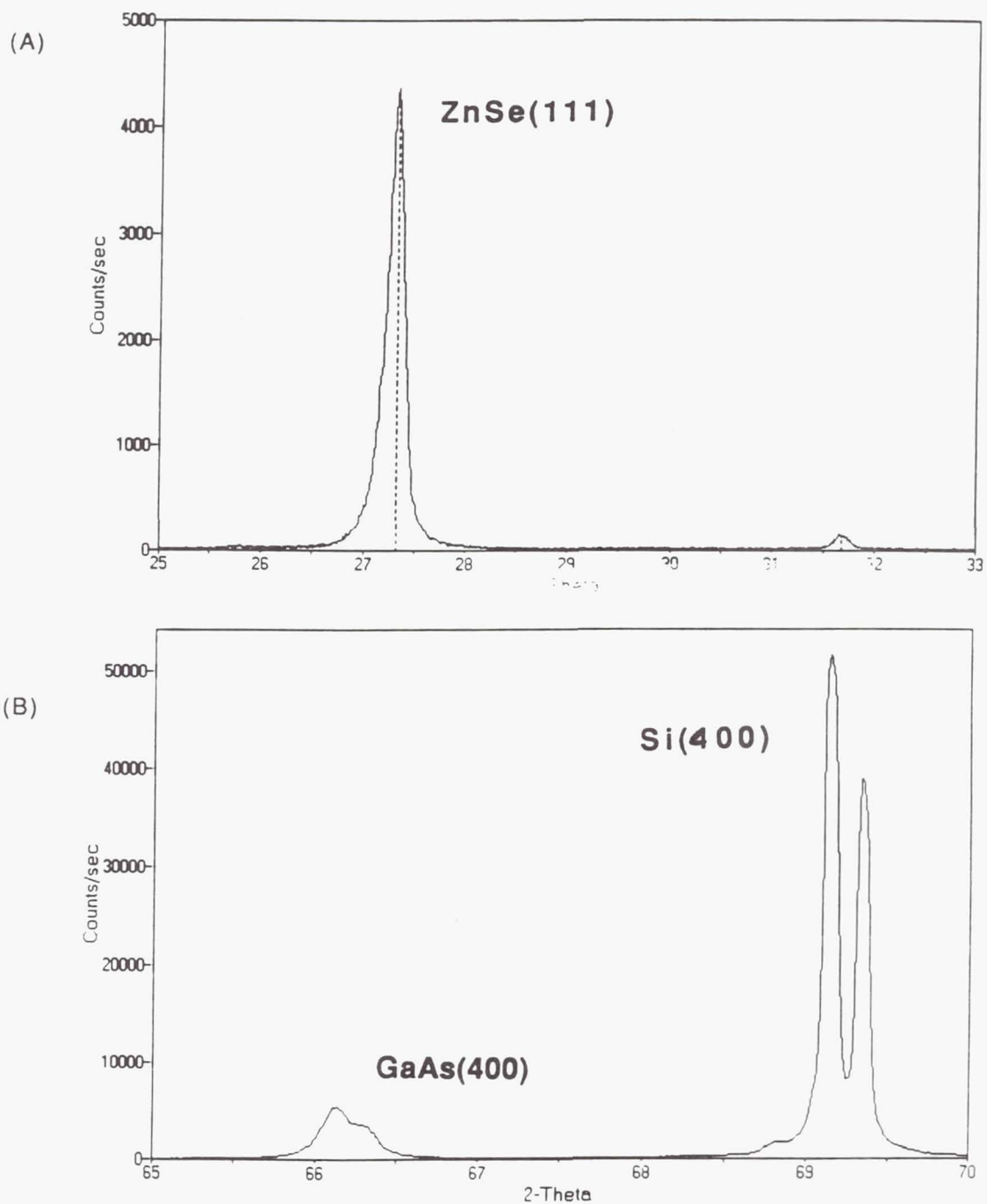


Figure 3. (A) XRD Spectrum for 92ZS070 Showing the Strong (111) Diffraction Peak;
(B) XRD Spectrum for the GaAs Film Grown on 92ZS070 (Giving Sample 92GZS070).

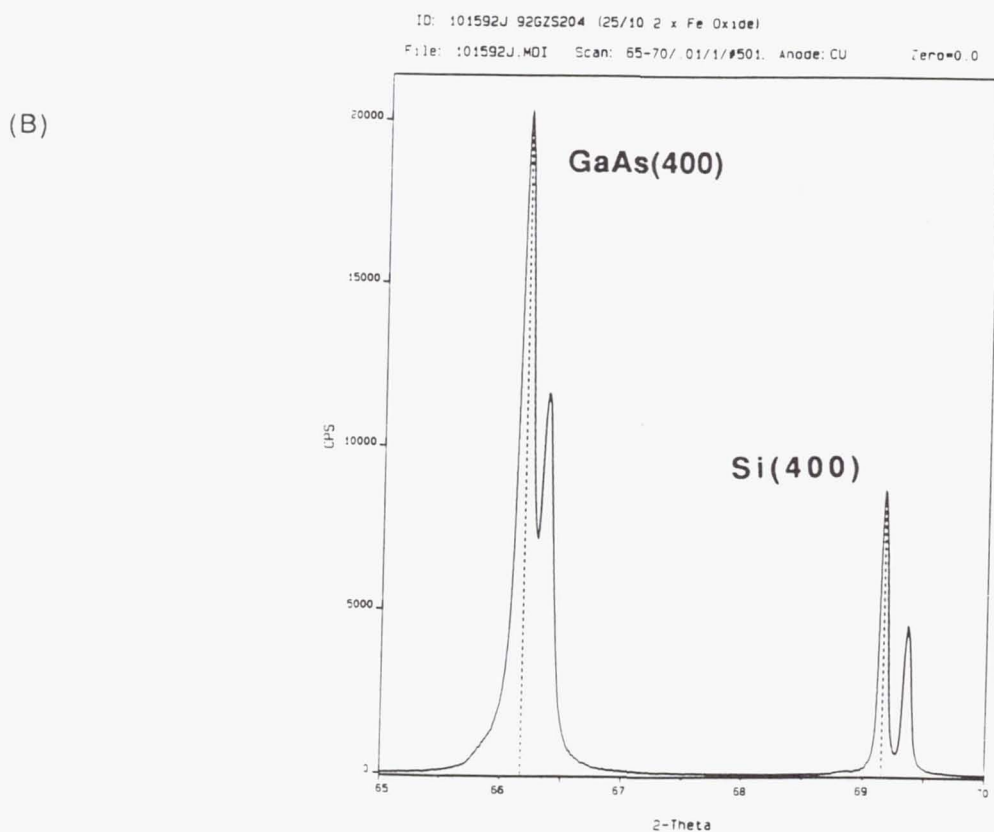
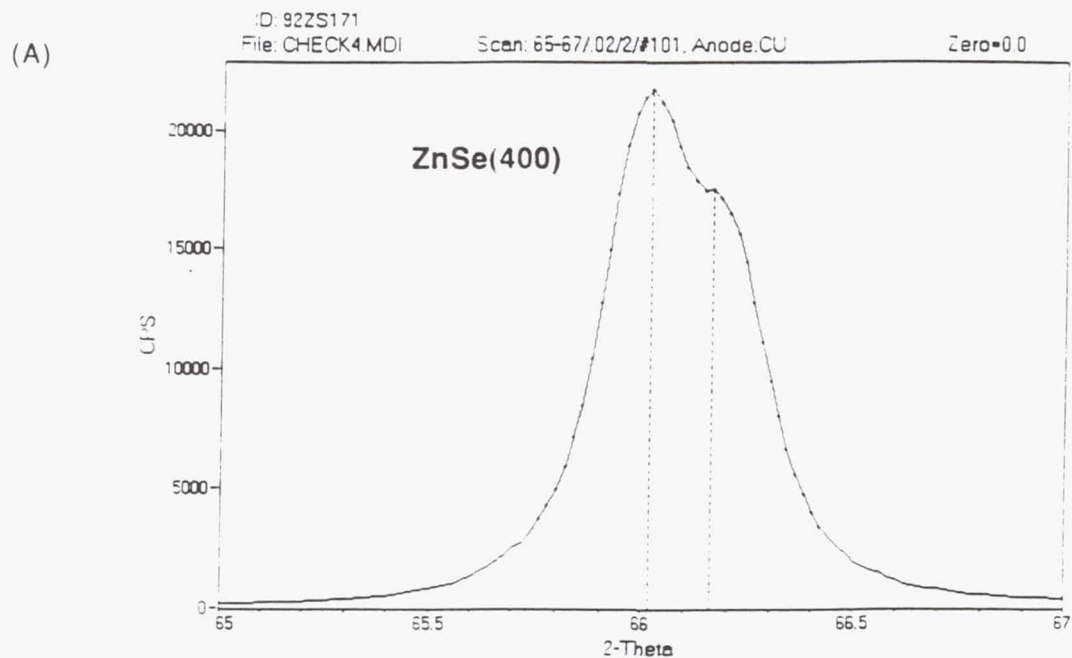
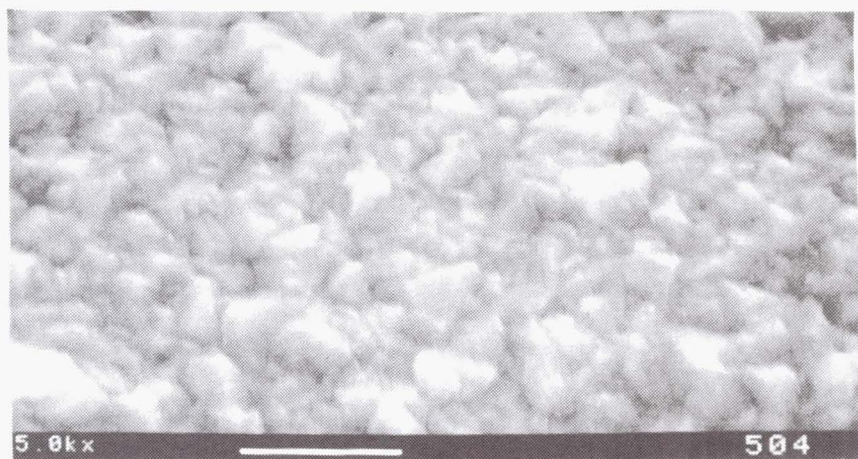
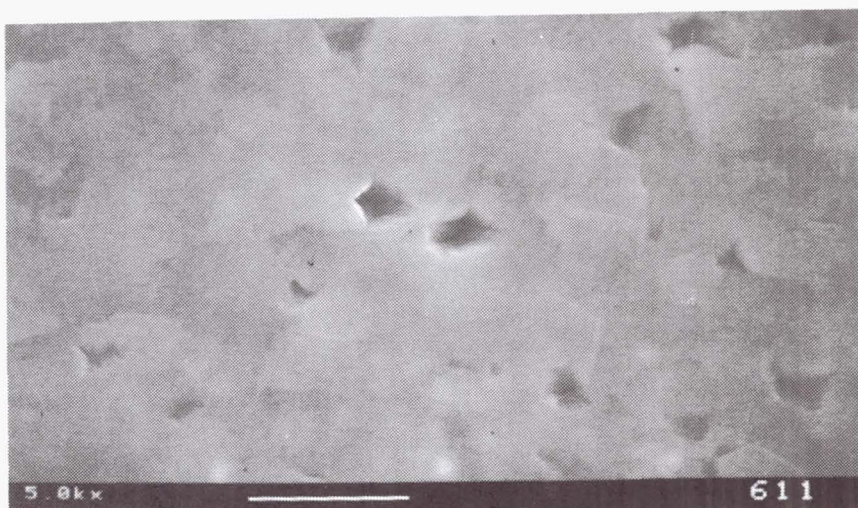


Figure 4 (A) XRD Spectrum for 92ZS171 Showing the ZnSe (400) Reflection with $K_{\alpha 1}$, $K_{\alpha 2}$ Peaks Just Resolved. Only (100) Type Peaks Were Observed. (B) XRD Spectrum for Sample 92GZS204 with Single Crystal GaAs Film Grown On ZnSe/Si Substrate.

(A)



(B)



(C)

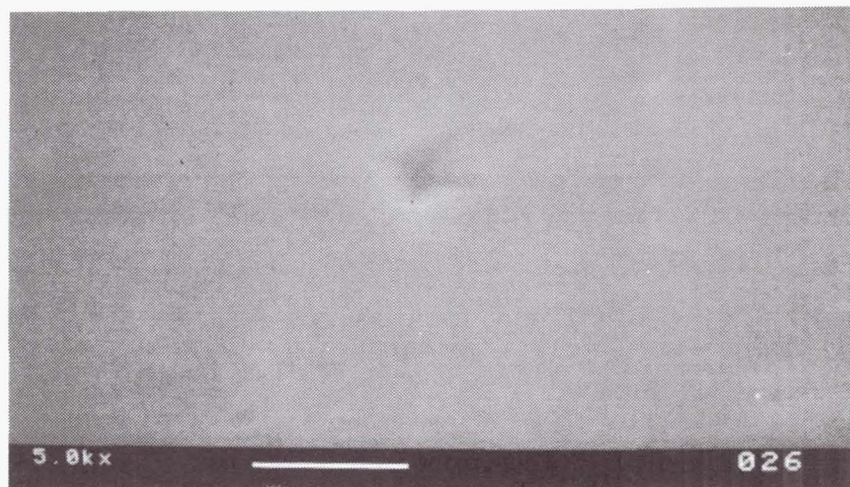
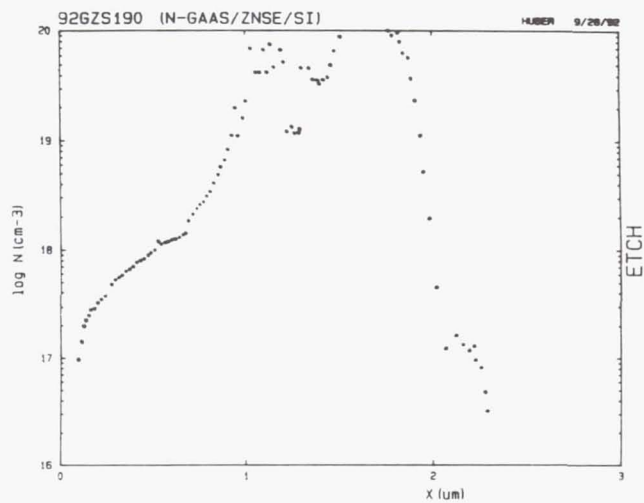


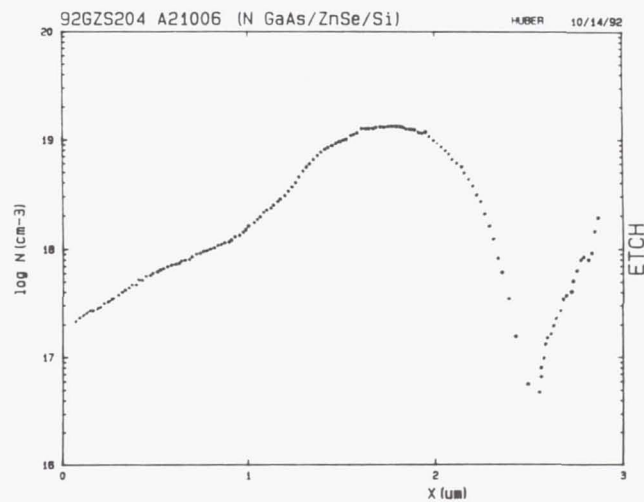
Figure 5.

Scanning Electron Micrographs for Three GaAs Films Grown on ZnSe/Si Substrates: (A) Sample 92GZS094, a GaAs Film Grown On ZnSe/Si with the ZnSe Having (111) Orientation; (B) Sample 92GZS165, a GaAs Film Grown on (100) ZnSe/Si (see text) ; (C) Sample 92GZS190, a GaAs Film Grown on (100) ZnSe/Si and an Improved Process (see text).

(A)



(B)



(C)

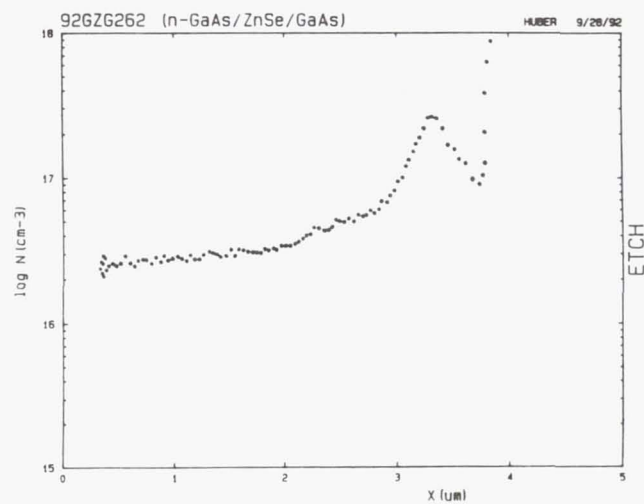


Figure 6. Charged Impurity Concentration Profiles Acquired for; (A) Sample 92GZS190; (B) Sample 92GZS204; (C) Sample 92GZG262.

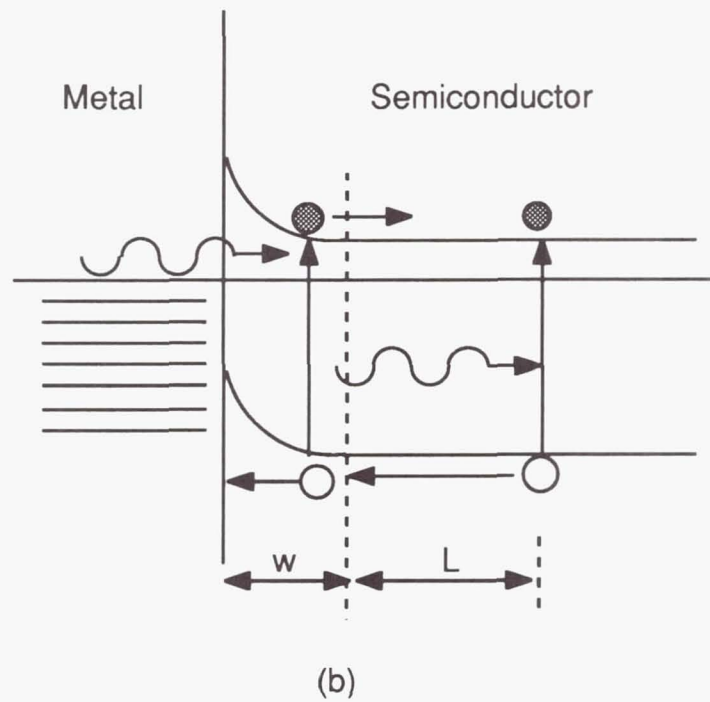
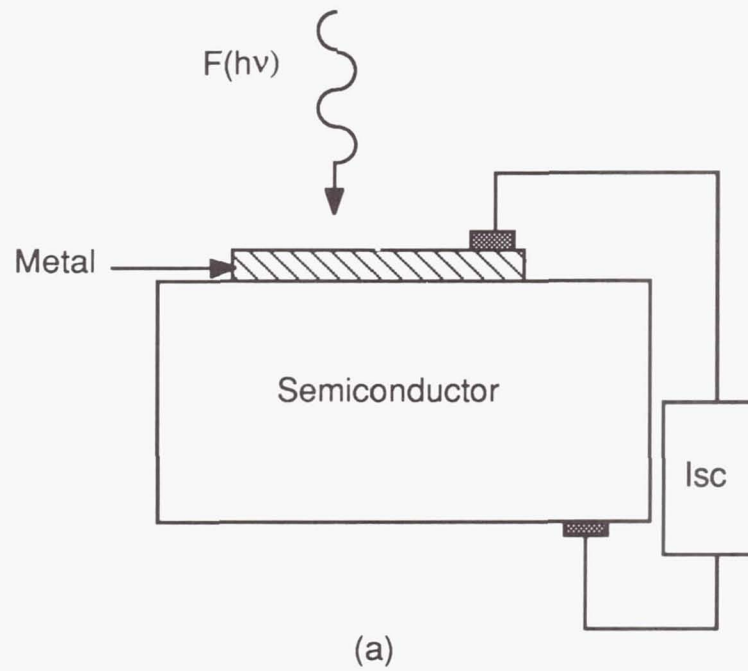


Figure 7. (A) Measurement of Short-Circuit Current for a Schottky Barrier Device; (B) The Associated Band Diagram.

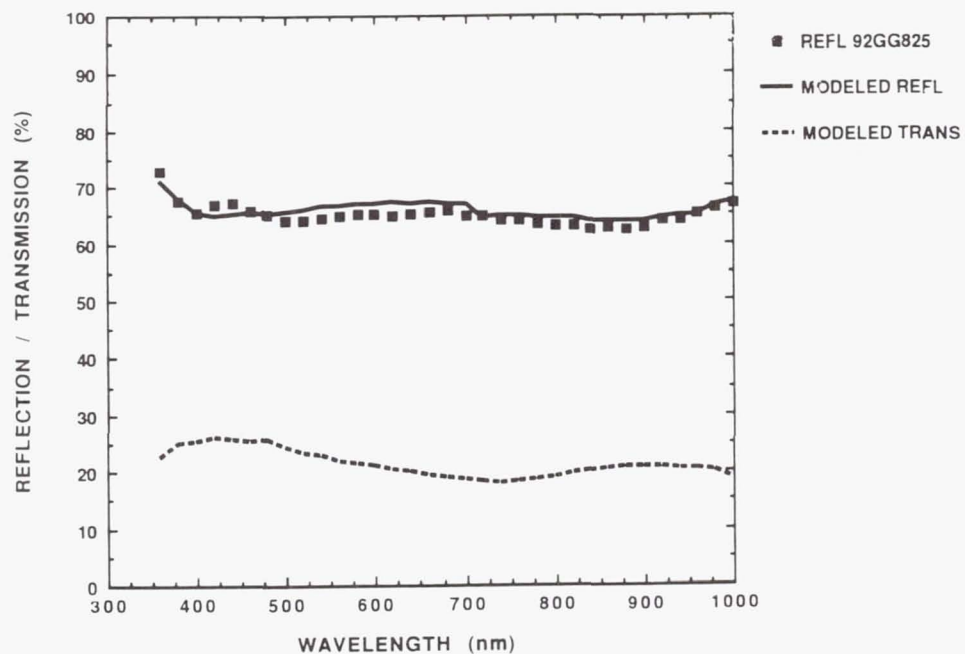


Figure 8. Measured reflection from 90Å Al film on n-GaAs with Modeled reflection and transmission from n and k of Al film deposited on quartz witness.

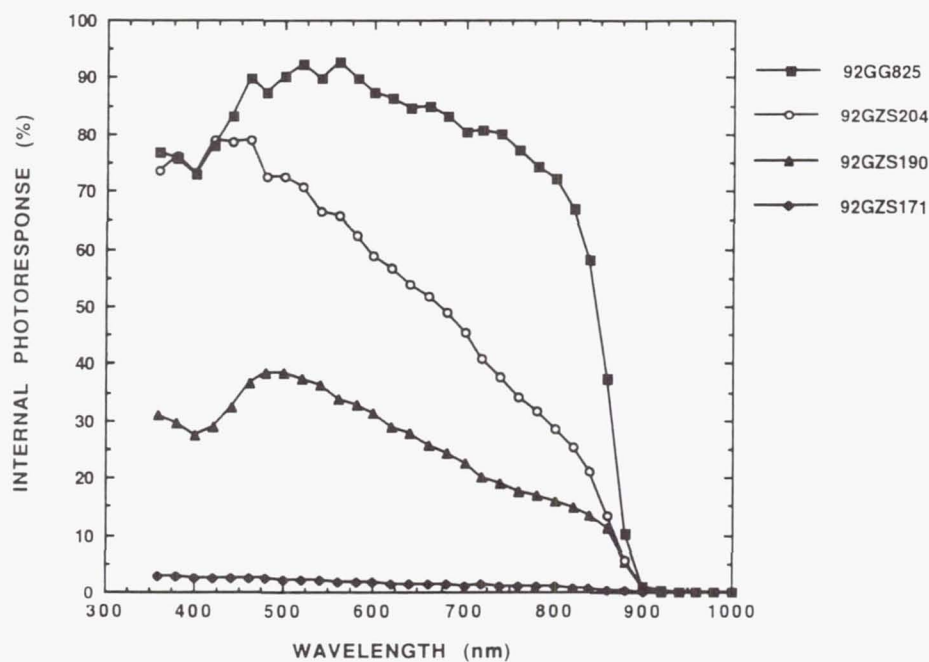


Figure 9. Internal Photoresponse for Al/GaAs Schottky Barriers. The GaAs Films were Grown on ZnSe/Si Substrates.

HETEROEPITAXIAL InP, AND ULTRATHIN, DIRECTLY GLASSED, GaAs III-V SOLAR CELLS.

C.M. Hardingham, T.A. Cross
EEV Ltd
Chelmsford, Essex, England CM1 2QU.

Abstract:

The commercial application of Indium Phosphide solar cells in practical space missions is crucially dependant upon achieving a major cost reduction which could be offered by heteroepitaxy on cheaper, more rugged substrates. Furthermore, significant mass reduction, compatibility with mechanically stacked multijunction cells, and elimination of the current loss through glue discoloration, is possible in III-V solar cells by the development of ultrathin, directly glassed cells.

This paper describes the progress of a UK collaborative program to develop high efficiency, homojunction InP solar cells, grown by MOCVD on Si substrates. Results of homoepitaxial cells (>17% 1 Sun AM0) are presented, together with progress in achieving low dislocation density heteroepitaxy.

Also, progress in a UK program to develop ultrathin directly-glassed GaAs cells is described. Ultrathin (5 micron) GaAs cells, with 1 Sun AM0 efficiencies up to 19.1%, are presented, together with progress in achieving a direct (adhesive-less) bond between the cell and coverglass. Consequential development to, for example, cell grids, are also discussed.

Keywords:

InP, GaAs, Heteroepitaxy, Ultrathin, Direct Glassing.

III-V solar cells vs Si.

It is well established that some III-V solar cell materials, such as GaAs or InP, offer substantial performance improvements over conventional Si cells, due to three main reasons [ref 1]. The band-gap for both materials is closer to the optimum for single-cell performance - in the case of GaAs (1.43eV) the maximum predicted beginning-of-life (BOL) 1 sun AM0 efficiency is as high as 26% compared to a more modest predicted maximum of around 22% for Silicon.

Secondly, it is well established that some III-V solar cell materials offer much higher radiation resistance, compared to conventional Si cells, which enhances their relative performance at end-of-life (EOL). This is a very significant factor, particularly for InP which appears to have higher radiation resistance than other materials.

Thirdly, the degradation in performance at elevated temperatures, for the higher bandgap cell such as GaAs, is much smaller than for Si cells.

Furthermore, some III-V solar cell materials, including both GaAs and InP, have a direct band-gap. The consequences of this are much higher absorption coefficients than is the case for indirect band-gap materials such as silicon. Thus all the light useful to the cell is absorbed within the first few microns, resulting in the bulk of the cell material being redundant, leading to the possibility of ultrathin (<10 micron) cells.

InP Solar Cell types:

There are three main types of InP cell. These comprise the epitaxially grown cells, (by MOCVD, MBE or related growth techniques), diffused junction cells (in which the junction is formed within the bulk substrate by diffusion), and surface junction cells, where the junction is formed substantially at the surface, by deposition of material (eg Schottky barrier type cells, or ITO cells).

The present program¹ addresses both epitaxially grown cells (MOCVD growth, both homoepitaxial and heteroepitaxial), and ITO/InP cells heteroface cells.

ITO/InP cells:

The Indium Tin Oxide /InP (ITO/InP) solar cells under consideration within the present program comprise an RF sputter deposited layer of ITO on p-type InP (Figure 1), and have been discussed more fully previously [ref 2-4]. Analysis of eg CV measurements leads to the theory that a shallow homojunction cell is formed, through the creation of a damaged layer just underneath the surface. The potential advantage of such cells is that the requirement for expensive epitaxy processing is redundant, although to-date, BOL efficiencies achieved with this type of cell have, in general, been lower than for epitaxial cells.

Epitaxial InP cells:

The epitaxial cells upon which the program has focused are shallow homojunction n⁺-p-p⁺ cells, fabricated with a lattice-matched InGaAs cap layer (Figure 2), with efficiencies approaching 18% 1 sun AM0 BOL (Figures 3, 4). The program baseline is 2x2 cm cells. The baseline cell structure has been established following pseudo-three dimensional modelling of the cell [ref 7]; this has incorporated lifetime values derived from test structures closely emulating the cell conditions. Furthermore, series resistance effects have been accurately taken into account using a distributed element approach, resulting in better optimisation of collection grid design.

Irradiation Studies:

1 MeV electron irradiation studies have been carried out on both types of cell; further electron and proton studies are scheduled for autumn '92, and spring '93. As expected, both types of cell stand up well to electron irradiation, better than either Silicon or GaAs [refs 5,6], with over 75% power remaining after a dose of 1E15 electrons (bare cells, in the dark) (Figure 5). The evidence suggests that still lower degradation is experienced for cells under load [ref C]. Furthermore, significant recovery of the cell parameters has been achieved at moderate temperatures (90°C).

¹ This work has been supported in part by the UK Department of Trade and Industry and the Science and Engineering Research Council under the LINK Advanced Semiconductor Materials Programme, and EEV acknowledge the contributions of the other participants in this program: Newcastle Photovoltaics Applications Centre; Epitaxial Products International; University of Wales College Cardiff; and Pilkington Group Research and Pilkington Space Technology.

Commercial Applicability:

In order for Indium Phosphide solar cells to be commercially applicable for practical space missions their cost must be significantly reduced below current levels. The (significant) cost of epitaxy can be eliminated through use of ITO/InP cells as described above, or diffused junction cells. (For example, the only mission to baseline InP cells for power production is the Japanese MUSES-A lunar orbiter using 1x2cm diffused junction InP cells [ref 8].) However, performance of the former type of cell has so far failed to match that of epitaxial cells, the cells on MUSES-A averaging 16% (BOL).

The cost of InP cells is heavily dependant on material costs. Thus the greatest cost benefit will be through heteroepitaxy on cheaper, more rugged, substrates. To this end, the program includes development of InP grown heteroepitaxially on Si (with and without intermediate layers).

InP/Si Heteroepitaxy:

The critical problem to be addressed in heteroepitaxy is how to accommodate lattice mismatch between the different materials. In the case of InP (5.869Å) on Si (5.431Å), this amounts to some 8%. The approaches being considered, within the present program, to accommodate this include: (a) direct growth of InP on Si via a "two-step" growth process; (b) growth of InP/GaAs/Si via a double "two-step" process, and (c), growth of InP/GaInAs/GaAs/Si, where the InP is grown on graded-composition InGaAs, (0-53% to provide lattice matching at the InP interface).

Experiments have confirmed the critical nature of the mismatch, with dislocation densities 2 orders of magnitude higher than acceptable being obtained for graded layers, and polycrystallinity evident on InP/Si.

However, for the case of InP/GaAs/Si, initial growths have produce films giving double crystal x-ray rocking curves with FWHM of 500 arc sec, and FWHM of 320 arc secs has been achieved with post-growth annealed samples, (although it is possible that the reduction seen on annealing is due to twin annihilation, which gives rise to threading dislocations, and therefore will not provide "better" material quality than that in the un-annealed state). Furthermore, growth of the intermediate GaAs layers on Si has produced x-ray FWHM of 152 arc sec.

Ultrathin InP Cells:

One of the potential advantages of heteroepitaxial InP is the possibility of removing the bulk of the heteroface material, leaving an ultrathin (5-10 micron) cell. This will facilitate mechanically stacked multijunction cells, with little sub-bandgap absorption in the InP cell.

However, some manufacturing issues in ultrathin InP cells remain to be addressed, such as interconnection techniques, supporting structure, etc. These issues are already being addressed for (related) ultrathin GaAs cells.

Ultrathin GaAs cells:

Several workers have already reported ultra-thin GaAs solar cells [refs 9-13]. EEV have been developing chemically etch-stopped GaAs cells grown on GaAs and Ge [ref 11], and have produced ultrathin (8 micron) cells up to 19.7% efficient, based on measured cell area of 3.7cm² (Figure 6). The technology is readily transferable to heteroepitaxial InP cells.

Directly Glassed GaAs cells:

Critically important for their use, is the ability of ultrathin cells to withstand handling and integration processes. Furthermore, one of the causes of current degradation over a cell's lifetime in space, is discoloration of the coverglass adhesive. These two issues combine, to raise interest in adhesiveless bonding of cells. One technique that has been tried is use of teflon bonding [refs 11,14]; however, of more interest is the possibility of completely doing away with any bonding medium, and relying on a direct bond between the coverglass and cell [ref 12].

This approach has been greatly facilitated by the advent of a coverglass material with expansion coefficient matched to GaAs [ref 15], and EEV are involved a program² to develop direct glassing of ultrathin GaAs cells, following on from the adhesive-bonded ultrathin work. The bond is formed by ionic diffusion formed by an electrostatic field applied during compression at elevated temperatures, requiring the cell to withstand somewhat higher temperatures than standard for a short time (seconds/a few minutes).

Interconnecting ultrathin Cells:

The ease of interconnection of such cells is under consideration; when made in conjunction with direct glassing, there is no adhesive-matrix to support the interconnect near the cell, and the problems associated with the interconnect flexing and cracking the cell are significant. The option of providing interconnection via metal attached to the coverglass rather than (primarily) to the cell is being considered (figure 7).

References:

1. T.A.Cross, Proc 2nd World Renewable Energy Conference, Reading, England, Sept.'92
2. N.M.Pearsall, Proc 4th Int Conference on InP and Related Materials, Newport RI, April 92
3. C.Hardingham et al, Proc 2nd ESPC, Florence, Sept. '91.
4. N.M.Pearsall et al, Proc 22nd IEEE PVSC, Las Vegas, Oct. '91.
5. K.A.Bertness et al, Proc 21st IEEE PVSC, Kissimmee, May '90
6. K.Ando & M.Yamaguchi, Appl. Phys. Lett., 47 (8), pp846-8, '85.
7. J.E.Parrott & A.Potts, Proc 22nd IEEE PVSC, Las Vegas, Oct.'91.
8. K.Takahashi et al, Proc 2nd ESPC, Florence, Sept.'91.
9. R.W.McClelland et al, Proc 21st IEEE PVSC, Kissimmee, May '90.
10. N.P.Kim et al, Proc 22nd IEEE PVSC, Las Vegas, Oct.'91
11. C.Huggins et al, *ibid*
12. M.J.Nowlan et al, *ibid*
13. R.L.Bell et al, Sandia Report No 7460, '84.
14. P.White, Proc 2nd ESPC, Florence, Sept.'91, p551
15. P.White, *ibid*, p547

² Part of this work has been carried out with the support of the procurement executive, Ministry of Defence;

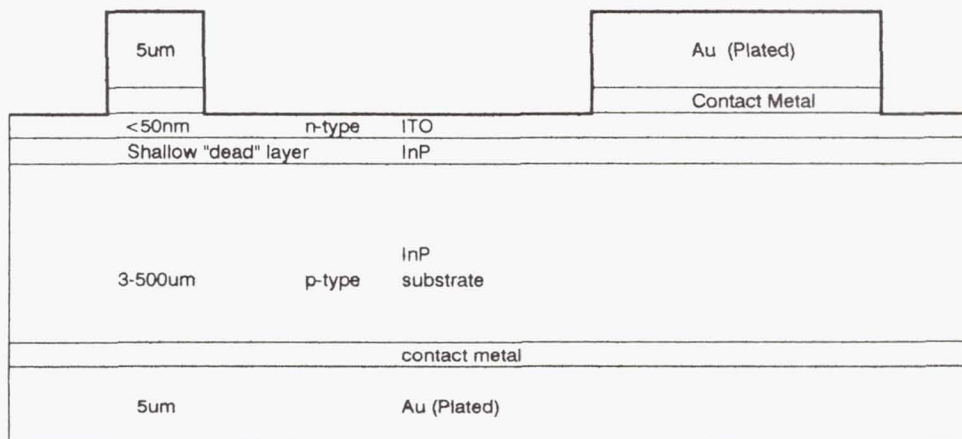


Figure 1: Schematic of ITO/InP Solar Cell

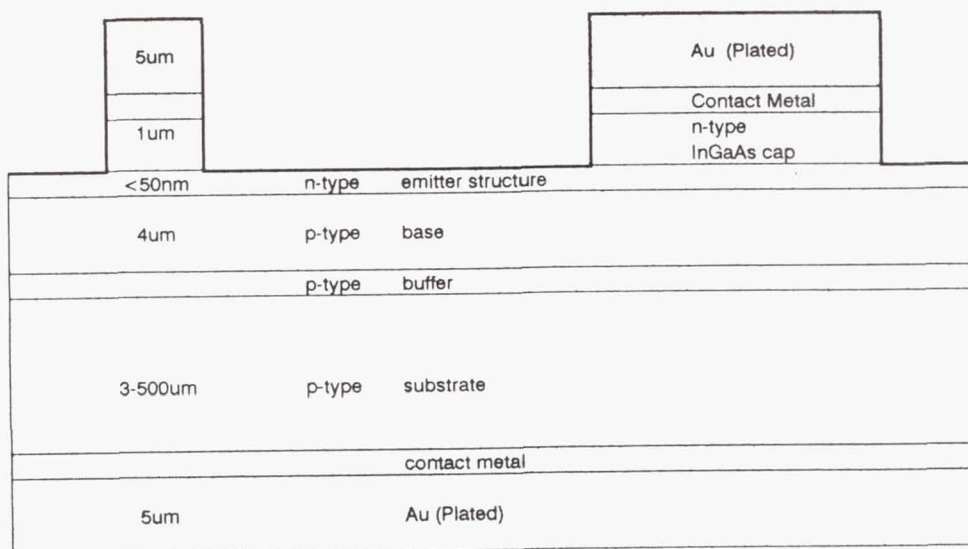


Figure 2: Schematic of Epitaxial InP Solar Cell

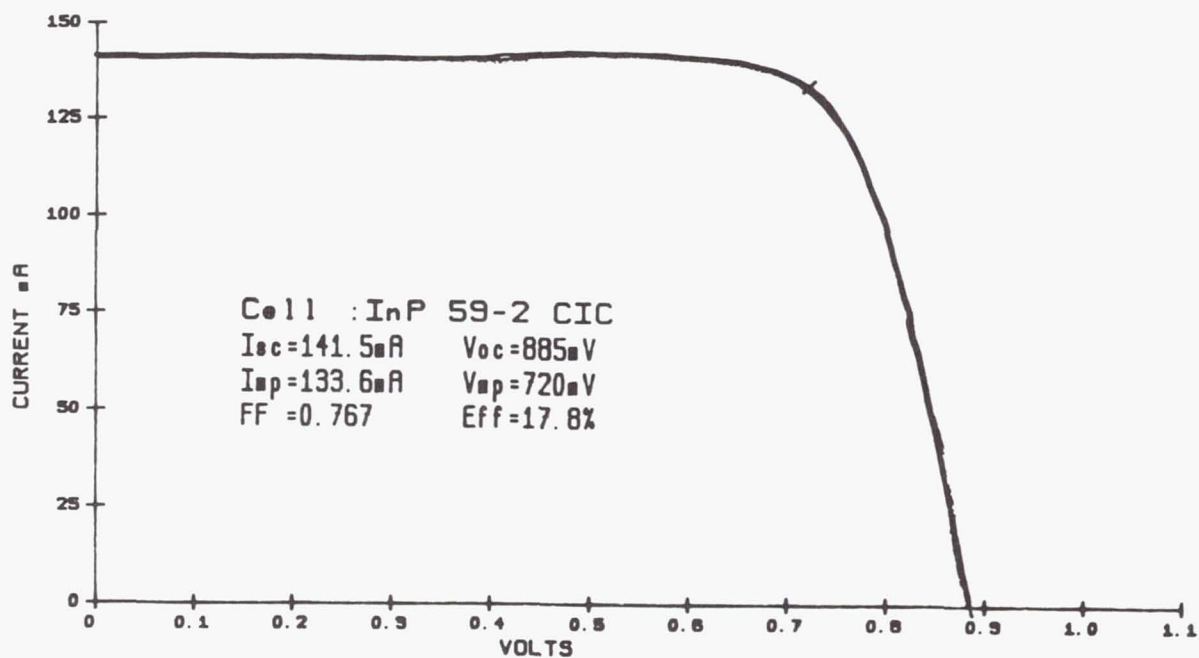


Figure 3: 1 Sun AM0 Photovoltaic measurement of 2x2 cm homoepitaxial n⁺-p-p⁺ Solar Cell

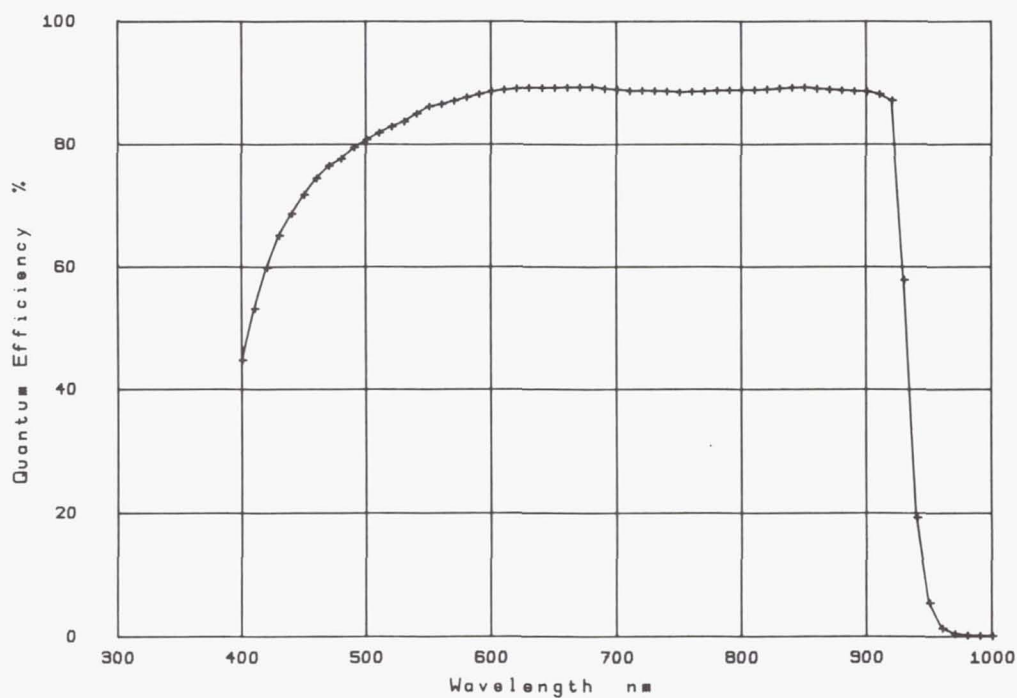


Figure 4: Quantum Efficiency of 2x2 cm homoepitaxial n⁺-p-p⁺ Solar Cell

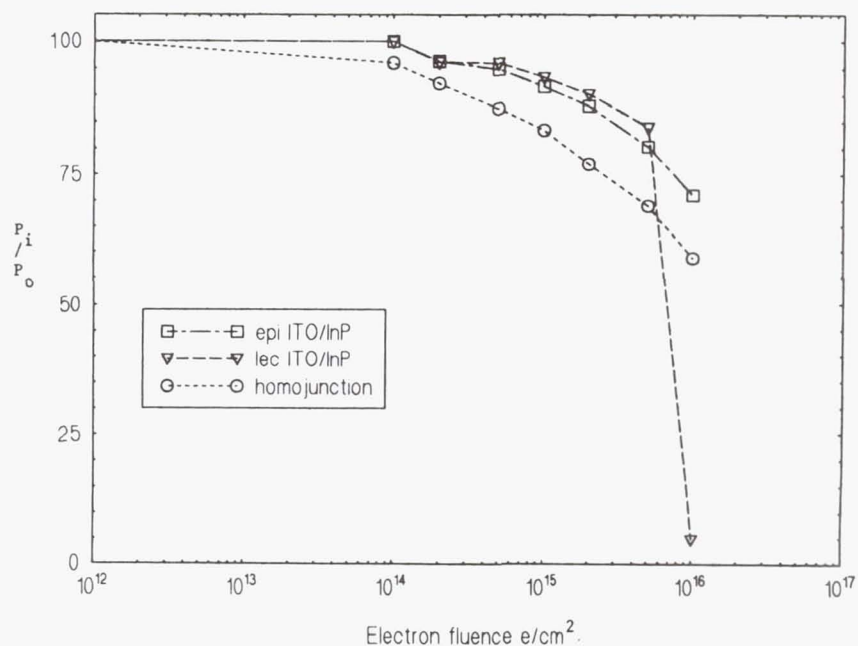


Figure 5: Percentage Power remaining for InP Solar Cells after 1 MeV electron irradiation.

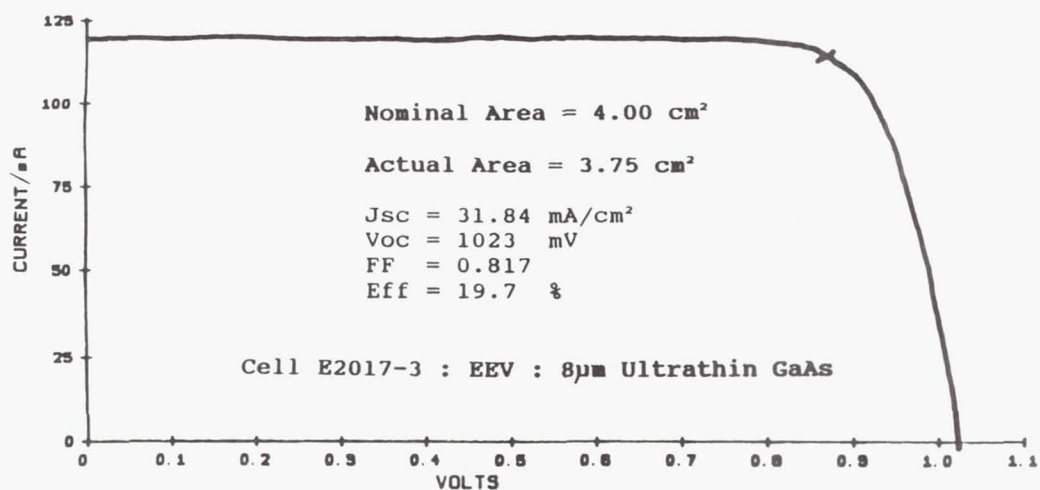


Figure 6: 1 Sun AM0 Photovoltaic measurement of 2x2cm ultrathin GaAs Solar Cell

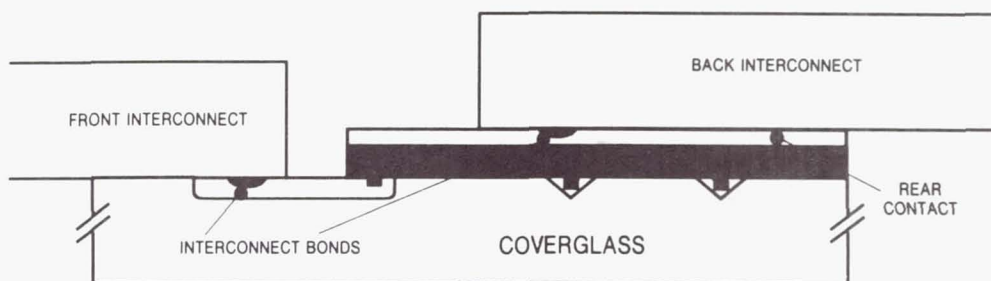


Figure 7: Interconnection to an ultrathin GaAs (or InP) cell, with interconnect supported on the coverglass.

REVIEW OF BETAVOLTAIC ENERGY CONVERSION

Larry C. Olsen

Washington State University / Tri-Cities
100 Sprout Road
Richland, WA 99352

Betavoltaic energy conversion refers to the generation of power by coupling a beta source to a semiconductor junction device. This paper briefly reviews the theory of betavoltaic energy conversion and some past studies of the subject. Calculations of limiting efficiencies for semiconductor cells versus bandgap are presented along with specific studies for Pm-147 and Ni-63 fueled devices. The approach used for fabricating Pm-147 fueled batteries by the author in the early 1970's is reviewed. Finally, the potential performance of advanced betavoltaic power sources is considered.

INTRODUCTION

Betavoltaic energy conversion refers to the generation of power by coupling a beta source to a semiconductor junction device. Some interest has been shown in this approach to energy conversion at the last two SPRAT meetings. As a result, it seemed timely to review the subject. This paper briefly reviews the theory of betavoltaic energy conversion, past studies in the field and discusses the potential performance of betavoltaic systems based on the availability of beta sources and currently available solar cell materials.

PAST BETAVOLTAIC STUDIES

The first report of an electron-voltaic effect was given by Ehrenberg, et al., in 1951 (ref. 1). They were primarily interested in the current magnification that resulted when selenium photocells were bombarded by an electron beam. Rappaport was the first to describe betavoltaic studies, that is, investigations involving beta sources coupled to semiconductor junction devices (ref. 2). He reported in 1953 on characteristics of silicon alloy junctions coupled to a 50 milliecurie $\text{Sr}^{90}\text{-Y}^{90}$ radioactive source. One cell produced 0.8 microwatts with an overall efficiency of 0.2 % being attained. The overall efficiency is based on the total power produced by the radioisotope source. Pfan and Roosbroeck reported on similar studies about the same time (ref. 3). They discussed the general problem of betavoltaics and gave experimental results for $\text{Sr}^{90}\text{-Y}^{90}$ sources combined silicon and germanium devices.

A more detailed report on the work by Rappaport and coworkers at RCA was given in 1956 (ref. 4). Further results were described for silicon and germanium alloy junctions coupled to $\text{Sr}^{90}\text{-Y}^{90}$ beta sources. In addition, the theory of betavoltaic devices was formulated. The interdependence of beta source parameters such as self absorption coefficient, beta energy

spectrum and activity, and semiconductor parameters such as energy gap and minority carrier properties were emphasized. The RCA group also identified the potential of Pm-147 betavoltaics in the 1956 paper. This was partially motivated by the negative results obtained with Sr⁹⁰-Y⁹⁰ sources coupled to Si devices. As a result of radiation damage, the maximum power produced by a Si/Sr-90 system was found to decay to one-tenth of its initial value within one week of life. The final contribution of the RCA group is contained in a 1964 paper by Flicker, et al. (ref. 5). Si and GaAs diffused junction devices were coupled to Pm-147 sources. Beta sources were made by precipitating Pm-147 as the hydrated oxide (Pm₂O₃·6H₂O) onto a substrate. Betavoltaic studies with GaAs cells yielded very poor results. Studies with silicon cells included the fabrication of prototype power sources consisting of a Pm-147 source combined with one or two silicon cells. Overall efficiencies of 0.4 % and 0.77 % were achieved. Lifetime studies with these prototypes showed only a slight effect due to radiation damage.

The most extensive effort concerning betavoltaic energy conversion appears to have occurred in a program led by the author at Donald W. Douglas Laboratories, Richland, WA, from 1968 to 1974 (ref. 6 and 7). This effort was based on the use of Pm-147 beta sources combined with Si n/p cells to produce nuclear batteries that were utilized as power sources for heart pacemakers. A brief description of this effort is discussed in a subsequent section.

PRINCIPLES OF BETAVOLTAIC ENERGY CONVERSION

The basic entity in a betavoltaic power source consists of a beta-emitting material coupled to a junction device as depicted in Figure 1. Some of the key aspects of betavoltaic energy conversion are described by Figure 2. An equivalent circuit for a betavoltaic cell is essentially the same as that for a solar cell, except that the current source is due to collection of electron-hole pairs generated by high energy beta particles. The importance one places on the series resistance R_s and the shunt resistance R_{sh} are reversed when comparing betavoltaics and photovoltaics. The value of R_s can be relatively large in the case of betavoltaics since the value of J_{sc} will typically be in the range of 1 μ A/sq.cm. to 100 μ A/sq.cm., whereas in photovoltaic applications J_{sc} is typically in the range of 10 to 40 mA/sq.cm.. Thus, R_s can be 100 ohms in a betavoltaic cell and cause a problem. On the other hand, it is important to minimize the shunt conductance -- that is, maximize the shunt resistance. Since a loss current of 1 μ A may be significant, it is necessary to utilize devices based on single crystal material. In the remainder of this section, a synopsis of the theory of betavoltaics will be presented, and then utilized to calculate the maximum efficiency of betavoltaic power sources versus semiconductor band gap.

The current supplied to a load by a betavoltaic cell is given by

$$J = J_{sc} - J_{Loss}(V) \quad (1)$$

J_{sc} is the short circuit current and J_{Loss} is the loss current given by

$$J_{Loss} = J_0 \exp(qV/kT) + J_{or} \exp(qV/2kT) + J_{ot} \exp(BV) + V/R_{sh} \quad (2)$$

where the loss terms refer to minority carrier injection, depletion layer recombination, tunneling and current loss through the effective shunt resistance. Since betavoltaic power sources typically provide low current, the dominant loss mechanism is typically tunneling or depletion layer recombination.

The short-circuit current is given by

$$J_{sc} = (1-r) Q J_{max} \quad (3)$$

where 'r' is the reflection coefficient for beta particles from the semiconductor surface, Q is the collection efficiency and J_{max} is the maximum possible current. The beta particle reflection depends primarily on the atomic number of the semiconductor. The collection efficiency is the fraction of electron-hole (EH) pairs collected as current relative to the total number of EH created by the beta particle flux that enters the semiconductor device. Since the decrease of beta particle flux within the semiconductor is proportional to $\exp(-\alpha x)$, where α is the absorption coefficient, analytical expressions for Q for a given device structure are essentially the same as those derived for solar cells. In particular, the beta flux passing through a material can be written as

$$N(x) = (1-r) N_0 \exp(-\alpha x) \quad (4)$$

If the beta particles penetrate only on the order of a minority carrier diffusion length, then values of Q can approach 1.0. For example, since betas from Pm-147 only penetrate silicon to a depth of 60 μm , Q-values can approach 0.8 to 1.0. If Pm-147 is coupled to a direct bandgap material, however, the collection efficiency will be significantly less since the diffusion length will be much smaller. Thus the value of Q depends on properties of both the source and the semiconductor.

In order to calculate the maximum efficiency of a system, we must know the maximum possible current. The key considerations concerning the calculation of J_{max} are described in Figure 3. One can define an effective ionization energy ϵ which is the average amount of energy expended to create one electron-hole pair. An empirical relationship exists which relates ϵ to semiconductor bandgap, namely,

$$\epsilon = (2.8) E_g + 0.5 \quad \text{eV} \quad (5)$$

If N_β and E_β are the incident beta flux and the average beta particle energy, respectively, then the maximum possible current that one can derive from a betavoltaic device is given by

$$J_{max} = q N_\beta (E_\beta / \epsilon) \quad (6)$$

The maximum power delivered by a cell can be written as

$$P_{max} = J_{sc} V_{oc} FF \quad (7)$$

Once a beta source and device structure are defined, J_{max} , r and Q can be calculated. Finally, V_{oc} and FF can be calculated if the dominant loss current term(s) is identified. The overall efficiency is defined by

$$\eta = (P_{\max}/P_{\text{in}}) \times 100 \quad (8)$$

where

$$P_{\text{in}} = q N_0 E_{\beta} \quad (9)$$

where N_0 refers to the number of beta particles emitted by the source per second, per square cm. of device area.

It is convenient to write the overall efficiency as a product of three terms, or efficiencies,

$$\eta = \eta_{\beta} \eta_c \eta_s \quad (10)$$

$$\eta_{\beta} = N_{\beta} / N_0 \quad (11)$$

$$\eta_c = (1-r) Q \quad (12)$$

$$\eta_s = [V_{oc} FF / \epsilon] \times 100 \quad \% \quad (13)$$

The term η_{β} expresses the fraction of all betas created that are actually emitted from the source and directed towards the device, and is therefore referred to as the beta source efficiency. η_c is a coupling efficiency since it involves properties of both beta source and the semiconductor device. The term is designated as the semiconductor efficiency, since it determines the maximum possible efficiency that can be attained with a given semiconductor coupled to a particular beta source.

The maximum possible efficiency of a given betavoltaic system as a function of bandgap if one assumes that the semiconductor device is an ideal homojunction. In this case, the current loss term is dictated by minority carrier injection. Following Green (ref.8), we estimate that J_0 can be written as

$$J_0 = 1.5 \times 10^5 \exp(-E_g/kT) \quad \text{A/sq.cm.} \quad (14)$$

The fill-factor can be accurately calculated as follows (ref.5)

$$FF = [v_{oc} - \ln(v_{oc} + 0.72)] / [v_{oc} + 1], \quad v_{oc} = V_{oc}/kT \quad (15)$$

Thus, once a given beta source is selected and an ideal device is assumed, the semiconductor efficiency (η_s) becomes a function only of bandgap. The potential efficiency of some systems will be examined after possible beta sources are considered. One can calculate an upper limit to betavoltaic device efficiency that is independent of the beta source, however. In particular, it can be shown that

$$\eta_s \leq E_g / \epsilon(E_g) \quad (16)$$

This limiting value of η is plotted in Figure 4 versus bandgap. Due to the functional dependence of the effective ionization energy, the limiting value of efficiency rises with bandgap and then levels off at a value slightly over 30 %. Thus, in principle, it is advantageous to utilize large bandgap devices. One must remember, however, that ideal cell behavior is being assumed.

BETA SOURCE CONSIDERATIONS

The process of selecting a beta emitter involves simultaneous consideration of isotope, half-life and the effects of radiation damage of semiconductor devices. To fabricate long lived power sources, it is clearly desirable to utilize isotopes with long half-lives. On the other hand, since the beta flux derivable from a source material is inversely proportional to the half-life, the value of J_{\max} and thus P_{\max} are inversely proportional to the half-life. One must also consider the beta particle energies relative to the semiconductor radiation damage threshold (E_{th}). In general, it is preferable to have the maximum beta particle energy (E_{\max}) less than E_{th} . Typically, E_{th} is on the order of 200 keV to 400 keV. Other key considerations are the availability of the radioisotope and the potential dose rate that might exist near the power source. Table 1 lists some possible beta emitters that meet some of the criteria that have been identified. Availability has become a key issue. The only isotopes that are readily available are tritium and Kr-85. Both are available in gaseous form, and tritium can be obtained in the form of tritiated Ti foils. If one were interested in one of the other isotopes, the Department of Energy would need to be consulted.

THEORETICAL EFFICIENCY OF Pm-147 AND NI-63 BETAVOLTAICS

Considerable attention has been given to the use of Pm-147 and Ni-63 in betavoltaic systems. As noted above Pm-147 fueled batteries were actually reduced to practice. Ni-63 has been considered in the past because of its long half-life. The use of both of these isotopes is hindered because of the complex processes required to generate the isotope. Calculated efficiencies are considered here because of interest shown in these materials in the past, and for the purpose of illustration.

Figure 5 gives a plot of theoretical efficiency of Pm-147 fueled devices versus bandgap assuming ideal semiconductor junctions and bidirectional sources. By bidirectional sources, it is implied that the beta flux from both sides of a slab of beta emitting material is utilized. Due to the ideal cell assumption, the efficiency vs bandgap curve has a similar shape as the limiting efficiency curve given in Figure 4.

Figure 6A and 6B describe calculated results for Ni-63 fueled cells. The device efficiencies are much lower in this case because of the beta source efficiency. As a result of the low beta energy, Ni-63 sources would suffer from effects of self absorption. The low values of current and power are results of the long half-life and low beta particle energy. Similar results are obtained when one considers properties of tritium fueled betavoltaic devices.

Pm-147 FUELED BETAVOLTAIC BATTERIES

The author led a program to develop Pm-147 fuelled betavoltaic batteries at the Donald W. Douglas Laboratories, Richland, WA, from 1968 to 1974. Pm-147 was available in the form of Pm_2O_3 from the U.S. Government. Custom made silicon cells were obtained from Heliotek (now Spectrolab) and from Centralab (now ASEC). The cells had n/p junctions with a mesa around the device periphery to minimize leakage currents at low voltages. The author benefited from interactions with Gene Ralph at Heliotek and Peter Isles at Centralab.

The basic approach to battery construction is illustrated by Figure 7. The n/p cells and beta sources were stacked in tandem so that the devices were connected in series. The Pm-147 sources actually consisted of Pm_2O_3 deposited onto Ta sheet. Thus the sources were unidirectional. Self-standing bidirectional Pm_2O_3 sources were under development when the program was terminated. Properties of a typical silicon cell coupled to a unidirectional source are described in Figures 8A and 8B. Batteries were typically designed with 5 mg/cm^2 Pm_2O_3 sources. Figure 9 shows a picture of three of the batteries that were made in reasonable quantities. Their properties are summarized in Table 2. These batteries were referred to as Betacel batteries and were nominally 2 % efficient (overall efficiency). With bidirectional sources, they would have had efficiencies of 4 %. The Model 400 Betacel was considered seriously for powering heart pacemakers by companies in the United States and Germany. The short-circuit current and maximum power versus time for a typical Model 400 Betacel are plotted in Figure 10. Since the power required by the pacemaker circuitry was approximately $10 \mu\text{watts}$, the potential lifetime was ten years. Over 100 people received Betacel powered pacemakers, and many of the units lasted 10 years. Although the potential use of Betacel batteries for pacemakers appeared very promising, the lithium battery was developed about the same time. Lithium batteries lasted only 7 years, but since they were non-nuclear they were preferred by the pacemaker industry. The Betacel batteries were also utilized to a limited extent for military purposes.

CONCLUSIONS

Interest in the use of betavoltaic energy conversion seems to 'pop up' every few years. When the right application emerges, it may finally be utilized extensively. Many more choices are now available for the semiconductor cell than were available when the Pm-147 fuelled batteries were developed. Unfortunately, the choice of beta emitting material would appear to be more limited. To place the potential use of betavoltaic power sources in perspective, it is useful to estimate the power density versus time for some possible advanced systems. Figure 11 describes results of calculated properties of some advanced concepts. The thin film AlGaAs cells are assumed to be self standing devices. There are many other devices that one could consider. For example, GaP with an indirect bandgap, and thus potentially long diffusion length, would certainly be of interest for coupling to Pm-147. InP with its radiation resistant properties could be interesting for coupling to high energy beta emitters such as Ti-204 . Nevertheless, the power density curves shown in Figure 11 can be used to make a few key points. Betavoltaic systems should only be considered for low power applications. For example, if one is interested in power levels on the order of one watt for ten years, it is clear that on the order of 1000 cm^3 of Pm-147 fueled devices must be considered. The size may not be a problem, but the cost might be

prohibitive. If one considers an application for which 1 milliwatt or 10 microwatts are required, tritium or Pm-147 fueled systems seem reasonable.

REFERENCES

1. W. Ehrenberg, et al., "The Electron Voltaic Effect," Proc. Roy. Soc. **64**, 424(1951).
2. P. Rappaport, "The Electron-Voltaic Effect in p-n Junctions Induced by Beta Particle Bombardment," Phys. Rev. **93**, 246(1953).
3. W.G. Pfann and W. Van Roosbroeck, "Radioactive and Photoelectric p-n Junction Power Sources," J. Appl. Phys. **25**, 1422 (1954).
4. P. Rappaport, J. J. Loferski and E. G. Linder, "The Electron-Voltaic Effect in Germanium and Silicon P-N Junctions," RCA Rev. **17**, 100 (1956).
5. H. Flicker, J. J. Loferski and T. S. Elleman, "Construction of a Promethium-147 Atomic Battery," IEEE Trans, **ED-11**, 2 (1964).
6. L. C. Olsen, "Betavoltaic Energy Conversion," Energy Conversion **13**, 117 (1973).
7. L.C. Olsen, "Advanced Betavoltaic Power Sources," Proc. 9th Intersociety Energy Conversion Engineering Conference, page 754 (1974).
8. Martin A. Green, "Solar Cells," Prentice-Hall, Inc., 1982, Chapter 5.

TABLE 1 -- POSSIBLE BETA SOURCES

ISOTOPE	E_{\max} (MeV)	$\tau_{1/2}$ (yr)	Maximum J_{sc} for Si (arbitrary units)
H^3	0.018	12.3	3×10^{-3}
Ni^{63}	0.067	92	10^{-3}
Pm^{147}	0.230	2.62	1
Tl^{204}	0.765	3.75	17
Kr^{85}	0.670	10.9	28

TABLE 2 -- BETACEL CHARACTERISTICS

Characteristic	Model 50	Model 200	Model 400
Performance characteristics†			
Maximum power (μW)	50	200	400
Voltage at maximum power (V)	1.3	3.3	4.0
Open circuit voltage (V)	1.7	4.7	4.9
Short circuit current (μA)	45	72	112
Curies Pm^{147}	12	73	66
Efficiency (%)	1.0	0.7	1.7
Physical characteristics			
Diameter (cm)	1.52	2.03	2.29
(in)	0.60	0.80	0.90
Overall height (cm)	1.02	1.65	2.44
(in)	0.40	0.65	0.96
Mass (g)	17	55	98
Radiation dose rate at 2.5 cm from battery center‡			
BOL (mrem/h)	2.3	8.1	6.1
At end of 5 years (mrem/h)	1.2	4.3	3.3
5 year time averaged (mrem/h)	1.7	5.9	4.4

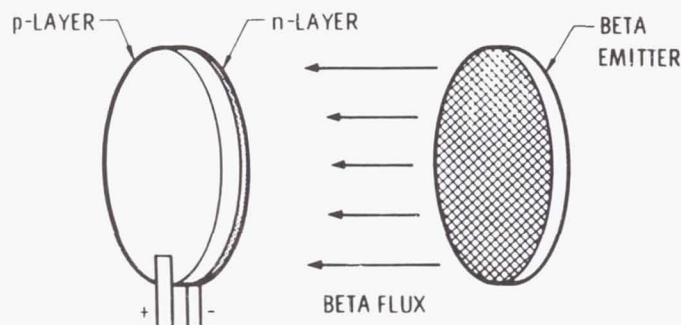
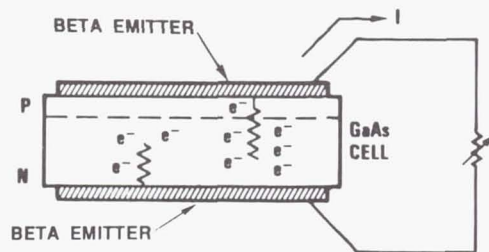


Figure 1. Basic Approach To Betavoltaic Energy Conversion.

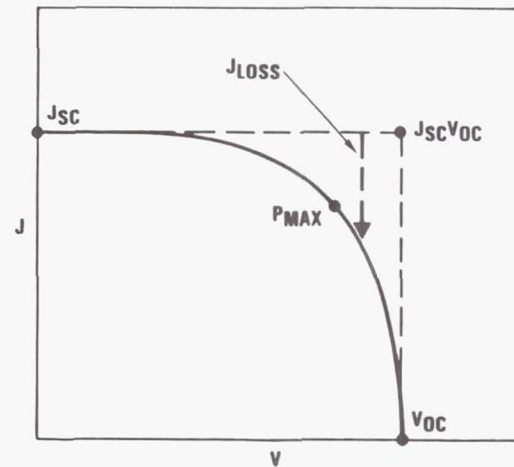
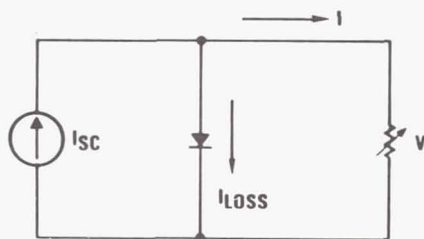


$$J = I / \text{CELL AREA}$$

$$J = J_{SC} - J_{LOSS}(V)$$

$$P_{MAX} = FF \cdot J_{SC} \cdot V_{OC}$$

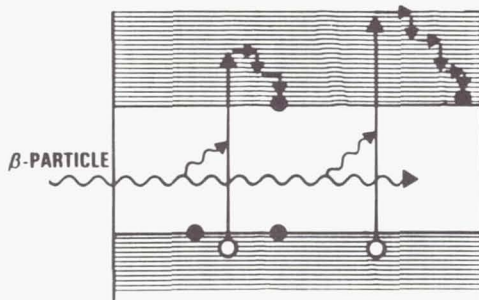
CIRCUIT MODEL



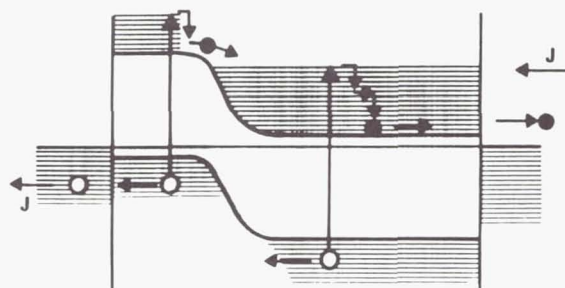
- High energy electrons (beta rays) produce electron/hole pairs in semiconductor cell
- Diode characteristics, $J_{LOSS}(V)$, of junction determine the current, I , to external load
- $J_{LOSS}(V)$ must be small in order to produce useful power

Figure 2. Betavoltaic Principles.

HOMOGENEOUS SEMICONDUCTOR



P/N JUNCTION



Electron-hole pairs

$$N_{EH} = (\text{No electron-hole pairs/cm}^2/\text{sec})$$

$$= N_{\beta} \left(\frac{\bar{E}_{\beta}}{\epsilon} \right)$$

$$\epsilon = \text{Effective ionization energy}$$

$$= (2.8) E_g + 0.5 \text{ eV}$$

$$N_{\beta} = \text{Beta flux entering junction device}$$

Maximum current

$$J_{max} = I_{max} / \text{cell area}$$

$$= e N_{EH} = e N_{\beta} \left(\frac{\bar{E}_{\beta}}{\epsilon} \right)$$

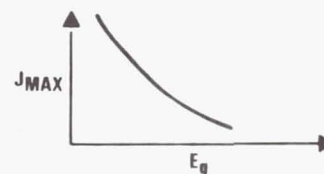


Figure 3. Considerations For Maximum Current.

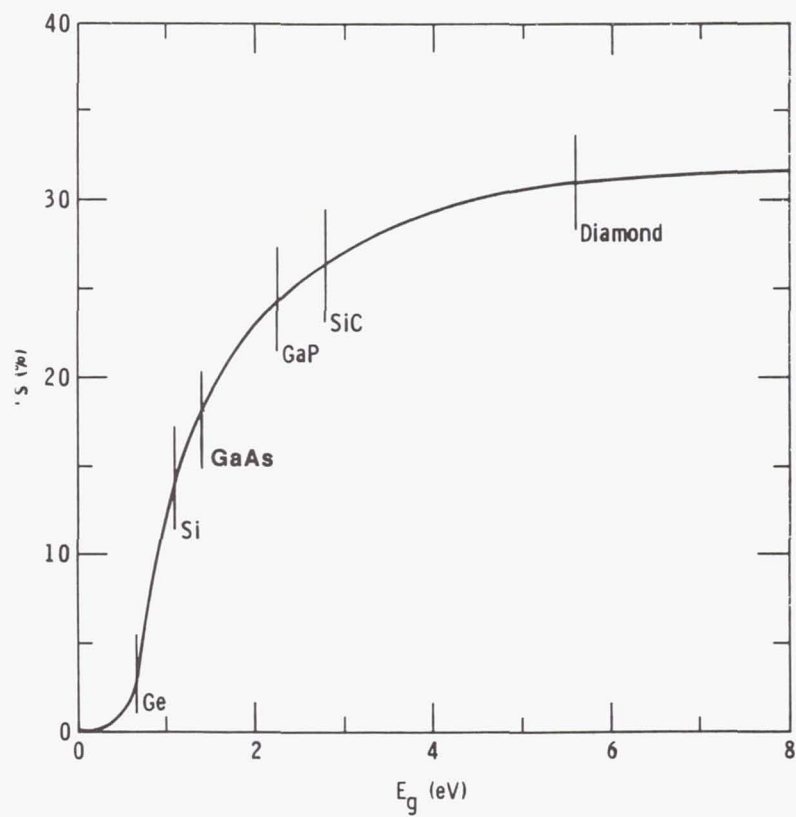


Figure 4. Limiting Betavoltaic Efficiency Versus Semiconductor Bandgap.

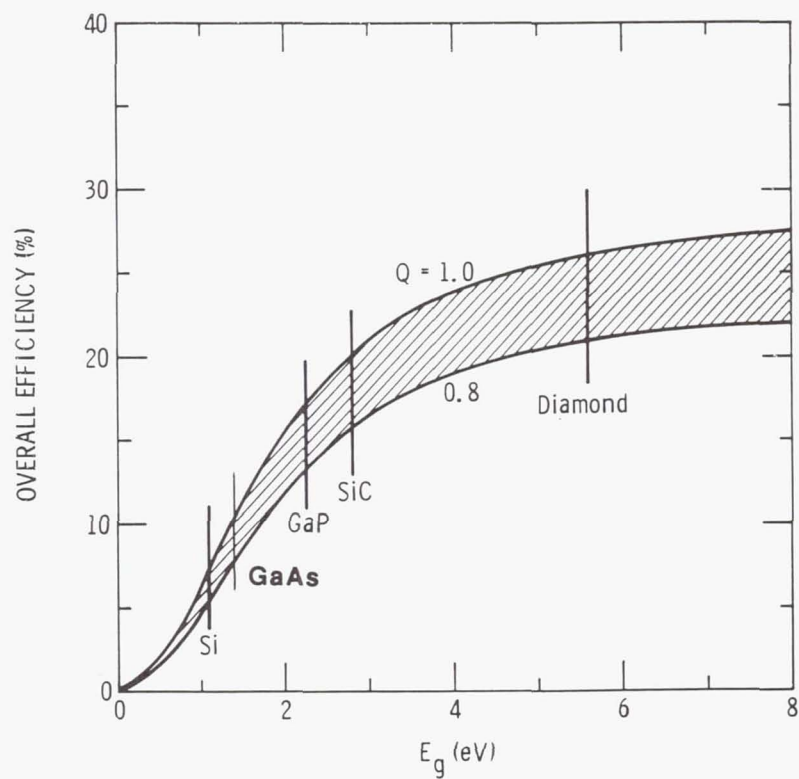
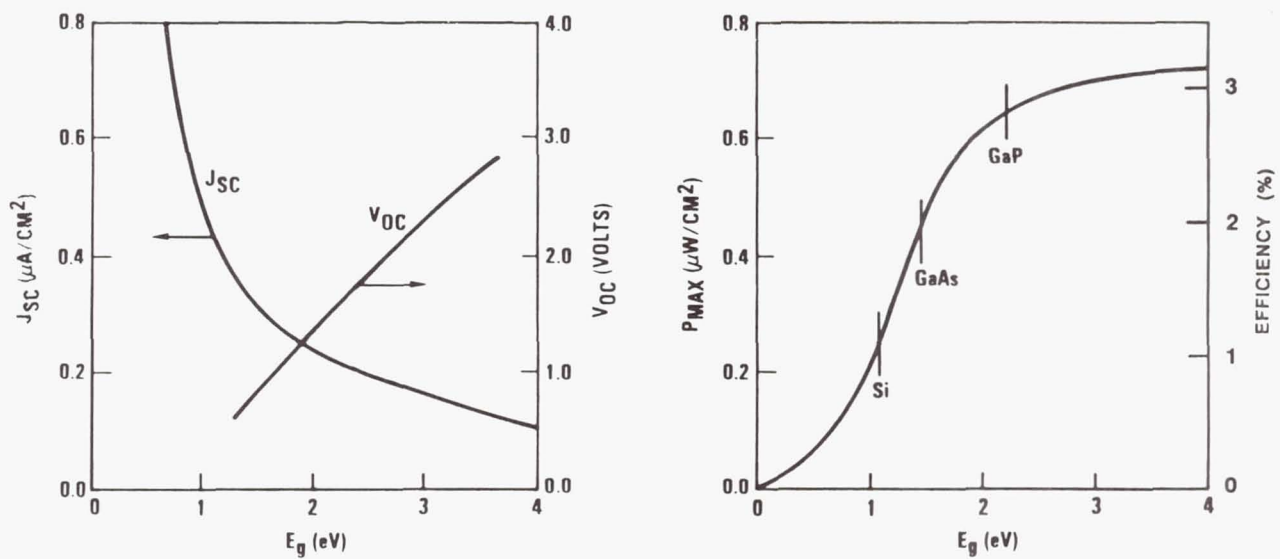


Figure 5. Calculated Efficiency For Pm-147 Betavoltaic Systems Versus Bandgap.



Assumptions: 1. Ideal Diode Characteristics
2. Two-Sided Beta Source With 100% Nickel 63

Figure 6. Calculated Properties Of Ni-63 Betavoltaic Systems Versus Bandgap.

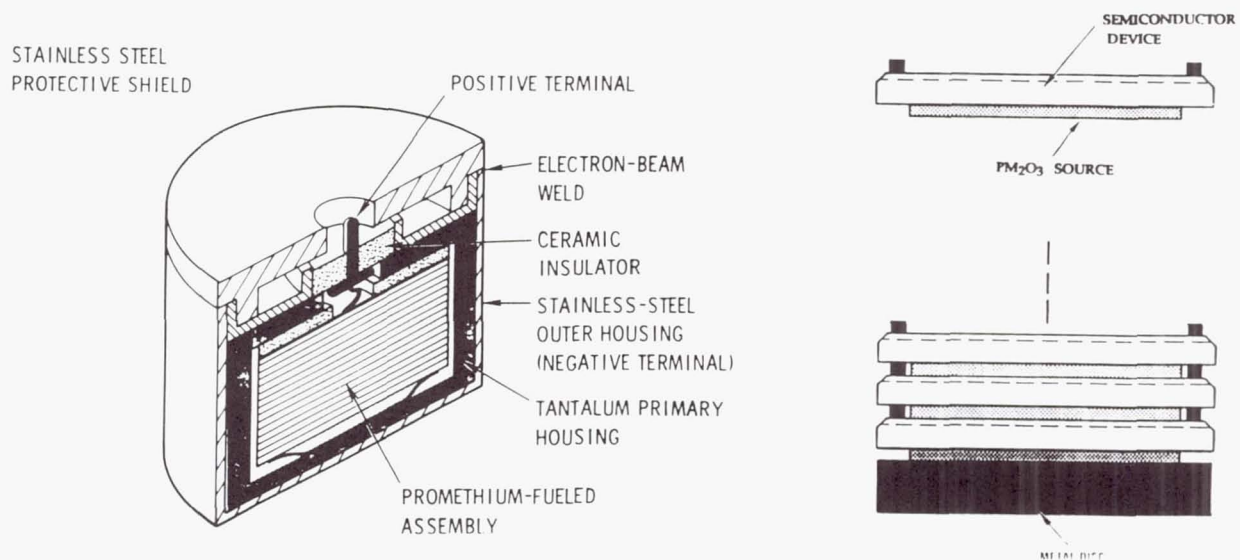


Figure 7. Approach Used For Betacel Construction.

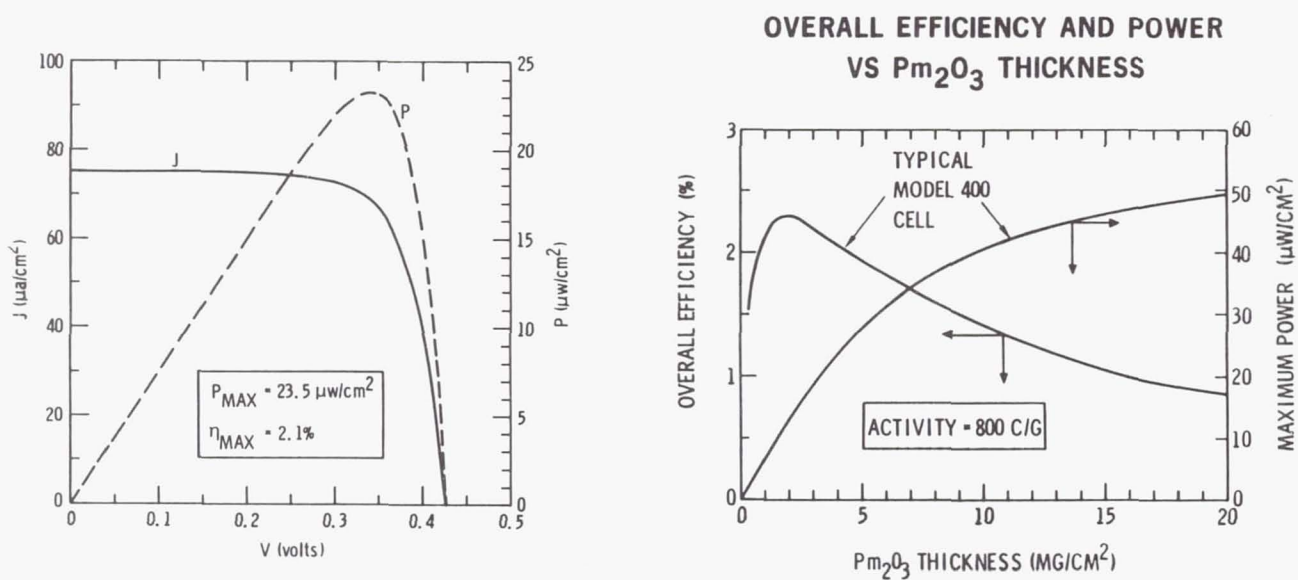


Figure 8. Betavoltaic Properties Of Silicon n/p Cells Coupled To Pm-147 Sources.

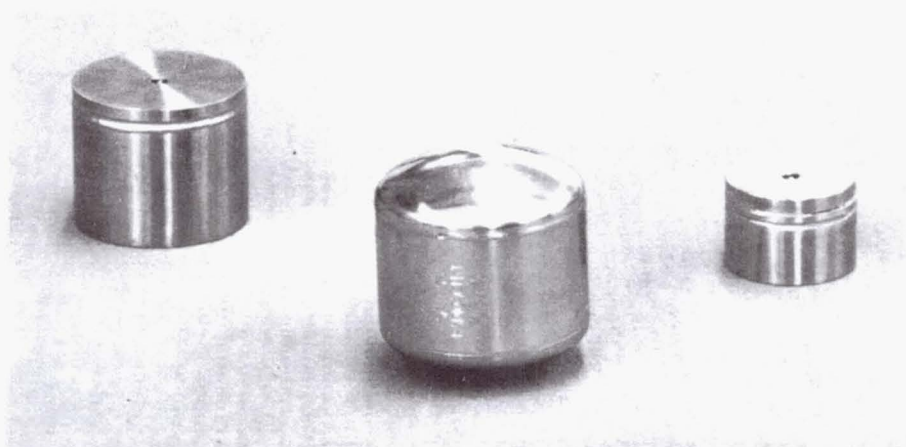


Figure 9. Betacel Batteries Developed At Donald W. Douglas Laboratories. Left to Right: Model 200, Model 400 and Model 50.

UV TESTING OF SOLAR CELLS: EFFECTS OF ANTIREFLECTIVE COATING, PRIOR IRRADIATION, AND UV SOURCE¹

A. Meulenberg
COMSAT Laboratories
Clarksburg, MD 20871

ABSTRACT

Short-circuit current degradation of electron irradiated double-layer antireflective-coated cells after 3000 hours ultraviolet (UV) exposure exceeds 3 percent; extrapolation of the data to 10^5 hours (11.4 yrs.) gives a degradation that exceeds 10 percent. Significant qualitative and quantitative differences in degradation were observed in cells with double- and single-layer antireflective coatings. The effects of UV-source age were observed and corrections were made to the data. An additional degradation mechanism was identified that occurs only in previously electron-irradiated solar cells since identical unirradiated cells degrade to only 6 ± 3 percent when extrapolated 10^5 hours of UV illumination.

INTRODUCTION

Previous testing (1989–1990) of INTELSAT VII preflight cells, performed under contract to MITSUBISHI, had indicated an unexpectedly high degradation to double-layer antireflective (DAR)-coated cells when compared to single-layer antireflective (SAR)-coated cells in the same test. If real, such high degradation would eliminate any advantage of using DAR coatings in space. A second extended ultraviolet (UV) degradation test (>3000 UV sun hours or UVSH)* was therefore conducted on covered, unirradiated and electron irradiated, solar cells provided by INTELSAT. The two tests had identical procedures and equipment, but a few things were changed in the hopes of identifying a possible source of the high degradation observed. First, the cells were limited to a 60°C infrared (IR) soak prior to start of UV exposure. This IR soak was used to aid outgassing of the system and heating the solar cells to prevent deposition of any outgassed contaminants on their surfaces. The earlier test was heated above 80°C since temperature coefficient measurements up to 75°C were to be made of these cells before and after the UV test. One vacuum chamber in the earlier test had produced visible contamination of the quartz window and solar cells when heated to 85°C for an extended period. Second, the UV test was conducted at 40°C rather than the 63°C of the earlier test. This was done to reduce possible contamination from the system over time, and to bring the test temperature closer to that of tests performed during the last 15 years. Third, a small set of unirradiated test cells was included in the UV test along with the electron irradiated cells. The earlier UV test had been conducted using only irradiated test cells from a prior 1 MeV-electron degradation test. Fourth, a larger group of SAR control cells (4 rather than 1) was included in the test to confirm and quantify the observed difference in shape between the DAR and SAR solar cell degradation curves of the earlier test. The DAR-coated cells, which displayed a lower degradation rate up to 2000 hours of UV, degraded more rapidly thereafter and, when the data were extrapolated, they indicated nearly twice the degradation at 10^5 hours.

The similarities in the two test procedures and solar cells allowed a confirmation of the earlier test results and pointed to a failure of the DAR coating to survive a space-UV environment. The differences that were introduced allowed

¹Work sponsored by the COMSAT Corporation.

*One UV sun is the UV content of 1 sun air mass zero (AM0). To get proper UV output from the UV source, no filters were used. This results in an excess intensity in the near-infrared region which causes large differences from AM0 in the output spectrum.

identification of several effects that alter extrapolated degradation predications and raised questions about how UV testing should be conducted.

SOLAR CELL DESCRIPTION

The UV test contained three groups of solar cells: Group 1—10- Ω -cm AEG (now Telefunken System Technic [TST]) INTELSAT V cells; Group 2—2 Ω -cm AEG DAR-coated INTELSAT VII primary power cells; and Group 3—10- Ω -cm AEG DAR-coated INTELSAT VII battery charge cells. The INTELSAT V test control cells are of a type used as test controls in other UV tests performed by COMSAT, are well behaved over many years of testing, and were included in a 23,000-hr UV test. These are SAR-coated cells and have always displayed a monotonically decreasing degradation with UV exposure.

Eleven 2- Ω -cm cells were selected from a larger set of 1-MeV-electron irradiated cells and their unirradiated controls. Four 10- Ω -cm cells were all irradiated to 1.2×10^{15} 1-MeV electrons/cm². Prior to the UV test, all INTELSAT VII cells had been exposed to at least 24 hours of 60°C annealing under an infrared (IR) lamp and for another 120 hours at 65°C at the beginning of the UV test during a vacuum bake out procedure.

A single AEG INTELSAT V cell was used as an unexposed control (secondary reference) cell. During UV exposure, it was kept covered by a rotatable flap within the vacuum chamber. The flap was moved out of the way while electrical measurements were being made.

DESCRIPTION OF TEST

The UV illumination test was performed in a COMSAT-designed vacuum chamber which incorporates a UV-grade quartz window. The system was rough pumped with a turbomolecular pump system (pressure at 10^{-6} torr) prior to starting the UV system and was operated continuously throughout the test with an ULTEK Model 202-2500 ion pump at a measured pressure of less than 10^{-6} torr and temperature of 40°C ($<2 \times 10^{-6}$ torr at the very start of test).

UV illumination for the test was obtained with a Kratos LH 153 source (1-kW bulb). Intensity levels were checked several times each week using a pyroheliometer covered with a calibrated UV bandpass filter and a quartz cover (to compensate for window reflection in the vacuum system). Intensity adjustments were made when necessary. Beam intensity did not deviate across the test cells by more than ± 10 percent.

A Hewlett-Packard computer and data acquisition system was used to monitor test parameters and to measure solar cell current/voltage (I/V) curves. The measured parameters used for comparison during the tests were short-circuit current (I_{sc}) and open-circuit voltage (V_{oc}). These measurements were made while the solar cells were illuminated with a Spectrolab X-25L solar simulator maintained at one sun AM0 using a primary solar cell standard. An internal control cell (mounted inside the test chamber) was shielded from the UV light source and only exposed to direct light while I_{sc} and V_{oc} measurements were being made on the solar cells under test.

After being installed with low-temperature solder on the vacuum chamber baseplate (water heated during the test), each solar cell was measured (without window) at $40^\circ\text{C} \pm 0.5^\circ\text{C}$ using the X-25L solar simulator (prior to pumpdown). Additional I_{sc} measurements were made under vacuum before and after an infrared bake-out ($\geq 65^\circ\text{C}$) for 120 hours, prior to exposure to UV. All I_{sc} measurements could be corrected with the internal control cell current (measured within 10 ms) to average out any short-term effects of X-25L light intensity fluctuation with time. Multiple measurements, taken 24 hours after the bake-out and averaged, constitute the initial (1 UVSH) measurement. Vacuum was not broken until after final measurements at the conclusion of the test.

Measurements were performed on cells *soldered* to the test fixture to improve temperature control and electrical reproducibility of the data. Initially, full I/V measurements of each solar cell were made to determine cell fill factors, hence I_{sc} measurement reliability. This technique required 30 seconds per cell measurement and as much as 5 minutes

between cell measurements. The normal test measurements were performed automatically by computer, scanning only the V_{oc} and I_{sc} of each solar cell, a process which takes about 20 seconds for the full set of cells. Each cell was measured 10 times, and the results averaged, to create a data point. Cells were in open-circuit condition while under UV illumination.

TEST RESULTS

UV degradation resulting from the test, after 3,340 UVSH, for the three groups of solar cells was: 2- Ω -cm primary power cells, 3.0 ± 0.2 percent; 10- Ω -cm battery charge cells, 3.8 ± 0.2 percent; and 10- Ω -cm AEG SAR-coated test control cells, 3.5 ± 0.2 percent. The error limits represent extremes of statistical error of the mean values for each cell type, but does not include systematic error or variation in the individual cells (typically $< \pm 0.5$ percent). The degradation of these control cells in other tests (for approximately 2,500 UVSH) was 3.2 ± 0.7 percent (systematic error included). The test-control cell results thus fall well within the range of similar cells in previous tests.

Comparison of the SAR- and DAR-coated cell test averages (Figure 1) indicate the reason for our concern about DAR-coated cells. The impact on results extrapolated to 100,000 hours (11.4 years) is particularly disturbing if the last few points (>3000 UVSH) are included. Figure 1 also includes a difference curve comparing the 2- and 10- Ω -cm DAR cells (2 minus 10- Ω -cm). The last data point for each cell type is the average of five readings from 3102 to 3342 hours. The error bars indicate the extreme values for the measurements. This format is used here to keep the plot from being cluttered in a region where the data crowd together and overlap. Note that the error limits are on the order of ± 0.25 percent.

UV DEGRADATION DATA

Results of the test are plotted along with extrapolations to 100,000 UVSH that encompass two cases. First, the extrapolated degradation based on a simple curve fit to data <3000 UVSH is plotted for each cell type (Figure 2). Second, the extrapolations, including the data >3000 UVSH, are provided (Figure 3). The differences in curve shape between the SAR- and DAR-coated cells are striking. First, the DAR cells appear to increase in I_{sc} during the first 100 hours, whereas the SAR cells degrade during this period. Both type cells degrade at about the same rate during the next 1000 hours, but the DAR-coated cells begin to degrade at a higher rate over the next 2000 hours. While the actual degradation after 3000 UVSH is similar for both cell types, the rate of degradation, which strongly affects extrapolated values, is of greater importance.

DISCUSSION

In a comprehensive and extended (>3000 hour) UV degradation test of DAR-coated silicon solar cells, both systematic and experimental errors were detected. Four sources of error were determined (Appendix A) to warrant correction.

- The greatest source of uncertainty resulted from the use of electron irradiated cells for the UV test. Contrary to expectation, the UV degradation was much more severe for such cells. This effect was identified and found to be extensive (nearly a factor of two), but quantitative evaluation cannot yet be made since only three nonirradiated DAR-coated cells were exposed to UV during this test.
- The second most important correction is related to the age of the UV source bulb. Degradation to the solar cell stack is greatest when the bulb is new. While the actual changes in cell current are not greatly affected by changes in the degradation rate, the extrapolated values can be strongly affected (by as much as a factor of two).
- The third major correction is also associated with prior electron irradiation damage. UV degradation is defined in terms of percent degradation of short circuit current or 100-percent $\Delta I_{sc}/I_{sc}$. Since the irradiated cells averaged 15-percent less I_{sc} than did the unirradiated cells, the percent degradation of these cells is calculated to be 15-percent higher.

- The last correction accounts for contamination and subsequent darkening on this contamination on the cells and vacuum system quartz window during the test. The correction is assumed to be twice the degradation observed by the internal control cell for the window alone.

CONCLUSION

Figure 4 is the corrected average data and fitted curves for the 2- and 10- Ω -cm DAR-coated INTELSAT VII solar cells, along with the unirradiated SAR-coated AEG cells from the INTELSAT V program used as exposure controls. The modifications made to correct the data are: a shift in the time base, a reduction of the electron irradiated cell degradation by 15 percent, and a subtraction of twice the control cell degradation from the test cell data. An unirradiated subset of the 2- Ω -cm DAR-coated cells is shown separately, to indicate the magnitude of the difference between irradiated and unirradiated cells. Being a smaller group, its error limit is percentage-wise greater, but there is little possibility of overlap in the two data sets.

Conclusions of this report are as follows:

- Previously irradiated DAR-coated solar cells made from 2- Ω -cm Wacker silicon degrade more severely than do identical, but unirradiated, cells.
 - Unirradiated 2 Ω -cm 6 ± 3 percent at 10^5 UVSH
 - Irradiated 2 and 10 Ω -cm 11 ± 3 percent at 10^5 UVSH
 - Unirradiated SAR 10 Ω -cm 6 ± 1 percent at 10^5 UVSH
- The use and age of UV source bulbs and optics must be controlled to prevent major errors in extrapolated data.
- The use of linear-linear plots can no longer be condoned in predicting UV degradation for extended missions. Extrapolated results of data plotted with such scales can be an order of magnitude off.
- There appears to be no statistically significant difference in UV degradation between the tested 10- and 2- Ω -cm solar cells. Although such a possibility is suggested by the data in this test, it is not the case in Reference 1. (The 2- Ω -cm DAR-coated cell average data in Figure 4 of this paper includes unirradiated cells.)
- A preference of UV testing for irradiated vs nonirradiated solar cells has not been established. Material type has an effect and crucible-grown silicon may not display any difference.
- Contrary to predictions based on the initial analysis of test data, we can no longer unequivocally claim that DAR coated cells degrade under UV more than do SAR-coated cells when extrapolated to 10^5 hours.

REFERENCES

1. Crabb, R. L., "Photon Induced Degradation of Electron Irradiated Silicon Solar Cells," Conference Record of the 9th Photovoltage Specialists Conference, *PVSC* (1972) pp. 329–330.
2. Crabb, R. L., "Photon Induced Degradation of Electron and Proton Irradiated Silicon Solar Cells," Conference Record of the 10th Photovoltage Specialists Conference, *PVSC* (1973) pp. 396–403.
3. Fisher, H. and Pschunder, W., "Investigation of Photon and Thermal Induced Changes in Silicon Solar Cells," Conference Record of the 10th Photovoltage Specialists Conference, *PVSC* (1973) pp. 404–411.
4. Pschunder, W. and Fisher, H., "Influence of Silicon Impurity Content on Photon Induced Variation of Solar Cell Parameters After Particle Irradiation," Conference Record of the 12th Photovoltage Specialists Conference, *PVSC* (1976) pp. 270–275.

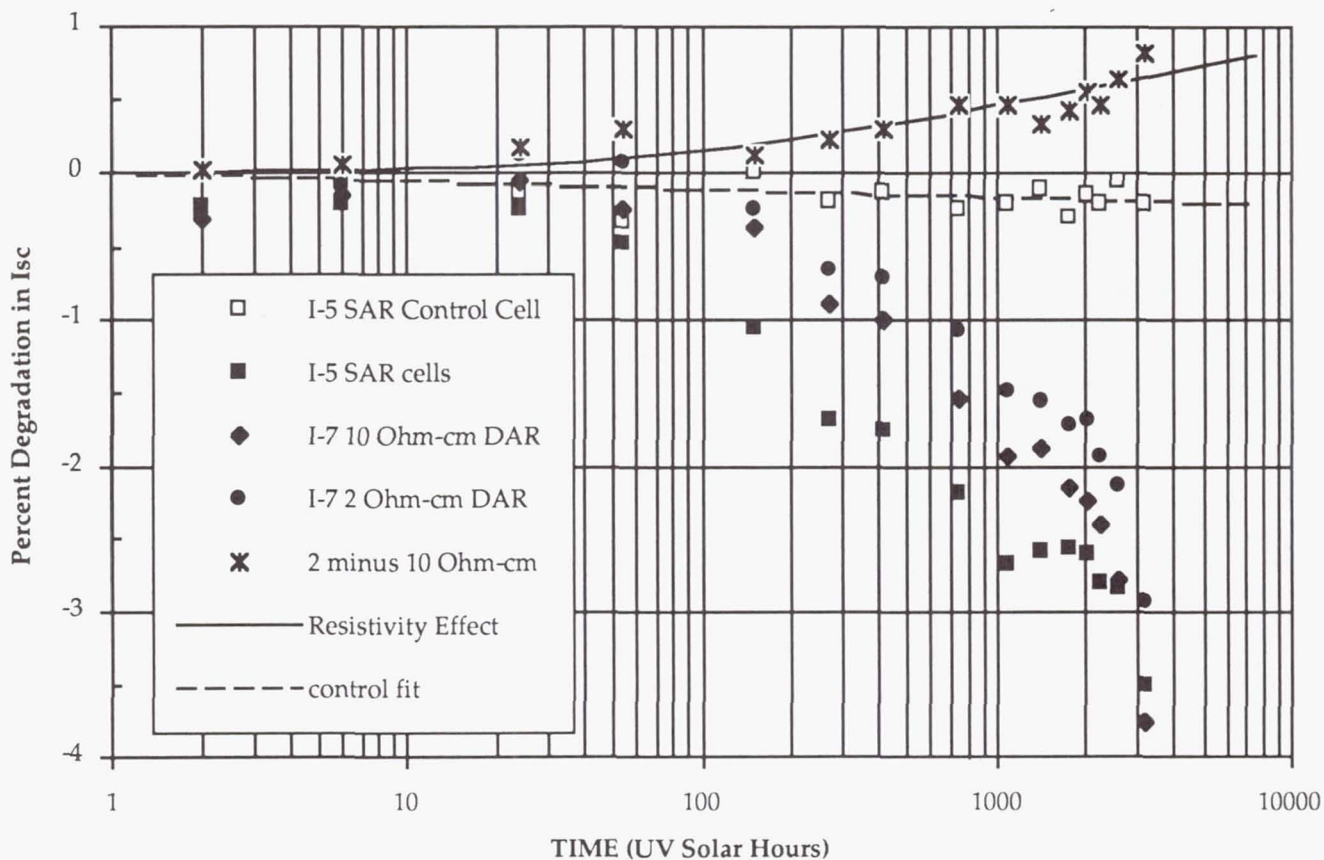


Figure 1. Raw data for UV degradation test (plus a difference curve)

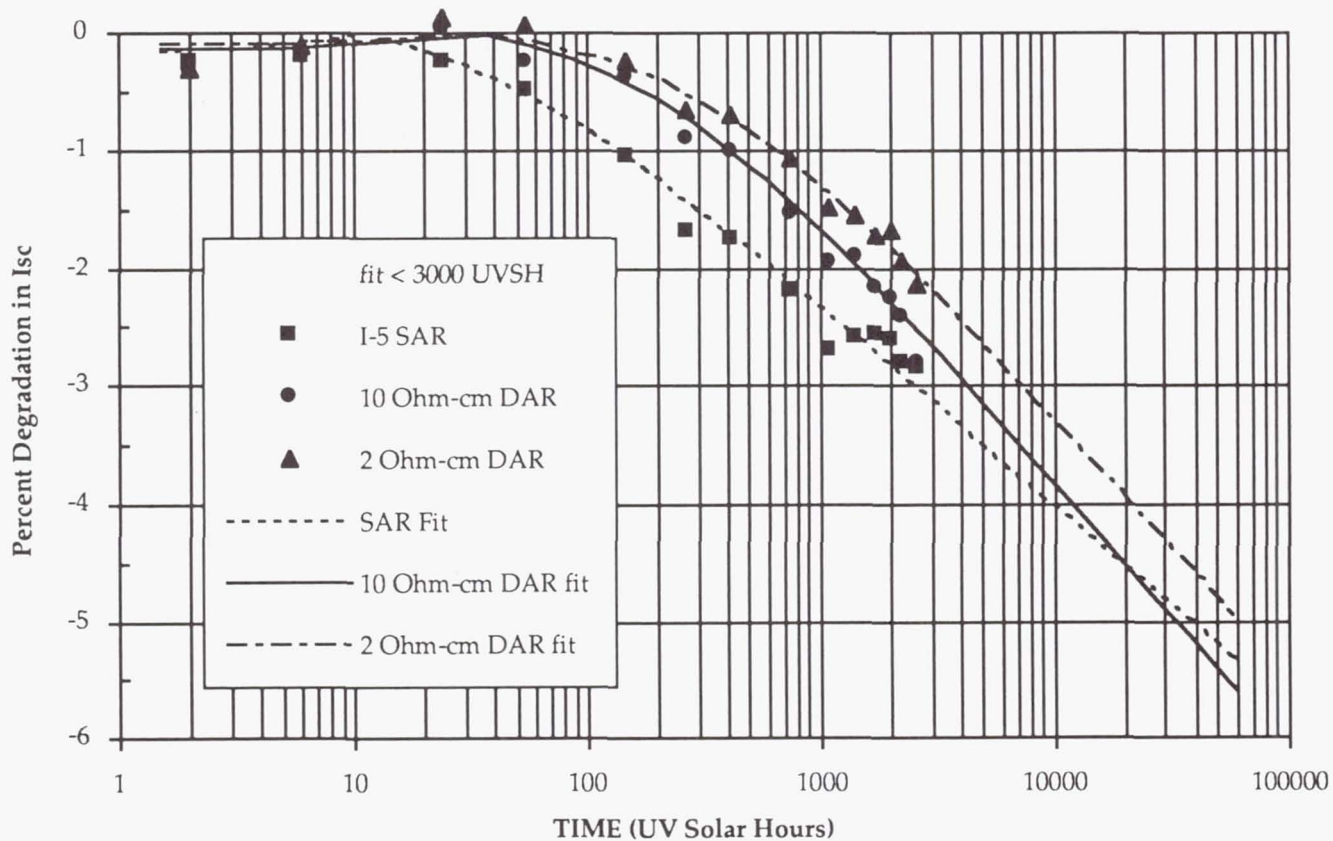


Figure 2. UV degradation for INTELSAT VII and AEG INTELSAT V cells for data <3000 UVSH

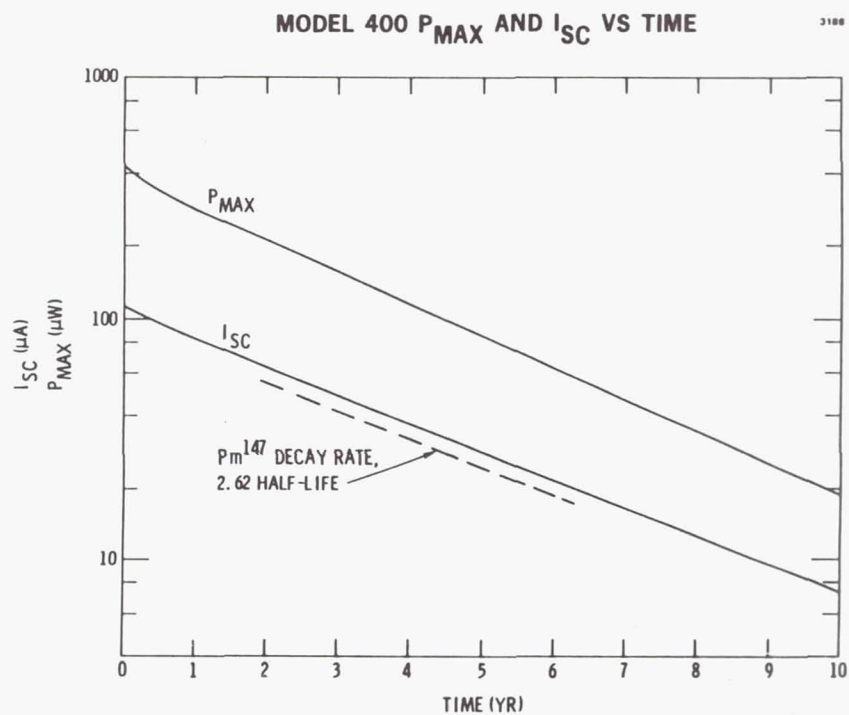


Figure 10. Short Circuit Current and Maximum Power Versus Time For a Model 400 Battery.

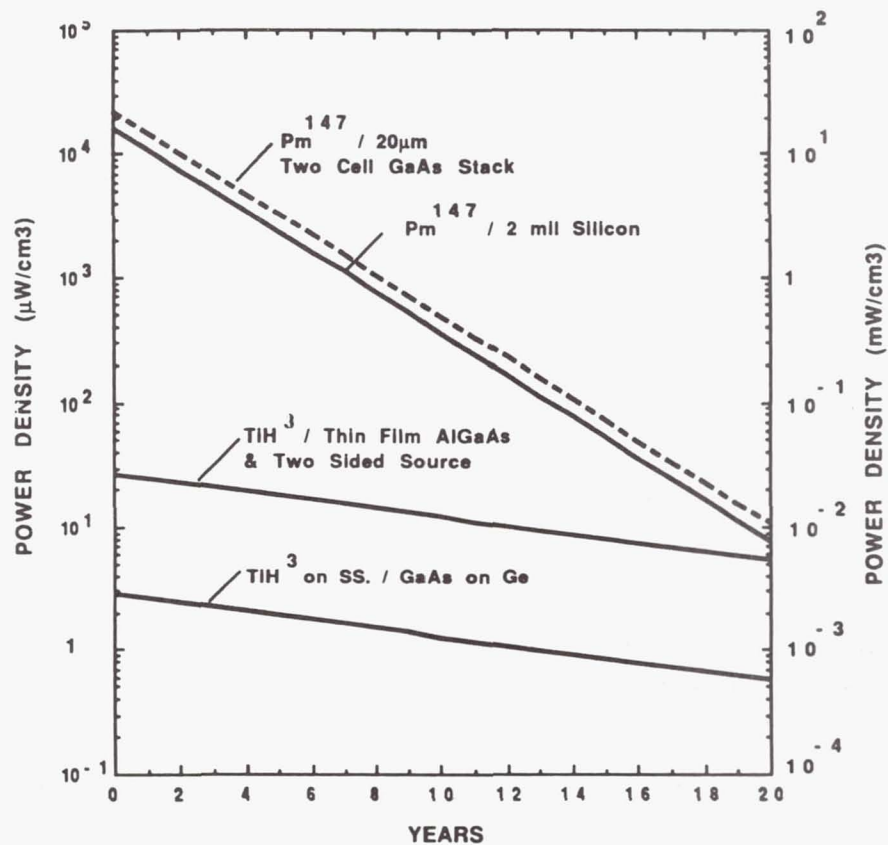


Figure 11. Power Density Versus Time For Advanced Betavoltaic Concepts.

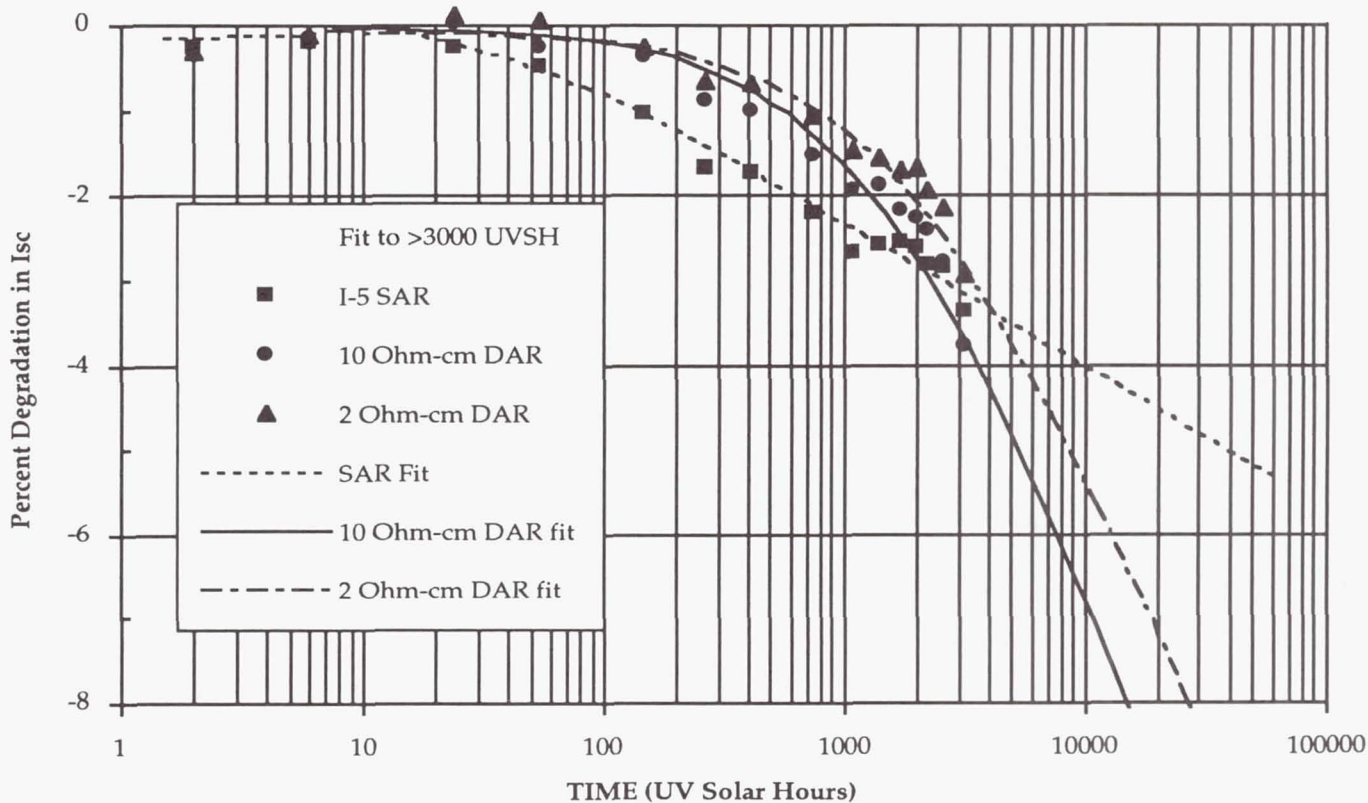


Figure 3. UV degradation for INTELSAT VII and AEG INTELSAT V cells including data >3000 UVSH

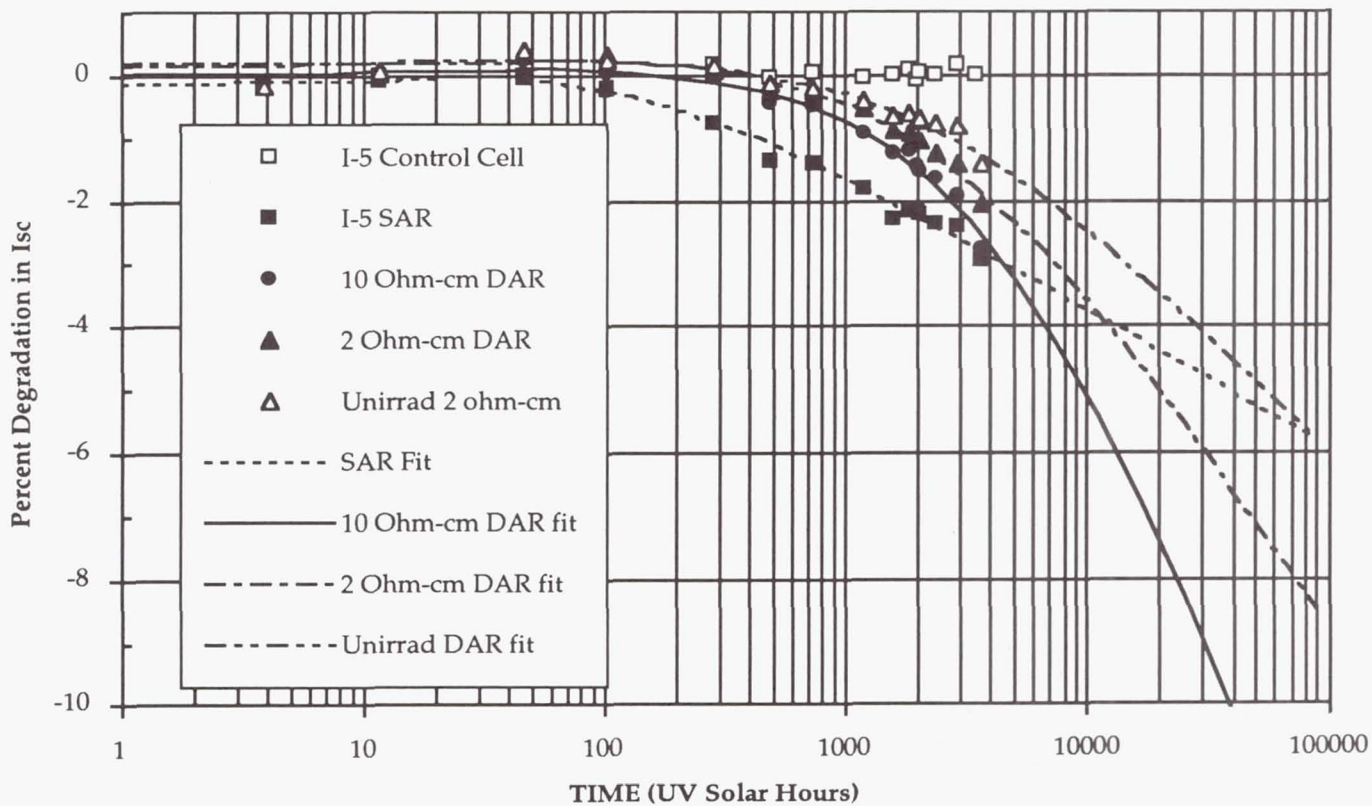


Figure 4. UV degradation (with modifications) for INTELSAT VII DAR and INTELSAT V SAR cells

APPENDIX A

CORRECTIONS TO DATA

Before analyzing the differences in results for the two cell types, it is important to examine the similarities (to determine systematic errors) and to determine the statistical fluctuation to be expected in the data. The fluctuation in results for the single AEG unirradiated internal control cell is less than ± 0.2 percent (Figure 1). If this is purely statistical, then the average of n cells should be $0.2 \text{ percent}/n^{1/2}$. Thus the four SAR and four 10- Ω -cm DAR cell averages should fluctuate about the best fit by about 0.1 percent and the average of eleven 2- Ω -cm DAR-coated cells by 0.06 percent. It is clear from Figures 2 and 3 that the larger cell samples do not have smaller fluctuations about the fitted curves as drawn. Therefore, a combination of statistical and systematic errors must be present. If systematic errors from the solar simulator strongly dominated, then the data could be safely normalized to the control cell. However, the other data sets would then display the statistical uncertainty of a single cell. A fitted curve through the internal control cell data reduces the apparent statistical error and indicates at least one component of systematic error. Temperature stability over the test period and during measurement is within $\pm 0.25^\circ\text{C}$; hence neither statistical nor systematic error can be attributed to this source.

CONTAMINATION

The systematic error displayed by the non-zero degradation of the internal control cell is less than 10 percent of the degradation observed in the test cells. If the source of this control cell degradation is contamination buildup inside the quartz window, then a similar layer is probably building up over all of the window and all of the cells. Since the control cell does not see UV light (except for the brief periods during electrical measurement), the contamination on its surface will not darken as much as that on the window and other cells would. Therefore, the degradation measured for the control cell is about only one-half that likely to be observed from this source on the other cells.

Correction for this systematic error would affect both SAR- and DAR-coated cells. A realistic correction would be to fit the internal control cell data with the same degradation function as used for the test cells (since it fits many different types of cells) and then subtract twice this value from the test cell results. Such a correction is made in the Conclusion.

SOLAR SIMULATOR SPECTRUM

Other systematic errors must be examined. A change in solar simulator spectral output with time could cause only the test cell outputs to decrease during the test, but this is unlikely since the test cells, the control cell and primary reference cell all have different, but similar, spectral responses. A feature in both SAR- and DAR-coated cells is the unusual curve shape beyond 1000 hours. Elimination of the data point at 1100 hours reduces the anomaly to some extent but does not resolve it. Therefore, a number of nonstatistical error sources have been examined in detail to better determine the true shape of the curves (and their extrapolated values) as well as to identify sources of the difference between SAR- and DAR-coated cell degradation.

RADIATION DAMAGE

The INTELSAT VII test cells, experiencing UV exposure, displayed a loss of voltage with time (2.5 mV average). The expected loss in V_{oc} for a 5-percent loss in I_{sc} is ≈ 1.3 mV, which is confirmed by the changes in voltage of ≈ 1.5 mV observed when the quartz window is removed and replaced ($\Delta I_{sc} \approx 5$ percent) at the end of the test. However, the change in I_{sc} of 3–4 percent for the cells under test resulted in an average change in V_{oc} of over 2 mV for the INTELSAT VII cells and less than 0.4 mV for the INTELSAT V cells. In examining the data, a pattern was observed. The INTELSAT VII cells had been irradiated with a few exceptions. These exceptions (some of the 2- Ω -cm cells) were degraded in I_{sc} like the irradiated cells; but, they displayed the same low drop in V_{oc} as did the INTELSAT V cells which also were not irradiated.

With this distinction, a clear separation in the extent of UV degradation to I_{sc} between the irradiated and unirradiated cells is possible. If no distinction is made, the maximum cell-to-cell variation in I_{sc} of the 2- Ω -cm cells at 2000 and 3300 UVSH is ± 1.5 percent. However, after separating the groups (Figure A-1), the difference between the groups at 3300 hours is 1.4 percent (~1.9-percent degradation for the unirradiated group VS ~3.3 percent for the irradiated) and the unirradiated group (three 2- Ω -cm cells) group has a maximum internal variation of ± 0.5 percent. While one irradiated cell has less UV degradation than the average of the three unirradiated cells (data not shown), the difference between the groups is clear.

The four 10- Ω -cm INTELSAT VII cells (which were all irradiated to $1.2 \times 10^{15} \text{ e/cm}^2$) had a spread in UV degradation of only ± 0.5 percent and the four unirradiated INTELSAT V cells had a spread of less than ± 0.3 percent. The larger set of 2- Ω -cm cells has a larger spread in degradation, as expected. Since the numbers of cells in any group is too small for statistical analysis, no standard deviation for cell variance can be calculated. The 2- Ω -cm set contains four levels of irradiation (0, 8, 10, $12 \times 10^{14} \text{ e/cm}^2$) but, other than with the unirradiated cells, no correlation can be made between UV degradation and electron dose. However, there is a strong correlation between the change in open-circuit voltage and the change in short-circuit current under UV exposure. This implies that the internal radiation damage to the solar cell itself is affected by extended UV exposure. Since the UV does not penetrate to the cell junction, the change in cell output would be dominated by the n^+ surface layer and its interface with the AR coating. However, the dominant term affecting V_{oc} in 10- Ω -cm cells is from the base, or p-layer. Therefore, a change in surface layer is not likely to strongly affect V_{oc} in 10- Ω -cm cells as it would affect 2- Ω -cm cells which are less base dominated. (The 2- Ω -cm cells are affected by both base and emitter, or surface regions.) Since the 10- Ω -cm cells show an effect as strongly as the 2- Ω -cm cells, the possibility of influence from the longer wavelength (more penetrating) component of the UV source must be considered.

Such photon redegradation was first reported in 1972 [1] for 10- Ω -cm float zone silicon solar cells and shown to be related to the bulk minority carrier lifetime. Crabb later reported [2] that dopant type (and levels) and dislocation density of the starting material was important and that the effect (up to 8-percent change in I_{sc}) saturates within 24 hours at 60°C. Space data indicated the need to produce such photon redegradation during electron irradiation tests to best predict array degradation. Fisher and Pschunder [3] confirmed the effect in 1- Ω -cm crucible-grown material (but to a lesser extent) and noted a reversible effect in this material prior to irradiation. In addition, they [4] found a correlation between carbon and oxygen content and photon stability in float-zone solar cells. This material difference showed up in our 1989 test where Shinetsu-supplied silicon was compared to Wacker silicon when made into solar cells by AEG and then electron irradiated and exposed to UV light.

Figure A-2 demonstrates the correlation between degradation in I_{sc} and in V_{oc} with UV exposure. Two groupings are observed. The data with least change in V_{oc} consists of the unirradiated 2- Ω -cm DAR and INTELSAT V (SAR) cells. A second group consists of the electron irradiated 10- Ω -cm DAR cells and most of the irradiated 2- Ω -cm DAR cells.

The major change in V_{oc} occurs between 200 and 1000 hours. At 270 hours (Xs in Figure A-2) the groups are already beginning to separate. The four cells in this set with highest change in I_{sc} are the SAR-coated cells. The three cells with lowest change in V_{oc} are the three unirradiated DAR cells.

UV SOURCE AGE

In examining the data to determine why the UV degradation appears to increase strongly beyond 2000 UVSH, one source of systematic error stood out. This was the fact that the quartz-xenon bulbs, used to provide ultraviolet light, normally last about 2000 hours. As they age, the UV output decreases and the source input power must be turned up. The bulb manufacturer feels that the worst degradation (from tungsten electrode sputtering) occurs in the region near $0.35 \mu\text{m}$; just the region where the coverslide adhesives, and perhaps the AR coatings, are most sensitive to degradation. Since the simulator UV output is set with a filtered detector (~ 0.30 to $0.47 \mu\text{m}$), adjustments to maintain a constant solar UV level are, in fact, not valid for the short wavelength region which has lower power than the upper portion of the filter passband.

To correct for this effect, a first order adjustment was made to the UVSH values which were originally considered linear with time of exposure. The algorithm used is to multiply any increment of UV bulb use by $(1.9 - 0.9t/1000)$ UVSH/bulb hours, where t is the average number of hours on the bulb during that increment. This means that a new bulb will provide 1.9 UVSH for each hour of use. UV solar hours from a bulb at 1000 hours will have a 1 to 1 relationship with exposure hours and at 2000 hours a 0.1 to 1 relationship. Figure A-3 displays four models of UV source degradation with age of the bulb. The 1:1 curve assumes that the UV detector used to establish the UV source intensity properly reflects the damaging component of the output spectrum. Consequently, adjustments in UV source input power, to maintain a fixed UV level on the cell surfaces, would be correct. The other curves assume that, despite the increases in source power made as the bulb ages, the damaging UV light output decreases with bulb age. The abrupt rise in these curves at 2100 hours results from a change of bulbs. The nonuniformity in the curves is a consequence of the approximation made in calculating the effective bulb age between measurement points. The 1.9:1, and 3:1 initial value curves fit the test data best. This implies that little or no damaging UV remains to a bulb by 2,000 hours.

Figure A-4 shows the combined DAR cell average plotted against hours exposure (A) and against corrected UVSH (B and C). It is possible to fit the corrected data with a single function (B or C), but the uncorrected data deviates greatly (± 0.5 percent) from such a fitted curve (A). While the algorithm for the effects of bulb degradation is crude (a linear fit for B) and the actual values selected are somewhat arbitrary, the model provides some insight into expectations for most UV testing. A nonlinear relationship (C) is included to provide a greater initial ratio (3:1) while still permitting some effect beyond 2000 hours ($0.2:1$). $[UVSH / \text{exposure time} = 3 - 2(t/1000)^{1/2}]$. In comparing the latter two relationships, it is seen in Figure A-3 that they really are not that different beyond the first 500 hours of bulb life.

EXTRAPOLATION

In most UV testing, the exposure is limited to 1000 UVSH and the results are plotted against a linear time scale. The UV lamp is generally changed prior to the test so that degradation rates are higher at the beginning. Figure A-5 is the first 2000 UVSH of the SAR and DAR cell percent degradation plotted against the time on a linear scale. Looking at these data allows one to understand the reported claims that UV degradation is saturated by 1000 UVSH and that DAR-coated cells display less degradation than do SAR-coated cells. Figure A-6 compares the fitted curves for these cell types, corrected for statistical fluctuation and the slight degradation in the control cell and plotted against corrected UVSH. While the SAR cells still appear saturated near 2000 UVSH, a claim for saturation of the DAR cells now becomes untenable.

While the DAR-coated cell data (beyond 2500 hours) indicate degradation to be less than the linear fit provided in Figure A-6, a somewhat less severe linear degradation does fit (within ± 0.3 percent) the modified-time-base data out to 4000 hours. Linear extrapolation of these data to 10^5 hours would indicate above 50-percent degradation at 10 years. While the linear fit-to-data is better than that of a saturated model, the extrapolation based on either assumption is unacceptable. The simple function, used in our best estimate of extrapolated UV degradation, has been found to fit results of nearly all our tests, even those of a 23,000 hour test; therefore, we feel comfortable using it here.

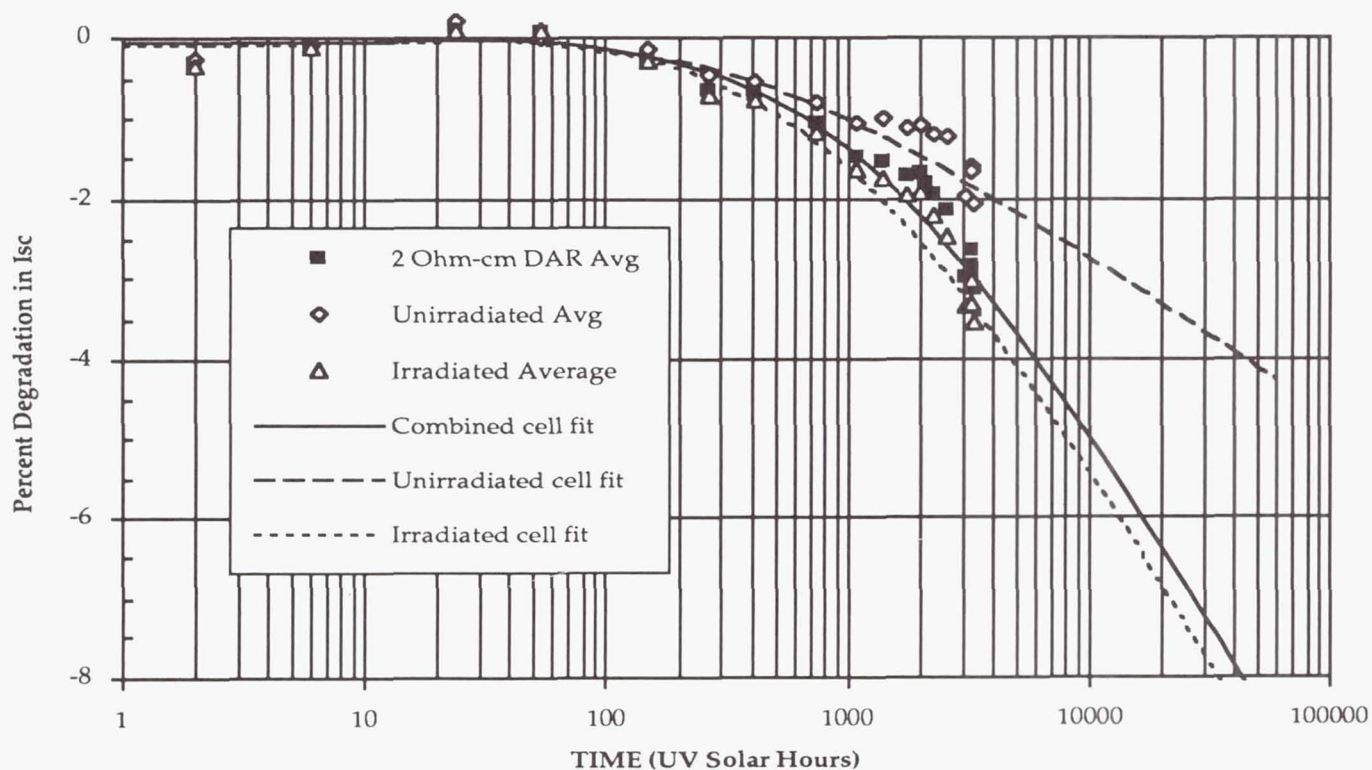


Figure A-1. UV degradation of electron irradiated and nonirradiated cells

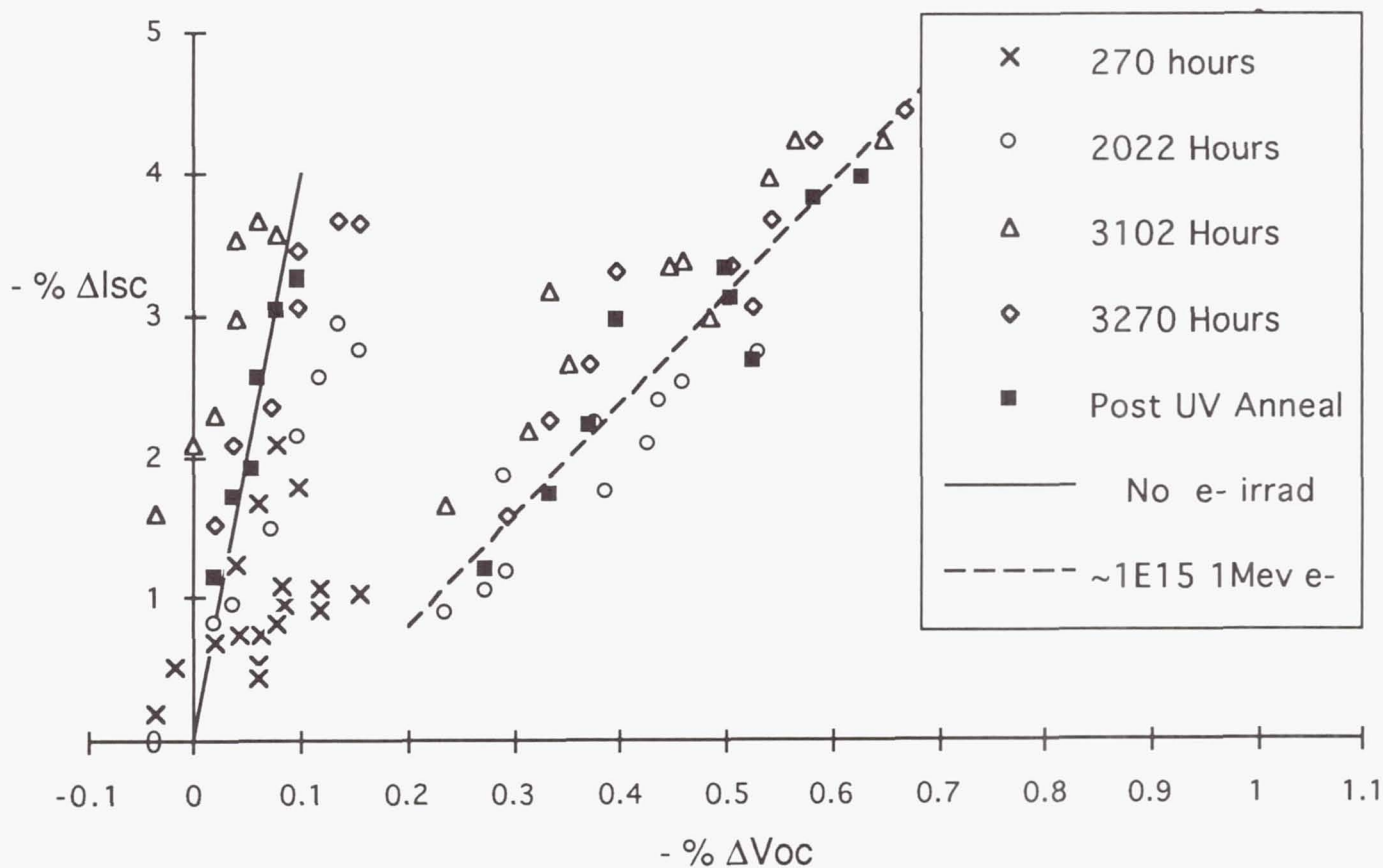


Figure A-2. ΔV_{oc} vs ΔI_{sc} during UV test and anneal

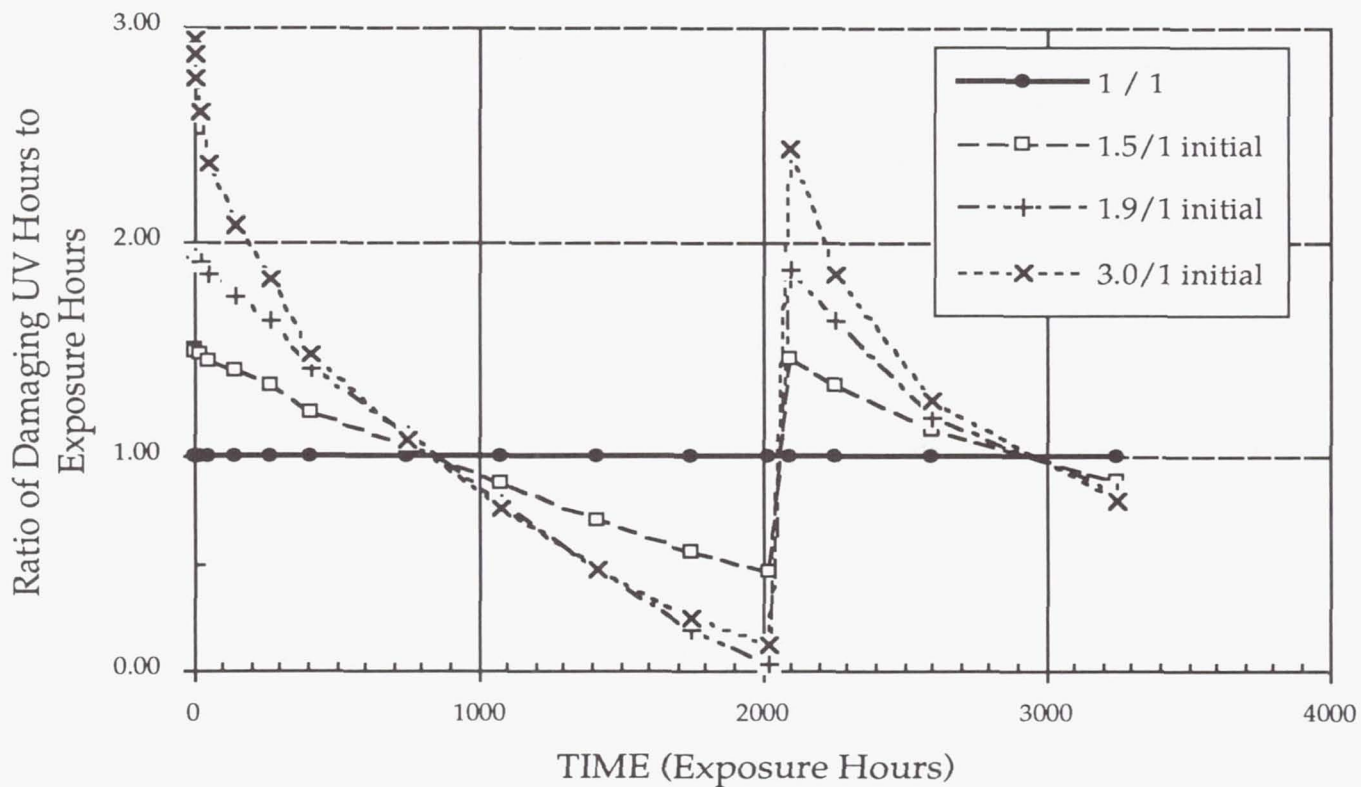


Figure A-3. Four models of UV simulator damaging radiation as a function of time

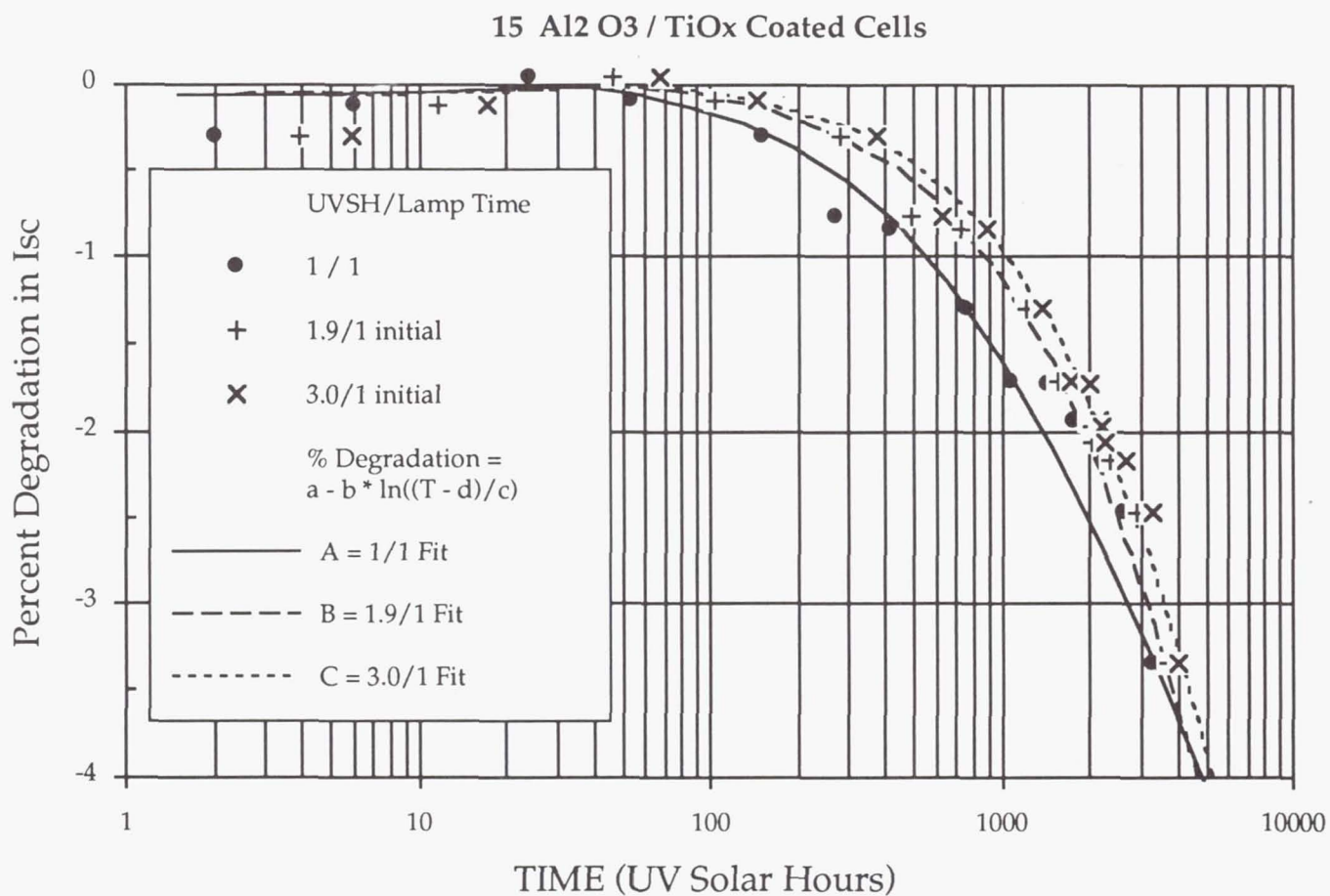


Figure A-4. DAR-coated solar cell data with corrected time bases

THE UoSAT-5 SOLAR CELL EXPERIMENT - FIRST YEAR IN ORBIT

C. Goodbody
Defence Research Agency, Space Technology Department,
Farnborough, Hants, GU14 6TD, United Kingdom

This paper describes the results for the first year in orbit of the DRA solar cell experiment flying on the Surrey University UoSAT-5 satellite. Several problems have been identified with the measured data, which are discussed along with the techniques used to remove or minimise the effect of the problems.

After 1 year in orbit the majority of the cells flying on the experiment have undergone little or no degradation. The exception to this are all the ITO/InP cells, supplied by two different manufacturers, they are showing more degradation than the GaAs cells. This result is unexpected and currently unexplainable.

It will be necessary to retrieve data from the experiment for several years to obtain the best results due to the relatively benign radiation environment.

1. INTRODUCTION

The solar cell experiment on the UoSAT-5 satellite was launched into a 770 km Sun Synchronous orbit on 16 July 1991 on an Ariane 4 launcher as a secondary payload to ERS-1. UoSAT-5 is a 50 kg microsatellite manufactured and controlled by Surrey University (ref. 1). The satellite is powered by three Spectrolab GaAs/Ge solar panels and a half panel of EEV IMLPE GaAs. The remaining half panel was used for the solar cell experiments.

The experiment consists of various types of silicon, gallium arsenide and indium phosphide solar cells from the UK, Europe and the USA, see Table 1. The purpose of the flight is to compare the performances of these various cell types in the space environment and to determine whether there is any degradation of different types of Pilkington coverglasses and coatings.

2. DATA

The data received back from the satellite are corrected to a temperature of 25°C and to an intensity of 1 solar constant (135.3 mW/cm²). After processing the first batch of data it quickly became apparent that there were several problems: firstly the I-V curve was measured incorrectly as it approached Voc. It was also found that the temperature resolution was 6° rather than the specified 2° and there was a large scatter in the day to day current, voltage and power values.

Instead of a 2° resolution and a temperature range centred around 0°C, due to a misunderstanding the temperature range was set to cover the maximum and minimum temperatures of the satellite and not the temperatures of the solar cell experiment. When the temperature measurement was checked on the ground the room temperature unfortunately coincided with a temperature at which the bit count changed and so this problem was not noticed. Attempts to improve the resolution by calibrating the temperature sensors of the cells against other temperature sensors on the panel have been made, all of which have proven to be unsatisfactory.

The incorrect I-V curve gives a higher Voc value than is expected. Surrey University, who designed and built the electronics package, undertook some fundamental modelling work on the circuit and its interaction with

the solar cells. The conclusion from this was that the difference was due to the slope resistance as one moves down the curve. Due to the measurement speed there is insufficient time for the current to stabilise at a voltage point and hence the measured current is higher than it ought to be. Unfortunately this was not identified in the ground testing.

A large part of the data scatter on Voc and to a lesser extent Pmax can be attributed to the measurement problems discussed above, the scatter on the Voc values is typically 10-20 mV, but the scatter on the Isc values is due to Earth albedo, giving rise to current variations of up to 6-7%.

The position of the satellite relative to the Earth was determined when each measurement was made in order to assess what landmass or ocean was in sunlight and visible to the satellite. The solar cell experiment measurement conditions are met when the satellite is nominally over the North or South Poles $\pm 23^\circ$ due to time of year, and the stability of the spin axis of the satellite relative to the sun. This showed that in most instances there is the possibility of earth albedo affecting the experiment. However in the early phase of the mission the solar cell experiment was activated and measurements made when the satellite had not been fully stabilised and several measurements were made when the likelihood of albedo was very small.

On the experiment are three cells which are heavily irradiated Mitsubishi GaAs cells (irradiated with 10^{15} 1 MeV e/cm²) to act as a measurement reference. By taking the average of the Isc values for these cells on the 'no' albedo days it has been possible to establish a baseline current for each of these cells. The % increase in these current values on the measurements days is then assumed to be due to albedo. This value is then subtracted from the measured values to correct the data for the albedo contribution.

3. RESULTS AND DISCUSSION

Figure 1 shows the variation of Isc with time in orbit for cell 22 after correction for the seasonal variation in solar intensity and temperature, figure 2 shows the reduction in scatter after correction for albedo and figure 3 shows the data as a percentage of initial in orbit value (the in orbit value has been taken to be the average of the first 30 days measurement).

The corrected Isc values for most but not all of the GaAs cells become very similar with little scatter. However on a large number of the Si and InP cells and one or two of the GaAs cells the scatter is reduced but the data splits into two distinct bands as shown in figure 2. The upper band is typically of values measured at the North Pole and the lower band of values measured at the South Pole. The banding is thought to occur due to the difference in the spectral responses of the cells and the reference cells used to estimate the albedo and the albedo having a different spectral content between the North and South Pole.

When cells other than GaAs are used to estimate the albedo level, this banding can be closed up or the data split into bands depending upon which cell is chosen. When silicon cell 18 is used to estimate the albedo for the silicon cells, the bands on cells 14 and 22 are closed up and the scatter on the current values is small. Due to this complication and the fact that the other cells will degrade, all the data remains corrected for albedo using the GaAs reference cells.

Figures 4-9 show typical results for Si, GaAs and InP cells on the experiment, the data has been averaged every four consecutive days to aid clarity and to remove the banding introduced with the albedo correction.

3.1 Comparison with pre-flight data

Table 2 shows the comparison of the in-orbit first 30 day average values with the pre-flight values measured at DRA using a Large Area Pulsed Solar Simulator (LAPSS). All the GaAs cells were calibrated against the same GaAs primary standard solar cell, produced by DRA using a terrestrial global irradiance calibration technique in Cyprus (ref. 2). The silicon cells were calibrated against DRA silicon Cyprus primary standards chosen

to match spectral responses as close as possible. Unfortunately no InP primary standard was available and so a calibration value for the LAPSS was assumed.

The in-flight values for the silicon cells are between -0.2 and +1.2% higher than predicted values, *ie.* there is very good agreement with the calibration technique. However the in-flight values for the GaAs cells are all lower than predicted ranging from -0.2% to -3.1%. Given the accuracy of the standard calibration technique, differences in spectral responses between some of the GaAs cells and the standard, and possible errors introduced by the albedo correction this is a reasonable result. The InP cell data are all lower than predicted but this is not unexpected given the lack of a standard.

All the Voc values are higher than predicted, ranging from 1-4.5%. This is to be expected given the measurement and temperature problems. The in-flight Pmax values typically vary from the predicted values by $\pm 3\%$ and is influenced by the difference in the Isc values and by the temperature measurement problem, given this there is a reasonable agreement between flight and predicted. This also shows that the effect of the measurement problem on Pmax is minimal.

3.2 Predicted degradation

The radiation environment has been predicted for the UoSAT-5 orbit with the UNIRAD short orbital flux integration program using the standard NSSDC proton and electron environment models for solar minimum. EQFRUX was then used to calculate the annual equivalent 1 MeV electron fluxes as a function of CMX coverglass thickness using a standard set of silicon damage coefficients. The environment is proton dominated, the equivalent electron fluxes for protons being two orders of magnitude higher. The 1 MeV electron fluences for silicon cells with a 100 micron CMX coverglass has been estimated to be:

$$\begin{array}{ll} \text{ISC} & 1 \times 10^{13} \text{ e cm}^{-2} \text{ year}^{-1} \\ \text{VOC/PMAX} & 2 \times 10^{13} \text{ e cm}^{-2} \text{ year}^{-1}. \end{array}$$

The damage coefficients for Si, GaAs and InP at 10 MeV protons are typically 3000, 1000 and 650 respectively (ref. 3). By taking the appropriate ratio of these it is possible to obtain a first order estimate of the equivalent 1 MeV electron fluences for the GaAs and InP cells. From this it can be seen that the radiation environment is relatively benign for silicon cells and therefore should be even more so for the GaAs and InP cells, we do not expect to see any significant degradation from the InP cells over the life time of the mission.

3.3 Comparison of cell types

The degradation of Isc, Voc and Pmax for all the cell types after 1 year in orbit has been estimated and the results are shown in Table 3. The estimate has been made to the nearest 0.5% and where there is a + this indicates that the performance has increased rather than decreased relative to the in-orbit initial value. It was expected that the unirradiated silicon cells would have degraded the most followed by the GaAs cells and then the InP cells (little or no degradation).

Cell 9 is a typical silicon cell and has degraded by approximately 3% in Pmax, (fig. 4). Most of the GaAs cells have undergone little or no degradation. Cells 15 and 19 show no signs of degradation at all while cells 13 and 17 show only slight degradation of Pmax (100-200 micron coverglass). Cells 3, 6 and 24 are showing signs of Isc and Voc degradation of approximately 0.5% and 1.5% degradation in Pmax (50-80 micron coverglass), see figures 5 and 6.

The most surprising results are from the Indium Phosphide cells. Ground based irradiation testing (ref. 4,5,6) has shown that InP is considerably more radiation resistant than either GaAs or silicon and that homojunction (HJ) and ITO cells behave in a similar manner. This is confirmed for the HJ cells: cells 2 and 4 show little sign of degrading and HJ cells 7 and 8 are showing approximately 1% degradation in Pmax, (fig. 2). Both these cells have 50 micron coverglasses and should be compared to GaAs cells 3, 6 and 24.

ITO/InP cells 1, 12 and 16 however are totally different, the cells degrading by 1.5 to 2.5% in Pmax which is worse than the GaAs cells, (fig. 7-8). There appears however to be a difference between the different manufacturers. Cell 1, the NREL cell flown by NASA, has undergone both current and voltage degradation whereas the Newcastle Polytechnic (NP) cells have only undergone voltage degradation, in fact the current on cell 12 appears to have improved slightly. InP cells are susceptible to low energy proton irradiation but as the base material and junction depths are similar to the homojunction cells one would have expected these cells to be showing signs of degradation as well. The ITO/INP cells on LIPS 3 (ref. 7) are showing only 1% degradation after 4 years in a more severe radiation environment, although only the Isc is being measured. The unexpected NP results are currently under investigation and may be due to other factors apart from radiation.

3.4 Comparison of coverglasses

All of the Pilkington coverglasses are mounted on the same type and batch of silicon solar cell. The cells were all irradiated prior to flight with 1 MeV electrons (except cell 9) to ensure that any degradation in performance was due to either the coverglass material darkening or changes to the coating on the coverglass. Cells 9 and 23 both over-ranged on the current values during the middle 6 months data giving rise to either no data points or data subject to a very large amount of scatter.

There are no signs of degradation on the CMX, CMZ and CMX with an ultra violet rejection coating (UVR) cells after the first year, (fig. 3). Cell 23 is showing signs of current and Pmax degradation, both of 0.5%. As the cell was nominally only 1% degraded before launch this is reasonable given that the unirradiated cell 9 has dropped by 1.5% in current. There are two anomalous results, for Teflon bonded cell 20 and directly glassed cell 21. These cells are currently being investigated.

4. CONCLUSIONS

After a successful launch the UoSAT-5 solar cell experiment is returning regular data. After processing the initial data it was found that there are several measurement problems. The temperature range was incorrectly set before flight giving a resolution of 6°C and all efforts to improve this have proven to be unsatisfactory. A fundamental design flaw has been found in the electronics affecting the shape of the I-V curve especially around Voc. The effect is to give a good Isc measurement, a slight error in the Pmax and a large error in Voc. It is not possible to correct the data for this error and so the correct in-orbit Voc values cannot be determined. It is believed however that the relative change in the measured Voc values with time in orbit is still valid although they will need to be used with caution.

The data is subjected to scatter due to variable Earth albedo, estimates of the albedo intensity have been made using 3 GaAs reference cells. When these estimates are used the scatter is considerably reduced.

The ground measured Isc and Pmax values agree reasonably well with the in-flight values. The ground measured Voc values are all considerably lower than the derived in-flight values, due to the temperature resolution and the measurement problems.

When the data is displayed as a percentage of initial value and averaged every four consecutive days the degradation trend in the curve becomes much clearer. From these curves it can be seen that most of the cells are behaving generally as expected. The standard silicon cell has degraded by approximately 3% in Pmax, the GaAs cells by 1.5% in Pmax and the homojunction Indium Phosphide cells by 0-1% in Pmax. Most of the coverglass cells have not degraded as is expected.

The main anomaly however is that all three ITO/InP cells have degraded more than the GaAs cells. All results to date have indicated that they should be far superior to GaAs cells in terms of their radiation resistance and this result is completely unexpected and currently unexplainable.

REFERENCES

- 1 Sweeting, M.N.: "UoSAT microsatellite missions", Electronics Communication Engineering Journal, Vol 4, no 3, p. 141-149.
- 2 Davies, M.A.H.; Goodbody, C.: "The calibration of solar cells in terrestrial sunlight," p. 583, European Space Power Conference, Florence, 1991.
- 3 Flood, D.J.: "Radiation damage resistance requirements for advanced space solar cell development," ??
- 4 Weinberg, I.; Swartz, C.K.; Hart Jnr, R.E.; Coutts, T.J.: "Radiation resistance and comparative performance of ITO/INP and N/P INP homojunction solar cells," p. 893, 20th IEEE Photovoltaic Specialists Conference, 1988.
- 5 Pearsall, N.M.; Goodbody, C.; Oparaku, O.; Dollery, A.A.; Hill, R.: "Effect of isotropic proton irradiation on the performance of ITO/INP solar cells," p. 898, 20th IEEE Photovoltaic Specialists Conference, 1988.
- 6 Pearsall, N.M.; Goodbody, C.; Robson, N.; Forbes, I.; Hill, R.: "Radiation and flight testing of ITO/INP solar cells," p. 1172, 21st IEEE Photovoltaic Specialists Conference, 1990.
- 7 Pearsall, N.M.; Robson, N.; Forbes, I.: "Flight and irradiation studies of ITO/INP solar cells," p. 689, European Space Power Conference, Florence, 1991.

Table 1
List of Cells Flying on the Experiment

1	NASA Lewis ITO/InP (NREL cell)
2	NASA Lewis HJ InP (Spire/NRL cell)
3	NASA Lewis cleft GaAs (Kopin cell)
4	Wright Lab. (USAF) InP (Spire cell)
5	Wright Lab. (USAF) GaAs (ASEC LPE cell)
6	Wright Lab. (USAF) GaAs (ASEC LPE cell replaced by DRA)
7	NASA Lewis HJ InP (Spire/NRL cell)
8	Link HJ Inp
9	PST - CMX unirradiated Si
10	Irradiated reference GaAs
11	Irradiated reference GaAs
12	Newcastle Polytechnic ITO/InP
13	EEV IMLPE GaAs - 100 micron CMG
14	PST - CMZ irradiated Si
15	EEV IMLPE GaAs - Teflon bonded CMG
16	Newcastle Polytechnic ITO/InP
17	EEV IMLPE GaAs - 200 micron CMG
18	PST - CMX irradiated Si
19	EEV IMLPE GaAs - 0.5 micron junction depth
20	PST - CMZ Teflon bonded irradiated Si
21	PST - CMZ directly glassed irradiated Si
22	PST - CMX UVR2 coated CMX irradiated Si
23	PST - CMX high emissivity coated CMX irradiated Si
24	NASA Lewis GaAs/Ge (Spectrolab cell)
25	Ex-Cyprus standard GaAs reference
26	EML/BAe/TST MOVPE GaAs
27	TST high ETA silicon

Table 2
Comparison of the In-Flight Initial Isc Values with the Pre-Flight Values
Measured at DRA

Cell No.		Pre-Flight	In-Flight	% Difference
1	INP	123.0	119.6	-2.7
2	INP	129.6	128.8	-0.6
3	GAAS	128.9	126.2	-2.1
4	INP	136.3	134.3	-1.5
5	GAAS	120.6	117.9	-2.2
6	GAAS	122.9	119.6	-2.6
7	INP	113.5	110.4	-2.7
8	INP	125.3	121.9	-2.7
9	SI	164.6	165.9	+0.8
10	GAAS	86.3	84.4	-2.2
11	GAAS	85.6	83.2	-2.8
12	INP	110.4	107.8	-2.3
13	GAAS	245.3	236.7	-3.5
14	SI	137.9	137.6	-0.2
15	GAAS	210.6	210.1	-0.2
16	INP	108.9	106.1	-2.6
17	GAAS	236.2	232.0	-1.8
18	SI	144.7	144.3	-0.2
19	GAAS	210.6	209.8	-0.3
20	SI	148.5	149.6	+0.7
21	SI	150.7	152.5	+1.2
22	SI	145.5	147.2	+1.2
23	SI	162.9	164.5	+0.9
24	GAAS/GE	259.1	250.8	-3.2
25	GAAS	166.1	163.4	-1.6

Table 3
Estimated Degradation of Isc, Voc and Pmax after 1 year in orbit
 Estimated to the nearest 0.5%, a '+' indicates performance has increased over the initial value rather than degraded

	Isc	Voc	Pmax
ITO/INP cells:			
1	1.5	1.0	2.5
12	+0.5	1.0	2.5
16	0.0	1.0	1.5
HJ INP cells:			
2	0.0	0.0	0.0
4	0.0	0.0	0.0
7	0.0	0.0	1.0
8	0.5	0.0	1.0
GaAs cells:			
6	0.5	0.0	1.5
13	0.0	0.0	0.5
17	0.0	0.0	0.5
24	0.0	0.5	1.0
Coverglass Si cells (pre-irradiated):			
14	+0.5	0.0	0.0
18	0.0	+1.0	0.0
22	0.0	+0.5	0.0
23	0.5	0.0	0.5
Silicon cells:			
9	1.5	0.0	3.0

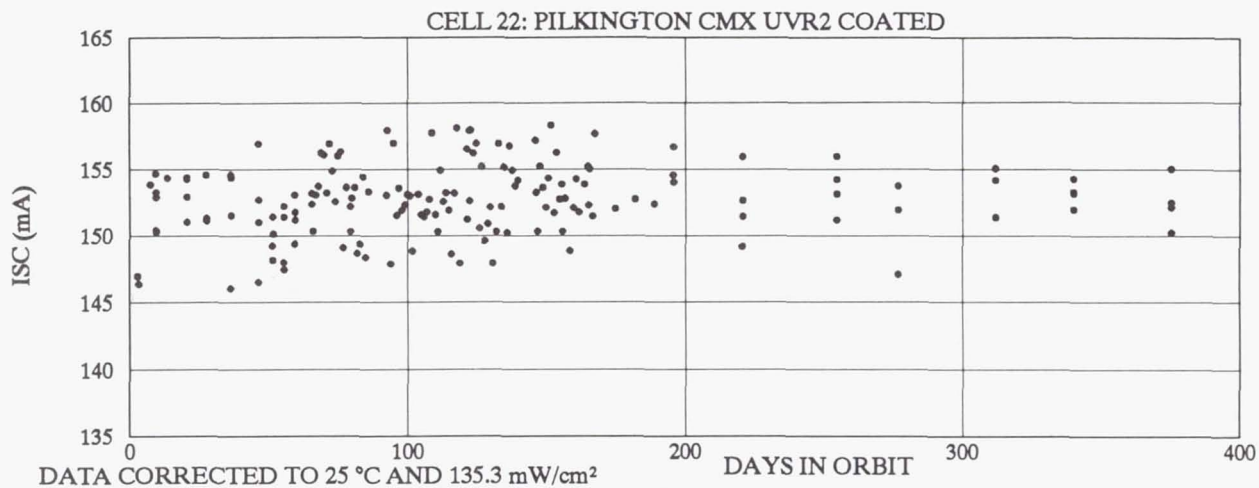


FIGURE 1.

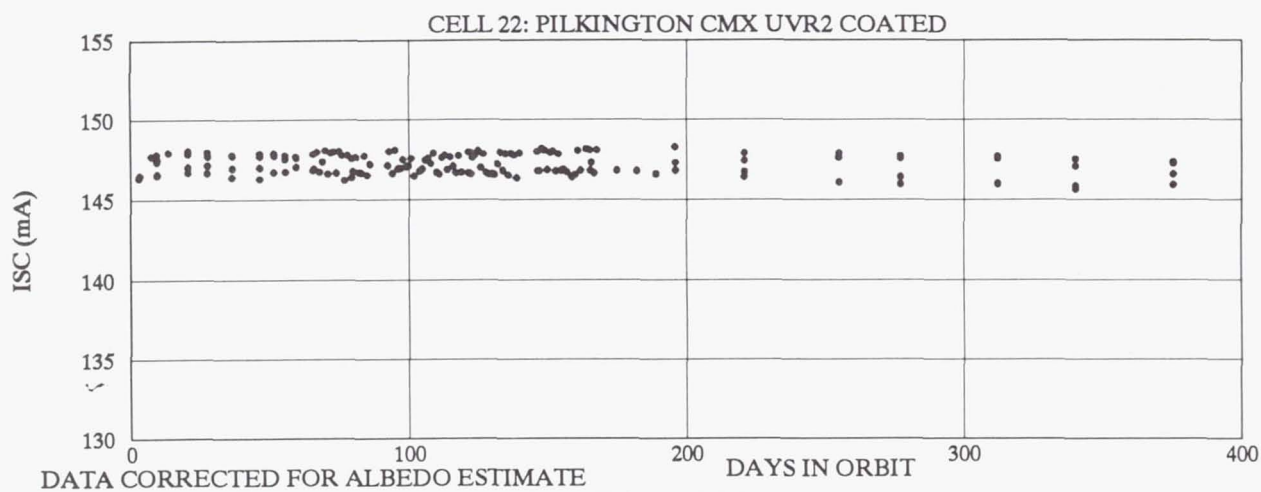


FIGURE 2.

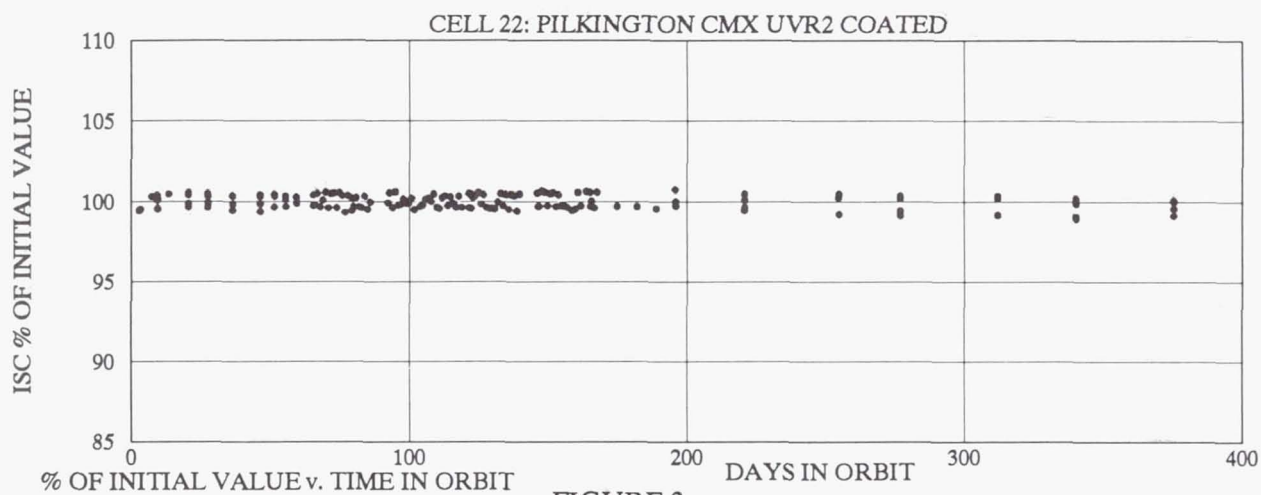


FIGURE 3.

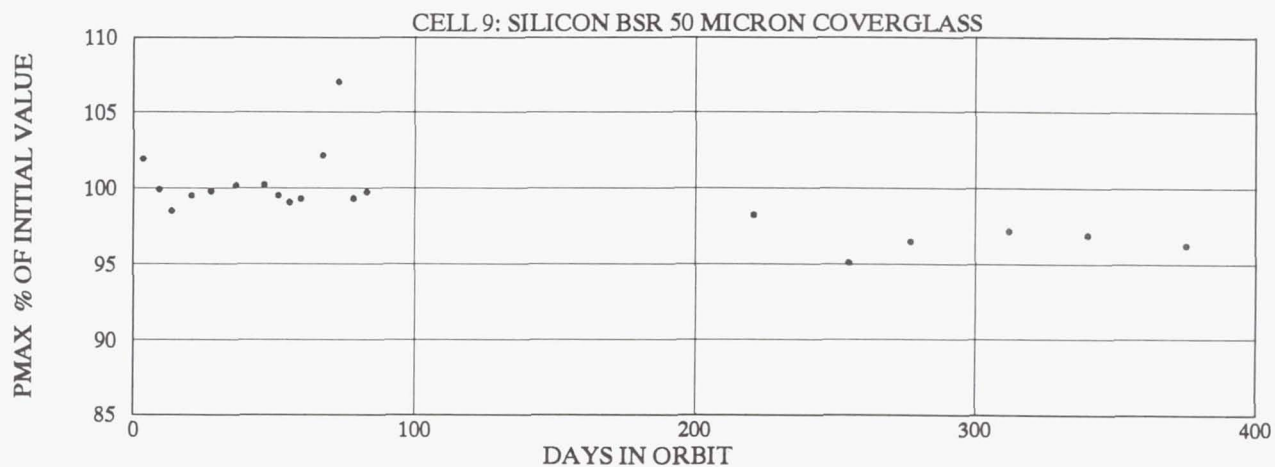


FIGURE 4.

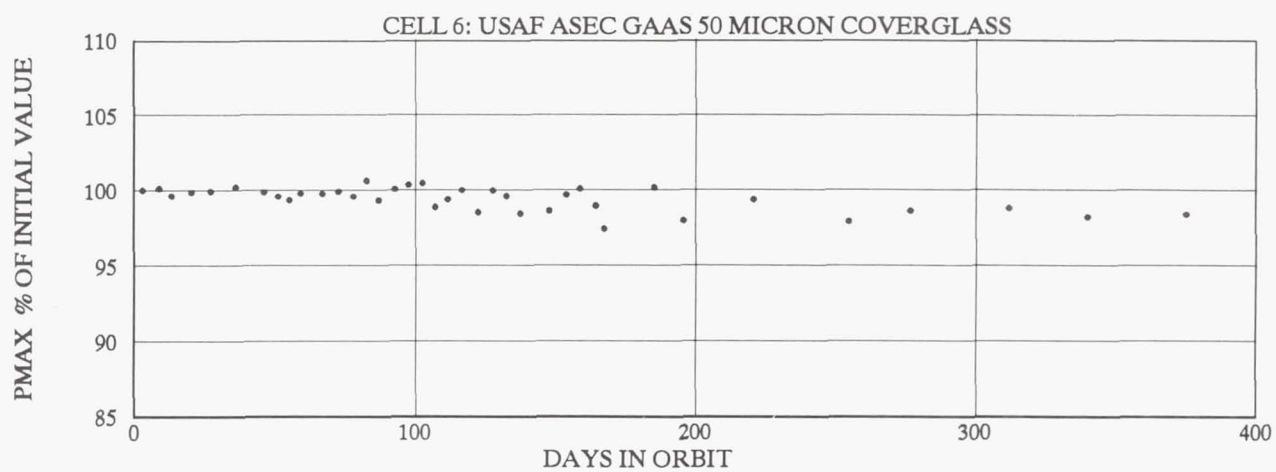


FIGURE 5.

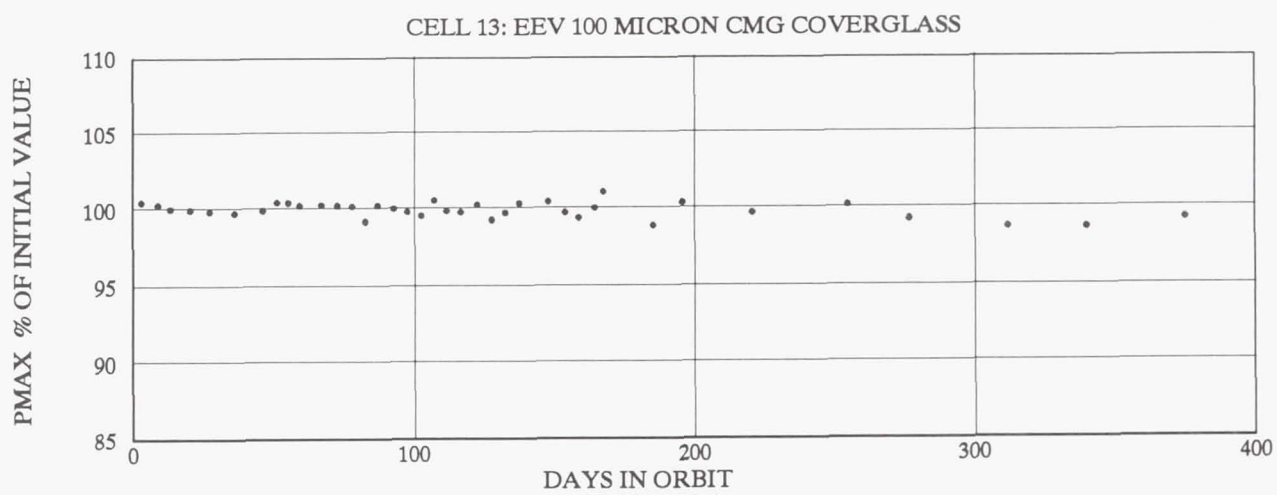


FIGURE 6.

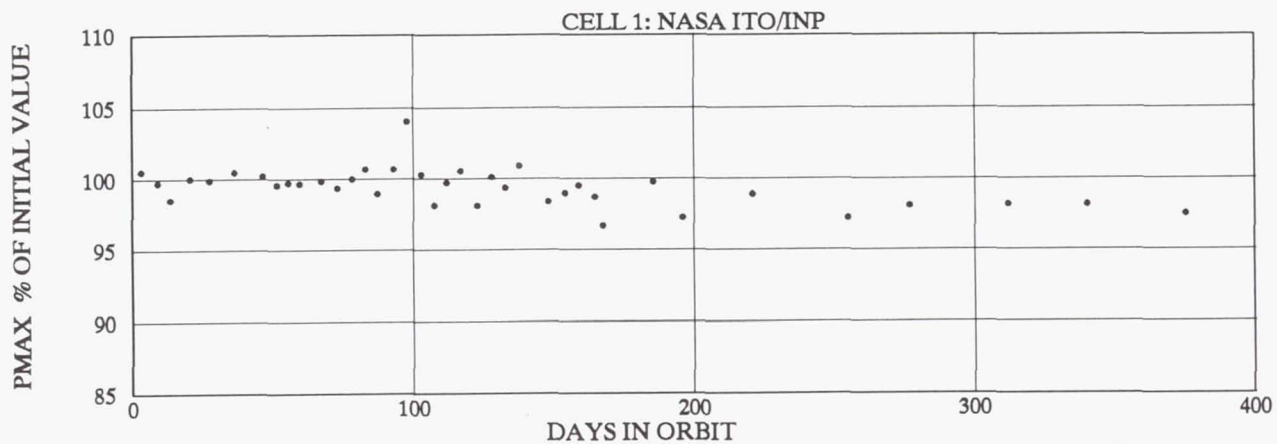


FIGURE 7.

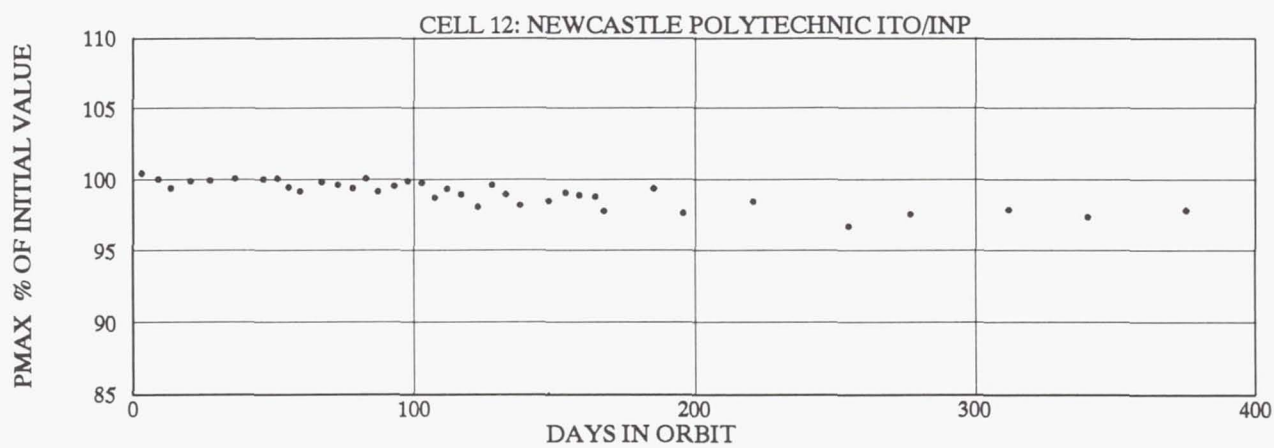


FIGURE 8.

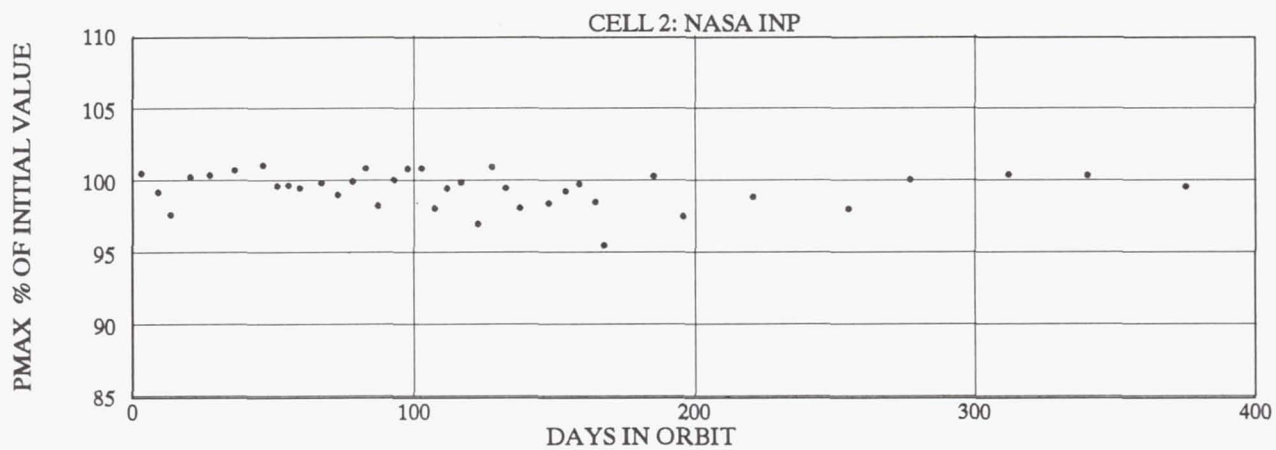


FIGURE 9.

RESULTS OF THERMAL VACUUM TESTS FOR THE PASP+ FLIGHT MODULES

Henry Curtis¹, Don Guidice², Paul Severance²,
and Michael Piszczor¹

1) NASA Lewis Research Center
2) Phillips Lab, Geophysics Directorate

INTRODUCTION

The PASP PLUS (Photovoltaic Array Space Power Plus Diagnostics) program is a photovoltaic experiment which will be flown on the Air Force satellite APEX (Advanced Photovoltaic And Electronic Experiment). APEX will be launched with a Pegasus during the summer of 1993. There are two other small experiments on APEX but PASP+ is the largest, uses the most power and accounts for over 90% of the data requirements. The orbit is elliptical with apogee and perigee of 1050 and 190 nautical miles respectively. The inclination is 70 degrees. The two main objectives of PASP+ are to determine the interactions between high voltage arrays and the space plasma environment and to determine the radiation damage characteristics of several newer types of solar cells.

In order to determine the interactions with the space plasma, several of the individual cell strings will be biased to voltages up to plus or minus 500 V, and leakage currents and arcing rates will be measured. The radiation degradation characteristics will be determined by the continuous monitoring of I-V data for all of the cell strings. As part of an overall testing program, the PASP+ panels and controller were put through a thermal vacuum test in order to check the thermal analysis, obtain temperature coefficients for the individual modules, and have an end-to-end test of the entire PASP+ experiment. This paper will describe briefly this thermal vacuum test and discuss the results obtained during that testing.

PASP+ DESCRIPTION

The PASP+ experiment consists of twelve photovoltaic modules with sixteen separate cell strings. Table I lists the sixteen different cell strings. There are a wide variety of cell types as well as two concentrator modules. Among the different cell types are silicon, GaAs on germanium substrates, InP, amorphous silicon, and three multi-bandgap cells, AlGaAs/GaAs, GaAs/GaSb, and GaAs/CIS.

As noted in Table I, not all of the individual modules will be biased for plasma interaction effects. Six of the individual modules will never be biased and only their radiation degradation will be measured. There are three modules with two or three individual strings. #'s 0, 1, and 2 are all 2x4 cm older silicon cell strings on the same module, while #'s 4 and 6 are GaAs strings on the same module. The other module with two strings is the GaAs/CIS module with two mechanically stacked multi-bandgap cell strings. Eight of the

Table I PASP+ Individual Cell Strings.

<u>PASP+ #</u>	<u>Cell Type</u>	<u>Array Type</u>	<u>Bias</u>	<u>Cells</u>
0	Silicon 2x4 cm	Planar	No	20
1	Silicon 2x4 cm	Planar	Yes	20
2	Silicon 2x4 cm	Planar	Yes	60
3	Silicon 8x8 cm	Space Station	Yes	4
5	Silicon 2.6x5 cm	APSA	Yes	12
4	GaAs 4x4 cm	Planar	Yes	20
6	GaAs 4x4 cm	Planar	Yes	12
8	GaAs 4x4 cm WT	Planar	Yes	4
11	GaAs 4x4 cm	Planar	Yes	8
10	InP 2x2 cm	Planar	No	10
9	Amorphous Si 4x4 cm	Planar	No	1
7	AlGaAs/GaAs	Planar	No	20
12	GaAs/CIS 2x2 cm	Planar	No	9
13	GaAs/CIS 2x4 cm	Planar	No	3
14	GaAs concentrator	Cassegrainian	Yes	8
15	GaAs/GaSb	Mini-dome Concentrator	Yes	12

individual strings are on a deployed panel (#'s 0-7), while the others are on the top surface of the APEX spacecraft.

Along with the photovoltaic modules, PASP+ has several diagnostic instruments to measure the environment or help determine the plasma interactions with the biased arrays. A Langmuir probe will be used to measure plasma properties; A dosimeter will measure the radiation environment in several energy bands; and a quartz crystal balance will be used to determine any contamination. A transient pulse monitor, an electrostatic analyzer and an electron emitter will be used in the plasma interaction portions of the experiment.

The last major portion of the PASP+ experiment is the controller, which will measure all the I-V curves, control the plus or minus bias voltages to the arrays, and in general run the experiment.

THERMAL VACUUM TEST DESCRIPTION

The thermal vacuum test was performed at the Boeing facility in Kent Washington during late June and early July of 1992. The work was supported by NASA contract NAS3-26604. The work was divided into three separate tests due to size limitations. The area covered by the solar simulator beam was not large enough to illuminate the entire PASP+ experiment, or even the deployed panel. Hence the first two tests were with the right half then the left half of the deployed panel illuminated, while the third test was with the payload shelf illuminated. During each test, only the panel being tested was in the chamber. In the two tests with the deployed panel, the half of the panel which was not being illuminated by the solar simulator was maintained at the required temperatures by a set of lamp banks built into the test support fixture.

Each of the three separate tests included the following:

- 1) A thermal balance cycle to determine the hot and cold operating temperatures.

- 2) Three thermal soak cycles at temperatures of 10 degrees higher than the hot operating temperature and 10 degrees lower than the cold operating temperature. The dwell time at each hot and cold temperature was 90 minutes.
- 3) Eight thermal cycles between the operating temperatures with no dwell time. (Four cycles for each of the deployed panel tests).

During each of the three tests, chamber pressure was maintained near 10^{-7} torr. The solar simulator irradiance was monitored with blackbody detectors (water cooled) in the chamber. Between the first and second and between the second and third tests, the solar simulator irradiance was measured (in air) at the test plane with three reference cells. The reference cells were silicon, GaAs, and InP. The Isc was measured to calibrate the flux detectors while the Voc was measured as a temperature sensor to adjust the reference cell Isc data. The test fixture also included lamp banks to simulate the earth's albedo.

Each of the PASP+ modules has an RTD platinum temperature sensor. These were continuously monitored by the PASP+ controller. Several thermocouples were also added to the panel structure to monitor temperatures during the tests. These thermocouples were continuously monitored by the Boeing test instrumentation. Since each of the modules could obtain different temperatures at different rates, there was one panel thermocouple designated to indicate when the simulator and lamp banks should be turned off and on. During the tests, the controller was in the test chamber and it was maintained near room temperature with auxiliary heaters.

During each of the three tests, between 40 and 50 I-V curves were taken for each of the modules under test. This data was stored in a small computer which was connected to the controller. The computer was in the main control room, which allowed near immediate viewing of the I-V data. The controller also continuously monitored the module temperatures, and displayed them in real time. The data was analyzed later at either NASA Lewis Research Center or Phillips Lab at Hanscom AFB.

MODULE TEMPERATURES

Figure 1 shows the temperature for the module which had the three silicon cell strings (#'s 0, 1, & 2). This data is typical for all the modules in all three tests. We first reached a hot temperature equilibrium, then turned the solar simulator off and waited 30 minutes for a cold temperature. 30 minutes was chosen because this is the longest expected eclipse during the PASP+ flight. After the thermal balance determination we did the hot and cold temperature soaks followed by the either four or eight rapid temperature cycles.

The data in figure 2 is just the thermal balance portion of the data in figure 1. Note the hot equilibrium temperature obtained after about 50 minutes and the 30 minutes of cooling before the simulator was turned back on. This data is typical of most of the PASP+ modules with ordinary thermal masses. Figure 3 shows the thermal balance portion for the APSA module, a very low thermal mass array. Note that the hot temperature equilibrium is reached in about three to four minutes and a cold balance temperature is reached in about 10 minutes. APSA is one of two low thermal mass modules on PASP+, the other one being the Space Station module. Table II shows the thermal balance temperatures for each of the PASP+ modules.

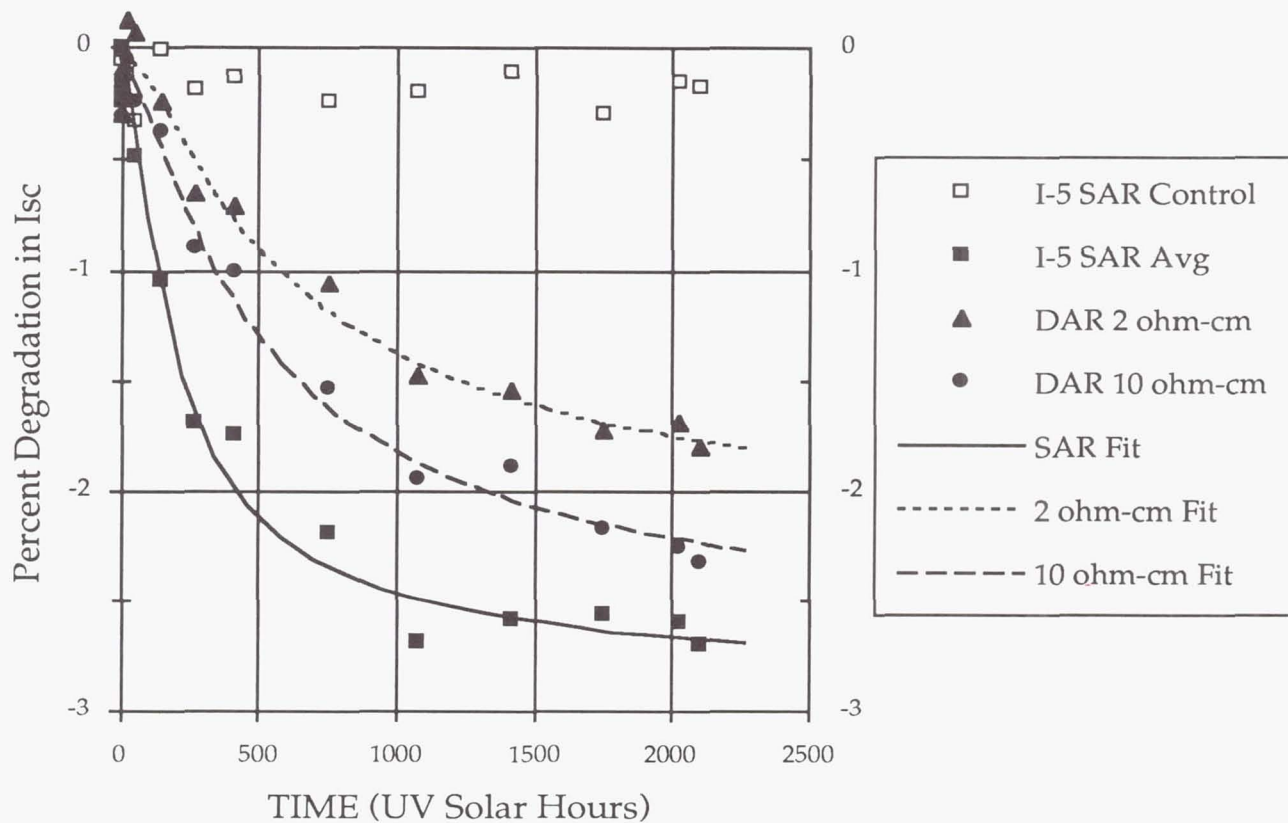


Figure A-5. Degradation from first UV lamp, on a linear scale

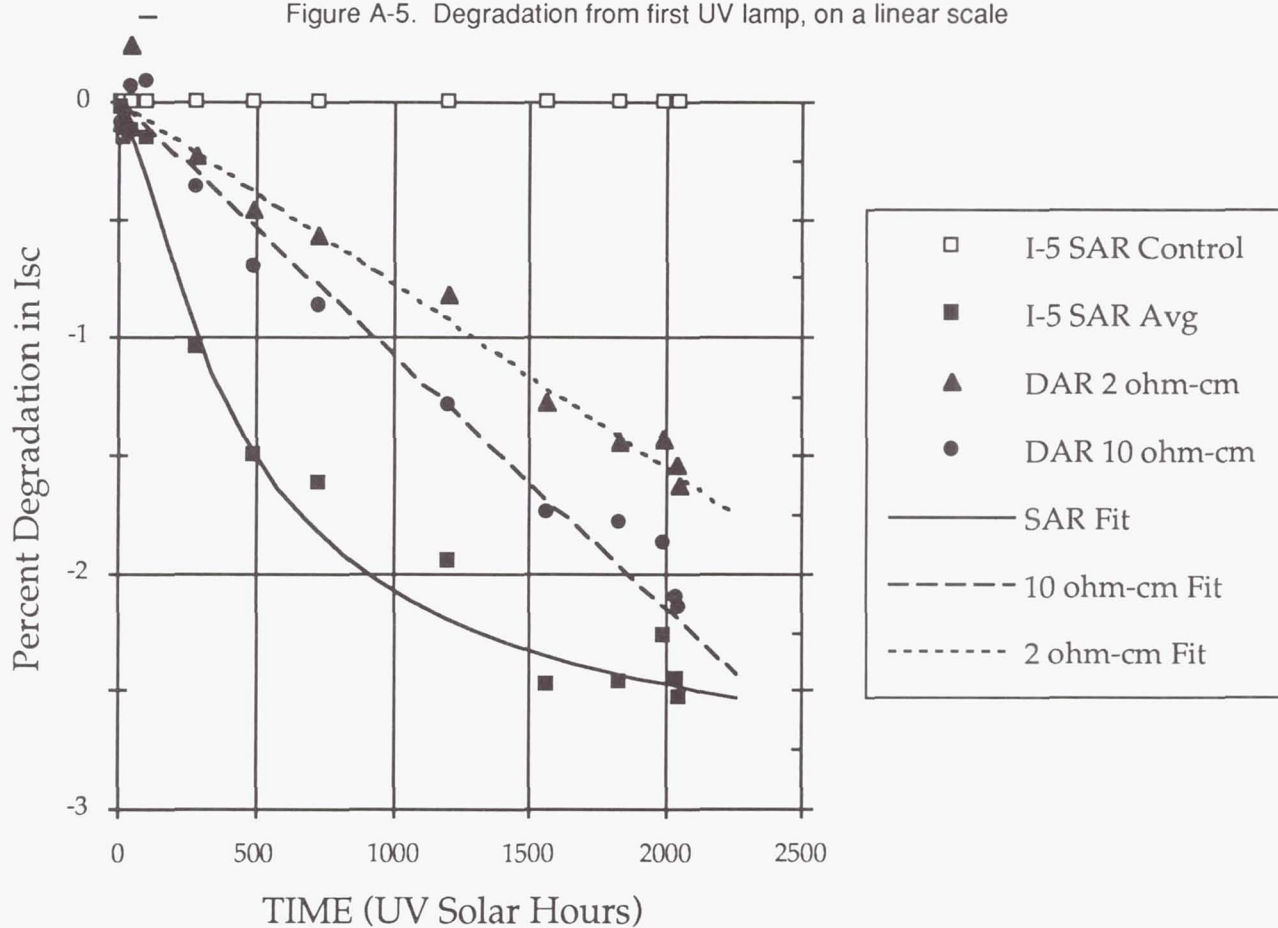


Figure A-6. Normalized and time base corrected degradation from first UV lamp, on linear scale

Table II Hot & Cold Thermal Balance Temperatures.

<u>PASP+ #</u>	<u>Cell Type</u>	<u>Hot Temp</u>	<u>Cold Temp.</u>
0, 1, 2	Silicon	44.4C	-57.7C
3	Silicon	62.7	-88.6
4, 6	GaAs	59.8	-43.0
5	Silicon	64.3	-85.8
7	AlGaAs/GaAs	35.2	-47.9
8	GaAs WT	37.9	-55.2
9	Amorphous Si	36.3	-36.8
10	InP	45.7	-35.0
11	GaAs	42.0	-54.2
12,13	GaAs/CIS	40.2	-36.8
14	GaAs Conc.	46.1	-21.8
15	GaAs/GaSb Conc.	49.4	-50.3

The Cassegrainian concentrator (#14) has a high thermal mass and after 30 minutes of simulated eclipse, the temperature dropped to only -21.8C. All the other modules had reached a cold equilibrium temperature after 30 minutes. During the 90 minute cold soaks however, the Cassegrainian reached a final cold temperature near -55C.

In general, the measured thermal balance temperatures offer no major surprises. Comparison with the predicted temperature from the thermal analysis is ongoing. After the three temperature soaks and the eight rapid temperature cycles, there was no measurable degradation in any module due to the thermal vacuum test.

MODULE ELECTRICAL PERFORMANCE

During each of the three thermal vacuum tests, between 40 and 50 I-V curves were taken for each module in that particular test. Sometimes, immediately after turning on the simulator after a cold soak, we would take a series of I-V curves to obtain data as the temperature changed. Hence, for each module, we have a collection of performance data at a wide variety of temperatures. From this data, we can generate plots of I_{sc} , V_{oc} , P_{max} , and fillfactor vs. temperature and eventually, from straight line curve fits, determine the temperature coefficients.

Figures 4 and 5 are representative of the bulk of the electrical performance data. Figure 4 shows short-circuit current vs. temperature for module #0, a silicon module, while figure 5 shows open circuit voltage vs. temperature for the InP module #10. In both cases, the data is well represented by a straight line curve fit, leading to meaningful temperature coefficients. Table III lists the I_{sc} , V_{oc} , & P_{max} temperature coefficients for each of the planar PASP+ modules in units of %/K. The temperature coefficients for the two concentrator modules are not included due to some data inconsistencies. The Cassegrainian module had a loose interconnection which changed the data from time to time. Since each element of the Cassegrainian has its own bypass diode, I-V data was always available. The mini-dome concentrator module showed a very large change in current with temperature and will be discussed later. There is no I_{sc} data for the Space Station module due to an incorrect current sensing resistor in the controller. This has been replaced and we will be able to measure all the currents during the PASP+ flight.

In Table III, the modules are grouped into cell types. The first group of five modules are all made with silicon cells, while the second group of four modules are all made with GaAs cells. The last group contains the multi-junction cells and the third group contains the InP and the amorphous silicon modules. Note the silicon modules, as expected degrade faster with temperature than the GaAs modules, due mainly to a

higher percentage Voc degradation. The InP module has intermediate Pmax and Voc temperature coefficients, again as expected due to its individual cell Voc being between silicon and GaAs.

Table III PASP+ Module Temperature Coefficients (%/K)

Module		Isc	Voc	Pmax
0	Silicon	0.055	-0.359	-0.410
1	Silicon	0.058	-0.362	-0.404
2	Silicon	0.054	-0.357	-0.439
3	Space Station	----	-0.315	-0.403
5	APSA	0.042	-0.314	-0.431
4	GaAs	0.029	-0.198	-0.226
6	GaAs	0.024	-0.173	-0.179
8	GaAs WT	0.038	-0.176	-0.135
11	GaAs	0.036	-0.179	-0.204
10	InP	0.028	-0.235	-0.295
9	Amorphous Si	0.149	-0.246	+0.339
7	AlGaAs/GaAs	0.122	-0.216	-0.145
12	GaAs/CIS	0.031	-0.214	-0.312
13	GaAs/CIS	0.031	-0.201	-0.229

The most noteworthy temperature coefficients are for the multi-junction cell modules and the amorphous silicon module, which actually is a multi-junction cell. It had been expected that multi-junction cells would degrade faster than single junction cells due to the multiple voltage drops. However the GaAs/CIS modules have a lower degradation with temperature than silicon, and only slightly more than single junction GaAs. This is due mainly to the relatively low drop in Voc with temperature. These cells are also connected somewhat differently than conventional monolithic multi-junction cells. For instance, the basic building block for module #12 is three CIS cells in series which are in parallel with three parallel GaAs cells. Module #13 is similar except the ratio is 4:1 rather than 3:1.

Figure 6 shows the maximum power for the AlGaAs/GaAs monolithic multi-junction cell module (#7) vs. temperature. Note that the power decreases with increasing temperature for temperatures above 0C. For this portion of the curve, the Pmax temperature coefficient (shown in Table III), is quite low, at -0.145%/C. Below 0C, the power increases with increasing temperature. The low Pmax temperature coefficient is the result of the relatively large Isc positive temperature coefficient, 0.122%/C, which is twice as large as any other PASP+ Isc temperature coefficient except amorphous silicon. The change in Pmax at 0C is reflected in the fillfactor as shown in figure 7. Note that the fillfactor decreases significantly as the temperature decreases below 0C.

This change in both Pmax and fillfactor behavior at 0C has two possible explanations, both dealing with the change in bandgap of the two cells (AlGaAs & GaAs) with temperature. The first explanation is that as the bandgaps change with temperature, the monolithic cell matching currents become mismatched and affect the fillfactor and Pmax. The second explanation is similar except the changing bandgaps could see different portions of a non-perfect solar simulator spectrum produced by high pressure xenon lamps. In either case, the actual flight data will determine if there is a real break in the Pmax vs. temperature curve for AlGaAs/GaAs multi-junction cells.

The amorphous silicon module (#9) also exhibits some interesting behavior. Figure 8 shows Pmax vs. temperature for the amorphous silicon module while figure 9 shows the fillfactor. The Pmax increases

dramatically with temperature while the fillfactor does the same. As noted in Table III, The I_{sc} also increases rapidly with temperature. Since the amorphous silicon cell is a monolithic multi-junction cell, similar arguments concerning bandgap shifts with temperature and non perfect solar simulation discussed above also apply. Again the flight data will be the final deciding factor. Nonetheless, it should be noted that the maximum measured P_{max} is near the operating temperature for the amorphous silicon module.

The I-V curves generated during the thermal vacuum tests are all fairly ordinary with the exception of the mini-dome concentrator. Figure 10 shows I-V curves for the mini-dome concentrator module at five temperatures covering the entire temperature range encountered during the test. The voltage portion of the curves is quite normal with the small decrease with increasing temperature. The current however shows a very large increase with temperature more than doubling in the temperature range of -49C to 59C. It is expected that the lenses got quite cold during the tests and along with the simulated solar irradiance not being collimated to 32 minutes they somewhat defocused the light. Again, we will have the flight data as a final check. At operating temperatures, the module had a normal performance and there were no effects due to the thermal cycling.

SUMMARY

A series of thermal vacuum tests were performed on the PASP+ modules and flight controller. Three thermal soaks for 90 minutes at 10 degrees beyond the measured hot and cold extreme temperatures were performed as well as 8 thermal cycles. There were no damaging effects of the test on any of the modules and a few problem areas with the controller were corrected. We obtained excellent performance data for each module as a function of temperature and temperature coefficients were calculated. Some non-predicted data were observed but on further analysis, plausible explanations were found. The experiment is ready for launch.

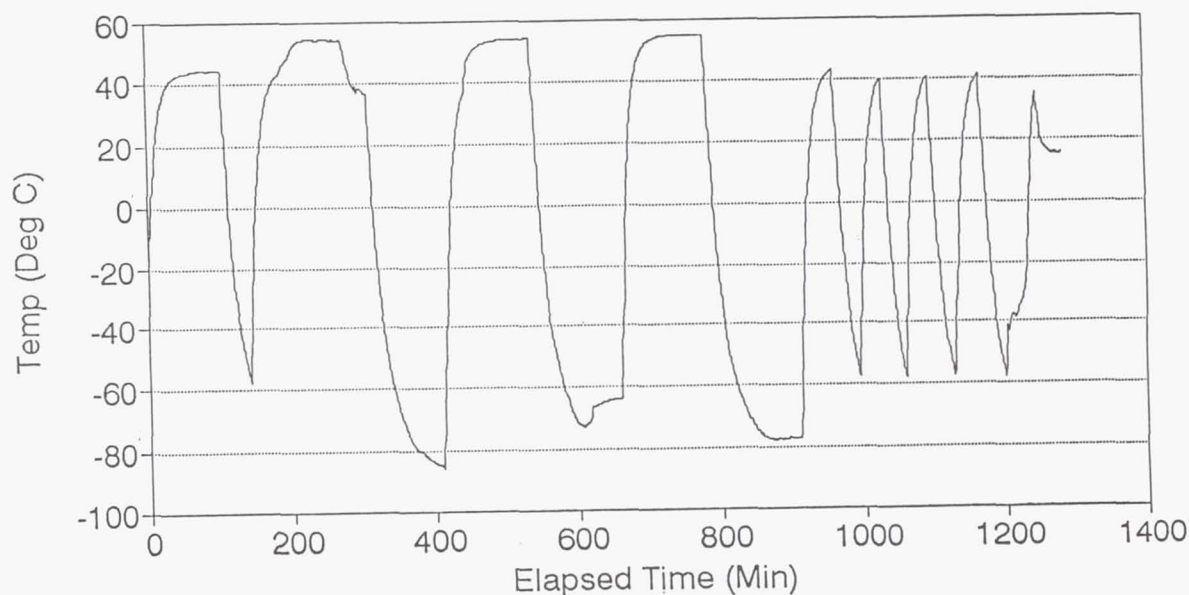


Figure 1. Temperature history for modules 0, 1, and 2, --- entire test.

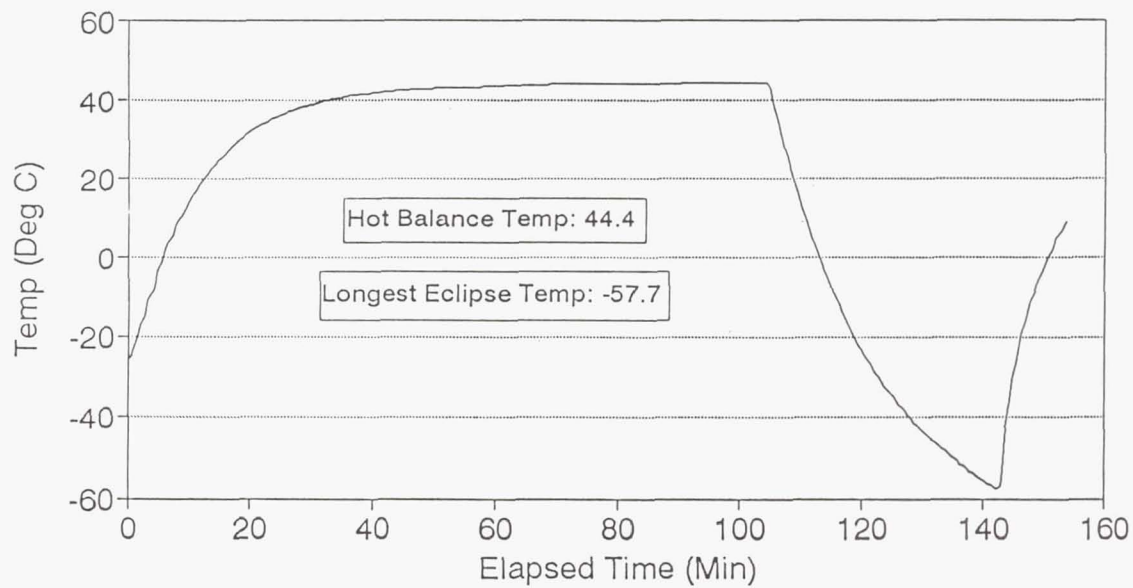


Figure 2. Temperature history for modules 0, 1, and 2, --- thermal balance.

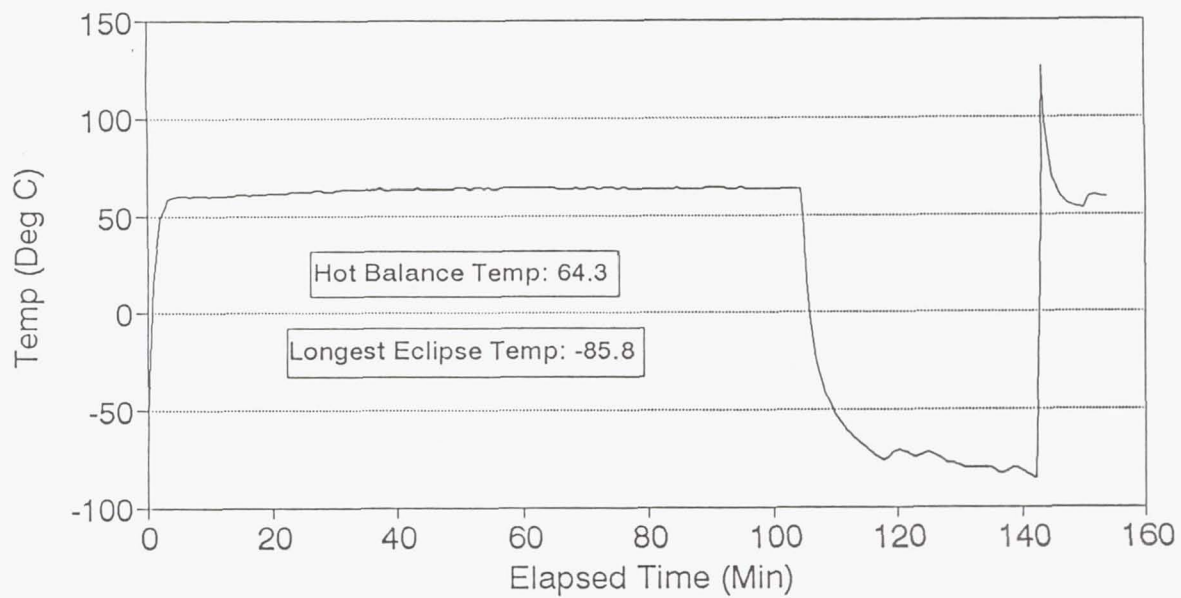


Figure 3. Temperature history for APSA module --- thermal balance.

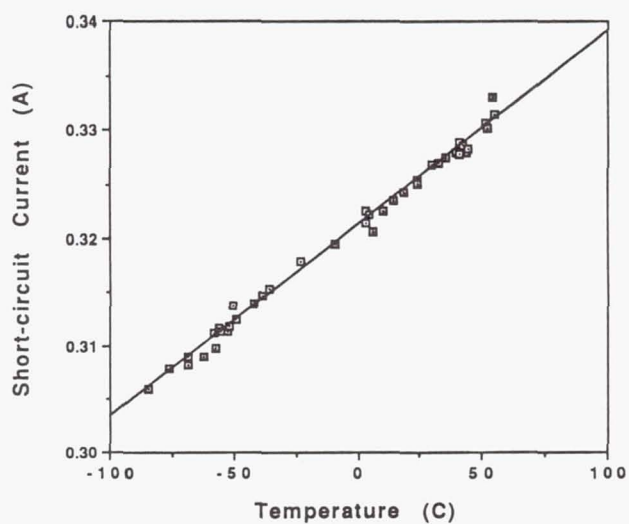


Figure 4. Short-circuit Current vs. Temperature for Module #0, Silicon.

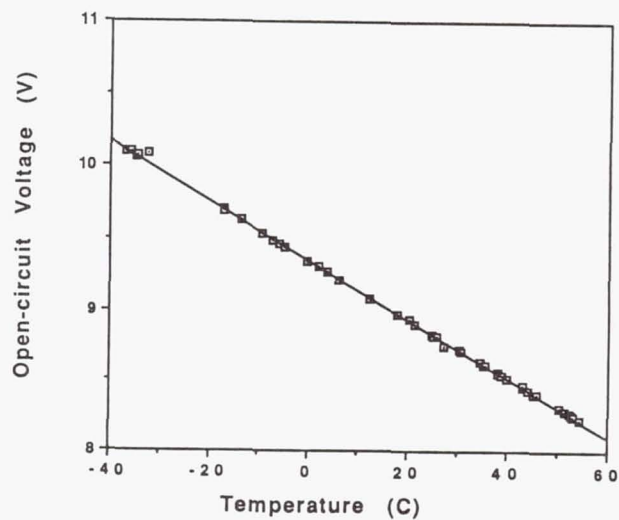


Figure 5. Open-circuit Voltage vs. Temperature for Module #10, InP.

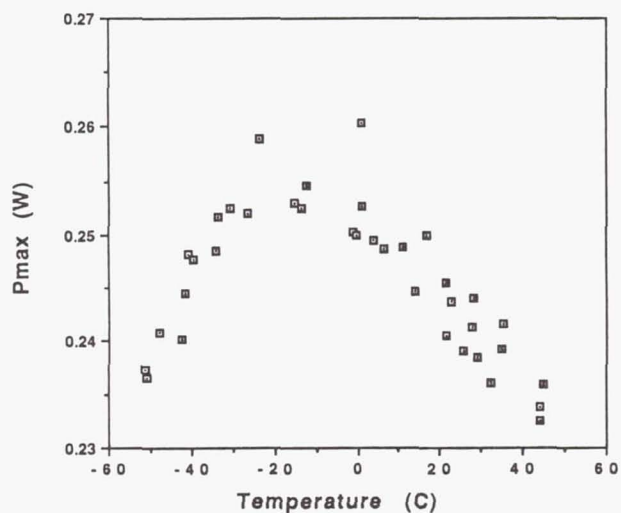


Figure 6. Maximum Power vs. Temperature for Module #7, AlGaAs/GaAs.

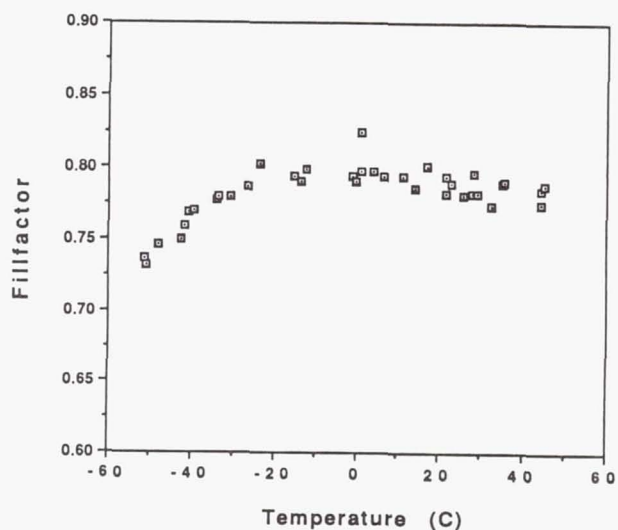


Figure 7. Fillfactor vs. Temperature for Module #7, AlGaAs/GaAs.

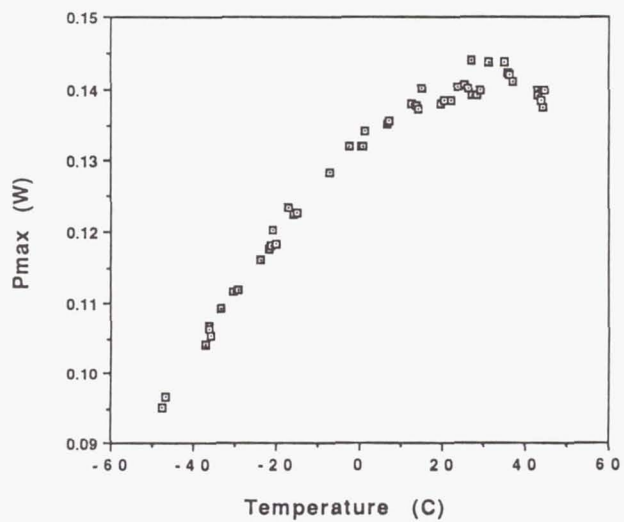


Figure 8. Maximum Power vs. Temperature for Module #9, Amorphous Si.

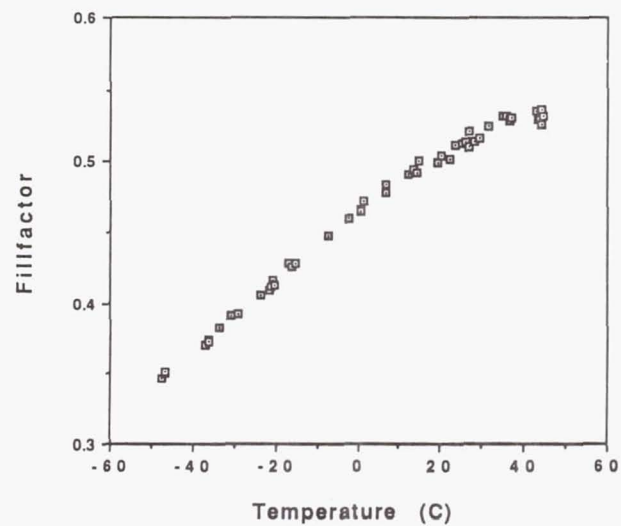


Figure 9. Fillfactor vs. Temperature for Module #9, Amorphous Si.

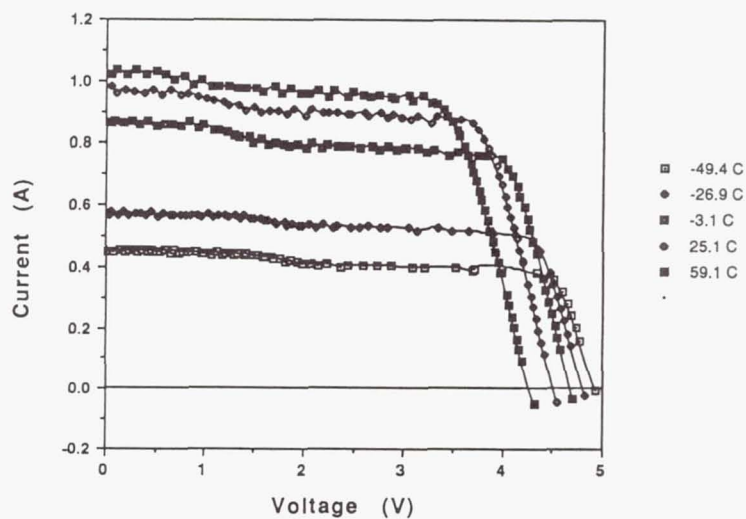


Figure 10. I-V Curves for Different Temperatures for Module #14, Mini-dome.

COMPUTATION OF PHOTOVOLTAIC PARAMETERS UNDER LUNAR TEMPERATURE VARIATION¹

Neelkanth G. Dhere, James V. Santiago
Florida Solar Energy Center
Cape Canaveral, FL 32920-4099

Photovoltaic (PV) arrays with regenerative-fuel-cell energy storage is a prime, power-system, candidate for lunar photo-power. The PV module performance decreases at higher temperatures. Surface temperature variations of the moon are extreme, the maximum (noon) temperature being 384 K. The present work utilizes detailed computations of photovoltaic parameters with computer program developed earlier for the computation of optimum bandgaps of single- and two-junction solar cells at different temperatures; and calculates the power output of single- and two-junction solar modules under different configurations which constitutes an improvement over the assumption of a linear variation of efficiency with temperature. The program also calculates the necessary PV-array size to satisfy stipulated levels of day- and night-time power consumption.

INTRODUCTION

Photovoltaic (PV) arrays with regenerative-fuel-cell energy storage is a prime, power-system, candidate in a lunar base development plan that does not require high power levels initially (ref. 1). The advantages of PV arrays are modularity, lightweight, and a long record of reliable power production in space with a reduced technical risk. They have the disadvantage of necessitating a storage system for the long (~354.36 hours) lunar night and possibly for the early morning and late afternoon when the incident energy on an horizontal array is small. Lunar surface temperatures are extreme in comparison to the surface temperatures on earth because of the slow synodic rotation period, lack of atmosphere, and low conductivity of lunar soil (ref. 1,2). The PV module performance decreases at higher temperatures. The earlier calculations of lunar photopower arrays did not take into account the continuous variation of cell parameters during the lunar day (ref. 1). Moreover the temperature dependence of the characteristics of solar cells cannot be described adequately by a linear approximation (ref. 5). Osterwald et al (ref. 3) have given a linear fit for the variation of the measured basic parameters for Si, GaAs, InP, and CuInSe₂ solar cells with the temperature and calculated the temperature coefficients over a limited temperature range of 15-60 °C. In most cases, the measured parameters showed a non-linear behavior at temperatures above 50 °C (ref. 3). When studying the efficiency of a solar cell on the moon, the temperature variation on the lunar surface and its effects on the solar cell conversion efficiency must be taken into consideration (ref. 4). The short circuit current mainly depends on the intensity of light, and therefore will have little temperature dependence except for minor corrections due to bandgap variation and diffusion-length changes. The main temperature effect is due to the change in open-circuit voltage. The fill factor FF and the photovoltaic conversion efficiency vary with temperature in a complex manner. The present paper carries out detailed computations of photovoltaic parameters; and calculates the power output and PV-array size of single- and two-junction solar modules necessary to satisfy stipulated levels of day- and night-time power consumption, under different configurations.

LUNAR TEMPERATURE CONDITIONS

Surface temperature variations of the moon are extreme, the maximum (noon) temperature at the lunar

¹ This work was supported by Technological Research and Development Authority, Titusville, FL.

equator being ~384 K and the temperature at sunrise being ~220 K (ref. 2,6,7). The surface-temperature variation of the moon depends on the exact position of the earth-moon system from the sun (ref. 6). The temperature equation can be written in a simple form as follows:

$$T = T_d + T_0 \cos^{1/6}(\theta) \quad (1)$$

where $T_0 = T_n - T_d$, T_n is the temperature at noon and T_d the temperature at sunrise of the latitude under consideration. θ , is the angular position of the sun with respect to zenith.

The variation of temperature at a given latitude can be determined using the equation (1) described above, along with the information of the maximum and minimum temperature at that particular latitude.

THEORY

Single Junction Solar Cell

The bandgap of a material at any given temperature is calculated using the following equation (ref. 5):

$$E_g(T) = E_{g0} - \alpha T^2 / (T + \beta) \quad (2)$$

where E_{g0} is the bandgap of the material in electron volts at 0 K, α and β are empirical constants specific to the material, and T is the absolute temperature in Kelvin. For most materials α is positive, hence the bandgap usually decreases with temperature.

The dark reverse saturation current of a solar cell, $J_0(T)$ at any given temperature is calculated using the following equation (ref. 5):

$$J_0(T) = K' T^3 \exp [-E_g(T) / kT] \quad (3)$$

where k is the Boltzmann's constant, K' is an empirical factor dependent on the quality of the material used for the solar cell. K' has a lower value for highly crystalline materials and a higher value for polycrystalline or amorphous materials. For the calculations which were not material specific, a value of 0.005 was chosen. Calculations that were specific to a particular material have used values that are appropriate to that material.

The short-circuit current density, $J_{sc}(T)$ is calculated using the following equation (ref. 8):

$$J_{sc}(T) = q N_{ph}(T) \quad (4)$$

where q is the electronic charge, $N_{ph}(T)$ is the effective photon flux incident on the solar cell that is used in the generation of current at temperature T . N_{ph} at temperature T was calculated as follows. The wavelength, $\lambda(T)$ equivalent to the bandgap $E_g(T)$ at a given temperature T is calculated by using $\lambda(T) = hc / E_g(T)$, where h is the Planck's constant, c is the speed of light in free space. The theoretical photovoltaic parameters viz. short circuit current, J_{sc} , open circuit voltage, V_{oc} , fill factor, FF, efficiency, η , and their normalized temperature coefficients in the absence of atmosphere (air mass zero AM 0) were calculated using AM0 spectral data (ref. 9) and standard equations and procedures (ref. 5).

The open-circuit voltage, V_{oc} is calculated using the following equation (ref. 5):

$$V_{oc}(T) = (kT / q) \ln [J_{sc}(T) / J_0(T) + 1] \quad (5)$$

Because of the exponential increase in the dark-reverse-saturation current $J_0(T)$ with temperature, $V_{oc}(T)$ decreases significantly with temperature.

The optimum voltage, V_m is calculated using the following equation (ref. 5):

$$\exp[qV_m(T)/k T] [1 + qV_m(T)/k T] = J_{sc}(T) / J_0(T) + 1 \quad (6)$$

The fill factor, FF is calculated using the following equation (ref. 5):

$$FF(T) = \{ V_m(T)/V_{oc}(T) \} \{ 1 - [(\exp(qV_m(T) / k T) - 1) / (\exp(qV_{oc}(T) / k T) - 1)] \} \quad (7)$$

The efficiency, $\eta(T)$ is calculated using the following equation (ref. 5):

$$\eta(T) = [V_{oc}(T) J_{sc}(T) FF(T)] / P_{in} \quad (8)$$

where P_{in} is the solar constant = 1.353 kW m^{-2} (AM0 value) (ref. 9).

Two-Junction Cell

Various combinations of materials can be employed in the fabrication of a two-junction cell from two different materials having different bandgaps. The bandgap of the top cell E_{g1} in a two-junction cell must be larger than the bandgap of the bottom cell E_{g2} (ref. 8). Incident light with energy larger than the bandgap of the top cell will generate a current and the corresponding voltage. The bottom cell generates electricity using photons having wavelengths within the window of energies falling between the bandgaps of the top- and the bottom-cells. The efficiencies for top cell, the bottom cell, and the two-junction cell are calculated as a function of three parameters: the temperature, and the bandgap of the top- and of the bottom-material. This calculation is useful in finding the optimum combination of materials (or bandgaps) that would give the best efficiency of the cell.

The values for the top cell (J_{01} , J_{sc1} , V_{oc1} , V_{m1}) and the corresponding values for the bottom cell (J_{02} , J_{sc2} , V_{oc2} , V_{m2}) are calculated. The equations and the procedures followed in the calculation of J_{sc1} , J_{01} , J_{02} , V_{oc1} and V_{oc2} are the same as those outlined above. The current, J_m corresponding to the optimum voltage for both the top and bottom cell is calculated using the following equations:

$$J_{m1}(T) = J_{01}(T) [\exp(qV_{m1}(T) / (kT)) - 1] - J_{sc1}(T) \quad (9)$$

$$J_{m2}(T) = J_{02}(T) [\exp(qV_{m2}(T) / (kT)) - 1] - J_{sc2}(T) \quad (10)$$

In making the calculation for the two-junction cell, it may be noted that the current passing through both top and bottom cells must be of the same magnitude (ref. 8). This magnitude is determined in the following way. The smaller of the values of J_{m1} and J_{m2} is assigned to J_{min} and the larger is assigned to J_{max} . The value of J_{min} is successively incremented till the value of J_{max} is reached. In each case the voltage corresponding to the current is evaluated for both the top and bottom cell so as to obtain the maximum value for the sum of the individual voltages V_{opt1} and V_{opt2} generated by the top and bottom cells respectively corresponding to the current J_{opt} where J_{opt} is the optimum value of current passing through both the cells. Care must be taken to assign $V_{opt} = 0$ whenever the corresponding J_{sc} is exceeded. The optimum power, P_{opt} is obtained by the following equation:

$$P_{opt} = J_{opt} (V_{opt1} + V_{opt2}) \quad (11)$$

Various Solar Array Configurations and Equations

Of the various designs for array configurations proposed in the literature, the most common configurations are flat-plate, 60-degree-triangular, constant-tracking, and incremental-tracking. The flat-plate and the 60-degree-triangular configurations are the simplest ones requiring no moving parts. Hence maintenance is negligible and the configurations are very cost effective. The tracking array would be gimballed and synchronized with the relative

movement of the sun ~ 1.97 hrs/degree (ref. 1). At sunset the panels could be reset to sunrise. The incremental tracking array would be either manually or automatically adjusted in a certain incremental angular steps. If the angular step is 30 degree, then the automatic adjustment would be done 6 times per lunar day. Thus the incident angle of the sunlight would continuously vary over $\pm 15^\circ$. Both the continuous tracking and incremental tracking require mounting and tracking mechanisms, increasing the cost. The array configurations are mounted on structures and hence positioned a few feet above the surface of the Moon. The efficiency of PV arrays will be affected by the lunar dust suspended and transported by the movement of astronauts, rovers, and the rocket launch and landing activities (ref. 10). Lunar base activities like rocket launching can be especially troublesome if the dust settles on moving parts. The particles have 5 times larger parabolic trajectories because of the lower gravity. Small dust particles, charged by the solar wind can adhere to the panels by electrostatic attraction (ref. 10). The adhesion can be reduced by grounding the electrostatic charge with a transparent conductive coating.

The temperature of the solar cell will be different, for different configurations and it will be different from that on the surface of the moon. The solar-array temperature is calculated based on the amount of incident solar energy and irradiation from the lunar surface, and the energy lost by photovoltaic conversion and irradiation neglecting the difference between the absorptivity and emissivity, using the following equation (ref. 11):

$$A_p \sigma T_{\text{sun}}^4 6.85 \times 10^{-5} (1-\eta) \cos(\theta)/\pi + A_p \sigma T_{\text{moon}}^4 2\pi/4\pi = 2 A_p \sigma T_{\text{cell}}^4 \quad (12)$$

where $\sigma = 2\pi^5 k^4 / 15 h^3 c^2$, A_p is the area of the solar cell inclined to solar rays at an angle θ , and T_{sun} is the temperature of the sun. The temperature of the solar array in the horizontal configuration is calculated by using the following equation (ref. 11):

$$T_{\text{cellhor}} = \{0.5 [6.85 \times 10^{-5} T_{\text{sun}}^4 (1 - \eta) \cos(\theta) / \pi + T_{\text{moon}}^4 / 2] \}^{1/4} \quad (13)$$

To begin with the efficiency η is assumed to be equal to 0.3. The temperature obtained above will be an approximate value (i.e., $T_{\text{cx}} = T_{\text{cellhor}}(\eta = 0.3)$). Using this approximate value, the efficiency of the solar cell is calculated. This calculated value of efficiency is substituted for the value of ' η ' in the equation for T_{cellhor} , and the refined value for the temperature (T_{ct}) of the cell is determined (i.e., $T_{\text{ct}} = T_{\text{cellhor}}(\eta = \eta(T_{\text{cx}}))$). The temperature of the solar array in the tracking configuration is calculated by using the following equation:

$$T_{\text{celltrk}} = \{0.5 [6.85 \times 10^{-5} T_{\text{sun}}^4 (1 - \eta)/\pi + T_{\text{moon}}^4 / 2] \}^{1/4} \quad (14)$$

The refined value of the cell temperature is obtained by the same procedure mentioned under horizontal configuration. The temperature of the solar array in the triangular configuration is calculated by using following equation:

$$T_{\text{celltrg}} = \{0.5 [6.85 \times 10^{-5} T_{\text{sun}}^4 (1 - \eta) (\text{Side1} + \text{Side2})/\pi + T_{\text{moon}}^4 / 2] \}^{1/4} \quad (15)$$

where $\text{Side1} = \cos(\phi_1)/2$, $\phi_1 = \theta + \pi/3$; and $\text{Side2} = \cos(\phi_2)/2$, $\phi_2 = \theta - \pi/3$.

Only one side of the solar cell array arranged in a triangular configuration produces electrical energy during the first and the last 60° relative movement of the sun. Both the sides of the solar cell array produce electrical energy during the middle 60° movement of the sun. This is taken into consideration by the factors Side1 and Side2. The refined value of the cell temperature is obtained using the procedure mentioned above.

The electrical energy obtained from the solar array in horizontal configuration, during an interval of 1.968 hours, corresponding to 0.5 degree increase in θ , is calculated using the following equation:

$$dEn_{\text{hor}} = (0.5 P_{\text{in}} H_{\text{pd}} \eta(T)) \cos(\theta) \quad (16)$$

where H_{pd} ($= 1.968$ hours/degree) is the rate of relative solar movement at the lunar equator. This incremental energy is summed through the whole lunar day comprising of approximately 14 earth days (~ 354.36 hours), to

obtain the total energy, E_{hor} .

The electrical energy obtained from the solar array in tracking configuration, during an interval of 1.968 hours is calculated using the following equation:

$$dE_{trk} = 0.5 P_{in} H_{pd} \eta(T) \quad (17)$$

This incremental energy is summed through one whole lunar day, to obtain the total energy, E_{trk} . The electrical energy obtained from the solar array in triangular configuration, during an interval of 1.968 hours is calculated using the following equation:

$$dE_{trg} = (0.5 P_{in} H_{pd} \eta(T)) (\text{Side1} + \text{Side2}) \quad (18)$$

This incremental energy is summed through one whole lunar day, to obtain the total energy, E_{trg} .

Computer Program

Computer programs were developed for the calculation of parameters required for the design of a lunar photopower system. The development started with a program for single-junction, solar-cell design. Using that another program was written for the two-junction solar cell. The lunar photopower program combines the calculations at different temperatures for both the single-junction and the two-junction cell performance with the calculation of temperatures of different solar array configurations. The programs were also customized for system design, by adding queries for the user and default parameters. Default values for the bandgap of the material used in the solar cell were chosen based on the highest efficiency obtained in the calculations and analysis that were carried out using the computer program. The following default values were used for the other parameters: day-time power consumption = 100 kW, night-time power consumption = 50 kW, regenerative-fuel-storage-cell efficiency = 60%.

RESULTS

The flat plate, tracking array, and 60° triangular configurations which have been proposed for lunar photopower were utilized for the analysis (ref. 1). The single-junction and two-junction programs developed above were utilized to compute the solar-cell-performance parameters during a lunar day for single-junction arrays of specific materials and two-junction arrays having the optimum bandgaps mounted at lunar equator in the three configurations.

The solar cell parameters such as α and β , etc. were calculated using specific material parameters for single-junction solar cells of known materials. The empirical value of K' were calculated on the basis of the best reported AM0 solar-cell parameters for single-crystal GaAs, InP, and Si solar cells; and AM1.5 parameters for polycrystalline-thin-film CuInSe₂ solar cells. The chosen K' values utilized for calculations of dark-reverse-saturation current J_0 were 0.005 for GaAs and InP single-crystal solar cells, 0.05 for Si single-crystal cells; and 0.5 for CuInSe₂ thin-film solar cells. These were approximately equal to those obtained from the reported parameters. The K' value of 0.5 was also utilized for polycrystalline-thin-film CdTe solar cells even though the calculated value was significantly higher for the best CdTe cell. It is expected that with improvements in the quality of CdTe thin-film solar cells, cell parameters and hence K' values will approach the chosen values.

As expected, the small decrease in the bandgap with temperature $E_g(T)$ was found to result in a gradual increase in the short-circuit current, J_{sc} values. The open circuit voltage, V_{oc} dropped considerably with an increase in temperature mainly due to a significantly increased dark-reverse-saturation current. The behavior of fill factor and efficiency reflected these changes. The drop in the conversion efficiencies of the lower bandgap CuInSe₂ and Si cells was much larger than that in higher bandgap InP, GaAs, and CdTe cells.

Figure 1 a and b show the variation of temperatures, short circuit current density J_{sc} , open circuit voltage V_{oc} , fill factor, FF, and efficiency, Eff from lunar sunrise to noon for CdTe solar arrays in the horizontal configuration and CuInSe₂ solar arrays in the triangular configuration respectively. Table I shows the sizes of solar array of Si, GaAs, InP, CuInSe₂, and CdTe single-junction solar cells mounted in the three configurations required for providing 100 kW of power during 354.36 hour lunar day and 50 kW of power during the 354.36 hour lunar night using 60%-efficient regenerative-fuel-cell storage.

In the calculations of two-junction solar cell parameters, the default values chosen for α and β were 4.01×10^{-4} and 0 respectively and E_{g0} was varied continuously. The chosen value for the empirical parameter K' was 0.05 for these calculations. Figure 2 a and b show the variation of temperatures and photovoltaic parameters for a two-junction array having optimum bandgaps $E_{g1} = 1.81$ eV, $E_{g2} = 1.18$ eV and $E_{g1} = 1.83$ eV, $E_{g2} = 1.2$ eV for the maximum power output in the horizontal and tracking configurations respectively. The behavior was found to be similar for each of the configurations for the different types of cells. Table I also provides the sizes of solar array of two-junction solar cells having the optimum bandgaps mounted in the three configurations required for providing the above power levels.

Practical efficiencies are expected to be lower than the calculated efficiencies because of the effects of series and parallel resistance losses which have not been considered in this analysis. However, variation of the efficiencies is expected to show a similar trend. The calculated theoretical parameters show a slightly non-linear behavior similar to the calculations of Fan (ref. 5).

TABLE I

Sizes of single-junction-solar cell arrays of Si, GaAs, InP, CuInSe₂, and CdTe, and two-junction solar cell arrays having optimum bandgaps mounted in the horizontal, tracking, and triangular configurations, required for providing 100 kW of power during 354.36 hour lunar day and 50 kW of power during the 354.36 hour lunar night using 60%-efficient regenerative-fuel-cell storage.

Material		Area of Solar Cell Arrays in square meters		
		Horizontal	Tracking	Triangular
Si		1084.8	725.7	1269.8
GaAs		885.7	579.1	1076.3
InP		901.4	592.2	1086.2
CuInSe ₂		1438.0	988.4	1616.0
CdTe		1034.5	682.4	1239.0
Two-Junction Cells	$E_{g1} = 1.83$ eV, $E_{g2} = 1.20$ eV	676.6	443.3	855.1
	$E_{g1} = 1.81$ eV, $E_{g2} = 1.18$ eV	676.2	443.5	853.0
	$E_{g1} = 1.77$ eV, $E_{g2} = 1.14$ eV	677.1	444.8	851.2

The lunar surface temperatures increase considerably immediately after the sunrise. The calculated photovoltaic module temperatures increased continuously for horizontal arrays (Figures 1a and 2a). The tracking array temperatures were found to rise sharply at sunrise following a gradual increase to the same maximum value as in the horizontal case (Figure 2 b). The increase of temperatures for triangular array was intermediate following a similar pattern as the tracking array (Figure 1b). The optimum values of bandgaps E_{g1} and E_{g2} for obtaining the maximum power output during the lunar day were found to be higher for the tracking and horizontal configurations than for the triangular configuration. This has been attributed to the higher overall operating temperatures in the tracking and horizontal configurations. The calculations can be refined further by choosing actual material parameters of semiconductors having bandgap values in the vicinity of the optimum values.

Even though the tracking array would be the most effective, it requires a complex structure and tracking mechanism. Horizontal array is the simplest configuration. In this geometry, the power output would increase slowly reaching a maximum at local noon and decreasing slowly afterwards. The energy output from the triangular array would be the lowest. However, it has the advantage of a constant power supply. The average effectivities normalized with respect to the tracking arrays were found to be in the ranges of 0.654-0.687 and 0.518-0.612 for the horizontal and triangular arrays respectively, compared to the respective estimated values of 0.635 and 0.46 (ref. 1).

REFERENCES

1. "Conceptual Design of a Lunar Base Solar Power Plant", Task 3.3 Report, NASA Contract Number NASA-17878, EEI Report 88-199, Eagle Engineering, Inc., Houston, Texas, August 14 (1988).
2. Taylor, S.R.: "Lunar Science: A Post-Apollo View", Pergamon Press Inc. (1975).
3. Osterwald, C.R., Glatfelter, T. and Burdick, J. "Comparison of the Temperature Coefficients of the Basic I-V Parameters for Various Types of Solar Cells", Proc. 19th IEEE PVS Conf., p. 188 (1987).
4. "Solar Photo Power Systems for Lunar Applications", Final Report, FSEC-CR-498-92, Technological Research and Development Authority, Titusville, Florida 32780 (May 1992).
5. Fan, J.C.C., "Theoretical Temperature Dependence of Solar Cell Parameters", Solar Cells 17, p. 309 (1986).
6. Weil, N.A., "Lunar and Planetary Surface Conditions", Academic Press (1965).
7. Heiken, G., Vaniman, D., and French, B.M., "Lunar Sourcebook", Cambridge University Press, 1991.
8. Fan, J.C.C., Tsaur, B-Y., and Palm, B.J., "High-Efficiency Crystalline Tandem Cells", Proc. of SPIE Vol. 407, Photovoltaics for solar energy applications II, April 5-6, 1983, Arlington, Virginia.
9. Thekaekara, M.P., "The Solar Constant and the Solar Spectrum Measured from a Research Aircraft", NASA Goddard Space Flight Center, NASA Technical Report X-322-68-304, (1968).
10. Katzan, C.M., Brinker, D.J., and Kress, R., "The Effects of Lunar Dust Accumulation on the Performance of Photovoltaic Arrays", SPRAT XI, NASA Lewis Research Center, Cleveland, Ohio, May 7-9, 1991.
11. Shockley, W., and Queisser, H.J., "Detailed Balance Limit of Efficiency of p-n Junction Solar Cells", J. Appl. Phys., Vol. 32, p.510-519, March 1961.

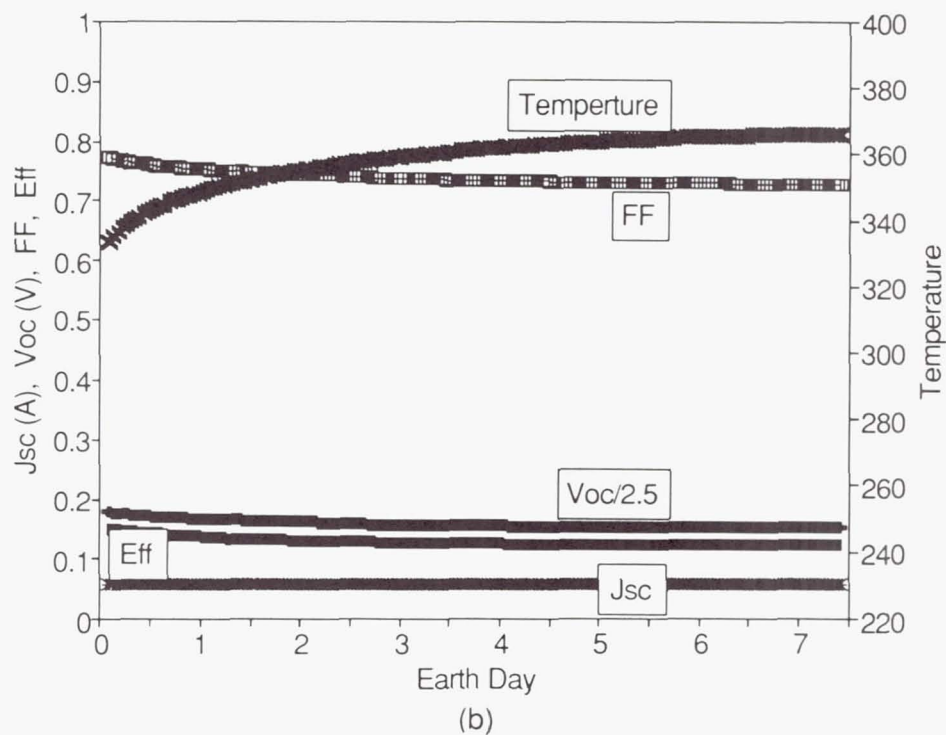
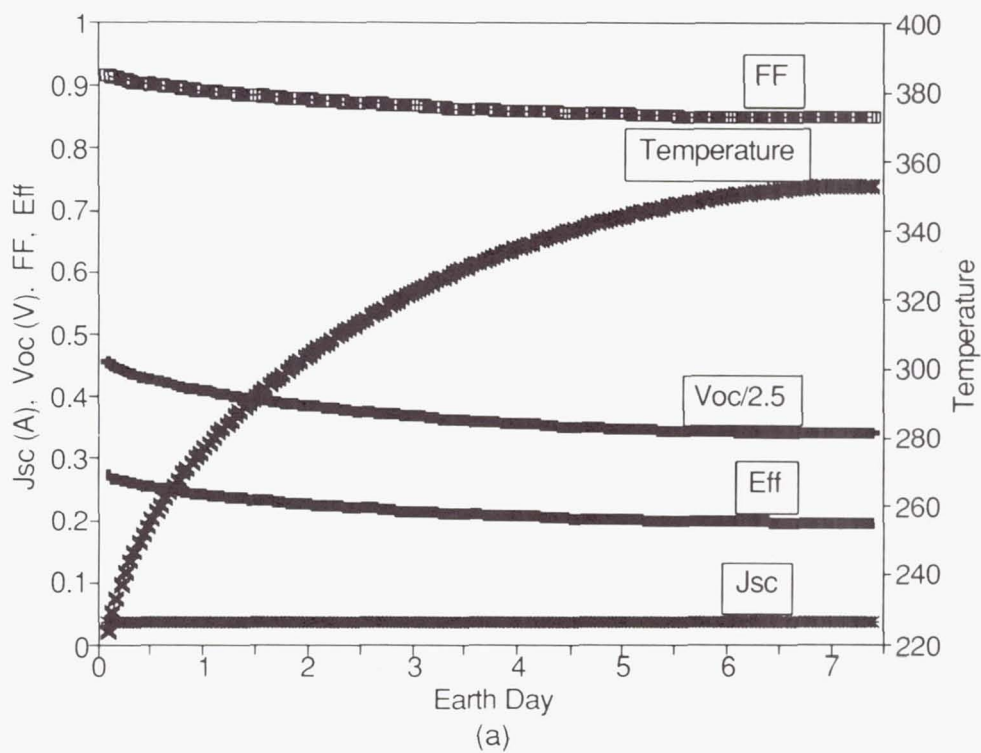


Fig. 1. Variation of the module temperature and the photovoltaic parameters short circuit current, J_{sc} , open circuit voltage, V_{oc} , fill factor, FF, and efficiency, η , from the lunar sunrise to noon of single-junction solar-cell arrays of: a) CdTe mounted in the horizontal flat plate configuration, and b) CuInSe₂ mounted in 60° triangular configuration.

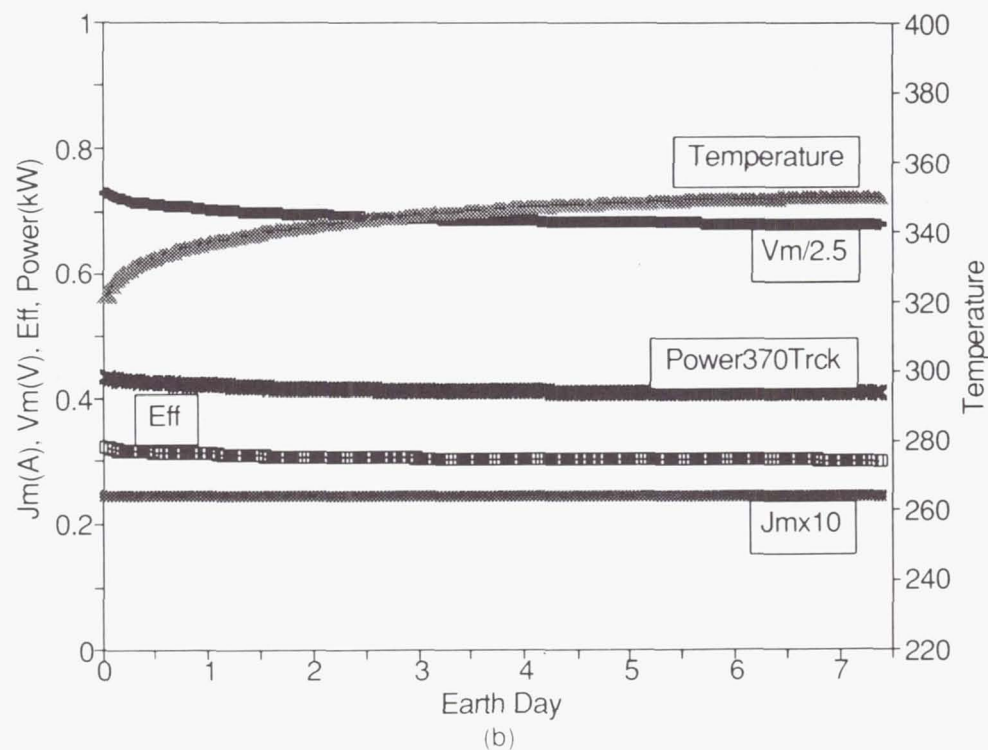
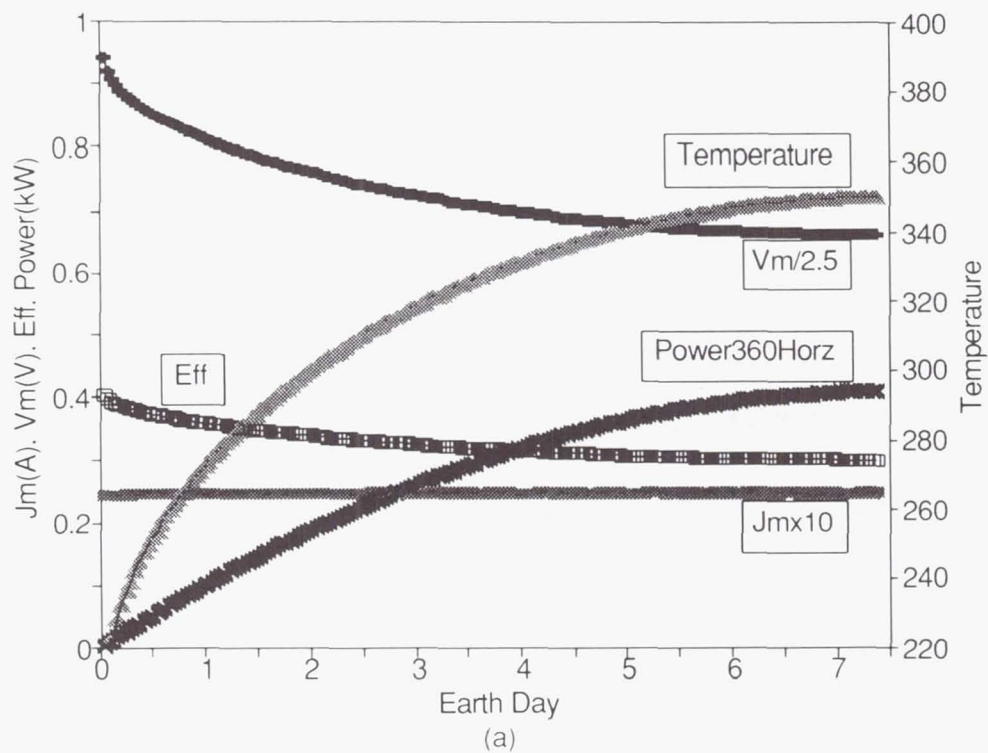


Fig. 2. Variation of the module temperature and the photovoltaic parameters optimum current, J_m , optimum voltage, V_m , efficiency, η , and power, P , from the lunar sunrise to noon, for two-junction solar-cell arrays having the optimum bandgaps mounted in: a) horizontal flat plate configuration with $E_{g1} = 1.81$ eV, $E_{g2} = 1.18$ eV, and b) tracking configuration with $E_{g1} = 1.83$ eV, $E_{g2} = 1.20$ eV.

AN OVERVIEW OF THE DEFENCE RESEARCH AGENCY PHOTOVOLTAIC PROGRAMME

C. Goodbody and M.A.H. Davies
Space Technology Department, Defence Research Agency
Farnborough, Hampshire, GU14 6TD, UK

INTRODUCTION

The DRA has been active in the photovoltaic field since the early 1960's, then as the Royal Aircraft Establishment (RAE). The early work was aimed at developing silicon cells, solar panels and light-weight flexible arrays in support of the "UK" and "X" series of British scientific and technology satellites (ref. 1), for which the RAE was either the design authority or technical advisor. The X3 satellite - Prospero, (fig. 1), launched in 1971 test flew 50 micron wrap-round silicon cells (ref. 2). The X4 satellite - Miranda, launched in 1974 test flew a deployable flexible silicon array which was developed at the DRA (ref. 3). During this period an extensive range of test equipment was developed which has been maintained, modernised and extended to date.

Following a period of reduced activity in the late 1970's and early 1980's the current programme has evolved. This paper briefly summarises the programmes that have been undertaken since 1983. These range from various cell developments, new types of coverglasses, flight experiments, radiation testing, primary cell calibration and environmental testing.

The current photovoltaic programme is mainly funded by the UK Ministry of Defence and by the Department of Trade and Industry through the British National Space Centre (BNSC). The programme is aimed at research and development, both internally and with Industry, to meet the customer's technical objectives and requirements and to provide them with technical advice. The facilities are also being used on contract work for various national and international organisations.

CELL DEVELOPMENT

SILICON

Due to the lack of a UK manufacturer very little has been carried out on silicon cells. The only work carried out was a study into the effects of incorporating an oxygen denuded zone and a defect gettering zone into a silicon cell to improve the radiation resistance (ref. 4). DLTS studies had shown that the main recombination defects involved oxygen and by removing this oxygen it was hoped that the radiation resistance would be improved. The initial results showed that the cells were very radiation hard but suffered from a poor performance. The cell efficiency only matched that of a conventional cell at a fluence of $1 \times 10^{15} \text{ e/cm}^2$ 1 MeV electrons. This technology is currently being looked at again to see if by varying the depth of the denuded zone the performance can be improved and still retain the radiation resistance.

GALLIUM ARSENIDE

The main cell development has been the development of GaAs cells at EEV. The first phase was the development of infinite melt liquid phase epitaxy (IMLPE) cells, (fig. 2), which has resulted in the commissioning of a 1 kW pilot production line with batch averages of over 18% and a best production cell of 19.6%, as measured at DRA (refs. 5,6). A 15 W power panel of these cells is being flight tested on the UoSAT-5 satellite and is performing

as expected. A production run in excess of twelve hundred 22 x 20 mm cells has been made to demonstrate the production line and to provide cells for three panels on the STRV-1A satellite (ref. 7).

The second phase is the development of MOCVD GaAs and GaAs/Ge cells. This is a joint DRA-European Space Agency (ESA) programme which consists of the installation and commissioning of a Quantax MOCVD reactor, the development of a mathematical model for GaAs/Ge cells, and the production of both 2 x 2 cm MOCVD GaAs and GaAs/Ge cells. The programme has recently been extended to include the development of 40 x 40 mm GaAs/Ge cells and is currently scheduled to be completed in March 1993. To date GaAs cells of over 19% efficiency have been produced through this programme.

The third phase is the development of ultra-thin GaAs cells. This involves the etching away of the substrate to leave a 10-20 micron thick solar cell supported by the coverglass. Initial trials using an adhesive bonded coverglass resulted in a best cell of 19.7%. Current activities concern the use of directly glassed coverglasses on a GaAs/Ge cell grown with an etch stop layer to produce ultra-thin devices. Work is also being undertaken into various interconnection methods as there are problems associated with the ultra-thin cells cracking at the contact pads.

INDIUM PHOSPHIDE

A development programme into ITO/InP cells was undertaken at Newcastle Polytechnic (ref. 8) which produced small area devices over 16% efficient and 2 x 2 cm devices over 13% efficient. It also resulted in the first flight of ITO/InP cells in space on the LIPS III satellite, which is discussed later. In addition to developing the cells, radiation studies were performed to assess their resistance compared to GaAs and Si cells (refs. 9-11). On completion of this programme a consortium of UK Industry and academia have continued the development of the ITO/InP cells along with new work aimed at developing homojunction InP and InP/Si cells under the UK Department of Trade and Industry LINK advanced semiconductor materials programme (refs. 12,13).

COVERGLASS DEVELOPMENT

DRA's involvement in solar cell coverglasses technology has over the years resulted in the development of various types of coverglass and coatings at Pilkington Space Technology.

The first coverglass to be developed was the CMS coverglass in the early 1970's, a borosilicate glass stabilised with cerium oxide against darkening induced by electron, proton and UV irradiation. This was followed in the early 1980's by a new composition designated CMX with improved transmission properties over the CMS glass (ref. 14).

With the introduction of larger area silicon cells and new coverglass bonding techniques the difference in thermal coefficient of expansion between CMX and Si can cause interface stresses. This led to the development of the CMZ coverglass which has the same optical properties and radiation stability as the CMX glass but with the thermal coefficient of expansion matched to that of silicon from -200°C to 500°C (refs. 15,16).

After completion of the CMZ development a programme was started into the direct glassing of silicon cells using electrostatic bonding (refs. 17,18). Several problems were incurred due to the anti-reflection coating on the cells, silver migration from the fingers into the coverglass and the grid finger height. This resulted in collaboration with ESA and Telefunken System Technik (TST). On completion of the first phase under the UK national programme, the second phase became a joint UK-German programme run through ESTEC with DRA providing support. A viable bonding process has been produced from this programme (refs. 19,20).

With the introduction of GaAs cells a new glass was developed to be thermally matched to GaAs. The resulting glass designated CMG has superior optical and thermo-optical properties to CMX and same radiation stability but has a thermal coefficient of expansion matched to GaAs from -180°C to 520°C (refs. 21,22).

Following the successful development of the CMG glass and the results of the silicon direct glassing programme a new DRA programme has commenced on the direct glassing of GaAs cells at Pilkington Space Technology and EEV.

In addition to the coverglass development two optical coatings have been developed to improve the thermo-optical properties of the glasses, an ultra-violet reflection (UVR) coating and a high emissivity (HE) coating. The ceria doped coverglasses absorb UV preventing coverglass adhesive darkening but in the process generate heat. The purpose of the UVR coating is to reflect the UV and so reducing the solar absorptance and hence lowering the temperature of the solar cell assembly. The HE coating increases the absorptance in the 8-12 micron region where the reststrahlen reflection bands from the silicon oxide in the glass occur. These bands lower the emittance of the glass, by suppressing them it is possible to increase the emittance (ref. 23).

All the glass types and coatings described above were subjected to an environmental test programme at DRA to demonstrate their suitability in the space environment.

FLIGHT EXPERIMENTS

LIPS-III

The DRA flight testing programme began with the flight of a small panel on the Naval Research Laboratory LIPS-III satellite (ref. 24), launched in Spring 1987. The panel was made up of four strings of silicon cells each with a different type of coverglass: standard CMX, CMX with an ultra-violet rejection coating, CMX with a high emissivity coating and CMZ. In addition to this were a string of radiation hard denuded zone silicon cells and four 2 x 2 cm ITO/InP cells. Unfortunately I-V and temperature measurement problems have been experienced which have limited the usefulness of the results from the experiment. After four years in orbit it is believed that the ITO/InP and denuded zone silicon cells have possibly degraded by 1% in Isc and all the coverglass strings by approximately 6% in Isc (see fig. 3), which is in broad agreement with the predicted degradation (refs. 11,12).

UoSAT-4

LIPS-III was followed by the UoSAT-4 solar cell experiment. UoSAT-4 was a 50 kg microsatellite designed and built by the University of Surrey. The satellite was powered by two panels of Mitsubishi LPE GaAs, a panel of CISE LPE GaAs and a half panel of LPE GaAs from the DRA development contract at EEV. DRA was responsible for the design, manufacture and acceptance testing of the Mitsubishi and EEV panels. DRA also undertook the design, manufacture and testing of the solar cell experiment (Surrey University provided the measurement electronics). The time period from the start of the design to delivery of the experiment was 9 months.

The purpose of the experiment was to test fly the cell and coverglass components currently under development and to compare them with devices from other international organisations. The experiment comprised of six strings of silicon cells, different types of coverglasses and coverglass bonding techniques, GaAs from EEV, CISE and ASEC, and InP from Newcastle Polytechnic and the Nippon Mining Company.

UoSAT-4 was successfully launched into an 800 km polar orbit on 22 January 1990 by an Ariane-4 launcher. Unfortunately 25 hours after activation all telemetry was lost from the satellite and has never been recovered.

UoSAT-5

Following the loss of UoSAT-4 the opportunity arose to fly an experiment on UoSAT-5 as a replacement (fig. 4). The experiment was redesigned to fly individual cells instead of strings and the electronics redesigned to be similar to the STRV electronics. The experiment is comprised of silicon cells with different types of coverglasses and coverglass bonding techniques, IMLPE GaAs, MOCVD GaAs, GaAs/Ge, Cleft GaAs, ITO/InP and homojunction InP (fig. 5). The cells and coverglasses were supplied by UK Industry and in collaboration with NASA Lewis and Wright Laboratory.

UoSAT-5 was successfully launched into a 770 km sun-synchronous orbit on 17 July 1991 by an Ariane-4 launcher as a secondary payload to ERS-1. Unfortunately I-V and temperature measurement problems have again been experienced on the experiment, although not as serious as on LIPS-III. Good Isc data is being received, reasonable Pmax data but the Voc is subject to an offset due to a measurement problem and the temperature resolution is too coarse. None of these problems are serious and good in-orbit performance data is being produced. After 1 year in orbit degradation is being seen on the cells roughly in line with that expected with one major anomaly: all three ITO/InP cells, from two different manufacturers are showing far more degradation than was expected, ground results have implied that little or no degradation should be seen. This result is currently under investigation. Data is continuing to be received from the experiment.

EURECA

The next experiment was the Advanced Solar GaAs Array (ASGA) experiment on the European Space Agency EURECA retrievable platform which was launched in the summer 1992 by the Space Shuttle on a 6 month flight and will then be recovered. The ASGA experiment is a collaboration between DRA and ASI (the Italian Space Agency) to fly a panel containing three cassegrainian concentrator modules (refs. 25,26). Pilkington Space Technology under contract to DRA manufactured the concentrator modules and integrated them onto the panel, see Figure 6. The completed panel was then electrically tested at DRA before shipping to ASI for integration on to EURECA. Post flight analysis will be undertaken to determine the effect of the LEO environment on the materials used and electrical tests on the modules to assess any degradation.

STRV-1

These flight experiments will be followed by a solar cell experiment on STRV-1B which should be launched into Geostationary Transfer Orbit (GTO) at the end of 1993. STRV-1B is a 50 kg microsatellite being developed at the DRA, see Figure 7 (ref. 27). Its purpose is to act as a test vehicle for new satellite technologies. Due to the GTO orbit, see Figure 8, the radiation environment is very severe. This allows for lifetime radiation testing of solar cell technologies to be performed in a short time scale. The nominal mission life is one year. The solar cell experiment will have the capability to measure the I-V curve and temperature of a maximum of 47 cells.

The list of cells to fly is still being drawn up but is likely to be made up of a wide range of technologies, Si, GaAs and its derivatives, InP, CIS, etc. supplied via Phillips Laboratory, NASA Lewis or DRA.

In addition to this the current at 28 V will be monitored on solar panels of STRV-1B and it's sister satellite STRV-1A which will be launched at the same time. These panels will be EEV IMLPE GaAs, EEV MOCVD GaAs or GaAs/Ge, CISE/FIAR IMLPE GaAs supplied via ESTEC, Spectrolab GaAs/Ge and ASEC GaAs/Ge supplied via Phillips Laboratory.

ENVIRONMENTAL TESTING

RADIATION EFFECTS

Radiation studies have been performed since the late 1960's (refs. 28,29,30). More recent work has concentrated on an internal programme of isotropic proton irradiation of silicon, GaAs and InP cells (refs. 9,10,11) and defect studies using Deep Level Transient Spectroscopy (DLTS) on silicon and GaAs cells at Southampton University.

We have access to several facilities at AEA Technology, Harwell, to perform electron and proton irradiations. We use a 0.6-1.2 MeV Van De Graaff accelerator for electrons, a 0.5-1.8 MeV Van De Graaff accelerator and a 2-10 MeV tandem Van De Graaff accelerator for protons. To simulate isotropic irradiation a 'rocker' is used on the end of the proton beam line (ref. 9).

The defect study at Southampton University used DLTS on proton and electron irradiated silicon and GaAs solar cells to identify the nature of the defects causing the electrical degradation (ref. 31). A new technique was

used, recombination DLTS which uses a laser to inject minority carriers into the device. This allows both majority and minority recombination centres to be identified.

The current programme consists of three main activities: an annealing study into the removal of proton damage from silicon and GaAs cells, an investigation into the radiation characteristics of advanced cell types and the production of accurate damage coefficients for cells which will fly on the STRV-1B solar cell experiment to allow a comparison between the predicted and actual degradation to be made.

The annealing study is aimed at determining the minimum temperatures required to remove low energy proton damage from silicon and GaAs and to determine whether it is possible to lower the temperature when large currents are injected, recombination enhanced annealing.

TEST FACILITIES

To support the above activities an extensive test laboratory is maintained at the DRA for electrical and thermal testing.

For I-V measurement two simulators are available: a Spectrolab X25 continuous simulator and a Large Area Pulsed Solar Simulator (LAPSS). The X25 beam is directed onto a temperature controlled block enabling the I-V curve for cells from 2 x 2 cm to 10 x 10 cm to be measured at temperatures ranging from +10°C to +115°C. A similar block is used on the LAPSS allowing 2 x 2 cm cells to be measured but in addition panels can also be tested, a maximum of 50 A and 100 V output.

The LAPSS facility is not suitable for testing a commercial satellite solar array however after it has been integrated on to the satellite. To overcome this a smaller version of the LAPSS was developed at DRA (ref. 32) to measure the performance of the solar panels before and after the satellites go through their environmental testing and to perform a pre-launch check at the launch sites. This was successfully used on the three MOD Skynet-4 and the two NATO-4 communications satellites.

In addition to the I-V measurements the relative spectral response (RSR) of cells can be measured using monochromatic light from a narrow band filtered xenon lamp at 25 nm steps from 300 to 1200 nm with or without AMO white light bias.

Standard solar cells are used to calibrate the simulators. DRA has for many years calibrated solar cells using terrestrial sunlight in either Cyprus or Malta (ref. 33). The DRA calibration method uses total radiation from sky and sun. This technique involves the measurement of the cell's RSR, I_{sc} in sunlight, solar intensity and the relative spectral energy distribution of the sunlight. From these measurements, the solar cell's short circuit current can be calculated for any AM0 or terrestrial spectrum. The advantage of the DRA terrestrial method is that a large number of cells, up to 10 x 10 cm in size, can be calibrated reasonably quickly at a relatively low cost per cell, at least 150 cells during a two week period.

A comparison was carried out in 1980 to compare this method with the JPL and CNES balloon flights and NASA's high altitude aircraft (ref. 34), the outcome was that all the methods agreed to $\pm 1\%$. Current activities are the improvement of the equipment and a repeat of the 1980 comparison, including a comparison of predicted performance using the standards against actual in-flight results on the solar cell experiments.

Besides the electrical measurement equipment, the section has a range of thermal test facilities: a rapid thermal cycling rig, a thermal vacuum chamber and a solar thermal vacuum chamber. These are for testing individual cells and coverglass, coupons and small solar panels, eg. STRV and UoSAT size.

The rapid thermal cycling equipment can cycle small test coupons up to 22 x 11 cm or individual components between a maximum of +150 and a minimum of -170°C in a nitrogen gas atmosphere. The cycle time depends upon the temperatures and the mass of the samples, a typical Al panel will take approximately 10 minutes a cycle between $\pm 100^\circ\text{C}$.

The thermal vacuum chamber is used to outgas and thermal cycle coupons or small solar panels. The maximum panel size is 60 x 40 cm. The maximum temperature is +200°C and the minimum temperature is -130°C.

The Solar Thermal Vacuum chamber can thermally cycle a panel of up to 27 x 26 cm between temperatures of +100 and -200°C in vacuum. The heating part of the cycle is achieved by illuminating the front of the panel through a port with light from an X25 solar simulator, supplementary heating from an internal wire heater is available if required. The rear of the panel faces a liquid nitrogen shroud, *ie* the front is in 'sunlight' and the rear 'deep space'. The light beam and heaters are shut off to go into 'eclipse'. If a deep eclipse is to be simulated, *eg* for GEO then the sample is lowered into a separate part of the chamber where it is completely surrounded by a liquid nitrogen shroud and also cooled by a helium refrigeration unit to improve the cooling rate. Using computer control GEO or LEO representative thermal cycling can be achieved. Future work is planned as part of an ESA activity on thermal control.

The above facilities are currently being used to qualify the EEV cells and panels which are to fly on STRV-1A and 1B. Along with other equipment, qualification tests can be performed in accordance with the ESA Generic specification for silicon solar cells PSS-01-604 and the USAF MIL-C-83443B general specification for Space solar cells and assemblies.

CONCLUDING REMARKS

The DRA photovoltaic programme has been wide ranging in its activities: developing new coverglasses, developing GaAs and InP solar cells, performing flight experiments, radiation testing, primary cell calibration and environmental testing. Further activities are planned in these areas to meet requirements of the British military and civil space programmes and other national and international bodies.

REFERENCES

- 1 Semple, E.C.: "British spacecraft projects - past, present and future", RAE Technical Report 74092 (1974)
- 2 Sketch, H.J.H.: "The Black Arrow X3 spacecraft", RAE Technical Report 69203 (1969)
- 3 Treble, F.C.: "The RAE lightweight solar array", RAE Technical Report 73172 (1973)
- 4 Markvart, T., Willoughby, A., Dollery, A.A.: "Silicon cells with improved radiation resistance", p.709, 19th IEEE Photovoltaic Specialists Conference, 1987
- 5 Burrage, J., *et al.*: "Gallium arsenide solar cell development", p.37, Photovoltaic Generators in Space Conference, The Hague, The Netherlands, 1986
- 6 Cross, T.A., *et al.*: "GaAs space solar cells - A European pilot production facility", p.507, European Space Power Conference, Florence, Italy, 1991
- 7 Cross, T.A., Hardingham, C.M.: "Gallium arsenide space solar cell panels using ultrasonic welding: Manufacturing technology and flight experience", 6th Photovoltaic Science and Engineering Conference, New Delhi, India, February 1992
- 8 Pearsall, N.M., Hill, R., Dollery, A.A.: "The status and prospects of indium phosphide based solar cells for space use", p.257, Photovoltaic Generators in Space Conference, The Hague, The Netherlands, 1986
- 9 Pearsall, N.M., *et al.*: "Effect of isotropic proton irradiation on the performance of ITO/InP solar cells", p.898, 20th IEEE Photovoltaic Specialists Conference, 1988

REFERENCES (continued)

- 10 Pearsall, N.M., *et al.*: "Radiation effects in ITO/InP solar cells", p.531, European Space Power Conference, Madrid, Spain, 1989
- 11 Pearsall, N.M., *et al.*: "Radiation and flight testing of ITO/InP solar cells", p.1172, 21st IEEE Photovoltaic Specialists Conference, 1990
- 12 Pearsall, N.M., *et al.*: "Flight and irradiation studies of ITO/InP solar cells", p.689, European Space Power Conference, Florence, Italy, 1991
- 13 Pearsall, N.M.: "Recent advances in UK InP solar research", p.182-185, 4th International Conference on Indium Phosphide and Related Materials, Newport, USA, April 1992
- 14 Taylor, H., Simpson, A.F., Dollery, A.A.: "CMX-50: A new ultrathin solar cell cover for lightweight arrays", p.211, Photovoltaic Generators in Space Conference, Bath, England, 1982
- 15 Kitchen, C.A., *et al.*: "A new generation of coverglass", p.271, Photovoltaic Generators in Space Conference, The Hague, The Netherlands, 1986
- 16 Kitchen, C.A., *et al.*: "CMZ - A new generation of coverglass", p.485, 19th IEEE Photovoltaic Specialists Conference, 1987
- 17 White, P.A., Dollery, A.A., Davies, R.T.: "Direct glassing of solar cells", p.87, Photovoltaic Generators in Space Conference, The Hague, The Netherlands, 1986
- 18 White, P.A., Crabb, R.C., Dollery, A.A.: "Direct glassing of silicon solar cells", p.949, 20th IEEE Photovoltaic Specialists Conference, 1988
- 19 White, P.A.: "Electrostatic bonding of silicon cells", p.575, European Space Power Conference, Florence, Italy, 1991
- 20 Koch, J.W., White, P.A.: "Direct glassing of silicon space solar cells - Approach and manufacturing experiences", p.1294, 21st IEEE Photovoltaic Specialists Conference, 1990
- 21 White, P.A.: "A coverglass for gallium arsenide cells", p.1300, 21st IEEE Photovoltaic Specialists Conference, 1990
- 22 White, P.: "CMG - Coverglass for GaAs cells", p.547, European Space Power Conference, Florence, Italy, 1991
- 23 Whalley, A.M., *et al.*: "Improved CMX solar cell coverglasses and optical solar reflectors", p.463, 19th IEEE Photovoltaic Specialists Conference, 1987
- 24 Severns, J., *et al.*: "LIPS-III - A solar cell test bed", p.807, 20th IEEE Photovoltaic Specialists Conference, 1988
- 25 Bertotti, L., *et al.*: "ASGA experiment on EURECA: Flight objectives and instrument configuration", p.197, Photovoltaic Generators in Space Conference, The Hague, The Netherlands, 1986
- 26 Bertotti, L., *et al.*: "The ASGA experiment on EURECA platform: Testing of advanced GaAs solar cells in LEO", p.1002, 20th IEEE Photovoltaic Specialists Conference, 1988

REFERENCES (concluded)

- 27 Ryden, K.A.: "The space technology research vehicle (STRV-1)", p.4.1-4.11, Proceedings of the Royal Aeronautical Society Conference on Small Satellites, 24 January 1991
- 28 Crabb, R.L., Walkden, M.W.: "Energy dependence of electron damage in silicon solar cells", RAE Technical Report 68139 (1968)
- 29 Walkden, M.W.: "Proton/electron damage ratios for some violet, black and thin silicon solar cells", RAE Technical Report 79133 (1979)
- 30 Markvart, T., *et al.*: "Electron and photon degradation of boron doped FZ silicon solar cells", p.109, Photovoltaic Generators in Space Conference, Bath, England, 1982
- 31 Peters, J.W., *et al.*: "Defect interactions in silicon solar cells", Proceedings of 2nd Workshop on Radiation Induced Defects in Semiconductor - Insulator Systems, North Carolina, USA, September 1989
- 32 Wharf, J.H., Davies, M.A.H., Roe, P.J.: "The development of a mobile pulsed solar simulator", p.437, Photovoltaic Generators in Space Conference, The Hague, The Netherlands, 1986
- 33 Photograph courtesy of Prof M.N. Sweeting, Surrey Satellite Technology, University of Surrey

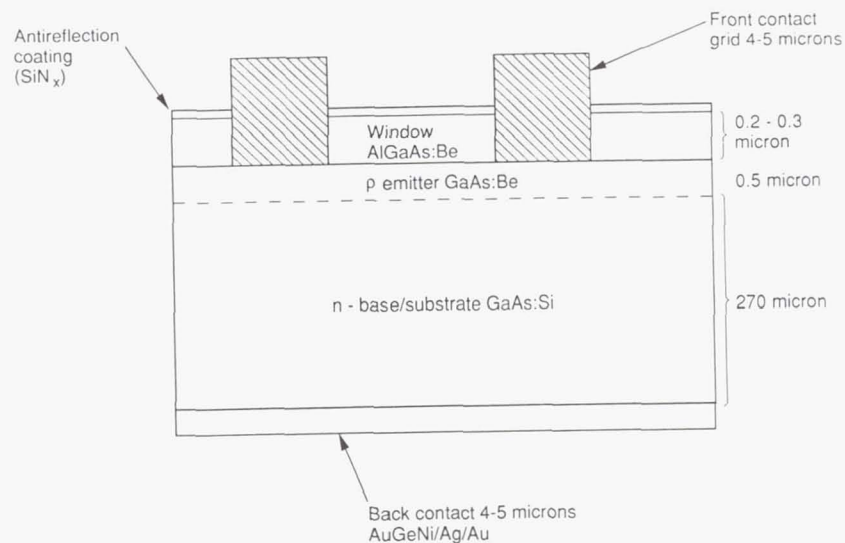


Fig 2 **The EEV IMPL GaAs solar cell**

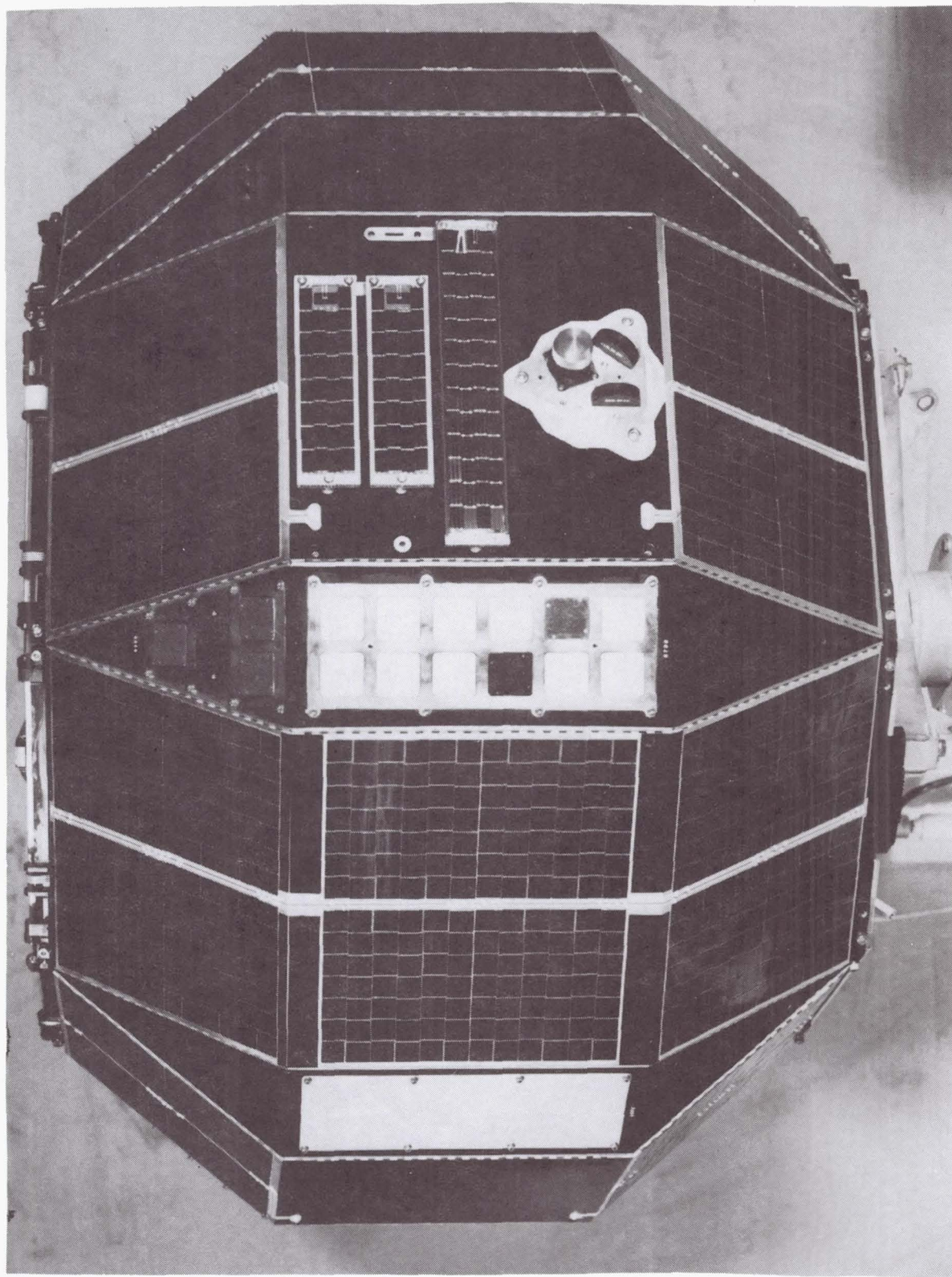


Fig 1 The UK-3 satellite - Prospero

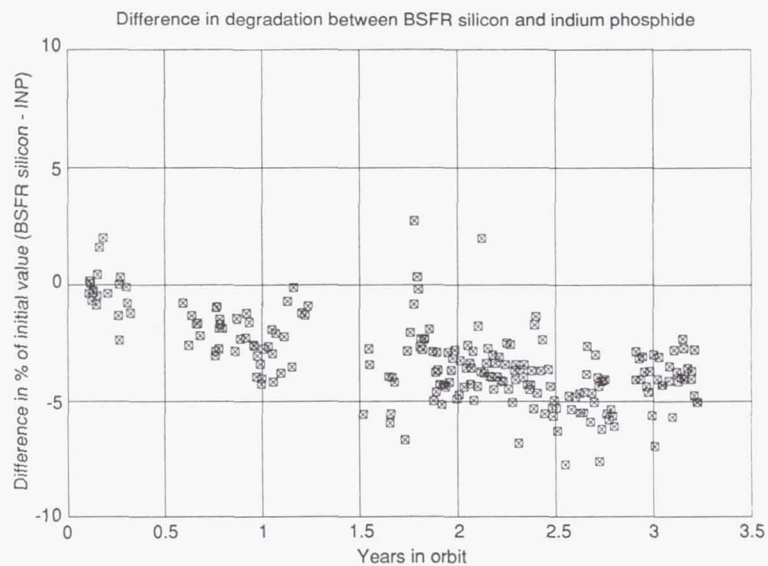


Fig 3 Lips III solar cell experiment

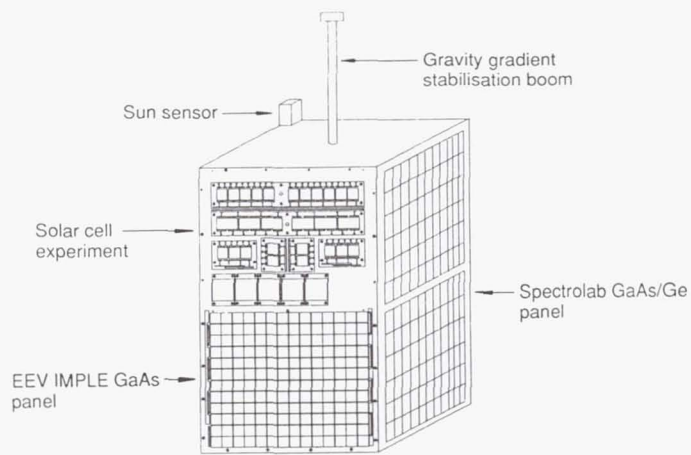


Fig 4 UoSAT - 5

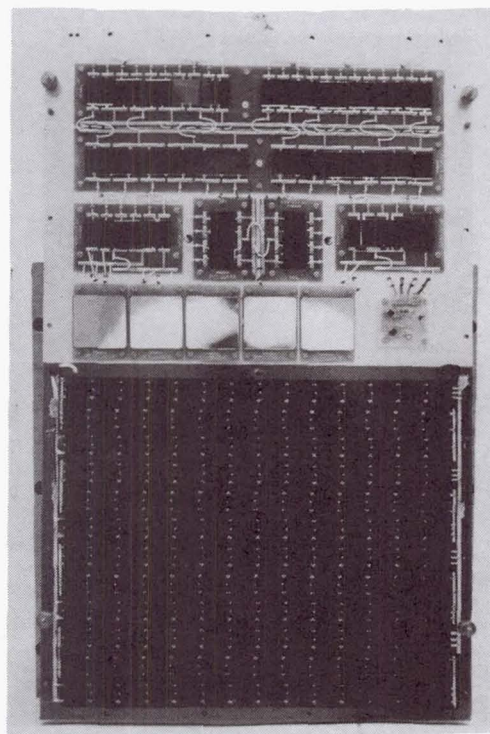


Fig 5 UoSAT-5 solar cell experiment - (Ref.33)

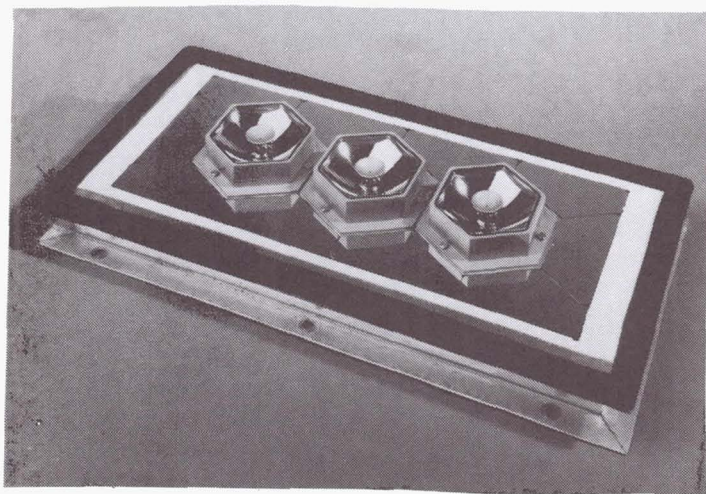


Fig 6 The Eureka concentrator experiment

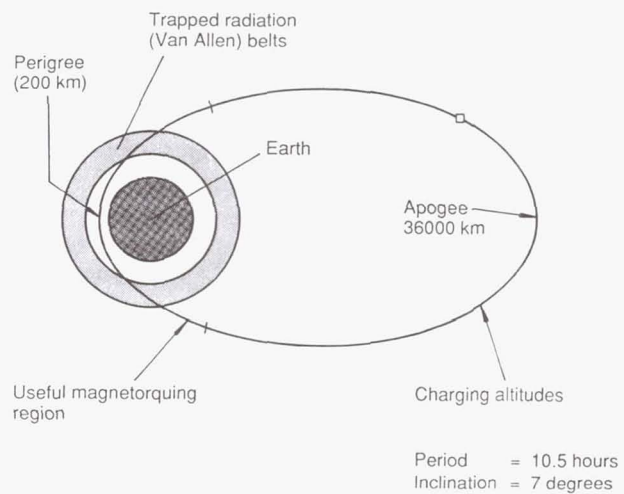


Fig 8 STRV - 1 geostationary transfer orbit

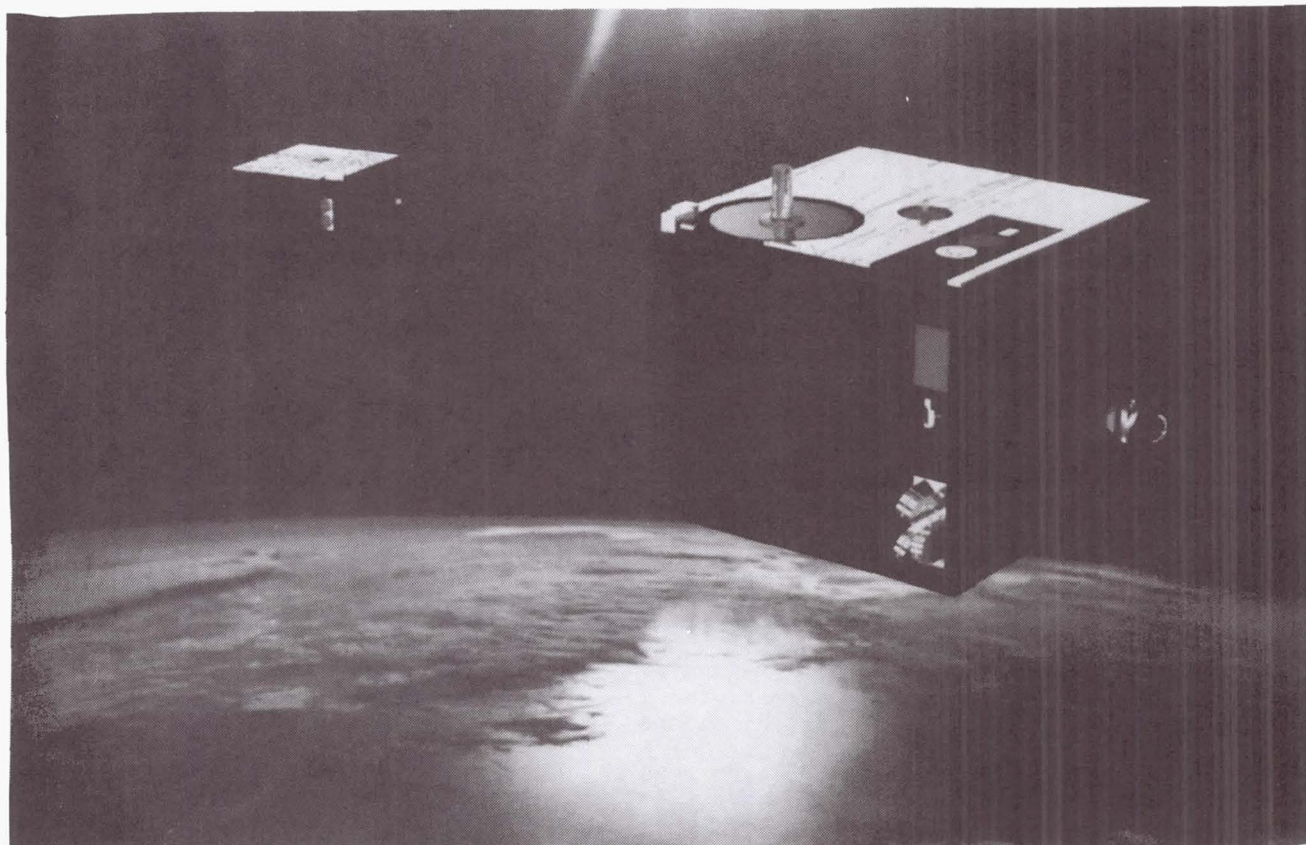


Fig 7 STRV - 1 satellites

NASDA Activities in Space Solar Power System Research, Development and Applications

Sumio MATSUDA, Yasunari YAMAMOTO, Masato UESUGI
TSUKUBA SPACE CENTER, NASDA¹

Abstract

This paper describes NASDA activities in solar cell research, development and applications. First, we review current technologies for space solar cells such as Si, GaAs and InP. Second, we discuss future space solar cell technologies intended to be used on satellites of 21st century. Next, we show the flight data of solar cell monitor on ETS-V. Finally, we propose to establish the universal space solar cell calibration system.

1. Introduction

Solar cells have been a dependable power source for use in space for the last 30 years, and have served as the primary power source for satellites. The performance of Si solar cells has increased from 10% air mass zero(AM0) solar energy conversion efficiency in the early 1960s to almost 15% on today's spacecraft. However, as larger satellites with greater output and longer life are developed, their power supplies will strongly require solar cells with higher efficiency, lighter weight, and longer life to increase the specific power (W/Kg) and the areal power density(W/m²) of the solar array. Reduction of solar array mass is especially important for high earth altitude or geosynchronous orbit missions due to launch vehicle cost and a restricted launch vehicle capability to boost payloads into high earth orbit. In addition, a reduction in solar array mass and/or increase in specific power enables a greater allocation for more sensors, transponders, or additional payload on existing spacecraft. Furthermore, higher areal power densities are important for low-altitude earth orbit due to the environmental drag on the surface of the solar array, causing altitude adjustments with an auxiliary reactor control gas thruster subsystem and decreasing the fuel supply and mission life.

Gallium Arsenide (GaAs) and Indium Phosphide (InP) solar cells have been expected to supplant Si solar cells because of their high efficiency and high radiation tolerance. GaAs solar cells were adopted for main solar arrays to satisfy the requirement Japanese domestic communications satellites(CS-3), which were successfully launched in 1988 and have been generating almost the expected power. Meanwhile InP solar cells are also being used as a photovoltaic power

source with output power of 10-20 watts on the lunar mission of the Japanese scientific satellite MUSES-A, which was launched in January 1990 by Institute of Space and Astronautical Science.

The photovoltaic element of the space energy conversion programs designed to provide the technology for efficiency improvement, mass and cost reduction, and operating life extension for solar cells and arrays. This paper describes the state of the technology of advanced solar cells for space applications.

2. Technology for Space Solar Cells

The status and trends in development of several kinds of solar cells for space use are shown in Table 1. Here, the status of production and technology for Si, GaAs, and InP solar cells, which are currently available for space use, are introduced.

2.1 Si Solar Cells

(1) Thin Si solar cells

Thin silicon solar cells have the advantages of lighter weight and higher radiation resistance than conventional thick (200μm) solar cells. Since the development of 50μm thin silicon solar cells in 1983, the thin solar cells have been used for Japanese satellite programs, ERS-1, ETS-VI and ADEOS of NASDA. (see Table 2)

(2) Improvement of thin solar cells

To meet the requirement of high efficiency from solar array side, the electrical performance of the thin solar cells was improved in 1990 by introducing fine gridlines forming method which used the photolithographic masks and lift off technique. The gridlines of the former cells were formed by evaporation through the metallic masks. The gridlines through metallic masks were minimum 20μm wide and 1mm spacing. The gridline penumbra originated from small gaps between metallic masks and silicon surfaces was

¹2-1-1 SENGEN, TSUKUBA-SHI IBARAKI-KEN 305 JAPAN

5 to 20 μ m wide and caused output current loss. The improved new cells showed about 6% higher output power than the former cells. The characteristics and electrical performance of the new cells are given in Table 3. The 4cmx6cm thin silicon solar cells were newly fabricated from the 4 inch silicon wafer process.

The qualification tests and characterization of the thin solar cells were performed according to NASDA specification, NASDA-QTS-1013 and they satisfied all test requirements.

The production of the improved solar cells (about 60000 2cmx4cm 100 μ m thick CIC's) started for ADEOS program in 1991.

Table 1 Status and trends in solar cells for space applications

Solar Cell		Current	Goal or trend
Si	In Production	13% to 15%	High power to weight ratio
	Efficiency		Low cost
	Size/Thickness	4x6cm/50 μ m	Large Area/Light Weight
	In development	17.5% efficiency (2x2cm)	High efficiency(20%)
GaAs	In production	18% to 20% efficiency	Light weight concentrator
	Size/Thickness	2x4cm/200 μ m	
InP	In pilot-production	16% to 17% (1x2cm) efficiency	Higher efficiency(20%) Low cost
GaAs on Si	In development	18% efficiency (2x2cm)	Higher efficiency Light weight

* Conversion Efficiency is for AM0

Table 2 Solar Cell Applications of NASDA Satellite

	ETS-V	CS-3a CS-3b	GMS-4	MOS-1b	BS-3a BS-3b	JERS-1	ETS-VI	GMS-5	ADEOS	COMETS
Launch Date	87.8.27	88.2.19 88.9.16	89.9.6	90.2.7	90.8.28 91.2.25	92.2.11	94 SUMMER	95 WINTER	96 WINTER	97 WINTER
Satellite Shape	Box	Cylindrical	Cylindrical	Box	Box	Box	Box	Cylindrical	Box	Box
Satellite Weight	550kg	550kg	325kg	740kg	550kg	1340kg	2000kg	345kg	3500kg	2000kg
Satellite Life	1.5y	7y	5y	2y	7y	2y	10y	5y	3y	3y
Satellite Power (EOL)	845W	628W	265W	540W	1482W	2053W	4100W	-	4500W	5400W
Solar Cell Type	Si BSFR	GaAs	Si BSFR	Si BSF	Si BSR	Si BSFR	Si BSFR	Si BSFR	Si BSFR	GaAs
Solar Cell Size	2cmx4cm	2cmx2cm	6.2cmx2.2cm ^{*1} 2cmx2cm	2cmx4cm	2cmx4cm	2cmx4cm	2cmx4cm	2.43cmx6.2cm	2cmx4cm	2cmx4cm
Solar Cell Thickness	280 μ m	280 μ m	200 μ m ^{*1} 280 μ m ^{*2}	280 μ m	200 μ m	50 μ m	50 μ m	200 μ m	100 μ m	200 μ m
Cover-glass	CMX150	CMS150	OCLI 150 μ m	CMS150	OCLI 150 μ m	AS100	AS50	OCLI 150 μ m	AS100	AS100

*1:main array

*2:charge array

The 4 inch diameter, CZ, (100) oriented, 200 μ m thick, chemically polished silicon wafers were etched to the target thickness in a hot sodium hydroxide solution. The fine gridlines on the surface were formed by the photolithography technique. The outline of fabrication process is shown below.

1. Thinning etch
2. Texturing etch
(formation of NRS)
3. Passivation of rear surface
4. p and n diffusion
5. Contact formation
6. A.R.C. formation
7. Cutting to 2cmx2cm

(2) Experimental Results

The electrical performance data of the solar cells are shown in Table 5. The 100 μ m thick solar cells with random pyramid surface showed the highest efficiency (17.5%) of all cells. The electrical parameters at the operating temperature were also calculated from the energy balance equation of the flat solar cell array considering the solar absorptance (α_s : measured values in Table 5) and the hemispherical emittance (ϵ_h : 0.80) of the solar cell and the hemispherical (ϵ_h : 0.80) of rear surface of the array substrate. The V-groove cells showed higher power at the operating temperature due to their low solar absorptance (0.77-0.79) than the other solar cells.

The spectral reflectance of the 50 μ m thick solar cell with three types of NRS is shown in Fig. 2. The V-groove cell showed the highest reflectance in the infrared spectrum (1100nm-2500nm) and gave the lowest solar absorptance (0.77). The inverted pyramid cell showed intermediate reflectance in the infrared spectrum. The random pyramid cell showed the lowest reflectance for whole wavelength range and generated the highest power of all the cells.

The random pyramid cells were irradiated by 1MeV electrons to 3×10^{15} e/cm². Degradation curves of maximum power of 50 μ m, 70 μ m and 100 μ m thick solar cells are shown in Fig. 3. After electron irradiation to more than 1×10^{14} e/cm², thinner cells showed higher Pmax similarly as the conventional BSFR cells with the whole area BSF layer and the back surface reflector (BSR) of aluminum thin layer and without the NRS and passivated rear surface. Degradation rates of the high efficiency solar cells were a little higher than those of the conventional BSFR cells, but absolute Pmax values after electron irradiation were fairly larger than those of the conventional BSFR cells.

From these data, we think that thin (50 μ m, 70 μ m and 100 μ m) silicon solar cells with nonreflective surface (NRS), passivated rear surface and locally diffused p⁺ BSF layer are hopeful candidates for space applications.

Table 5 Electrical performance of high efficiency thin silicon solar cells

Configuration of Solar Cell				Electrical Performance at 28°C					α_s	Performance at Top		
NRS	Resistivity (Ω cm)	Thickness (μ m)	BSF	Voc(mV)	Isc(mA)	Pmax(mW)	Fill Factor	Efficiency		Top (°C)	Pmax(mW) @ Top	Efficiency @ Top
RANDOM	10	50	localized	633.0	188.4	93.0	0.790	17.2%	0.85	45.2	86.5	16.0%
		70		629.0	191.6	93.7	0.794	17.3%	0.85	45.6	87.0	16.1%
		100		628.0	193.1	94.6	0.785	17.5%	0.86	46.8	87.5	16.2%
INVERTED	10	50	localized	641.0	180.7	90.2	0.787	16.7%	0.80	39.2	86.1	15.9%
		70		630.0	186.4	91.6	0.791	16.9%	0.82	41.8	86.5	16.0%
		100		632.0	188.4	93.2	0.784	17.2%	0.83	42.8	87.6	16.2%
V-GROOVE	10	50	localized	634.0	181.8	89.7	0.795	16.6%	0.77	36.2	86.8	16.0%
		70		630.0	185.8	91.3	0.790	16.9%	0.78	37.0	88.1	16.3%
		100		629.0	186.3	91.3	0.784	16.9%	0.79	37.4	87.8	16.2%
without NRS	10	50	whole	605.0	160.0	76.5	0.790	14.1%	0.75	36.3	73.9	13.7%
		70		605.0	163.0	78.0	0.791	14.4%	0.75	35.9	75.6	14.0%
		100		605.0	166.0	79.5	0.792	14.7%	0.76	36.9	76.7	14.2%

Note. Cell Dimensions : 20 × 20 mm

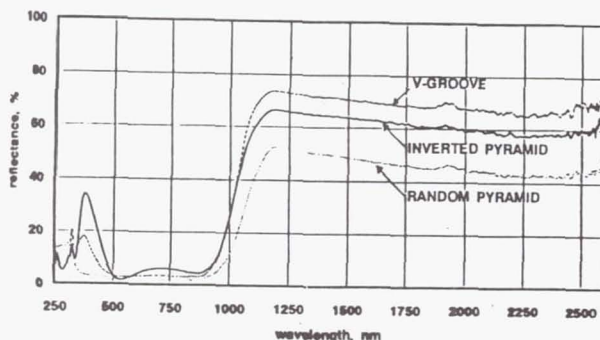


Fig. 2 Spectral reflectance of solar cells

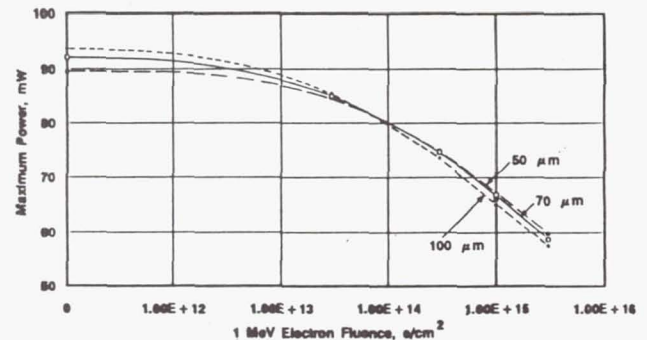


Fig. 3 Degradation curves of Pmax of the 50 μ m, 70 μ m and 100 μ m thick random pyramid cells.

Table 3 Cell Electrical Parameter

Solar Cell Type	200 μ m BSR (2 Ω cm)	200 μ m BSR (10 Ω cm)	100 μ m BSFR	70 μ m BSFR	50 μ m BSFR
Open Circuit Voltage(V_{oc}), mV	592	548	610	610	610
Short Circuit Current(J_{sc}), mA/cm ²	40.0	40.0	42.2	41.4	40.7
Cell Load Voltage(V_L), mV	490	450	500	500	500
Cell Load Current(J_L), mA/ cm ²	38.1	38.1	40.2	39.5	38.7
Cell Power(P), mW/cm ²	18.7	17.1	20.2	19.8	19.4
Efficiency(η), %	13.8	12.7	14.9	14.6	14.3

Note : Measuring Conditions ; Cell Temperature 28°C,
AM0 135.3mW/cm²

2.2 GaAs solar cells

GaAs solar cells have been expected to serve as future space power sources because of high efficiency, high radiation tolerance, and ability to operate at high temperature. High efficiency GaAs solar cells with an average efficiency of 18.9% at AM0 have been obtained by liquid phase epitaxy (LPE), and AM0 efficiency as high as 22.5% has been reported by using metalorganic chemical vapor deposition (MOCVD). As mentioned above, GaAs solar cells were adopted as primary power sources for Japanese communications satellites, which were successfully launched in 1988, and the cells have been generating nearly the expected power. The flight data of CS-3 have proved that radiation damage to a GaAs solar cell is less than that of a Si solar cell (thickness is over 200 μ m). The production of the improved GaAs solar cells (about 40,800 2cmx4cm 200 μ m thick) started for COMETS program in 1992. This is thought to stem from differences in the optical-absorption and photocarrier generation mechanism of GaAs and Si: in GaAs the diffusion length is sufficiently large compared with the thickness of the region where most of the photo-carriers are produced, and the junction depth of 0.5 \pm 0.1 μ m is shallow, so damage is small and degradation of the diffusion length is slight, resulting in little drop in the efficiency. While the diffusion length in silicon is comparable with the thickness of the active region, the efficiency decreases with the decrease of diffusion length.

GaAs solar cells with 18% to 20% efficiency, 2cmx4cm in size and 200 μ m in thickness, have been fully qualified for space use and are being mass-produced. This cell has the AlGaAs/GaAs heteroface structure, which

consists of p-AlGaAs/p-GaAs/n-GaAs buffer layer/n-GaAs substrate. This type of heteroface AlGaAs/GaAs solar cell can be produced by the liquid phase epitaxy process named VSTC-LPE. CS-3 solar array is covered with 36,671 2cmx2cm GaAs solar cells.

2.3 InP solar cells

Recently, much effort has been devoted to the study of InP solar cells for space applications owing to the radiation resistance and annealing properties of InP. The radiation resistance of InP solar cells are superior to that of GaAs or Si solar cells under 1 MeV electron and 10 MeV proton irradiation. Furthermore, the degradation can be removed by annealing at a relatively low temperature.

As mentioned above, 1300 pieces of 2cmx1cm InP solar cells with AM0 efficiency of 16% to 17% were used as the power source of a satellite for a lunar mission. These cells have a n/p homojunction of InP, which was formed by diffusing sulfur into p-type substrates.

One obstacle to the production of InP solar cells is the high cost of the InP substrate. For this reason much effort has been devoted to work on heteroepitaxy such as InP-on-Si and to the CLEFT (Cleavage of Lateral Epitaxial Films for Transfer) process for removal and recovery of the substrate.

3. Future space solar cell technology

Solar arrays are expected to become larger in area, lighter in weight, and longer-lived. In addition, the cost/watt of such solar arrays needs to be decreased from the present level. Major advances in the performance and fabrication technology for solar cells

must be made in order to meet the above broad system needs. The main areas of activity for solar cells for space applications in the near future fall into the following three categories:

3.1 Si high efficiency solar cells

The first research program to improve thin silicon solar cell performance (target efficiency: 17% on 100 μ m cell) started in November 1990. Main aim of this program was a basic research of high efficiency thin solar cells for future spacecraft. After completion of this program in April of 1992, the second research program (target efficiency: 18% on 100 μ m cell) started in June of this year. The

qualification test program of the high efficiency thin silicon solar cells for space application will be performed in the next fiscal year.

The basic design of the solar cell with nonreflective surface (NRS), passivated rear surface and locally P⁺ diffused BSF layer was confirmed to be very effective for improving characteristics of the space solar cells.

(1) Cell design and process

Three types of NRS (normal pyramid, inverted pyramid and V-groove) and the above basic design as shown in Figure 1. The main features of these thin solar cells are given in Table 4.

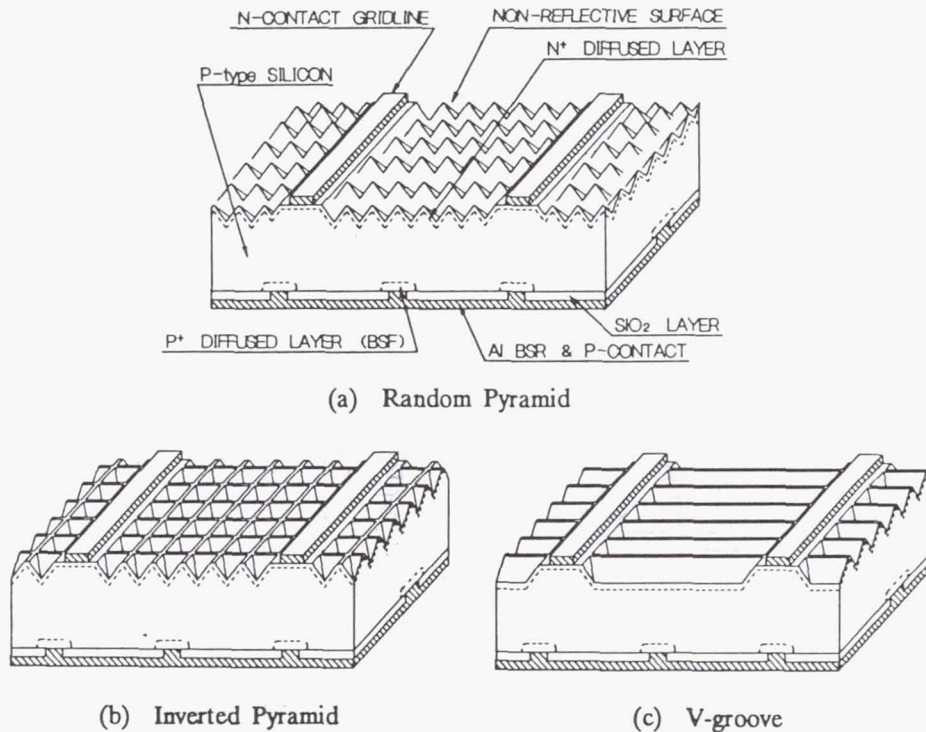


Figure 1 Solar cell structure with various NRS.

Table 4 Main features of high efficiency thin silicon solar cells

Item	Feature
Cell dimension	- 2cmx2cm
Cell thickness	- 50 μ m, 70 μ m and 100 μ m
Substrate	- CZ, P type, 10 Ω cm
Surface	- NRS (normal pyramid, inverted pyramid and V-groove)
PN junction	- Shallowly diffused with phosphorous ($X_j=0.15\mu$ m)
Rear P ⁺ layer	- Locally diffused with boron
Passivation	- Rear surface passivation by SiO ₂
N contact	- Ti-Pd-Ag
P contact	- Al-Ti-Pd-Ag
A.R. Coating	- Dual layer coating

In addition to the high efficiency, the solar cell structure which enables prevention of an accident caused by a reverse bias has been proposed. When a part of solar cell array is shadowed, shadowed submodule are reverse biased. If the reverse bias voltage is higher than the breakdown reverse bias voltage is higher than the breakdown voltage of the cell, breakdown of cell submodule occurs and may results in permanent failure of the module. "The solar cell with bypass diode operation" has a structure in which a breakdown due to the reverse bias voltage is less liable to occur. Fig. 4 shows an equivalent circuit of this cell. The cell is connected in parallel with a diode which has plural small P-N junctions. This can prevent a permanent failure of the solar cell. Fig. 5 shows one of the structures of this ideas.

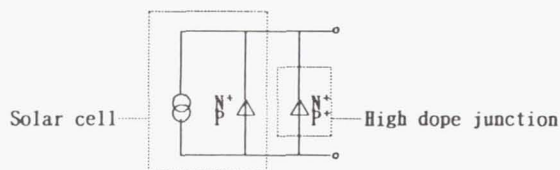


Fig. 4 Equivalent circuit of the solar cell with bypass diode operation

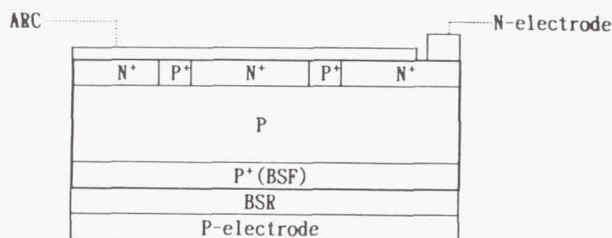


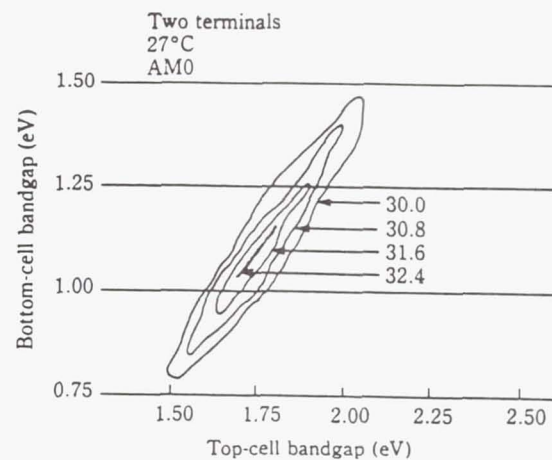
Fig. 5 One of the structures of the solar cell with bypass diode operation

3.2 Thin film GaAs solar cells

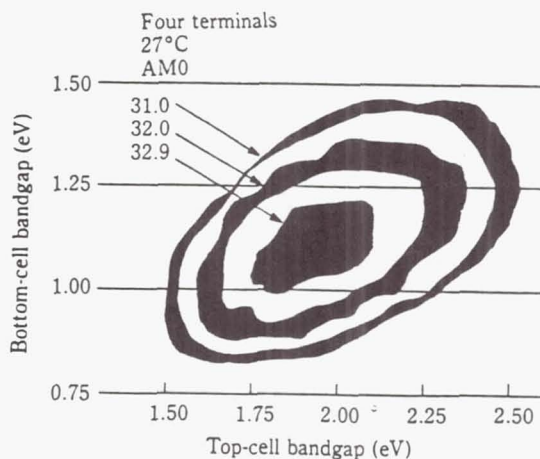
Since the optical absorption coefficient of GaAs is large, GaAs solar cells are generally able to minimize material cost without degrading efficiency. They are on-going either by the CLEFT process or by fabricating GaAs solar cells on substrate such as silicon. The GaAs-on-Si solar cells are expected to provide low weight, low cost and large area, and an efficiency rate of 18.3% has been obtained by combining in-situ thermal cycling and strained superlattices in the laboratory. However, there are problems with lattice mismatch and the thermal expansion coefficient between GaAs and Si. Emphasis should be placed on developing techniques for assembling thin GaAs for the CLEFT process and the crystal growth technique of high quality GaAs on Si substrate for the GaAs-on-Si solar cell.

3.3 Multi-junction solar cells

Substantial efficiency increases are expected for two-cell tandem structures in comparison with single-junction cells. Figure 6 shows the efficiency contour map of a two-junction tandem solar cell in a two-terminal and a four-terminal configuration. The maximum theoretical efficiency is 32.4% at AM0 for a two-terminal and 32.9% at AM0 for a four-terminal. The top cell should have an energy gap of 1.7 to 1.8 eV and the bottom cell should have a gap of about 1.0 to 1.1 eV. The top cell could be fabricated from $\text{Al}_{1-x}\text{Ga}_x\text{As}$ or $\text{Ga}_{1-x}\text{P}_x\text{As}$. The bottom cell of a Si cell will be utilized for economic reasons.



(a) AMO iso-efficiency plots for the two-cell, two-terminal tandem structure at 27°C and one sun (J.C.C. Fan et al.)



(b) AMO iso-efficiency plots for the two-cell, four-terminal tandem structure at 27°C and one sun (J.C.C. Fan et al.)

Fig. 6

A two-terminal cell requires current matching between the top and bottom cells for optimum performance. Anything which causes current mismatch,

such as radiation damage, will lead quickly to degraded total performance. In a four-terminal configuration two cells are electrically independent of each other, so that the effect will not be compounded as rapidly. Complexity will increase at the array level, however, because essentially two power conditioning circuits must be employed. The presumption is that the increased performance will be worth the extra effort.

4. Solar Cell Monitor on ETS-V

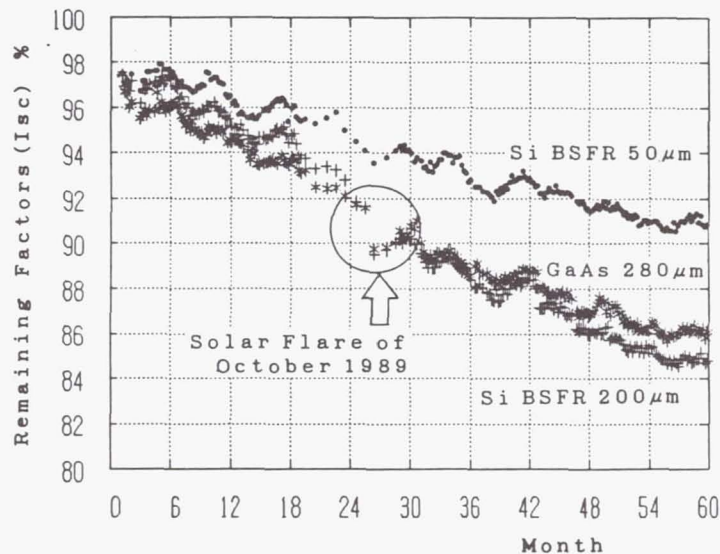
NASDA had launched Engineering Test Satellite-V (ETS-V) on 27 August 1987 and had put it into a geostationary orbit at longitude 150 degrees east. This satellite has the technical Data Acquisition Equipment (TEDA) to obtain technical data for developing satellites. The TEDA consists of 8 monitors and one of them is Solar Cell Monitor(SCM).

In the sensor parts of SCM, 24 solar cells are attached to Aluminum panels.

These cells differ in the cell thickness, cell structure, growth method of epitaxial layer, cover glass thickness and cell material (GaAs and Si) so as to investigate the effects of these parameters. In SCM the generated currents and voltages are measured on ten load conditions for each cell. Fig.7 shows the flight data of remarkable three cells which are GaAs LPE cell, Si BSFR 200 μ m and Si BSFR 50 μ m after correction. Observation data must be corrected because of following reasons.

- (1) incident solar power correction
- (2) angle correction
- (3) temperature correction

On 27 August 1992 (5 years after launched) the remaining factors of GaAs, Si BSFR 200 μ m and Si BSFR 50 μ m are about 86%, 85% and 91% respectively. These data also show degradation by solar flare of 19 October 1989.



(The day of origin = August 27, 1987)

Fig.7 The Flight Data of Remarkable Three Cells

5. Universal Space Solar Cell Calibration System

(1) Background

From the design of the space solar cell to the assemble of the array, it is necessary to high accuracy measurement of the solar cell performance. Small errors in measuring solar cell performance and its variation due to the effects of temperature and radiation damage can be significant to a solar array designer or manufacturer. Poor estimates of solar cell performance can lead to incorrect power estimates and as a result errors in optimizing costs and mass.

When testing a large variety of

space solar cells of different types and from various manufacturers of solar cell, it is necessary to choose with some care the standard against which the cell be calibrated in AMO condition.

The solar cells can be tested on the ground, in a balloon, in a high altitude aircraft or on board of a free-flying satellite. The satellite calibration is more complete than any of the other, suffering only one disadvantage; the test article cannot be recovered.

We are now thinking about the possibility to establish a standard universal calibration system of space solar cells, the outdoor calibration method of reference solar cells (Global

Sunlight Method) for terrestrial application, and the measurement method of solar modules with the calibrated reference solar cells by developing stable solar simulators and precise spectro-radiometers.

We suggest the following items to be carried out this year as the first step:

To identify the difference between each calibration system of NASA/JPL, NASA/Lewis, CNES, and NASDA, we will provide some Si solar cells to each facility with electrical data obtained by the our solar simulator. The cells will be calibrated by each facility using their usual calibration method. The calibrated values will be compared with each other quantitatively and the difference will be discussed to establish a good standard method next year.

(2) Proposed Plan of Round Robin Calibration

The purpose of this proposed plan which is to compare "the calibrated value by Indoor Calibration Method" with "the calibrated value by Balloon Flight or Aircraft Calibration". By using the calibration results, we would like to confirm which AMO condition (WMO, Johnson, Neckel & Labs, Thekaekara and so on) is preferable.

We compare the results of Indoor Calibration Method (Solar Simulator Method) with Balloon Flight & Aircraft Calibration Method respective which AMO (WMO, Johnson, Neckel & Labs, Thekaekara and so on) is preferable by the Indoor Calibration Method. We send back the results of comparison to each calibration facilities.

6. Conclusion

We can reach that efficiency of Si solar cells become 17-18%. Next target is a large area solar cell such as 8cmx8cm or 10cmx10cm, on condition that thickness is less than 100 μ m. We will try that GaAs and InP solar cells are planned to thin film on Si or Ge on this century. Next, we will plan to carry TEDA on satellites of NASDA development. We will collect the flight data about space radiation environment and this data will be useful for satellite design. We would like to establish the universal space solar cell calibration system similar to ground solar cell calibration system. We believe 21st century is era of solar power system.

NASDA will continue to develop new solar cells for space applications in the future.

References

- [1] S.Yoshida and S.Matsuda, Optoelectronics Devices and Technologies (1990) 285
- [2] S.Yoshida, N.Imura, M.Goto, and S.Matsuda, Proc.4th European Symp. Photovoltaic Generators in Space (1984)65.
- [3] S.Matsuda, S.Yoshida, and A.Kawakami, Proc.5th European Symp. Photovoltaic Generators in Space (1986)31.
- [4] M.Yamaguchi, C.Uemura, A.Yamamoto, and A.Shibukawa, Jpn.J.Appl. Phys.,23(1984)302.
- [5] L.Weinberg,C.K.Swartz,and R.E.Hart,Jr.,Proc.18th IEEE Photovoltaic Specialists Conf.(1985).
- [6] S.Yoshida, H.Matsumoto, M.Goto, M.Ohmura, N.Takata, H.Kurahata, S.Matsuda, and T.Okuno, Proc.21th IEEE Photovoltaic Specialists Conf.(1990),(to be published).
- [7] M.Yamaguchi, T.Hayashi, A.Ushirokawa, Y.Takahashi, M.Koubata, M.Hashimoto, and H.Okazaki, Proc.21th IEEE Photovoltaic Specialists Conf.(1990)
- [8] S.Yoshida, H.Matsumoto, K.Sato, S.Hokuyo, M.Ohkubo, and S.Matsuda, AIAA 12th International Satellite Syst. Conf.(1988)63.
- [9] S.Matsuda, H.Matsumoto, S.Hokuyo, and S.Yoshida, Proc.3rd Int'l. PVSEC Tokyo(1987)191.
- [10] S.Yoshida, H.Matsumoto, M.Okubo, and Y.Okawa, Proc. European Space Power Conf.(1989)623.
- [11] M.Yamaguchi, Proc.20th IEEE Photovoltaic Specialists Conf.(1988)880.
- [12] H.Okazaki, T.Takamoto, H.Takamura, T.Kamei, M.Ura, A.Yamamoto, and M.Yamaguchi, Proc.20th IEEE Photovoltaic Specialists Conf.(1988)886.
- [13] J.C.C.Fan, Proc.15th IEEE Photovoltaic Specialists Conf.(1981)666.
- [14] H.Ohmachi, T.Ohhara, and Y.Kadota, Proc.21th IEEE Photovoltaic Specialists Conf.(1990).
- [15] H.Okamoto, Y.Kadota, Y.Watanabe, Y.Fukuda, T.Ohhara, and Y.Ohmachi, Proc.20th IEEE Photovoltaic Specialists Conf.(1988)475.
- [16] J.C.C.Fan, B.Y.Tsaur, and B.J.Palm, Proc.15th IEEE Photovoltaic Specialists Conf.(1982)692.
- [17] S.Matsuda et al, Proceeding of the European Space Power Conference, (1991) 609
- [18] M.Uesugi et al, Proceeding of the 22nd IEEE Photovoltaic Specialists Conference, (1991)1521
- [19] T.Katsu et al, 18th International Symposium on Space Technology and Science e (ISTS), Kagoshima, Japan, May 18, 1992
- [20] H.Washio et al, 11th European Solar Energy Conference, Oct.13, 1992

SUMMARY

WORKSHOP ON HETEROEPITAXIAL InP SOLAR CELLS

Cochairmen

I.Weinberg

NASA Lewis Research Center
Cleveland, Ohio 44135

And

R.W.Walters

Naval Research Laboratory
Washington, DC 20375

The workshop considered the following topics.

JUSTIFICATION FOR WORK IN THIS AREA

RESULTS TO DATE

DESIREABLE SUBSTRATE CHARACTERISTICS

REALISTICALLY ACHIEVABLE EFFICIENCIES

THE DISLOCATION PROBLEM

PEELED FILMS

FUTURE RESEARCH POSSIBILITIES

A summary of the workshop discussions follows.

Justification: In a generic sense, the justification for any sort of InP solar cell research applies here; i.e. to take advantage of the inherently high radiation resistance and efficiency of InP solar cells. To be more specific; the approach is justified by its potential for significant cost reduction and the availability of greatly increased cell area afforded by substrates such as Si and Ge. The use of substrates, such as the latter two, would result in increased ruggedness, ease of handling and improved manufacturability. The use of more rugged substrates would lead to a greatly increased capability for cell thinning leading to the desirable feature of reduced array weight.

Results to Date: The highest 1 sun AMO efficiency reported to date was 13.7%.^{1,2} This was achieved with a GaAs substrate and $Ga_xIn_{1-x}As$ transition layers. The latter is lattice matched to InP

when $x=0.47$. A similar cell, with an anti-obscuration cell cover achieved an efficiency of 19.9% under 71.8X AMO concentration at 25 °C.³ Considering multibandgap cells, A three terminal arrangement with an InP top cell and $\text{Ga}_{0.47}\text{In}_{0.53}\text{As}$ bottom cell achieved a combined efficiency of 31.8% at 50X AM1.5 and $T=50$ °C.⁴ In addition, a two terminal multibandgap device with InP top and GaInAsP bottom cell, yielded an AM1.5 (global) efficiency of 14.8%.⁵

Substrate Characteristics: Low cost, light weight, ruggedness and availability in large area were deemed to be desirable substrate characteristics. Ideally, all of these characteristics should be combined with close matching of lattice constant and thermal expansion coefficient to InP. Since the cell is processed at a relatively high temperature, it is also desirable that the substrate thermal expansion coefficient be such that the InP would cool down in compression.

Efficiencies: In theory, AMO efficiencies over 21% are predicted if dislocation densities below $10^5/\text{cm}^2$ are achievable together with surface recombination velocities of 10^5 cm/sec or lower. However, it was concluded that 18% is a realistic near term goal with dislocation densities on the order of $10^6/\text{cm}^2$. A far term goal of 20% appears achievable.

Dislocations: The workshop participants considered methods to reduce the harmful effects of dislocations on cell performance. At present, $3 \times 10^7/\text{cm}^2$ is the lowest dislocation density reported for a heteroepitaxial InP cell.^{1,2} Obviously, there is room for improvement in this area. Dislocation passivation by hydrogen, which has in the past worked for Si, is a technique which deserves close attention for InP. It was also recommended that more effort be expended on the use of lattice matching transition layers. Aside from these two techniques, there is a scarcity of ideas on how to attack this difficult problem. There is ample room here for creative material science.

Peeled Films: The cell processing would entail epitaxial thin film deposition on an ultra thin release layer deposited on InP. A selective etch separates cell from substrate. The completed cell can be used in a stand alone mode with a glass superstrate or attached to a heterogeneous substrate such as Si. Advantages are decreased dislocation density and reduced cost through substrate reuse. Difficulty in handling is a principal disadvantage.

Future Research Possibilities: It is surprising that no results have been reported using Ge as a substrate. From the viewpoint of ruggedness, price and availability in large areas, it is preferable to GaAs. In addition, when compared to Si, it has the advantages of a much closer match, to InP, of lattice constant and thermal expansion coefficient. Use of a buffer layer of ZnSe on Ge or Si was also suggested. With regard to choice of cell

configuration, one should bear in mind that Ge and Si are n-dopants in InP and GaAs. Hence, one should chose a configuration which avoids the creation of a performance limiting counterdiode. Aside from this caveat, the workshop expressed no preference for either the p/n or n/p configuration nor was any preference expressed for either planar, multibandgap or concentrator cells. With respect to a goal at which to aim for SRV's, 10^4 cm/sec is desireable. With respect to dislocations, $10^6/\text{cm}^2$ is a realistic goal, with $10^5/\text{cm}^2$ desireable but extremely difficult to achieve. Finally for the EOL efficiency goal, it was decided that 16% would be desireable after 5 years in a mid-altitude orbit.

REFERENCES

1. M.W.Wanlass, U.S. Patent No. 4,963,949 (1990)
2. T.J.coutts, Proceedings 3rd Int'l Conf. on InP and Related Compounds, IEEE, Piscataway, N.J., 1991, p209
3. M.W.Wanlass, T.J.Coutts, J.S.Ward and K.A.Emery, Proc. 11th Space Photovoltaic Res. and Technology Conf., NASA Lewis Research Center, 1991, p27-1
4. M.W.Wanlass, T.J.Coutts, J.S.Ward, K.A.Emery, T.Gessert and C.R.Osterwald, Proc. 22nd IEEE Photovoltaic Spec. Conf., IEEE, Piscataway, N.J. 1991, p38
5. C.C.Shen Ibid p381
6. R.K.Jain and D.J.Flood, Proc. 22nd IEEE Photovoltaic Spec. Conf., IEEE Piscataway, N.J., 1991, p250

THIN FILM SOLAR CELL WORKSHOP

Joe Armstrong[†] and Frank Jeffrey[‡]
†Martin Marietta
‡Iowa Thin Film technologies

The following is a summation of responses to questions posed to the thin-film workshop and the ensuing discussion. Participants in the workshop included PV manufacturers (both thin film and crystalline), cell performance investigators, and consumers (spacecraft designers, program managers).

(1) Will Amorphous Silicon (a-Si) Ever Be Stable?

Maybe. In the worst-case scenario, long term efficiency will stabilize 10% below annealed efficiency. But the more relevant question is: what will be the end of life (EOL) efficiency for a typical mission? Presently, the highest stabilized efficiency for a 1 ft² module is 8.5%. Based on studies from JPL and Wayne State, combination of radiation created defects and annealing at operating temperature will cause typical EOL efficiencies slightly lower than this. An end of life array efficiency of 8% might be expected with current a-Si technology.

(2) What is Required to Establish Use of Thin-Film Cells in Space?

As is the case with any new photovoltaic technology, a full battery of standard space qualification testing on a given cell design must be conducted. In addition, flexible thin-film devices must also be subjected to extensive mechanical and thermal cycling testing. Ultimately, it is important that spacecraft designers be confident in the thin-film technologies. Thus, flight experience must be gained to establish a heritage with these devices before serious consideration is given to thin-film solar cells and modules.

However, other considerations must be given to thin-film technologies. Unlike conventional crystalline devices, thin-film PV technologies are strongly linked to an accompanying array design to utilize their properties fully. This is particularly the case with flexible devices which usually are linked with novel array designs. For this reason, it may be necessary to qualify the thin-film PV technology with an associated array design.

Finally, as was the case with the introduction of gallium-arsenide (GaAs), use of thin-film devices may not occur until a given application absolutely requires it due to its combination of low installed cost, high specific power, and improved radiation resistance when compared to conventional crystalline technology.

(3) What Thin-Film Cells Can Be Put on Lightweight Substrates? Key Technical Barriers? Status?

All of the thin-film cells, including a-Si, copper-indium-diselenide (CIS), and cadmium-telluride (CdTe) can be deposited onto lightweight substrates. Selection of substrates for most of the devices is limited by processing temperature and processing environments which may damage the substrate. Furthermore, some surface texture may also be detrimental to device fabrication.

Amorphous silicon has been demonstrated on both metal foils and polyimide substrates. Fully-integrated, large-area modules have been demonstrated on polyimides. CIS solar cells have been manufactured onto metal foils (aluminum, titanium, molybdenum), while large-area modules have been demonstrated on glass substrates. Until recently, lightweight CdTe has not been manufactured for space applications because of its superstrate structure. Now, lightweight CdTe cells have been manufactured on polyimides.

(4) What are Realistic Cost Goals, Given Space Market Volume?

The general consensus is that thin-film PV can have significant impact on cost, particularly due to monolithic integration and its associated reduced installed labor and reporting cost. Some calculations indicate that a 1

ft² module can result in an 80% installed cost reduction, even on a limited space volume. It would be particularly helpful if a thin-film space PV program can "piggyback" onto an existing terrestrial program for a larger production volume.

A minimum order will be required to make it attractive for manufacturers to make the effort for a space-based device. Such an order may be on the order of \$10,000 to \$100,000, depending upon the type of qualification and the deviation from standard processing required.

(5) Potential Space Applications?

Because the devices exhibit the important qualities of high specific end-of-life power and low cost, they can be used in most applications. In particular, missions such as orbit transfer vehicles which dwell for a significant time in radiation-rich environments are ideally suited for thin-film PV. Furthermore, any surface-based (lunar, martian) power stations which require low mass will also be ideal for these technologies.

Quite possibly, the only missions for which thin-film PV might not apply are array area critical missions, such as low earth orbit where array drag is critical in station-keeping requirements. Attempts at array size reduction, at present, is inhibited by lower device efficiency, although technologies such as CdTe have been demonstrated at efficiencies above 16%.

(6) Are Tandem Thin-Film Cells Practical?

Tandem cells for a-Si are required for the 10% stability noted above. Because of the continuous in-line processing used for thin-film devices, the addition of another device is not as cost-prohibitive as compared to crystalline technologies.

CIS has been used in a tandem cell configuration as well, and it is possible to manufacture a CIS/CdTe tandem cell. As is the case with a-Si, it is possible to make a cost-effective process which can manufacture such devices.

(7) Are Space-Qualified Encapsulants Needed? Are They Available?

At present, data are not yet available on the requirements of thin-film device encapsulants. Furthermore, flexible devices cannot use conventional cover glass technology used with crystalline devices. Because polymers are affected by atomic oxygen and radiation, conventional thin-film encapsulants probably cannot be used for orbital use. Some fluoropolymer encapsulants may be usable on surface power missions.

(8) Is There a Required Minimum Efficiency?

Quite probably, this question is the most difficult to answer. Spacecraft designers in the workshop indicated that efficiencies comparable to silicon, which is most commonly used in space, would warrant immediate use of thin-film devices. However, the high specific power, low stowage volume, low cost, and radiation damage resistance may drive this efficiency requirement much lower than the typical 14.5% Si efficiency. An efficiency of 9% end-of-life with the crystalline thin-film technologies may be a guideline.

Workshop on Solar Electric Propulsion

Dean Marvin
Aerospace Corporation
El Segundo, California

David Bents
NASA Lewis Research Center
Cleveland Ohio

This workshop was well-attended, with over thirty participants. The meeting room was filled to capacity. Latecomers were forced to go across the hall and fetch extra chairs.

As the meeting opened, Dr. Marvin introduced himself and his co-chairperson (D.J. Bents) and presented some opening questions that Drs. Flood and Bailey had collected to challenge the group. Mr. Bents then asked the participants how many of them considered themselves to be photovoltaic technologists, and how many considered themselves to be SEP advocates. The technologists would be persons basically interested in learning more about SEP and application of their technology to electric propulsion. Advocates would be those who not only were already familiar with SEP, but also of the strong opinion that it is a useful concept, with merit in being considered for upcoming missions. To the definition of Technologist, approximately twenty people raised their hands. To the definition of Advocate, 6 people raised their hands.

Dr. Marvin then delivered a few advocacy viewgraphs about the advantages of SEP over chemical propulsion for orbit-raising. This presentation culminated in a lengthy discussion of the ELITE SEP flight experiment, an electric propulsion technology demonstration program executed by the Air Force Phillips Lab in Albuquerque. During the discussion, which was sparked with spirited interactions from several members of the group, the technical objectives of this program and details of the anticipated flight experiments were presented to the participants as an example of the issues pertinent to SEP solar array development.

The purpose of ELITE is to demonstrate operation of solar array powered electric thrusters for raising spacecraft from parking orbit to higher altitudes, leading to definition of an operational SEP OTV for Air Force missions. According to Dr. Marvin, many of the problems or potential problems that may be associated with SEP are not well understood nor clearly identified, and system level phenomena such as interaction of thruster plume with the solar arrays cannot be simulated in a ground test. Therefore, an end-to-end system flight test is required to demonstrate solar electric propulsion.

The ELITE project is being carried out on a cost-share basis with TRW, who will provide the spacecraft bus. The Air Force will provide a Titan II launch vehicle and is procuring the electric thruster system (ammonia arcjet is baselined) and a solar array, through an RFP due to be released in November. An array of approximately 10 kWe is required, with scalability to larger sizes as would be used on an operational SEP OTV. The anticipated launch date is the end of FY1996. ELITE will be launched into a LEO parking orbit, then spiral to a final altitude of 2150 nmi. Various on-orbit maneuvers, including repositioning and orbital plane changes, will be demonstrated during the test. The maneuvers are an important application of EP to military space missions, according to Air Force Space Command. When final orbit is reached, the thrusters will be turned off and the vehicle will remain there until it fails due to Van Allen radiation. There is also the option of a thruster restart demonstration following a radiation exposure period equivalent to LEO to GEO transfer. Since the ELITE spacecraft would have a large amount of electrical power available at end of its mission to service experimental packages, the program office is actively seeking outside experiments for spacecraft payloads.

As Dr. Marvin finished his presentation, some discussion arose concerning the solar array for ELITE. Due to the spacecraft's destination, an opportunity for definitive degradation tests of the various competing space cell types has been presented. Should ELITE be considered mainly a demonstration of electric propulsion or could it also be considered an experiment for solar arrays in a severe radiation environment? Dr. Marvin responded that spacecraft bus requirements, integration and packaging concerns would most likely drive array selection to a single array technology despite the desirability of creating a solar cell testbed that demonstrates several technologies.

Discussion then turned to cell and array design. Which approach is more favorable for operation in a high natural radiation environment -- concentrator PV arrays with their inherent capability for shielding and temperature control, or thin planar arrays using the newer, more radiation-resistant materials? One of the participants then asked whether single concentrator arrays should be considered. Others replied that the single versus multi-concentrator PV array issue had been considered years ago in previous (mainly terrestrial) array development programs. Multiconcentrator designs had proven to be superior in all cases considered. An example was cited from a DoE/Sandia program in the early 80's where the experience with large single concentrators had been singularly disappointing.

A question was then raised about the Topaz flight experiment sponsored by SDIO. Mention of Topaz sparked a lively discussion, since this proposed flight demonstration would use a Russian space reactor to power an electric thruster equipped spacecraft from a medium low (nuclear safe) orbit to higher altitudes. Since this project also anticipates a 1996 launch date, it appears to compete with the ELITE program. Does demonstration of nuclear electric propulsion (such as Topaz flight experiment) support, or undermine a solar electric propulsion demonstration for the same mission?

Since the competitive potential of NEP versus SEP orbit raising could not be easily resolved in a photovoltaics conference, discussion turned back to the solar array. One stated objective of ELITE is scalability of the 10 kWe SEP flight experiment to a larger orbital tug that would be competitive with the chemical upper stages presently in use. However, packaging of larger array that is required for a SEP upper stage is a potential show-stopper. To be competitive with existing chemical propulsion upper stages, the deployed array would have to provide tens of kWe, but when stowed it would have to fit inside the shroud of a launch vehicle that is considerably smaller than the original one (that carried a chemical upper stage) it replaces. Several of the participants voiced the opinion that a 30 kWe array could not be made to fit inside the limited payload shroud of smaller launch vehicles such as a Delta.

Discussion's focus on ELITE finally ended when it was pointed out that there won't be much influence on the flight experiment since the array RFP for ELITE is already presently in final preparation and the workshop discussions, which may be of some benefit to potential competitors, comes too late to influence the RFP itself. It will be up to the government's proposal team to determine the level of technology and programmatic risk that is acceptable when these proposals are evaluated.

In the closing minutes of the workshop, one last question on the agenda was discussed. Are there any missions where EP offers such major benefits that the arguments in favor of EP over chemical thrusters are compelling? Most of the participants agreed that EP would look more attractive for higher delta V missions such as interplanetary flight than for orbit-raising. As an example, a recent study that considered sending a 200 kg scientific payload to the asteroid

Anteros was mentioned. If a chemical upper stage was used to fly this satellite, a Delta launch vehicle would be required. If an SEP upper stage was available, however, the mission could be launched on a Taurus rocket instead. For this mission, the trip times were nearly identical for both upper stages. Unfortunately, nearly all of the marketplace for launch and boost stage propulsion appears to be in earth orbit raising. For earth orbit raising missions, the increased trip time associated with EP is not considered acceptable from an operational standpoint. The bottom line is that time, in terms of the infrastructure and support personnel required to navigate the satellite to its final destination, is money. Therefore the dilemma: how can the perceived operational disadvantage of SEP compared to a chemical upper stage (trip time of weeks rather than hours from parking to operation orbit) be ameliorated or reduced? The discussion highlighted the reluctance of mission users to try new technology unless there is a major tangible benefit.

WORKSHOP SUMMARY NEW SILICON CELLS

A. Meulenberg
COMSAT Laboratories
Clarksburg, MD 20871
P.A. Iles
Applied Solar Energy Corporation
City of Industry, CA 91749-1212

This report summarizes the workshop on new silicon cells held during SPRAT XII. A smaller than average group attended this workshop reflecting the reduction in research dollars available to this portion of the photovoltaics community. Despite the maturity of the silicon technology, a core of the group maintained an excitement about new developments and potential opportunities. The group addressed both the implications and the applications of recent developments.

LIGHT TRAPPING AND ULTRATHIN SILICON CELLS

Discussion of these two topics is combined because of their potential interaction. Benefits from ultrathin silicon cells include lightweight, high V_{oc} (for $L_n \gg W_B$), and potentially higher end-of-life performance when exposed to radiation. To achieve these benefits, back-surface fields, back-surface reflectors, and light trapping are required. The problems associated with these cells are difficulty in fabrication, handling, and assembly; radiation sensitivity of V_{oc} ; and high costs associated with production and the techniques required to obtain and maintain high cell efficiencies.

Light trapping is a particularly nice concept to couple with ultrathin cells. First-order light trapping (e.g., nonreflective surfaces, antireflective coatings, and reflective back contacts) are already incorporated into cells in a cost-effective manner. Its effectiveness may increase with decreasing cell thickness; but below a certain thickness, the difficulty in its implementation may become prohibitive. To compound the problem, many of the techniques for light trapping and fabricating ultra-thin cells are incompatible. Furthermore, cost-containment techniques generally destroy the very benefits sought in both light trapping and ultra-thin cells. Unless some new techniques are developed, it is not likely that higher-order light trapping (e.g., orthogonal grooving, front and back) will be feasible for high production. Any devices produced using such techniques must also be lightweight, cost effective, and radiation stable to find an adequate customer base. Solar cell vendors will incorporate any option that a customer base will support. However, a major effort is not likely to be made to create such a base unless a clearly superior technology, that is also inexpensive, presents itself.

DIFFERENT USES FOR SILICON CELLS

Two uses for silicon cells were discussed that, while not new, were different applications of a conventional technology. As a medium bandgap material, silicon is appropriate as a bottom cell of a favorable pair (e.g., 1.7:1.1 eV) for either one sun or concentrator application. In this latter application, some of the constraints of normal use are relaxed. Without concern about blue response, the junction can be made deeper to perhaps improve red response, V_{oc} , and fill factor. If a two-terminal monolithic tandem cell is being designed, the tunnel junction necessary to connect the two parts eliminates the need for a highly conductive emitter layer in the silicon. The need to conduct current to grids in the silicon cell may vanish and methods for reducing surface recombination velocity are greatly altered. The use of nonreflective (pyramid or, maybe, V-groove) surfaces could, in addition to improving longwave length response, provide a means of

stress relief and thereby increase the number of useful top cell materials. Two terminal, mechanically stacked tandem cells, using Si as the under-cell, are being evaluated.

As a stable, sturdy, heat-conductive, well-characterized material, silicon has much going for it as a bottom cell. However, the very thing that recommends it, good long-wavelength response, makes it radiation sensitive. Fortunately, some of the techniques for increasing normal silicon cell efficiencies (e.g., light trapping, cell thinning, optimized doping, etc.) work here as well and could actually improve radiation hardness. In a concentrator configuration, heat which limits silicon cell performance, has much less effect if silicon is used as a bottom cell rather than alone. The bandgap narrowing, which lowers V_{oc} , also increases IR response. In this application, the reduction in silicon cell V_{oc} is proportionately less (because of the higher combined cell voltage) and the increase in I_{sc} is proportionately higher (because of the division in cell current between the two cells).

A second "different" use for silicon cells is that of a thermal photovoltaic (TPV) converter in conjunction with a selective emitter (SE). SEs have, in addition to the normal black body radiation spectrum, characteristic emission lines in the shorter wavelength region. Some materials, such as Yb_2O_3 , have emission lines below the silicon absorption edge and, therefore, could convert thermal energy into wavelengths that experience a high conversion efficiency in silicon. A SETPV converter in space has advantages in that thermal isolation between source and converter is simpler than within an atmosphere. However, it is not likely to compete with sunlight, if available, since heat sources still add weight.

Of the two different uses of silicon cells discussed in the workshop, the space application as a bottom cell appears to be more immediately appropriate and commercially important. The use of silicon in a SETPV converter would appear to be more limited in its application (e.g., deep space or low earth orbit where array drag is unacceptable). Future research in this latter case would need to be in the source rather than in the converter area.

NEW SILICON CELL DEVELOPMENTS

Four new silicon cell developments were discussed in the workshop. Two were material oriented, for cost reduction, and two were optimized for high efficiency. The two material-oriented developments were the Spheral™ cell and the Si Film™ cell. Both use lower grade silicon as the starting material and production techniques capable of significant economies when scaled up. The Spheral cell has limitations in that the small silicon balls (typically on the order of 25-mils across) are not high-grade single-crystal silicon, despite dramatic improvement in quality by-process steps; are not lightweight; and have low packaging densities relative to normal solar cell arrays. However, they are flexible and radiation resistant (poor starting material) and the technology has not been optimized.

The Si Film cells are not yet highly efficient, but they have more promise in this area than do the Spheral cells. They are expected to be low-cost, thin, poly-silicon sheet on a flexible substrate that is compatible with very large scale production.

The two high-efficiency Si cell developments, from Stanford University and the University of New South Wales (UNSW), have a lot of features in common and are getting even closer together with time. Both utilize high-diffusion-length silicon, very good surface passivations, reduced contact and emitter areas, and carrier trapping. They are both extremely sensitive to radiation damage (ionizing as well as displacement) and degrade much further than conventional silicon cells. While there are techniques available to reduce damage from ionizing radiation, these cells will have their application in nonradiation solar environments and in nonsolar (e.g., TPV, laser, etc.) areas.

Of the four new developments discussed, the Si Film cells seemed to have the greatest potential for general space use (in lightweight deployable arrays) but would be competing with CIS and a-Si sheet arrays for that slot. The terrestrial applications of this technology could greatly reduce costs and, therefore, increase its viability for space.

A fifth new silicon cell development discussed, the buried defect cell, is burdened with a large question mark. The source of the claim for major improvements in a silicon cell is basically unknown and untested in the West; no cells supporting the claim exist; no single investigator has seen the fabrication and test processes through even a major portion of their cycles; the cell on which the claim is based is very small (~2mm on a side); and the technology is unlike

any applied to solar cells heretofore. However, the claims of very high efficiencies and long wavelength response beyond the silicon bandedge, if verified, could revolutionize silicon solar cell technology.

Briefly the process consists of a high-dose proton implant (180 keV , 10^{16} p/cm^2) with grid lines masked, a flash anneal to form voids beneath the surface, a high temperature anneal (carefully controlled to $\sim 1430^\circ\text{C}$) to regrow the single crystal silicon and to passivate the void surfaces; and an extended boron diffusion and drive-in.

In addition to the uncertainty in measurement technique and results, there are inconsistencies in the fabrication process (e.g. implant energies and defect layer depth do not agree). To compound the problem of general application to space, the material costs are greatly increased if large area implant and long-term anneal and diffusion steps are required. Nevertheless, if even half the claims are valid, cost-effective means of achieving them might well be found.

RADIATION TOLERANT HIGH EFFICIENCY CELLS

Typically, as the efficiency of a solar cell is improved, its susceptibility to radiation damage is also increased. Sometimes the changes offer no improvement in end-of-life (EOL) performance so that beginning of life (BOL) improvements mean higher degradation rates. Sometimes the changes actually decrease the EOL performance. Occasionally a cell improvement for one purpose reduces performance in another area, but gives net gains in EOL performance. The high-efficiency silicon cells discussed in the workshop are not likely to be radiation tolerant. The possible exception is a variant of the buried-defect-layer solar cell. The UNSW and Stanford cells could be made less radiation sensitive than they are presently; but they will always drop below the normal cell output at some fluence (between 10^{14} and $5 \times 10^{14} \text{ 1 MeV e-/cm}^2$). The buried defect layer cell may display higher performance despite a lower performance starting material. If this is the case, onset of degradation will be at higher fluences and EOL performance will be higher than that of normal cells, if passivation of the buried surfaces are not critical or if they can be radiation hardened.

CONCLUSIONS

As presently manufactured, space-grade silicon solar cells are unlikely to be changed drastically unless the buried defect layer cell, or derivative ideas, can be verified and implemented in a reasonable manner. The low-cost, low-weight possibilities presented by the Si Film cells may make them a viable option in the future.

MULTI-BAND GAP AND NEW SOLAR CELL OPTIONS WORKSHOP

J. Hutchby and M. Timmons
Research Triangle Institute
Research Triangle Park, NC

J.M. Olson
National Renewable Energy Laboratory
Golden, CO

Question 1. Are greater than 2 terminal (2T) cells really useful?

Number of terminals	Advantages/disadvantages
2T	direct replacements for existing cells
3T	no interest; no perception of useful applications; good for separate cell analysis during development
4T	could be useful; 4T controllers and power conditioning equipment could be developed; even if cells are 4T, module level will likely be 2T; users want 2T. Cost must be in line with advantages.

For most missions, 2T are preferred, but for compelling reason (radiation resistance, efficiency?), 4T cells could be preferred and used.

Questions 2. Will radiation damage prevent development of MBG cells for space?

Probably not.

-Junctions in MBG cells will degrade at different rates. Cells can be designed for BOL or EOL matching. This adds flexibility to MBG designs but requires attention to detail.

-GEO likely to be most populated orbit with increasing use of LEO. Not as radiation intense. High efficiency in "hot" mid orbits make MBG attractive if radiation resistant.

-Ground testing needs to be realistic to convince users that MBG cells are radiation resistance and 1-meV electron equivalent testing is useful; MBG cells **must** reach a level of performance (25%?) to justify radiation testing.

Question 3. Is lattice matching critical for MBG cells?

Yes, for monolithic cells. No, for mechanically stacked cells

Threading dislocations that result from mismatch will degrade cells, i.e., lower BOL. However, may have smaller efficiency deltas at EOL.

Concentrator cells can tolerate some dislocations.

Related questions:

- Are monolithic cells far-term and stacked cells near-term or vice-versa?
- What are the capitalization costs of automation?
- What is the cost differential between monolithic and stacked cells?
- What is the interconnect cost difference? reliability difference?

Tandem technology is still in development stage;

- 2-junction (2-J) monolithic devices probably will not reach 30 percent; 3-J devices may.
- 2-J stacked cells may reach 30 percent

When the payloads increase to the points that arrays must be redesigned, then there exists a cost delta drive for higher efficiency cells. There are current applications where 22-23% efficient radiation hard cells would be attractive.

Question 4. How is true performance measured?

The problem is with the spectral content of simulators, particularly for low-band-gap cells. Calibration requires single junction reference cells for each of the subcells in the stack. Reference cells for buried subcells in the stack must be calibrated with simulated top cells in place.

Cells should be measured at intended operating temperature.

More frequent NASA jet flights and independent measurements are needed.

Question 5. Can greater than 30% be achieved in planar cells? Cost?

Yes. It is theoretically possible, 3-J, AlGaInP/GaAs/Ge, for example.

-High operating temperatures will make 3rd, low band gap cell almost useless.

-2-J devices will probably not exceed 30%, unless concentrated.

Cost?

-Boeing estimated \$70M development costs for GaAs/GaSb concentrator.

-A monolithic MGB may will only be 10-20% more than 1-J analog.

-There will be associated costs related to yields, throughput, etc.

-TBD!

Question 6. What is the future of II-VI materials for MGB devices ?

Viewed as far-term; not much interest. II-VI's may be useful for buffer layers or window layers in the near-term.

Question 7. Quaternaries?

-e.g., AlGaInP, GaInAsP

-If there is a real need for 30% flatplate cells, it will likely require the use of AlGaInP or GaInAsP in 3-J cells.

-The main problem with quaternaries is the necessity to control composition and for AlGaInP, the sensitivity of the electronic quality to oxygen and water contamination.

CLOSING REMARKS:

If we are to fly MBG cells by year 2000, we need to freeze design soon, begin characterization and bring to production.

Cost of this? Hard to say. Maybe \$15-\$20M. Could be answered by man-tech program.

RECEIVERS FOR LASER POWER BEAMING

Summary of the Workshop at SPRAT-XII

Geoffrey A. Landis
Sverdrup Technology
NASA Lewis Research Center 302-1
21000 Brookpark Rd., Cleveland, OH 44135

Abstract

At the Space Photovoltaics Research and Technology [SPRAT] conference at NASA Lewis Research Center, a workshop session was held to discuss issues involved in using photovoltaic arrays ("solar cells") to convert laser power into electrical power for use as receiving elements for beamed power.

Introduction

Photovoltaic cells could potentially be used as power receivers for several laser sources. At NASA Langley, Conway and Walker has investigated use of space-based lasers, both direct solar-pumped [1] and diode lasers [2], for power transmission. Coomes, Bamberger, and co-workers at DOE have proposed a space-based nuclear reactor to power diode lasers which beam power to photovoltaic receivers [3]. Use of diode lasers to transmit power down optical fibers to remote GaAs receivers [4] for use on airplanes wingtips and other fiber-linked remote applications is a technology with many near-term applications. Finally, recent suggestions that adaptive optics technology could be used in conjunction with ground-based lasers to beam power to photovoltaic receivers in space [5,6] has resulted in the NASA SELENE (Space Laser Energy) project [7]. SELENE has concentrated on the use of 100-kW to MW-class free-electron lasers (FELs) for transmission to geosynchronous orbit satellites, electric-propulsion orbital transfer vehicles, and (in the long term) to a photovoltaic array powering a lunar base. The consensus of the workshop was that the technology for space-based lasers would not be available until well past the year 2000, and thus the workshop focussed mainly on PV receivers for ground-based laser transmitters, which were felt to have the possibility of a near-term payoff.

Near-term Applications

The most-discussed applications were to geosynchronous orbit satellites. The remark was made that many organizations have satellites that could possibly benefit from laser power beaming, and that the options should not be restricted only to communications satellites, or even only to U.S. satellites. A difficulty in near-term demonstrations is that only satellites in range of U.S. laser sites such as the White Sands testing range can be considered.

The need to make a near-term demonstration of the feasibility of the system, even if only at a low power level, was emphasized. It was suggested that operation of a single transponder on a communication satellite by laser power through a full eclipse would be a convincing demonstration. A typical satellite has 24 transponders drawing roughly 17 watts, and requires 62 watts of housekeeping power [12]. Thus, operation of a single transponder would require only 9% of full power. At 532 nm (doubled YAG wavelength), 9% of full power would require 14 kW of laser power if a 2.5 meter mirror is used [12], assuming perfect atmospheric compensation. Although many issues need to be resolved, perhaps this could be done with lasers now existing or under development in the laboratory, such as the AVLIS copper-vapor laser or frequency-doubled YAG lasers, with existing beam-directors and adaptive optical systems used for the test.

Finally, during the discussion of radiation damage, another application was suggested, that of using a ground-based laser to heat up solar cells to anneal radiation damage. This could even use laser types which operate at wavelengths that are not good for power conversion but are now available in high power. It would, however, require high-temperature design of the arrays, which is possible, but has not been currently implemented on existing satellites.

Experiments Needed

The next workshop question was, what experiments needed to be done now in order to verify key assumptions about laser receivers? All high-powered lasers available now or in the near future at the wavelength range of interest are pulsed. Investigation of the effect of the pulse format on the cell response is a major concern. The AVLIS copper vapor laser, currently the highest continuous average-power laser in operation at wavelengths below 1 micron, has a pulse format with a pulse width of ~50 nS and a repetition rate up to 26 kHz. The wavelength can be varied somewhat by pumping a dye with the copper-vapor light at 511 and 578 nm. Of the free-electron lasers under consideration, the RF FEL will typically have a pulse width of 10 pS, with a repetition rate on the order of a GHz, while the induction FEL would have a pulse width on the order of 20 nS, with a repetition rate of twenty kHz. A frequency-doubled Nd:YAG laser would require a pulsed output in order to achieve high efficiency on the doubling crystal without thermal distortion, since the efficiency of frequency doubling is directly proportional to the intensity. Various pulse formats would be possible for this laser, as long as the peak-to-average ratio is sufficiently high to reach good doubling efficiency.

If cell operation at 1.06 microns is possible, it may be possible to use a Nd:YAG laser without frequency doubling in CW operation.

Experiments reported at this SPRAT showed the response of cells to pulsed lasers is significantly different than the response to CW laser illumination [8,9], and suggested that this response may be dependent on laser wavelength [10]. Thus, it was suggested that pulsed laser experiments in the wavelength range of 750-850 nm GaAs cells should be done, to learn as much as possible about GaAs cell response at the most efficient operating wavelength of GaAs cells. This could potentially be done using a Ti-sapphire laser or a dye laser.

Experiments done previously showed difficulties with lasers using the induction FEL or copper-vapor pulse formats, and suggested that novel cell and circuit design techniques, such as monolithically integrated cells, wide flat conductors, and integral capacitors, could ameliorate some of the difficulties. Experiments should be done to test some of these possibilities, as well as to gather further data on cell response at these pulse formats.

Few tests so far have been done using the RF laser format, and the tests done to date have not resolved the picosecond micropulse structure of the laser. Since this is an increasingly attractive laser format, further tests on RF lasers should be done.

Operating wavelengths were discussed later in the workshop. It was suggested that if cell operation at longer wavelengths is desirable, cell testing at the desired wavelength should begin immediately.

Cell Types and Operating Wavelength

Silicon cells showed better response than GaAs cells to the induction format pulses, and it was suggested that, in the near term, the pulse format problem should probably be solved by simply going to silicon cells. The feeling was, it works and it's available. Silicon was also desirable since it is already flying, although it was noted that cells now flying are relatively old designs which have been further radiation damaged, and thus will not have significant response to 1.06 micron radiation.

A wavelength of 1.06 micron has been suggested [11] as being considerably better (from the point of view of laser technology and atmospheric transparency and compensation) than the 840 nm chosen for the baseline SELENE system. The atmosphere is known to be extremely transparent at some specific wavelengths near 1.06 microns. It is important to start testing cells at this wavelength. Cell possibilities include both silicon and InGaAs cells. It is noteworthy that, while silicon has low optical absorption at 1.06 microns at room temperature, the absorption constant rapidly increases at elevated temperatures. For Si cells at 1.06 microns, it may be desirable to operate at high temperature.

It was agreed that it would be possible to operate photovoltaic cells that respond in the "eyesafe" wavelength range of 1.5 to 1.7 microns, but that this will result in a very large loss in performance due to the lower efficiency (figure 1), and that these cells would not be able to operate at high laser intensities due to the adverse temperature coefficient. It is important to know just how advantageous operation at this wavelength is. Operation in the eyesafe wavelength range may be required if a relay mirror is used, since an error in the mirror pointing would direct the beam back toward the ground.

On "exotic" cell types, production will be a big problem. For anything except silicon or conventional GaAs cells, the capability for production of large (square meters) arrays is nonexistent. In many cases technologies such as cell to cell interconnections have not been addressed. Cells that have only been produced on a laboratory scale will take considerable time and effort to bring to production readiness and space-qualify.

Conclusions

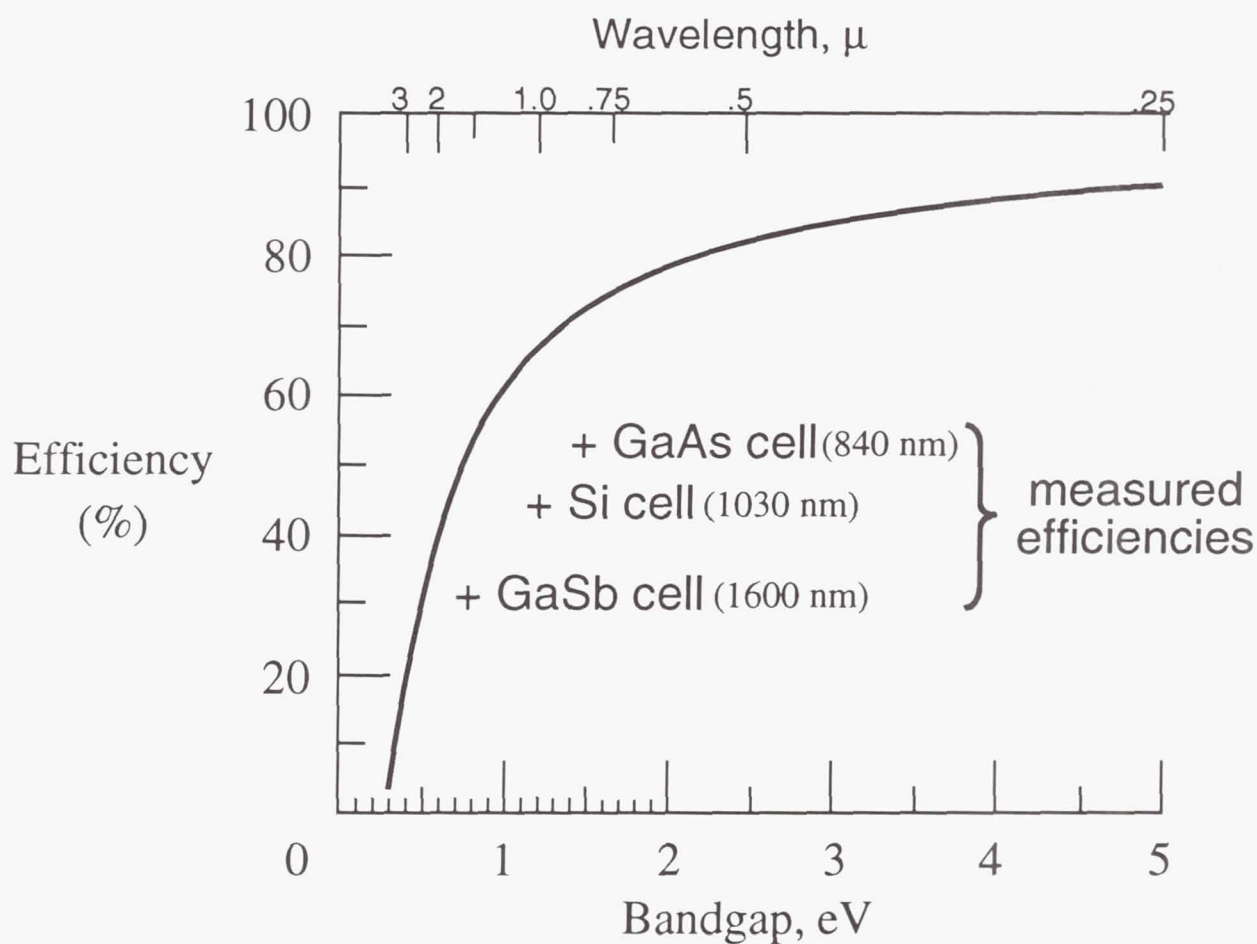
The possibilities for laser power beaming engendered a lively discussion, and it was agreed that there were likely to be many applications that have not yet been thought of. The idea of an early technology demonstration to stimulate interest in the technology, was particularly well received. It was cautioned that, despite the cutting-edge nature of the technology, mundane solar array considerations such as space qualification and manufacturing readiness cannot be ignored.

References

- [1] E.J. Conway, "Solar Pumped Laser Technology Options for Space Power Transmission," paper 869423, *Proc. 21st Intersociety Energy Conversion Engineering Conference*, Vol. 3, 1862-1868, American Chemical Society, 1986.
- [2] G.H. Walker, M.D. Williams, G.L. Schuster and P.A. Iles, "Potential Converter for Laser-Power Beaming Using Diode Lasers," *Space Photovoltaic Research and Technology 1991, NASA Conference Publication 3121*, 25-1 to 25-5 (1991).
- [3] J.A. Bamberger *et al.*, "A Power Beaming Based Infrastructure for Space Power," paper 91-2-116, *Proc. 26th Intersociety Energy Conversion Engineering Conference*, American Nuclear Society, 1991.
- [4] M.B. Spitzer *et al.*, "Monolithic Series-Connected Gallium Arsenide Converter Development, Conf. Record 22nd IEEE Photovoltaic Specialists Conference, Vol. 1, 142-146, IEEE, 1991.
- [5] G.A. Landis, "Space Power By Ground-Based Laser Illumination," *IEEE Aerospace and Electronics Systems Magazine*, Vol. 6, No. 6, Nov. 1991, 3-7; presented at *26th Intersociety Energy Conversion Engineering Conference*, Vol. 1, 1-6, American Nuclear Society, 1991.
- [6] G.A. Landis, "Space Power by Laser Illumination of PV Arrays," *Space Photovoltaic Research and Technology 1991, NASA Conference Publication 3121*, 24-1 to 24-5 (1991).
- [7] E.E. Montgomery, ed., *Proc. of the SELENE Advocacy Briefing and Progress Review*, July 16 1992, Washington D.C., George C. Marshall Space Flight Center, 1992.
- [8] R.L. Lowe, G.A. Landis and P. Jenkins, "The Efficiency of Photovoltaic Cells Exposed to Pulsed Laser Light," *Space Photovoltaic Research and Technology Conference 1992*, NASA Lewis Research Center, Cleveland, OH, October 20-22, 1992.
- [9] D. Willoughby, D. Alexander, T. Edge and K. Herren, "Response of Si Solar Cell to Pulsed Laser Illumination," *Space Photovoltaic Research and Technology Conference 1992*, NASA Lewis Research Center, Cleveland, OH, October 20-22, 1992.
- [10] G.A. Landis and R.K. Jain, "Solar Cell Design for Pulsed Laser Power Receivers," *Space Photovoltaic Research and Technology Conference 1992*, NASA Lewis Research Center, Cleveland, OH, October 20-22, 1992.
- [11] R.R. Parenti and C.A. Primmerman, "Power Beaming System Analysis Update," MIT Lincoln Laboratory Project Memorandum 54PM-PBP-001, 15 May 1992.
- [12] G.A. Landis and L. Westerlund, "Laser Beamed Power: Satellite Demonstration Applications," paper IAF-92-0600, *43rd Congress of the International Astronautics Federation*, Washington DC, Aug. 28-Sept. 5, 1992.

Figure 1: Theoretical and Measured Conversion Efficiency of Photovoltaic Cells for Monochromatic Light

Intensity = 500 mW/cm², temperature = 25 °C



Theoretical curve from Larry Olsen, *Space Photovoltaic Research and Technology* 1991

REPORT DOCUMENTATION PAGE			Form Approved OMB No. 0704-0188	
Public reporting burden for this collection of information is estimated to average 1 hour per response, including the time for reviewing instructions, searching existing data sources, gathering and maintaining the data needed, and completing and reviewing the collection of information. Send comments regarding this burden estimate or any other aspect of this collection of information, including suggestions for reducing this burden, to Washington Headquarters Services, Directorate for Information Operations and Reports, 1215 Jefferson Davis Highway, Suite 1204, Arlington, VA 22202-4302, and to the Office of Management and Budget, Paperwork Reduction Project (0704-0188), Washington, DC 20503.				
1. AGENCY USE ONLY (Leave blank)	2. REPORT DATE May 1993	3. REPORT TYPE AND DATES COVERED Conference Publication		
4. TITLE AND SUBTITLE Proceedings of the XII Space Photovoltaic Research and Technology Conference (SPRAT XII)		5. FUNDING NUMBERS WU 506-41-11		
6. AUTHOR(S)				
7. PERFORMING ORGANIZATION NAME(S) AND ADDRESS(ES) National Aeronautics and Space Administration Lewis Research Center Cleveland, Ohio 44135-3191		8. PERFORMING ORGANIZATION REPORT NUMBER E-7551		
9. SPONSORING/MONITORING AGENCY NAME(S) AND ADDRESS(ES) National Aeronautics and Space Administration Washington, D.C. 20546-0001		10. SPONSORING/MONITORING AGENCY REPORT NUMBER NASA CP-3210		
11. SUPPLEMENTARY NOTES Responsible person, Navid Fatemi, Lewis Research Center, (216) 433-5586.				
12a. DISTRIBUTION/AVAILABILITY STATEMENT Unclassified - Unlimited Subject Category 76, 20		12b. DISTRIBUTION CODE		
13. ABSTRACT (Maximum 200 words) The Twelfth Space Photovoltaic Research and Technology conference was held at the NASA Lewis Research Center from October 20 to 22, 1992. The papers and workshops presented in this volume report substantial progress in a variety of areas in space photovoltaics. Technical and review papers were presented in many areas, including high efficiency GaAs and InP solar cells, GaAs/Ge cells as commercial items, flexible amorphous and thin film solar cells (in the early stages of pilot production), high efficiency multiple bandgap cells, laser power converters, solar cell and array technology, heteroepitaxial cells, betavoltaic energy conversion, and space radiation effects in InP cells. Space flight data on a variety of cells were also presented. Six workshops were held to discuss the following topics: <ul style="list-style-type: none"> • Heteroepitaxial InP Solar Cell Development • Thin Film Solar Cell development • Solar Electric Propulsion • New Silicon Solar Cell Development • Multi-Bandgap and New Solar Cell Options • Photovoltaic Receivers for Laser Power Converters 				
14. SUBJECT TERMS Space power; Photovoltaic cells; Solar cells; Solar arrays		15. NUMBER OF PAGES 352		
		16. PRICE CODE A16		
17. SECURITY CLASSIFICATION OF REPORT Unclassified	18. SECURITY CLASSIFICATION OF THIS PAGE Unclassified	19. SECURITY CLASSIFICATION OF ABSTRACT Unclassified	20. LIMITATION OF ABSTRACT	

National Aeronautics and
Space Administration
Code JTT
Washington, D.C.
20546-0001

Official Business

Penalty for Private Use, \$300

SPECIAL FOURTH-CLASS RATE
POSTAGE & FEES PAID
NASA
PERMIT No. G27



POSTMASTER: If Undeliverable (Section 158
Postal Manual) Do Not Return